Transactions of the ASME, Journal of Heat Transfer (ISSN 0022-1481) is published monthly by The American Society of Mechanical Engineers, Three Park Avenue, New York, NY 10016. Periodicals postage paid at New York, NY and additional mailing offices. POSTMASTER: Send address changes to Transactions of the ASME, Journal of Heat Transfer, c/o THE AMERICAN SOCIETY OF MECHANICAL ENGINEERS, 22 Law Drive, Box 2300, Fairfield, NJ 07007-2300. **CHANGES OF ADDRESS** must be received at Society headquarters seven weeks before they are to be effective. Please send old label and new address.

Journal of Heat Transfer

Published Monthly by ASME

VOLUME 131 • NUMBER 10 • OCTOBER 2009

Special Issue on Recent Advances in Porous Media Transport

GUEST EDITORIAL

RESEARCH PAPERS

(**Contents continued on inside back cover**)

This journal is printed on acid-free paper, which exceeds the ANSI Z39.48-1992 specification for permanence of paper and library materials. ♾™
♻ 85% recycled content, including 10% post-consumer fibers.

Journal of Heat Transfer **Volume 131, Number 10** **OCTOBER 2009**

TECHNICAL BRIEFS

The ASME Journal of Heat Transfer is abstracted and indexed in the following:

Applied Science and Technology Index, Chemical Abstracts, Chemical Engineering and Biotechnology Abstracts (Electronic equivalent of Process and Chemical Engineering), Civil Engineering Abstracts, Compendex (The electronic equivalent of Engineering Index), Corrosion Abstracts, Current Contents, E & P Health, Safety, and Environment, Ei EncompassLit, Engineered Materials Abstracts, Engineering Index, Enviroline (The electronic equivalent of Environment Abstracts), Environment Abstracts, Environmental Engineering Abstracts, Environmental Science and Pollution Management, Fluidex, Fuel and Energy Abstracts, Index to Scientific Reviews, INSPEC, International Building Services Abstracts, Mechanical & Transportation Engineering Abstracts, Mechanical Engineering Abstracts, METADEX (The electronic equivalent of Metals Abstracts and Alloys Index), Petroleum Abstracts, Process and Chemical Engineering, Referativnyi Zhurnal, Science Citation Index, SciSearch (The electronic equivalent of Science Citation Index), Theoretical Chemical Engineering

Journal of Heat Transfer

Guest Editorial

Recent Advances in Porous Media Transport

This special issue of *Journal of Heat Transfer* focuses on the recent advances in Porous Media Transport as related to applications in industry and biology. Transport phenomena through porous media have been the subject of various studies due to the wide range of applicability of these research areas in contemporary technology, for example, biological, electronics cooling, thermal insulation engineering, geothermal and environmental engineering, heat pipes, underground spreading of chemical waste, nuclear waste repository, grain storage and enhanced recovery of petroleum reservoirs. This interest is further driven by practical applications that can be modeled as transport through porous media such as packed bed heat exchangers, drying technology, catalytic reactors, petroleum industries, geothermal systems, tissue engineering, drug delivery, and advanced medical imaging as related to brain stroke.

The Porous Media theory has been involved in cutting-edge basic and applied research in Thermal and Fluid sciences, with a particular emphasis in developing systems that are compact in size and volume. Some examples include electronics and avionics, heat pipes, miniature refrigerators, nanoparticles added to dielectric coolants for enhanced heat transfer in nanofluids, microtextured surfaces for enhanced boiling, base stations in cellular communications, power electronics, automotive electronics, wearable electronics, etc. In the area of natural and forced convection, forced convection in a parallel plate channel occupied by a layered saturated porous medium with laminar pulsating flow is analyzed analytically in this issue. It is found from this study that the fluctuating part of the Nusselt number changes in magnitude and phase as the dimensionless frequency increases. An alternative way of modeling form-drag in a porous medium saturated by a power-law fluid is also discussed in this issue. In the area of phase change flow, a simple semi-theoretical method for calculating two-phase frictional pressure gradient in porous media is presented. The proposed model can be transformed into either a two-phase frictional multiplier for liquid flowing alone or two-phase frictional multiplier for gas flowing alone as a function of the Lockhart–Martinelli parameter. Another investigation includes the use of a nano- and micro-porous surface layer to enhance boiling heat transfer mechanism in a plate heat exchanger. The plate heat exchanger with the enhancement structure appears to have displayed a substantially enhanced heat transfer coefficient in the refrigerant channel. In an associated study, the topology and geometry of microstructures, which play a significant role in determining the heat transfer, performance in passive cooling devices such as heat pipes has been studied. Hexagonally packed spheres on a surface are identified to be the most efficient microstructure geometry for wicking and thin-film evaporation.

Porous media modeling has been applied in many biomedical applications. Examples include macromolecular transport in arterial walls, biofilms, characterization of heat transport through biological media, drug delivery, hyperthermia treatment, tissue replacement production, diffusion-weighted magnetic resonance imaging, biodegradable porous drug delivery devices, porous scaffolds for tissue engineering, polymerase chain reaction nucleic acid amplification applications, computational biology, and advanced medical imaging. The onset of electrothermoconvection in a dielectric porous medium, which is favorable for the design of artificial organs, and the onset of thermo-magnetic convection in a ferrofluid porous medium are covered in this issue. Decrease in magnetic field as well as Darcy number is found to delay the onset of ferrconvection. The application of porous media in a human lung is also addressed here. A porous media approach is proposed to investigate the bifurcating airflow and mass transfer within a lung.

In the geological applications, water coning is a serious problem encountered in active bottom-water drive reservoirs. A depletion strategy is developed in this issue for an active bottom-water drive reservoir to improve oil recovery and to reduce water production due to coning. In a related study, porous medium's geological model is developed to model fluid flow and energy transport in a large-scale porous medium such as oil and geothermal reservoirs. In another study, dual-permeability modeling of capillary diversion and drift shadow effects in unsaturated fractural rock is analyzed numerically. The drift-shadow effects describe capillary diversion of water flow around a drift or cavity in porous or fractured rock resulting in lower water flux directly beneath the cavity.

In this issue we cite Professor Adrian Bejan's accomplishments in the porous media area on the occasion of his 60^{th} birthday. Adrian has worked in the field of designed porous media more recently as a branch of constructal theory and design, which he exudes. He introduced convection in porous media for the first time as a chapter in a course on convective heat transfer (in the book *Convection Heat Transfer*, Wiley, 1984, 1995, 2004). Adrian Bejan's contributions are best summarized by his methods of fundamental research on transport in porous media (e.g., scale analysis, constructal design of porous media, heatlines and masslines, intersection of asymptotes), and his books, *Convection in Porous Media* which is the most cited book in the field, and *Porous and Complex Flow Structures in Modern Technologies*, both published by Springer.

In conclusion, I would like to thank many reviewers that had helped us a lot with their careful and detailed critical reviews of the papers that were considered in this issue. I am thankful for all their helpful comments in improving the quality of the presentations in this issue.

Kambiz Vafai
Department of Mechanical Engineering,
University of California, Riverside

Analysis of the Wicking and Thin-Film Evaporation Characteristics of Microstructures

Ram Ranjan

Jayathi Y. Murthy

Suresh V. Garimella[1]
e-mail: sureshg@purdue.edu

School of Mechanical Engineering and
Birck Nanotechnology Center,
Purdue University,
West Lafayette, IN 47907-2088

The topology and geometry of microstructures play a crucial role in determining their heat transfer performance in passive cooling devices such as heat pipes. It is therefore important to characterize microstructures based on their wicking performance, the thermal conduction resistance of the liquid filling the microstructure, and the thin-film characteristics of the liquid meniscus. In the present study, the free-surface shapes of the static liquid meniscus in common microstructures are modeled using SURFACE EVOLVER *for zero Bond number. Four well-defined topologies, viz., surfaces with parallel rectangular ribs, horizontal parallel cylinders, vertically aligned cylinders, and spheres (the latter two in both square and hexagonal packing arrangements), are considered. Nondimensional capillary pressure, average distance of the liquid free-surface from solid walls (a measure of the conduction resistance of the liquid), total exposed area, and thin-film area are computed. These performance parameters are presented as functions of the nondimensional geometrical parameters characterizing the microstructures, the volume of the liquid filling the structure, and the contact angle between the liquid and solid. Based on these performance parameters, hexagonally-packed spheres on a surface are identified to be the most efficient microstructure geometry for wicking and thin-film evaporation. The solid-liquid contact angle and the nondimensional liquid volume that yield the best performance are also identified. The optimum liquid level in the wick pore that yields the highest capillary pressure and heat transfer is obtained by analyzing the variation in capillary pressure and heat transfer with liquid level and using an effective thermal resistance model for the wick.* [DOI: 10.1115/1.3160538]

1 Introduction

Heat pipes have proven to be one of the most efficient passive cooling devices for electronics cooling and other applications. Heat pipes use porous media for wicking fluid from the condenser to the evaporator section. Wicking is caused by capillary forces acting at the solid-liquid-vapor contact line in the fluid-filled interstices in a porous medium. Wicking action, combined with evaporation in the evaporator section, causes fluid to move from the condenser to the evaporator; the amount of fluid flow that results depends on the permeability of the wicking medium. Furthermore, the effective thermal conductivity of the porous medium determines the effectiveness with which the heat is transferred to the evaporating fluid. With the increasing power density of critical electronic components, there is a need to optimize heat pipe microstructures to maximize the heat transfer rate and to minimize thermal resistance.

Avoiding dryout and overheating in heat pipes is a critical consideration and has been the focus of much research over the past few years. Many studies have proposed methods to develop permeability measurement techniques, to characterize wick porosity, and to quantify the overall performance of heat pipes. Most have focused on determining dryout heat fluxes and the limits of operation for a given wicking mechanism. Iverson et al. [1] quantified wick performance, including evaporation rates, for sintered-copper powder wicks under conditions of operation in heat pipes. They compared the performance of four different sintered wicks of varying porosity. The evaporative thermal resistance across thin layers of sintered-copper wicks of varying porosity was experimentally measured under saturated conditions by Davis and Garimella [2]. Numerical models for the effective thermal conductivity for various types of wicks have also been developed [3,4]. Garimella and Sobhan [5] reviewed the state of the art in the understanding and analysis of a large variety of heat pipes, and also identified the respective limitations. Maximum heat transfer rates for wrapped wire screen, square axial grooves, and sintered metal powder wicks were reported by Gupta and Upadhya [6]. They found sintered metal powder wicks to be the most effective for heat transfer. Abhat and Seban [7] performed experiments to study boiling and evaporation from heat pipe wicks with water and acetone. They postulated that the evaporative performance of a wick can be limited as much by a failure of capillary suction as due to fluid friction in the wick.

Thin-film evaporation, which takes place near a solid-liquid-vapor junction, is believed to be the dominant mode of heat transfer in such systems. Thin-film evaporation has been reported to affect the overall heat transfer capability in sintered porous media [8]. A theoretical model for thin-film evaporation was developed by Wang et al. [9,10]. The model predicts that more than 50% of the total heat transfer from the evaporating meniscus occurs in the microregion of the meniscus.

Numerical and theoretical models have also been developed for the operation of heat pipes [11] and to delineate the role of thin-film evaporation in such systems [8]. Kim et al. [12] proposed a one-dimensional mathematical model for a miniature heat pipe with a grooved wick structure to predict its thermal performance characteristics. Do et al. [13] presented a mathematical model to analyze the thermal characteristics of a flat microheat pipe with a grooved wick. Axial variations in wall temperature and the evaporation and condensation rates were also included in the model. Mwaba et al. [14] studied the influence of wick characteristics on heat pipe performance using numerical methods. They considered screen-mesh and sintered-copper wicks as the porous medium in heat pipes and pointed out that a heat pipe with a composite wick structure gives the best performance. Hanlon and Ma [8] presented a two-dimensional model to predict the overall heat trans-

[1]Corresponding author.

Manuscript received September 5, 2008; final manuscript received February 19, 2009; published online July 28, 2009. Review conducted by Kambiz Vafai.

fer capability of a sintered wick structure. They concluded that thin-film evaporation from the top surface of the sintered wick plays a major role in enhancing heat transfer. Failure to establish an adequate thin-film evaporation condition on the top surface of the wicks was shown to result in a significant decrease in the rate of evaporation.

Evaporation from liquid menisci in complex geometries has also been studied [15,16]. Morris [17] developed a theoretical model to predict apparent contact angles for evaporating liquids. Another study by Morris [18] provided a relationship between heat flow, apparent contact angle, interface curvature, superheat, and material properties for a perfectly wetting system; a conduction model with a fixed liquid-vapor interface was considered for estimating heat flow across the interface for small capillary number flows with thermocapillary and bulk flow effects being ignored. Transport from a volatile meniscus inside an open microtube was modeled by Wang et al. [19]. This work delineated the structure of fluid flow near an evaporating meniscus, including Marangoni and buoyancy-driven instabilities. Recently, Dhavaleswarapu et al. [20] visualized flow patterns near an evaporating meniscus using μPIV techniques and compared the influence of buoyancy and thermocapillarity on the overall flow structure. These studies have led to a better understanding of an evaporating liquid meniscus and are useful in providing guidelines for the design of efficient microstructures for passive cooling devices.

We seek to develop the basis for reverse-engineering the porous-medium microstructure to yield the optimum combination of capillary pressure, permeability, and thermal conductivity. In this paper, we address the issue of which microstructure geometries yield the maximum wicking action, as well as optimal thin-film heat transfer characteristics. We use SURFACE EVOLVER [21] for computing the static liquid meniscus shapes in different microstructures. This program has been used in the literature [22,23] to compute liquid capillary surfaces in packed beds of uniform spheres. Although the present work addresses only static free-surface shapes, the results are likely to yield important insights into optimal wick structures under dynamic conditions. In steady operation, liquid is fed to the evaporator section of the heat pipe from the adiabatic section with a constant mass flow rate, and constant time-independent free-surface shape results. The free-surface shape determines the capillary pressure generated, as well as important heat transfer parameters, such as the extent of the thin-film region, the total exposed area for evaporation heat transfer, and the conduction resistance of the liquid. These performance parameters are computed as functions of the microstructure geometry, the solid-liquid contact angle, and the liquid volume. A comparative study of four different well-defined microstructured surfaces is performed. The microstructure with the best performance for the evaporator section is determined from these computations. An effective thermal resistance model for the evaporator section is used to study the variation in the wick thermal resistance with changing liquid level in the pores. Based on this model, the optimum liquid level in the wick pore, which provides the greatest wicking action, as well as low thermal resistance, is identified.

2 Microstructure Topologies

Some of the common microstructured wicks used in cooling devices are made of wire meshes, sintered powders, grooves, and felts/fibers. These microstructures are generally multilayered. In this paper, the free-surface shape of the liquid filling these microstructures is assumed to be little-affected by the number of layers, and only one layer of the microstructure is considered for the four geometries studied. The porosity, defined as the ratio of void volume to the total volume, is taken to be same in all four cases. The unit cells for the four surfaces are shown in Fig. 1 and are described below.

Topology 1. Uniform spheres on a surface in both hexagonal packing (HP) (Figs. 1(*a*) and 1(*b*)) and square packing (SP) arrangements (Figs. 1(*c*) and 1(*d*)).

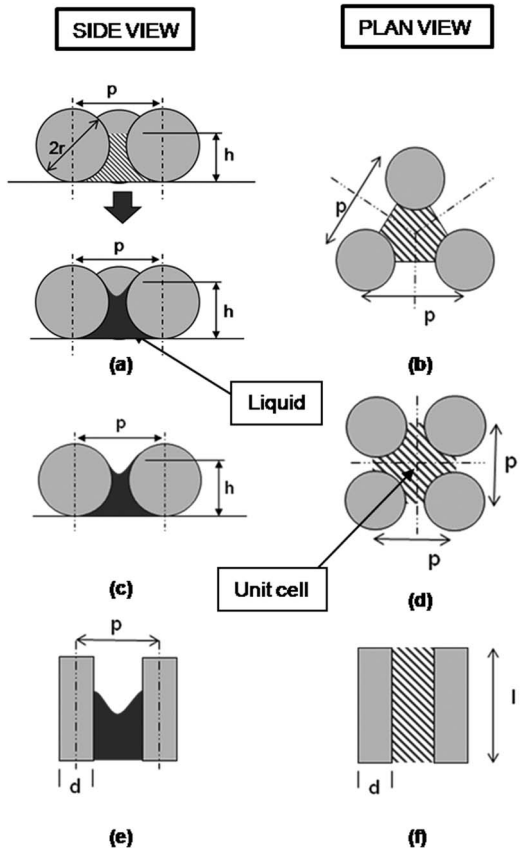

Fig. 1 Side views of surface with (*a*) spheres (hexagonally packed), (*c*) spheres (square packed) and horizontal cylinders, (*e*) vertical cylinders, and parallel rectangular ribs. Plan views of surface with (*b*) spheres and cylinders (both hexagonally packed), (*d*) spheres and cylinders (both square packed), and (*f*) horizontal cylinders and rectangular ribs. The corresponding unit cell is also shown in each case.

Topology 2. Surface with vertical cylinders in both hexagonal (Fig. 1(*b*)) and square packing arrangements (Figs. 1(*e*) and 1(*d*)).

Topology 3. Surface with parallel horizontal cylinders (Figs. 1(*c*) and 1(*f*)).

Topology 4. Surface with parallel horizontal rectangular ribs (Figs. 1(*e*) and 1(*f*)).

In Fig. 1(*a*), h is the initial height of the filling liquid measured from the substrate, and r is the radius of the cylinder or sphere. In Fig. 1(*f*), the length, l, of the cylinders and ribs is not significant, as the meniscus shape is independent of l. We choose l such that the base area of the unit cell in these cases matches the base area in Topology 1 (*SP*). The pitch, p, is defined as the distance between centers of adjacent spheres/cylinders/ribs. In the square-packed spheres case, we assume that the pitch is the same in both the longitudinal and transverse directions and that $p=2.4r$. This leads to a porosity of 0.64. The same porosity is maintained for all other topologies. Geometrical parameters for all topologies are shown in Table 1.

3 Problem Formulation

3.1 Wicking. The capillary pressure developed in a wick is governed by the Young–Laplace equation

Table 1 Geometrical parameters chosen for different topologies with a porosity=0.64. The base area is the area of the flat surface containing the unit cell.

Topology	L	$P(p/L)$	(base area)$/L^2$
1. Spheres a. HP	r	2.56	2.83
b. SP		2.4	5.75
2. Vertical cylinders a. HP	r	3.16	4.32
b. SP		2.94	8.64
3.Horizontal cylinders	r	4.32	5.75
4. Rectangular ribs	d	2.75	5.75

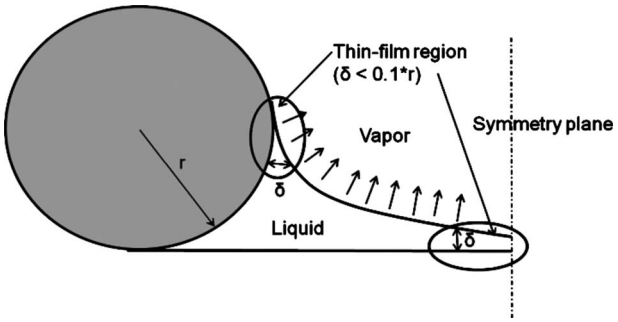

Fig. 2 Schematic illustration and definition of the thin-film region of a liquid meniscus formed over a sphere

$$\Delta p = \gamma_{LV}\left(\frac{1}{r_1} + \frac{1}{r_2}\right) = 2H'\gamma_{LV} \tag{1}$$

where Δp is the capillary pressure defined as $(p_{\text{liq}} - p_{\text{vap}})$, γ_{LV} is the surface tension between liquid and vapor phases, r_1 and r_2 are any two orthogonal radii of curvature at a point on the meniscus, and H' is the mean curvature at any point.

For a static liquid free surface in equilibrium with the vapor phase, in the absence of external forces (e.g., gravity), the mean curvature at any point of the free surface is constant. The mean curvature is defined by the liquid free-surface shape, which depends on the solid-liquid contact angle, the geometry of the microstructure, and the volume of liquid filling the microstructure. The capillary pressure Δp is nondimensionalized as $\Delta P = \Delta p L/\gamma_{LV}$. Other dimensionless parameters are

$$V = \frac{v}{L^3}, \quad \text{Bo} = \frac{\rho g L^2}{\gamma_{LV}}, \quad Z = \frac{z}{L}, \quad P = \frac{p}{L}, \quad H = \frac{h}{L} \tag{2}$$

in which V is the nondimensional volume of the liquid filling the unit cell of the microstructure, as shown in Fig. 1. The Bond number, Bo, is the ratio of gravitational to surface tension forces, while the nondimensional height at any point on the meniscus in its equilibrium position is denoted by Z, and H is the nondimensional height of the liquid meniscus measured from the substrate when the meniscus is horizontal (i.e., in the nonequilibrium initial condition). The characteristic length L is taken to be the radius r of the spheres/cylinders for Topologies 1, 2, and 3, and as the width of the ribs d for Topology 4. The contact angle, θ, along with the parameters described in Eq. (2), determines the shape of the equilibrium liquid meniscus. Furthermore, the nondimensional capillary pressure ΔP is given by

$$\Delta P = 2H'L = L\frac{\Delta p}{\gamma_{LV}} + \text{Bo}\ Z \tag{3}$$

Thus, ΔP can be computed at any point of the meniscus for a given θ and V if Bo and Z are known.

3.2 Heat Transfer Characteristics. The most important parameters, which affect evaporation heat transfer in a wicking microstructure, are the conduction resistance offered by the filling liquid, the total exposed free-surface area for evaporation, and the extent of the liquid meniscus that is in the thin-film region. These parameters are computed from the free-surface shape of the liquid meniscus, as described in Secs. 3.2.1–3.2.3.

3.2.1 Conduction Resistance of Liquid. Heat is transferred from the solid walls (the substrate wall, as well as the microstructure surface) to the surroundings through the shortest path from the walls to the liquid free surface. This distance is indicative of the conduction resistance of the liquid. We compute the area-averaged minimum distance of the liquid free-surface from the solid walls. For each point on the meniscus, the shortest distance from the solid walls is computed and averaged over the liquid free-surface area. This quantity signifies the conduction resistance of the liquid and is computed as a function of V and θ. It is nondimensionalized by the characteristic length L of the microstructure.

3.2.2 Total Exposed Free-Surface Area. The total free-surface area of the liquid meniscus is the exposed area through which evaporation occurs and hence it is a crucial parameter for heat transfer. We compute the total free-surface area of the liquid meniscus as a function of V and θ and nondimensionalize it by the base area of the unit cell of a microstructure.

3.2.3 Thin-Film Percentage Area. The thin-film region of a liquid meniscus has been defined variously in different studies in the literature, with the width of the film ranging from 30 nm to 20 μm [24,9,15]. In the present work, we define the thin-film region based on a nondimensional thickness of $\delta = 0.1 * L$ (see Fig. 2). We note that the exact definition of the thin-film region is in itself not significant, since the aim of the present work is to conduct a comparative study of different microstructures. However, a range of nondimensional thin-film thickness values (defined as $0.05 * L$, $0.1 * L$, and $0.15 * L$) are also considered in order to demonstrate the effect of this definition on the conclusions drawn here. The most common wick microstructures used in cooling devices have a characteristic length of the order of 100 μm [1]. According to our definition, therefore, the thickness of the thin-film region is on the order of 10 μm; such a region has been identified as a microregion in other studies [9]. A schematic representation of an evaporating meniscus is shown in Fig. 2. We compute the thin-film percentage area, which is defined as the percentage of the total exposed area that satisfies our thin-film definition.

The porosity is fixed at 0.64 for all the microstructures considered here. A unit cell, which defines the microstructure, is used in SURFACE EVOLVER and is explained in Sec. 4. Unit cells for different geometries are shown in Fig. 1. Only wetting liquids are considered, with wetting angles ranging from 15 deg to 90 deg. Nonwetting liquids produce unfavorable capillary pressure for evaporation and do not give rise to thin-film regions, which makes them unsuitable for evaporative heat transfer applications. The bottom wall is assumed to be perfectly wetting in all cases. Also, gravity is taken to be zero in all computations. For microstructure length scales of the order 100 μm [1], a Bond number (Bo) of the order of 10^{-3} results for a copper-water combination. This indicates that capillary forces are far greater than gravitational forces in these geometries, and that the Bond number may be assumed to be zero at such scales.

4 Numerical Approach

In the present work, we model the liquid meniscus using the program SURFACE EVOLVER [21]. SURFACE EVOLVER works on the principle of surface-energy minimization. It calculates surface energy and volume as functions of the liquid meniscus and solid configurations and evolves the free surface toward the minimum energy configuration by a gradient-descent method. SURFACE

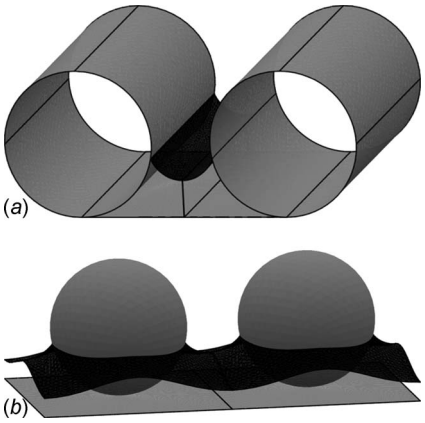

Fig. 3 Final liquid meniscus shape (dark gray) in (*a*) Topology 3, $r=1$, $V=3.54$($H=0.6$), $P=2.8$, and $\theta=30$ deg, and (*b*) Topology 1 (SP), $r=1$, $V=3.6$ ($H=0.5$), $P=2.8$, and $\theta=45$ deg

EVOLVER is a powerful and computationally efficient tool for investigating liquid free surfaces in static equilibrium in complicated capillary structures. However, it should be noted that SURFACE EVOLVER cannot be used to simulate dynamic problems, that is, problems in which fluid flow occurs.

In the program, a surface is implemented as a simplical complex, i.e., a union of triangles. The energy can be due to surface tension and/or gravity or in the form of any other user-defined surface integral. SURFACE EVOLVER admits arbitrary topologies and geometrical constraints on vertex positions, as well as constraints on integral quantities, such as volume. We use the volume and level-set constraints in our modeling. The unit cell of the microstructure geometry, along with a prescribed liquid volume, is specified as the initial geometry for SURFACE EVOLVER. The free-surface shape is iterated upon, tuning the surface mesh using procedures, such as equi-angulation, vertex averaging, and mesh refinement, to obtain the final equilibrium free surface. During every iteration, SURFACE EVOLVER adjusts the vertex positions to minimize the faceted meniscus area. An equilibrium free surface is considered obtained when the surface area of the meniscus changes by less than 0.01% over 10 iterations. Figures 3(*a*) and 3(*b*) show the final surface shapes for parallel horizontal cylinders and square-packed spheres, respectively.

5 Results and Discussion

The liquid meniscus shapes for four microstructured surface topologies have been modeled using SURFACE EVOLVER. In the calculations, V is varied for the unit cell such that H varies from 0.2 to 1.8 for Topologies 1 and 3. For Topologies 2 and 4, capillary pressure and heat transfer parameters are not a strong function of V (except for very low values of V), so V is varied until volume independence of output parameters is achieved. The contact angle θ is varied from 15 deg to 90 deg. Efficient wicking surfaces with the highest thin-film percentage area are determined for a fixed porosity (0.64). We then present the behavior of these performance parameters with varying V and θ in the most efficient microstructures. Porosity is also varied for the most efficient geometry in order to understand its effect on wicking and heat transfer characteristics. A special case of low liquid volumes, which leads to a dryout condition on a part of the flat surface, is discussed. The effect of the number of layers and liquid level on wicking and heat transfer characteristics are analyzed and discussed for the case of hexagonally-packed spheres.

5.1 Free-Surface Shapes. In general, the liquid meniscus shape in any microstructure is a function of liquid volume, solid-liquid contact angle, and the surface tension between the liquid and vapor phases; the specific shape is achieved by minimizing the surface-energy subject to these constraints.

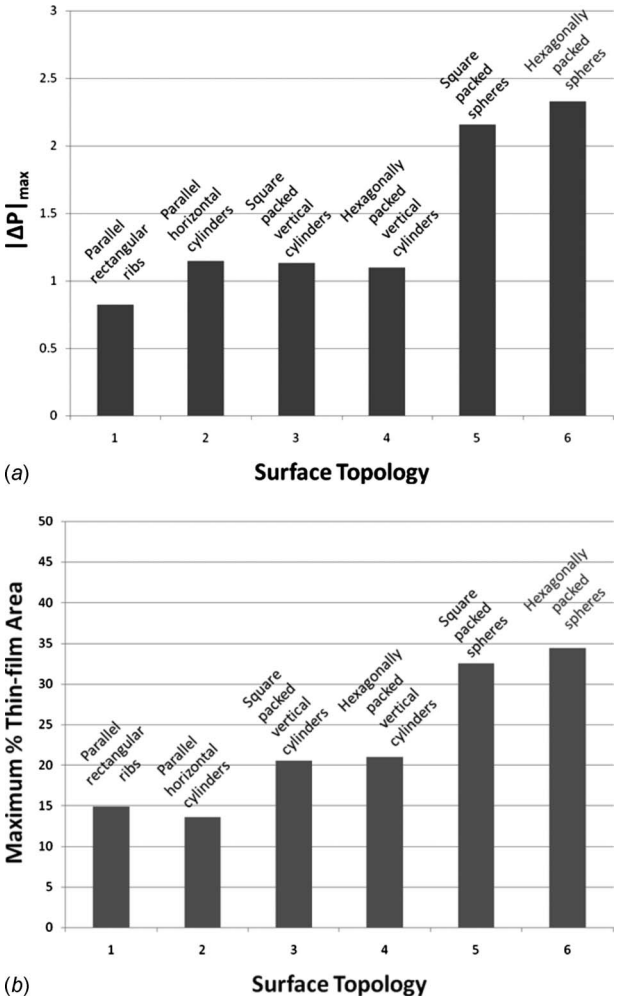

Fig. 4 (*a*) $|\Delta P|_{max}$ and (*b*) maximum percentage thin-film area achieved in different topologies at any liquid volume for porosity=0.64 and $\theta=15$ deg

In Fig. 3, we show the final liquid meniscus shapes in two topologies (3 and 1). The meniscus shape is a strong function of liquid volume in these cases. In contrast, V does not affect the meniscus shape in Topologies 2 and 4 except when V is very low (corresponding to $H<0.2$), and a dryout condition occurs on the substrate wall due to wicking action. Pore shapes in Topologies 3 and 4 are uniform in the plane parallel to substrate. Analytical expressions exist for the meniscus shapes in these topologies [22], and the meniscus is cylindrical in these cases. Pore shapes in Topologies 1 and 3 are more complex. In the case of close-packed (planar) spheres, the pore between spheres has a complex nonaxisymmetric convergent-divergent geometry, while the pore shape is nonaxisymmetric in the case of vertical cylinders. This leads to the formation of menisci that deviate significantly from spherical/cylindrical shapes. In these cases, the meniscus is puckered, exhibiting anticlastic curvature in the narrower spaces between two adjacent spheres/cylinders, while the surface is synclastic (i.e., orthogonal radii have the same sign at a point) in the central pore region. Analytical expressions for the meniscus shapes are not available in these cases and a numerical approach must be used.

5.2 Maximum Capillary Pressure and Maximum Thin-Film Percentage Area. The maximum capillary pressure ($|\Delta P|$) in all topologies is observed to be lowest for the lowest value of θ(=15 deg). Figure 4(*a*) shows the maximum $|\Delta P|$ attained in all

topologies for any liquid volume. Though ΔP is a function of liquid volume V for Topologies 1 and 3, our concern is to achieve the maximum $|\Delta P|$ irrespective of the liquid volume. From the histogram, it can be seen that the highest $|\Delta P|$ is achieved in the case of hexagonally-packed spheres on a surface. The trigonal pores formed in the case of hexagonally-packed spheres provide the smallest pore size among all microstructures for the same porosity and, hence, generate the highest capillary pressure. A similar, though somewhat lower, $|\Delta P|$ is achieved with the square-packed spheres. The highest $|\Delta P|$ achieved is nearly half of the maximum value for the rest of the microstructures considered. Thus, a surface with close-packed (planar) spheres appears to be the best wicking microstructure among all the ones considered here. Similar to the capillary pressure, the percentage thin-film area in any topology is found to be maximum for the smallest contact angle ($\theta=15$ deg). Again, the histogram in Fig. 4(*b*) shows the maximum attainable percentage thin-film area in different topologies irrespective of the liquid volume. The maximum thin-film area is again achieved by close-packed (planar) spheres (Topology 1). Use of a lower value of the nondimensional thin-film thickness ($\delta=0.05*L$) to define the thin-film region was found to result in a decreased thin-film percentage area for all microstructures; conversely, use of a higher value of $0.15*L$ for thin-film thickness resulted in an increased thin-film percentage area as expected. However, the definition adopted for nondimensional thin-film thickness is not found to affect the conclusions drawn from this comparative study of microstructures. The maximum thin-film percentage area is always observed to occur for hexagonally close-packed spheres on a surface. The maximum thin-film percentage area for the three cases is 19.02% ($0.05*L$), 34.39% ($0.1*L$), and 48.01% ($0.15*L$).

5.3 Performance Parameters for Packed Spheres on a Surface (HP and SP Configurations). As shown in Fig. 4, packed spheres on a surface are the best class of microstructures from wicking and thin-film evaporation points of view. We find that the values of conduction resistance of the filling liquid and the total exposed surface area are less sensitive to the choice of microstructure. Therefore, the best performing microstructure is decided on the basis of the maximum capillary pressure and maximum thin-film area condition. We now present in detail the behavior of wicking and heat transfer parameters with respect to θ and V for the packed-sphere topology for a porosity of 0.64. This will lead to a determination of V for the best wicking and heat transfer performance.

5.3.1 Capillary Pressure. Figure 5 shows the variation in ΔP with V for square- and hexagonally-packed spheres. Each curve represents a different contact angle θ. A negative value of ΔP implies suction, and is desirable for wicking. For each curve and for each type of packing, we observe that the nondimensional capillary pressure reaches its minimum value at a certain liquid volume. ΔP first decreases with increasing liquid volume (or increasing H) and reaches a minimum near V corresponding to $H=1$. For a contact angle of 15 deg, ΔP decreases from point (a) to (b) (see Fig. 5), as the liquid meniscus develops increasing net positive curvature. ΔP is minimum at point (b), which lies between a liquid height H of 0.8 and 1. As V increases from 0 to 1.5, the pore size between spheres continues to decrease and hence the absolute capillary pressure increases. In the larger pore spaces between spheres, the meniscus develops synclastic curvature (i.e., the curvatures in orthogonal directions at a point have the same sign) while being saddle-shaped or anticlastic in the narrower spaces between spheres. The net curvature reaches a maximum at point (b). With increasing volume ($H>1, V>1.5$), ΔP starts to increase as the pore size continues to increase and hence the meniscus curvature decreases. ΔP reaches its maximum at point (c) where the meniscus curvature is lowest. It is interesting to note that positive capillary pressure can be achieved with high wetting

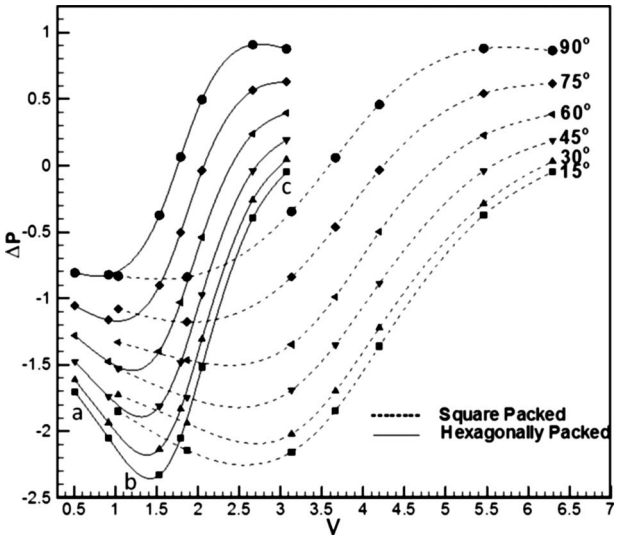

Fig. 5 Capillary pressure versus nondimensional liquid volume for square and hexagonally-packed spheres for various contact angles (15–90 deg)

contact angles (>30 deg) when V is high (corresponding to $H>1.2$, in general). A maximum $|\Delta P|$ is attained in the hexagonally-packed case for $\theta=15$ deg near $V=1.5$ (corresponding to $H\sim1$), and this is the desired operating condition for maximum wicking. Dryout on the flat surface is observed for the lowest contact angle (15 deg) in the square packing arrangement. Dryout conditions due to wicking will be discussed further in Sec. 5.5.

5.3.2 Thin-Film Percentage Area. The percentage of the total exposed area defined as a thin film is presented in Figs. 6(*a*) and 6(*b*) as a function of V and θ in the HP and SP arrangements, respectively. A higher thin-film area is obtained for smaller contact angles. Also, the percentage thin-film area is the highest for the smallest liquid volumes. This is because for low liquid volumes, the liquid meniscus shape is similar to the one shown in Fig. 2, and the thin-film condition is satisfied both at the sphere and the unit-cell substrate surface. However, in the hexagonally-packed case, the thin-film condition is not satisfied at the substrate surface for higher contact angles (>60 deg) and lower values of $V(<1)$. As we increase V, the bottom wall stops contributing to the thin-film area and the percentage thin-film area decreases. However, it again reaches a maximum at a certain V. It is clear that if the substrate wall is not taken into consideration for the meniscus distance computations, we would obtain a perfectly symmetric curve with a maximum in the middle. Again, we observe that the maximum percentage thin-film area is achieved in the hexagonally-packed case near $V=1.5$. Hence, we conclude that $V=1.5$ and $\theta=15$ deg in the hexagonally-packed case provides the maximum wicking, as well as the maximum thin-film area.

5.3.3 Area-Averaged Minimum Meniscus Distance. As discussed before, the area-averaged minimum meniscus distance from the solid surface is a measure of the heat conduction resistance of the liquid filling the microstructure. Figure 7 shows the variation in this quantity with V for square- and hexagonally-packed spheres on a surface. Each curve represents a different contact angle θ. It can be observed from the curves that the distance is smaller for lower contact angles and lower liquid volumes. This is again because of the substrate-wall effect for lower liquid volumes. The wall effect can be observed for $H<0.5$ in both packing arrangements. The resistance increases as we further increase V and reaches a maximum. Once the substrate wall no

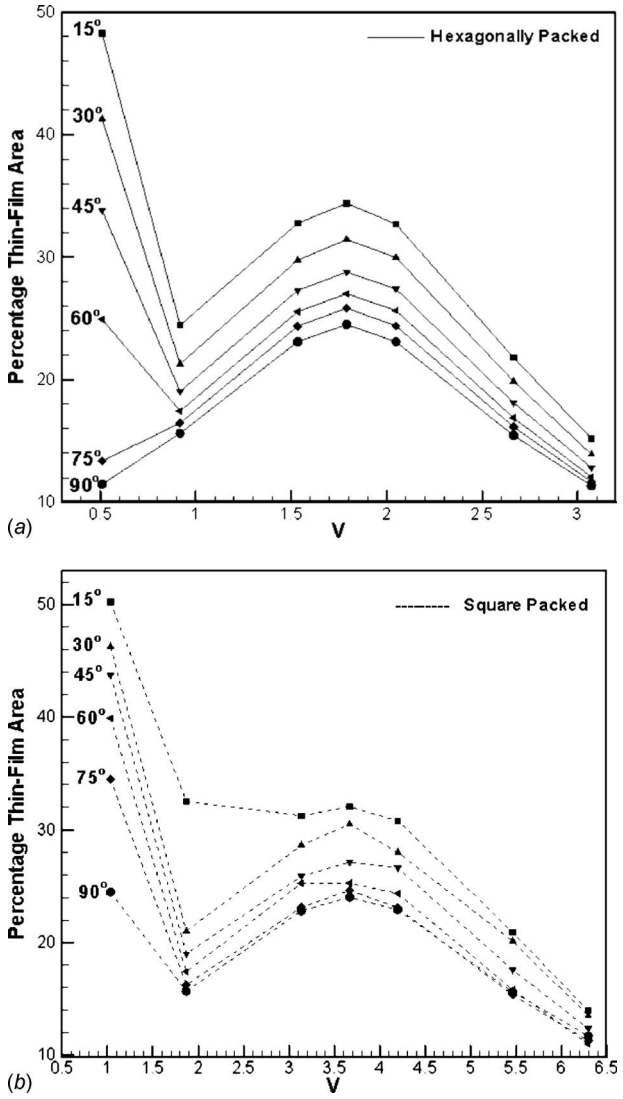

Fig. 6 Percentage thin-film area versus nondimensional liquid volume for (*a*) hexagonally packed and (*b*) square-packed spheres for various contact angles (15–90 deg)

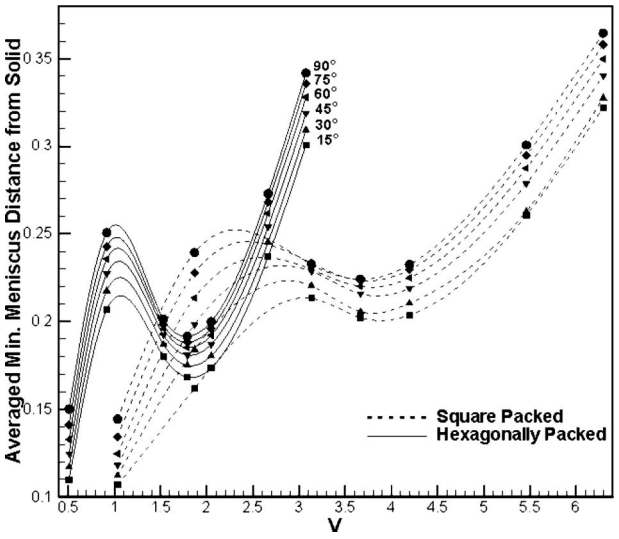

Fig. 7 Non-dimensional area-averaged minimum meniscus distance versus nondimensional liquid volume for square- and hexagonally-packed spheres for various contact angles (15–90 deg)

longer has the shortest path to the liquid free surface, the resistance value is characterized only by the distance between the meniscus and the sphere surface. This distance starts decreasing with increase in V and attains a second minimum at a liquid volume corresponding to $H \sim 1$. It can be observed that the hexagonally-packed case gives a very low conduction resistance near $V=1.5$, which was also found to be the volume for which the highest capillary pressure and high thin-film area were obtained.

5.3.4 Exposed Surface Area. The total liquid free-surface area exposed to evaporation, nondimensionalized by the base area of the unit cell, is presented in Fig. 8 as a function of V and θ in the SP and HP arrangements. The total free-surface area increases with decreasing θ and for each θ, it decreases as we increase V, with a minimum achieved at $H \sim 1$. This is because initially the effective pore radius decreases as we increase H from 0 to 1. However, the pore radius increases as we increase H from 1 to 2. It can be observed that the minimum occurs near $V=1.5$ for the hexagonally-packed case. From the variation in capillary pressure, percentage thin-film area, and conduction resistance of the filling liquid (Figs. 5–7) for hexagonally-packed spheres on a surface, the optimum operation point for maximum evaporation appears to occur at $\theta=15$ deg near $V=1.5$. However, from Fig. 8, we observe that the exposed area for evaporation is lowest near $V=1.5$. Hence, a trade-off exists, and the optimum value of V can be obtained by minimizing a formal cost function formulated by assigning appropriate weights to the various performance parameters.

5.4 Effect of Porosity. We now address wicking and heat transfer characteristics for hexagonally-packed spheres as a function of microstructure porosity. Iverson et al. [1] used wick samples with porosities ranging from 0.46 to 0.6. We vary porosity from 0.39 (corresponding to the case of close hexagonally-packed spheres) to 0.64, with $\theta=15$ deg held constant for all cases. Figures 9(*a*) and 9(*b*) show, respectively, the maximum $|\Delta P|$ and the maximum percentage thin-film area achieved at any porosity, irrespective of the liquid volume. It is observed that, as would be expected, a lower porosity leads to a higher capillary

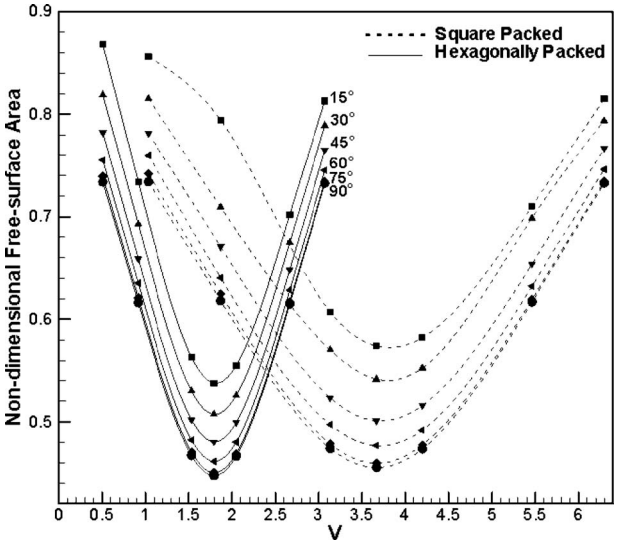

Fig. 8 Total exposed liquid free-surface area versus nondimensional liquid volume for square- and hexagonally-packed spheres for various contact angles (15–90 deg)

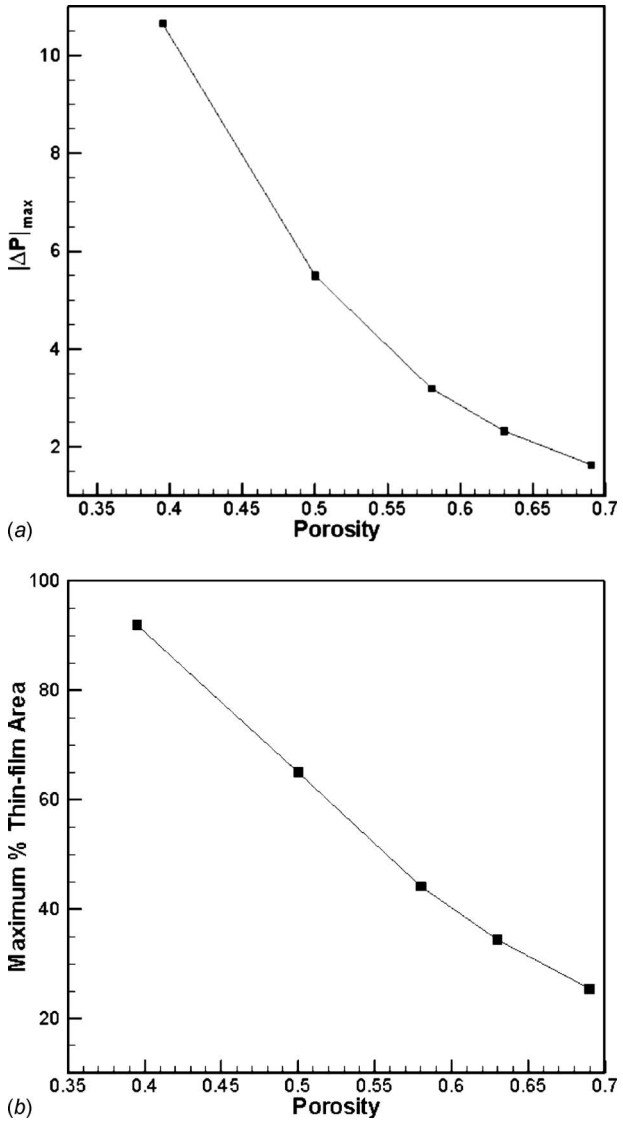

Fig. 9 (*a*) Maximum $|\Delta P|$ and (*b*) maximum percentage thin-film area versus porosity in hexagonally-packed spheres on a surface, $\theta=15$ deg

pressure and a higher thin-film percentage area. Hence, the closest packed case is the ideal case for wicking and also provides the largest thin-film area.

5.5 Special Case of Low Liquid Volumes. When the volume of the liquid filling the microstructure is very low (corresponding to $H<0.2$) and the contact angle is small (≤ 15 deg), a part of the bottom wall may dry out due to wicking. We show two such cases in Figs. 10(*a*) and 10(*b*). It is observed that the liquid is wicked up on to the cylinder/sphere surface, and a part of the bottom wall is depleted of liquid, depending on the contact angle between the liquid and bottom wall surface. Figure 10(*a*) shows a case with a contact angle of $\theta=15$ deg between the solid surfaces and the liquid. Under this condition, the liquid free surface breaks up at the symmetry plane between adjacent cylinders and moves toward the cylinder surface. Figure 10(*b*) shows the case of square-packed spheres when the bottom surface is perfectly wetting. In this case, a part of the bottom surface is perfectly wetted and the liquid recedes from the sphere surface. Since a perfectly wetting surface is difficult to achieve, dryout situations are expected to be more common with low liquid volumes. It should be noted that very low liquid volumes are unfavorable for heat transfer applications, as the portions that dry out do not contribute to evaporation heat transfer, and heat loss in these regions would be due to natural convection alone.

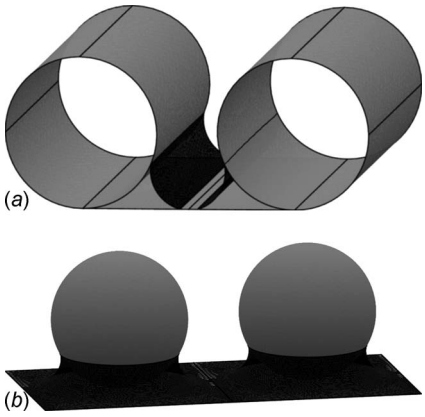

Fig. 10 Final liquid meniscus shape (dark gray) for (*a*) Topology 3, $r=1$, $V=1.58$($H=0.2$), $P=2.8$; $\theta=15$ deg between cylinder surface and liquid and $\theta=15$ deg between bottom surface and liquid, and (*b*) Topology 1 (SP), $r=1$, $V=0.75$($H=0.1$), $P=2.8$; $\theta=15$ deg between sphere's surface and liquid, and $\theta=0$ deg between the bottom surface and liquid

5.6 Effect of Number of Layers. The number of sphere layers typically used in sintered-copper wicks is approximately 8–10. The effect of the number of layers on the static meniscus shapes and heat transfer parameters must be understood in order to simulate heat pipe conditions. Two layers of spheres in the microstructure (Topology 1, HP) are considered now. Liquid meniscus shapes in the second layer of spheres are computed and the four performance parameters (capillary pressure, thin-film percentage area, area-averaged minimum meniscus distance and total meniscus area) are obtained as functions of H (initial liquid level in the second layer). A hexagonal packing arrangement is assumed for every layer of spheres since it provides the maximum wicking and thin-film percentage area. In the vertical direction, a simple-cubic packing arrangement is assumed. The final meniscus shape for one such case is shown in Fig. 11.

A porosity of 0.56, corresponding to $P=1.28$, is chosen, corresponding to the average porosity (range of porosity=0.46–0.6 [1]) of practical wicks (Topology 1, HP). It is observed that the liquid meniscus shapes formed in the second layer of spheres remain unaffected by the lower layer of spheres and are only determined by the second layer's configuration. This is why the capillary pressure and exposed meniscus area do not change for the second layer from those for single layers. However, the area-averaged minimum meniscus distance and thin-film percentage area are different for the second layer of spheres when $H<0.5$

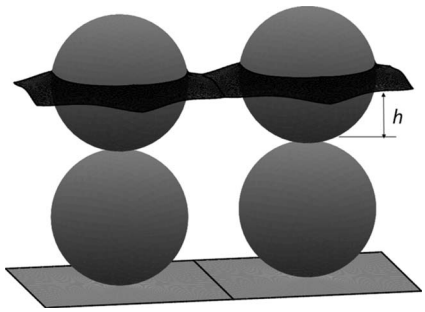

Fig. 11 Final liquid meniscus shape (dark gray) for Topology 1 (HP), $r=1$, $H=1$, $P=2.8$; $\theta=15$ deg between sphere surface and liquid

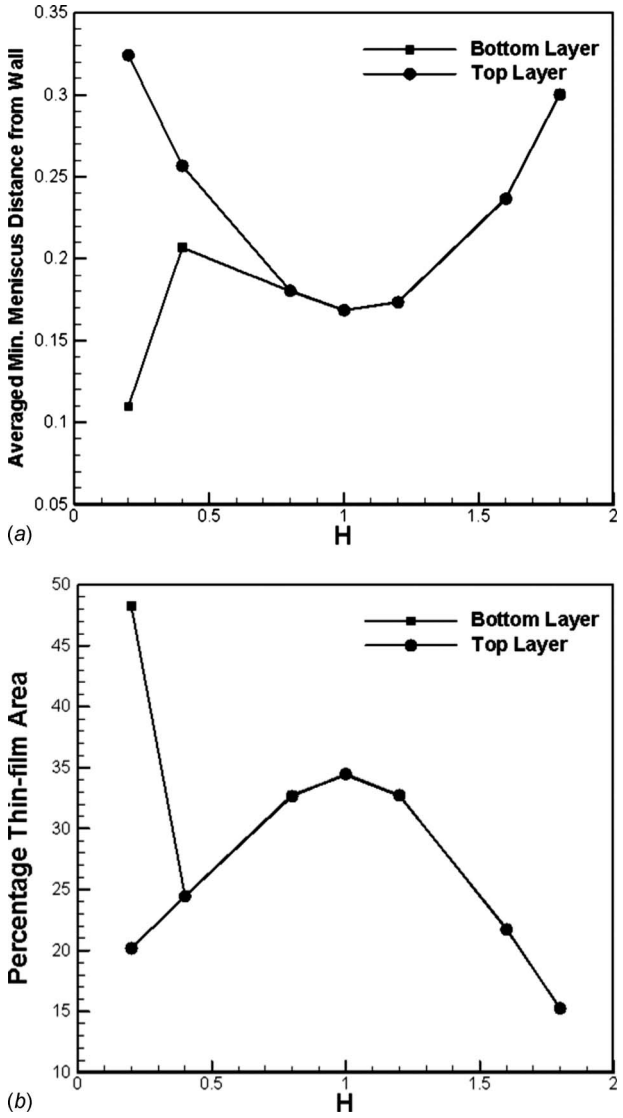

Fig. 12 (*a*) Area-averaged meniscus distance from solid walls versus nondimensional liquid height, and (*b*) percentage thin-film area of the meniscus for top and bottom layers of spheres in two-layer configuration versus nondimensional liquid height; θ=15 deg, porosity=0.56

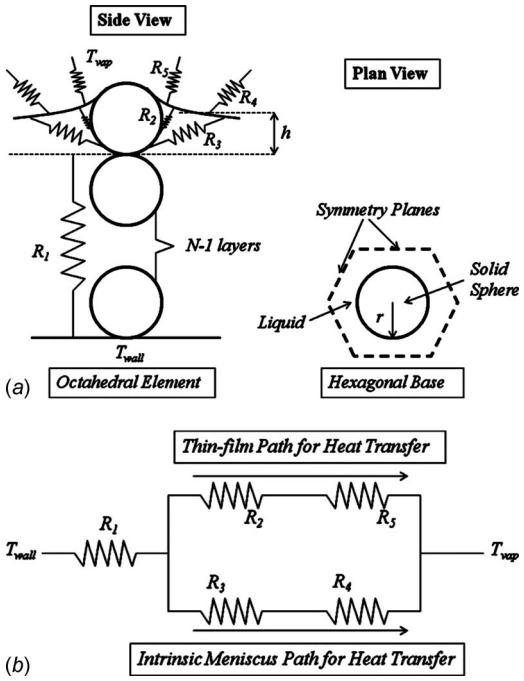

Fig. 13 (*a*) Thermal resistance model for heat transfer in a wick (shown for hexagonally-packed spheres on a surface with simple-cubic packing in the *z*-direction), and (*b*) equivalent resistance network

(Figs. 12(*a*) and 12(*b*)). This is because of the presence of spheres below the liquid meniscus formed in the second layer of spheres. This affects the minimum meniscus distance from the solid walls.

5.7 Effective Thermal Resistance of the Wick. As discussed earlier, liquid meniscus shape is a strong function of the liquid level (H) in hexagonally-packed spheres (Topology 1, HP). We observed that $V=1.5$ corresponds to maximum capillary pressure for a single layer of spheres and also yields a small conduction resistance and a high thin-film percentage area. Nevertheless, the exposed meniscus area is nearly the smallest at this value of V. Hence, determination of the optimum liquid level for any layer of spheres requires the formulation of a cost function for wick performance as a function of H. The optimum liquid volume can also be determined if optimum H and N are known. The two important parameters for the performance of wick microstructures in cooling devices are their maximum wicking capability and the thermal resistance: The optimum liquid level is that which provides maximum wicking, as well as the lowest thermal resistance for conduction and evaporation heat transfer.

In Fig. 13(*a*), an approximate thermal resistance model for conduction and evaporation through the wick in Topology 1 (HP) is shown. An octahedral volume around a sphere is chosen as the representative unit cell. A three-dimensional packing of spheres, similar to the one discussed in the two-layer configuration, is assumed. Heat flows from the hot bottom wall to the liquid-vapor interface by conduction. For the present analysis, convection can be ignored in comparison to conduction through the solid sintered material. Also, thermocapillary convection is not considered. Heat transfer from liquid to vapor occurs at the interface by evaporation. The five thermal resistances R_1, R_2, R_3, R_4, and R_5, as shown in Fig. 13(*a*), result from (i) the conduction resistance due to $(N-1)$ layers of spheres (solid) and interstitial liquid, (ii) the thermal resistance offered by the liquid for conduction from the top layer of spheres to meniscus, and (iii) the evaporation resistance of the liquid meniscus. Temperature varies along the liquid meniscus because of the variation in evaporation rate resulting from the variations in film thickness. In the present model, the liquid meniscus is assumed to be at two different temperatures, one corresponding to the thin-film region, and the other to rest of the meniscus. Hence, there are two separate paths, viz., the thin-film path and the intrinsic meniscus path (or the non-thin-film path), for heat transfer from the top layer of spheres to the vapor. These resistances can be represented in terms of the three heat transfer parameters computed from the static meniscus shape. We have used a functional notation for the three heat transfer parameters, viz., $F_1(h)$ for nondimensional area-averaged minimum meniscus distance, $F_2(h)$ for nondimensional meniscus area, and $F_3(h)$ for percentage thin-film area. The resistance R_1 is the thermal resistance due to $(N-1)$ layers of spheres and interstitial liquid; R_2 is the thermal resistance offered by the liquid between the sphere wall and the thin-film region; R_3 is the thermal resistance offered by the liquid between the sphere wall and the intrinsic region of the meniscus (i.e., the non-thin-film region); R_4 is the thermal resistance accounting for evaporation from the intrinsic meniscus

region; and R_5 is the thermal resistance accounting for evaporation from the thin-film region of the meniscus. The definitions of these resistances are given below

$$R_1 = \frac{(N-1)2r}{k_{\text{eff}}\text{area}_{\text{hexagon}}r^2}, \quad R_2 = \frac{0.1r}{2k_w(0.01F_2F_3)r^2}$$

$$R_3 = \frac{(F_1F_2 - 0.001F_2F_3)r}{(F_2 - 0.01F_2F_3)^2k_w2r^2} \tag{4}$$

$$R_4 = \frac{1}{h_{\text{meniscus}}(F_2 - 0.01F_2F_3)(2r^2)}$$

$$R_5 = \frac{1}{h_{\text{meniscus}}(0.01F_2F_3)(2r^2)}$$

The values used in the above expressions are now discussed. The number of sphere layers is taken to be $N=10$, the radius of spheres is assumed to be $r=100$ μm, and the porosity is assumed to be 0.56. $\text{area}_{\text{hexagon}}$ is the base area of the octahedral volume shown in Fig. 13(*a*). The effective thermal conductivity k_{eff} of a sphere-liquid layer is obtained using FLUENT [25] and is found to be 42.8 W/m K for a copper-water combination ($k_w=0.6$ W/m K, $k_{\text{cu}}=387.6$ W/m K). It should be noted that the analysis presented later using this resistance model is independent of R_1 and so the details of the computation of k_{eff} are not included here. h_{meniscus} is the convective heat transfer coefficient accounting for evaporation from the meniscus and is taken to be 10^6 W/m^2 K [9]. We note that the present model does not account for contact resistance between the spheres.

Figure 13(*b*) shows the thermal resistance network for heat transfer in the wick. The total or effective thermal resistance of the wick is calculated using

$$R_{\text{eff}} = R_1 + \frac{(R_2 + R_5)(R_3 + R_4)}{(R_2 + R_3 + R_4 + R_5)} \tag{5}$$

The effective thermal resistance (R_{eff}) of the wick for conduction and evaporation can now be represented in terms of $F_1(h)$, $F_2(h)$, and $F_3(h)$. Optimization of the liquid level, h, is performed by creating a cost function and assigning equal weights to capillary pressure and heat transfer. This cost function is minimized to achieve maximum $|\Delta P|$ and minimum thermal resistance, R_{eff}.

5.8 Optimum Liquid Level in the Wick Pore. Figure 14(*a*) shows the variation of resistances with nondimensional liquid level, H. Variations are shown for a solid-liquid contact angle of 45 deg. It is observed that R_1 is independent of the liquid level. Also, it is smaller than R_2 and R_3. R_2 and R_3 are quite large due to the very small meniscus area. At $H=1$, R_2 is lowest because of highest thin-film area at this H value. R_3 is highest at $H=1$ because of lowest total meniscus area at this liquid level. R_4 and R_5 (evaporative resistances) are very small compared with other resistances. R_4 (due to evaporation from intrinsic meniscus) is smaller than R_5 (due to thin-film evaporation) because the thin-film area is much smaller than the intrinsic meniscus area.

Figure 14(*b*) shows the variation in the thermal resistances in the thin-film and non-thin-film paths with changing H. It is observed that the thin-film path resistance is lowest at $H=1$ because the thin-film percentage area reaches a maximum at this meniscus position (Figs. 6(*a*) and 12(*b*)). However, the non-thin-film path resistance attains a maximum at $H=1$ because the exposed meniscus area is minimum at this H value. The latter leads to the maximum in R_{eff} seen at $H=1$. When H is in the range of 0.8–1.2, the thin-film path gives a lower resistance to heat flow than the intrinsic meniscus or non-thin-film path, indicating that more than 50% of heat transfer occurs through the thin-film portion of liquid meniscus. At other values of H, more than 30–40% of heat transfer occurs from the thin-film region. Thin-film evaporation is suppressed at H values other than those in the range of 0.8–1.2. However, the total heat transfer is governed by the total resistance, R_{eff}.

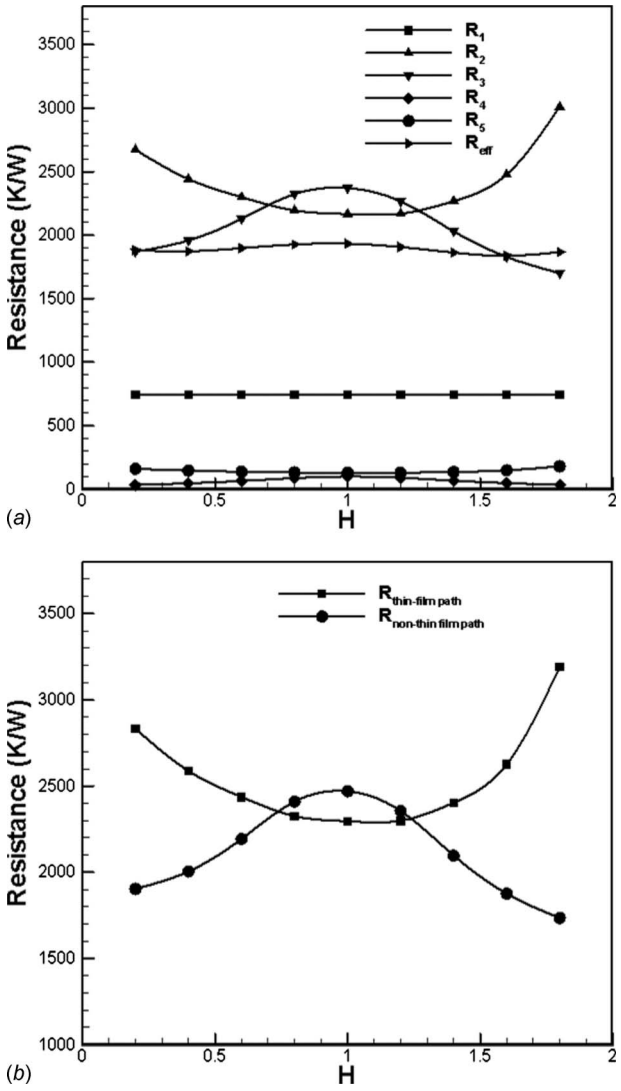

Fig. 14 (*a*) Thermal resistance variation with nondimensional liquid level (H) in the wick pore, and (*b*) thermal resistances in thin-film and non-thin-film (extrinsic meniscus) paths for heat transfer versus nondimensional liquid level; $\theta=45$ deg, porosity=0.56

The variation of R_{eff} with H is shown in Fig. 15 for a porosity of 0.56 and for $\theta=15$, 30, and 45 deg. It is observed that effective resistance to heat transfer is lowest for the lowest contact angle. Also, the effective thermal resistance at any contact angle is highest when liquid fills the wick pore half-way through, i.e., $H=1$. Although the thin-film resistance is lowest at $H\sim1$, the total resistance is highest here because of the smallest total meniscus area. The total resistance increases beyond $H\sim1.6$ as the thin-film area decreases drastically in the range $H=1.6-1.8$. R_{eff} exhibits two minima for higher values of contact angle as H varies from 0.2 to 1.8 while only one minimum is observed in case of lower contact angles (<30 deg). R_{eff} is a combination of the resistances in the thin-film and non-thin-film paths. The variation in R_{eff} depends on how these resistances change with H. The variations in thin-film and non-thin-film path resistances with H are governed by the corresponding variations in thin-film area and total meniscus area and are presented in Fig. 14(*b*). As can be observed in Fig. 14(*b*), for a contact angle of 45 deg, the thin-film path resis-

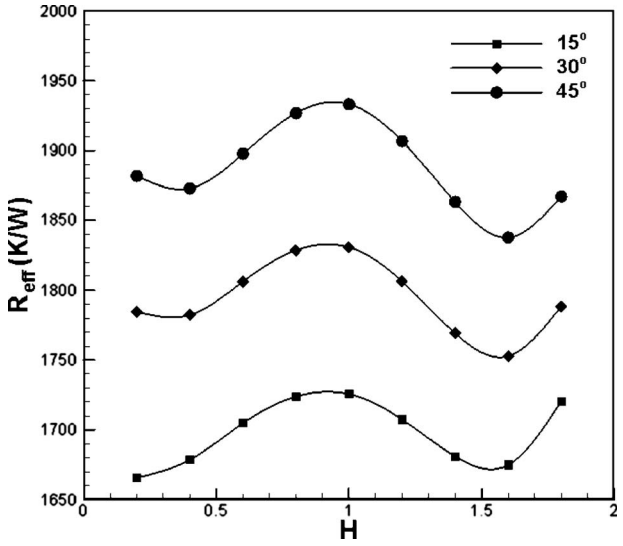

Fig. 15 Total thermal resistance for evaporation and conduction in the wick versus nondimensional liquid height in the wick pore for θ=15, 30, and 45 deg, porosity=0.56

tance decreases while the non-thin-film path resistance increases as H varies from 0.2 to 0.5. The decrease in thin-film path resistance compensates and swamps the increase in non-thin-film path resistance, and leads to an overall decrease in R_{eff}. Therefore, a minimum in the R_{eff} curve is observed near $H \sim 0.5$. This minimum is not observed in case of the 15 deg contact angle because the decrease in thin-film path resistance for 15 deg fails to overcome the increase in non-thin-film path resistance. The second minimum in R_{eff} is observed at $H \sim 1.5$ for all contact angles and is caused by the increase in thin-film path resistance as H increases from 1.5 to 1.8 (Fig. 14(*b*)).

An important point to note here is that the maximum percentage change in R_{eff} with the variation in H is only about 5% at any contact angle. However, $|\Delta P|$ varies from 0 (minimum) to 3.2 (maximum) with H for θ=15 deg and porosity=0.56. Hence, the variation in liquid level in the wick pore does not affect the total heat transfer from the wick as much as it affects the capillary pressure. Therefore, the optimum liquid level should be determined based on the capillary pressure variation with meniscus height and is found to be optimum at $H \sim 0.8-1$ ($V \sim 1.5$, Topology 1, HP).

6 Conclusions

The wicking and heat transfer characteristics of four well-defined microstructures have been studied by computing the static liquid free-surface shapes using SURFACE EVOLVER. The wicking characteristics of the microstructure are characterized by the capillary pressure. The heat transfer characteristics of the static liquid meniscus are characterized by the percentage of the liquid meniscus that is in the thin-film region, the conduction resistance of the liquid, and the total exposed surface area of the meniscus for evaporation. The solid-liquid contact angle and the liquid volume are varied for all microstructures to determine the most efficient geometry for evaporation. Among all the microstructures considered, hexagonally-packed uniform spheres on a surface are found to generate the maximum favorable capillary pressure for evaporation at a contact angle of θ=15 deg. The liquid meniscus is also found to possess the maximum thin-film area for this case. We have studied the effect of contact angle and liquid volume variation on wicking and heat transfer performance for packed spheres on a surface. The effects of porosity and low liquid volumes in the microstructure are also presented. The effect of the number of sphere layers in Topology 1 (HP) on wicking, and heat transfer performance is investigated. Finally, a thermal resistance model of the wick is proposed and the optimum liquid level H in the wick pore is obtained for maximum wicking and heat transfer. The main conclusions drawn from the study of packed spheres (Topology 1) on a surface are as follows.

- Capillary pressure and heat transfer parameters are strong functions of θ and V. The highest favorable capillary pressure is realized for the hexagonally-packed case.
- For high values of $V(H>1.2)$, positive and hence unfavorable capillary pressure for evaporation can be generated even for wetting contact angles (30 deg$<\theta<$90 deg). This condition must be avoided for efficient device operation.
- V=1.5 is the optimum liquid volume for maximum wicking (θ=15 deg) for the case of hexagonally-packed spheres. The highest thin-film percentage area and the lowest liquid conduction resistance are also observed at the same value of V. However, the exposed surface area of the liquid meniscus is near its minimum for V=1.5. Hence, an optimum V must be determined to maximize overall performance.
- Capillary pressure and percentage thin-film area increase with decreasing porosity. Hence, hexagonal close-packed spheres on a surface appear to be the most favorable geometry for evaporation. However, this arrangement also offers the maximum resistance to flow. Permeability is thus an important factor in determining the optimum wick porosity. This consideration will be a part of our future investigations.
- The static liquid meniscus shape does not depend on the number of layers of spheres in the wick but only depends on the sphere arrangement at the liquid free surface. Hence, the wick pores at the free surface determine the capillary pressure and thin-film characteristics of the liquid meniscus.
- An approximate effective thermal resistance model developed for the wick (Topology 1, HP) shows that wick heat transfer performance is nearly independent of the liquid level in the wick pore. Hence, the optimum liquid level should be determined on the basis of capillary pressure variation with liquid level and is found to be $H \sim 0.8-1$ at any porosity.

Nomenclature

$\text{area}_{\text{hexagon}}$ = base area of octahedral volume used in effective resistance model
Bo = Bond number ($=\rho g L^2/\gamma_{LV}$)
d = width of rectangular ribs
D = dimensionless width of rectangular ribs
F = notation for heat transfer parameters associated with free surface of the liquid meniscus
g = acceleration due to gravity
h = height of liquid free-surface from substrate
h_{meniscus} = convective heat transfer coefficient of meniscus accounting for evaporation
H = dimensionless height of liquid free-surface ($=h/L$)
H' = mean curvature of meniscus at any point
HP = hexagonally-packed configuration
N = number of sphere layers for hexagonally-packed spheres
k = thermal conductivity
l = length of cylinders/ribs in unit cell
L = characteristic length
p = pitch
P = dimensionless pitch ($=p/L$)
P_{liq} = liquid pressure
P_{vap} = vapor pressure
r = radius of cylinders/spheres
r_1, r_2 = orthogonal radii of curvature at any point on liquid meniscus

R = notation for thermal resistances in effective thermal resistance model
SP = square-packed configuration
v = liquid volume filling unit cell measured from substrate
V = dimensionless liquid volume ($=v/L^3$)
z = height of any point on liquid meniscus from substrate
Z = dimensionless height of any point on liquid meniscus ($=z/L$)

Greek

Δp = capillary pressure
ΔP = nondimensional capillary pressure ($=L\Delta p/\gamma_{LV}$)
γ_{LV} = surface tension between liquid and vapor phases
ρ = density of liquid
θ = contact angle between liquid and solid surfaces

Subscripts

cu = copper
eff = effective
max = maximum
w = water

References

[1] Iverson, B. D., Davis, T. W., Garimella, S. V., North, M. T., and Kang, S. S., 2007, "Heat and Mass Transport in Heat Pipe Wick Structures," J. Thermophys. Heat Transfer, **21**(2), pp. 392–404.
[2] Davis, T. W., and Garimella, S. V., 2008, "Thermal Resistance Measurement Across a Wick Structure Using a Novel Thermosyphon Test Chamber," Exp. Heat Transfer, **21**, pp. 143–154.
[3] Bauer, T. H., 1993, "General Analytical Approach Toward the Thermal Conductivity of Porous Media," Int. J. Heat Mass Transfer, **36**(17), pp. 4181–4191.
[4] Abo El-Nasr, A., and El-Haggar, S. M., 1996, "Effective Thermal Conductivity of Heat Pipes," Heat Mass Transfer, **32**(1–2), pp. 97–101.
[5] Garimella, S. V., and Sobhan, C. B., 2001, "Recent Advances in the Modeling and Applications of Nonconventional Heat Pipes," Adv. Heat Transfer, **35**, pp. 249–308.
[6] Gupta, A., and Upadhya, G., 1999, "Optimization of Heat Pipe Wick Structures for Low Wattage Electronics Cooling Applications," *Advances in Electronic Packaging 1999, Pacific RIM/ASME International Intersociety Electronics Photonic Packaging Conference*, ASME, New York, **26**, pp. 2129–2137.
[7] Abhat, A., and Seban, R. A., 1974, "Boiling and Evaporation From Heat Pipe Wicks With Water and Acetone," ASME J. Heat Transfer, **96**(3), pp. 331–337.
[8] Hanlon, M. A., and Ma, H. B., 2003, "Evaporation Heat Transfer in Sintered Porous Media," ASME J. Heat Transfer, **125**, pp. 644–652.
[9] Wang, H., Garimella, S. V., and Murthy, J. Y., 2007, "Characteristics of an Evaporating Thin Film in a Microchannel," Int. J. Heat Mass Transfer, **50**, pp. 3933–3942.
[10] Wang, H., Garimella, S. V., and Murthy, J. Y., 2008, "An Analytical Solution for the Total Heat Transfer in the Thin-film Region of an Evaporating Meniscus," Int. J. Heat Mass Transfer, **51**, pp. 6317–6322.
[11] Vadakkan, U., Garimella, S. V., and Murthy, J. Y., 2004, "Transport in Flat Heat Pipes at High Heat Fluxes From Multiple Discrete Sources," ASME J. Heat Transfer, **126**, pp. 347–354.
[12] Kim, S. J., Seo, J. K., and Do, K. H., 2003, "Analytical and Experimental Investigation on the Operational Characteristics and the Thermal Optimization of a Miniature Heat Pipe With a Grooved Wick Structure," Int. J. Heat Mass Transfer, **46**, pp. 2051–2063.
[13] Do, K. H., Kim, S. J., and Garimella, S. V., 2008, "A Mathematical Model for Analyzing the Thermal Characteristics of a Flat Micro Heat Pipe With a Grooved Wick," Int. J. Heat Mass Transfer, **51**(19–20), pp. 4637–4650.
[14] Mwaba, M. G., Huang, X., and Gu, J., 2006, "Influence of Wick Characteristics on Heat Pipe Performance," Int. J. Energy Res., **30**, pp. 489–499.
[15] Xu, X., and Carey, V. P., 1990, "Film Evaporation From a Micro-Grooved Surface—An Approximate Heat Transfer Model and Its Comparison With Experimental Data," J. Thermophys. Heat Transfer, **4**, pp. 512–520.
[16] Ma, H. B., and Peterson, G. P., 1997, "Temperature Variation and Heat Transfer in Triangular Grooves With an Evaporating Film," J. Thermophys. Heat Transfer, **11**, pp. 90–97.
[17] Morris, S. J. S., 2001, "Contact Angles for Evaporating Liquids Predicted and Compared With Existing Experiments," J. Fluid Mech., **432**, pp. 1–30.
[18] Morris, S. J. S., 2003, "The Evaporating Meniscus in a Channel," J. Fluid Mech., **494**, pp. 297–317.
[19] Wang, H., Murthy, J. Y., and Garimella, S. V., 2008, "Transport From a Volatile Meniscus Inside an Open Microtube," Int. J. Heat Mass Transfer, **51**, pp. 3007–3017.
[20] Dhavaleswarapu, H. K., Chamarthy, P., Garimella, S. V., and Murthy, J. Y., 2007, "Experimental Investigation of Steady Buoyant-Thermocapillary Convection Near an Evaporating Meniscus," Phys. Fluids, **19**, p. 082103.
[21] Brakke, K. A., 1992, "The Surface Evolver," Exp. Math., **1**(2), pp. 141–165.
[22] Hilden, J. L., and Trumble, K. P., 2003, "Numerical Analysis of Capillarity in Packed Spheres: Planar Hexagonal-Packed Spheres," J. Colloid Interface Sci., **267**, pp. 463–474.
[23] Slobozhanin, L. A., Alexander, J. I. D., Collicott, S. H., and Gongalez, S. R., 2006, "Capillary Pressure of a Liquid in a Layer of Square-Packed Uniform Spheres," Phys. Fluids, **18**(8), p. 082104.
[24] Potash, M., Jr., and Wayner, P. C., 1972, "Evaporation From a 2-Dimensional Extended Meniscus," Int. J. Heat Mass Transfer, **15**(10), pp. 1851–1863.
[25] Fluent Inc., 2004, FLUENT 6.2 User's Guide.

Thermodynamically Constrained Averaging Theory Approach for Heat Transport in Single-Fluid-Phase Porous Medium Systems

William G. Gray
e-mail: graywg@unc.edu

Cass T. Miller
e-mail: casey_miller@unc.edu

Department of Environmental Sciences and Engineering,
University of North Carolina,
Chapel Hill, NC 27599-7431

The recently developed thermodynamically constrained averaging theory is briefly summarized as a tool for the building of rigorous macroscale models of transport phenomena in complex systems. The specific case of thermal transport in a single-fluid-phase porous medium system is considered. Key results from the application of this theory are used to develop a simplified entropy inequality, which is in turn used to guide the development of closure relations. The decomposition of exchange terms is considered, and closed models for internal energy are derived for the case of nonequilibrium and local thermal equilibrium conditions. Since all variables are expressed in terms of precisely defined averages of microscale quantities, the resultant models can be compared with highly resolved microscale simulations to determine the range of validity of the upscaled models.
[DOI: 10.1115/1.3160539]

Keywords: averaging theory, TCAT, averaged thermodynamics, model formulation, heat transport, porous media

1 Introduction

Modeling of transport phenomena in porous media requires that governing equations be formulated at a length scale consistent with the desired resolution and with closure relations that accurately represent subscale processes. Equations can be formulated at the microscale that describe fluid flow and chemical or thermal transport within the pore space and in the solid medium. However, simulation of these processes in natural systems typically requires that the equations be formulated at a larger scale due to both lack of detailed information regarding the morphology and topology of the pore space and computational limitations.

To facilitate this change in scale in a rigorous framework, the thermodynamically constrained averaging theory (TCAT) approach has been developed [1]. Making use of this formalism, one is able to develop closed models at a larger scale that are consistent with microscale conservation equations, a system entropy balance, and thermodynamics. This formalism overcomes issues of ambiguity associated with the heuristic definition of quantities such as temperature and pressure at the larger scale that are inconsistent with microscale definitions and may not be readily measurable quantities.

Since the integrity of the equations is preserved across scales, data collected at a small scale can be used in efforts to obtain experimental verification for the theoretical models. A series of papers has appeared, which provides the basic elements of the TCAT approach and then applies the method to obtain closed flow and species transport models for a single-fluid-phase system [1–5]. In these formulations, the examples of closure of the general sets of equations were restricted to isothermal systems.

The overall goal of this work is to extend the previously derived TCAT single-phase flow model to include energy transport. The specific objectives of this work are (1) to outline the steps involved with the TCAT approach, (2) to summarize the development of a simplified entropy inequality that is applicable to nonisothermal systems, (3) to examine alternative ways in which interentity exchange terms can be decomposed, (4) to develop closure relations for energy transport that are developed from the entropy inequality, (5) to combine conservation equations and closure relations to produce closed models for energy transport, and (6) to summarize additional extensions to this work that warrant consideration.

2 TCAT Approach

The macroscale system considered in this work is a porous medium saturated with a single fluid phase. Microscale conservation equations, the energy balance, and thermodynamic relations describe the system behavior. These equations are averaged over representative larger scale domains identified as a macroscale domain Ω that is centered at each microscale point in the domain and is invariant with respect to time and location; a subvolume of Ω occupied by a solid phase, Ω_s; a subvolume of Ω occupied by the fluid phase, Ω_w; and an interfacial region within Ω between the solid and fluid phases, Ω_{ws}. Microscale conservation and balance equations are written for each of these regions and averaged to the macroscale. The explicit inclusion of the interface between phases allows for more complete modeling of the important mechanisms of system behavior.

The length scale of the averaging region is considered to be large enough that all average quantities that appear are essentially invariant with respect to small changes in the extent of the averaging region. By averaging over such a representative elementary volume (REV), equations are formulated that do not require detailed knowledge of pore structure but do require macroscale closure relations that represent the essential features of the microscale processes as a function of some set of averaged macroscale variables. By basing all elements of the model development procedure on a rigorous transformation from the microscale to the macroscale, the TCAT method assures an unambiguous and consistent formulation between scales. This feature is in marked contrast to other methods that involve averaging of some quantities and equations along with heuristic, and sometimes physically indefensible, definitions of some symbols directly at the larger scale. Although conditions for which a well-defined REV does not exist occur routinely in nature, these conditions are outside the scope of

Manuscript received September 9, 2008; final manuscript received November 3, 2008; published online July 28, 2009. Review conducted by Kambiz Vafai.

this study. Nevertheless, by invoking the existence of an REV, we are explicitly stating a condition under which the derived equations will apply.

The TCAT approach for a single-fluid-phase volume in a porous medium, without consideration of chemical species transport within phases or the interface, makes use of the following steps [1].

1. An entropy inequality (EI) for the entire system is generated by averaging the entropy balances for each phase volume and the interface and then summing these over these entities to eliminate the interentity exchange terms.
2. A set of mass, momentum, and total energy conservation equations is formulated at the microscale for each phase and the interface and then averaged to the macroscale.
3. A microscale thermodynamic theory is averaged to the macroscale, and differential forms of the macroscale relations are developed.
4. The EI is constrained using the product of Lagrange multipliers with conservation equations and differential, consistent-scale thermodynamic equations to produce the augmented EI (AEI).
5. The set of Lagrange multipliers is determined consistent with the combination of conservation equations that describes the physics of interest and to eliminate time derivatives from the AEI to produce the constrained EI (CEI).
6. A simplified entropy inequality (SEI) is produced from the general CEI by making some approximations appropriate to the system of interest to provide a form that is useful in developing closure relations.
7. The resultant SEI is used to guide the formulation of closed macroscale conservation equations consistent with the second law of thermodynamics.
8. The validity and applicability of the macroscale equations and closure relations are examined in conjunction with microscale and macroscale modeling and experimentation.

This general approach applied to a single-fluid-phase system makes use of averaging theorems for phases and the interface as well as careful definitions of each macroscale quantity in terms of its microscale precursor and other macroscale quantities. The manipulations involved in arriving at averaged equations, the CEI, and finally the SEI are complex and lengthy. The details of these fundamental manipulations for a general multiphase system are provided elsewhere [1,4], while the specific application to flow in a single-fluid-phase porous medium has also been developed [2].

3 Elements of the TCAT Derivation

In this section we will provide the elements of the full TCAT derivation outlined above that are employed in the analysis of single-phase flow in porous media.

3.1 Entropy Inequality. The entropy inequality is written at the microscale for each of the system entities—*w* phase, *s* phase, and *ws* interface. These equations are then averaged to the macroscale making use of appropriate averaging theorems [4]. As a result of this process, the exchanges of entropy between entities appear explicitly in each of the entropy equations. Rather than modeling each of these exchange processes, the three equations are summed over all entities such that the exchanges will cancel thereby producing the system entropy inequality

$$\sum_{\alpha\in\mathcal{I}} \mathcal{S}^{\alpha} = \sum_{\alpha\in\mathcal{I}} \left(\frac{\mathrm{D}^{\bar{\alpha}}\bar{\bar{\eta}}^{\bar{\alpha}}}{\mathrm{D}t} + \bar{\bar{\eta}}^{\bar{\alpha}}\mathbf{I}:\bar{\bar{\mathbf{d}}}^{\bar{\alpha}} - \nabla\cdot(\epsilon^{\alpha}\bar{\bar{\varphi}}^{\bar{\alpha}}) - \epsilon^{\alpha}b^{\alpha} \right) = \Lambda \geq 0 \tag{1}$$

where $\bar{\bar{\eta}}^{\bar{\alpha}}$ is the entropy per volume, $\bar{\bar{\mathbf{d}}}^{\bar{\alpha}}$ is the rate of strain tensor, $\epsilon^{\alpha}\bar{\bar{\varphi}}^{\bar{\alpha}}$ is the nonadvective entropy flux, $\epsilon^{\alpha}b^{\alpha}$ is the entropy source term, and Λ is the entropy production rate. The use of superscripts with quantities indicates that they are macroscale properties. Simple integral averages taken over the domain in which a quantity is defined are denoted with an unadorned superscript. The overbar on a superscript means that the quantity is a mass-weighted average. Double overbars on a quantity indicate that this macroscale quantity is specially defined at the macroscale. All the definitions of macroscale quantities are given in the Nomenclature with the general meaning of a term being adequate to allow one to follow the flow of the derivation. Equation (1) provides a constraint on the system behavior. However, additional constraints are provided by the equations of conservation of mass, momentum, and energy that are not accounted for by the entropy inequality.

3.2 Conservation Equations. The conservation equations are first stated at the microscale and then integrated, making use of averaging theorems, to the macroscale. At the macroscale, all the equations may be represented by the general form

$$\mathcal{F}^{\alpha} = \frac{\mathrm{D}^{\bar{\alpha}}\bar{\bar{F}}^{\bar{\alpha}}}{\mathrm{D}t} + \bar{\bar{F}}^{\bar{\alpha}}\mathbf{I}:\bar{\bar{\mathbf{d}}}^{\bar{\alpha}} - \nabla\cdot\bar{\bar{\mathbf{f}}}^{\bar{\alpha}} - \bar{\bar{f}}^{\bar{\alpha}} - \sum_{\kappa\in\mathcal{I}_{c\alpha}} \overset{\kappa\to\alpha}{X} = 0 \tag{2}$$

where $\bar{\bar{F}}^{\bar{\alpha}}$ is the macroscale property of entity α per unit volume that is being conserved, $\bar{\bar{\mathbf{f}}}^{\bar{\alpha}}$ is the nonadvective flux, $\bar{\bar{f}}^{\bar{\alpha}}$ is the entity source term, and $\overset{\kappa\to\alpha}{X}$ accounts for the transfer of the conserved quantity from the entity κ that bounds entity α into entity α. The quantities that appear in this equation for the various particular conservation equations are given in the table. The new terms that appear in the table are defined such that ϵ^{α} is the extent of entity α per volume, ρ^{α} is the mass of entity α per α extent, $\bar{\bar{E}}^{\bar{\alpha}}$ is the internal energy associated with α per volume, $\bar{\bar{K}}_E^{\bar{\alpha}}$ is the kinetic energy associated with subscale velocities, $\bar{\psi}^{\bar{\alpha}}$ is the potential energy associated with entity α, which will here be taken to be due only to gravitational effects, $\bar{\bar{\mathbf{t}}}^{\bar{\alpha}}$ is the macroscale stress tensor, $\epsilon^{\alpha}\bar{\bar{\mathbf{q}}}^{\bar{\alpha}}$ is the nonadvective heat flux vector, $\bar{\mathbf{g}}^{\bar{\alpha}}$ is the mass averaged body force acceleration vector (gravity for this application), and $\epsilon^{\alpha}h^{\alpha}$ is the energy source term. The exchange terms have been broken down into components for each equation. For the mass conservation equation, the exchange is due to mass transfer between entities and is indicated as $\overset{\kappa\to\alpha}{M}$. Part of the momentum and energy exchange between entities is associated with mass transfer, and these are indicated as $\overset{\kappa\to\alpha}{\mathbf{M}}_v$ and $\overset{\kappa\to\alpha}{M}_E$, respectively. Momentum exchange due to mechanical interactions between entities is designated as $\overset{\kappa\to\alpha}{\mathbf{T}}$, and the energy exchange that accompanies these interactions is denoted as $\overset{\kappa\to\alpha}{T}_v$. The exchange of energy due to heat transfer is indicated as $\overset{\kappa\to\alpha}{Q}$. The components of these exchange terms will be discussed in more detail subsequently, since the decomposition of the exchange terms into these various parts is nonunique.

3.3 Decomposition of Exchange Terms. The exchange terms that appear in the conservation equations account for the subscale interactions between entities. These terms are among the most complex that arise in form; therefore they are decomposed so that the processes embodied in these interaction terms can be both represented clearly and separated into components. The decomposition is nonunique, and a slightly different version will be employed here than has been used previously [2]. For these reasons, the exchange terms are treated explicitly here.

The exchange terms in the mass conservation equation are relatively straightforward and describe mass transfer from the *ws* interface to the κ phase, where $\kappa\in\{w,s\}$, as

$$\overset{ws\to\kappa}{M} = -\overset{\kappa\to ws}{M} = \langle \rho_\kappa \mathbf{n}_\kappa \cdot (\mathbf{v}_{ws} - \mathbf{v}_\kappa) \rangle_{\Omega_{ws},\Omega} \quad \text{for } \kappa \in \{w,s\} \tag{3}$$

where the subscripted variables are microscale quantities and $\mathbf{n}_\kappa$ is the unit vector normal to the *ws* interface positive outward from the κ phase.

For the momentum equation, the exchange terms from the interface to the phases are obtained as

$$\begin{aligned} \overset{ws\to\kappa}{\mathbf{M}_v} + \overset{ws\to\kappa}{\mathbf{T}} &= -\left(\overset{\kappa\to ws}{\mathbf{M}_v} + \overset{\kappa\to ws}{\mathbf{T}}\right) \\ &= \langle \mathbf{n}_\kappa \cdot [\mathbf{t}_\kappa + \rho_\kappa (\mathbf{v}_{ws} - \mathbf{v}_\kappa)\mathbf{v}_\kappa] \rangle_{\Omega_{ws},\Omega} \quad \text{for } \kappa \in \{w,s\} \end{aligned} \tag{4}$$

This expression may be decomposed by introducing an arbitrary macroscale velocity, designated as $\mathbf{v}^{\overline{\text{arb}}}$, in a way that does not change the equality, since it is added in and subtracted out

$$\begin{aligned} \overset{ws\to\kappa}{\mathbf{M}_v} + \overset{ws\to\kappa}{\mathbf{T}} &= -\left(\overset{\kappa\to ws}{\mathbf{M}_v} + \overset{\kappa\to ws}{\mathbf{T}}\right) = \langle \mathbf{n}_\kappa \cdot [\rho_\kappa (\mathbf{v}_{ws} - \mathbf{v}_\kappa)\mathbf{v}^{\overline{\text{arb}}}] \rangle_{\Omega_{ws},\Omega} \\ &\quad + \langle \mathbf{n}_\kappa \cdot [\mathbf{t}_\kappa + \rho_\kappa (\mathbf{v}_{ws} - \mathbf{v}_\kappa)(\mathbf{v}_\kappa - \mathbf{v}^{\overline{\text{arb}}})] \rangle_{\Omega_{ws},\Omega} \\ &\quad \text{for } \kappa \in \{w,s\} \end{aligned} \tag{5}$$

Then we identify

$$\overset{ws\to\kappa}{\mathbf{M}_v} = -\overset{\kappa\to ws}{\mathbf{M}_v} = \langle \mathbf{n}_\kappa \cdot [\rho_\kappa (\mathbf{v}_{ws} - \mathbf{v}_\kappa)\mathbf{v}^{\overline{\text{arb}}}] \rangle_{\Omega_{ws},\Omega} \quad \text{for } \kappa \in \{w,s\} \tag{6}$$

and

$$\begin{aligned} \overset{ws\to\kappa}{\mathbf{T}} &= -\overset{\kappa\to ws}{\mathbf{T}} = \langle \mathbf{n}_\kappa \cdot [\mathbf{t}_\kappa + \rho_\kappa (\mathbf{v}_{ws} - \mathbf{v}_\kappa)(\mathbf{v}_\kappa - \mathbf{v}^{\overline{\text{arb}}})] \rangle_{\Omega_{ws},\Omega} \\ &\quad \text{for } \kappa \in \{w,s\} \end{aligned} \tag{7}$$

Because a macroscale quantity may be removed from the averaging operator, Eq. (6) may be expressed as

$$\overset{ws\to\kappa}{\mathbf{M}_v} = -\overset{\kappa\to ws}{\mathbf{M}_v} = \mathbf{v}^{\overline{\text{arb}}} \overset{ws\to\kappa}{M} \quad \text{for } \kappa \in \{w,s\} \tag{8}$$

The remaining task is to select the value for $\mathbf{v}^{\overline{\text{arb}}}$. The simplest choice would be to set $\mathbf{v}^{\overline{\text{arb}}} = \mathbf{v}^{\overline{\kappa}}$. However, this choice does not provide the best physical decomposition. With reference to Eq. (7) it can be seen that the best specification would be

$$\mathbf{v}^{\overline{\text{arb}}} = \langle \mathbf{v}_\kappa \rangle_{\Omega_{ws},\Omega_{ws},\mathbf{n}_\kappa \cdot [\rho_\kappa (\mathbf{v}_{ws} - \mathbf{v}_\kappa)]} \tag{9}$$

This choice would cause $\overset{ws\to\kappa}{\mathbf{T}}$ to depend only on the average of $\mathbf{n}_\kappa \cdot \mathbf{t}_\kappa$ over the *ws* interface. Nevertheless, the weighting function used for the averaging in Eq. (9) is cumbersome and obscures the physical meaning. Therefore, we select a slightly simpler form

$$\mathbf{v}^{\overline{\text{arb}}} = \mathbf{v}_\kappa^{\overline{ws}} = \langle \mathbf{v}_\kappa \rangle_{\Omega_{ws},\Omega_{ws},\rho_\kappa} \tag{10}$$

This expression is the mass average of the phase velocity over the interface. In most cases, this quantity will be small. With this selection, the definitions of the exchange terms for the momentum equation are

$$\begin{aligned} \overset{ws\to\kappa}{\mathbf{T}} &= -\overset{\kappa\to ws}{\mathbf{T}} = \langle \mathbf{n}_\kappa \cdot [\mathbf{t}_\kappa + \rho_\kappa (\mathbf{v}_{ws} - \mathbf{v}_\kappa)(\mathbf{v}_\kappa - \mathbf{v}_\kappa^{\overline{ws}})] \rangle_{\Omega_{ws},\Omega} \\ &\quad \text{for } \kappa \in \{w,s\} \end{aligned} \tag{11}$$

along with

$$\overset{ws\to\kappa}{\mathbf{M}_v} = -\overset{\kappa\to ws}{\mathbf{M}_v} = \mathbf{v}_\kappa^{\overline{ws}} \overset{ws\to\kappa}{M} \quad \text{for } \kappa \in \{w,s\} \tag{12}$$

For the total energy equation, the exchange terms from the interface to the phases are

$$\begin{aligned} &\overset{ws\to\kappa}{Q} + \overset{ws\to\kappa}{T_v} + \overset{ws\to\kappa}{M_E} \\ &\quad = -\left(\overset{\kappa\to ws}{Q} + \overset{\kappa\to ws}{T_v} + \overset{\kappa\to ws}{M_E}\right) \\ &\quad = \langle \mathbf{n}_\kappa \cdot \mathbf{q}_\kappa + \mathbf{n}_\kappa \cdot \mathbf{t}_\kappa \cdot \mathbf{v}_\kappa \rangle_{\Omega_{ws},\Omega} \\ &\qquad + \left\langle \left(\frac{E_\kappa}{\rho_\kappa} + \frac{1}{2}\mathbf{v}_\kappa \cdot \mathbf{v}_\kappa + \psi_\kappa \right) \rho_\kappa (\mathbf{v}_{ws} - \mathbf{v}_\kappa) \cdot \mathbf{n}_\kappa \right\rangle_{\Omega_{ws},\Omega} \end{aligned} \tag{13}$$

The objective for the decomposition of this expression is to introduce macroscale quantities such that the mass and momentum exchange terms previously defined emerge within this expression. This is achieved by adding and subtracting macroscale quantities and then regrouping terms. In working with the momentum exchange term, we made use of an arbitrary macroscale velocity that, in the end, was chosen to be the mass-weighted entity velocity averaged over the interface. For the energy exchange terms, we additionally introduce an arbitrary macroscale internal energy, body force potential, and subscale kinetic energy. Then, in order to associate physical processes with each of the symbols employed, we select these arbitrary variables to be phase variables averaged over the interface. With this set of conventions we obtain

$$\begin{aligned} \overset{ws\to\kappa}{Q} &= -\overset{\kappa\to ws}{Q} \\ &= \langle \mathbf{n}_\kappa \cdot \mathbf{q}_\kappa + \mathbf{n}_\kappa \cdot \mathbf{t}_\kappa \cdot (\mathbf{v}_\kappa - \mathbf{v}_\kappa^{\overline{ws}}) \rangle_{\Omega_{ws},\Omega} \\ &\quad + \left\langle \left(\frac{E_\kappa}{\rho_\kappa} - \frac{E_\kappa^{\overline{\overline{ws}}}}{\epsilon^\kappa \rho_\kappa^{ws}} \right) \rho_\kappa (\mathbf{v}_{ws} - \mathbf{v}_\kappa) \cdot \mathbf{n}_\kappa \right\rangle_{\Omega_{ws},\Omega} \\ &\quad + \left\langle \frac{1}{2}(\mathbf{v}_\kappa - \mathbf{v}_\kappa^{\overline{ws}}) \cdot (\mathbf{v}_\kappa - \mathbf{v}_\kappa^{\overline{ws}}) \rho_\kappa (\mathbf{v}_{ws} - \mathbf{v}_\kappa) \cdot \mathbf{n}_\kappa \right\rangle_{\Omega_{ws},\Omega} \\ &\quad + \langle (\psi_\kappa - \psi_\kappa^{\overline{ws}} - K_{E\kappa}^{\overline{\overline{ws}}}) \rho_\kappa (\mathbf{v}_{ws} - \mathbf{v}_\kappa) \cdot \mathbf{n}_\kappa \rangle_{\Omega_{ws},\Omega} \quad \text{for } \kappa \in \{w,s\} \end{aligned} \tag{14}$$

$$\overset{ws\to\kappa}{T_v} = -\overset{\kappa\to ws}{T_v} = \mathbf{v}_\kappa^{\overline{ws}} \cdot \overset{ws\to\kappa}{\mathbf{T}} \quad \text{for } \kappa \in \{w,s\} \tag{15}$$

and

$$\begin{aligned} \overset{ws\to\kappa}{M_E} &= -\overset{\kappa\to ws}{M_E} \\ &= \frac{1}{\epsilon^{ws}\rho_\kappa^{ws}} \left[E_\kappa^{\overline{\overline{ws}}} + \epsilon^{ws}\rho_\kappa^{ws} \left(\frac{1}{2}\mathbf{v}_\kappa^{\overline{ws}} \cdot \mathbf{v}_\kappa^{\overline{ws}} + K_{E\kappa}^{\overline{\overline{ws}}} + \psi_\kappa^{\overline{ws}} \right) \right] \overset{ws\to\kappa}{M} \\ &\quad \text{for } \kappa \in \{w,s\} \end{aligned} \tag{16}$$

Recall that a different selection of any of the arbitrary macroscale quantities that appears in these final three equations may be made without altering the definition of the sum of the three terms provided that the different definition is applied in all of the equations. The selection made here ensures that in considering exchanges between phases and interfaces, $\overset{ws\to\kappa}{Q}$ models heat transfer and work associated with changes in entity extents, $\overset{ws\to\kappa}{T_v}$ models the work due to frictional effects, and $\overset{ws\to\kappa}{M_E}$ accounts for the exchange of energy that accompanies phase change.

Alternatively, one could use the standard decompositions that have previously been defined [2]. While these earlier decompositions are less conceptually satisfying, they have the advantage of being expressed in terms of macroscale quantities that will naturally appear in the final form of TCAT models, which are more

easily accessible than the alternative forms posed above. Ultimately, approximate closure relations will be posed for the exchange quantities regardless of the exact decomposition form that is written.

3.4 Thermodynamic Relations. The TCAT approach starts with a microscale thermodynamic description of the phases and the interfaces. This may be chosen from various proposals for irreversible formulations [1]. Here we employ the simplest formulation, classical irreversible thermodynamics (CIT). The CIT forms are averaged to the macroscale. The process of averaging the thermodynamic relations is one feature that distinguishes TCAT from other procedures for obtaining macroscale models. The derived Euler equations for the fluid w and elastic solid s phases and for the ws interface are, respectively [5–7],

$$E^{\bar{\bar{w}}} = \eta^{\bar{\bar{w}}}\theta^{\bar{\bar{w}}} - \epsilon^w p^w + \epsilon^w \rho^w \mu^{\bar{w}} \tag{17}$$

$$E^{\bar{\bar{s}}} = \eta^{\bar{\bar{s}}}\theta^{\bar{\bar{s}}} + \epsilon^s \boldsymbol{\sigma}^{\bar{\bar{s}}} : \frac{\mathbf{C}^s}{j^s} + \epsilon^s \rho^s \mu^{\bar{s}} \tag{18}$$

$$E^{\overline{ws}} = \eta^{\overline{ws}}\theta^{\overline{ws}} + \epsilon^{ws}\gamma^{ws} + \epsilon^{ws}\rho^{ws}\mu^{\overline{ws}} \tag{19}$$

where θ is the temperature, p^w is the pressure of the wetting fluid phase, μ is the chemical potential, $\boldsymbol{\sigma}^{\bar{\bar{s}}}$ is the Lagrangian stress tensor, $\mathbf{C}^s$ is Green's deformation tensor, j^s is the solid-phase Jacobian, and γ^{ws} is the interfacial tension of the ws interface. The material derivatives of these expressions are also of importance. Because the Euler expressions involve averages, the dependence of the macroscale energy on the macroscale variables is more complex than the corresponding type of dependence at the microscale. The expressions obtained for the w and s phase volumes and for the interface are, respectively [1,6,7],

$$\mathcal{T}^w = \frac{\mathrm{D}^{\bar{w}}E^{\bar{\bar{w}}}}{\mathrm{D}t} - \theta^{\bar{\bar{w}}}\frac{\mathrm{D}^{\bar{w}}\eta^{\bar{\bar{w}}}}{\mathrm{D}t} - \mu^{\bar{w}}\frac{\mathrm{D}^{\bar{w}}(\epsilon^w\rho^w)}{\mathrm{D}t} + p^w\frac{\mathrm{D}^{\bar{w}}\epsilon^w}{\mathrm{D}t} + \left\langle \eta_w\frac{\mathrm{D}^{\bar{w}}(\theta_w - \theta^{\bar{\bar{w}}})}{\mathrm{D}t} + \rho_w\frac{\mathrm{D}^{\bar{w}}(\mu_w - \mu^{\bar{w}})}{\mathrm{D}t} - \frac{\mathrm{D}^{\bar{w}}(p_w - p^w)}{\mathrm{D}t} \right\rangle_{\Omega_w,\Omega} = 0 \tag{20}$$

$$\mathcal{T}^s = \frac{\mathrm{D}^{\bar{s}}E^{\bar{\bar{s}}}}{\mathrm{D}t} - \theta^{\bar{\bar{s}}}\frac{\mathrm{D}^{\bar{s}}\eta^{\bar{\bar{s}}}}{\mathrm{D}t} - \mu^{\bar{s}}\frac{\mathrm{D}^{\bar{s}}(\epsilon^s\rho^s)}{\mathrm{D}t} + \left\langle \eta_s\frac{\mathrm{D}^{\bar{s}}(\theta_s - \theta^{\bar{\bar{s}}})}{\mathrm{D}t} + \rho_s\frac{\mathrm{D}^{\bar{s}}(\mu_s - \mu^{\bar{s}})}{\mathrm{D}t} \right\rangle_{\Omega_s,\Omega} - \left\langle \left(\frac{\mathbf{C}_s}{j_s} : \boldsymbol{\sigma}_s\right)(\mathbf{v}_{ws} - \mathbf{v}_s)\cdot\mathbf{n}_s \right\rangle_{\Omega_{ws},\Omega} - \left\langle \mathbf{n}_s \cdot \left[\frac{2}{j_s}\boldsymbol{\sigma}_s : (\nabla_X\mathbf{x}\nabla_X\mathbf{x})\cdot(\mathbf{v}_s - \mathbf{v}^{\bar{s}})\right] \right\rangle_{\Omega_{ws},\Omega} + \left\langle \left\{\nabla\cdot\left[\frac{2}{j_s}\boldsymbol{\sigma}_s : (\nabla_X\mathbf{x}\nabla_X\mathbf{x})\right] - \nabla\boldsymbol{\sigma}_s : \frac{\mathbf{C}_s}{j_s}\right\}\cdot(\mathbf{v}_s - \mathbf{v}^{\bar{s}}) \right\rangle_{\Omega_s,\Omega} + \epsilon^s\boldsymbol{\sigma}^{\bar{\bar{s}}} : \frac{\mathbf{C}^s}{j^s}\mathbf{I} : \mathbf{d}^{\bar{\bar{s}}} - \left\langle \frac{2}{j_s}\boldsymbol{\sigma}_s : (\nabla_X\mathbf{x}\nabla_X\mathbf{x}) \right\rangle_{\Omega_s,\Omega} : \mathbf{d}^{\bar{\bar{s}}} - \nabla\cdot\left\langle \left[\frac{2}{j_s}\boldsymbol{\sigma}_s : (\nabla_X\mathbf{x}\nabla_X\mathbf{x}) - \boldsymbol{\sigma}_s : \frac{\mathbf{C}_s}{j_s}\mathbf{I}\right]\cdot(\mathbf{v}_s - \mathbf{v}^{\bar{s}}) \right\rangle_{\Omega_s,\Omega} = 0 \tag{21}$$

and

Table 1 Conservation equation variables

Symbol	Mass	Momentum	Energy
$\mathcal{F}^\alpha$	$\mathcal{M}^\alpha$	$\boldsymbol{\mathcal{P}}^\alpha$	$\mathcal{E}^\alpha$
$F^{\bar{\bar{\alpha}}}$	$\epsilon^\alpha\rho^\alpha$	$\epsilon^\alpha\rho^\alpha\mathbf{v}^{\bar{\alpha}}$	$E^{\bar{\bar{\alpha}}} + \epsilon^\alpha\rho^\alpha\left(\frac{1}{2}\mathbf{v}^{\bar{\alpha}}\cdot\mathbf{v}^{\bar{\alpha}} + K_E^{\bar{\bar{\alpha}}} + \psi^{\bar{\alpha}}\right)$
$\mathbf{f}^{\bar{\bar{\alpha}}}$	—	$\epsilon^\alpha\mathbf{t}^{\bar{\bar{\alpha}}}$	$\epsilon^\alpha\mathbf{t}^{\bar{\bar{\alpha}}}\cdot\mathbf{v}^{\bar{\alpha}} + \epsilon^\alpha\mathbf{q}^{\bar{\bar{\alpha}}}$
$f^{\bar{\alpha}}$	—	$\epsilon^\alpha\rho^\alpha\mathbf{g}^{\bar{\alpha}}$	$\epsilon^\alpha h^\alpha$
$\kappa\to\alpha$	$\kappa\to\alpha$	$\kappa\to\alpha \quad \kappa\to\alpha$	$\kappa\to\alpha \quad \kappa\to\alpha \quad \kappa\to\alpha$
X	M	$\mathbf{M}_v + \mathbf{T}$	$M_E + T_v + Q$

$$\mathcal{T}^{ws} = \frac{\mathrm{D}^{\overline{ws}}E^{\overline{\bar{ws}}}}{\mathrm{D}t} - \theta^{\overline{\bar{ws}}}\frac{\mathrm{D}^{\overline{ws}}\eta^{\overline{\bar{ws}}}}{\mathrm{D}t} - \mu^{\overline{ws}}\frac{\mathrm{D}^{\overline{ws}}(\epsilon^{ws}\rho^{ws})}{\mathrm{D}t} - \gamma^{ws}\frac{\mathrm{D}^{\overline{ws}}\epsilon^{ws}}{\mathrm{D}t} + \left\langle \eta_{ws}\frac{\mathrm{D}'^{\overline{ws}}(\theta_{ws} - \theta^{\overline{\bar{ws}}})}{\mathrm{D}t} + \rho_{ws}\frac{\mathrm{D}'^{\overline{ws}}(\mu_{ws} - \mu^{\overline{ws}})}{\mathrm{D}t} \right\rangle_{\Omega_{ws},\Omega} + \left\langle \frac{\mathrm{D}'^{\overline{ws}}(\gamma_{ws} - \gamma^{ws})}{\mathrm{D}t} \right\rangle_{\Omega_{ws},\Omega} - \nabla\theta^{\overline{\bar{ws}}}\cdot\langle\mathbf{n}_w\mathbf{n}_w\cdot(\mathbf{v}^{\overline{ws}} - \mathbf{v}_{ws})\eta_{ws}\rangle_{\Omega_{ws},\Omega} - \nabla\mu^{\overline{ws}}\cdot\langle\mathbf{n}_w\mathbf{n}_w\cdot(\mathbf{v}^{\overline{ws}} - \mathbf{v}_{ws})\rho_{ws}\rangle_{\Omega_{ws},\Omega} - \nabla\gamma^{ws}\cdot\langle\mathbf{n}_w\mathbf{n}_w\cdot(\mathbf{v}^{\overline{ws}} - \mathbf{v}_{ws})\rangle_{\Omega_{ws},\Omega} \tag{22}$$

In these expressions, the primed material derivative involves derivatives within the surface as defined in the Nomenclature. For a case where the variations of the microscale quantities within the averaging region are small, the terms in the averaging operators will also be small and the macroscale derivative expressions become analogous to their microscopic precursors. These equations may also be subjected to variational analysis [8–10] so that equilibrium conditions may be developed. These equilibrium relations have been developed [7] and also employed [11] previously.

3.5 Augmented Entropy Inequality. In the TCAT approach, the entropy inequality for the system, Eq. (1), is required to also satisfy the conservation and thermodynamic equations. This condition is imposed by adding these relations to Eq. (1) as constraints. The conservation equations expressed as Eq. (2)—particularized for mass, momentum, and energy of each phase volume and interface using the definitions in Table 1, and the thermodynamic relations in Eqs. (20)–(22) are added to the EI as products of Lagrange multipliers. The addition of these equations does not alter the inequality since each term being added is, itself, equal to zero. The AEI may be written as

$$\sum_{\alpha\in\mathcal{I}}\left(\mathcal{S}^\alpha + \lambda^\alpha_{\mathcal{M}}\mathcal{M}^\alpha + \boldsymbol{\lambda}^\alpha_{\mathcal{P}}\cdot\boldsymbol{\mathcal{P}}^\alpha + \lambda^\alpha_{\mathcal{E}}\mathcal{E}^\alpha + \lambda^\alpha_{\mathcal{T}}\mathcal{T}^\alpha\right) = \Lambda \geq 0 \tag{23}$$

where the sub- and superscripted λs are the Lagrange multipliers of the corresponding conservation equations $\mathcal{M}^\alpha$, $\boldsymbol{\mathcal{P}}^\alpha$, and $\mathcal{E}^\alpha$ and the thermodynamic expressions $\mathcal{T}^\alpha$.

3.6 Specify Lagrange Multipliers. The Lagrange multipliers are selected with the intent of having the terms that survive on the left side of the EI be in the form of products of forces and fluxes such that the equation has the appearance

$$\sum_i J_i F_i + \sum_j \mathbf{J}_j\cdot\mathbf{F}_j + \sum_k \mathbf{J}_k : \mathbf{F}_k = \Lambda \tag{24}$$

where J_i, $\mathbf{J}_j$, and $\mathbf{J}_k$ are the thermodynamic fluxes corresponding to scalar, vector, and tensor types, respectively; and F_i, $\mathbf{F}_j$, and $\mathbf{F}_k$ are the thermodynamic forces of the scalar, vector, and tensor types, respectively. The reduction to this form is achieved by eliminating time derivatives to the degree possible through astute selection of values of the Lagrange multipliers. The values of the Lagrange multipliers employed are [11]

$$\lambda_{\mathcal{M}}^{\alpha} = \frac{1}{\theta^{\bar{\bar{\alpha}}}}\left[K_E^{\bar{\bar{\alpha}}} + \mu^{\bar{\alpha}} + \psi^{\bar{\alpha}} - \frac{(\mathbf{v}^{\bar{\alpha}} \cdot \mathbf{v}^{\bar{\alpha}})}{2}\right] \tag{25}$$

$$\boldsymbol{\lambda}_{\mathcal{P}}^{\alpha} = \frac{\mathbf{v}^{\bar{\alpha}}}{\theta^{\bar{\bar{\alpha}}}} \tag{26}$$

$$\lambda_{\mathcal{E}}^{\alpha} = -\frac{1}{\theta^{\bar{\bar{\alpha}}}} \tag{27}$$

$$\lambda_{\mathcal{T}}^{\alpha} = \frac{1}{\theta^{\bar{\bar{\alpha}}}} \tag{28}$$

3.7 Constrained Entropy Inequality. The values of the Lagrange multipliers are substituted into Eq. (23) and the summations are expanded to yield the CEI. Some manipulations are required for this step, which involve grouping terms in force-flux form and arranging groupings of terms that correspond to given physical processes. The CEI does not depend on any approximations in addition to those mentioned previously. The resulting equation serves as a starting point for closure of any single-fluid-phase system when species transport is not a consideration. The resulting CEI is

$$
\begin{aligned}
&-\nabla\cdot\left[\epsilon^{w}\left(\boldsymbol{\varphi}^{\bar{\bar{w}}}-\frac{\mathbf{q}^{\bar{\bar{w}}}}{\theta^{\bar{\bar{w}}}}\right)\right]-\nabla\cdot\left[\epsilon^{ws}\left(\boldsymbol{\varphi}^{\overline{\bar{w}s}}-\frac{\mathbf{q}^{\overline{\bar{w}s}}}{\theta^{\overline{\bar{w}s}}}\right)\right]-\nabla\cdot\left\{\epsilon^{s}\boldsymbol{\varphi}^{\bar{\bar{s}}}-\frac{1}{\theta^{\bar{\bar{s}}}}\left[\epsilon^{s}\mathbf{q}^{\bar{\bar{s}}}-\left\langle\left(\mathbf{t}_s-\boldsymbol{\sigma}_s:\frac{\mathbf{C}_s}{j_s}\mathbf{I}\right)\cdot(\mathbf{v}_s-\mathbf{v}^{\bar{s}})\right\rangle_{\Omega_s,\Omega}\right]\right\}\\
&-\epsilon^{w}b^{w}+\frac{1}{\theta^{\bar{\bar{w}}}}\left[\epsilon^{w}h^{w}+\left\langle\eta_w\frac{\mathrm{D}^{\bar{s}}(\theta_w-\theta^{\bar{\bar{w}}})}{\mathrm{D}t}\right\rangle_{\Omega_w,\Omega}\right]+\frac{1}{\theta^{\bar{\bar{w}}}}\left\langle\rho_w\frac{\mathrm{D}^{\bar{s}}(\mu_w+\psi_w-\mu^{\bar{w}}-K_E^{\bar{\bar{w}}}-\psi^{\bar{w}})}{\mathrm{D}t}\right\rangle_{\Omega_w,\Omega}\\
&-\epsilon^{s}b^{s}+\frac{1}{\theta^{\bar{\bar{s}}}}\left[\epsilon^{s}h^{s}+\left\langle\eta_s\frac{\mathrm{D}^{\bar{s}}(\theta_s-\theta^{\bar{\bar{s}}})}{\mathrm{D}t}\right\rangle_{\Omega_s,\Omega}\right]+\frac{1}{\theta^{\bar{\bar{s}}}}\left\langle\rho_s\frac{\mathrm{D}^{\bar{s}}(\mu_s+\psi_s-\mu^{\bar{s}}-K_E^{\bar{\bar{s}}}-\psi^{\bar{s}})}{\mathrm{D}t}\right\rangle_{\Omega_s,\Omega}\\
&-\epsilon^{ws}b^{ws}+\frac{1}{\theta^{\overline{\bar{w}s}}}\left[\epsilon^{ws}h^{ws}+\left\langle\eta_{ws}\frac{\mathrm{D}'^{\bar{s}}(\theta_{ws}-\theta^{\overline{\bar{w}s}})}{\mathrm{D}t}\right\rangle_{\Omega_{ws},\Omega}\right]+\frac{1}{\theta^{\overline{\bar{w}s}}}\left\langle\rho_{ws}\frac{\mathrm{D}'^{\bar{s}}(\mu_{ws}+\psi_{ws}-\mu^{\overline{ws}}-K_E^{\overline{\bar{w}s}}-\psi^{\overline{ws}})}{\mathrm{D}t}\right\rangle_{\Omega_{ws},\Omega}+\frac{\epsilon^{w}}{\theta^{\bar{\bar{w}}}}(\mathbf{t}^{\bar{\bar{w}}}+p^{w}\mathbf{I}):\mathbf{d}^{\bar{\bar{w}}}\\
&+\frac{\epsilon^{s}}{\theta^{\bar{\bar{s}}}}(\mathbf{t}^{\bar{\bar{s}}}-\mathbf{t}^{s}):\mathbf{d}^{\bar{\bar{s}}}+\frac{\epsilon^{ws}}{\theta^{\overline{\bar{w}s}}}(\mathbf{t}^{\overline{\bar{w}s}}-\gamma^{ws}\mathbf{I}):\mathbf{d}^{\overline{\bar{w}s}}-\epsilon^{w}\mathbf{q}^{\bar{\bar{w}}}\cdot\nabla\left(\frac{1}{\theta^{\bar{\bar{w}}}}\right)-\epsilon^{ws}\mathbf{q}^{\overline{\bar{w}s}}\cdot\nabla\left(\frac{1}{\theta^{\overline{\bar{w}s}}}\right)\\
&-\left[\epsilon^{s}\mathbf{q}^{\bar{\bar{s}}}-\left\langle\left(\mathbf{t}_s-\boldsymbol{\sigma}_s:\frac{\mathbf{C}_s}{j_s}\mathbf{I}\right)\cdot(\mathbf{v}_s-\mathbf{v}^{\bar{s}})\right\rangle_{\Omega_s,\Omega}\right]\cdot\nabla\left(\frac{1}{\theta^{\bar{\bar{s}}}}\right)+\frac{1}{\theta^{\overline{\bar{w}s}}}\left\{\left[K_E^{\overline{\bar{w}s}}+\mu^{\overline{ws}}+\psi^{\overline{ws}}-\frac{(\mathbf{v}^{\overline{ws}}-\mathbf{v}_w^{\overline{ws}})\cdot(\mathbf{v}^{\overline{ws}}-\mathbf{v}_w^{\overline{ws}})}{2}\right]\right.\\
&\left.-\left[K_E^{\bar{\bar{w}}}+\mu^{\bar{w}}+\psi^{\bar{w}}-\frac{(\mathbf{v}^{\bar{w}}-\mathbf{v}_w^{\overline{ws}})\cdot(\mathbf{v}^{\bar{w}}-\mathbf{v}_w^{\overline{ws}})}{2}\right]\right\}^{ws\to w}M+\frac{1}{\theta^{\overline{\bar{w}s}}}\left\{\left[K_E^{\overline{\bar{w}s}}+\mu^{\overline{ws}}+\psi^{\overline{ws}}-\frac{(\mathbf{v}^{\overline{ws}}-\mathbf{v}_s^{\overline{ws}})\cdot(\mathbf{v}^{\overline{ws}}-\mathbf{v}_s^{\overline{ws}})}{2}\right]\right.\\
&\left.-\left[K_E^{\bar{\bar{s}}}+\mu^{\bar{s}}+\psi^{\bar{s}}-\frac{(\mathbf{v}^{\bar{s}}-\mathbf{v}_s^{\overline{ws}})\cdot(\mathbf{v}^{\bar{s}}-\mathbf{v}_s^{\overline{ws}})}{2}\right]\right\}^{ws\to s}M-\frac{1}{\theta^{\bar{\bar{s}}}}\left\langle\left[\mathbf{n}_s\cdot\mathbf{t}_s\cdot\mathbf{n}_s-\boldsymbol{\sigma}_s:\frac{\mathbf{C}_s}{j_s}\right]\mathbf{n}_s\cdot(\mathbf{v}_s-\mathbf{v}_{ws})\right\rangle_{\Omega_{ws},\Omega}\\
&+\left(\frac{1}{\theta^{\bar{\bar{w}}}}-\frac{1}{\theta^{\overline{\bar{w}s}}}\right)\left\{{}^{ws\to w}Q+(\mathbf{v}_w^{\overline{ws}}-\mathbf{v}^{\bar{s}})\cdot{}^{ws\to w}\mathbf{T}+\left[\frac{E_w^{\overline{\bar{w}s}}}{\rho_w^{ws}\epsilon^{ws}}-\mu^{\bar{w}}+\frac{(\mathbf{v}^{\bar{w}}-\mathbf{v}_w^{\overline{ws}})\cdot(\mathbf{v}^{\bar{w}}-\mathbf{v}_w^{\overline{ws}})}{2}+\psi_w^{\overline{ws}}+K_{Ew}^{\overline{\bar{w}s}}-\psi^{\bar{w}}-K_E^{\bar{\bar{w}}}\right]{}^{ws\to w}M\right\}\\
&+\left(\frac{1}{\theta^{\bar{\bar{s}}}}-\frac{1}{\theta^{ws}}\right)\left\{{}^{ws\to s}Q+(\mathbf{v}_s^{\overline{ws}}-\mathbf{v}^{\bar{s}})\cdot{}^{ws\to s}\mathbf{T}+\left[\frac{E_s^{\overline{\bar{w}s}}}{\rho_s^{ws}\epsilon^{ws}}-\mu^{\bar{s}}+\frac{(\mathbf{v}^{\bar{s}}-\mathbf{v}_s^{\overline{ws}})\cdot(\mathbf{v}^{\bar{s}}-\mathbf{v}_s^{\overline{ws}})}{2}+\psi_s^{\overline{ws}}+K_{Es}^{\overline{\bar{w}s}}-\psi^{\bar{s}}-K_E^{\bar{\bar{s}}}\right]{}^{ws\to s}M\right\}\\
&-\frac{1}{\theta^{\bar{\bar{w}}}}\{{}^{ws\to w}\mathbf{T}+\epsilon^{w}\rho^{w}\mathbf{g}^{\bar{w}}+\epsilon^{w}\rho^{w}\nabla(\psi^{\bar{w}}+\mu^{\bar{w}}+K_E^{\bar{\bar{w}}})-\nabla(\epsilon^{w}p^{w})+\eta^{\bar{\bar{w}}}\nabla\theta^{\bar{\bar{w}}}\}\cdot(\mathbf{v}^{\bar{w}}-\mathbf{v}^{\bar{s}})+\frac{1}{\theta^{\overline{\bar{w}s}}}\{{}^{ws\to w}\mathbf{T}+{}^{ws\to s}\mathbf{T}-\epsilon^{ws}\rho^{ws}\mathbf{g}^{\overline{\bar{w}s}}\\
&-\epsilon^{ws}\rho^{ws}\nabla(\mu^{\overline{ws}}+K_E^{\overline{\bar{w}s}}+\psi^{\overline{ws}})-\eta^{\overline{\bar{w}s}}\nabla\theta^{\overline{\bar{w}s}}-\nabla(\epsilon^{ws}\gamma^{ws})\}\cdot(\mathbf{v}^{\overline{ws}}-\mathbf{v}^{\bar{s}})-\frac{1}{\theta^{\bar{\bar{s}}}}\langle\mathbf{n}_s\cdot\mathbf{t}_s\cdot\mathbf{I}'\cdot(\mathbf{v}_s-\mathbf{v}^{\bar{s}})\rangle_{\Omega_{ws},\Omega}+\frac{1}{\theta^{\bar{\bar{s}}}}\left\langle\left[\nabla\cdot\mathbf{t}_s\right.\right.\\
&\left.\left.-\nabla\boldsymbol{\sigma}_s:\frac{\mathbf{C}_s}{j_s}\right]\cdot(\mathbf{v}_s-\mathbf{v}^{\bar{s}})\right\rangle_{\Omega_s,\Omega}-\frac{1}{\theta^{\overline{\bar{w}s}}}\langle[p_w+\mathbf{n}_s\cdot\mathbf{t}_s\cdot\mathbf{n}_s+\gamma_{ws}\nabla'\cdot\mathbf{n}_s-\rho_{ws}\mathbf{g}_{ws}\cdot\mathbf{n}_s](\mathbf{v}_{ws}-\mathbf{v}^{\bar{s}})\cdot\mathbf{n}_s\rangle_{\Omega_{ws},\Omega}-\langle p_w(\mathbf{v}_{ws}\\
&-\mathbf{v}^{\bar{s}})\cdot\mathbf{n}_s\rangle_{\Omega_{ws},\Omega}\left(\frac{1}{\theta^{\bar{\bar{w}}}}-\frac{1}{\theta^{\overline{\bar{w}s}}}\right)-\langle\mathbf{n}_s\cdot\mathbf{t}_s\cdot\mathbf{n}_s(\mathbf{v}_{ws}-\mathbf{v}^{\bar{s}})\cdot\mathbf{n}_s\rangle_{\Omega_{ws},\Omega}\left(\frac{1}{\theta^{\bar{\bar{s}}}}-\frac{1}{\theta^{\overline{\bar{w}s}}}\right)+\frac{1}{\theta^{\overline{\bar{w}s}}}[\nabla\cdot\langle\mathbf{n}_s\mathbf{n}_s\cdot(\mathbf{v}_{ws}-\mathbf{v}^{\bar{s}})\gamma_{ws}\rangle_{\Omega_{ws},\Omega}\\
&+\langle\mathbf{n}_s\mathbf{n}_s\gamma_{ws}\rangle_{\Omega_{ws},\Omega}:\mathbf{d}^{\bar{\bar{s}}}]+\frac{1}{\theta^{\overline{\bar{w}s}}}\nabla\theta^{\overline{\bar{w}s}}\cdot\langle\mathbf{n}_w\mathbf{n}_w\cdot(\mathbf{v}_{ws}-\mathbf{v}^{\bar{s}})\eta_{ws}\rangle_{\Omega_{ws},\Omega}+\frac{1}{\theta^{\overline{\bar{w}s}}}\nabla(\mu^{\overline{ws}}+K_E^{\overline{\bar{w}s}}+\psi^{\overline{ws}})\cdot\langle\mathbf{n}_w\mathbf{n}_w\cdot(\mathbf{v}_{ws}-\mathbf{v}^{\bar{s}})\rho_{ws}\rangle_{\Omega_{ws},\Omega}=\Lambda\geq 0
\end{aligned}
\tag{29}
$$

3.8 Simplified Entropy Inequality. The SEI is produced from the CEI by making restrictions and approximations about the system behavior. A more detailed example is presented elsewhere [2], and here the elements are merely stated.

The system is defined to be a simple system [12] so that the relations between the nonadvective entropy and energy fluxes are proportional to the temperature as are the relations between the entropy and energy source terms. For the simple system we specify the relations between the entropy and energy fluxes as

$$\boldsymbol{\varphi}^{\bar{\bar{w}}} - \frac{\mathbf{q}^{\bar{\bar{w}}}}{\theta^{\bar{\bar{w}}}} = 0 \tag{30}$$

$$\epsilon^s \boldsymbol{\varphi}^{\bar{\bar{s}}} - \frac{1}{\theta^{\bar{\bar{s}}}}\left[\epsilon^s \mathbf{q}^{\bar{\bar{s}}} - \left\langle \left(\mathbf{t}_s - \boldsymbol{\sigma}_s : \frac{\mathbf{C}_s}{j_s}\mathbf{I}\right)\cdot(\mathbf{v}_s - \mathbf{v}^{\bar{s}})\right\rangle_{\Omega_s,\Omega}\right] = 0 \tag{31}$$

$$\boldsymbol{\varphi}^{\bar{\bar{ws}}} - \frac{\mathbf{q}^{\bar{\bar{ws}}}}{\theta^{\bar{\bar{ws}}}} = 0 \tag{32}$$

and the relations between the entropy and entropy sources as

$$-\epsilon^w b^w + \frac{1}{\theta^{\bar{\bar{w}}}}\left[\epsilon^w h^w + \left\langle \eta_w \frac{\mathrm{D}^{\bar{s}}(\theta_w - \theta^{\bar{\bar{w}}})}{\mathrm{D}t}\right\rangle_{\Omega_w,\Omega}\right] + \frac{1}{\theta^{\bar{\bar{w}}}}\left\langle \rho_w \frac{\mathrm{D}^{\bar{s}}(\mu_w + \psi_w - \mu^{\bar{w}} - K_E^{\bar{\bar{w}}} - \psi^{\bar{w}})}{\mathrm{D}t}\right\rangle_{\Omega_w,\Omega} = 0 \tag{33}$$

$$-\epsilon^s b^s + \frac{1}{\theta^{\bar{\bar{s}}}}\left[\epsilon^s h^s + \left\langle \eta_s \frac{\mathrm{D}^{\bar{s}}(\theta_s - \theta^{\bar{\bar{s}}})}{\mathrm{D}t}\right\rangle_{\Omega_s,\Omega}\right] + \frac{1}{\theta^{\bar{\bar{s}}}}\left\langle \rho_s \frac{\mathrm{D}^{\bar{s}}(\mu_s + \psi_s - \mu^{\bar{s}} - K_E^{\bar{\bar{s}}} - \psi^{\bar{s}})}{\mathrm{D}t}\right\rangle_{\Omega_s,\Omega} = 0 \tag{34}$$

$$-\epsilon^{ws} b^{ws} + \frac{1}{\theta^{\bar{\bar{ws}}}}\left[\epsilon^{ws} h^{ws} + \left\langle \eta_{ws} \frac{\mathrm{D}'^{\bar{s}}(\theta_{ws} - \theta^{\bar{\bar{ws}}})}{\mathrm{D}t}\right\rangle_{\Omega_{ws},\Omega}\right] + \frac{1}{\theta^{\bar{\bar{ws}}}}\left\langle \rho_{ws} \frac{\mathrm{D}'^{\bar{s}}(\mu_{ws} + \psi_{ws} - \mu^{\bar{ws}} - K_E^{\bar{\bar{ws}}} - \psi^{\bar{ws}})}{\mathrm{D}t}\right\rangle_{\Omega_{ws},\Omega} = 0 \tag{35}$$

Since species transport is not being considered, we will also neglect phase change that could be important if a melting, freezing, or evaporation process is occurring. This stipulation is applied by requiring

$$\overset{ws\to w}{M} = \overset{ws\to s}{M} = 0 \tag{36}$$

and also the fact that when no phase change is occurring the microscale condition that applies is

$$\mathbf{n}_s \cdot (\mathbf{v}_s - \mathbf{v}_{ws}) = \mathbf{n}_s \cdot (\mathbf{v}_w - \mathbf{v}_{ws}) = 0 \tag{37}$$

Thus the SEI under consideration is

$$\begin{aligned}
&+ \frac{\epsilon^w}{\theta^{\bar{\bar{w}}}}(\mathbf{t}^{\bar{\bar{w}}} + p^w\mathbf{I}):\mathbf{d}^{\bar{\bar{w}}} + \frac{\epsilon^s}{\theta^{\bar{\bar{s}}}}(\mathbf{t}^{\bar{\bar{s}}} - \mathbf{t}^s):\mathbf{d}^{\bar{\bar{s}}} + \frac{\epsilon^{ws}}{\theta^{\bar{\bar{ws}}}}(\mathbf{t}^{ws} - \gamma^{ws}\mathbf{I}):\mathbf{d}^{ws} - \epsilon^w \mathbf{q}^{\bar{\bar{w}}}\cdot\nabla\left(\frac{1}{\theta^{\bar{\bar{w}}}}\right) - \epsilon^{ws}\mathbf{q}^{\bar{\bar{ws}}}\cdot\nabla\left(\frac{1}{\theta^{\bar{\bar{ws}}}}\right)\\
&- \left[\epsilon^s\mathbf{q}^{\bar{\bar{s}}} - \left\langle\left(\mathbf{t}_s - \boldsymbol{\sigma}_s:\frac{\mathbf{C}_s}{j_s}\mathbf{I}\right)\cdot(\mathbf{v}_s - \mathbf{v}^{\bar{s}})\right\rangle_{\Omega_s,\Omega}\right]\cdot\nabla\left(\frac{1}{\theta^{\bar{\bar{s}}}}\right) + \left(\frac{1}{\theta^{\bar{\bar{s}}}} - \frac{1}{\theta^{\bar{\bar{ws}}}}\right)\left[\overset{ws\to w}{Q} + (\mathbf{v}_w^{\bar{ws}} - \mathbf{v}^{\bar{s}})\cdot\overset{ws\to w}{\mathbf{T}} - \langle p_w(\mathbf{v}_{ws} - \mathbf{v}^{\bar{s}})\cdot\mathbf{n}_s\rangle_{\Omega_{ws},\Omega}\right]\\
&+ \left(\frac{1}{\theta^{\bar{\bar{s}}}} - \frac{1}{\theta^{\bar{\bar{ws}}}}\right)\left[\overset{ws\to s}{Q} + (\mathbf{v}_s^{\bar{ws}} - \mathbf{v}^{\bar{s}})\cdot\overset{ws\to s}{\mathbf{T}} - \langle\mathbf{n}_s\cdot\mathbf{t}_s\cdot\mathbf{n}_s(\mathbf{v}_{ws} - \mathbf{v}^{\bar{s}})\cdot\mathbf{n}_s\rangle_{\Omega_{ws},\Omega}\right] - \frac{1}{\theta^{\bar{\bar{w}}}}\left\{\overset{ws\to w}{\mathbf{T}} + \epsilon^w\rho^w\mathbf{g}^{\bar{w}} + \epsilon^w\rho^w\nabla(\psi^{\bar{w}} + \mu^{\bar{w}} + K_E^{\bar{\bar{w}}})\right.\\
&\left. - \nabla(\epsilon^w p^w) + \eta^{\bar{\bar{w}}}\nabla\theta^{\bar{\bar{w}}}\right\}\cdot(\mathbf{v}^{\bar{w}} - \mathbf{v}^{\bar{s}}) + \frac{1}{\theta^{\bar{\bar{ws}}}}\left\{\overset{ws\to w}{\mathbf{T}} + \overset{ws\to s}{\mathbf{T}} - \epsilon^{ws}\rho^{ws}\mathbf{g}^{\bar{ws}} - \epsilon^{ws}\rho^{ws}\nabla(\mu^{\bar{ws}} + K_E^{\bar{\bar{ws}}} + \psi^{\bar{ws}}) - \eta^{\bar{\bar{ws}}}\nabla\theta^{\bar{\bar{ws}}} - \nabla(\epsilon^{ws}\gamma^{ws})\right\}\\
&\cdot(\mathbf{v}^{\bar{ws}} - \mathbf{v}^{\bar{s}}) - \frac{1}{\theta^{\bar{\bar{s}}}}\langle\mathbf{n}_s\cdot\mathbf{t}_s\cdot\mathbf{l}'\cdot(\mathbf{v}_s - \mathbf{v}^{\bar{s}})\rangle_{\Omega_{ws},\Omega} + \frac{1}{\theta^{\bar{\bar{s}}}}\left\langle\left[\nabla\cdot\mathbf{t}_s - \nabla\boldsymbol{\sigma}_s:\frac{\mathbf{C}_s}{j_s}\right]\cdot(\mathbf{v}_s - \mathbf{v}^{\bar{s}})\right\rangle_{\Omega_s,\Omega}\\
&- \frac{1}{\theta^{\bar{\bar{ws}}}}\langle[p_w + \mathbf{n}_s\cdot\mathbf{t}_s\cdot\mathbf{n}_s + \gamma_{ws}\nabla'\cdot\mathbf{n}_s - \rho_{ws}\mathbf{g}_{ws}\cdot\mathbf{n}_s](\mathbf{v}_{ws} - \mathbf{v}^{\bar{s}})\cdot\mathbf{n}_s\rangle_{\Omega_{ws},\Omega} + \frac{1}{\theta^{\bar{\bar{ws}}}}[\nabla\cdot\langle\mathbf{n}_s\mathbf{n}_s\cdot(\mathbf{v}_{ws} - \mathbf{v}^{\bar{s}})\gamma_{ws}\rangle_{\Omega_{ws},\Omega} + \langle\mathbf{n}_s\mathbf{n}_s\gamma_{ws}\rangle_{\Omega_{ws},\Omega}:\mathbf{d}^{\bar{\bar{s}}}]\\
&+ \frac{1}{\theta^{\bar{\bar{ws}}}}\nabla\theta^{\bar{\bar{ws}}}\cdot\langle\mathbf{n}_w\mathbf{n}_w\cdot(\mathbf{v}_{ws} - \mathbf{v}^{\bar{s}})\eta_{ws}\rangle_{\Omega_{ws},\Omega} + \frac{1}{\theta^{\bar{\bar{ws}}}}\nabla(\mu^{\bar{ws}} + K_E^{\bar{\bar{ws}}} + \psi^{\bar{ws}})\cdot\langle\mathbf{n}_w\mathbf{n}_w\cdot(\mathbf{v}_{ws} - \mathbf{v}^{\bar{s}})\rho_{ws}\rangle_{\Omega_{ws},\Omega} = \Lambda \geq 0
\end{aligned} \tag{38}$$

To further develop this analysis, we define the geometric orientation tensor for the *ws* interface, $\mathbf{G}^{ws}$, as

$$\epsilon^{ws}\mathbf{G}^{ws} = \langle\mathbf{G}_{ws}\rangle_{\Omega_{ws},\Omega} = \langle\mathbf{n}_w\mathbf{n}_w\rangle_{\Omega_{ws},\Omega} = \langle\mathbf{n}_s\mathbf{n}_s\rangle_{\Omega_{ws},\Omega} \tag{39}$$

For the current system consisting of a single fluid and solid, when the orientation of the surface of the solid grains is random, $\mathbf{G}^{ws} = \mathbf{I}/3$. When the principal directions of solid grain orientation are aligned with the coordinate system, $\mathbf{G}^{ws}$ is a diagonal tensor. The trace of $\mathbf{G}^{ws}$ is invariant and equal to 1. Knowledge of the microscale geometry is sufficient to compute $\mathbf{G}^{ws}$ without error and thereby test the macroscale models derived from this theory. This tensor is a useful indicator of the isotropy of the system for both flow and transport processes.

In general, $\mathbf{G}_{ws}$ appears within averaging operators as a product involving other terms. An approximation will be used here that assumes the product terms are independent, such that the orientation of the interface does not depend on interfacial tension or velocities. This allows us to estimate the integral of the product as being equal to a product of the integrals of the terms. Applying these approximations and similar product-splitting integral approximations, and relating changes in ϵ^s to changes in ϵ^{ws}, we reduce Eq. (38) to

$$+\frac{\epsilon^w}{\bar{\bar{\theta}}^w}(\bar{\bar{\mathbf{t}}}^w+p^w\mathbf{I}):\mathbf{d}^{\bar{\bar{w}}}+\frac{\epsilon^s}{\bar{\bar{\theta}}^s}(\bar{\bar{\mathbf{t}}}^s-\mathbf{t}^s):\mathbf{d}^{\bar{\bar{s}}}+\frac{\epsilon^{ws}}{\bar{\bar{\theta}}^{ws}}[\mathbf{t}^{\overline{\bar{ws}}}-\gamma^{ws}(\mathbf{I}-\mathbf{G}^{ws})]:\mathbf{d}^{\overline{\bar{ws}}}-\epsilon^w\mathbf{q}^{\bar{\bar{w}}}\cdot\nabla\left(\frac{1}{\bar{\bar{\theta}}^w}\right)-\epsilon^{ws}\mathbf{q}^{\overline{\bar{ws}}}\cdot\nabla\left(\frac{1}{\bar{\bar{\theta}}^{ws}}\right)$$

$$-\left[\epsilon^s\mathbf{q}^{\bar{\bar{s}}}-\left\langle\left(\mathbf{t}_s-\boldsymbol{\sigma}_s:\frac{\mathbf{C}_s}{j_s}\mathbf{I}\right)\cdot(\mathbf{v}_s-\mathbf{v}^{\bar{s}})\right\rangle_{\Omega_s,\Omega}\right]\cdot\nabla\left(\frac{1}{\bar{\bar{\theta}}^s}\right)+\left(\frac{1}{\bar{\bar{\theta}}^w}-\frac{1}{\bar{\bar{\theta}}^{ws}}\right)[\overset{ws\to w}{Q}+(\mathbf{v}_w^{\overline{\bar{ws}}}-\mathbf{v}^{\bar{s}})\cdot\overset{ws\to w}{\mathbf{T}}-\langle p_w(\mathbf{v}_{ws}-\mathbf{v}^{\bar{s}})\cdot\mathbf{n}_s\rangle_{\Omega_{ws},\Omega}]$$

$$+\left(\frac{1}{\bar{\bar{\theta}}^s}-\frac{1}{\bar{\bar{\theta}}^{ws}}\right)[\overset{ws\to s}{Q}+(\mathbf{v}_s^{\overline{\bar{ws}}}-\mathbf{v}^{\bar{s}})\cdot\overset{ws\to s}{\mathbf{T}}-\langle\mathbf{n}_s\cdot\mathbf{t}_s\cdot\mathbf{n}_s(\mathbf{v}_{ws}-\mathbf{v}^{\bar{s}})\cdot\mathbf{n}_s\rangle_{\Omega_{ws},\Omega}]-\frac{1}{\bar{\bar{\theta}}^w}\{\overset{ws\to w}{\mathbf{T}}+\epsilon^w\rho^w\mathbf{g}^{\bar{w}}+\epsilon^w\rho^w\nabla(\psi^{\bar{w}}+\mu^{\bar{w}}+K_E^{\bar{\bar{w}}})-\nabla(\epsilon^w p^w)$$

$$+\eta^{\bar{\bar{w}}}\nabla\theta^{\bar{\bar{w}}}\}\cdot(\mathbf{v}^{\bar{w}}-\mathbf{v}^{\bar{s}})+\frac{1}{\bar{\bar{\theta}}^{ws}}\{\overset{ws\to w}{\mathbf{T}}+\overset{ws\to s}{\mathbf{T}}-\epsilon^{ws}\rho^{ws}\mathbf{g}^{\overline{\bar{ws}}}-\epsilon^{ws}\rho^{ws}(\mathbf{I}-\mathbf{G}^{ws})\cdot\nabla(\mu^{\overline{\bar{ws}}}+K_E^{\overline{\bar{ws}}}+\psi^{\overline{\bar{ws}}})-\eta^{\overline{\bar{ws}}}(\mathbf{I}-\mathbf{G}^{ws})\cdot\nabla\theta^{\overline{\bar{ws}}}-\nabla\cdot[\epsilon^{ws}\gamma^{ws}(\mathbf{I}$$

$$-\mathbf{G}^{ws})]\}\cdot(\mathbf{v}^{\overline{\bar{ws}}}-\mathbf{v}^{\bar{s}})-\frac{1}{\bar{\bar{\theta}}^s}\langle\mathbf{n}_s\cdot\mathbf{t}_s\cdot\mathbf{I}'\cdot(\mathbf{v}_s-\mathbf{v}^{\bar{s}})\rangle_{\Omega_{ws},\Omega}+\frac{1}{\bar{\bar{\theta}}^s}\left\langle\left[\nabla\cdot\mathbf{t}_s-\nabla\sigma_s:\frac{\mathbf{C}_s}{j_s}\right]\cdot(\mathbf{v}_s-\mathbf{v}^{\bar{s}})\right\rangle_{\Omega_s,\Omega}$$

$$-\frac{1}{\bar{\bar{\theta}}^{ws}}\langle p_w+\mathbf{n}_s\cdot\mathbf{t}_s\cdot\mathbf{n}_s+\gamma_{ws}\nabla'\cdot\mathbf{n}_s-\rho_{ws}\mathbf{g}_{ws}\cdot\mathbf{n}_s\rangle_{\Omega_{ws},\Omega_{ws}}\frac{\mathrm{D}^{\bar{s}}\epsilon^s}{\mathrm{D}t}=\Lambda\geq 0 \tag{40}$$

We will use this SEI by relating it to Eq. (24) and linearizing with respect to the force variables. If we therefore eliminate the higher order terms from Eq. (40) (i.e., those involving products of force variables that go to zero at equilibrium) we obtain the linearized SEI that we will employ to obtain closure relations as

$$+\frac{\epsilon^w}{\bar{\bar{\theta}}^w}(\bar{\bar{\mathbf{t}}}^w+p^w\mathbf{I}):\mathbf{d}^{\bar{\bar{w}}}+\frac{\epsilon^s}{\bar{\bar{\theta}}^s}(\bar{\bar{\mathbf{t}}}^s-\mathbf{t}^s):\mathbf{d}^{\bar{\bar{s}}}+\frac{\epsilon^{ws}}{\bar{\bar{\theta}}^{ws}}[\mathbf{t}^{\overline{\bar{ws}}}-\gamma^{ws}(\mathbf{I}-\mathbf{G}^{ws})]:\mathbf{d}^{\overline{\bar{ws}}}-\epsilon^w\mathbf{q}^{\bar{\bar{w}}}\cdot\nabla\left(\frac{1}{\bar{\bar{\theta}}^w}\right)-\epsilon^{ws}\mathbf{q}^{\overline{\bar{ws}}}\cdot\nabla\left(\frac{1}{\bar{\bar{\theta}}^{ws}}\right)-\epsilon^s\mathbf{q}^{\bar{\bar{s}}}\cdot\nabla\left(\frac{1}{\bar{\bar{\theta}}^s}\right)+\overset{ws\to w}{Q}\left(\frac{1}{\bar{\bar{\theta}}^w}-\frac{1}{\bar{\bar{\theta}}^{ws}}\right)$$

$$+\overset{ws\to s}{Q}\left(\frac{1}{\bar{\bar{\theta}}^s}-\frac{1}{\bar{\bar{\theta}}^{ws}}\right)-\frac{1}{\bar{\bar{\theta}}^w}[\overset{ws\to w}{\mathbf{T}}+\epsilon^w\rho^w\mathbf{g}^{\bar{w}}+\epsilon^w\rho^w\nabla(\psi^{\bar{w}}+\mu^{\bar{w}})-\nabla(\epsilon^w p^w)]\cdot(\mathbf{v}^{\bar{w}}-\mathbf{v}^{\bar{s}})$$

$$+\frac{1}{\bar{\bar{\theta}}^{ws}}\{\overset{ws\to w}{\mathbf{T}}+\overset{ws\to s}{\mathbf{T}}-\epsilon^{ws}\rho^{ws}\mathbf{g}^{\overline{\bar{ws}}}-\epsilon^{ws}\rho^{ws}(\mathbf{I}-\mathbf{G}^{ws})\cdot\nabla(\mu^{\overline{\bar{ws}}}+\psi^{\overline{\bar{ws}}})-\nabla\cdot[\epsilon^{ws}\gamma^{ws}(\mathbf{I}-\mathbf{G}^{ws})]\}\cdot(\mathbf{v}^{\overline{\bar{ws}}}-\mathbf{v}^{\bar{s}})$$

$$-\frac{1}{\bar{\bar{\theta}}^{ws}}\langle p_w+\mathbf{n}_s\cdot\mathbf{t}_s\cdot\mathbf{n}_s+\gamma_{ws}\nabla'\cdot\mathbf{n}_s-\rho_{ws}\mathbf{g}_{ws}\cdot\mathbf{n}_s\rangle_{\Omega_{ws},\Omega_{ws}}\frac{\mathrm{D}^{\bar{s}}\epsilon^s}{\mathrm{D}t}=\Lambda\geq 0 \tag{41}$$

In this equation, each term consists of a flux followed by its conjugate force.

4 Closed Equations

An objective of this work is to produce closed TCAT models for heat transport in a porous medium system. One aspect of the problem is to make use of coupling between processes in forming Onsager-like closure relations. For example, $\epsilon^w\mathbf{q}^{\bar{\bar{w}}}$ could be expressed as a linear function of each of the temperature gradients and of the relative velocities. This coupling can be important in instances when the gradients or velocities are large. Here, the simpler case will be considered where the coupling between processes can be neglected. Thus, the linearization will assume that only the conjugate flux-force relation need be considered. One exception to this choice is that the term designated $\overset{ws\to\kappa}{Q}$ accounts for heat transfer plus work. This must be accounted for in the closure process. We will consider two different cases. In the first case, the temperatures of the phases and interface will be allowed to be different. In the second case, a single temperature will be assumed to characterize the system at all macroscale locations in space. In the heat transfer literature, these two cases are often termed the two equation or local thermal nonequilibrium model and the single equation or local thermal equilibrium model, respectively.

4.1 Linearized Closure Relations Without Coupling. At the microscale, the stress is modeled as being related to the rate of strain (e.g., for a Newtonian fluid). At the macroscale, the length scale of the viscous effects is small enough that the stress tensors may be considered to be independent of these strains. In this case, the multipliers of each of the rate of strain tensors, $\mathbf{d}^{\bar{\bar{\alpha}}}$, in Eq. (41) must be zero; and we obtain the closure relations

$$\bar{\bar{\mathbf{t}}}^w+p^w\mathbf{I}=0 \tag{42}$$

$$\bar{\bar{\mathbf{t}}}^s-\mathbf{t}^s=0 \tag{43}$$

$$\mathbf{t}^{\overline{\bar{ws}}}-\gamma^{ws}(\mathbf{I}-\mathbf{G}^{ws})=0 \tag{44}$$

The linearized heat fluxes are all of the same form

$$\mathbf{q}^{\bar{\bar{\alpha}}}=-\hat{\mathbf{K}}_q^{\alpha}\cdot\nabla\left(\frac{1}{\bar{\bar{\theta}}^{\alpha}}\right)\quad\text{for}\quad\alpha\in\{w,s,ws\} \tag{45}$$

where $\hat{\mathbf{K}}_q^{\alpha}$ are symmetric, positive, semidefinite, second-rank effective heat conduction tensors that also account for tortuosity and dispersive effects due to velocity fluctuations.

The two expressions for energy exchange between the phases and the interface account for heat transfer and the work of volume change. Therefore, $\overset{ws\to\kappa}{Q}$ will be linearized in terms of both its conjugate force and the force associated with work of volume change to obtain

$$\overset{ws\to\kappa}{Q}=\hat{k}_q^{\kappa}\left(\frac{1}{\bar{\bar{\theta}}^{\kappa}}-\frac{1}{\bar{\bar{\theta}}^{ws}}\right)-\hat{k}_W^{\kappa}\frac{\mathrm{D}^{\bar{s}}\epsilon^{\kappa}}{\mathrm{D}t}\quad\text{for}\quad\kappa\in\{w,s\} \tag{46}$$

where the scalars $\hat{k}_q^{\kappa}$ are non-negative heat transfer coefficients and the fact that $\epsilon^w=1-\epsilon^s$ has been employed.

For momentum transfer involving the w phase, the linearized exchange term is

$$\overset{ws\to w}{\mathbf{T}}+\epsilon^w\rho^w\mathbf{g}^{\bar{w}}+\epsilon^w\rho^w\nabla(\psi^{\bar{w}}+\mu^{\bar{w}})-\nabla(\epsilon^w p^w)=-\hat{\mathbf{R}}^w\cdot(\mathbf{v}^{\bar{w}}-\mathbf{v}^{\bar{s}}) \tag{47}$$

while for the exchange due to interface movement the closed expression is

$$\overset{ws\to w}{\mathbf{T}} + \overset{ws\to s}{\mathbf{T}} - \epsilon^{ws}\rho^{ws}\mathbf{g}^{\overline{ws}} - \epsilon^{ws}\rho^{ws}(\mathbf{I}-\mathbf{G}^{ws})\cdot\nabla(\mu^{\overline{ws}}+\psi^{\overline{ws}}) - \nabla\cdot[\epsilon^{ws}\gamma^{ws}(\mathbf{I}-\mathbf{G}^{ws})] = \hat{\mathbf{R}}^{ws}\cdot(\mathbf{v}^{\overline{ws}}-\mathbf{v}^{\bar{s}}) \tag{48}$$

In these last two equations, $\hat{\mathbf{R}}^{w}$ and $\hat{\mathbf{R}}^{ws}$ are symmetric, positive semidefinite, second-rank flow resistance tensors that simplify to scaled unit tensors under conditions of entity isotropy. The final closure relation involves the balance of forces on the surface of the solid and is linearized to

$$-\langle p_w + \mathbf{n}_s\cdot\mathbf{t}_s\cdot\mathbf{n}_s + \gamma_{ws}\nabla'\cdot\mathbf{n}_s - \rho_{ws}\mathbf{g}_{ws}\cdot\mathbf{n}_s\rangle_{\Omega_{ws},\Omega_{ws}} = \hat{c}\frac{\mathrm{D}^{\bar{s}}\epsilon^{s}}{\mathrm{D}t} \tag{49}$$

where $\hat{c}$ is a non-negative compressibility parameter.

4.2 Momentum Equation Closure. Closure relations (42) and (47) are employed to eliminate $\mathbf{t}^{\bar{\bar{w}}}$ and $\overset{ws\to w}{\mathbf{T}}$ from the momentum equation for the w phase to obtain [2]

$$\frac{\mathrm{D}^{\bar{w}}(\epsilon^{w}\rho^{w}\mathbf{v}^{\bar{w}})}{\mathrm{D}t} + \epsilon^{w}\rho^{w}\mathbf{v}^{\bar{w}}\mathbf{I}:\mathbf{d}^{\bar{\bar{w}}} + \hat{\mathbf{R}}^{w}\cdot(\mathbf{v}^{\bar{w}}-\mathbf{v}^{\bar{s}}) + \epsilon^{w}\rho^{w}\nabla(\psi^{\bar{w}}+\mu^{\bar{w}}) = 0 \tag{50}$$

When the local and advective acceleration terms are negligible, this equation simplifies to a Darcy-like equation

$$\hat{\mathbf{R}}^{w}\cdot(\mathbf{v}^{\bar{w}}-\mathbf{v}^{\bar{s}}) + \epsilon^{w}\rho^{w}\nabla(\psi^{\bar{w}}+\mu^{\bar{w}}) = 0 \tag{51}$$

Further manipulations with this equation for use in analyzing flow in porous media, including the solid matrix compression, the form of the stress tensor for the elastic solid, and the use of this fluid phase momentum equation with the mass conservation equations, have been presented [2]. Since the goal of the present exposition is to focus on the energy equation, these issues relating to flow will not be considered further. Instead, we turn our attention to closure conditions for total energy.

4.3 Energy Equation Closure: Entity-Based Temperatures. From the general conservation equation expression in Eq. (2) and with the specific information in the table and for the exchange terms, the total energy conservation equations for the w and s phases are

$$\frac{\mathrm{D}^{\bar{\alpha}}\left[E^{\bar{\bar{\alpha}}} + \epsilon^{\alpha}\rho^{\alpha}\left(\frac{1}{2}\mathbf{v}^{\bar{\alpha}}\cdot\mathbf{v}^{\bar{\alpha}} + K_E^{\bar{\bar{\alpha}}} + \psi^{\bar{\alpha}}\right)\right]}{\mathrm{D}t} + \left[E^{\bar{\bar{\alpha}}} + \epsilon^{\alpha}\rho^{\alpha}\left(\frac{1}{2}\mathbf{v}^{\bar{\alpha}}\cdot\mathbf{v}^{\bar{\alpha}} + K_E^{\bar{\bar{\alpha}}} + \psi^{\bar{\alpha}}\right)\right]\mathbf{I}:\mathbf{d}^{\bar{\bar{\alpha}}} - \nabla\cdot(\epsilon^{\alpha}\mathbf{t}^{\bar{\bar{\alpha}}}\cdot\mathbf{v}^{\bar{\alpha}} + \epsilon^{\alpha}\mathbf{q}^{\bar{\bar{\alpha}}}) - \epsilon^{\alpha}h^{\alpha} - \frac{1}{\epsilon^{ws}\rho_{\alpha}^{ws}}\left[E_{\alpha}^{\overline{\overline{ws}}} + \epsilon^{ws}\rho_{\alpha}^{ws}\left(\frac{1}{2}\mathbf{v}_{\alpha}^{\overline{ws}}\cdot\mathbf{v}_{\alpha}^{\overline{ws}} + K_{E\alpha}^{\overline{\overline{ws}}} + \psi_{\alpha}^{\overline{ws}}\right)\right]\overset{ws\to\alpha}{M} - \mathbf{v}_{\alpha}^{\overline{ws}}\cdot\overset{ws\to\alpha}{\mathbf{T}} - \overset{ws\to\alpha}{Q} = 0 \quad \text{for } \alpha\in\{w,s\} \tag{52}$$

For simplicity, we will consider the case where the energy transport in the interface between phases is small so that the ws energy equation need not be included in the analysis. We note in passing that it may be convenient to work with the internal energy equation in a particular application. This equation, denoted $\mathcal{U}^{\alpha}$, is obtained from the energy, momentum, and mass equations of a phase as

$$\mathcal{U}^{\alpha} = \mathcal{E}^{\alpha} - \mathbf{v}^{\bar{\alpha}}\cdot\boldsymbol{\mathcal{P}}^{\alpha} + \tfrac{1}{2}\mathbf{v}^{\bar{\alpha}}\cdot\mathbf{v}^{\bar{\alpha}}\mathcal{M}^{\alpha} - \mathcal{G}^{\alpha} = 0 \quad \text{for } \alpha\in\{w,s\} \tag{53}$$

where $\mathcal{G}$ is the identity that applies when the body force potential is due to gravitational effects and the correlation between gravitational potential on the interface with the phase velocities at the interfaces is negligible such that

$$\mathcal{G}^{\alpha} = \epsilon^{\alpha}\rho^{\alpha}\mathbf{g}^{\bar{\alpha}}\cdot\mathbf{v}^{\bar{\alpha}} + \frac{\mathrm{D}^{\bar{\alpha}}(\epsilon^{\alpha}\rho^{\alpha}\psi^{\bar{\alpha}})}{\mathrm{D}t} + \epsilon^{\alpha}\rho^{\alpha}\psi^{\bar{\alpha}}\mathbf{I}:\mathbf{d}^{\bar{\bar{\alpha}}} - \psi_{\alpha}^{\overline{ws}}\overset{ws\to\alpha}{M} = 0 \tag{54}$$

Thus, the internal energy equation may be expanded out to

$$\mathcal{U}^{\alpha} = \frac{\mathrm{D}^{\bar{\alpha}}(E^{\bar{\bar{\alpha}}} + \epsilon^{\alpha}\rho^{\alpha}K_E^{\bar{\bar{\alpha}}})}{\mathrm{D}t} + (E^{\bar{\bar{\alpha}}} + \epsilon^{\alpha}\rho^{\alpha}K_E^{\bar{\bar{\alpha}}})\mathbf{I}:\mathbf{d}^{\bar{\bar{\alpha}}} - \epsilon^{\alpha}\mathbf{t}^{\bar{\bar{\alpha}}}:\mathbf{d}^{\bar{\bar{\alpha}}} - \nabla\cdot(\epsilon^{\alpha}\mathbf{q}^{\bar{\bar{\alpha}}}) - \epsilon^{\alpha}h^{\alpha} - \left[\frac{E_{\alpha}^{\overline{\overline{ws}}}}{\epsilon^{ws}\rho_{\alpha}^{ws}} + \frac{1}{2}(\mathbf{v}^{\bar{\alpha}}-\mathbf{v}_{\alpha}^{\overline{ws}})\cdot(\mathbf{v}^{\bar{\alpha}}-\mathbf{v}_{\alpha}^{\overline{ws}}) + K_{E\alpha}^{\overline{\overline{ws}}}\right]\overset{ws\to\alpha}{M} + (\mathbf{v}^{\bar{\alpha}}-\mathbf{v}_{\alpha}^{\overline{ws}})\cdot\overset{ws\to\alpha}{\mathbf{T}} - \overset{ws\to\alpha}{Q} = 0 \quad \text{for } \alpha\in\{w,s\} \tag{55}$$

The velocities of the phases averaged over the solid-fluid interface surface, $\mathbf{v}_{w}^{\overline{ws}}$ and $\mathbf{v}_{s}^{\overline{ws}}$, are small and will be assumed to be equal to the macroscale solid-phase velocity itself, $\mathbf{v}^{\bar{s}}$. Additionally, we will assume that mass transfer between phases is negligible and that the subscale kinetic energy term $K_E^{\bar{\bar{\alpha}}}$ is negligible. With these simplifications, Eq. (55) becomes

$$\mathcal{U}^{\alpha} = \frac{\mathrm{D}^{\bar{\alpha}}E^{\bar{\bar{\alpha}}}}{\mathrm{D}t} + (E^{\bar{\bar{\alpha}}}\mathbf{I} - \epsilon^{\alpha}\mathbf{t}^{\bar{\bar{\alpha}}}):\mathbf{d}^{\bar{\bar{\alpha}}} - \nabla\cdot(\epsilon^{\alpha}\mathbf{q}^{\bar{\bar{\alpha}}}) - \epsilon^{\alpha}h^{\alpha} + (\mathbf{v}^{\bar{\alpha}}-\mathbf{v}^{\bar{s}})\cdot\overset{ws\to\alpha}{\mathbf{T}} - \overset{ws\to\alpha}{Q} = 0 \quad \text{for } \alpha\in\{w,s\} \tag{56}$$

With the interface properties not being considered, Eqs. (47) and (48) may be combined to write

$$\overset{ws\to\alpha}{\mathbf{T}} = e_{w\alpha}[-\epsilon^{w}\rho^{w}\mathbf{g}^{\bar{w}} - \epsilon^{w}\rho^{w}\nabla(\psi^{\bar{w}}+\mu^{\bar{w}}) + \nabla(\epsilon^{w}p^{w}) - \hat{\mathbf{R}}^{w}\cdot(\mathbf{v}^{\bar{w}}-\mathbf{v}^{\bar{s}})] \quad \text{for } \alpha\in\{w,s\} \tag{57}$$

where $e_{w\alpha}=1$ when $\alpha=w$ and $e_{w\alpha}=-1$ when $\alpha=s$. Elimination of $\overset{ws\to\alpha}{\mathbf{T}}$ and $\overset{ws\to\alpha}{Q}$ from Eq. (56) using Eqs. (46) and (57) and also employing the flow model of Eq. (51) give

$$\mathcal{U}^{\alpha} = \frac{\mathrm{D}^{\bar{\alpha}}E^{\bar{\bar{\alpha}}}}{\mathrm{D}t} + (E^{\bar{\bar{\alpha}}}\mathbf{I} - \epsilon^{\alpha}\mathbf{t}^{\bar{\bar{\alpha}}}):\mathbf{d}^{\bar{\bar{\alpha}}} - \nabla\cdot(\epsilon^{\alpha}\mathbf{q}^{\bar{\bar{\alpha}}}) - \epsilon^{\alpha}h^{\alpha} + (\mathbf{v}^{\bar{\alpha}}-\mathbf{v}^{\bar{s}})\cdot[-\epsilon^{w}\rho^{w}\mathbf{g}^{\bar{w}} + \nabla(\epsilon^{w}p^{w})] - \hat{k}_{q}^{\alpha}\left(\frac{1}{\theta^{\bar{\bar{\alpha}}}} - \frac{1}{\theta^{\overline{\overline{ws}}}}\right) + \hat{k}_{W}^{\alpha}\frac{\mathrm{D}^{\bar{s}}\epsilon^{\alpha}}{\mathrm{D}t} = 0 \quad \text{for } \alpha\in\{w,s\} \tag{58}$$

The Appendix indicates that the parameter $\hat{k}_{W}^{\alpha}$ can be specified as

$$\hat{k}_{W}^{\alpha} = -\langle\mathbf{n}_{\alpha}\cdot\mathbf{t}_{\alpha}\cdot\mathbf{n}_{\alpha}\rangle_{\Omega_{ws},\Omega_{ws}} \tag{59}$$

With this condition and a rearrangement of $(\mathbf{v}^{\bar{\alpha}}-\mathbf{v}^{\bar{s}})\cdot[\nabla(\epsilon^{w}p^{w})]$ to a difference in material derivatives yields the internal energy equation

$$\mathcal{U}^{\alpha} = \frac{\mathrm{D}^{\bar{\alpha}}E^{\bar{\bar{\alpha}}}}{\mathrm{D}t} + \frac{\mathrm{D}^{\bar{\alpha}}(\epsilon^{w}p^{w})}{\mathrm{D}t} - \frac{\mathrm{D}^{\bar{s}}(\epsilon^{w}p^{w})}{\mathrm{D}t} - \langle\mathbf{n}_{\alpha}\cdot\mathbf{t}_{\alpha}\cdot\mathbf{n}_{\alpha}\rangle_{\Omega_{ws},\Omega_{ws}}\frac{\mathrm{D}^{\bar{s}}\epsilon^{\alpha}}{\mathrm{D}t} + (E^{\bar{\bar{\alpha}}}\mathbf{I} - \epsilon^{\alpha}\mathbf{t}^{\bar{\bar{\alpha}}}):\mathbf{d}^{\bar{\bar{\alpha}}} - \nabla\cdot(\epsilon^{\alpha}\mathbf{q}^{\bar{\bar{\alpha}}}) - \epsilon^{\alpha}h^{\alpha} - \epsilon^{w}\rho^{w}\mathbf{g}^{\bar{w}}\cdot(\mathbf{v}^{\bar{\alpha}}-\mathbf{v}^{\bar{s}}) - \hat{k}_{q}^{\alpha}\left(\frac{1}{\theta^{\bar{\bar{\alpha}}}} - \frac{1}{\theta^{\overline{\overline{ws}}}}\right) = 0 \quad \text{for } \alpha\in\{w,s\} \tag{60}$$

We make use of Eqs. (42) and (45) in Eq. (60) with $\alpha=w$ to obtain the internal energy equation for the w phase

$$\mathcal{U}^w = \frac{\mathrm{D}^{\bar{w}}(E^{\bar{\bar{w}}} + \epsilon^w p^w)}{\mathrm{D}t} - \epsilon^w \frac{\mathrm{D}^{\bar{w}} p^w}{\mathrm{D}t} - (p^w + \langle \mathbf{n}_w \cdot \mathbf{t}_w \cdot \mathbf{n}_w \rangle_{\Omega_{ws},\Omega_{ws}}) \frac{\mathrm{D}^{\bar{s}} \epsilon^w}{\mathrm{D}t} + (E^{\bar{\bar{w}}} + \varepsilon^w p^w)\mathbf{I}:\mathbf{d}^{\bar{\bar{w}}} + \nabla \cdot \left[\epsilon^w \hat{\mathbf{K}}_q^w \cdot \nabla \left(\frac{1}{\theta^{\bar{\bar{w}}}} \right) \right] - \epsilon^w h^w + \epsilon^w (\nabla p^w - \rho^w \mathbf{g}^{\bar{w}}) \cdot (\mathbf{v}^{\bar{w}} - \mathbf{v}^{\bar{s}}) - \hat{k}_q^w \left(\frac{1}{\theta^{\bar{\bar{w}}}} - \frac{1}{\theta^{\bar{\bar{w}}\bar{\bar{s}}}} \right) = 0 \tag{61}$$

The term involving $\mathbf{v}^{\bar{w}} - \mathbf{v}^{\bar{s}}$ is second order in velocity and thus can be eliminated. Additionally, the macroscale enthalpy of w phase per total volume is defined as

$$H^{\bar{\bar{w}}} = E^{\bar{\bar{w}}} + \epsilon^w p^w \tag{62}$$

Finally, let us assume that the microscale stress tensor is represented as

$$\mathbf{t}_w = -p_w \mathbf{I} + \boldsymbol{\tau}_w \tag{63}$$

where $\boldsymbol{\tau}_w$ accounts for the frictional forces. Then Eq. (61) may be written conveniently as

$$\mathcal{U}^w = \frac{\mathrm{D}^{\bar{w}} H^{\bar{\bar{w}}}}{\mathrm{D}t} + H^{\bar{\bar{w}}}\mathbf{I}:\mathbf{d}^{\bar{\bar{w}}} - \epsilon^w \frac{\mathrm{D}^{\bar{w}} p^w}{\mathrm{D}t} - (p^w - p_w^{ws} + \langle \mathbf{n}_w \cdot \boldsymbol{\tau}_w \cdot \mathbf{n}_w \rangle_{\Omega_{ws},\Omega_{ws}}) \frac{\mathrm{D}^{\bar{s}} \epsilon^w}{\mathrm{D}t} + \nabla \cdot \left[\epsilon^w \hat{\mathbf{K}}_q^w \cdot \nabla \left(\frac{1}{\theta^{\bar{\bar{w}}}} \right) \right] - \epsilon^w h^w - \hat{k}_q^w \left(\frac{1}{\theta^{\bar{\bar{w}}}} - \frac{1}{\theta^{\bar{\bar{w}}\bar{\bar{s}}}} \right) = 0 \tag{64}$$

Usually, the term involving the material derivative of ϵ^w is absent. This may often be a reasonable approximation since the w phase pressure averaged over the solid surface, p_w^{ws}, may approximately equal the w phase pressure averaged over the phase, p^w, and the component of the frictional stress indicated is also typically small. However, without averaging the equations, the presence of this term and its possible importance is easily overlooked.

For the solid phase, the internal energy equation provided by Eq. (60) with the restrictions mentioned becomes

$$\mathcal{U}^s = \frac{\mathrm{D}^{\bar{s}} E^{\bar{\bar{s}}}}{\mathrm{D}t} - \langle \mathbf{n}_s \cdot \mathbf{t}_s \cdot \mathbf{n}_s \rangle_{\Omega_{ws},\Omega_{ws}} \frac{\mathrm{D}^{\bar{s}} \epsilon^s}{\mathrm{D}t} + (E^{\bar{\bar{s}}}\mathbf{I} - \epsilon^s \mathbf{t}^{\bar{\bar{s}}}):\mathbf{d}^{\bar{\bar{s}}} + \nabla \cdot \left[\epsilon^s \hat{\mathbf{K}}_q^s \cdot \nabla \left(\frac{1}{\theta^{\bar{\bar{s}}}} \right) \right] - \epsilon^s h^s - \hat{k}_q^s \left(\frac{1}{\theta^{\bar{\bar{s}}}} - \frac{1}{\theta^{\bar{\bar{w}}\bar{\bar{s}}}} \right) = 0 \tag{65}$$

The enthalpy of a solid is defined as

$$H^{\bar{\bar{s}}} = E^{\bar{\bar{s}}} - \epsilon^s \boldsymbol{\sigma}^{\bar{\bar{s}}}:\frac{\mathbf{C}^s}{j^s} \tag{66}$$

Thus the solid-phase thermal energy equation may be written in terms of enthalpy as

$$\mathcal{U}^s = \frac{\mathrm{D}^{\bar{s}} H^{\bar{\bar{s}}}}{\mathrm{D}t} + H^{\bar{\bar{s}}}\mathbf{I}:\mathbf{d}^{\bar{\bar{s}}} + \frac{\mathrm{D}^{\bar{s}}}{\mathrm{D}t}\left(\epsilon^s \boldsymbol{\sigma}^{\bar{\bar{s}}}:\frac{\mathbf{C}^s}{j^s} \right) - \langle \mathbf{n}_s \cdot \mathbf{t}_s \cdot \mathbf{n}_s \rangle_{\Omega_{ws},\Omega_{ws}} \frac{\mathrm{D}^{\bar{s}} \epsilon^s}{\mathrm{D}t} + \left[\left(\epsilon^s \boldsymbol{\sigma}^{\bar{\bar{s}}}:\frac{\mathbf{C}^s}{j^s} \right)\mathbf{I} - \varepsilon^s \mathbf{t}^{\bar{\bar{s}}} \right]:\mathbf{d}^{\bar{\bar{s}}} + \nabla \cdot \left[\epsilon^s \hat{\mathbf{K}}_q^s \cdot \nabla \left(\frac{1}{\theta^{\bar{\bar{s}}}} \right) \right] - \epsilon^s h^s - \hat{k}_q^s \left(\frac{1}{\theta^{\bar{\bar{s}}}} - \frac{1}{\theta^{\bar{\bar{w}}\bar{\bar{s}}}} \right) = 0 \tag{67}$$

An identity for the material derivative of $\epsilon^s \boldsymbol{\sigma}^{\bar{\bar{s}}}:\mathbf{C}^s/j^s$ can be found in Appendix A of Ref. [7]. With some rearrangement of this identity, we obtain

$$\frac{\mathrm{D}^{\bar{s}}}{\mathrm{D}t}\left(\epsilon^s \boldsymbol{\sigma}^{\bar{\bar{s}}}:\frac{\mathbf{C}^s}{j^s} \right) - \langle \mathbf{n}_s \cdot \mathbf{t}_s \cdot \mathbf{n}_s \rangle_{\Omega_{ws},\Omega_{ws}} \frac{\mathrm{D}^{\bar{s}} \epsilon^s}{\mathrm{D}t} + \left[\left(\epsilon^s \boldsymbol{\sigma}^{\bar{\bar{s}}}:\frac{\mathbf{C}^s}{j^s} \right)\mathbf{I} - \epsilon^s \mathbf{t}^{\bar{\bar{s}}} \right]:\mathbf{d}^{\bar{\bar{s}}} = \epsilon^s \frac{\mathbf{C}^s}{j^s}:\frac{\mathrm{D}^{\bar{s}} \boldsymbol{\sigma}^{\bar{\bar{s}}}}{\mathrm{D}t} + \left\langle \frac{\mathbf{C}_s}{j_s}:\frac{\mathrm{D}^{\bar{s}}(\boldsymbol{\sigma}_s - \boldsymbol{\sigma}^{\bar{\bar{s}}})}{\mathrm{D}t} \right\rangle_{\Omega_s,\Omega} + \langle (\mathbf{n}_s \cdot \mathbf{t}_s \cdot \mathbf{n}_s - \langle \mathbf{n}_s \cdot \mathbf{t}_s \cdot \mathbf{n}_s \rangle_{\Omega_{ws},\Omega_{ws}})\mathbf{n}_s \cdot (\mathbf{v}_s - \mathbf{v}^{\bar{s}}) \rangle_{\Omega_{ws},\Omega} + \langle \mathbf{n}_s \cdot \mathbf{t}_s \cdot \mathbf{I}' \cdot (\mathbf{v}_s - \mathbf{v}^{\bar{s}}) \rangle_{\Omega_{ws},\Omega} - \left\langle \left\{ \nabla \cdot \mathbf{t}_s - \nabla \boldsymbol{\sigma}_s:\frac{\mathbf{C}_s}{j_s} \right\} \cdot (\mathbf{v}_s - \mathbf{v}^{\bar{s}}) \right\rangle_{\Omega_s,\Omega} + \nabla \cdot \left\langle \left[\mathbf{t}_s - \boldsymbol{\sigma}_s:\frac{\mathbf{C}_s}{j_s}\mathbf{I} \right] \cdot (\mathbf{v}_s - \mathbf{v}^{\bar{s}}) \right\rangle_{\Omega_s,\Omega} \tag{68}$$

The last four terms in this identity will be neglected for the present case because, in the first two terms, the multipliers of the velocity difference in the averages over the ws interface are negligible; and, in the last two terms, the average of the velocity difference over the solid phase will also be small. With these terms eliminated, substitution of Eq. (68) into Eq. (67) yields

$$\mathcal{U}^s = \frac{\mathrm{D}^{\bar{s}} H^{\bar{\bar{s}}}}{\mathrm{D}t} + H^{\bar{\bar{s}}}\mathbf{I}:\mathbf{d}^{\bar{\bar{s}}} + \epsilon^s \frac{\mathbf{C}^s}{j^s}:\frac{\mathrm{D}^{\bar{s}} \boldsymbol{\sigma}^{\bar{\bar{s}}}}{\mathrm{D}t} + \left\langle \frac{\mathbf{C}_s}{j_s}:\frac{\mathrm{D}^{\bar{s}}(\boldsymbol{\sigma}_s - \boldsymbol{\sigma}^{\bar{\bar{s}}})}{\mathrm{D}t} \right\rangle_{\Omega_s,\Omega} + \nabla \cdot \left[\epsilon^s \hat{\mathbf{K}}_q^s \cdot \nabla \left(\frac{1}{\theta^{\bar{\bar{s}}}} \right) \right] - \epsilon^s h^s - \hat{k}_q^s \left(\frac{1}{\theta^{\bar{\bar{s}}}} - \frac{1}{\theta^{\bar{\bar{w}}\bar{\bar{s}}}} \right) = 0 \tag{69}$$

Equations (64) and (69) can be solved together when thermodynamic information is available for the two phases. Additionally, since the interface properties are being neglected, the heat transferred between phases must be preserved with

$$\overset{ws\to w}{Q} + \overset{ws\to s}{Q} = 0 \tag{70}$$

This condition may be used to solve for $\theta^{\bar{\bar{w}}\bar{\bar{s}}}$ by making use of the closure conditions of Eq. (46) subject to Eq. (59) and the fact that $\epsilon^w + \epsilon^s = 1$. Substitution of the closure conditions into Eq. (70) gives

$$\hat{k}_q^w \left(\frac{1}{\theta^{\bar{\bar{w}}}} - \frac{1}{\theta^{\bar{\bar{w}}\bar{\bar{s}}}} \right) + \hat{k}_q^s \left(\frac{1}{\theta^{\bar{\bar{s}}}} - \frac{1}{\theta^{ws}} \right) + (\langle \mathbf{n}_s \cdot \mathbf{t}_s \cdot \mathbf{n}_s \rangle_{\Omega_{ws},\Omega_{ws}} - \langle \mathbf{n}_w \cdot \mathbf{t}_w \cdot \mathbf{n}_w \rangle_{\Omega_{ws},\Omega_{ws}}) \frac{\mathrm{D}^{\bar{s}} \epsilon^s}{\mathrm{D}t} = 0 \tag{71}$$

such that the solution for $1/\theta^{\bar{\bar{w}}\bar{\bar{s}}}$ is

$$\frac{1}{\theta^{\bar{\bar{w}}\bar{\bar{s}}}} = \frac{1}{\hat{k}_q^w + \hat{k}_q^s} \left[\frac{\hat{k}_q^w}{\theta^{\bar{\bar{w}}}} + \frac{\hat{k}_q^s}{\theta^{\bar{\bar{s}}}} + \langle \mathbf{n}_s \cdot (\mathbf{t}_s - \mathbf{t}_w) \cdot \mathbf{n}_s \rangle_{\Omega_{ws},\Omega_{ws}} \frac{\mathrm{D}^{\bar{s}} \epsilon^s}{\mathrm{D}t} \right] \tag{72}$$

We will assume that any discontinuity in the normal stress multiplied by the rate of change in porosity makes a negligibly small contribution to $\theta^{\bar{\bar{w}}\bar{\bar{s}}}$ so that the last term in this equation may be neglected. We will also ignore the body source term for energy (e.g., radiation effects) so that h^w and h^s are eliminated. Finally, we introduce a thermal conductivity scaled by the square of the temperature such that

$$\hat{\mathbf{K}}_\theta^\alpha = \frac{\hat{\mathbf{K}}_q^\alpha}{\theta^{\bar{\alpha}2}} \tag{73}$$

Thus the equations of interest for modeling the thermal behavior of the w and s phases independently are, respectively,

$$\mathcal{U}^w = \frac{\mathrm{D}^{\bar{w}}H^{\bar{\bar{w}}}}{\mathrm{D}t} + H^{\bar{\bar{w}}}\mathbf{I}:\mathbf{d}^{\bar{\bar{w}}} - \epsilon^w\frac{\mathrm{D}^{\bar{w}}p^w}{\mathrm{D}t} - \nabla\cdot(\epsilon^w\hat{\mathbf{K}}^w_\theta\cdot\nabla\theta^{\bar{\bar{w}}}) - \left(\frac{1}{\hat{k}^w_q}+\frac{1}{\hat{k}^s_q}\right)^{-1}\left(\frac{1}{\theta^{\bar{\bar{w}}}}-\frac{1}{\theta^{\bar{\bar{s}}}}\right) = 0 \tag{74}$$

and

$$\mathcal{U}^s = \frac{\mathrm{D}^{\bar{s}}H^{\bar{\bar{s}}}}{\mathrm{D}t} + H^{\bar{\bar{s}}}\mathbf{I}:\mathbf{d}^{\bar{\bar{s}}} + \epsilon^s\frac{\mathbf{C}^s}{j^s}:\frac{\mathrm{D}^{\bar{s}}\boldsymbol{\sigma}^{\bar{\bar{s}}}}{\mathrm{D}t} + \left\langle \frac{\mathbf{C}_s}{j_s}:\frac{\mathrm{D}^{\bar{s}}(\boldsymbol{\sigma}_s-\boldsymbol{\sigma}^{\bar{\bar{s}}})}{\mathrm{D}t}\right\rangle_{\Omega_s,\Omega} - \nabla\cdot(\epsilon^s\hat{\mathbf{K}}^s_\theta\cdot\nabla\theta^{\bar{\bar{s}}}) - \left(\frac{1}{\hat{k}^w_q}+\frac{1}{\hat{k}^s_q}\right)^{-1}\left(\frac{1}{\theta^{\bar{\bar{s}}}}-\frac{1}{\theta^{\bar{\bar{w}}}}\right) = 0 \tag{75}$$

It is common to express these two equations in terms of differentials in temperature. With the TCAT approach, this differential can be obtained by integrating the differential expression for microscale enthalpy to obtain a differential expression in terms of macroscale variables. This procedure has been explained previously [5–7] so the full derivation will not be presented here. The result of averaging the microscale representations of the differential of water phase enthalpy is

$$\frac{\mathrm{D}^{\bar{w}}H^{\bar{\bar{w}}}}{\mathrm{D}t} + H^{\bar{\bar{w}}}\mathbf{I}:\mathbf{d}^{\bar{\bar{w}}} - \frac{H^{\bar{\bar{w}}}}{\epsilon^w\rho^w}\overset{ws\to w}{M} = \epsilon^w\rho^w C_p^{\bar{w}}\frac{\mathrm{D}^{\bar{w}}\theta^{\bar{\bar{w}}}}{\mathrm{D}t} + \epsilon^w(1-\beta^{\bar{\bar{w}}}\theta^{\bar{\bar{w}}})\frac{\mathrm{D}^{\bar{w}}p^w}{\mathrm{D}t} - \left\langle \rho_w\frac{\mathrm{D}^{\bar{w}}}{\mathrm{D}t}\left(\frac{H_w}{\rho_w}-\frac{H^{\bar{\bar{w}}}}{\epsilon^w\rho^w}\right) - \rho_w C_{pw}\frac{\mathrm{D}^{\bar{w}}(\theta_w-\theta^{\bar{\bar{w}}})}{\mathrm{D}t} - (1-\beta_w\theta_w)\frac{\mathrm{D}^{\bar{w}}(p_w-p^w)}{\mathrm{D}t}\right\rangle_{\Omega_w,\Omega} \tag{76}$$

where β_w and $\beta^{\bar{\bar{w}}}$ are the microscopic and macroscopic coefficients of thermal expansion, respectively, and C_{pw} and $C_p^{\bar{w}}$ are the microscale and mass averaged heat capacities. For the solid phase, averaging of the microscale differential of solid-phase enthalpy yields

$$\frac{\mathrm{D}^{\bar{w}}H^{\bar{\bar{s}}}}{\mathrm{D}t} + H^{\bar{\bar{s}}}\mathbf{I}:\mathbf{d}^{\bar{\bar{s}}} - \frac{H^{\bar{\bar{s}}}}{\epsilon^s\rho^s}\overset{ws\to s}{M} = \epsilon^s\rho^s C_p^{\bar{s}}\frac{\mathrm{D}^{\bar{s}}\theta^{\bar{\bar{s}}}}{\mathrm{D}t} - \frac{\epsilon^s}{j^s}(\mathbf{C}^s-\boldsymbol{\beta}^{\bar{\bar{s}}}\theta^{\bar{\bar{s}}}):\frac{\mathrm{D}^{\bar{s}}\boldsymbol{\sigma}^{\bar{\bar{s}}}}{\mathrm{D}t} - \left\langle \rho_s\frac{\mathrm{D}^{\bar{s}}}{\mathrm{D}t}\left(\frac{H_s}{\rho_s}-\frac{H^{\bar{\bar{s}}}}{\epsilon^s\rho^s}\right) - \rho_s C_{ps}\frac{\mathrm{D}^{\bar{s}}(\theta_s-\theta^{\bar{\bar{s}}})}{\mathrm{D}t} + \frac{1}{j_s}(\mathbf{C}_s-\boldsymbol{\beta}_s\theta_s):\frac{\mathrm{D}^{\bar{s}}(\boldsymbol{\sigma}_s-\boldsymbol{\sigma}^{\bar{\bar{s}}})}{\mathrm{D}t}\right\rangle_{\Omega_s,\Omega} \tag{77}$$

where

$$\boldsymbol{\beta}_s = \left(\frac{\partial\mathbf{C}_s}{\partial\theta_s}\right)_{\boldsymbol{\sigma}_s,\mathbb{M}} \tag{78}$$

and $\boldsymbol{\beta}^{\bar{\bar{s}}}$ is the macroscale tensor value of this coefficient of thermal expansion.

Note that by averaging the microscale relations rather than simply hypothesizing some sort of macroscale formula, we are able to retain a connection between microscale and macroscale variables. The price for this feature is the presence of the terms that remain in the averaging operators in Eqs. (76) and (77). These terms account for the absence of local equilibrium at the macroscale. Typically, these terms are implicitly overlooked in the energy equation formulation. Here, we will substitute the respective derivatives of the enthalpy into Eqs. (74) and (75). For the *w* entity, the resulting thermal energy equation is

$$\mathcal{U}^w = \epsilon^w\rho^w C_p^{\bar{w}}\frac{\mathrm{D}^{\bar{w}}\theta^{\bar{\bar{w}}}}{\mathrm{D}t} - \epsilon^w\theta^{\bar{\bar{w}}}\beta^{\bar{\bar{w}}}\frac{\mathrm{D}^{\bar{w}}p^w}{\mathrm{D}t} - \nabla\cdot(\epsilon^w\hat{\mathbf{K}}^w_\theta\cdot\nabla\theta^{\bar{\bar{w}}}) - \left\langle \rho_w\frac{\mathrm{D}^{\bar{w}}}{\mathrm{D}t}\left(\frac{H_w}{\rho_w}-\frac{H^{\bar{\bar{w}}}}{\epsilon^w\rho^w}\right) - \rho_w C_{pw}\frac{\mathrm{D}^{\bar{w}}(\theta_w-\theta^{\bar{\bar{w}}})}{\mathrm{D}t} - (1-\beta_w\theta_w)\frac{\mathrm{D}^{\bar{w}}(p_w-p^w)}{\mathrm{D}t}\right\rangle_{\Omega_w,\Omega} - \left(\frac{1}{\hat{k}^w_q}+\frac{1}{\hat{k}^s_q}\right)^{-1}\left(\frac{1}{\theta^{\bar{\bar{w}}}}-\frac{1}{\theta^{\bar{\bar{s}}}}\right) = 0 \tag{79}$$

The term involving deviations that is in the averaging operator could be important for systems where the dynamics are fast. Here, we will assume that the change in properties is slow enough that these terms are negligible. With this assumption, subject to review depending on the problem under consideration, the energy equation simplifies to

$$\mathcal{U}^w = \epsilon^w\rho^w C_p^{\bar{w}}\frac{\mathrm{D}^{\bar{w}}\theta^{\bar{\bar{w}}}}{\mathrm{D}t} - \epsilon^w\theta^{\bar{\bar{w}}}\beta^{\bar{\bar{w}}}\frac{\mathrm{D}^{\bar{w}}p^w}{\mathrm{D}t} - \nabla\cdot(\epsilon^w\hat{\mathbf{K}}^w_\theta\cdot\nabla\theta^{\bar{\bar{w}}}) - \left(\frac{1}{\hat{k}^w_q}+\frac{1}{\hat{k}^s_q}\right)^{-1}\left(\frac{1}{\theta^{\bar{\bar{w}}}}-\frac{1}{\theta^{\bar{\bar{s}}}}\right) = 0 \tag{80}$$

Next, we substitute Eq. (77) into Eq. (75) and neglect interentity exchange to obtain the thermal energy equation for the solid in the form

$$\mathcal{U}^s = \epsilon^s\rho^s C_p^{\bar{s}}\frac{\mathrm{D}^{\bar{s}}\theta^{\bar{\bar{s}}}}{\mathrm{D}t} + \frac{\epsilon^s}{j^s}\theta^{\bar{\bar{s}}}\boldsymbol{\beta}^{\bar{\bar{s}}}:\frac{\mathrm{D}^{\bar{s}}\boldsymbol{\sigma}^{\bar{\bar{s}}}}{\mathrm{D}t} - \left\langle \rho_s\frac{\mathrm{D}^{\bar{s}}}{\mathrm{D}t}\left(\frac{H_s}{\rho_s}-\frac{H^{\bar{\bar{s}}}}{\epsilon^s\rho^s}\right) - \rho_s C_{ps}\frac{\mathrm{D}^{\bar{s}}(\theta_s-\theta^{\bar{\bar{s}}})}{\mathrm{D}t} - \frac{1}{j_s}\theta_s\boldsymbol{\beta}_s:\frac{\mathrm{D}^{\bar{s}}(\boldsymbol{\sigma}_s-\boldsymbol{\sigma}^{\bar{\bar{s}}})}{\mathrm{D}t}\right\rangle_{\Omega_s,\Omega} - \nabla\cdot(\varepsilon^s\hat{\mathbf{K}}^s_\theta\cdot\nabla\theta^{\bar{\bar{s}}}) - \left(\frac{1}{\hat{k}^w_q}+\frac{1}{\hat{k}^s_q}\right)^{-1}\left(\frac{1}{\theta^{\bar{\bar{s}}}}-\frac{1}{\theta^{\bar{\bar{w}}}}\right) = 0 \tag{81}$$

As with the *w* phase, we will assume that the system dynamics are slow enough that the material derivatives of the deviation terms inside the averaging operator in Eq. (81) can be neglected so that the thermal energy equation for the solid is

$$\mathcal{U}^s = \epsilon^s\rho^s C_p^{\bar{s}}\frac{\mathrm{D}^{\bar{s}}\theta^{\bar{\bar{s}}}}{\mathrm{D}t} + \frac{\epsilon^s}{j^s}\theta^{\bar{\bar{s}}}\boldsymbol{\beta}^{\bar{\bar{s}}}:\frac{\mathrm{D}^{\bar{s}}\boldsymbol{\sigma}^{\bar{\bar{s}}}}{\mathrm{D}t} - \nabla\cdot(\epsilon^s\hat{\mathbf{K}}^s_\theta\cdot\nabla\theta^{\bar{\bar{s}}}) - \left(\frac{1}{\hat{k}^w_q}+\frac{1}{\hat{k}^s_q}\right)^{-1}\left(\frac{1}{\theta^{\bar{\bar{s}}}}-\frac{1}{\theta^{\bar{\bar{w}}}}\right) = 0 \tag{82}$$

In most cases, the velocity of the solid phase is considered to be so small that the material derivatives in Eq. (82) can be replaced with partial time derivatives. Equations (80) and (82) constitute the two-temperature model for temperature in a single-fluid-phase porous media system with heat exchange between entities of a form analogous to Newton's law of cooling.

4.4 Energy Equation Closure: Single Temperature. When the heat transfer between the phases is fast enough that the phases can be considered to be at the same temperature, a single internal energy equation may be used for modeling. This equation is obtained by adding Eqs. (80) and (82) so that the term for heat exchange between the phases cancels, and we obtain

$$\mathcal{U}^w + \mathcal{U}^s = \epsilon^w\rho^w C_p^{\bar{w}}\frac{\mathrm{D}^{\bar{w}}\theta^{\bar{\bar{w}}}}{\mathrm{D}t} + \epsilon^s\rho^s C_p^{\bar{s}}\frac{\mathrm{D}^{\bar{s}}\theta^{\bar{\bar{s}}}}{\mathrm{D}t} - \epsilon^w\theta^{\bar{\bar{w}}}\beta^{\bar{\bar{w}}}\frac{\mathrm{D}^{\bar{w}}p^w}{\mathrm{D}t} + \frac{\epsilon^s}{j^s}\theta^{\bar{\bar{s}}}\boldsymbol{\beta}^{\bar{\bar{s}}}:\frac{\mathrm{D}^{\bar{s}}\boldsymbol{\sigma}^{\bar{\bar{s}}}}{\mathrm{D}t} - \nabla\cdot(\epsilon^w\hat{\mathbf{K}}^w_\theta\cdot\nabla\theta^{\bar{\bar{w}}} + \epsilon^s\hat{\mathbf{K}}^s_\theta\cdot\nabla\theta^{\bar{\bar{s}}}) = 0 \tag{83}$$

Although we could now replace the indicated temperatures in

each phase with a common temperature, it may be useful to examine the system more closely to obtain some insight about the conduction tensors.

The total conduction vector is identified from the last equation as

$$\bar{\bar{\mathbf{q}}}^{T} = \epsilon^{w}\hat{\mathbf{K}}_{\theta}^{w} \cdot \nabla \bar{\bar{\theta^{w}}} + \epsilon^{s}\hat{\mathbf{K}}_{\theta}^{s} \cdot \nabla \bar{\bar{\theta^{s}}} \tag{84}$$

This can be decomposed making use of the orientation tensor to

$$\bar{\bar{\mathbf{q}}}^{T} = \mathbf{G}^{ws} \cdot (\epsilon^{w}\hat{\mathbf{K}}_{\theta}^{w} \cdot \nabla \bar{\bar{\theta^{w}}} + \epsilon^{s}\hat{\mathbf{K}}_{\theta}^{s} \cdot \nabla \bar{\bar{\theta^{s}}}) + (\mathbf{I} - \mathbf{G}^{ws}) \cdot (\epsilon^{w}\hat{\mathbf{K}}_{\theta}^{w} \cdot \nabla \bar{\bar{\theta^{w}}} + \epsilon^{s}\hat{\mathbf{K}}_{\theta}^{s} \cdot \nabla \bar{\bar{\theta^{s}}}) \tag{85}$$

Note that the term in the first set of parentheses is the heat transfer due to flow normal to the interface between the phases. The second term on the right is due to heat transfer in the direction tangent to the interface. We want to write both of these fluxes in terms of a single temperature Θ.

Consider the first term, which accounts for flow normal to layers (e.g., from *w* into *s*). We want to represent this part making use of the fact that for local steady state

$$\mathbf{G}^{ws} \cdot \bar{\bar{\mathbf{q}}}^{T} = \mathbf{G}^{ws} \cdot \bar{\bar{\mathbf{q}}}^{w} = \mathbf{G}^{ws} \cdot \bar{\bar{\mathbf{q}}}^{s} \tag{86}$$

with

$$\mathbf{G}^{ws} \cdot (\epsilon^{w}\hat{\mathbf{K}}_{\theta}^{w} \cdot \nabla \bar{\bar{\theta^{w}}} + \epsilon^{s}\hat{\mathbf{K}}_{\theta}^{s} \cdot \nabla \bar{\bar{\theta^{s}}}) = \mathbf{G}^{ws} \cdot \hat{\mathbf{K}}_{\theta} \cdot \nabla\Theta \tag{87}$$

Additionally, the continuity of the heat being transferred requires

$$\mathbf{G}^{ws} \cdot \hat{\mathbf{K}}_{\theta}^{\alpha} \cdot \nabla \bar{\bar{\theta^{\alpha}}} = \mathbf{G}^{ws} \cdot \hat{\mathbf{K}}_{\theta} \cdot \nabla\Theta \quad \text{for} \quad \alpha \in \{w,s\} \tag{88}$$

We also know that in approximating the two-temperature gradients using a single gradient in the direction across layers that

$$\epsilon^{w}\mathbf{G}^{ws} \cdot \nabla \bar{\bar{\theta^{w}}} + \epsilon^{s}\mathbf{G}^{ws} \cdot \nabla \bar{\bar{\theta^{s}}} = \mathbf{G}^{ws} \cdot \nabla\Theta \tag{89}$$

or

$$\epsilon^{w}\mathbf{G}^{ws} \cdot \hat{\mathbf{K}}_{\theta} \cdot \nabla \bar{\bar{\theta^{w}}} + \epsilon^{s}\mathbf{G}^{ws} \cdot \hat{\mathbf{K}}_{\theta} \cdot \nabla \bar{\bar{\theta^{s}}} = \mathbf{G}^{ws} \cdot \hat{\mathbf{K}}_{\theta} \cdot \nabla\Theta \tag{90}$$

Eliminating the gradients of $\bar{\bar{\theta^{w}}}$ and $\bar{\bar{\theta^{s}}}$ from this equation using Eq. (88) gives

$$\mathbf{G}^{ws} \cdot \hat{\mathbf{K}}_{\theta} \cdot (\epsilon^{w}\hat{\mathbf{K}}_{\theta}^{w-1} + \epsilon^{s}\hat{\mathbf{K}}_{\theta}^{s-1}) \cdot \hat{\mathbf{K}}_{\theta} \cdot \nabla\Theta = \mathbf{G}^{ws} \cdot \hat{\mathbf{K}}_{\theta} \cdot \nabla\Theta \tag{91}$$

Therefore we can use the relation

$$\mathbf{G}^{ws} \cdot \hat{\mathbf{K}}_{\theta} = \mathbf{G}^{ws} \cdot (\epsilon^{w}\hat{\mathbf{K}}_{\theta}^{w-1} + \epsilon^{s}\hat{\mathbf{K}}_{\theta}^{s-1})^{-1} \tag{92}$$

so that substitution into Eq. (87) followed by substitution into the first term on the right side of Eq. (85) yields

$$\bar{\bar{\mathbf{q}}}^{T} = \mathbf{G}^{ws} \cdot (\epsilon^{w}\hat{\mathbf{K}}_{\theta}^{w-1} + \epsilon^{s}\hat{\mathbf{K}}_{\theta}^{s-1})^{-1} \cdot \nabla\Theta + (\mathbf{I} - \mathbf{G}^{ws}) \cdot (\epsilon^{w}\hat{\mathbf{K}}_{\theta}^{w} \cdot \nabla \bar{\bar{\theta^{w}}} + \epsilon^{s}\hat{\mathbf{K}}_{\theta}^{s} \cdot \nabla \bar{\bar{\theta^{s}}}) \tag{93}$$

In the direction tangent to the materials, (i.e., in directions $\mathbf{I} - \mathbf{G}^{ws}$ at the macroscale), all the temperature gradients are equal when using a single temperature formulation. Thus, Eq. (93) becomes

$$\bar{\bar{\mathbf{q}}}^{T} = \mathbf{G}^{ws} \cdot (\epsilon^{w}\hat{\mathbf{K}}_{\theta}^{w-1} + \epsilon^{s}\hat{\mathbf{K}}_{\theta}^{s-1})^{-1} \cdot \nabla\Theta + (\mathbf{I} - \mathbf{G}^{ws}) \cdot (\epsilon^{w}\hat{\mathbf{K}}_{\theta}^{w} + \varepsilon^{s}\hat{\mathbf{K}}_{\theta}^{s}) \cdot \nabla\Theta \tag{94}$$

Substitution of this expression for the conduction vector into Eq. (83) and replacing the individual phase temperatures with the common temperature provide the energy conservation equation

$$\mathcal{U}^{w} + \mathcal{U}^{s} = \epsilon^{w}\rho^{w}C_{p}^{w}\frac{\mathrm{D}^{\bar{w}}\Theta}{\mathrm{D}t} + \epsilon^{s}\rho^{s}C_{p}^{s}\frac{\mathrm{D}^{\bar{s}}\Theta}{\mathrm{D}t} - \epsilon^{w}\Theta\bar{\bar{\beta^{w}}}\frac{\mathrm{D}^{\bar{w}}p^{w}}{\mathrm{D}t} + \frac{\epsilon^{s}}{j^{s}}\Theta\bar{\bar{\boldsymbol{\beta}}}^{s}:\frac{\mathrm{D}^{\bar{s}}\bar{\bar{\sigma^{s}}}}{\mathrm{D}t} - \nabla \cdot [\mathbf{G}^{ws} \cdot (\epsilon^{w}\hat{\mathbf{K}}_{\theta}^{w-1} + \epsilon^{s}\hat{\mathbf{K}}_{\theta}^{s-1})^{-1} \cdot \nabla\Theta + (\mathbf{I} - \mathbf{G}^{ws}) \cdot (\epsilon^{w}\hat{\mathbf{K}}_{\theta}^{w} + \epsilon^{s}\hat{\mathbf{K}}_{\theta}^{s}) \cdot \nabla\Theta] = 0 \tag{95}$$

There are several attractive features associated with the form of the conductivity as it appears in Eq. (94) and then in energy equation (95). First if the system is layered and conduction is orthogonal to the layers, the first term will dominate. When conduction is parallel to the layers, the second term will dominate, and the orientation tensor $\mathbf{G}^{ws}$ will assure this behavior. When the matrix structure is isotropic, $\mathbf{G}^{ws} = \mathbf{I}/3$ and

$$\mathcal{U}^{w} + \mathcal{U}^{s} = \epsilon^{w}\rho^{w}C_{p}^{w}\frac{\mathrm{D}^{\bar{w}}\Theta}{\mathrm{D}t} + \epsilon^{s}\rho^{s}C_{p}^{s}\frac{\mathrm{D}^{\bar{s}}\Theta}{\mathrm{D}t} - \epsilon^{w}\Theta\bar{\bar{\beta^{w}}}\frac{\mathrm{D}^{\bar{w}}p^{w}}{\mathrm{D}t} + \frac{\epsilon^{s}}{j^{s}}\Theta\bar{\bar{\boldsymbol{\beta}}}^{s}:\frac{\mathrm{D}^{\bar{s}}\bar{\bar{\sigma^{s}}}}{\mathrm{D}t} - \nabla \cdot \left\{ \left[\frac{1}{3}(\epsilon^{w}\hat{\mathbf{K}}_{\theta}^{w-1} + \epsilon^{s}\hat{\mathbf{K}}_{\theta}^{s-1})^{-1} + \frac{2}{3}(\epsilon^{w}\hat{\mathbf{K}}_{\theta}^{w} + \epsilon^{s}\hat{\mathbf{K}}_{\theta}^{s}) \right] \cdot \nabla\Theta \right\} = 0 \tag{96}$$

If, additionally, each phase behaves isotropically and dispersion is also isotropic, then the effective conduction tensors reduce to scaled unit tensors so that the internal energy equation is

$$\mathcal{U}^{w} + \mathcal{U}^{s} = \epsilon^{w}\rho^{w}C_{p}^{w}\frac{\mathrm{D}^{\bar{w}}\Theta}{\mathrm{D}t} + \epsilon^{s}\rho^{s}C_{p}^{s}\frac{\mathrm{D}^{\bar{s}}\Theta}{\mathrm{D}t} - \epsilon^{w}\Theta\bar{\bar{\beta^{w}}}\frac{\mathrm{D}^{\bar{w}}p^{w}}{\mathrm{D}t} + \frac{\epsilon^{s}}{j^{s}}\Theta\bar{\bar{\boldsymbol{\beta}}}^{s}:\frac{\mathrm{D}^{\bar{s}}\bar{\bar{\sigma^{s}}}}{\mathrm{D}t} - \nabla \cdot \left\{ \left[\frac{1}{3}\left(\frac{\epsilon^{w}}{\hat{K}_{\theta}^{w}} + \frac{\epsilon^{s}}{\hat{K}_{\theta}^{s}}\right)^{-1} + \frac{2}{3}(\epsilon^{w}\hat{K}_{\theta}^{w} + \varepsilon^{s}\hat{K}_{\theta}^{s}) \right] \nabla\Theta \right\} = 0 \tag{97}$$

5 Discussion

Heat transport in porous media is an area of research rich in both applications and scholarly examination [13–16]. Recent work has focused on understanding conditions under which a one equation, or a local thermal equilibrium, model applies, solving a variety of cell problems to provide approximate closure relations [13,16], and improving the understanding of non-Darcy effects on thermal transport [15].

Similar to some previous work [14–17], a multiscale approach based on formal averaging is used in this work. However, as a departure from previous work, the TCAT approach is employed, which provides a framework in which conservation equations, an entropy inequality, and thermodynamic relations are jointly and consistently used to formulate models, which may include both phases and also interfaces. In addition, unlike previous work [17], we have not assumed an incompressible solid phase, leading to differences in the final form of the formulated models. The TCAT approach provides a description of all macroscale variables in terms of well-defined averages with appropriate weighting depending on the quantity. Based on this work and previous TCAT work, a hierarchy of models can be developed and examined. This hierarchy can be compared with results from and advanced through the solution of subscale problems by a process analogous to traditional subscale computational or analytical approaches. This aspect of this TCAT work has not yet been considered for the case of heat transport.

To complete the TCAT development of a macroscale model for heat transport in a single-fluid-phase porous medium system, the validity and applicability of the macroscale equations and closure relations developed here must be studied in conjunction with microscale and macroscale modeling and experimentation. We note

that additional manipulations involving the solid-phase motion may be examined, as in Ref. [11], so that the solid consolidation is considered as a consequence of the fluid phase that is modeled explicitly. Additionally, although the closure relations of Eqs. (42)–(49) were applied to the thermal energy equation here, those same relations may also close the total energy equation if that equation is to be used in a model.

Finally, closure of the energy equation for the interface between phases was not considered in this manuscript. The needed conservation equations and closure relations appear, but the actual inclusion of the closed equations is not provided. This is consistent with the case of flow and heat transport in a natural porous medium. For a situation where a coating of highly conductive or insulating material is applied to the surface of the porous media grains, for example, the interface equations could be important in describing the overall system performance. Additionally, if porous media flow containing two or more fluids is to be studied, the work involved in deforming the interfaces may contribute to the total energy balance.

6 Conclusions

The previously developed TCAT approach has been shown to be applicable to the derivation of closed models involving energy transport in porous medium systems. TCAT models are formulated in terms of well-defined averages of all quantities that appear in the model. Both the local-equilibrium and local nonequilibrium cases are considered and conditions under which the TCAT formulation reduce to models similar in form to traditional models based on volume averaging are shown.

The general nature of the mass, momentum, and energy equations considered and the closure schemes advanced provide a means to investigate a wide variety of physical phenomena, including systems not in local thermal equilibrium, systems involving non-Darcy behavior, systems in which compressibility of the solid is important, and systems in which interfacial effects are important. Such investigations warrant further consideration.

Acknowledgment

This work was supported by the National Science Foundation Grant No. DMS-0327896 and by the National Institute of Environmental Health Sciences Grant No. P42 ES05948.

Nomenclature

Roman Letters

- b = entropy source density
- $\mathbf{C}$ = Greens' deformation tensor
- C_p = heat capacity at constant pressure on a per unit mass basis
- $\hat{c}$ = compressibility parameter
- $\mathbf{d}$ = rate of strain tensor
- $\mathbf{d}^{\bar{\bar{\alpha}}}$ = macroscale rate of strain tensor, $[\nabla \mathbf{v}^{\bar{\alpha}} + (\nabla \mathbf{v}^{\bar{\alpha}})^T]/2$
- E = internal energy density
- $E^{\bar{\bar{\alpha}}}$ = macroscale internal energy density of entity α, $\langle E_\alpha \rangle_{\Omega_\alpha,\Omega}$
- $E_\kappa^{\bar{\bar{ws}}}$ = macroscale internal energy density for entity κ obtained as an average over interface ws, $\epsilon^\kappa \langle E_\kappa \rangle_{\Omega_{ws},\Omega_{ws}}$
- $\mathcal{E}^\alpha$ = macroscale conservation of total energy equation for entity α
- F = scalar thermodynamic force
- $\mathbf{F}$ = vector thermodynamic force
- $\mathbf{F}$ = tensor thermodynamic force
- $\mathcal{F}^\alpha$ = macroscale conservation equation for property $F^{\bar{\bar{\alpha}}}$
- $F^{\bar{\bar{\alpha}}}$ = macroscale density of a general property of entity α being conserved
- $\mathbf{f}^{\bar{\bar{\alpha}}}$ = nonadvective flux of $F^{\bar{\bar{\alpha}}}$ in entity α
- $f^{\bar{\bar{\alpha}}}$ = source term for property $F^{\bar{\bar{\alpha}}}$ in entity α
- $\mathbf{G}_{ws}$ = microscale orientation tensor for the ws interface, $\mathbf{n}_s\mathbf{n}_s$
- $\mathbf{G}^{ws}$ = macroscale orientation tensor for the ws interface, $\langle \mathbf{n}_s\mathbf{n}_s \rangle_{\Omega_{ws},\Omega_{ws}}$
- $\mathcal{G}$ = identity relating material derivative of macroscale gravitational potential to macroscale gravity
- $\mathbf{g}$ = body force acceleration vector (gravity for this application)
- $H^{\bar{\bar{s}}}$ = enthalpy of entity s per unit volume, $E^{\bar{\bar{s}}} - \epsilon^s \boldsymbol{\sigma}^{\bar{\bar{s}}} : \mathbf{C}^s / j^s$
- $H^{\bar{\bar{w}}}$ = enthalpy of entity w per unit volume, $E^{\bar{\bar{w}}} + \epsilon^w p^w$
- h = energy source density
- $\mathbf{I}$ = identity tensor
- $\mathbf{I}'$ = surface identity tensor
- $\mathcal{I}$ = index set of entities, $\{w,s,ws\}$
- J = scalar thermodynamic flux
- $\mathbf{J}$ = vector thermodynamic flux
- $\mathbf{J}$ = tensor thermodynamic flux
- $j_{\bar{s}}$ = solid-phase Jacobian
- $K_E^{\bar{\bar{\alpha}}}$ = macroscale kinetic energy of entity α per unit mass of entity α due to microscale velocity fluctuations, $\left\langle \frac{1}{2}(\mathbf{v}_\alpha - \mathbf{v}^{\bar{\alpha}}) \cdot (\mathbf{v}_\alpha - \mathbf{v}^{\bar{\alpha}}) \right\rangle_{\Omega_\alpha,\Omega_\alpha,\rho_\alpha}$
- $K_{E\kappa}^{\bar{\bar{ws}}}$ = macroscale kinetic energy of phase entity κ per unit mass of entity κ due to microscale velocity fluctuations obtained as an average over entity ws, $\left\langle \frac{1}{2}(\mathbf{v}_\kappa - \mathbf{v}^{\bar{\kappa}}) \cdot (\mathbf{v}_\kappa - \mathbf{v}^{\bar{\kappa}}) \right\rangle_{\Omega_{ws},\Omega_{ws},\rho_\kappa}$
- $\hat{\mathbf{K}}_q^\alpha$ = effective macroscale heat conduction tensor for entity α
- $\hat{\mathbf{K}}_\theta^\alpha$ = scaled effective heat conduction tensor for entity α, $\hat{\mathbf{K}}_q^\alpha / \bar{\theta}^{\bar{\bar{\alpha}}2}$
- $\hat{k}_q^\kappa$ = interentity coefficient for heat transfer between entities ws and κ
- $\hat{k}_W^\kappa$ = interentity coefficient for work of expansion of entity κ impacting interface ws
- $\mathcal{M}^\alpha$ = macroscale conservation of mass equation for entity α
- $M^{\kappa\to\alpha}$ = transfer of mass in the κ entity to the α entity per unit volume per unit time
- $M_E^{\kappa\to\alpha}$ = transfer of energy from the κ entity to the α entity due to interentity mass transfer per unit volume per unit time
- $\mathbf{M}_v^{\kappa\to\alpha}$ = transfer of momentum from the κ entity to the α entity due to interentity mass transfer per unit volume per unit time
- $\mathbf{n}_\alpha$ = outward unit normal vector from entity α
- $\mathcal{P}^\alpha$ = macroscale conservation of momentum equation for entity α
- p = fluid pressure
- $Q^{\kappa\to\alpha}$ = transfer of energy from entity κ to entity α by heat transfer and work of expansion per unit volume per unit time
- $\mathbf{q}$ = nonadvective heat flux density vector

$\bar{\bar{\mathbf{q}}}^{\alpha}$ = macroscale nonadvective energy flux vector, $\langle \mathbf{q}_\alpha - (E_\alpha/\rho_\alpha - \bar{\bar{E}}^{\alpha}/\epsilon^\alpha\rho^\alpha + 1/2(\mathbf{v}_\alpha - \bar{\mathbf{v}}^{\alpha})\cdot(\mathbf{v}_\alpha - \bar{\mathbf{v}}^{\alpha}))\rho_\alpha(\mathbf{v}_\alpha - \bar{\mathbf{v}}^{\alpha})\rangle_{\Omega_\alpha,\Omega_\alpha} - \langle(-\bar{\bar{K}}_E^{\alpha} + \psi_\alpha - \bar{\psi}^{\alpha})\rho_\alpha(\mathbf{v}_\alpha - \bar{\mathbf{v}}^{\alpha}) - \mathbf{t}_\alpha\cdot(\mathbf{v}_\alpha - \bar{\mathbf{v}}^{\alpha})\rangle_{\Omega_\alpha,\Omega_\alpha}$

$\bar{\bar{\mathbf{q}}}^{T}$ = total heat conduction vector, $\epsilon^w\bar{\bar{\mathbf{q}}}^{w} + \epsilon^s\bar{\bar{\mathbf{q}}}^{s}$

$\hat{\mathbf{R}}^{\alpha}$ = resistance tensor for flow of entity α

$\mathcal{S}$ = entropy balance equation

$\mathcal{T}^{\alpha}$ = CIT-based material derivative of macroscale thermodynamic equation for internal energy equation of entity α

$\overset{\kappa\to\alpha}{\mathbf{T}}$ = transfer of momentum from entity κ to entity α due to interentity stress and per unit volume per unit time

$\overset{\kappa\to\alpha}{T_v}$ = transfer of energy from entity κ to the entity α due to frictional effects per unit volume per unit time

$\mathbf{t}$ = stress tensor

$\bar{\bar{\mathbf{t}}}^{\alpha}$ = macroscale stress tensor for entity α, $\langle \mathbf{t}_\alpha - \rho_\alpha(\mathbf{v}_\alpha - \bar{\mathbf{v}}^{\alpha})(\mathbf{v}_\alpha - \bar{\mathbf{v}}^{\alpha})\rangle_{\Omega_\alpha,\Omega_\alpha}$

t = time

$\mathcal{U}^{\alpha}$ = macroscale equation of thermal energy conservation for entity α

$\mathbf{v}$ = velocity

$\overset{\kappa\to\alpha}{X}$ = transfer of property of entity α being conserved from entity κ to entity α

$\mathbf{X}$ = material coordinate position vector

$\mathbf{x}$ = spatial coordinate position vector

Greek Letters

α = entity identifier that takes on values of w, s, or ws to denote fluid, solid, or interface, respectively

β = coefficient of thermal expansion for a fluid

$\bar{\bar{\beta}}^{w}$ = macroscale coefficient of thermal expansion for a fluid, $\langle \beta_w\theta_w\rangle_{\Omega_w,\Omega_w}/\bar{\bar{\theta}}^{w}$

$\boldsymbol{\beta}_s$ = microscale solid-phase tensor coefficient of thermal expansion and stress

$\bar{\bar{\boldsymbol{\beta}}}^{s}$ = microscale solid-phase tensor coefficient of thermal expansion and stress, $\langle \theta_s\boldsymbol{\beta}_s\rangle_{\Omega_s,\Omega_s}/\bar{\bar{\theta}}^{s}$

γ = interfacial tension

ϵ^{α} = measure of quantity of entity α per macroscale volume

η = entropy density

$\bar{\eta}^{\alpha}$ = macroscale entropy of entity α per total volume, $\langle \eta_\alpha\rangle_{\Omega_\alpha,\Omega}$

$\bar{\bar{\eta}}_{\kappa}^{ws}$ = macroscale entropy of entity κ obtained as an average over interface ws, $\epsilon^{\kappa}\langle \eta_\kappa\rangle_{\Omega_{ws},\Omega_{ws}}$

Θ = macroscale temperature when all entities are modeled as having the same temperature at any macroscale point

θ = temperature

$\bar{\theta}^{\alpha}$ = macroscale temperature of entity α, $\langle \theta_\alpha\rangle_{\Omega_\alpha,\Omega_\alpha,\eta_\alpha}$

Λ = entropy production rate density

$\lambda_{\mathcal{E}}^{\alpha}$ = Lagrange multiplier for macroscale total energy conservation equation of entity α

$\lambda_{\mathcal{M}}^{\alpha}$ = Lagrange multiplier for macroscale mass conservation equation of entity α

$\boldsymbol{\lambda}_{\mathcal{P}}^{\alpha}$ = Lagrange multiplier for macroscale momentum conservation equation of entity α

$\lambda_{\mathcal{T}}^{\alpha}$ = Lagrange multiplier for material derivative of macroscale thermodynamic equation for energy of entity α

μ = chemical potential

ρ = mass density

$\boldsymbol{\sigma}$ = Lagrangian stress tensor for the solid phase

$\bar{\bar{\boldsymbol{\sigma}}}^{s}$ = macroscale Lagrangian stress tensor, $\bar{\bar{\boldsymbol{\sigma}}}^{s} : \mathbf{C}^s/j^s = \langle \boldsymbol{\sigma}_s : \mathbf{C}_s/j_s\rangle_{\Omega_s,\Omega_s}$

$\bar{\bar{\boldsymbol{\varphi}}}$ = nonadvective entropy density flux vector

$\boldsymbol{\varphi}^{\alpha}$ = macroscale nonadvective entropy density flux vector, $\langle \boldsymbol{\varphi}_\alpha - \eta_\alpha(\mathbf{v}_\alpha - \bar{\mathbf{v}}^{\alpha})\rangle_{\Omega_\alpha,\Omega_\alpha}$

ψ = acceleration potential (e.g., gravitational potential)

Ω = macroscale spatial domain or REV

Ω_s = subvolume of Ω occupied by solid

Ω_w = subvolume of Ω occupied by fluid

Ω_{ws} = interfacial region within Ω between the solid and fluid phases

Subscripts and Superscripts

s, w, ws, α, κ = as subscript, refers to microscale property of corresponding entity; as superscript, refers to macroscale property of corresponding entity; as superscript with overbar, refers to mass averaged property of corresponding entity; and as superscript with double overbar, refers to macroscale property defined uniquely for different properties in the Nomenclature

Macroscale Quantities Obtained as Integral Averages

$\langle P_\alpha\rangle_{\Omega_\kappa,\Omega_\beta,m}$ = general average of some microscale property, P, of entity α, using a weighting factor, m, $\int_{\Omega_\kappa} mP_\alpha d\mathfrak{r}/\int_{\Omega_\beta} m d\mathfrak{r}$

$\langle P_\alpha\rangle_{\Omega_\kappa,\Omega_\beta}$ = average with weighting factor $m=1$, $\int_{\Omega_\kappa} P_\alpha d\mathfrak{r}/\int_{\Omega_\beta} d\mathfrak{r}$

P^{α} = entity average, $\langle P_\alpha\rangle_{\Omega_\alpha,\Omega_\alpha}$

$\bar{P}^{\alpha}$ = mass-weighted average, $\langle P_\alpha\rangle_{\Omega_\alpha,\Omega_\alpha,\rho_\alpha}$

P_{α}^{ws} = surface average over the interface, $\langle P_\alpha\rangle_{\Omega_{ws},\Omega_{ws}}$

$P_{\alpha}^{\overline{ws}}$ = mass-weighted surface average over the interface, $\langle P_\alpha\rangle_{\Omega_{ws},\Omega_{ws},\rho_\alpha}$

Material Derivatives

$D\bar{}^{\alpha}/Dt$ = material derivative with velocity $\bar{\mathbf{v}}^{\alpha}$, $\partial/\partial t + \bar{\mathbf{v}}^{\alpha}\cdot\nabla$

$D'\bar{}^{\alpha}/Dt$ = material derivative restricted to an interface, $D\bar{}^{\alpha}/Dt + (\mathbf{v}_{ws} - \bar{\mathbf{v}}^{\alpha})\cdot\mathbf{n}_s\mathbf{n}_s\cdot\nabla$

Appendix A: Form of Energy Exchange Term

In the absence of mass exchange between phases, Eq. (14) simplifies to the definition

$$\overset{ws\to\kappa}{Q} = \langle \mathbf{n}_\kappa\cdot\mathbf{q}_\kappa\rangle_{\Omega_{ws},\Omega} + \langle \mathbf{n}_\kappa\cdot\mathbf{t}_\kappa\cdot(\mathbf{v}_\kappa - \bar{\mathbf{v}}_{\kappa}^{\overline{ws}})\rangle_{\Omega_{ws},\Omega} \tag{A1}$$

In positing closure relations for $\overset{ws\to\kappa}{Q}$, it is appropriate to make use of the fact that in this expression, the first term on the right side is associated with heat transfer while the second term is related to work. The purpose of this appendix is to examine the work term so that guidance can be provided for specifying $\hat{k}_W^{\kappa}$ that arises in Eq. (46).

As a first step in the analysis, decompose the stress tensor further into normal and tangential components to obtain

$$\langle \mathbf{n}_\kappa \cdot \mathbf{t}_\kappa \cdot (\mathbf{v}_\kappa - \mathbf{v}_\kappa^{\overline{ws}}) \rangle_{\Omega_{ws},\Omega} = \langle (\mathbf{n}_\kappa \cdot \mathbf{t}_\kappa \cdot \mathbf{n}_\kappa)\mathbf{n}_\kappa \cdot (\mathbf{v}_\kappa - \mathbf{v}_\kappa^{\overline{ws}}) \rangle_{\Omega_{ws},\Omega} + \langle (\mathbf{n}_\kappa \cdot \mathbf{t}_\kappa \cdot \mathbf{l}') \cdot (\mathbf{v}_\kappa - \mathbf{v}_\kappa^{\overline{ws}}) \rangle_{\Omega_{ws},\Omega} \tag{A2}$$

When there is no phase change occurring the microscale phase velocity at the interface is equal to the microscale velocity at the interface. Therefore $\mathbf{v}_\kappa = \mathbf{v}_{ws}$ and $\mathbf{v}_\kappa^{\overline{ws}} = \mathbf{v}^{\overline{ws}}$. With these notational changes, Eq. (A2) becomes

$$\langle \mathbf{n}_\kappa \cdot \mathbf{t}_\kappa \cdot (\mathbf{v}_\kappa - \mathbf{v}_\kappa^{\overline{ws}}) \rangle_{\Omega_{ws},\Omega} = \langle (\mathbf{n}_\kappa \cdot \mathbf{t}_\kappa \cdot \mathbf{n}_\kappa)\mathbf{n}_\kappa \cdot (\mathbf{v}_{ws} - \mathbf{v}^{\overline{ws}}) \rangle_{\Omega_{ws},\Omega} + \langle (\mathbf{n}_\kappa \cdot \mathbf{t}_\kappa \cdot \mathbf{l}') \cdot (\mathbf{v}_{ws} - \mathbf{v}^{\overline{ws}}) \rangle_{\Omega_{ws},\Omega} \tag{A3}$$

The second term on the right involves the tangential velocity at the interface. We assume that the difference between the averages of the tangent of the microscale velocity is equal to the average tangent multiplied by the macroscale velocity. Thus this term is negligibly small. For the first term on the right, we assume that the correlation between the microscale normal stress and the normal velocity difference is unimportant so that the average of the product is equal to the product of the average. With these minor approximations we obtain

$$\langle \mathbf{n}_\kappa \cdot \mathbf{t}_\kappa \cdot (\mathbf{v}_\kappa - \mathbf{v}_\kappa^{\overline{ws}}) \rangle_{\Omega_{ws},\Omega} = \langle \mathbf{n}_\kappa \cdot \mathbf{t}_\kappa \cdot \mathbf{n}_\kappa \rangle_{\Omega_{ws},\Omega_{ws}} \langle \mathbf{n}_\kappa \cdot (\mathbf{v}_{ws} - \mathbf{v}^{\overline{ws}}) \rangle_{\Omega_{ws},\Omega} \tag{A4}$$

From the averaging theorems for a two-phase system, we have the identity

$$\langle \mathbf{n}_\kappa \cdot (\mathbf{v}_{ws} - \mathbf{v}^{\overline{ws}}) \rangle_{\Omega_{ws},\Omega} = \frac{\mathrm{D}^{\overline{ws}} \epsilon^\kappa}{\mathrm{D}t} \tag{A5}$$

Therefore, Eq. (A3) becomes

$$\langle \mathbf{n}_\kappa \cdot \mathbf{t}_\kappa \cdot (\mathbf{v}_\kappa - \mathbf{v}_\kappa^{\overline{ws}}) \rangle_{\Omega_{ws},\Omega} = \langle \mathbf{n}_\kappa \cdot \mathbf{t}_\kappa \cdot \mathbf{n}_\kappa \rangle_{\Omega_{ws},\Omega_{ws}} \frac{\mathrm{D}^{\overline{ws}} \epsilon^\kappa}{\mathrm{D}t} \tag{A6}$$

Finally, with the solid movement being very small, we can make the approximation with minimal error that $\mathbf{v}^{\overline{ws}} \approx \mathbf{v}^{\overline{s}}$ so that the material derivative in Eq. (A6) is calculated at the macroscale solid velocity rather than the macroscale interface velocity. Then substitution of this result into Eq. (A1) yields

$$\overset{ws \to \kappa}{Q} = \langle \mathbf{n}_\kappa \cdot \mathbf{q}_\kappa \rangle_{\Omega_{ws},\Omega} + \langle \mathbf{n}_\kappa \cdot \mathbf{t}_\kappa \cdot \mathbf{n}_\kappa \rangle_{\Omega_{ws},\Omega_{ws}} \frac{\mathrm{D}^{\overline{s}} \epsilon^\kappa}{\mathrm{D}t} \tag{A7}$$

Comparison of this result with Eq. (46) suggests that $\hat{k}_W^\kappa = -\langle \mathbf{n}_\kappa \cdot \mathbf{t}_\kappa \cdot \mathbf{n}_\kappa \rangle_{\Omega_{ws},\Omega_{ws}}$ as stated in Eq. (59) in the main body of the text and subsequently employed.

References

[1] Gray, W. G., and Miller, C. T., 2005, "Thermodynamically Constrained Averaging Theory Approach for Modeling Flow and Transport Phenomena in Porous Medium Systems: 1. Motivation and Overview," Adv. Water Resour., **28**(2), pp. 161–180.

[2] Gray, W. G., and Miller, C. T., 2006, "Thermodynamically Constrained Averaging Theory Approach for Modeling Flow and Transport Phenomena in Porous Medium Systems: 3. Single-Fluid-Phase Flow," Adv. Water Resour., **29**(11), pp. 1745–1765.

[3] Gray, W. G., and Miller, C. T., 2009, "Thermodynamically Constrained Averaging Theory Approach for Modeling Flow and Transport Phenomena in Porous Medium Systems: 5. Single-Fluid-Phase Transport," Adv. Water Resour., **32**(5), pp. 681–711.

[4] Miller, C. T., and Gray, W. G., 2005, "Thermodynamically Constrained Averaging Theory Approach for Modeling Flow and Transport Phenomena in Porous Medium Systems: 2. Foundation," Adv. Water Resour., **28**(2), pp. 181–202.

[5] Miller, C. T., and Gray, W. G., 2008, "Thermodynamically Constrained Averaging Theory Approach for Modeling Flow and Transport Phenomena in Porous Medium Systems: 4. Species Transport Fundamentals," Adv. Water Resour., **31**(3), pp. 577–597.

[6] Gray, W. G., 2002, "On the Definition of Derivatives of Macroscale Energy for the Description of Multiphase Systems," Adv. Water Resour., **25**(8–12), pp. 1091–1104.

[7] Gray, W. G., and Schrefler, B. A., 2007, "Analysis of the Solid Phase Stress Tensor in Multiphase Porous Media," Int. J. Numer. Analyt. Meth. Geomech., **31**, pp. 541–581.

[8] Alexander, J. I. D., and Johnson, W. C., 1985, "Thermomechanical Equilibrium in Solid-Fluid Systems With Curved Interfaces," J. Appl. Phys., **58**(2), pp. 816–824.

[9] Boruvka, L., 1975, "An Extension to Classical Theory of Capillarity," Ph.D. thesis, University of Toronto, Toronto, Canada.

[10] Boruvka, L., and Neumann, A. W., 1977, "Generalization of the Classical Theory of Capillarity," J. Chem. Phys., **66**(12), pp. 5464–5476.

[11] Gray, W. G., and Miller, C. T., 2007, "Consistent Thermodynamic Formulations for Multiscale Hydrologic Systems: Fluid Pressures," Water Resour. Res., **43**, W09408.

[12] Eringen, A. C., 1980, *Mechanics of Continua*, Krieger, Huntington, NY.

[13] Alazmi, B., and Vafai, K., 2001, "Analysis of Fluid Flow and Heat Transfer Interfacial Conditions Between a Porous Medium and a Fluid Layer," Int. J. Heat Mass Transfer, **44**(9), pp. 1735–1749.

[14] Amiri, A., and Vafai, K., 1998, "Transient Analysis of Incompressible Flow Through a Packed Bed," Int. J. Heat Mass Transfer, **41**(24), pp. 4259–4279.

[15] Nakayama, A., and Kuwahara, F., 2005, "Algebraic Model for Thermal Dispersion Heat Flux Within Porous Media," AIChE J., **51**(10), pp. 2859–2864.

[16] Quintard, M., Kaviany, M., and Whitaker, S., 1997, "Two-Medium Treatment of Heat Transfer in Porous Media: Numerical Results for Effective Properties," Adv. Water Resour., **20**(2–3), pp. 77–94.

[17] Quintard, M., and Whitaker, S., 2000, "Theoretical Analysis of Transport in Porous Media," *Handbook of Porous Media*, K. Vafai, ed., Dekker, New York, NY, pp. 1–52.

Effect of Boundary Conditions on the Onset of Thermomagnetic Convection in a Ferrofluid Saturated Porous Medium

I. S. Shivakumara[1]
Department of Mathematics,
UGC-Centre for Advanced Studies in Fluid Mechanics,
Bangalore University,
Bangalore 560 001, India
e-mail: shivakumarais@gmail.com

C. E. Nanjundappa
Department of Mathematics,
Dr. Ambedkar Institute of Technology,
Bangalore 560 056, India
e-mail: cenanju@hotmail.com

M. Ravisha
Department of Mathematics,
East Point College of Engineering and Technology,
Bangalore 560 049, India
e-mail: pmravisha@yahoo.co.in

The onset of thermomagnetic convection in a ferrofluid saturated horizontal porous layer in the presence of a uniform vertical magnetic field is investigated for a variety of velocity and temperature boundary conditions. The Brinkman–Lapwood extended Darcy equation, with fluid viscosity different from effective viscosity, is used to describe the flow in the porous medium. The lower boundary of the porous layer is assumed to be rigid-ferromagnetic, while the upper boundary is considered to be either rigid-ferromagnetic or stress-free. The thermal conditions include fixed heat flux at the lower boundary, and a general convective-radiative exchange at the upper boundary, which encompasses fixed temperature and heat flux as particular cases. The resulting eigenvalue problem is solved using the Galerkin technique and also by using regular perturbation technique when both boundaries are insulated to temperature perturbations. It is found that the increase in the Biot number and the viscosity ratio, and the decrease in the magnetic as well as in the Darcy number is to delay the onset of ferroconvection. Besides, the nonlinearity of fluid magnetization has no effect on the onset of convection in the case of fixed heat flux boundary conditions. [DOI: 10.1115/1.3160540]

Keywords: nanoparticle, ferrofluid, porous medium, viscosity ratio, fixed heat flux

1 Introduction

In the 1960s, scientists from the National Aeronautics and Space Administration (NASA) research center investigated methods for controlling liquids in space. They developed ferrofluids, which are colloidal suspensions of magnetic nanoparticles in a carrier fluid such as water, hydrocarbon (mineral oil or kerosene), or fluorocarbon. The nanoparticles typically have sizes of about 100 Å or 10 nm and they are coated with surfactants in order to prevent the coagulation. Ferrofluids respond to an external magnetic field and this enables to control the location of the fluid through the application of a magnetic field. Ferrofluids have been tailor-made and possess a wide variety of potential applications in various industries [1–5]. Mechanical engineering industries use them as fluids in vibration dampers, shock absorbers, and vacuum seals. Electrical and electronic industries use ferrofluids to improve hi-fi characteristic loud speakers as transformer coolants and also in miniaturizing inductive components. Computation industries use them as fluids in stepper motors. Therefore, studies on ferrofluids have received much attention in the scientific community over the years

The magnetization of ferrofluids depends on the magnetic field, temperature, and density. Hence, any variations in these quantities induce a change in body force distribution in the fluid and eventually give rise to convection in ferrofluids in the presence of a gradient of magnetic field. There have been numerous studies on thermal convection in a ferrofluid layer called ferroconvection analogous to Rayleigh–Benard convection in ordinary viscous fluids. Finlayson [6] studied convective instability of a magnetic fluid layer heated from below in the presence of a uniform vertical magnetic field. A linear stability analysis has been carried out to predict the critical gradient of temperature corresponding to the onset of convection when both buoyancy and magnetic forces are included, by considering the bounding surfaces of the magnetic fluid layer to be either shear free or rigid. Thermoconvective instability of ferrofluids without considering buoyancy effects has been investigated by Lalas and Carmi [7], whereas Shliomis [8] analyzed the linear relation for magnetized perturbed quantities at the limit of instability. A similar analysis but with the fluid confined between ferromagnetic plates has been carried out by Gotoh and Yamada [9] using linear stability analysis. Schwab et al. [10] experimentally investigated the problem of Finlayson in the case of a strong magnetic field and detected the onset of convection by plotting the Nusselt number versus the Rayleigh number. Stiles and Kagan [11] extended the problem to allow for the dependence of effective shear viscosity on temperature and colloid concentration. The effect of the different forms of basic temperature gradients on the onset of ferroconvection driven by combined surface tension and buoyancy forces has been discussed by Shivakumara et al. [12] in order to understand the control of ferroconvection. Kaloni and Lou [13] theoretically investigated the convective instability problem in a thin horizontal layer of magnetic fluid heated from below under alternating magnetic field, by considering the quasistationary model with internal rotation and vortex viscosity. Shivakumara and Nanjundappa [14] analyzed the effect of various forms of nonuniform initial temperature profiles on the onset of Marangoni convection in a ferrofluid layer. The influence of magnetic field on heat and mass transport in ferrofluids has been discussed by Volker et al. [15]. Recently, Sunil and Mahajan [16] performed a nonlinear stability analysis for a magnetized ferrofluid layer heated from below in the stress-free boundaries, while Nanjundappa and Shivakumara [17] analyzed the effects of different velocities and temperature boundary conditions on the onset of convection in a ferrofluid layer.

Thermal convection of ferrofluids saturating a porous medium has also attracted considerable attention in the literature, owing to its importance in controlled emplacement of liquids or treatment of chemicals, and emplacement of geophysically imageable liq-

[1]Corresponding author.

Manuscript received September 20, 2008; final manuscript received March 14, 2009; published July 28, 2009. Review conducted by Kambiz Vafai.

uids into particular zones for subsequent imaging. Rosensweig et al. [18] experimentally studied the penetration of ferrofluids in the Heleshaw cell. The stability of the magnetic fluid penetration through a porous medium in high uniform magnetic field oblique to the interface is studied by Zahn and Rosensweig [19]. The thermal convection of a ferrofluid saturating a porous medium in the presence of a vertical magnetic field is studied by Vaidyanathan et al. [20] by employing the Brinkman equation with effective viscosity (Brinkman viscosity) is the same as fluid viscosity and considering that the bounding surfaces of the porous layer are shear free. Qin and Chadam [21] carried out the nonlinear stability analysis of ferroconvection in a porous layer by including the inertial effects to accommodate high velocity. The laboratory-scale experimental results of the behavior of ferrofluids in porous media consisting of sands and sediments are presented by Borglin et al. [22]. The onset of centrifugal convection in a magnetic fluid-saturated porous medium under zero gravity condition is investigated by Sarvanan and Yamaguchi [23]. The effect of dust particles on the onset of ferroconvection in a porous medium has been studied by Sunil et al. [24].

All the abovementioned studies on ferroconvection in a porous medium have dealt with isothermal boundary conditions. However, consideration of actual situations suggests that these conditions may be too restrictive. For instance, if the heating at the lower surface is bypassing an electric current through a thin metallic foil, then the appropriate temperature boundary conditions would be a fixed heat flux rather than a fixed temperature. Besides, porous materials used in many technological applications of practical importance possess high permeability values. For example, for permeabilities of compressed foams as high as 8×10^{-6} m^2 and for a 1 mm thick foam layer, the equivalent Darcy number is equal to 8 (see Nield et al. [25] and references therein). For a high porosity porous medium ($\varepsilon = 0.972$), Givler and Altobelli [26] experimentally determined that $\tilde{\mu}_f = 7.5^{+3.4}_{-2.4}\mu_f$, where $\tilde{\mu}_f$ is the effective viscosity and μ_f is the fluid viscosity. Under the circumstances, a theoretical solution, which is general enough to yield accurate results for ferroconvection in porous media is of fundamental and practical interest. Such a study helps experimentalists in the proper design of miniature cores of transformers, generators, and armatures, in which the winding act as pores and ferrofluids flowing through them act as coolant as well as induction cores. The main objective of the present study is the desire to understand the criterion for the onset of ferroconvection in a ferrofluid saturated, sparsely packed porous medium for different types of velocity and temperature boundary conditions. The lower boundary is considered to be rigid with fixed heat flux condition, while the upper boundary is assumed to be either rigid or free with convective-radiative exchange condition, which encompasses both fixed heat flux and temperature conditions as particular cases. The resulting eigenvalue problem is solved numerically and also using regular perturbation technique when both boundaries are insulated to temperature perturbations.

To achieve the above objectives, the remainder of this paper proceeds are as follows. Section 2 is devoted to the formulation of the problem. The method of the solution is discussed in Sec. 3. In Sec. 4, the results obtained both numerically and analytically are discussed, and some important conclusions follow in Sec. 5.

2 Formulation of the Problem

The system considered is an initially quiescent incompressible constant viscosity ferrofluid saturated horizontal porous layer of characteristic thickness d in the presence of a uniform applied magnetic field H_0 in the vertical direction. The horizontal extension of the porous layer is sufficiently large so that edge effects may be neglected. A Cartesian coordinate system (x,y,z) is used with the origin at the bottom of the porous layer and the z-axis is directed vertically upward (Fig. 1). At the lower boundary $z=0$, a constant heat flux condition of the form

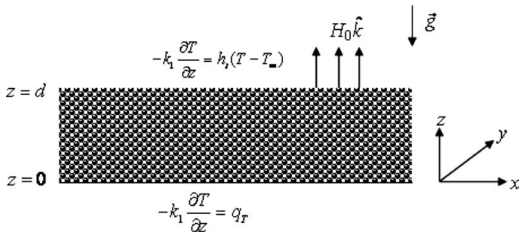

Fig. 1 Geometrical configuration

$$-k_1\frac{\partial T}{\partial z} = q_T \tag{1}$$

is used, while at the upper boundary $z=d$, a radiative-type of condition of the form

$$-k_1\frac{\partial T}{\partial z} = h_t(T - T_\infty) \tag{2}$$

is invoked. In the above equations, T is the temperature, q_T is the conductive thermal flux, k_1 is the overall thermal conductivity, h_t is the heat transfer coefficient, and T_∞ is the temperature in the bulk of the environment. The flow in the porous medium is described by the Brinkman–Lapwood extended Darcy equation with fluid viscosity different from effective viscosity, and the Oberbeck–Boussinesq approximation is assumed to be valid. In most of the studies, the Oberbeck–Boussinesq approximation has been quite mistreated, and the justifications that have been given for this approximation are largely incorrect. Rajagopal et al. [27] provided a systematic basis for this approximation and discussed some of the errors in the previous approaches.

The equations governing the flow of an incompressible ferrofluid in a porous medium are given as follows.

The continuity equation is

$$\nabla \cdot \boldsymbol{q} = 0 \tag{3}$$

where $\boldsymbol{q}$ is the velocity vector.

The momentum equation is

$$\rho_0\left[\frac{1}{\varepsilon}\frac{\partial \boldsymbol{q}}{\partial t} + \frac{1}{\varepsilon^2}(\boldsymbol{q}\cdot\nabla)\boldsymbol{q}\right] = -\nabla p + \rho_0[1-\alpha_t(T-T_0)]\boldsymbol{g} - \frac{\mu_f}{k}\boldsymbol{q} + \tilde{\mu}_f\nabla^2\boldsymbol{q} + \mu_0(\boldsymbol{M}\cdot\nabla)\boldsymbol{H} \tag{4}$$

where p is the pressure, $\boldsymbol{M}$ is the magnetization, $\boldsymbol{H}$ is the magnetic field intensity, ρ_0 is the reference density, k is the permeability of the porous medium, ε is the porosity of the porous medium, μ_f is the fluid viscosity, $\tilde{\mu}_f$ is the effective fluid viscosity, μ_0 is the magnetic permeability of vacuum, α_t is the thermal expansion coefficient, and $\nabla^2 = \partial^2/\partial x^2 + \partial^2/\partial y^2 + \partial^2/\partial z^2$ is the Laplacian operator. The term $\mu_0(\boldsymbol{M}\cdot\nabla)\boldsymbol{H}$ in the above equation is the magnetic body force, which appears as a result of the polarization of the ferrofluid in the presence of a magnetic field. In the present study, $\tilde{\mu}_f$ and μ_f are considered to be different and their ratio is taken as a separate parameter.

The temperature equation is

$$\varepsilon\left[\rho_0 C_{V,H} - \mu_0\boldsymbol{H}\cdot\left(\frac{\partial \boldsymbol{M}}{\partial T}\right)_{V,H}\right]\frac{DT}{Dt} + (1-\varepsilon)(\rho_0 C)_S\frac{\partial T}{\partial t} + \mu_0 T\left(\frac{\partial \boldsymbol{M}}{\partial T}\right)_{V,H}\cdot\frac{D\boldsymbol{H}}{Dt} = k_1\nabla^2 T \tag{5}$$

where C is the specific heat, $C_{V,H}$ is the specific heat at constant volume and magnetic field, and the subscript s represents the solid.

The Maxwell equations in the magnetostatic limit are

$$\nabla \cdot \boldsymbol{B} = 0 \tag{6a}$$

$$\nabla \times \boldsymbol{H} = 0 \quad \text{or} \quad \boldsymbol{H} = \nabla\varphi \tag{6b}$$

where $\boldsymbol{B}$ is the magnetic induction, and φ is the magnetic potential.

Further, $\boldsymbol{B}$, $\boldsymbol{M}$, and $\boldsymbol{H}$ are related by

$$\boldsymbol{B} = \mu_0(\boldsymbol{M} + \boldsymbol{H}) \tag{7}$$

It is assumed that the magnetization is aligned with the magnetic field, but allowed a dependence on the magnitude of the magnetic field as well as the temperature [6] and thus

$$\boldsymbol{M} = \frac{M}{H}(H,T)\boldsymbol{H} \tag{8}$$

The magnetic equation of state, following Ref. [6], is taken as

$$M = M_0 + \chi(H - H_0) - K(T - T_0) \tag{9}$$

where $\chi = (\partial M/\partial H)_{H_0,T_0}$ is the magnetic susceptibility, $K = -(\partial M/\partial T)_{H_0,T_0}$ is the pyromagnetic coefficient, and $M_0 = M(H_0, T_0)$.

It is clear that there exist the following solutions for the basic state:

$$\boldsymbol{q}_b = 0, \quad p_b(z) = p_0 - \rho_0 g z - \frac{1}{2}\rho_0\alpha_t g\beta z^2 - \frac{\mu_0 M_0 \kappa\beta}{1+\chi}z - \frac{\mu_0\kappa^2\beta^2}{2(1+\chi)^2}z^2$$

$$T_b(z) = T_0 - \beta z, \quad \boldsymbol{H}_b(z) = \left[H_0 - \frac{K\beta z}{1+\chi}\right]\hat{k},$$

$$\boldsymbol{M}_b(z) = \left[M_0 + \frac{K\beta z}{1+\chi}\right]\hat{k} \tag{10}$$

where $\beta = q_T/k_1$ is the temperature gradient, $T_0 = T_\infty + q_T(1 + h_t d/k_1)/h_t$, $\hat{k}$ is the unit vector in the z-direction, and the subscript b denotes the basic state.

To investigate the conditions under which the quiescent solution is stable against small disturbances, we consider a perturbed state such that

$$\boldsymbol{q} = \boldsymbol{q}', \quad p = p_b(z) + p', \quad T = T_b(z) + T', \quad \boldsymbol{H} = \boldsymbol{H}_b(z) + \boldsymbol{H}', \quad \boldsymbol{M} = \boldsymbol{M}_b(z) + \boldsymbol{M}' \tag{11}$$

where $\boldsymbol{q}' = (u', v', w')$, p', T', $\boldsymbol{H}' = (H_x', H_y', H_z')$, and $\boldsymbol{M}' = (M_x', M_y', M_z')$ are perturbed variables and are assumed to be small.

Substituting Eq. (11) into Eqs. (7) and (8), and using Eq. (6), we obtain (after dropping the primes)

$$H_x + M_x = (1 + M_0/H_0)H_x$$

$$H_y + M_y = (1 + M_0/H_0)H_y$$

$$H_z + M_z = (1+\chi)H_z - KT \tag{12}$$

Again, substituting Eq. (11) into momentum (Eq. (4)), linearizing, eliminating the pressure term by operating curl twice, and using Eq. (12), the z-component of the resulting equation can be obtained (after dropping the primes) as

$$\left(\rho_0\frac{\partial}{\partial t} + \frac{\mu_f}{k} - \tilde{\mu}_f\nabla^2\right)\nabla^2 w = -\mu_0 K\beta\frac{\partial}{\partial z}(\nabla_h^2\varphi) + \frac{\mu_0 K^2\beta}{1+\chi}\nabla_h^2 T + \rho_0\alpha_t g\nabla_h^2 T \tag{13}$$

where $\nabla_h^2 = \partial^2/\partial x^2 + \partial^2/\partial y^2$ is the horizontal Laplacian operator.

The temperature (Eq. (5)), after using Eq. (11) and linearizing, takes the following form (after dropping the primes):

$$(\rho_0 C)_1\frac{\partial T}{\partial t} - \mu_0 T_0 K\frac{\partial}{\partial t}\left(\frac{\partial\varphi}{\partial z}\right) = k_1\nabla^2 T + \left[(\rho_0 C)_2 - \frac{\mu_0 T_0 K^2}{1+\chi}\right]w\beta \tag{14}$$

where $(\rho_0 C)_1 = \varepsilon\rho_0 C_{V,H} + \varepsilon\mu_0 H_0 K + (1-\varepsilon)(\rho_0 C)_s$, and $(\rho_0 C)_2 = \varepsilon\rho_0 C_{V,H} + \varepsilon\mu_0 H_0 K$.

Equations (6*a*) and (6*b*), after substituting Eq. (11) and using Eq. (12), may be written as (after dropping the primes)

$$\left(1 + \frac{M_0}{H_0}\right)\nabla_h^2\varphi + (1+\chi)\frac{\partial^2\varphi}{\partial z^2} - K\frac{\partial T}{\partial z} = 0 \tag{15}$$

Since the principle of the exchange of stability is valid [6], the normal mode expansion of the dependent variables is assumed in the form

$$\{w, T, \varphi\} = \{W(z), \Theta(z), \Phi(z)\}\exp[i(\ell x + my)] \tag{16}$$

where ℓ and m are wave numbers in the x- and y-directions, respectively.

Substituting Eq. (16) into Eqs. (13)–(15), and nondimensionalizing the variables by setting

$$z^* = \frac{z}{d}, \quad w^* = \frac{d}{\nu A}w, \quad \Theta^* = \frac{\kappa}{\beta\upsilon d}\Theta, \quad \text{and} \quad \Phi^* = \frac{(1+\chi)\kappa}{K\beta\upsilon d^2}\Phi \tag{17}$$

where $\upsilon = \mu_f/\rho_0$ is the kinematic viscosity, $\kappa = k_1/(\rho_0 C)_2$ is the effective thermal diffusivity, and $A = (\rho_0 C)_1/(\rho_0 C)_2$ is the ratio of heat capacities, we obtain (after dropping the asterisks for simplicity) the following:

$$[\Lambda(D^2 - a^2) - \mathrm{Da}^{-1}](D^2 - a^2)W = -a^2 R[M_1 D\Phi - (1 + M_1)\Theta] \tag{18}$$

$$(D^2 - a^2)\Theta = -(1 - M_2 A)W \tag{19}$$

$$(D^2 - a^2 M_3)\Phi - D\Theta = 0 \tag{20}$$

Here, $D = d/dz$ is the differential operator, $a = \sqrt{\ell^2 + m^2}$ is the overall horizontal wave number, W is the amplitude of the vertical component of velocity, Θ is the amplitude of the temperature, Φ is the amplitude of magnetic potential, $R = \alpha_t g\beta d^4/\nu\kappa$ is the thermal Rayleigh number, $M_1 = \mu_0 K^2\beta/(1+\chi)\alpha_t\rho_0 g$ is the magnetic number, $M_2 = \mu_0 T_0 K^2/(1+\chi)(\rho_0 C)_1$ is the magnetic parameter, $\mathrm{Da} = k/d^2$ is the Darcy number, $M_3 = (1 + M_0/H_0)/(1+\chi)$ is the measure of nonlinearity of magnetization, and $\Lambda = \tilde{\mu}_f/\mu_f$ is the ratio of viscosities. The typical value of M_2 for ferrofluids with different carrier liquids turns out to be of the order of 10^{-6}, and hence, its effect is neglected as compared with unity.

The lower boundary is considered to be rigid-ferromagnetic with fixed heat flux, while the upper boundary is assumed to be either thin rigid lamina of negligible heat capacity or stress-free with convective-radiative transport to the environment. Accordingly, we impose the following conditions at the boundaries:

$$W = DW = \Phi = D\Theta = 0 \text{(on the lower rigid boundary)}$$

$$W = DW = \Phi = D\Theta + \mathrm{Bi}\Theta = 0 \text{(if the upper boundary is rigid)}$$

$$W = D^2 W = D\Phi = D\Theta + \mathrm{Bi}\Theta = 0 \text{(if the upper boundary is free)} \tag{21}$$

where $\mathrm{Bi} = h_t d/k_1$ is the Biot number. The case $\mathrm{Bi} = 0$ and $\mathrm{Bi} \to \infty$ correspond to the constant heat flux and isothermal conditions at the upper boundary, respectively.

3 Method of Solution

Equations (18)–(20), together with the chosen boundary conditions, constitute an eigenvalue problem, which has been solved by the Galerkin method. Accordingly, W, Θ, and Φ are written as

$$W = \sum_{i=1}^{n} A_i W_i(z), \quad \Theta(z) = \sum_{i=1}^{n} C_i \Theta_i(z), \quad \Phi(z) = \sum_{i=1}^{n} D_i \Phi_i(z) \tag{22}$$

where A_i, C_i, and D_i are unknown constants to be determined. The base functions $W_i(z)$, $\Theta_i(z)$, and $\Phi_i(z)$ are generally chosen such that they satisfy the corresponding boundary conditions but not the differential equations [28]. For both boundaries rigid (i.e., rigid-rigid) as well as the lower-rigid and upper-free boundaries (i.e., rigid-free), the base functions are chosen as

$$W_i = z^2(1-z)^2 T^*_{i-1}, \quad \Theta_i = z(1-z/2)T^*_{i-1}, \quad \Phi_i = z(1-z)T^*_{i-1} \tag{23a}$$

$$W_i = \left(z^4 - \frac{5}{2}z^3 + \frac{3}{2}z^2\right)T^*_{i-1}, \quad \Theta_i = z(1-z/2)T^*_{i-1},$$

$$\Phi_i = z^2(1-2z/3)T^*_{i-1} \tag{23b}$$

where T^*_i is are the modified Chebychev polynomial. The above trial functions satisfy all the boundary conditions except the natural one, namely $D\Theta + \mathrm{Bi}\Theta = 0$ at $z=1$ but the residual from this condition is included as the residual from the differential equation. Multiplying Eq. (18) by $W_j(z)$, Eq. (19) by $\Theta_j(z)$, and Eq. (20) by $\Phi_j(z)$, performing the integration by parts with respect to z between $z=0$ and 1, and using the boundary conditions, we obtain a system of linear homogeneous algebraic equations in A_i, C_i, and D_i. For such a system, nontrivial solution exists if and only if a given characteristic determinant is equal to zero. This leads to a relation involving the characteristic parameters R, Λ, Da^{-1}, Bi, M_1, M_3, and a in the following form:

$$f(R, \Lambda, \mathrm{Da}^{-1}, \mathrm{Bi}, M_1, M_3, a) = 0 \tag{24}$$

4 Results and Discussion

The critical stability parameters are obtained numerically, in general, for the different types of boundary conditions considered. Besides, analytical solutions are also obtained when the boundaries are kept at constant heat flux conditions and the results are compared with those obtained numerically. A discussion on the results is made in the Secs. 4.1 and 4.2.

4.1 Numerical Solution for General Thermal Conditions. It is observed that six terms (i.e., $n=6$) in the series expansion of Eq. (22) are required to have convergent results within the accuracy of 0.01% for both rigid-rigid and rigid-free boundary conditions. To validate the numerical procedure used, first, the test computations are carried out under the limiting cases of $M_1 = M_3 = 0$, $\mathrm{Da}^{-1} = 0$, and $\Lambda = 1$ for different values of Bi. This limiting case corresponds to the ordinary viscous fluid (i.e., classical Rayleigh–Benard problem), which has been studied by Sparrow et al. [29] using a different solution procedure. The critical Rayleigh number and the corresponding wave number obtained for the above limiting case for both rigid-rigid and rigid-free boundary conditions are found to be in excellent agreement with those of Sparrow et al. [29], and thus verify the accuracy of the numerical procedure employed in the present study to solve the eigenvalue problem. It is thus evident that the results of Sparrow et al. [29] turned out to be a particular case of our study.

The critical Rayleigh numbers and the corresponding wave numbers obtained for different values of Λ, Da^{-1}, Bi, M_1, and M_3 are presented graphically in Figs. 2–6, respectively. Figure 2 shows the variation in the critical Rayleigh number R_c as a function of Da^{-1} for both types of velocity boundary conditions (i.e., rigid-rigid and rigid-free boundaries) and for different values of Bi with $M_1 = 5$, $M_3 = 1$, and $\Lambda = 1$. From the figure it is evident that the variation in Bi from 0 to 1 significantly increases the critical Rayleigh numbers in both the cases of velocity boundary conditions considered; the least being for $\mathrm{Bi} = 0$ and the highest values correspond to those for $\mathrm{Bi} = 1$. Thus the system is found to be more unstable for the upper heat insulating boundary as compared with isothermal condition at the upper boundary. This behavior is not surprising as the nature of the upper boundary changes drastically from an insulated surface to a conductive boundary with an increase in the value of Bi. It is evident that with an increase in the value of Bi, the temperature perturbations will not grow so easily, and therefore higher values of R_c are needed for the onset of convection. Further, for a fixed value of Bi, the critical Rayleigh numbers for rigid-rigid boundaries are greater than those of rigid-free boundaries because the effect of the upper rigid boundary is to suppress the disturbances. Moreover, the deviation in the critical Rayleigh number for different values of Bi increases gradually with an increase in the value of Da^{-1}.

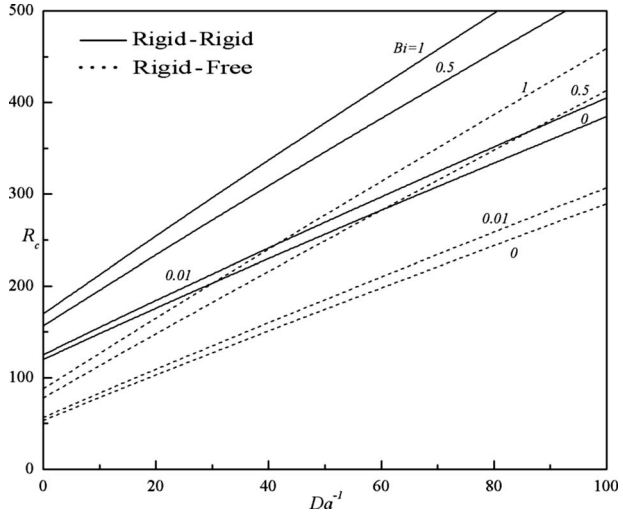

Fig. 2 Variation in critical Rayleigh number R_c as a function of Da^{-1} for different values of Bi when $M_3=1$, $M_1=5$, and $\Lambda=1$

As pointed out in the introduction, the model of Brinkman rests on an effective viscosity μ_e different from the fluid viscosity denoted through Λ in dimensionless form, and it has a determining influence on the onset of ferroconvection in porous media. Figure 3 indicates the variation in R_c as a function of Da^{-1} for the four values of $\Lambda = 1$, 3, 5, and 10 with $M_1 = 5$, $M_3 = 1$, and $\mathrm{Bi} = 2$. From the figure it is seen that an increase in the value of Λ is to increase

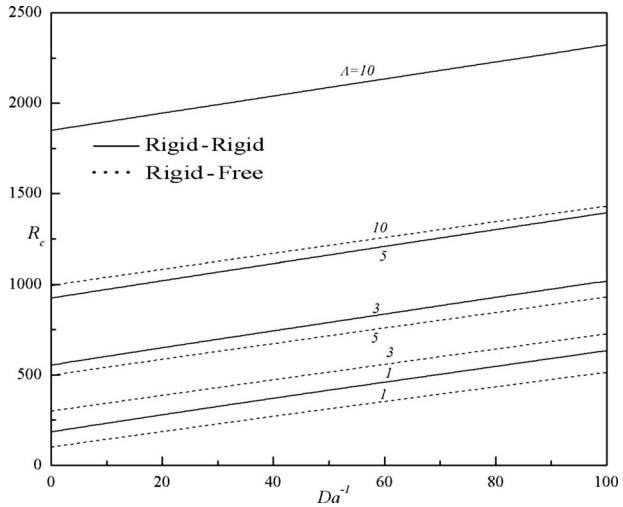

Fig. 3 Variation in critical Rayleigh number R_c as a function of Da^{-1} for different values of Λ when $M_3=1$, $M_1=5$, and $\mathrm{Bi}=2$

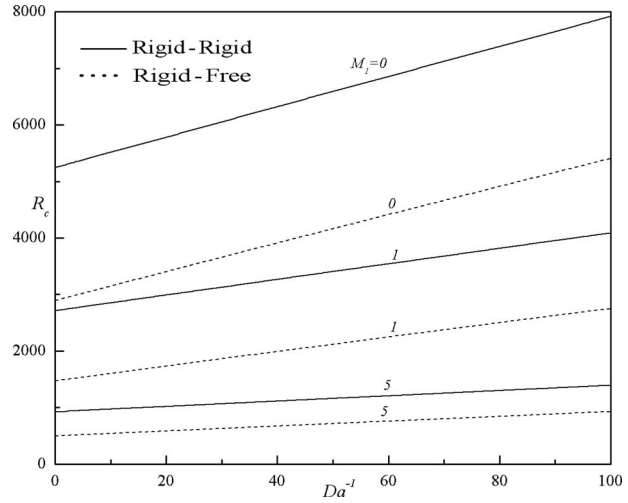

Fig. 4 Variation in critical Rayleigh number R_c as a function of Da^{-1} for different values of M_1 when M_3=1, Λ=5, and Bi=2

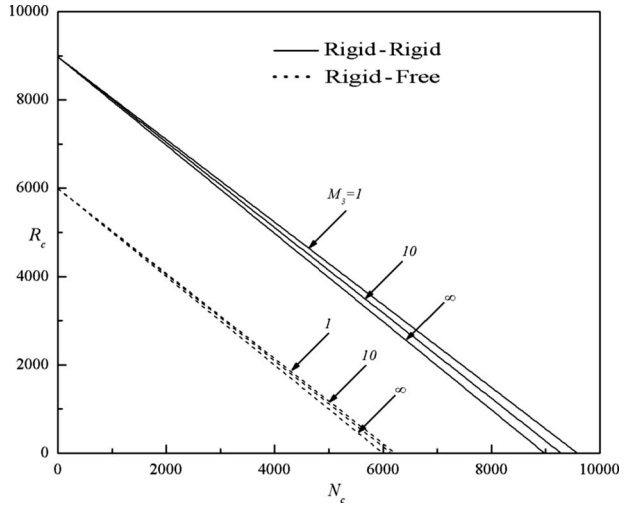

Fig. 6 Variation in critical Rayleigh number R_c as a function of N_c for different values of M_3 when Da^{-1}=100, Λ=6, and Bi=2

R_c, and hence its effect is to delay the onset of ferroconvection in a porous medium. Further inspection of the figure reveals that the deviation in the R_c values between the rigid-rigid and rigid-free boundaries goes on, increasing significantly with an increase in the value of Λ.

In Fig. 4, the critical Rayleigh numbers as a function of Da^{-1} are plotted for three values of M_1=0, 1, and 5 with M_3=1, Λ=5, and Bi=2. It is observed that an increase in the value of M_1 is to decrease the value of R_c, and thus leads to a more unstable system due to an increase in the magnetic force. Besides, it is interesting to note that the difference in the critical Rayleigh numbers between the rigid-rigid and rigid-free boundaries diminishes as the value of M_1 increases.

Figure 5 depicts R_c as a function of Da^{-1} for the different values of nonlinearity of fluid magnetization represented through the parameter M_3. The results presented here are for M_3=1, 10, and ∞ when M_1=5, Λ=6, and Bi=2. It can be seen that an increase in the value of M_3 is to decrease R_c, and thus it has a destabilizing effect on the stability of the system. This may be attributed to the fact that the application of magnetic field makes the ferrofluid acquire larger magnetization, which in turn interacts with the existing magnetic field to produce large energy and cause convection

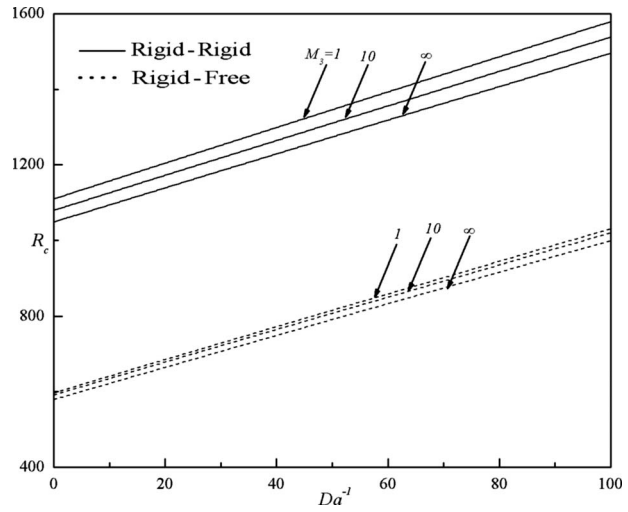

Fig. 5 Variation in critical Rayleigh number R_c as a function of Da^{-1} for different values of M_3 when M_1=5, Λ=6, and Bi=2

at a smaller temperature gradient. Nonetheless, the critical Rayleigh numbers are found to be independent of M_3 when Bi=0. In other words, the nonlinearity of fluid magnetization has no influence on the onset of ferroconvection in a porous medium if the boundaries are thermally adiabatic.

The complementary effects of the buoyancy and the magnetic forces are made clear in Fig. 6 by displaying the locus of the critical Rayleigh number R_c and the critical magnetic Rayleigh number N_c for different values of M_3 when Λ=6, Da^{-1}=100, and Bi=2 for both types of velocity boundary conditions considered. The magnetic Rayleigh number N is defined as $N=RM_1=\mu_0 K^2\beta^2 d^4/(1+\chi)\mu\kappa A$. From Fig. 6, we note that R_c is inversely proportional to N_c. As $M_3\to\infty$, irrespective of the boundaries considered, the data fit the following relation exactly

$$\frac{R_c}{R_{c0}}+\frac{N_c}{N_{c0}}=1$$

where R_{c0} is the critical Rayleigh number in the nonmagnetic case (N=0), and N_{c0} is the critical magnetic Rayleigh number in the nongravitational case (R=0), which depends on the value of Da^{-1} and Λ.

Figures 7–10 illustrate the variation in the critical wave number a_c as a function of Da^{-1} for different boundary conditions, and also for different values of Λ, Bi, M_1, and M_3. From these figures it is evident that an increase in Bi, Λ, and M_3 is to increase a_c, indicating their effect is to reduce the dimension of convection cells (see Figs. 7, 8, and 10). Whereas, an increase in M_1 is to decrease a_c, and thus its effect is to enlarge the size of convection cells (see Fig. 9). From further inspection of these figures it is seen that the critical wave number decreases with an increase in Da^{-1} when both boundaries are rigid, but opposite is the case for lower-rigid and upper-free boundaries. Moreover, the critical wave numbers for rigid-rigid boundaries are higher than those of rigid-free boundaries.

4.2 Analytical Solution for Constant Heat Flux Boundary Conditions. Since the critical wave number is negligibly small for constant-flux thermal boundary conditions (i.e., $D\Theta$=0 at z=0, 1), the eigenvalue problem is also solved analytically using regular perturbation technique with wave number a as a perturbation parameter. Accordingly, W, Θ, and Φ are expanded in powers of a^2 as

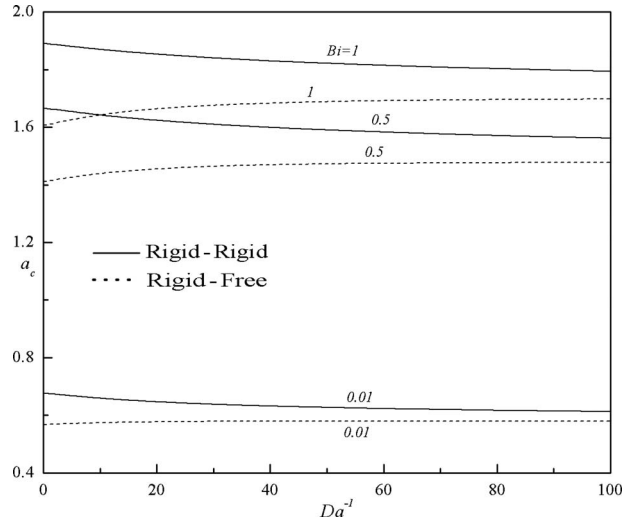

Fig. 7 Variation in critical wave number a_c as a function of Da^{-1} for different values of Bi when $M_3=1$, $M_1=5$, and $\Lambda=1$

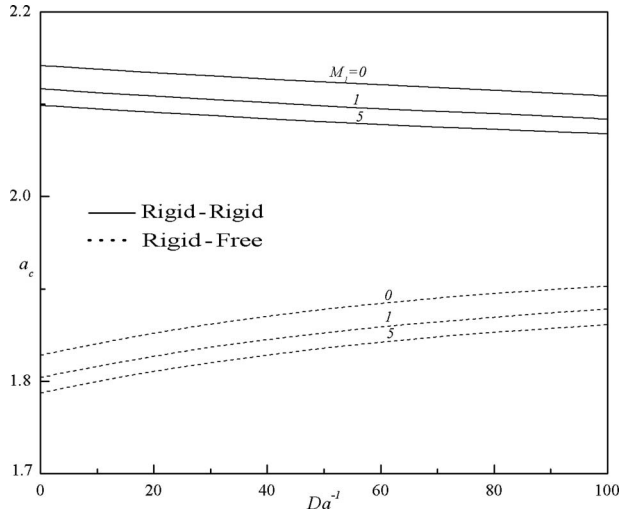

Fig. 9 Variation in critical wave number a_c as a function of Da^{-1} for different values of M_1 when $M_3=1$, $\Lambda=5$, and Bi=2

$$(W,\Theta,\Phi) = (W_0,\Theta_0,\Phi_0) + a^2(W_1,\Theta_1,\Phi_1) + \cdots \tag{25}$$

Substituting Eq. (25) into Eqs. (18)–(20) and also in the boundary conditions, and collecting the terms of 0th order in a^2, we obtain

$$D^4W_0 - \mathrm{Da}_e^{-1}D^2W_0 = 0 \tag{26a}$$

$$D^2\Theta_0 = -W_0 \tag{26b}$$

$$D^2\Phi_0 = D\Theta_0 \tag{26c}$$

where $\mathrm{Da}_e^{-1} = \mathrm{Da}^{-1}/\sqrt{\Lambda}$.

The corresponding boundary conditions are as follows:

(i) rigid-rigid boundaries

$$W_0 = DW_0 = 0 = D\Theta_0 = \Phi_0 \quad \text{at} \quad z = 0,1 \tag{27a}$$

(ii) rigid-free boundaries

$$W_0 = DW_0 = 0 = D\Theta_0 = \Phi_0 \quad \text{at} \quad z = 0 \tag{27b}$$

$$W_0 = D^2W_0 = 0 = D\Theta_0 = D\Phi_0 \quad \text{at} \quad z = 1 \tag{27c}$$

The solutions to the 0th order equations are $W_0=0$, $\Theta_0=1$, and $\Phi_0=0$ for the rigid-rigid boundaries, while $W_0=0$, $\Theta_0=1$, and $\Phi_0=1$ for the rigid-free boundaries.

The first order equations in a^2 are then

$$D^4W_1 - \mathrm{Da}_e^{-1}D^2W_1 = R_e(1+M_1) \tag{28a}$$

$$D^2\Theta_1 = 1 - W_1 \tag{28b}$$

$$D^2\Phi_1 = D\Theta_1 \tag{28c}$$

where $R_e = R/\Lambda$ with the boundary conditions $W_1 = DW_1 = \Phi_1 = D\Theta_1 = 0$ on the rigid boundary and $W_1 = D^2W_1 = D\Phi_1 = D\Theta_1 = 0$ on the free boundary.

The general solution of Eq. (28*a*) is given by

$$W_1 = c_1\cosh(\sigma_e z) + c_2\sinh(\sigma_e z) + c_3 + c_4 z - R_e(1+M_1)z^2/2\sigma_e^2 \tag{29}$$

where $\sigma_e = \sqrt{\mathrm{Da}_e^{-1}}$ and the arbitrary constants $c_1 - c_4$ are to be determined using the boundary conditions, and they are given by

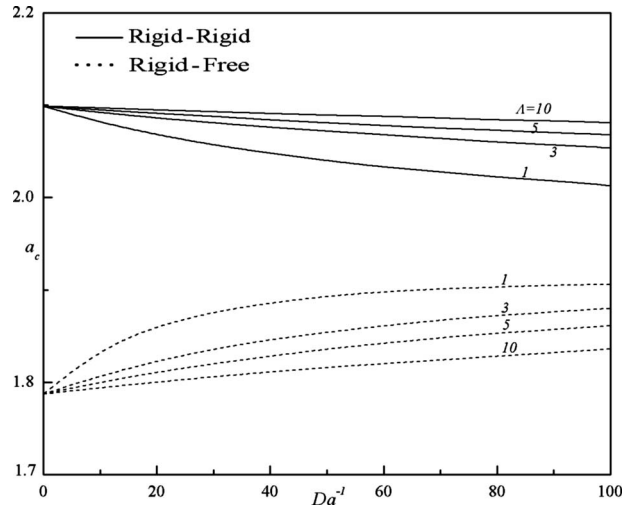

Fig. 8 Variation in critical wave number a_c as a function of Da^{-1} for different values of Λ when $M_3=1$, $M_1=5$, and Bi=2

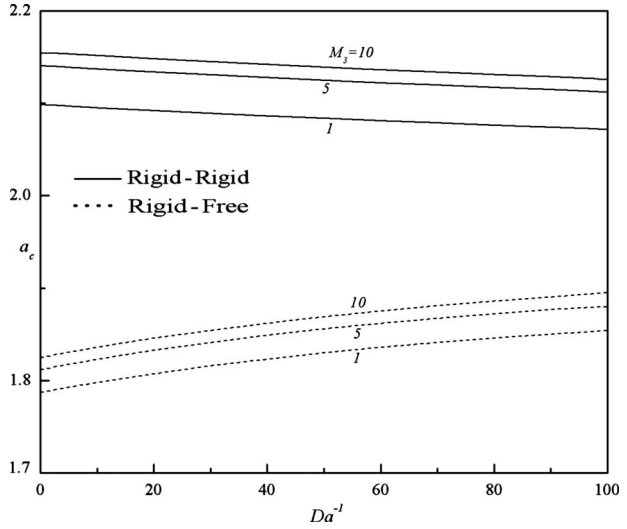

Fig. 10 Variation of critical wave number a_c as a function of Da^{-1} for different values of M_3 when $M_1=5$, $\Lambda=6$, and Bi=2

Table 1 Values of R_c obtained from Galerkin and regular perturbation techniques for different values of M_1, Λ, and Da^{-1} when Bi=0

		Rigid-rigid			Rigid-free		
M_1	Da^{-1}	$\Lambda=1$, R_c	$\Lambda=5$,R_c	$\Lambda=10$, R_c	$\Lambda=1$, R_c	$\Lambda=5$, R_c	$\Lambda=10$, R_c
0	10	889.511	3771.03	7371.23	470.404	1751.95	3352.16
	25	1137.57	4026.1	7627.32	690.258	1978.34	3579.61
	50	1538.35	4447.56	8052.2	1046.61	2352.02	3956.68
	75	1927.45	4864.477	8474.77	1394.8	2721.73	4331.43
	100	2307.96	5278.11	8895.11	1737.49	3088.01	4704.04
1	10	444.756	1885.51	3685.61	235.202	875.974	1676.08
	25	568.777	2013.05	3813.66	345.129	989.171	1789.80
	50	769.173	2223.78	4026.1	523.305	1176.01	1978.34
	75	963.725	2432.39	4237.38	697.398	1360.87	2165.72
	100	1153.98	2639.05	444.7.56	868.744	1544.00	2352.02
5	10	148.252	628.504	1228.54	78.401	281.991	558.694
	25	189.596	671.017	1271.22	115.043	329.724	596.601
	50	256.391	741.26	1342.03	174.435	392.004	659.447
	75	321.242	810.796	1412.46	232.466	453.622	721.906
	100	384.659	879.685	1482.52	289.581	514.668	784.007

(i) rigid-rigid boundaries

$$c_1 = \frac{R_e(1+M_1)(1+\cosh\sigma_e)}{2\sigma_e^3 \sinh\sigma_e}$$

$$c_2 = -\frac{R_e(1+M_1)}{2\sigma_e^3}$$

$$c_3 = -c_1$$

$$c_4 = -\sigma_e c_2 \tag{30}$$

(ii) rigid-free boundaries

$$c_1 = -\frac{R_e(1+M_1)[(\sigma_e^2-2)\sinh\sigma_e + 2\sigma_e]}{2\sigma_e^4(\sinh\sigma_e - \sigma_e\cosh\sigma_e)}$$

$$c_2 = \frac{R_e(1+M_1)[(\sigma_e^2-2)\cosh\sigma_e + 2]}{2\sigma_e^4(\sinh\sigma_e - \sigma_e\cosh\sigma_e)}$$

$$c_3 = -c_1$$

$$c_4 = -\sigma_e c_2 \tag{31}$$

Integrating Eq. (28*b*) between $z=0$ and 1 and using the boundary condition on temperature, it follows that

$$1 = \int_0^1 W_1 dz \tag{32}$$

Substituting for W_1 from Eq. (29) into Eq. (32) and carrying out the integration leads to an expression for critical Rayleigh numbers for rigid-rigid and rigid-free boundaries, respectively, in the following form:

$$R_{ec} = \frac{12\sigma_e^4 \sinh\sigma_e}{(1+M_1)[\sigma_e^2\sinh\sigma_e + 12\sinh\sigma_e - 6\sigma_e(1+\cosh\sigma_e)]} \tag{33}$$

and

$$R_{ec} = \frac{12\sigma_e^5(\sinh\sigma_e - \sigma_e\cosh\sigma_e)}{(1+M_1)[4\sigma_e(\sigma_e^2-6)\sinh\sigma_e + (24-\sigma_e^4)\cosh\sigma_e + 12(\sigma_e^2-2)]} \tag{34}$$

It is interesting to check the above relations for some special cases. When $M_1=0$ (i.e., ordinary viscous fluid case), then the above equations coincide with those obtained by Shivakumara and Nanjundappa [30].

Letting $\Lambda=1$ and $\sigma_e \to 0$, Eq. (33) becomes

$$R_c = \frac{720}{1+M_1} \tag{35}$$

and Eq. (34) becomes

$$R_c = \frac{320}{1+M_1} \tag{36}$$

thus recovering the results for nonporous case discussed by Nanjundappa and Shivakumara [17]. We note that the above two equations reduce to $R_c=720$ and $R_c=320$, respectively, when $M_1=0$, which are the known exact values for the ordinary viscous fluid layer [29]. From Eqs. (33) and (34), it is interesting to note that the nonlinearity of fluid magnetization (i.e., M_3) has no effect on the onset of convection, a result, which is revealed by numerical computations carried out in the Sec. 3. Since at the onset of convection $a_c=0$ (very large wavelength), one would expect that M_3 has no effect on the stability of the system (Eq. (20)). The numerically computed values of R_c for the different values of M_1, Da^{-1}, and Λ with Bi=0 are compared in Table 1 with those obtained using regular perturbation techniques. We note that the results obtained from simple regular perturbation techniques coincide exactly with those obtained from time consuming numerical methods, and thus provides a justification for the analytically obtained results for prescribed heat flux conditions (i.e., Bi=0). In other words, the solutions obtained analytically are exact. As noticed earlier, an increase in the value of Da^{-1} and Λ, as well as a decrease in M_1 is to increase R_c and raise the stability of the system.

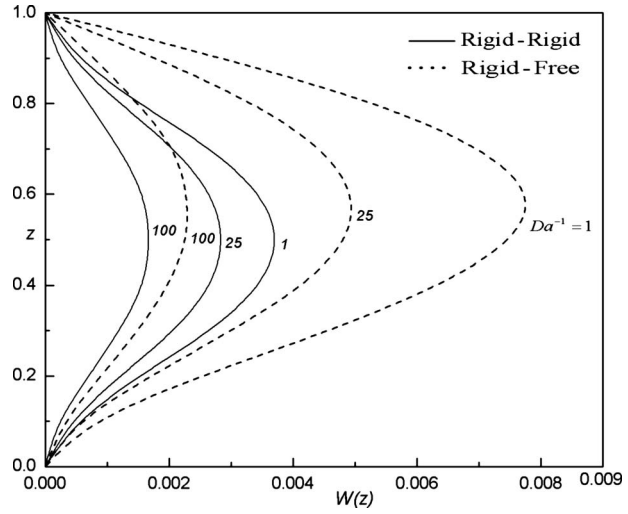

Fig. 11 Vertical velocity eigenfunctions for different values of Da^{-1} when $M_1=2$ and $\Lambda=2$

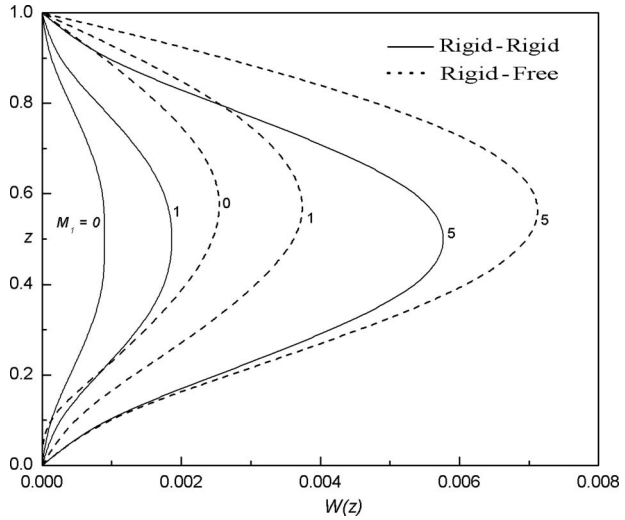

Fig. 13 Vertical velocity eigenfunctions for different values of M_1 when $\Lambda=2$ and $Da^{-1}=25$

The eigenfunctions of the vertical velocity $W(z)$ for rigid-rigid and rigid-free boundaries are presented in Figs. 11–13 for the different values of Da^{-1}, Λ, and M_1, respectively. As can be seen, $W(z)$ gets reduced more in the case of rigid-rigid boundaries when compared with the rigid-free boundaries for the different values of the physical parameters considered. Further, an increase in the values of the porous parameter Da^{-1} (see Fig. 11) and viscosity ratio Λ (see Fig. 12) is to decrease in the value of $W(z)$, while opposite is the case with an increase in the value of the magnetic parameter M_1 (see Fig. 13) for a chosen velocity boundary condition. This corroborates the effect of these parameters observed on the onset of ferroconvection in a ferrofluid saturated porous layer.

5 Conclusions

From the foregoing study, it is observed that nature of velocity and temperature boundary conditions significantly influence the onset of ferroconvection in a ferrofluid saturated porous medium. It is found that an increase in the value of M_1 and M_3 is to hasten, while an increase in Bi, Λ, and Da^{-1} is to delay the onset of ferroconvection in a porous medium. Nonetheless, the parameter M_3 has no effect on the stability of the system in the case of constant-flux thermal boundary conditions (i.e., Bi=0). Besides, the numerically and analytically obtained results for the case of constant-flux thermal boundary conditions coincide with each other, indicating that the critical stability parameters obtained from the analytical formula are exact. Further, a decrease in M_3, Λ, and Bi and an increase in M_1 is to decrease in the critical wave number, irrespective of the velocity boundary conditions. Whereas, the critical wave number decreases with an increase in Da^{-1} if both boundaries are rigid, and increases if the boundaries are of different types (i.e., lower-rigid and upper-free boundaries). Also, $(R_c \text{ and } a_c)_{\text{rigid-rigid}} > (R_c \text{ and } a_c)_{\text{rigid-free}}$.

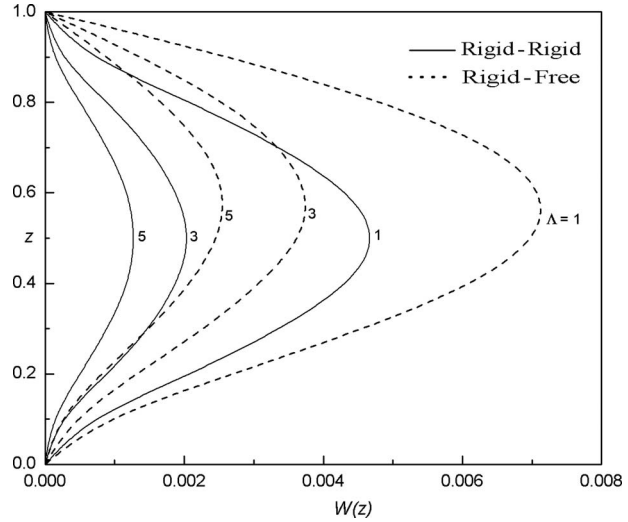

Fig. 12 Vertical velocity eigenfunctions for different values of Λ when $M_1=2$ and $Da^{-1}=25$

Acknowledgment

The work reported in this paper was supported by UGC under CAS Programme. The authors (C.E.N. and M.R.) wish to thank the management and principal of Dr. Ambedkar Institute of Technology and East Point College of Engineering and Technology, Bangalore, respectively, for the encouragement. The authors are thankful to the reviewers for their constructive comments.

References

[1] Rosensweig, R. E., 1985, *Ferrohydrodynamics*, Cambridge University Press, London.
[2] Berkovsky, B. M., Medvedev, V. F., and Krakov, M. S., 1993, *Magnetic Fluids, Engineering Applications*, Oxford University Press, New York.
[3] Blums, E., Cebers, A., and Maiorov, M. M., 1997, *Magnetic Fluids*, de Gruyter, New York.
[4] Hergt, R., Andrä, W., Ambly, C. G., Hilger, I., Kaiser, W. A., Richter, U., and Schmidt, H. G., 1998, "Physical Limitations of Hypothermia Using Magnetite Fine Particles," IEEE Trans. Magn., **34**, pp. 3745–3754.
[5] Alexiou, C., Arnold, W., Hulin, P., Klein, R., Schmidt, A., Bergemann, C., and Parak, F. G., 2001, "Therapeutic Efficacy of Ferrofluid Bound Anticancer Agent," Magnetohydrodynamics, **37**, pp. 318–322.
[6] Finlayson, B. A., 1970, "Convective Instability of Ferromagnetic Fluids," J. Fluid Mech., **40**, pp. 753–767.
[7] Lalas, D. P., and Carmi, S., 1971, "Thermoconvective Stability of Ferrofluids," Phys. Fluids, **14**, pp. 436–437.
[8] Shliomis, M. I., 1974, "Magnetic Fluids," Sov. Phys. Usp., **17**(2), pp. 153–169.
[9] Gotoh, K., and Yamada, M., 1982, "Thermal Convection in a Horizontal Layer of Magnetic Fluids," J. Phys. Soc. Jpn., **51**, pp. 3042–3048.
[10] Schwab, L., Hilderbrandt, U., and Stierstadt, K., 1983, "Magnetic Bénard Convection," J. Magn. Magn. Mater., **39**, pp. 113–114.
[11] Stiles, P. J., and Kagan, M., 1990, "Thermoconvective Instability of a Horizontal Layer of Ferrofluid in a Strong Vertical Magnetic Field," J. Colloid Interface Sci., **134**, pp. 435–448.
[12] Shivakumara, I. S., Rudraiah, N., and Nanjundappa, C. E., 2002, "Effect of Non-Uniform Basic Temperature Gradient on Rayleigh–Benard–Marangoni Convection in Ferrofluids," J. Magn. Magn. Mater., **248**, pp. 379–395.

[13] Kaloni, P. N., and Lou, J. X., 2004, "Convective Instability of Magnetic Fluids," Phys. Rev. E, **70**, p. 026313.
[14] Shivakumara, I. S., and Nanjundappa, C. E., 2006, "Marangoni Ferroconvection With Different Initial Temperature Gradients," J. Energy Heat Mass Transf., **28**, pp. 45–59.
[15] Volker, T., Blums, E., and Odenbach, S., 2007, "Heat and Mass Transfer Phenomena in Magnetic Fluids," Mitt. Ges. Angew. Math. Mech., **30**(1), pp. 185–194.
[16] Sunil, and Mahajan, A., 2008, "A Nonlinear Stability Analysis for Magnetized Ferrofluid Heated From Below," Proc. R. Soc. London, Ser. A, **464**, pp.83–98.
[17] Nanjundappa, C. E., and Shivakumara, I. S., 2008, "Effect of Velocity and Temperature Boundary Conditions on Convective Instability in a Ferrofluid Layer," ASME J. Heat Transfer, **130**, p. 104502.
[18] Rosensweig, R. E., Zahn, M., and Volger, T., 1978, "Stabilization of Fluid Penetration Through a Porous Medium Using Magnetizable Fluids," *Thermomechanics of Magnetic Fluids*, B. Berkovsky, ed., Hemisphere, Washington, DC, pp. 195–211.
[19] Zahn, M., and Rosensweig, R. E., 1980, "Stability of Magnetic Fluid Penetration Through a Porous Medium With Uniform Magnetic Field Oblique to the Interface," IEEE Trans. Magn., **16**, pp. 275–282.
[20] Vaidyanathan, G., Sekar, R., and Balasubramanian, R., 1991, "Ferroconvective Instability of Fluids Saturating a Porous Medium," Int. J. Eng. Sci., **29**, pp. 1259–1267.
[21] Qin, Y., and Chadam, J., 1995, "A Nonlinear Stability Problem for Ferromagnetic Fluids in a Porous Medium," Appl. Math. Lett., **8**(2), pp. 25–29.
[22] Borglin, S. E., Mordis, J., and Oldenburg, C. M., 2000, "Experimental Studies of the Flow of Ferrofluid in Porous Media," Transp. Porous Media, **41**, pp. 61–80.
[23] Saravanan, S., and Yamaguchi, H., 2005, "Onset of Centrifugal Convection in a Magnetic-Fluid-Saturated Porous Medium," Phys. Fluids, **17**, p. 084105.
[24] Sunil, Sharma, D., and Sharma, R. C., 2005, "Effect of Dust Particles on Thermal Convection in Ferromagnetic Fluid Saturating a Porous Medium," J. Magn. Magn. Mater., **288**, pp. 183–195.
[25] Nield, D. A., Junqueira, S. L. M., and Lage, J. L., 1996, "Forced Convection in a Fluid Saturated Porous Medium Channel With Isothermal or Isoflux Boundaries," *Proceedings of the International Conference on Porous Media and Their Applications in Science, Engineering and Industry*, K. Vafai and P. N. Shivakumar, eds., Engineering Foundation, New York, pp. 51–70.
[26] Givler, R. A., and Altobelli, S. A., 1994, "A Determination of the Effective Viscosity for the Brinkman–Forcheimer Flow Model," J. Fluid Mech., **258**, pp. 355–370.
[27] Rajagopal, K. R., Ruzicka, M., and Srinivas, A. R., 1996, "On the Oberbeck–Boussinesq Approximation," Math. Models Meth. Appl. Sci., **6**(8), pp. 1157–1167.
[28] Finlayson, B. A., 1972, *Method of Weighted Residuals and Variational Principles*, Academic, New York.
[29] Sparrow, E. M., Goldstein, R. J., and Jonsson, U. K., 1964, "Thermal Instability in a Horizontal Fluid Layer: Effect of Boundary Conditions and Non-Linear Temperature Profiles," J. Fluid Mech., **18**, pp. 513–528.
[30] Shivakumara, I. S., and Nanjundappa, C. E., 2001, "Onset of Convection in a Sparsely Packed Porous Layer With Throughflow," Arch. Mech., **53**(3), pp. 219–241.

How Good Is Open-Cell Metal Foam as Heat Transfer Surface?

Indranil Ghosh
Cryogenic Engineering Centre,
Indian Institute of Technology,
Kharagpur 721 302, India
e-mail: indranil@hijli.iitkgp.ernet.in

High porosity open-cell metal foam is considered to be an attractive choice for compact heat exchanger applications because of its high area density and superior thermal performance. A systematic study has been made in the present article to verify the suitability of the porous material as an extended heat transfer surface. The area goodness (j/f) factor has been chosen as performance evaluation criterion. This governing parameter has been computed using the existing correlations for the heat transfer and pressure drop coefficients. Conservative estimate shows that the thermohydraulic characteristics of high porosity open-cell metal foam are almost alike, if not better than those of the conventional heat transfer surfaces. Importantly, the analysis has been found to be consistent with the Reynolds analogy. This study helps the designer in making the initial selection of foam surfaces for the heat exchanger application. [DOI: 10.1115/1.3160537]

Keywords: metal foam, goodness factor, porosity, pore density, heat exchanger

1 Introduction

Use of extended heat transfer surfaces is a well-known means for augmenting heat exchange. Meticulously designed fin renders double benefits—compactness in size and augmentation in overall heat transfer coefficient. Plate fin type compact heat exchangers make use of such finned surfaces to achieve high thermal efficiency. Some of the commonly used high performance fin geometries include wavy fin, offset strip fin, louvered fin, pin fins, perforated fins, etc. Although such compact heat exchangers find wide applications in various process industries and equipment, there is hardly any addition to the list of finned surfaces over the past few decades. Technological advancement has helped in reducing the hydraulic diameter while the basic geometries of the flow passages remain unaltered. Process intensifications achieved by increasing heat transfer surface area density take its toll with corresponding rise in pressure drop. Nevertheless, a thermal engineer always aspires to design and fabricate a heat transfer surface, which will have ideal features like high area density, enhanced heat transfer coefficient, and minimum pressure drop. Recently developed high porosity open-cell metal foam is a promising alternative. It appears that the new class of material possesses all the positive qualities one looks for. A systemic study has been attempted in this manuscript to confirm this belief.

High area density is one of the basic criteria to call a heat transfer surface good. Compactness, following the recommendation of Shah [1], is quantified with an area density of 700 m^2/m^3. Open-cell metal foam, owing to its highly interconnected filamentlike structure, open porosity, and variable pore densities, can easily meet this criterion. The complexity of the foam structure makes it difficult to have an exact estimate of the area density. However, the complicated foam structure is often simplified with a repetitive cubic structure model. Then the expression for the foam area density [2,3] can be derived on the basis of the model

$$\sigma_s = 3\pi\left(\frac{d_f}{d_p{}^2}\right) = \frac{2\sqrt{3\pi}}{d_p}\rho_{\mathrm{rel}}{}^{1/2} \tag{1}$$

While the area density is directly proportional to the strut diameter, it is inversely proportional to the square of the pore diameter. It is worthwhile to mention that the pore density (often measured as pores per inch (PPI)) and porosity (ε) are the parameters commonly used by foam manufacturers to characterize open-cell porous materials. These two variables are related to the basic structural properties like strut diameter (d_f) and pore diameter (d_p). The typical area density of a 20 PPI foam with 85% porosity is nearly about 2000 m^2/m^3 [2]. Certainly, the compactness criterion is met by open porous metal foam.

Next to area density, the properties of paramount importance are the heat transfer and pressure drop characteristics. In the nondimensional form, they are represented traditionally by the Colburn factor j and friction-factor f. While compactness and thermal performance is closely associated with the heat transfer coefficient, the other one decides the pumping power requirement. An ideal heat transfer surface should have coefficients of high heat transfer and low pressure drop. This follows an obvious question—How good is open-cell foam with respect to its heat transfer and frictional properties?

Literature review does not provide any clear answer to this query. In response to this question, it is necessary to know the criterion for calling a heat transfer surface good or bad. There exists no unique index to define the "goodness" of heat transfer surfaces. Instead, the existence of more than 16 different performance evaluation criteria (PEC) has been reported by Shah [4]. "Area goodness factor" is one of the commonly used comparison criteria defined as the ratio of j factor to f factor. Heat transfer surface with high (j/f) ratio designates lower free-flow area and hence lower frontal area. "Volume goodness factor" is a more generalized technique suggested by London and Ferguson [5] for surfaces of equivalent hydraulic diameters. It is represented by a plot of heat transfer coefficient versus pumping power per unit heat transfer area. A high value on such a graph is an indicative of reduced core volume. Cowell [6] presented a family of methods for comparing compact heat transfer surfaces. The variables and constants have been chosen from the list of hydraulic diameter, frontal area, total volume, pumping power, and number of transfer units. According to him, a clear and compact indication of the relative merits of the different surfaces is possible by the proposed method. Hesselgreaves [7] listed different criteria for comparing heat transfer surfaces under various constraints. Sekulic et al. [8] attempted to establish a performance evaluation criterion using the thermodynamic irreversibility (entropy generation minimization). They also compared the results obtained through the conventional area goodness factor. Recently, Sahiti et al. [9] proposed a new technique based on the method developed by Soland et al. [10]. A direct comparison of the heat transfer rate and power input per unit heat exchanger volume has been used by Sahiti et al. [9] for the performance evaluation of the heat exchangers.

Manuscript received September 25, 2008; final manuscript received February 28, 2009; published online July 28, 2009. Review conducted by Kambiz Vafai.

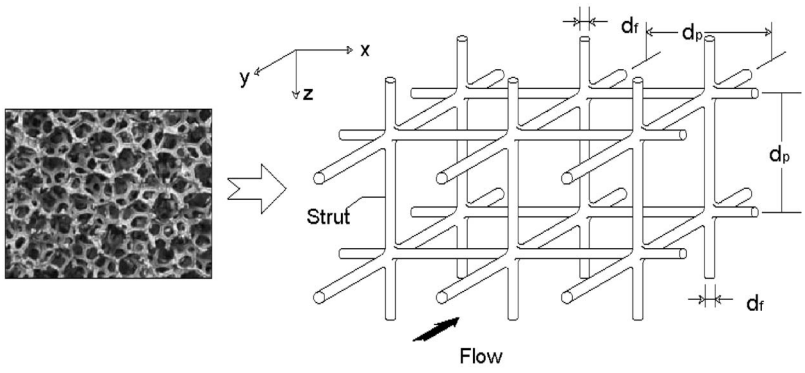

Fig. 1 Open-cell foam (*a*) actual structure and (*b*) unit cubic cell model

While the principal objective for selecting the optimum surface remains the same in all the suggested techniques, the constraints imposed upon achieving optimization are different. Comparison of surfaces using area goodness criteria, for example, is inherently associated with the assumption of fixed pressure drop, while the volume goodness criterion is linked with the postulation of equivalent hydraulic diameter. Imposition of constraints, in reality, is determined by the process requirement and the factors like compactness, etc. Depending on the process, one can often sacrifice heat transfer or tolerate enhance pressure loss at the cost of the other. In this article, it has been decided to adhere to the area goodness factor criterion. Since this study does not intend a multivariable optimization of a real heat exchanger, selection of area goodness is justified for comparative evaluation. The superiority of the new generation material as the heat transfer surface can be established if its thermal performance is found better than the prevailing one. The widely accepted heat transfer surfaces, benchmarked for yielding high performance, can be set as the reference. Literature review shows that the offset strip fins and wavy fins, because of their superior performance in various practical applications, have attracted the attention of researchers more than other geometries. Thermohydraulic characterization data for these two types of surfaces are also not rare [11–14]. The selection of these two types of fins as the standard reference surfaces has been made on that basis.

It is evident that the knowledge of heat transfer and pressure drop characteristics for metal form as well as for both fin types is necessary for the comparison of surfaces using the area goodness factor. The study reveals that substantial work has already been carried out both theoretically and experimentally on various aspects of the characterization of open porous materials. It includes thermohydraulic modeling and simulation [15–19], numerical analysis [20–23], thermophysical characterization [24], and experimental determination of heat transfer and pressure drop [25–27]. Attempts have also been made to develop heat transfer and pressure drop correlations involving different foam variables and process parameters. Porous media with porosity ranging between 0.3 and 0.6 has a few decade long history of research. An excellent review on this topic has been made by Kaviany [28]. However, the development of metal foam with porosity more than 0.9 is relatively new. Recently, Mahjoob and Vafai [29] reviewed the existing fluid and thermal transport models for metal foam heat exchangers and summarized the existing correlations for the open porous materials. Another such attempt has been reported very recently by Edouard et al. [30]. Wide variations in the expressions for heat transfer and pressure drop correlations often create confusion about the selection of the appropriate one. The use of different models representing the porous structure is primarily responsible for generating dissimilar correlations. In the present article, heat transfer and pressure drop analysis has been reviewed to find the suitable ones for this study. Based on that thermohydraulic analysis, the area goodness factor for the porous material has been calculated and compared with those of the wavy and offset strip fins.

2 Heat Transfer Models and Correlations

Open-cell metal, being a continuously connected structure of slender filaments, can be characterized by different parameters like cell size, cell shape, relative density, degree of anisotropy, etc. In practice, the manufacturers commonly specify two parameters, viz., pore density (in PPI) and relative density to describe the porous media. Conversely, the theoretical analysis of foam heat transfer and pressure drop is mostly based on the simplified, simulated porous structure. Foam assembly described by the original complex foam geometry renders the modeling difficult (Fig. 1(*a*)). Thermohydraulic simulation of an exact foam replica can only be handled with computational fluid dynamics (CFD) [31]. Otherwise, one needs to apply simplifying assumptions.

The characteristic dimension of the porous body has not been defined uniquely. Different models have diverse opinions about this parameter. While a group of researchers [17,23,31] has argued for the use of permeability, others [3,18] have preferred either the "mean pore diameter" or the "strut diameter" [24,27]. Under these circumstances, it is also not possible to have a uniquely defined Reynolds number. The strut diameter appears to be the appropriate characteristic dimension when the "simple cubic model" is used to represent the foam structure [2,3].

Small convective flow through the porous medium can be imagined to form a continuum between the solid and the liquid with local thermal equilibrium [32–34]. Recently, Dukhan et al. [35] proposed a macroscopic lumped-parameter engineering model to determine the temperature distribution within the open-cell metal foam. However, the assumption of local thermal equilibrium remains valid within a limited range of fluid flow. Alternatively, one has to consider nonequilibrium between the foam filaments and the fluid flowing over them. Then it becomes necessary to look at the porous structure on a microscopic scale. The intricate foam microstructure renders heat transfer and fluid flow modeling very difficult. Simple cubic representation can reduce the complexity of the foam geometry to a great extent. In this model, the porous structure is assumed to be a repetitive cubic block made with slender tubes of diameter d_f and length d_p, as shown in Fig. 1(*b*). The three-dimensional microstructure gets further simplified with the omission of the cross-connections between the struts [2]. Then the simple cubic struts assembly reduces into a bundle of unidirectional microtubes. Convective flow through the struts then resembles flow across the bank of tubes. Calmidi and Mahajan [36] also considered the local nonequilibrium between the solid and the fluid phase. Their heat transfer model is based on heat transfer correlations for cylinders on cross-flow. Recently, microstructure based heat transfer model retaining

the integrity of the foam structure has been analyzed by Ghosh [37]. The analysis revealed that the cross-connectivity plays an important role in heat transfer augmentation.

The selection of appropriate correlations for the dimensionless heat transfer coefficient such as j factor or Nusselt number is an essential part of thermal modeling. In principle, heat transfer data can be computed from CFD analysis of velocity and temperature field. However, even with the modern computers, the process is difficult and does not predict the performance of the complex surfaces accurately. Experimentally obtained data are considered to be most reliable until now. Empirical correlations are worked out to help the engineer in designing heat exchangers even in the absence of direct experimental data.

Heat transfer coefficients are, in general, dependent on the flow conduit, fluid velocity, and types of fluid. Starting with the simple cubic model, the effective Nusselt number ($\mathrm{Nu}_{\mathrm{eff}}$) for the porous medium has been predicted in terms of the empirical correlations for the cross-convective flow over the bank of smooth tubes [38]

$$\mathrm{Nu}_{\mathrm{eff}} = \sqrt{2}\mathrm{Nu}_{\mathrm{tube}} \tag{2}$$

where $\mathrm{Nu}_{\mathrm{tube}} = 0.8\ \mathrm{Re}^{0.4}\ \mathrm{Pr}^{1/3}$ for $10 < \mathrm{Re} < 100$, and the Reynolds number has been defined on the basis of the strut diameter. Heat transfer correlations obtained through separate heat and mass transfer experiments by Giani et al. [39,40] are almost identical to Eq. (2). The validity of Eq. (2) is further established through the similar expression predicted by Lu et al. [2].

Heat transfer coefficient can also depend on the model used for the analysis [38]. While deriving this Eq. (2), foam has been considered as a cluster of x-struts with protrusions of length ($d_p/2$) along the y- and z-directions. In order to take account of the roughness caused due to the protruding struts, the heat transfer coefficient (h_{tube}) for the cross-convective flow over the bank of smooth tubes is modified suitably. As an alternative to this approach, it may be presumed that the projected struts are acting as extended heat transfer surfaces. If the projected filaments act as fins, the heat transfer through the individual struts has to be considered independently. When conduction heat transfer through the cross struts is considered separately in the microstructure-based model [37,38], the effective heat transfer coefficient becomes

$$\mathrm{Nu} = \frac{\sqrt{2}\mathrm{Nu}_{\mathrm{tube}}}{1 + 4\eta_{1/2}} \tag{3}$$

where

$$\eta_{1/2} = \frac{\tanh\dfrac{md_p}{2}}{\dfrac{md_p}{2}}, \quad m = \sqrt{\frac{4h}{k_f d_f}}$$

Comparison between Eqs. (2) and (3) shows that the effective Nusselt number given by the former will have a higher value than its equivalent represented by the latter. The factor in the denominator of Eq. (3) arises due to the conduction heat transfer through cross connecting the y- and z-struts acting as fins attached to the x-strut. It has been shown in Ref. [38] that the end effects in both situations are the same. In the microstructured model, the heat transfer coefficient may become small, but explicit consideration of heat transfer through the cross struts maintains the heat balance. In contrast, an enhanced heat transfer coefficient takes care of the entire heat transport formalism in the "lumped parameter engineering" model [35]. It may be emphasized here that Eq. (3) represents a more appropriate form of convective heat transfer coefficient, although the outcomes of these two approaches are the same. It is because of the fact that the contributions of conductive and convective heat transfer could be separated out in Eq. (3). On the other hand, Eq. (2) signifies an overall heat transfer coefficient including the effect of conduction through the cross-connecting struts.

Equation (3) can be used to express heat transfer coefficient in another dimensionless form, i.e., j factor,

$$j = \frac{\mathrm{Nu}}{\mathrm{St}\ \mathrm{Pr}^{1/3}} = \frac{\sqrt{2}\mathrm{Nu}_{\mathrm{tube}}}{(1 + 4\eta_{1/2})\mathrm{St}\ \mathrm{Pr}^{1/3}} \tag{4}$$

Since Eq. (4) represents the porous media convective heat transfer exclusively, the present article has used it while comparing different heat transfer surfaces based on the area goodness factor.

3 Pressure Drop Models and Correlations

The friction-factor (f) is defined on the basis of an equivalent shear force in the flow direction per unit friction area. The force can be a viscous shear (skin friction), pressure force (form drag), or a combination of the two. Without making an attempt to differentiate them from each other, it is possible to express the overall effect by the Fanning friction-factor (f) given by the relation

$$f = \frac{\tau_s}{\left(\frac{1}{2}\rho u^2\right)} \tag{5}$$

with τ_s being is the surface shear stress. In engineering applications, pressure drop (ΔP) due to internal flow through a duct can be related to shear stress for obtaining Eq. (6) [41]:

$$\Delta P = \frac{4fL}{d_h} \cdot \left(\frac{1}{2}\rho u^2\right) \tag{6}$$

with d_h being the hydraulic diameter.

On the other hand, pressure drop in porous media is conventionally expressed by the Forchheimer equation

$$\frac{\Delta P}{L} = \frac{\mu u}{K} + \frac{\rho F u^2}{\sqrt{K}} \tag{7}$$

Equation (7) is a widely accepted pressure drop expression for the flow through porous medium. Permeability (K) and inertial coefficient (F) in the above equation are not really constants, instead they are strongly dependent on the foam's geometrical properties like pore density, porosity, etc. Differential pressure drop measurement across the porous body can be used for the experimental determination of those two factors [25]. Efforts have also been made for their theoretical estimation [18,42]. In either case, attempts are made to develop empirical or analytical correlations involving foam variables. Substantial literature has been found to exist on the pressure drop characterization of high porosity foams [18,24,25,42].

The history of fluid flow through porous media has been reviewed by Lage [43]. Another review on porous media with porosity ranging between 0.3 and 0.6 has been summarized by Kaviany [28]. Lu et al. [2] developed an analytical model with simple cubic unit cell for using metal foams in compact heat exchangers. In the process, they also estimated the pressure drop occurring in the fluid flow through the porous media. Assuming that the flow through the unit cubic cell and the bank of tubes are similar, pressure drop expression has been derived using the empirical friction-factor correlations for the tube bundles in cross-convective flow. Giani et al. [39,40] also followed the model proposed by Lu et al. [2] for analyzing the experimental pressure drop data. Derivation of the friction-factor coefficient is based on the analogy with pressure drop across tube banks. Theoretical model based on the simple cubic unit structure of foam has been proposed by Du Plessis et al. [18]. The model has been further improved by Fourie and Du Plessis [44]. Prediction of pressure gradient in terms of the permeability and inertial coefficient derived from their model is quite accurate. Hwang et al. [45] tried to fit the experimentally obtained the pressure drop data in a relation similar to Eq. (6). The characteristic dimension of the media has been taken as the length of the flow channel, and the corresponding Reynolds number has been used to develop empirical correlations relating different porosities. Bhattacharya et al. [24] con-

ducted analytical and experimental investigations for the determination of permeability and inertial coefficient. Their analytical model is based on the unit cubic cell model for the porous body. Paek et al. [17] experimentally determined the permeability and friction-factor for the flow of water through a porous body. The correlation obtained for the friction-factor is inline with those, which have been proposed by other researchers [33]. It depends on the Reynolds number defined on the basis of permeability. Boomsma et al. [46] studied experimentally the compressed and uncompressed foams, with water as the convective fluid. They reported substantial reduction in thermal resistance in the compressed foam without the additional cost of pumping power. In a separate article, they reported heat transfer and pressure drop simulation studies using the computational fluid dynamics [31]. Kim et al. [47] conducted experimental thermohydraulic studies on porous media. However, they correlated the experimental data using Darcy and Reynolds numbers based on the channel height. They also compared the performance of porous foam with the conventional louvered fins by plotting pumping power per unit volume versus heat transfer per unit volume per unit temperature difference. This is the performance evaluation criteria recommended by Kays and London [48]. They reported similar thermal performance when compared with the conventional louvered fins and also indicated that the performance of louvered fins in terms of pressure drop is better than foam. Dukhan et al. [26] reported pressure drop measurement for the airflow through compressed and uncompressed open-cell foam samples. They tried to fit experimental data in the Ergun-type model, originally developed for the pressure drop calculation in a porous bed made of spherical particles. The applicability of Ergun-like pressure drop expression for the porous material is justified, provided that an appropriate equivalent particle diameter is used [49]. Researchers have different opinions about the characteristic dimension. The list includes strut diameter, square root of permeability, equivalent spherical diameter, reciprocal of surface area density, etc. It has lead to the development of several Ergun-like pressure drop correlations for the ceramic foams to be used as catalytic substrates [30,50–52].

The complexity of the foam geometry in the present article has been simplified using unit cubic cell model of the porous structure. The diameter of the ligament in the transformed configuration has been taken as the characteristic dimension both for heat transfer and pressure drop analyses. This approach is in line to that has been adopted by Lu et al. [2], Ashby et al. [53], and Fourie and Du Plessis [44]. Pressure drops in Eqs. (8) and (9), suggested by Lu et al. [2] and Ashby et al. [53], respectively, have been used to determine the foam friction-factor:

$$\frac{\Delta P}{L} = \left(\frac{4\chi\rho u^2}{d_p}\right)\left(\frac{u d_p}{\nu}\right)^{-0.15} \frac{\left(\frac{d_p}{d_f} - 1\right)^{0.15}}{\left(1 - \frac{d_f}{d_p}\right)^2}\left\{0.044 + \frac{0.08\left(\frac{d_p}{d_f}\right)}{\left(\frac{d_p}{d_f} - 1\right)^n}\right\} \tag{8}$$

where

$$n = 0.43 + 1.13\left(\frac{d_f}{d_p}\right)$$

$$\frac{\Delta P}{L} = \frac{4}{a}\left[\frac{\nu^m \rho}{(1-\alpha)^{2-m}}\right] u^{2-m} d_f^{-m} \tag{9}$$

where

$$a = 1.24 d_f \sqrt{\frac{3\pi}{\rho_{\text{rel}}}}$$

The analytical prediction by Fourie and Du Plessis [44] for the foam permeability (K) and inertial coefficient (F) in the Forchheimer type equation can also be used to calculate the pressure drop:

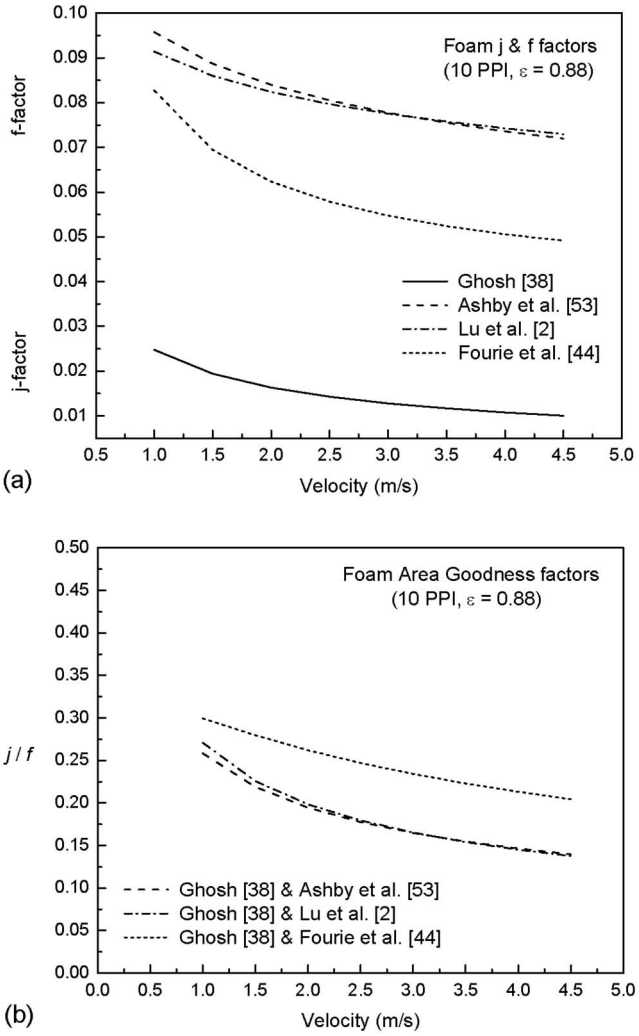

Fig. 2 Velocity variation in (*a*) *j* and *f* factors and (*b*) area goodness factor predicted by different correlations for 10 PPI foam with a porosity of 0.88

$$K = \frac{\varepsilon^2 (d_p + d_f)^2}{36(\chi - 1)\chi} \quad \text{and} \quad F = (3 - \chi)(\chi - 1)\frac{C_{D,f}\chi^{1.5}}{24\varepsilon^2} \tag{10}$$

Comparison of Eq. (6) with Eqs. (7)–(9) gives an estimate of the friction-factor (f) for the open-cell foam, provided that the hydraulic diameter d_h in Eq. (6) is replaced by the strut diameter (d_f):

$$f = \left(\frac{\Delta P}{L}\right)\left[\frac{d_f}{2\rho u^2}\right] \tag{11}$$

Pressure drop per unit length given by Eqs. (7)–(9) can be used in Eq. (11) while calculating the foam friction-factor and the area goodness factor.

4 Area Goodness Factor

The following assumptions have been made while calculating the area goodness factor.

(a) The fluid passing through porous medium is air at 300 K and 0.1 MPa.
(b) There is no phase change occurring in the fluid.
(c) The porous medium is homogeneous.

These assumptions become necessary to determine the thermophysical properties of the convective fluid for estimating the Rey-

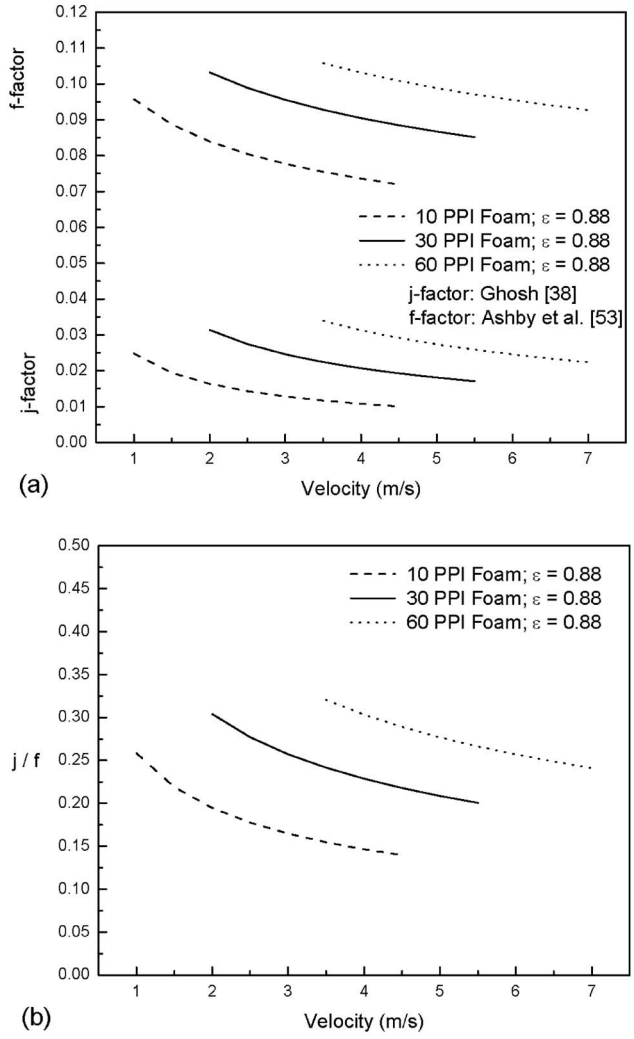

Fig. 3 Velocity variation in (*a*) *j* and *f* factors and (*b*) area goodness factor for 10, 30, and 60 PPI foams with a porosity of 0.88

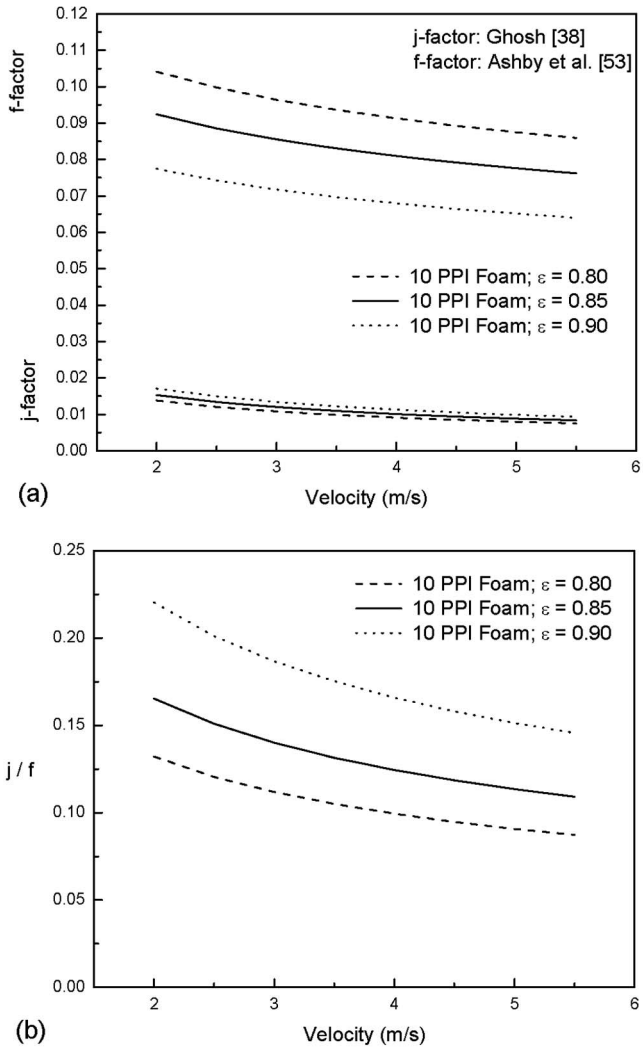

Fig. 4 Velocity variation in (*a*) *j* and *f* factors and (*b*) area goodness factor for 10 PPI foam having different porosities of 0.80, 0.85, and 0.90

nolds number, *j* factor, and *f* factor. Equations (4) and (11) have been used to calculate the *j* and *f* factors, respectively. Though it is customary to use Reynolds number for such presentation, the area goodness factor and the individual constituents have been plotted as a function of free stream velocity. The use of Reynolds number has been avoided in anticipation that other heat transfer surfaces like wavy fins and offset strip fins may have different hydraulic diameter than the foam characteristic dimension. That creates a nonuniform basis of comparison between different types of heat transfer surfaces.

Figure 2(*a*) shows the velocity variation in the *j* and *f* factors proposed by different researchers. Predictions of the friction-factor by Ashby et al. [53] and Lu et al. [2] are almost matching, whereas the same obtained through the pressure drop relation of Fourie and Du Plessis [44] is less. Consequently, the area goodness factor obtained through the pressure drop equation of Fourie and Du Plessis [44] becomes higher. Both the *j* and *f* factors are monotonically decreasing functions of velocity and the same trend has been observed to be followed also by the (j/f) ratio.

It must be emphasized here that the area goodness factor (j/f) has a limit. According to the Reynolds analogy, it can have a maximum value of 0.5 in the absence of the form drag [54]. However, the contribution of the form drag may be of the same order of magnitude for an interrupted surface. Thus the value of area goodness factor (j/f) should be limited within 0.25 or nearly 0.3 [54,55]. It is evident from Fig. 2 that the present foam heat transfer analysis is not violating the Reynolds analogy. This also shows that the heat transfer and pressure drop models used for the porous media are appropriate.

Variation in the area goodness factor with pore density (PPI) and porosity (ε) has been carried out parametrically. The velocity variations in thermohydraulic parameters and the area goodness factor have been shown in Fig. 3 for the porous materials having different pore densities. It may be noted that a single *f* factor corresponding to each pore density has been plotted using the pressure drop correlation of Ashby et al. [53]. In order to bring clarity in the plot, friction-factors relating other expressions have been dropped. The *f* factor corresponding to Fourie and Du Plessis [44] predicts a smaller value; however, a conservative approach has been adopted while presenting the data. According to Fig. 3(*b*), it is clear that the foam with the higher pore density is the better heat transfer surface insofar as the area goodness factor is the evaluation criterion. Since the surface area density increases with pore density, the overall heat transfer performance is also expected to be high. This fact is supported by the experimental results of Boomsma et al. [46], who reported significant improvement in the foam heat exchanger efficiency as compared with the existing ones when operated under nearly identical conditions.

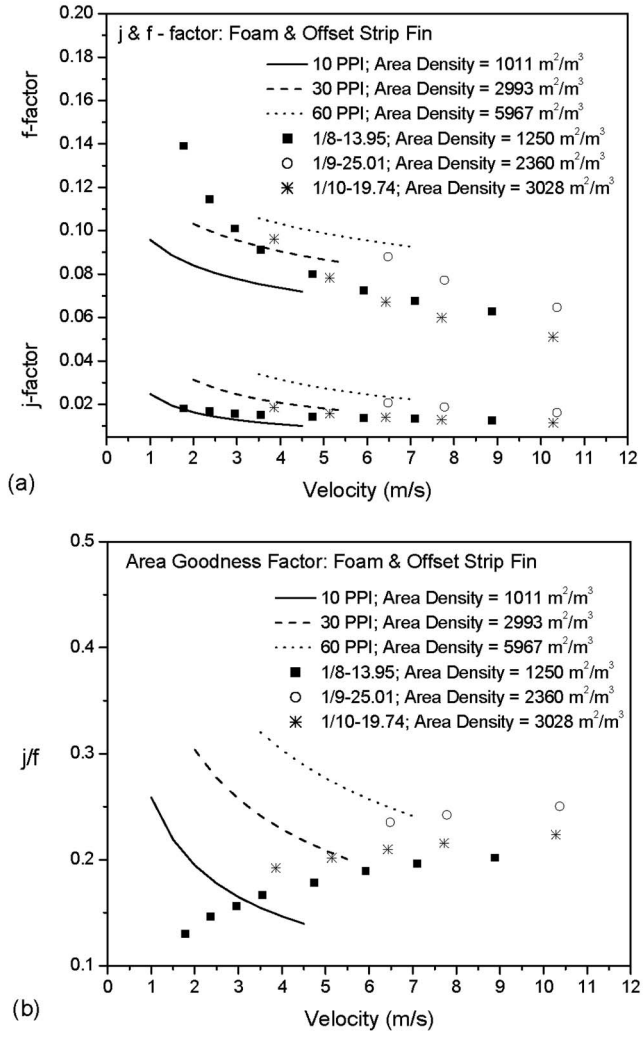

Fig. 5 Velocity variation in (*a*) *j* and *f* factors and (*b*) area goodness factor for foam and offset strip fins

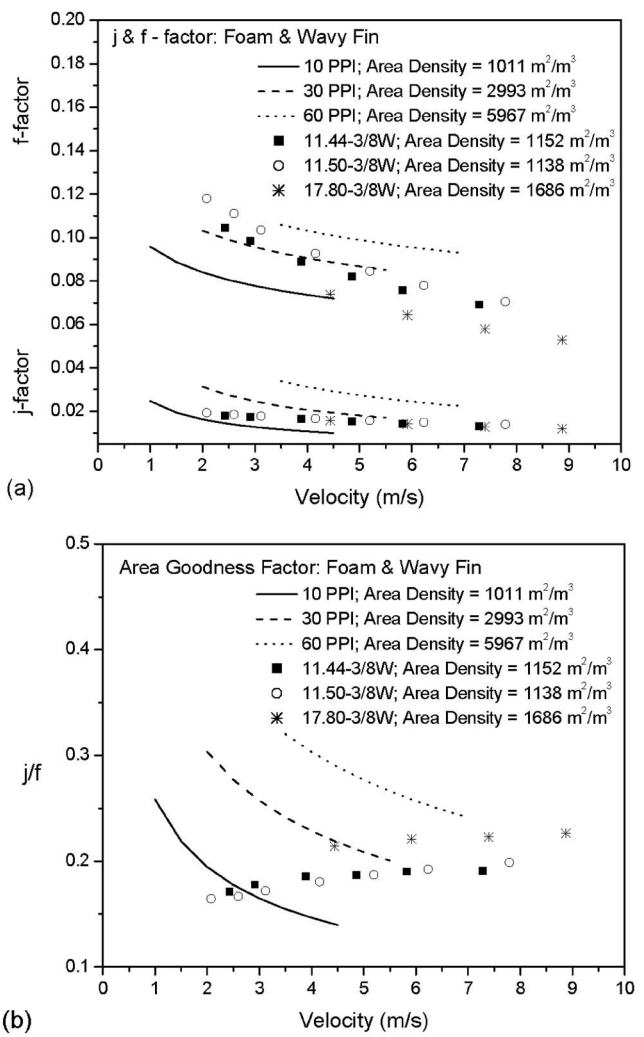

Fig. 6 Velocity variation in (*a*) *j* and *f* factors and (*b*) area goodness factor for foam and wavy fins

The effect of porosity on the heat transfer and pressure drop coefficients has been shown in Fig. 4(*a*) for different free stream velocities. Foam with higher porosity shows improvement in the area goodness factor (Fig. 4(*b*)). However, heat transfer area density strongly decreases with the increase in porosity. This feature may not desirable in view of the overall heat transfer performance.

Finally, the *j* and *f* factors and their ratio for few selective offset strip and wavy fin surfaces have been plotted using the experimental data from Ref. [13]. Heat transfer and pressure drop data for these commonly used heat transfer surfaces provide a reference for comparison with the porous material. Thermohydraulic data of offset strip and wavy fins along with those of foam surfaces have been plotted in Figs. 5 and 6, respectively. Figures 5(*a*) and 6(*a*) show that the individual heat transfer and pressure drop coefficients for the porous media are similar, if not better than those of wavy and offset strip fins. Additionally, metal foam, owing to its high area density, becomes a better choice for heat exchanger application. Figures 5(*b*) and 6(*b*) indicate that the foam area goodness factor is higher than that of wavy and offset strip fins in the low velocity range, making it most suitable for low Reynolds number applications. The ratio of *j* and *f* factors for offset (Fig. 5(*b*)) and wavy fins (Fig. 6(*b*)) shows an asymptotic increase in the velocity, while an opposite trend can be observed with the porous materials. It is probably due to the fact that the form drag component of the pressure drop increases fast with the velocity of the convective fluid. An increase in pressure drop due to form drag is not associated with a corresponding enhancement in heat transfer [55]. That is why foam area goodness factor falls quickly with higher velocity. On the other hand, when the velocity of the convective fluid is small, skin friction plays the dominant role toward pressure drop with an associated rise in heat transfer [55]. However, it does not necessarily mean that the porous materials are not suitable for high Reynolds number application in comparison to the conventional heat transfer surfaces. Since the individual heat transfer and pressure drop characteristics including the area goodness factor of high density metal sponge are favorable, the open-cell foam could be a better alternative for the actual heat exchangers when assessed with more generalized performance evaluation criteria pertaining to practical design conditions.

5 Conclusions

Open-cell metal foam is considered to be a promising alternative for compact heat exchanger applications, owing to its high heat transfer surface area density, superior thermohydraulic characteristics, and other favorable mechanical properties. A systematic analysis has been made to study the relative merits of porous medium in comparison to existing high performance heat transfer surfaces. The area goodness factor has been chosen for this comparative evaluation. The existing correlations for the heat transfer

and pressure drop coefficients have been used to compute this deciding factor. Careful selection of characteristic foam dimension and relevant thermohydraulic data becomes important to avoid erroneous prediction of results.

The parametric study reveals that the individual heat transfer and pressure drop characteristics for the high porosity open-cell foam are almost alike, if not better than those of conventional heat transfer surfaces like wavy or offset strip fin. This conclusion has been made on the basis of a conservative analysis. The high density foam has been found more suitable because of its favorable (j/f) ratio as well as its large surface area density. An increase in porosity shows positive gain in the area goodness factor. On the negative side, an increase in porosity is associated with a reduction in heat transfer surface area density. The selection of appropriate porosity needs optimization based on practical constraints.

The upper limit of the area goodness factor (j/f) is restricted by the Reynolds analogy. Its maximum value lies within 0.25 to nearly 0.3. The present analysis has been found to be in complete harmony with that analogy. This also authenticates that the models used for heat transfer and pressure drop in porous media are appropriate. In a nutshell, an affirmative answer has emerged out of this study for the question being raised at the beginning, and the design engineer can make preliminary selection of foam heat transfer surfaces on the basis of this study.

Nomenclature

d_f = strut diameter (m)
d_p = pore size (m)
F = inertia coefficient defined by Eq. (10)
f = friction-factor
h = heat transfer coefficient (W/m^2 K)
j = Colburn factor
k_f = fluid thermal conductivity (W/m K)
K = foam permeability (m^2)
L = length of foam (m)
Nu = Nusselt number (hd_f/k_f)
Pr = Prandtl number
PPI = pores per inch (m^{-1})
ΔP = pressure drop across heat exchanger surface ($kg\ m^{-1}\ s^{-2}$)
Re = Reynolds number based on d_f
St = Stanton number
u = free stream velocity (m/s)

Greek Symbols

α = thermal diffusivity (m^2/s)
χ = tortuosity
ε = porosity
$\eta_{1/2}$ = efficiency of half strut
μ = dynamic viscosity ($kg\ m^{-1}\ s^{-1}$)
ν = kinematic viscosity ($m^2\ s^{-1}$)
ρ_{rel} = relative foam density
ρ = fluid density (kg/m^3)
σ_s = area density (m^2/m^3)

References

[1] Shah, R. K., 1980, "Classification of Heat Exchangers," *Heat Exchangers, Thermal-Hydraulic Fundamentals and Design*, S. Kakac, A. Bergles, and F. Mayinger, eds., Hemisphere, Washington, DC, pp. 9–46.
[2] Lu, T. J., Stone, H. A., and Ashby, M. F., 1998, "Heat Transfer in Open-Cell Metal Foams," Acta Mater., **46**(10), pp. 3619–3635.
[3] Fuller, A. J., Kim, T., Hodson, H. P., and Lu, T. J., 2005, "Measurement and Interpretation of the Heat Transfer Coefficients of Metal Foams," Proc. Inst. Mech. Eng., Part C: J. Mech. Eng. Sci., **219**, pp. 183–191.
[4] Shah, R. K., 1978, "Compact Heat Exchanger Surface Selection Methods," *Proceedings of the Sixth International Heat Transfer Conference*, Toronto, Canada, pp. 193–199.
[5] London, A. L., and Ferguson, C. K., 1949, "Test Results of High-Performance Heat Exchanger Surfaces Used in Aircraft Intercoolers and Their Significance for Gas-Turbine Regenerator Design," Trans. ASME, **71**, pp. 17–26.
[6] Cowell, T. A., 1990, "A General Method for the Comparison of Compact Heat Transfer Surfaces," ASME Trans. J. Heat Transfer, **112**, pp. 288–294.
[7] Hesselgreaves, J. E., 2001, *Compact Heat Exchangers: Selection, Design and Operation*, Pergamon, Oxford, UK.
[8] Sekulic, D. P., Campo, A., and Morales, J. C., 1997, "Irreversibility Phenomena Associated With Heat Transfer and Fluid Friction in Laminar Flows Through Singly Connected Ducts," Int. J. Heat Mass Transfer, **40**(4), pp. 905–914.
[9] Sahiti, N., Durst, F., and Dewan, A., 2006, "Strategy for Selection of Elements for Heat Transfer Enhancement," Int. J. Heat Mass Transfer, **49**, pp. 3392–3400.
[10] Soland, G. J., Mack, W. M., Jr., and Rohsenow, W. M., 1978, "Performance Ranking of Plate-Fin Heat Exchanger Surfaces," ASME Trans. J. Heat Transfer, **100**, pp. 514–519.
[11] Joshi, H. M., and Webb, R. L., 1987, "Heat Transfer and Friction in the Offset Strip-Fin Heat Exchanger," Int. J. Heat Mass Transfer, **30**(1), pp. 69–84.
[12] Manglik, R. M., and Bergles, A. E., 1995, "Heat Transfer and Pressure Drop Correlations for the Rectangular Offset Strip Fin Compact Heat Exchanger," Exp. Therm. Fluid Sci., **10**, pp. 171–180.
[13] Kays, W. M., and London, A. L., 1984, *Compact Heat Exchangers*, 3rd ed., McGraw-Hill, New York.
[14] Muzychka, Y. S., and Yovanovich, M. M., 2001, "Modeling the F and J Characteristics for Transverse Flow Through an Offset Strip Fin at Low Reynolds Number," J. Enhanced Heat Transfer, **8**, pp. 261–277.
[15] Calmidi, V. V., and Mahajan, R. L., 1999, "The Effective Thermal Conductivity of High Porosity Metal Foams," ASME J. Heat Transfer, **121**, pp. 466–471.
[16] Lee, D. Y., and Vafai, K., 1999, "Analytical Characterisation and Conceptual Assessment of Solid and Fluid Temperature Differentials in Porous Media," Int. J. Heat Mass Transfer, **42**, pp. 423–435.
[17] Paek, J. W., Kang, B. H., Kim, S. Y., and Hyun, J. M., 2000, "Effective Thermal Conductivity and Permeability of Aluminum Foam Materials," Int. J. Thermophys., **21**(2), pp. 453–464.
[18] Du Plessis, P., Montilet, A., Comiti, J., and Legrand, J., 1994, "Pressure Drop Prediction for Flow Through High Porosity Metallic Foams," Chem. Eng. Sci., **49**(21), pp. 3545–3553.
[19] Bejan, A., 1993, *Heat Transfer*, Wiley, New York.
[20] Antohe, B. V., Lage, J. L., Price, D. C., and Weber, R. M., 1996, "Numerical Characterization Micro Heat Exchangers Using Experimentally Tested Porous Aluminum Layers," Int. J. Heat Fluid Flow, **17**(6), pp. 594–603.
[21] Kiwan, S., and Al-Nimr, M. A., 2001, "Using Porous Fins for Heat Transfer Enhancement," ASME J. Heat Transfer, **123**, pp. 790–795.
[22] Alkam, M. K., Al-Nimr, M. A., and Hamdan, M. O., 2001, "Enhancing Heat Transfer in Parallel-Plate Channels by Using Porous Inserts," Int. J. Heat Mass Transfer, **44**, pp. 931–938.
[23] Dukhan, N., Picon-Feliciano, R., and Alvarez, A. R. H., 2006, "Heat Transfer Analysis in Metal Foams With Low-Conductivity Fluids," ASME J. Heat Transfer, **128**, pp. 784–792.
[24] Bhattacharya, A., Calmidi, V. V., and Mahajan, R. L., 2002, "Thermophysical Properties of High Porosity Metal Foams," Int. J. Heat Mass Transfer, **45**, pp. 1017–1031.
[25] Tadrist, L., Miscevic, M., Rahli, O., and Topin, F., 2004, "About the Use of Fibrous Materials in Compact Heat Exchangers," Exp. Therm. Fluid Sci., **28**, pp. 193–199.
[26] Dukhan, N., Picon-Feliciano, R., and Alvarez, A. R. H., 2006, "Air Flow Through Compressed and Uncompressed Aluminum Foam: Measurements and Correlations," ASME J. Fluids Eng., **128**, pp. 1004–1012.
[27] Salas, K. I., and Wass, A. M., 2007, "Convective Heat Transfer in Open Cell Metal Foams," ASME J. Heat Transfer, **129**, pp. 1217–1229.
[28] Kaviany, M., 1991, *Principles of Heat Transfer in Porous Media*, Springer, New York.
[29] Mahjoob, S., and Vafai, K., 2008, "A Synthesis of Fluid and Thermal Transport Models for Metal Foam Heat Exchangers," Int. J. Heat Mass Transfer, **51**, pp. 3701–3711.
[30] Edouard, D., Lacroix, M., Huu, C. P., and Luck, F., 2008, "Pressure Drop Modeling on Foam: State-of-the Art Correlation," Chem. Eng. J., **144**, pp. 299–311.
[31] Boomsma, K., Poulikakos, D., and Ventikos, Y., 2003, "Simulations of Flow Through Open Cell Metal Foams Using an Idealized Periodic Cell Structure," Int. J. Heat Fluid Flow, **24**, pp. 825–834.
[32] Kaviany, M., 1985, "Laminar Flow Through a Porous Channel Bounded by Isothermal Parallel Plates," Int. J. Heat Mass Transfer, **28**, pp. 851–858.
[33] Vafai, K., and Tien, C. L., 1982, "Boundary and Inertia Effects on Convective Mass Transfer in Porous Media," Int. J. Heat Mass Transfer, **25**(8), pp. 1183–1190.
[34] Vafai, K., and Tien, C. L., 1981, "Boundary and Inertia Effects on Flow and Heat Transfer in Porous Media," Int. J. Heat Mass Transfer, **24**, pp. 195–203.
[35] Dukhan, N., Ramos, P. D., Cruz-Ruiz, E., Reyes, M. V., and Scott, E. P., 2005, "One-Dimensional Heat Transfer Analysis in Open-Cell 10-PPI Metal Foam," Int. J. Heat Mass Transfer, **48**, pp. 5112–5120.
[36] Calmidi, V. V., and Mahajan, R. L., 2000, "Forced Convection in High Porosity Metal Foams," ASME J. Heat Transfer, **122**, pp. 557–565.
[37] Ghosh, I., 2008, "Heat-Transfer Analysis of High Porosity Open-Cell Metal Foam," ASME J. Heat Transfer, **130**, p. 034501.
[38] Ghosh, I., 2009, "Heat-Transfer Analysis of High Porosity Open-Cell Metal Foam," Int. J. Heat Mass Transfer, **52**, pp. 1488–1494.
[39] Giani, L., Groppi, G., and Tronconi, E., 2005, "Mass Transfer Characterization

of Metal Foams," Ind. Eng. Chem. Res., **44**, pp. 4993–5002.
[40] Giani, L., Groppi, G., and Tronconi, E., 2005, "Heat Transfer Characterization of Metallic Foams," Ind. Eng. Chem. Res., **44**, pp. 9078–9085.
[41] White, F. M., 1986, *Fluid Mechanics*, McGraw-Hill, New York.
[42] Despois, J. F., and Mortensen, A., 2005, "Permeability of Open-Pore Microcellular Materials," Acta Mater., **53**, pp. 1381–1388.
[43] Lage, J. L., 1998, "The Fundamental Theory of Flow Through Permeable Media From Darcy to Turbulence," *Transport Phenomena in Porous Media*, D. B. Ingham, and I. Pop, eds., Elsevier, Oxford, pp. 1–30.
[44] Fourie, J. G., and Du Plessis, J. P., 2002, "Pressure Drop Modeling in Cellular Metallic Foams," Chem. Eng. Sci., **57**, pp. 2781–2789.
[45] Hwang, J. J., Hwang, G. J., Yeh, R. H., and Chao, C. H., 2002, "Measurement of Interstitial Convective Heat Transfer and Frictional Drag for Flow Across Metal Foams," ASME J. Heat Transfer, **124**, pp. 120–129.
[46] Boomsma, K., Poulikakos, D., and Zwick, F., 2003, "Metal Foams as Compact High Performance Heat Exchangers," Mech. Mater., **35**, pp. 1161–1176.
[47] Kim, S. Y., Paek, J. W., and Kang, B. H., 2000, "Flow and Heat Transfer Correlations for Porous Fin in a Plate-Fin Heat Exchanger," ASME J. Heat Transfer, **122**, pp. 572–578.
[48] Kays, W. M., and London, A. L., 1950, "Heat-Transfer and Flow-Friction Characteristics of Some Compact Heat-Exchanger Surfaces—Part 2," Trans. ASME, **72**, pp. 1087–1097.
[49] Dukhan, N., and Patel, P., 2008, "Equivalent Particle Diameter and Length Scale for Pressure Drop in Porous Metals," Exp. Therm. Fluid Sci., **32**(5), pp. 1059–1067.
[50] Lacroix, M., Nguyen, P., Schweich, D., Pham Huu, C., Savin-Poncet, S., and Edouard, D., 2007, "Pressure Drop Measurements and Modelling on SiC Foams," Chem. Eng. Sci., **62**, pp. 3259–3267.
[51] Richardson, J. T., Peng, Y., and Remue, D., 2000, "Properties of Ceramic Foam Catalyst Supports: Pressure Drop," Appl. Catal., A, **204**, pp. 19–32.
[52] Liu, J. F., Wu, W. T., Chiu, W. C., and Hsieh, W. H., 2006, "Measurement and Correlation of Friction Characteristic of Flow Through Foam Matrixes," Exp. Therm. Fluid Sci., **30**, pp. 329–336.
[53] Ashby, M. F., Evans, A., Fleck, N. A., Gibson, L. J., Hutchinson, J. W., and Wadley, H. N. G., 2000, *Metal Foams: A Design Guide*, Butterworth-Heinmann, Oxford, UK.
[54] Shah, R. K., 1980, "Compact Heat Exchangers," *Heat Exchangers, Thermal-Hydraulic Fundamentals and Design*, S. Kakac, A. Bergles, and F. Mayinger, eds., Hemisphere, Washington, DC, pp. 111–151.
[55] Shah, R. K., and Sekulic, D. P., 2003, *Fundamentals of Heat Exchanger Design*, Wiley, New York.

Forced Convection With Laminar Pulsating Counterflow in a Saturated Porous Channel

D. A. Nield
Department of Engineering Science,
University of Auckland,
Private Bag 92019,
Auckland 1142, New Zealand
e-mail: d.nield@auckland.ac.nz

A. V. Kuznetsov
Department of Mechanical and Aerospace Engineering,
North Carolina State University,
Campus Box 7910,
Raleigh, NC 27695-7910
e-mail: avkuznet@eos.ncsu.edu

An analytical solution is obtained for forced convection in a parallel-plate channel occupied by a layered saturated porous medium with counterflow produced by pulsating pressure gradients. The case of asymmetrical constant heat-flux boundary conditions is considered, and the Brinkman model is employed for the porous medium. A perturbation approach is used to obtain analytical expressions for the velocity, temperature distribution, and transient Nusselt number for convection produced by an applied pressure gradient that fluctuates with small amplitude harmonically in time about a nonzero mean. It is shown that the fluctuating part of the Nusselt number alters in magnitude and phase as the dimensionless frequency increases. The magnitude increases from zero, goes through a peak, and then decreases to zero. The height of the peak depends on the values of various parameters. The phase (relative to that of the steady component) decreases as the frequency increases. The phase angle at very low frequency can be $\pi/2$ or $-\pi/2$ depending on the degree of asymmetry of the heating and the values of other parameters.
[DOI: 10.1115/1.3180810]

Keywords: forced convection, pulsating flow, counterflow, parallel-plate channel

1 Introduction

Research on forced convection with laminar flow in a parallel-plate channel or a circular tube occupied by a saturated porous medium has been reviewed by Lauriat and Ghafir [1] and Nield et al. [2,3]. All of these studies are concerned with a time-independent applied pressure gradient, and consequently Nield and Kuznetsov [4,5] broke new grounds in discussing an applied pressure gradient that varies harmonically with time about a nonzero mean. Pulsating flow is of practical importance in biology (because of heart beating; see, for example, Ref. [6]), automotive industry (simulation of exhaust from IC engines), and heat transfer enhancement [7].

The paper by Nield and Kuznetsov [8] also broke new grounds, this time by considering counterflow in adjacent layers in the channel. This study was motivated by a desire to model an essential feature that distinguishes bioheat transfer from other forms of heat transfer in a porous medium [9–12].

The analysis in the present paper is a combination of the analyses in the papers by Kuznetsov and Nield [5,8]. A perturbation approach is followed. It is assumed that the relative amplitude ε of the pulsating pressure gradient is small compared with unity. The case of the uniform heat-flux boundary condition is considered. Asymmetric as well as symmetric heating is considered. The Peclet number is assumed to be large so that the axial heat conduction can be neglected. A Brinkman model with local thermal equilibrium is employed. Analytical expressions for the velocity and temperature and the transient Nusselt number are obtained, to first order in ε.

2 Analysis

For the steady-state fully-developed situation we have unidirectional flow in the x^*-direction between impermeable boundaries at $y^*=0$ and $y^*=H$. The asterisks denote dimensional variables. We assume that the permeability K and the effective thermal conductivity k are functions of y^* only.

We suppose that the applied pressure gradient is $G[1+\varepsilon\exp(i\Omega t^*)]$, where t^* is the time. We assume that the fluid is incompressible so that for this steady harmonic unidirectional flow the Brinkman momentum equation can be written as

$$\frac{\rho}{\phi}\frac{\partial u^*}{\partial t^*} = G[1+\varepsilon\exp(i\Omega t^*)] + \mu_e\frac{\partial^2 u^*}{\partial y^{*2}} - \frac{\mu}{K}u^* \tag{1}$$

Here, ρ is the fluid density, μ is the fluid viscosity, μ_e is the effective viscosity, ϕ is the porosity, and K is the permeability of the medium.

We suppose that the channel is divided into two layers and μ_{eff}, K, and G take different values in these. Explicitly, we assume that

$$K=K_1, \quad \mu_{\text{eff}}=\mu_{\text{eff1}}, \quad G=\gamma_1 G_{\text{ref}} \quad \text{for } 0<y^*<\xi H \tag{2a}$$

$$K=K_2, \quad \mu_{\text{eff}}=\mu_{\text{eff2}}, \quad G=-\gamma_2 G_{\text{ref}} \quad \text{for } \xi H<y^*<H \tag{2b}$$

where G_{ref} is a reference value.

We suppose that the interface at $y^*=\xi H$ is a solid plate so that there is no velocity slip there.

We define dimensionless variables

$$y=\frac{y^*}{H}, \quad u=\frac{\mu u^*}{G_{\text{ref}}H^2}, \quad t=\frac{\phi\mu t^*}{\rho H^2}, \quad \omega=\frac{\rho H^2\Omega}{\phi\mu} \tag{3}$$

This means that the reference velocity has been chosen to be $G_{\text{ref}}H^2/\mu$.

We note that the dimensionless frequency ω may be regarded as a Reynolds number based on $H\Omega$ as the velocity scale and H as the length scale. (The reader should note that here H denotes the channel width, whereas in Ref. [5] it denotes one-half of the channel width. Consequently ω as defined here is four times the ω used in Ref. [5]).

Then the dimensionless forms of the momentum equations are

$$\frac{1}{\gamma_1}\frac{\partial u_1}{\partial t} = 1+\varepsilon\exp(i\omega t) + M_1\frac{\partial^2 u_1}{\partial y^2} - N_1 u_1 \tag{4a}$$

Manuscript received April 1, 2008; final manuscript received July 23, 2008; published online July 29, 2009. Review conducted by Kambiz Vafai.

$$\frac{1}{\gamma_2}\frac{\partial u_2}{\partial t} = -1 - \varepsilon \exp(i\omega t) + M_2\frac{\partial^2 u_2}{\partial y^2} - N_2 u_2 \tag{4b}$$

where the pressure-gradient modified viscosity ratios M_1 and M_2 and the pressure-gradient modified reciprocal Darcy numbers N_1 and N_2 are defined by

$$M_1 = \frac{\mu_{\text{eff1}}}{\gamma_1 \mu} \tag{5a}$$

$$M_2 = \frac{\mu_{\text{eff2}}}{\gamma_2 \mu} \tag{5b}$$

$$N_1 = \frac{H^2}{\gamma_1 K_1} \tag{5c}$$

$$N_2 = \frac{H^2}{\gamma_2 K_2} \tag{5d}$$

It has been assumed that the Reynolds number based on the mean velocity is sufficiently small for the inertial terms to be neglected. It is also assumed that the Reynolds number based on the frequency is small. The usual convention, that it is the real part of complex quantities such as u_1 and u_2 that have physical significance, is adopted.

Equations (4*a*) and (4*b*) must be solved subject to the no-slip boundary conditions

$$u_1 = 0 \quad \text{at } y = 0 \tag{6a}$$

$$u_1 = 0 \quad \text{at } y = \xi \tag{6b}$$

$$u_2 = 0 \quad \text{at } y = \xi \tag{6c}$$

$$u_2 = 0 \quad \text{at } y = 1 \tag{6d}$$

For convenient shorthand we write

$$\lambda_1 = \sqrt{\frac{N_1}{M_1}} \tag{7a}$$

$$\lambda_2 = \sqrt{\frac{N_2}{M_2}} \tag{7b}$$

$$\sigma_1 = \left(\frac{N_1}{M_1} + \frac{i\omega}{\gamma_1 M_1}\right)^{1/2} \tag{7c}$$

$$\sigma_2 = \left(\frac{N_2}{M_2} + \frac{i\omega}{\gamma_2 M_2}\right)^{1/2} \tag{7d}$$

The solution of Eqs. (4*a*) and (4*b*) subject to Eqs. (6*a*)–(6*d*) is

$$u_1 = \frac{1 + e^{\lambda_1\xi} - e^{\lambda_1 y} - e^{\lambda_1(\xi - y)}}{N_1[1 + e^{\lambda_1\xi}]} + \frac{\varepsilon[1 + e^{\sigma_1\xi} - e^{\sigma_1 y} - e^{\sigma_1(\xi - y)}]}{M_1\sigma_1^2[1 + e^{\sigma_1\xi}]}e^{i\omega t} \tag{8a}$$

$$u_2 = -\frac{[1 + e^{-\lambda_2(1-\xi)} - e^{-\lambda_2(1-y)} - e^{-\lambda_2(y-\xi)}]}{N_2[1 + e^{-\lambda_2(1-\xi)}]} - \frac{\varepsilon[1 + e^{-\sigma_2(1-\xi)} - e^{-\sigma_2(1-y)} - e^{-\sigma_2(y-\xi)}]}{M_2\sigma_2^2[1 + e^{-\sigma_2(1-\xi)}]}e^{i\omega t} \tag{8b}$$

This solution is exact. Now suppose that $\varepsilon \ll 1$.

The spatial mean value of the velocity is

$$\bar{u} = \int_0^\xi u_1 dy + \int_\xi^1 u_2 dy = \frac{1}{N_1}\left\{\xi - \frac{2}{\lambda_1}\tanh\left(\frac{\lambda_1\xi}{2}\right)\right\} - \frac{1}{N_2}\left\{1 - \xi - \frac{2}{\lambda_2}\tanh\left(\frac{\lambda_2(1-\xi)}{2}\right)\right\} + \varepsilon\left[\frac{1}{M_1\sigma_1^2}\left\{\xi - \frac{2}{\sigma_1}\tanh\left(\frac{\sigma_1\xi}{2}\right)\right\} - \frac{1}{M_2\sigma_2^2}\left\{1 - \xi - \frac{2}{\sigma_2}\tanh\left(\frac{\sigma_2(1-\xi)}{2}\right)\right\}\right]e^{i\omega t} \tag{9}$$

Write

$$u_1 = f_1 + \varepsilon g_1 e^{i\omega t} \tag{10a}$$

$$u_2 = f_2 + \varepsilon g_2 e^{i\omega t} \tag{10b}$$

$$\bar{u} = \bar{f} + \varepsilon \bar{g} e^{i\omega t} \tag{11}$$

Thus

$$f_1 = \frac{1 + e^{\lambda_1\xi} - e^{\lambda_1 y} - e^{\lambda_1(\xi - y)}}{N_1[1 + e^{\lambda_1\xi}]} = \frac{1}{N_1}\left\{1 - \frac{\cosh[\lambda_1(\xi - 2y)/2]}{\cosh[\lambda_1\xi/2]}\right\} \tag{12a}$$

$$f_2 = -\frac{[1 + e^{-\lambda_2(1-\xi)} - e^{-\lambda_2(1-y)} - e^{-\lambda_2(y-\xi)}]}{N_2[1 + e^{-\lambda_2(1-\xi)}]} = -\frac{1}{N_2}\left\{1 - \frac{\cosh[\lambda_2(1 + \xi - 2y)/2]}{\cosh[\lambda_2(1-\xi)/2]}\right\} \tag{12b}$$

$$g_1 = \frac{1 + e^{\sigma_1\xi} - e^{\sigma_1 y} - e^{\sigma_1(\xi - y)}}{M_1\sigma_1^2[1 + e^{\sigma_1\xi}]} \tag{12c}$$

$$g_2 = -\left\{\frac{1 + e^{-\sigma_2(1-\xi)} - e^{-\sigma_2(1-y)} - e^{-\sigma_2(y-\xi)}}{M_2\sigma_2^2[1 + e^{-\sigma_2(1-\xi)}]}\right\} \tag{12d}$$

$$\bar{f} = \frac{1}{N_1}\left\{\xi - \frac{2}{\lambda_1}\tanh\left(\frac{\lambda_1\xi}{2}\right)\right\} - \frac{1}{N_2}\left\{1 - \xi - \frac{2}{\lambda_2}\tanh\left(\frac{\lambda_2(1-\xi)}{2}\right)\right\} \tag{12e}$$

$$\bar{g} = \left[\frac{1}{M_1\sigma_1^2}\left\{\xi - \frac{2}{\sigma_1}\tanh\left(\frac{\sigma_1\xi}{2}\right)\right\} - \frac{1}{M_2\sigma_2^2}\left\{1 - \xi - \frac{2}{\sigma_2}\tanh\left(\frac{\sigma_2(1-\xi)}{2}\right)\right\}\right] \tag{12f}$$

The normalized velocity is, to first order,

$$\hat{u}_1 = \frac{u_1}{\bar{u}} = \hat{u}_1^{(0)} + \hat{u}_1^{(1)} e^{i\omega t} \tag{13a}$$

$$\hat{u}_2 = \frac{u_2}{\bar{u}} = \hat{u}_2^{(0)} + \hat{u}_2^{(1)} e^{i\omega t} \tag{13b}$$

where

$$\hat{u}_1^{(0)} = \frac{f_1}{\bar{f}} \tag{14a}$$

$$\hat{u}_1^{(1)} = \varepsilon\left(\frac{g_1}{f_1} - \frac{\bar{g}}{\bar{f}}\right)\frac{f_1}{\bar{f}} \tag{14b}$$

$$\hat{u}_2^{(0)} = \frac{f_2}{\bar{f}} \tag{14c}$$

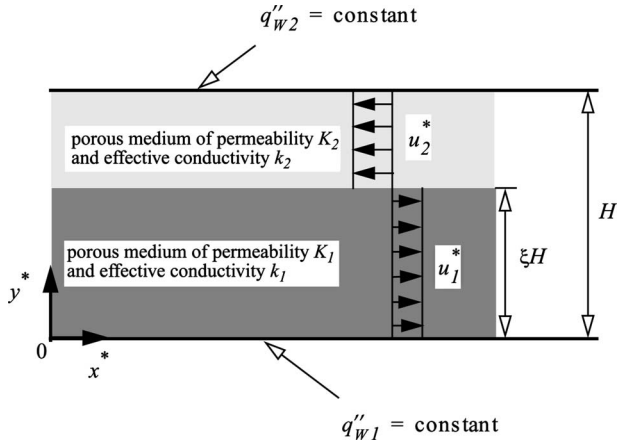

Fig. 1 Definition sketch

$$\hat{u}_2^{(1)} = \varepsilon\left(\frac{g_2}{f_2} - \frac{\bar{g}}{\bar{f}}\right)\frac{f_2}{\bar{f}} \tag{14d}$$

We now proceed to consider the thermal aspects. We assume that the frequency is sufficiently small for the assumption of local thermal equilibrium to be valid. We treat the case of asymmetric heating of the walls as well as the case of symmetric heating. In dealing with the former we follow the path taken by Nield [13].

Now suppose that the effective thermal conductivity is given by

$$k = k_1 \quad \text{for } 0 < |y^*| < \xi H \tag{15a}$$

$$k = k_2 \quad \text{for } \xi H < |y^*| < H \tag{15b}$$

so that the mean value is given by

$$\bar{k} = \xi k_1 + (1-\xi)k_2 \tag{16}$$

We write

$$\tilde{k}_1 = \frac{k_1}{\bar{k}} \tag{17a}$$

$$\tilde{k}_2 = \frac{k_2}{\bar{k}} \tag{17b}$$

Further we define the Nusselt number Nu based on the channel width as

$$\mathrm{Nu} = \frac{Hq''_\mu}{\bar{k}(T^*_{w\mu} - T^*_m)} \tag{18}$$

where q''_μ is the mean wall heat flux, defined in terms of Fig. 1 and

$$q''_\mu = \frac{1}{2}(q''_{w1} + q''_{w2}) \tag{19}$$

Here $T^*_{w\mu}$ is the mean wall temperature and T^*_m is the bulk temperature defined by

$$T^*_m = \frac{1}{\bar{u}H}\int_0^H u^* T^* dy^* \tag{20}$$

The reader should note that we have defined Nu in terms of the channel width rather than the hydraulic diameter (twice the channel width).

For the case of uniform flux boundaries, the thermal energy equation takes the form

$$(\rho c)_m \frac{\partial T^*}{\partial t*} + (\rho c_P)_f u^* \frac{\partial T^*}{\partial x^*} = k_m \frac{\partial^2 T^*}{\partial y^{*2}} \tag{21}$$

The Peclet number Pe has been assumed to be large so that thermal diffusion in the axial direction can be neglected. Provided that the Prandtl number is large, this assumption is consistent with our other assumption that the Reynolds number is small.

The first law of thermodynamics leads to

$$\frac{\partial T^*}{\partial x^*} = \frac{dT_m}{dx^*} = \frac{2q''_\mu}{\rho c_p H \bar{u}^*} = \text{const} \tag{22}$$

We define a dimensionless temperature

$$\hat{T} = \frac{T^* - T^*_{w\mu}}{T^*_m - T^*_{w\mu}} \tag{23}$$

and introduce the Prandtl number Pr, thermal capacity ratio σ_r, and a modified Prandtl number Λ defined by

$$\mathrm{Pr} = \frac{\mu/\rho}{k_m/(\rho c_P)_f}, \quad \sigma_r = \frac{(\rho c)_m}{(\rho c_P)_f}, \quad \Lambda = \phi\sigma_r \ \mathrm{Pr} \tag{24}$$

Then Eq. (21) takes the form

$$\frac{\partial^2 \hat{T}}{\partial y^2} - \Lambda\frac{\partial \hat{T}}{\partial t} = -2 \ \mathrm{Nu} \ \hat{u} \tag{25}$$

In this case the dimensionless form of the thermal energy equation may be written as

$$\frac{\partial^2 \hat{T}_1}{\partial y^2} - \Lambda_1\frac{\partial \hat{T}_1}{\partial t} = -\frac{2 \ \mathrm{Nu} \ \hat{u}_1}{\tilde{k}_1} \quad \text{for } 0 < y < \xi \tag{26a}$$

$$\frac{\partial^2 \hat{T}_2}{\partial y^2} - \Lambda_2\frac{\partial \hat{T}_2}{\partial t} = -\frac{2 \ \mathrm{Nu} \ \hat{u}_2}{\tilde{k}_2} \quad \text{for } \xi < y < 1 \tag{26b}$$

These equations must now be solved subject to the boundary conditions

$$\hat{T}_1(0) = \beta_T \tag{27a}$$

$$\hat{T}_2(1) = -\beta_T \tag{27b}$$

and the matching conditions (for temperature and heat flux)

$$\hat{T}_1(\xi) = \hat{T}_2(\xi) \tag{27c}$$

$$\tilde{k}_1\frac{d\hat{T}_1}{dy}(\xi) = \tilde{k}_2\frac{d\hat{T}_2}{dy}(\xi) \tag{27d}$$

where

$$\beta_T = \frac{T_{w1} - T_{w2}}{2(T_m - T_{w\mu})} \tag{28}$$

The solution to first order in ε is of the form

$$T_1 = \hat{T}_1^{(0)} + \hat{T}_1^{(1)}e^{i\omega t} \tag{29a}$$

$$T_2 = \hat{T}_2^{(0)} + \hat{T}_2^{(1)}e^{i\omega t} \tag{29b}$$

Then Eqs. (25a) and (25b) require that

$$\frac{d^2\hat{T}_1^{(0)}}{dy^2} = -\frac{2 \ \mathrm{Nu}}{\tilde{k}_1}\hat{u}_1^{(0)} \tag{30a}$$

$$\frac{d^2\hat{T}_1^{(1)}}{dy^2} - \beta_1^2\hat{T}_1^{(1)} = -\frac{2 \ \mathrm{Nu}}{\tilde{k}_1}\hat{u}_1^{(1)} \tag{30b}$$

$$\frac{d^2\hat{T}_2^{(0)}}{dy^2} = -\frac{2\ \mathrm{Nu}}{\tilde{k}_2}\hat{u}_2^{(0)} \tag{30c}$$

$$\frac{d^2\hat{T}_2^{(1)}}{dy^2} - \beta_2^2\hat{T}_2^{(1)} = -\frac{2\ \mathrm{Nu}}{\tilde{k}_2}\hat{u}_2^{(1)} \tag{30d}$$

where we have introduced the shorthand notation

$$\beta_i = (i\omega\Lambda_i)^{1/2} \quad \text{for } i = 1,2,\ldots \tag{31}$$

Also, Eqs. (27*a*)–(27*d*) require that

$$\hat{T}_1^{(0)}(0) = \beta_T \tag{32a}$$

$$\hat{T}_1^{(0)}(\xi) = \hat{T}_2^{(0)}(\xi) \tag{32b}$$

$$\tilde{k}_1\frac{d\hat{T}_1^{(0)}}{dy}(\xi) = \tilde{k}_2\frac{d\hat{T}_2^{(0)}}{dy}(\xi) \tag{32c}$$

$$\hat{T}_2^{(0)}(1) = -\beta_T \tag{32d}$$

$$\hat{T}_1^{(1)}(0) = 0 \tag{32e}$$

$$\hat{T}_1^{(1)}(\xi) = \hat{T}_2^{(1)}(\xi) \tag{32f}$$

$$\tilde{k}_1\frac{d\hat{T}_1^{(1)}}{dy}(\xi) = \tilde{k}_2\frac{d\hat{T}_2^{(1)}}{dy}(\xi) \tag{32g}$$

$$\hat{T}_2^{(1)}(1) = 0 \tag{32h}$$

The solution of Eqs. (30*a*)–(30*d*) subject to Eqs. (32*a*)–(32*e*) and (32*h*) is straightforward but algebraically complicated. It can be readily handled by the software package MATHEMATICA. The result is too complicated to present here. The solution is of the form

$$\hat{T}_1^{(0)} = \beta_T R_1^{(0)} + \mathrm{Nu}\ S_1^{(0)}, \quad \hat{T}_2^{(0)} = \beta_T R_2^{(0)} + \mathrm{Nu}\ S_2^{(0)}$$
$$\hat{T}_1^{(1)} = \varepsilon\ \mathrm{Nu}\ S_1^{(1)}, \quad \hat{T}_2^{(1)} = \varepsilon\ \mathrm{Nu}\ S_2^{(1)} \tag{33}$$

The compatibility condition (an identity required for consistency of Eqs. (18) and (20)) is

$$\langle\hat{u}\hat{T}\rangle = 1 \tag{34}$$

To first order, this gives

$$\mathrm{Nu}[\langle\hat{u}^{(0)}S^{(0)}\rangle + \varepsilon(\langle\hat{u}^{(0)}S^{(1)}\rangle + \langle\hat{u}^{(1)}S^{(0)}\rangle)e^{i\omega t}] + \beta_T[\langle\hat{u}^{(0)}R^{(0)}\rangle + \varepsilon\langle\hat{u}^{(1)}R^{(0)}\rangle > e^{i\omega t}] = 1 \tag{35}$$

Here

$$\langle\hat{u}^{(0)}S^{(0)}\rangle = \int_0^{\xi}\hat{u}_1^{(0)}S_1^{(0)}dy + \int_{\xi}^{1}\hat{u}_2^{(0)}S_2^{(0)}dy \tag{36}$$

etc. Then, to first order, Eq. (35) gives

$$\mathrm{Nu} = \mathrm{Nu}_0(1 + \nu\varepsilon e^{i\omega t}) \tag{37}$$

where

$$\mathrm{Nu}_0 = \frac{1 - \beta_T\langle\hat{u}^{(0)}R^{(0)}\rangle}{\langle\hat{u}^{(0)}S^{(0)}\rangle} \tag{38}$$

$$\nu = -\left\{\frac{\langle\hat{u}^{(0)}S^{(1)}\rangle + \langle\hat{u}^{(1)}S^{(0)}\rangle}{\langle\hat{u}^{(0)}S^{(0)}\rangle} + \frac{\beta_T\langle\hat{u}^{(1)}R^{(0)}\rangle}{1 - \beta_T\langle\hat{u}^{(0)}R^{(0)}\rangle}\right\} \tag{39}$$

For the case of $\xi=1$, one can recover the results in Ref. [5] by identifying $\lambda_1=2s$ and $\omega=4\omega'$, where s is defined in Ref. [5] and a prime has been placed on ω as defined in Ref. [5]. Also, when $\xi=1$, one can derive the analytic expressions

Table 1 Values of the mean Nusselt number Nu_0 for counterflow in the Darcy limit ($M_1\to 0, M_2\to 0$)

	$N_2/N_1=0.1$	$N_2/N_1=1.0$	$N_2/N_1=10$
$\beta=0$	4.35	0	4.36
$\beta=1$	7.01	0	1.69
$\beta=10$	30.97	0	−22.32

$$\hat{u}_1^{(0)} = \frac{\lambda_1 C - \lambda_1\cosh[\lambda_1(2y-1)/2]}{\lambda_1 C - 2S} \tag{40}$$

$$T_1^{(0)} = \beta_T(1-2y) - \frac{\mathrm{Nu}_0}{\lambda_1 C - 2S}\left\{\lambda_1 C(y^2-y) + \frac{2C - 2\cosh[\lambda_1(2y-1)/2]}{\lambda_1}\right\} \tag{41}$$

$$\mathrm{Nu}_0 = \frac{6\lambda_1(\lambda_1 C - 2S)^2}{\lambda_1^3 C^2 - 24\lambda_1 C^2 - 6\lambda_1 + 60SC} \tag{42}$$

where

$$C = \cosh(\lambda_1/2), \quad S = \sinh(\lambda_1/2) \tag{43}$$

3 Results and Discussion

We tested our MATHEMATICA code using the results for special cases available in Ref. [5] (for a single layer, $\xi=1$) and in Ref. [8] (for the nonpulsating case). In particular, when we took account of the different scaling, we recovered the results displayed in Fig. 2 in Ref. [5]. Likewise, the values in Tables 1 and 2 for the mean Nusselt number Nu_0 have been newly computed. They are closely the same as in Tables 1(a) and 2(a) in Ref. [8].

Because of the novelty of the hydrodynamic boundary conditions at the interface between the two streams, there are no other results in the literature for which we could compare our present results.

Because of the large number of parameters involved, of necessity we have been very selective in the set of parameter values for which results are reported. All of the results presented below are for the case where each layer occupies half the channel ($\xi=0.5$) and for which the modified Prandtl numbers Λ_1 and Λ_2 are unity.

For the pulsating counterflow situation, we first considered the Darcy flow limit. Figures 2 and 3 present the results for the cases corresponding to the first and third columns of Table 1. The general behavior is similar to what we found in the single layer case reported in Ref. [5]. The amplitude of ν first increases from zero with ω, goes through a maximum, and then reduces to zero as ω tends to infinity. For the case shown in Fig. 2, the value of the peak first decreases as β_T increases, and then increases. The argument of ν (a phase angle) generally decreases as ω increases. A feature not observed for the single layer situation is that now a jump of 2π occurs in the phase angle at some value of ω. Because of the periodicity, this does not correspond to a physical discontinuity. It is just a consequence of the fact that the jump occurs when the starting phase angle is $-\pi/2$ (as in the case $\beta_T=0$) rather than $\pi/2$ (as in the case $\beta_T=10$).

Table 2 Values of the mean Nusselt number Nu_0 for counterflow in the clear fluid limit ($N_1\to 0, N_2\to 0$)

	$M_2/M_1=0.1$	$M_2/M_1=1.0$	$M_2/M_1=10$
$\beta=0$	3.62	0	3.62
$\beta=1$	5.83	0	1.41
$\beta=10$	25.73	0	−18.50

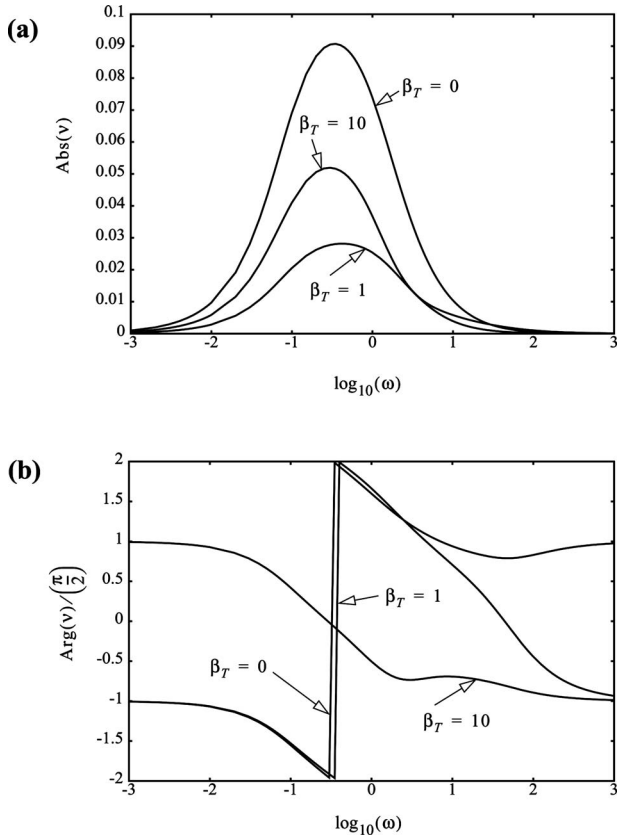

Fig. 2 Plots of (*a*) the modulus and (*b*) the argument as a fraction of $\pi/2$ of ν where $\mathrm{Nu}=\mathrm{Nu}_0(1+\nu\varepsilon e^{i\omega t})$ as functions of the frequency ω for various values of β_T for the case of the Darcy limit, $\xi=0.5$ and $N_2/N_1=0.1$. The values of Nu_0 are 4.35, 7.01, and 30.97 for the β_T values 0, 1, and 10, respectively.

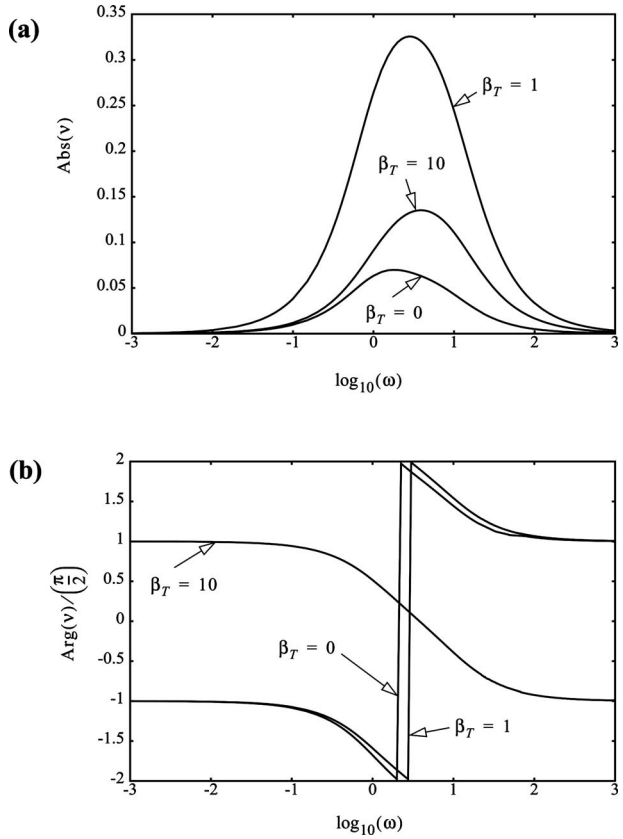

Fig. 3 Plots of (*a*) the modulus and (*b*) the argument as a fraction of $\pi/2$ of ν where $\mathrm{Nu}=\mathrm{Nu}_0(1+\nu\varepsilon e^{i\omega t})$ as functions of the frequency ω for various values of β_T for the case of the Darcy limit, $\xi=0.5$ and $N_2/N_1=10$. The values of Nu_0 are 4.36, 1.69, and -22.32 for the β_T values 0, 1, and 10, respectively.

A comparison of Fig. 3 with Fig. 2 reveals that a change from $N_2/N_1=0.1$ to $N_2/N_1=10$ does not change the general qualitative picture but it does change the details. Rather than the amplitude of ν going through a minimum as β_T increases, it now goes through a maximum. The values of the peaks are generally higher, and they occur at larger values of ω. Likewise the value of ω at which there is a rapid change in the phase angle is greater in Fig. 3 than in Fig. 2.

Figures 4 and 5 for the clear fluid limit are similar to Figs. 2 and 3 for the Darcy flow limit. The main change is that the peaks in the amplitude of ν and the jumps in the phase angles occur at larger values of ω.

To complete our report we present in Figs. 6–9 some results for general values of the modified reciprocal Darcy numbers N_1 and N_2. All of these are for the case of modified viscosity ratios M_1 and M_2 having the value unity. Figures 6 and 7 are for the case of symmetric heating ($\beta_T=0$) and Figs. 8 and 9 correspond to the case of asymmetric heating ($\beta_T=1$). In Fig. 6 (and Fig. 8) the values of N_1 and N_2 are varied with the ratio N_2/N_1 held constant at 0.1. In Fig. 7 (and Fig. 9) the values of N_1 and N_2 are varied with the ratio N_2/N_1 held constant at 10. As one would expect from the physical symmetry of the situation, Figs. 6 and 7 are essentially the same, while Figs. 8 and 9 differ significantly. A particular feature is the relatively large peak amplitude of ν when $(N_1,N_2)=(10,100)$. In fact here the peak amplitude exceeds unity. This means that in this case the Nusselt number Nu oscillates between positive and negative values.

As was noted in Ref. [8], the negative values arise in the case of strong thermal asymmetry and when the product of β_T and $\bar{u}$ is positive so that the more strongly heated boundary (and thus the hotter one) is adjacent to the layer in which the weaker flow occurs, other things being equal.

4 Conclusions

We investigated forced convection in a parallel-plate channel occupied by a layered saturated porous medium with counterflow produced by pulsating pressure gradients. For this pulsating flow, the amplitude of Nusselt number variation first increases from zero with the increase in the dimensionless pulsation frequency, goes through a maximum, and then reduces to zero as the pulsation frequency tends to infinity. The argument of the phase angle of the Nusselt number variation generally decreases as the pulsation frequency increases. A jump of 2π can occur in the phase angle at some value of the pulsation frequency. Because of the periodicity, this does not correspond to a physical discontinuity. The jump occurs when the phase angle at very low frequency is $-\pi/2$ (rather than $\pi/2$), an occurrence that depends on the degree of asymmetry of the heating and on the values of other parameters.

Our primary results are presented for the cases of the Darcy and clear fluid limits. These provide upper and lower bounds for the mean Nusselt number. Where the results for these two limits are in qualitative agreement, one can reasonably expect that the results for the intermediate cases will show the same qualitative behavior.

In our analysis we have assumed that the frequency is sufficiently small for the inertial and local thermal nonequilibrium effects to be neglected. In any case, it appears from our results

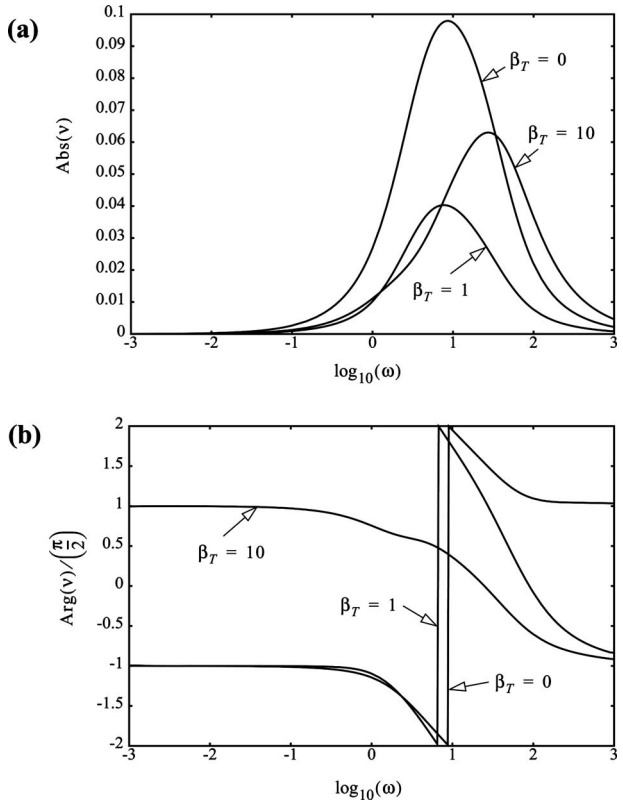

Fig. 4 Plots of (*a*) the modulus and (*b*) the argument as a fraction of $\pi/2$ of ν where $\mathrm{Nu}=\mathrm{Nu}_0(1+\nu\varepsilon e^{i\omega t})$ as functions of the frequency ω for various values of β_T for the case of the clear fluid limit, $\xi=0.5$ and $M_2/M_1=0.1$. The values of Nu_0 are 3.62, 5.83, and 25.73 for the β_T values 0, 1, and 10, respectively.

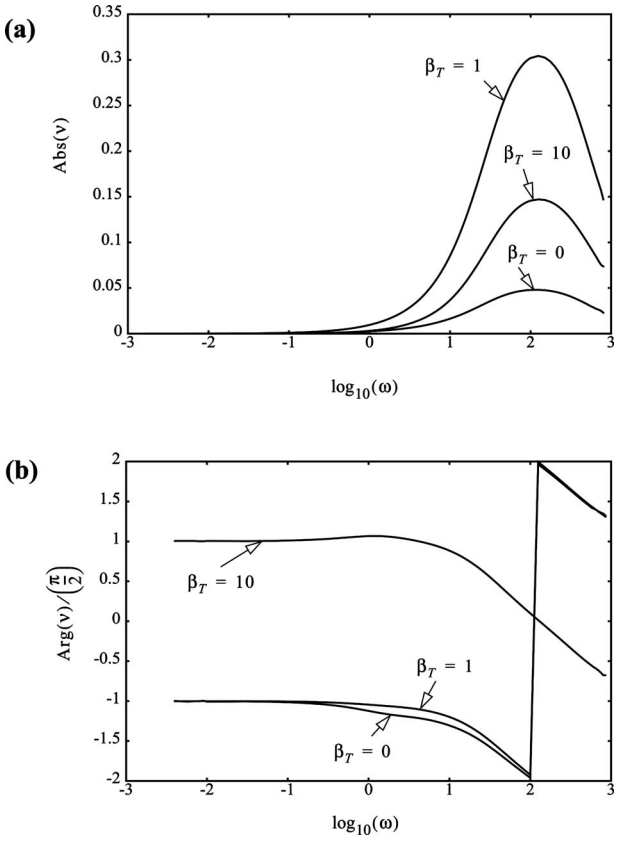

Fig. 5 Plots of (*a*) the modulus and (*b*) the argument as a fraction of $\pi/2$ of ν where $\mathrm{Nu}=\mathrm{Nu}_0(1+\nu\varepsilon e^{i\omega t})$ as functions of the frequency ω for various values of β_T for the case of the clear fluid limit, $\xi=0.5$ and $M_2/M_1=10$. The values of Nu_0 are 3.62, 1.41, and −18.50.

that the Nusselt number does not pulsate much when the frequency is large, so the case of very high frequency is not particularly interesting.

In our analysis we have also assumed that the pulsation frequency is the same for each stream and the pulsations are in phase. The effect of a phase lag is the subject of the current research. The case of different frequencies for the two streams is beyond the scope of our analysis.

Nomenclature

c_P = specific heat
f, g = functions defined in Eq. (10)
$G[1+\varepsilon \exp(i\Omega t^*)]$ = applied pressure gradient
G_{ref} = reference value of the applied pressure gradient
H = channel width
K = effective thermal conductivity
$\bar{k}$ = mean value of k
K = permeability
M = modified viscosity ratio defined in Eq. (5)
N = modified reciprocal Darcy number defined in Eq. (5)
Nu = Nusselt number $2Hq''_\mu/\bar{k}(T^*_{w\mu}-T^*_m)$
Nu_0 = mean Nusselt number
Pr = Prandtl number $\mu/\rho/k_m/(\rho c_P)_f$
q''_μ = mean wall heat flux $1/2(q''_{w1}+q''_{w2})$
t = dimensionless time $(\phi\mu t^*/\rho H^2)$
t^* = time
T^* = temperature
T^*_m = bulk temperature defined in Eq. (20)
T^*_w = wall temperature
$T^*_{w\mu}$ = mean wall temperature
$\hat{T}$ = dimensionless temperature $(T^*-T^*_{w\mu})/(T^*_m-T^*_{w\mu})$
u = dimensionless longitudinal velocity $(\mu u^*/G_{\mathrm{ref}}H^2)$
u^* = longitudinal velocity
$\bar{u}$ = spatial average of u
$\hat{u}$ = rescaled dimensionless longitudinal velocity $u/\bar{u}$
x^* = longitudinal coordinate
y^* = transverse coordinate
y = dimensionless transverse coordinate y^*/H

Greek Symbols

β = $(i\omega\Lambda)^{1/2}$
β_T = dimensionless boundary temperature defined in Eq. (28)
ε = amplitude
γ = pressure gradient ratio
Λ = modified Prandtl number ($\Lambda=\phi\sigma_r$ Pr)
λ = $(N/M)^{1/2}$
μ = fluid viscosity
μ_{eff} = effective viscosity
ν = Nusselt number variation function defined in Eq. (39)
ρ = density

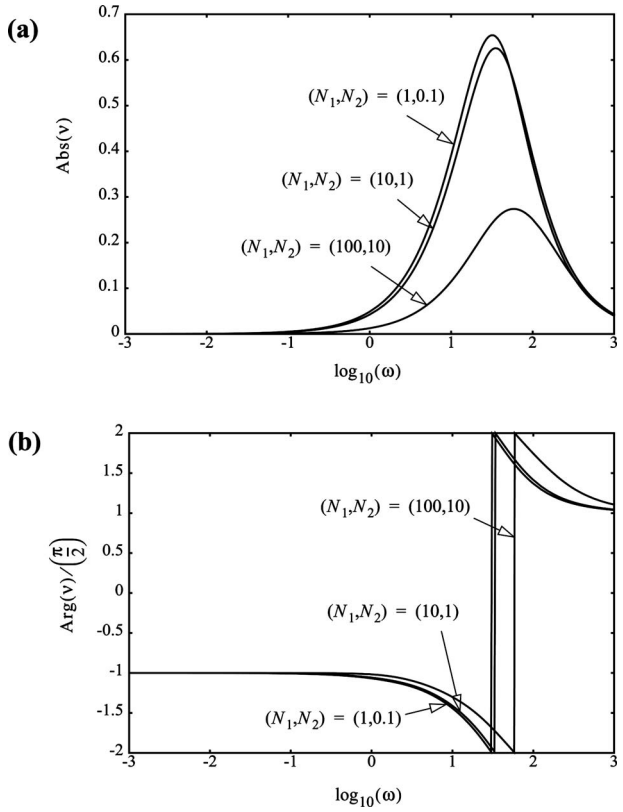

Fig. 6 Plots of (*a*) the modulus and (*b*) the argument as a fraction of $\pi/2$ of ν where $\mathrm{Nu}=\mathrm{Nu}_0(1+\nu\epsilon e^{i\omega t})$ as functions of the frequency ω for some general cases $\xi=0.5$, $\beta=0$, $M_1=1$, and $M_2=1$, and for $(N_1,N_2)=(1,0.1)$, (10,1), and (100,10). The values of Nu_0 are 0.00203, 0.156, and 2.175, respectively.

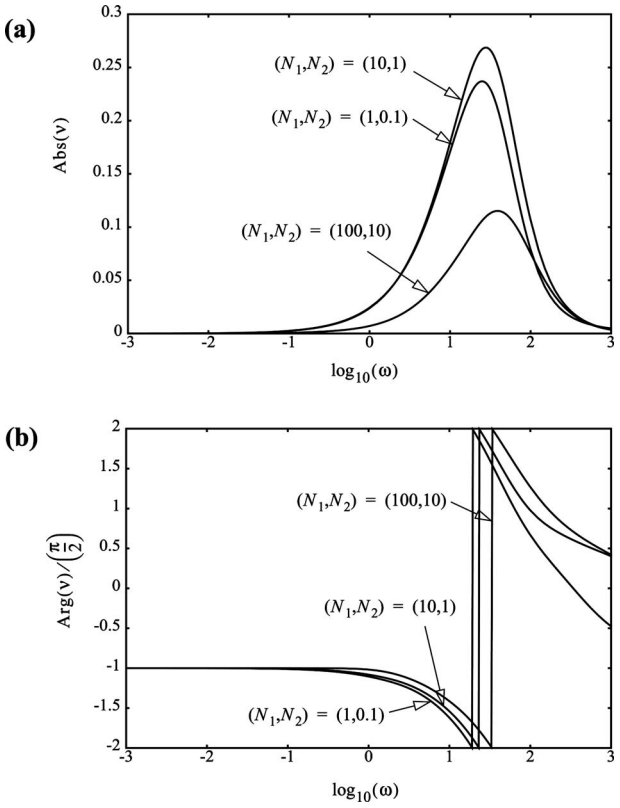

Fig. 8 As for Fig. 6, but now with $\beta_T=1$, the values of Nu_0 are 0.0934, 0.947, and 4.502, respectively

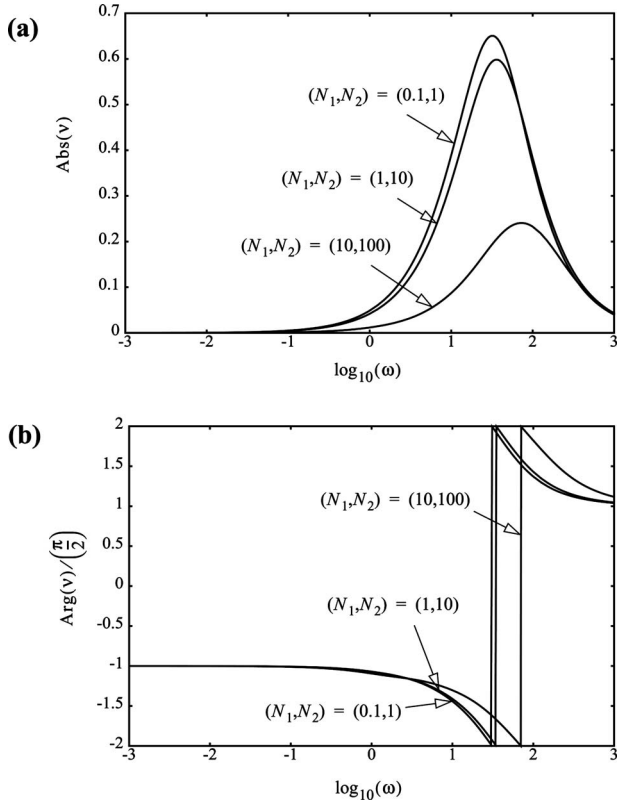

Fig. 7 As for Fig. 6, but now for $(N_1,N_2)=(0.1,1)$, (1,10), and (10,100), the values of Nu_0 are 0.00203, 0.156, and 2.175, respectively

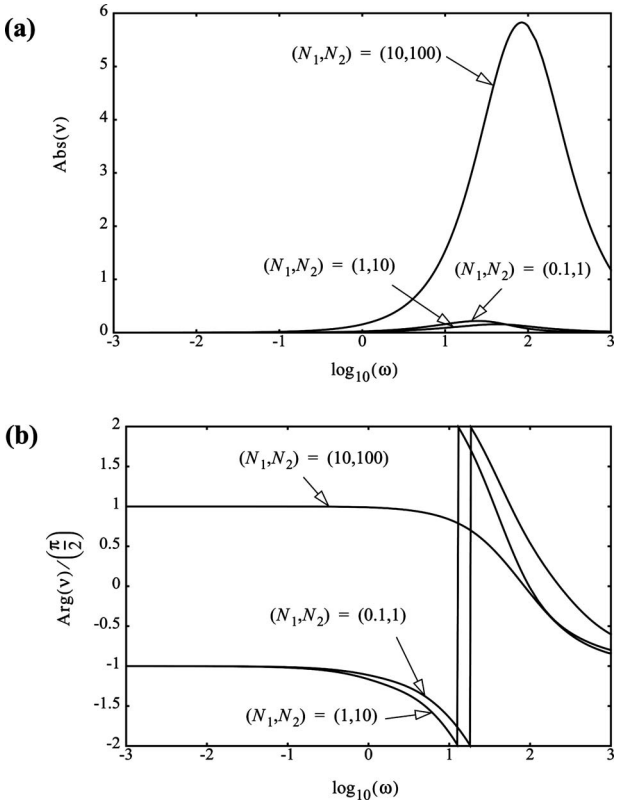

Fig. 9 As for Fig. 7, but now with $\beta_T=1$, the values of Nu_0 are -0.0893, -0.635, and -0.152, respectively

σ = $(N/M + i\omega/\gamma M)^{1/2}$
σ_r = thermal capacity ratio $(\rho c)_m/(\rho c_P)_f$
ϕ = porosity
ξ = y-coordinate value giving the position of the layer interface
ω = dimensionless pulsation frequency $(\rho H^2\Omega/\phi\mu)$
Ω = pulsation frequency

Superscripts

* = dimensional variable

Subscripts

1,2 = layer indices

References

[1] Lauriat, G., and Ghafir, R., 2000, "Forced Convective Heat Transfer in Porous Media," *Handbook of Porous Media*, K. Vafai, ed., Dekker, New York, pp. 201–267.

[2] Nield, D. A., and Kuznetsov, A. V., 2005, "Forced Convection in Porous Media: Transverse Heterogeneity Effects and Thermal Development," *Handbook of Porous Media*, 2nd ed., K. Vafai, ed., Taylor & Francis, Baton Rouge, LA, pp. 143–193.

[3] Nield, D. A., and Bejan, A., 2006, *Convection in Porous Media*, 3rd ed., Springer, New York.

[4] Nield, D. A., and Kuznetsov, A. V., 2007, "Forced Convection With Laminar Pulsating Flow in a Channel or Tube," Int. J. Therm. Sci., **46**, pp. 551–560.

[5] Kuznetsov, A. V., and Nield, D. A., 2006, "Forced Convection With Laminar Pulsating Flow in a Saturated Porous Channel or Tube," Transp. Porous Media, **65**, pp. 505–523.

[6] Han, Y., Ganatos, P., and Weinbaum, S., 2005, "Transmission of Steady and Oscillatory Fluid Shear Stress Across Epithelial and Endothelial Surface Structures," Phys. Fluids, **17**, p. 031508.

[7] Huang, P. C., Nian, S. H., and Yang, C. F., 2005, "Enhancement Heat-Source Cooling by Flow Pulsation and Porous Block," J. Thermophys. Heat Transfer, **19**, pp. 460–470.

[8] Nield, D. A., and Kuznetsov, A. V., 2008, "A Bioheat Transfer Model: Forced Convection in a Channel Occupied by a Porous Medium With Counterflow," Int. J. Heat Mass Transfer, **51**, pp. 5534–5541.

[9] Khaled, A. R. A., and Vafai, K., 2003, "The Role of Porous Media in Modeling Flow and Heat Transfer in Biological Tissues," Int. J. Heat Mass Transfer, **46**, pp. 4989–5003.

[10] Khanafer, K., and Vafai, K., 2005, "Transport Through Porous Media—A Synthesis of the State of the Art for the Past Couple of Decades," Annu. Rev. Heat Transfer, **14**, pp. 345–383.

[11] Khanafer, K., and Vafai, K., 2006, "The Role of Porous Media in Biomedical Engineering as Related to Magnetic Resonance Imaging and Drug Delivery," Heat Mass Transfer, **42**, pp. 939–953.

[12] Nakayama, A., Kuwahara, F., and Lui, W., 2007, "Macroscopic Governing Equations for Bioheat Transfer Phenomena," *Proceedings of the Second International Conference on Porous Media and Its Application in Science and Engineering*, Kauai, HI, Jun. 17–21.

[13] Nield, D. A., 2004, "Forced Convection in a Plane Plate Channel With Asymmetric Heating," Int. J. Heat Mass Transfer, **47**, pp. 5609–5612.

Banafsheh Barabadi
Department of Mechanical Engineering and Cellular Biomechanics and Sports Science Laboratory,
Villanova University,
800 Lancaster Avenue,
Villanova, PA 19085

Rungun Nathan
Cellular Biomechanics and Sports Science Laboratory,
800 Lancaster Avenue,
Villanova, PA 19085;
Division of Engineering,
Penn State Berks,
Reading, PA 19610

Kei-peng Jen
Department of Mechanical Engineering,
Villanova University,
800 Lancaster Avenue,
Villanova, PA 19085

Qianhong Wu[1]
Department of Mechanical Engineering and Cellular Biomechanics and Sports Science Laboratory,
Villanova University,
800 Lancaster Avenue,
Villanova, PA 19085
e-mail: qianhong.wu@villanova.edu

On the Characterization of Lifting Forces During the Rapid Compaction of Deformable Porous Media

*In a recent paper, Wu et al. (2005, "Dynamic Compression of Highly Compressible Porous Media With Application to Snow Compaction," J. Fluid Mech., **542**, pp. 281–304) developed a novel experimental and theoretical approach to investigate the dynamic lift forces generated in the rapid compression of highly compressible porous media, (e.g., snow layer), where a porous cylinder-piston apparatus was used to measure the pore air pressure generation and a consolidation theory was developed to capture the pore-pressure relaxation process. In the current study, we extend the approach of Wu et al. to various porous materials such as synthetic fibers. The previous experimental setup was completely redesigned, where an accelerometer and a displacement sensor were employed to capture the motion of the piston. The pore-pressure relaxation during the rapid compaction of the porous material was measured. The consolidation theory developed by Wu et al. was modified by introducing the damping effect from the solid phase of the porous materials. One uses Carman–Kozeny's relationship to describe the change in the permeability as a function of compression. By comparing the theoretical results with the experimental data, we evaluated the damping effect of the soft fibers, as well as that of the pore air pressure for two different porous materials, A and B. The experimental and theoretical approach presented herein has provided an important methodology in quantifying the contributions of different forces in the lift generation inside porous media and is an extension of the previous studies done by Wu et al.* [DOI: 10.1115/1.3167543]

Keywords: lift generation, porous media, permeability, compression, deformable

1 Introduction

Porous materials have a vast range of applications. Many natural substances, such as biological tissues (e.g., bones), and man-made materials, such as foams and ceramics, are considered to be porous media. Fluid flow in porous media has been one of the main research focuses of scientists for decades. There are a number of applications of porous media flow in biological, civil, and mechanical systems, such as cartilage biomechanics [1–3], fluid flow through the endothelial glycocalyx in the motion of red cells through capillaries [4–7], fluid flow past muscle cells in the artery wall [8], fluid flow through brush border microvilli in the proximal tubule [9], fluid flow through fenestral pores in the capillary wall and the internal elastic lamina of arteries [10], the transmission of fluid shear stress to the intracellular actin cytoskeleton of the endothelial cells [11,12], fluid flow in deformable porous media and its application in molding process [13], and soil mechanics [14,15]. Lift generation in soft porous media is a new concept in porous media flow. This concept was first proposed by the pioneering work of Feng and Weinbaum [5] who demonstrated that the excess pore pressure generated by a planing surface moving on a compressed porous layer scales as $\alpha^2 = h^2/K_p$, where h is the layer thickness and K_p is the Darcy permeability, and that α is 10^2 or larger for both red blood cells gliding over the endothelial glycocalyx that cover the lumen side of our capillaries and human skiing/snowboarding on fresh snow powder. Thus the lift forces generated can be more than four orders of magnitude greater than the classical lubrication theory. The huge enhancement in lift arises from the fact that as the porous medium (snow or glycocalyx) compresses, there is a dramatic increase in the lubrication pressure because of the marked increase in the hydrodynamic resistance that the fluid (air or blood plasma) encounters as it tries to escape from the confining boundary through the compressed porous layer. It explains the pop-out phenomenon for a red blood cell squeezing through a small capillary and the enhanced lift phenomenon for a human skiing/snowboarding. In later studies by Wu et al. [16], the authors developed a new experimental and theoretical approach with intent to understand the dynamic pore pressure that might build up in a snow layer on the time scale of loading associated with skiing, snowboarding or snow-shoeing. The time-scales are roughly 0.05–0.2 s in the first two applications and 0.5 s in the last application. A series of experiments was carried out in a specially designed porous-walled cylinder-piston apparatus. The excess pore pressure was captured through dynamic experiments where the piston was released and allowed to fall under its own weight on the snow sample in the porous cylinder to create a sudden compaction. It was shown that the pore-pressure generation inside a wind-packed snow layer occurs in a period of 0.1 s and pressure relaxation in 0.7 s. For a snowboarder gliding over wind-packed snow with a velocity of 10 m/s, if the length of the snowboard is equal to 1.5 m, the approximate time that the snowboard remains in contact with snow layer is 0.15 s. This infers that sufficient time is available to adequately support the weight of the snowboard by the generated pore air pressure. The basic physics underlying the lift generation in soft porous media proposed by Feng and Weinbaum [5] was verified experimentally.

The phenomena of pore pressure increase due to sudden compression on soft porous media and that of slow pressure venting due to viscous effects is a new concept. This concept was recently

[1]Corresponding author.
Manuscript received September 30, 2008; final manuscript received April 23, 2009; published online July 29, 2009. Review conducted by Kambiz Vafai.

applied in the development of a realistic model for the lift mechanics of downhill skiing and snowboarding [17,18], which incorporates lift contributions from both the transiently trapped air inside a snow layer and the compressed ice crystals. It captures the key physics of the stability and control during skiing or snowboarding and predicts that if the speed of the skier or snowboarder was 20 m/s, the lift force generated by the trapped air accounted for approximately 50% of the total lift force in the case of snowboarding and 40% for skiing. In a further study, Wu et al. [19] applied the lessons learned from red blood cells gliding over the endothelial glycocalyx and from a human skiing or snowboarding on fresh powder snow to the conceptual design of a future generation train that can glide on a soft porous track whose mechanical properties are similar to goose down. The key insight in the latter application is that one can greatly enhance the lift and reduce the drag due to friction in the solid phase if the lateral loss of pore pressure at the side walls of the track could be eliminated.

The work in Refs. [5,16] laid the foundation for the lift generation in highly compressible porous media, and the work in Refs. [17–19] extensively applied this concept in some extreme applications. However, much of these works have been focused on the contribution of pore fluid pressure to the total lift. The solid phase behavior during the compression process has yet to be examined. The specific limitations of these works are as follows.

First, the previous study on the dynamic compression of soft porous media concentrated only on two types of samples: wind-blown snow and fresh snow. One expects by intuition that, if the solid phase of the porous material is different, e.g., stiffer, the trapped air's contribution to the total lift would be different too. Thus, the obvious question following the work of Wu and his colleagues [16] is as follows: How would other soft porous materials with varying porosities behave when subjected to sudden compressive forces?

Second, when the theory in Ref. [5] was first developed, it was intended to apply to highly compressible porous media in the limit where the structure is so compressible that the normal forces generated by the compression of the solid phase were negligible compared with the pore-pressure forces generated within the porous media. In the dynamic compression study by Wu et al. [16], the authors took into account the lift generation from both the transiently trapped air and the solid phase; however, the damping effect was attributed solely to the fluid (air) while the solid phase was assumed to be elastic. Recently, Skotheim and Mahadevan [20] theoretically investigated the fluid-induced deformation of the soft interface and the resultant lift generation due to the draining of the fluid and the elastic response of the solid structures. In this study, the authors focused on the elastic properties of a soft interface under hydraulic pressure and hence preclude the damping forces from the solid phase. In other words, none of the existing literature, to our knowledge, treats the damping effects from both the trapped fluid and the solid structure. One would ask, how would the viscoelastic property of the solid phase affect the lift generation? If the solid phase contributes more damping effect, how would this affect the lift generation from the trapped fluid?

Third, in the experiment of Wu et al. [16], the motion of the dropping piston was predicted theoretically; the comparison between the theoretical model and the experimental data was only based on the pore air pressure response. If the damping effect from both the solid phase and the pore air pressure need to be determined, one would need another matching criterion besides the pressure response. What is that criterion?

In the current study we will explore these limitations. We shall first completely redesign the experimental setup in [16] by introducing a guiding system for the dropping piston. The new apparatus will be fully instrumented with pressure, acceleration, and displacement sensors. We shall perform thorough analyses on a more comprehensive set of experimental data obtained from trials conducted on various porous materials having different porosities and densities. The consolidation theory developed by Wu et al. [16] will be modified to include the damping force from the solid phase, $-\eta(dh/dt)mg$, where η is the damping coefficient, and dh/dt and mg are the velocity and weight of the piston, respectively. The initial Darcy permeability, K_{P0}, of the porous media, which is related to the damping effect of the pore air pressure, and the damping coefficient of the solid phase, η, are to be determined by requiring that the theoretical predictions for the motion of the piston as well as the pore air pressure response fit our experimental data. By performing detailed analyses of the pore air pressure distribution and the viscoelastic behavior of the solid phase, we shall provide a quantitative approach in characterizing different aspects that affect the lift generation in a soft porous medium.

2 Experiment

2.1 Experimental Setup. In order to obtain critical insight into the behavior of soft porous media in response to rapid compaction, a porous-walled cylinder-piston apparatus was designed, fabricated, and tested in the Cellular Biomechanics and Sports Science Laboratory at Villanova University. The design of this apparatus was based on the setup in Ref. [16] but with significant improvements. The previous experimental setup was a fairly accurate design and the experimental results were reasonable. However, it had several major limitations. First, the piston that provides sudden compaction on the porous media was released manually in the previous studies. Inconsistent drop rates were observed under similar initial conditions. Second, there was no direct measurement of the displacement of the piston in the previous study and the initial and final thicknesses of the porous media were measured manually. Third, the previous experiments were only performed on snow and goose down. Other types of porous media and particularly synthetic fibers have not been tested. Considering these limitations, a new modified and enhanced setup was built. A schematic of this apparatus is shown in Fig. 1(*a*). It consists of a porous cylindrical side wall of 40 cm diameter and 12.80 cm height, which is attached to a solid base plate. The porous side wall was made of Rigimesh® from Pall Corporation (East Hills, NY), which is an arrangement of several screens bonded together for rigidity. The mesh provided negligible resistance to the flow of air through it, which was confirmed during trial tests without the fibers when no pressure buildup was indicated by the pressure transducers during the free fall of the loaded and unloaded piston. A light piston that can be loaded with fixed weights on top of it can slide freely along the inner surface of the cylinder and provide a uniform loading to the porous media. In order to prevent any misplacement of the piston during the free fall, to minimize friction, and to have consistency in all experiments, the piston was guided by a linear bearing from the top, as shown in Fig. 1(*a*). A glider was attached to the rod that can glide through a vertical gliding path to create a uniform loading. The apparatus is designed with a small clearance gap between the piston and the cylinder side wall, which allows the trapped air to flow out of the cylinder only through the porous side walls in the radially outward direction. A high frequency response micro-electro-mechanical systems (MEMS)-based pressure transducer (Kulite Semiconductor Products (Leonia, NJ) Model MIC-062) was mounted at the center of the piston, and three other pressure transducers (SI Micro (Milpitas, CA) Model SM5652-015-G-3-L) were installed in the radial direction of the piston at distances 7 cm, 14 cm, and 18 cm from the center. The largest inner diameter of the transducers is 0.203 cm. This size was used to get a satisfying spatial resolution in local pressure measurements. All the pressure signals were measured relative to the ambient atmospheric pressure. In order to examine the motion of the piston, a dual-axis accelerometer (ADXL203), with a range of ± 1.7 g and a sensitivity of 1000 mV/g, was installed on the top surface of the piston, which allows the inertia of the piston to be determined directly from the experiment. A laser sensor from Micro-Epsilon (model ILD1300-200) with a range of 200 mm and a dynamic

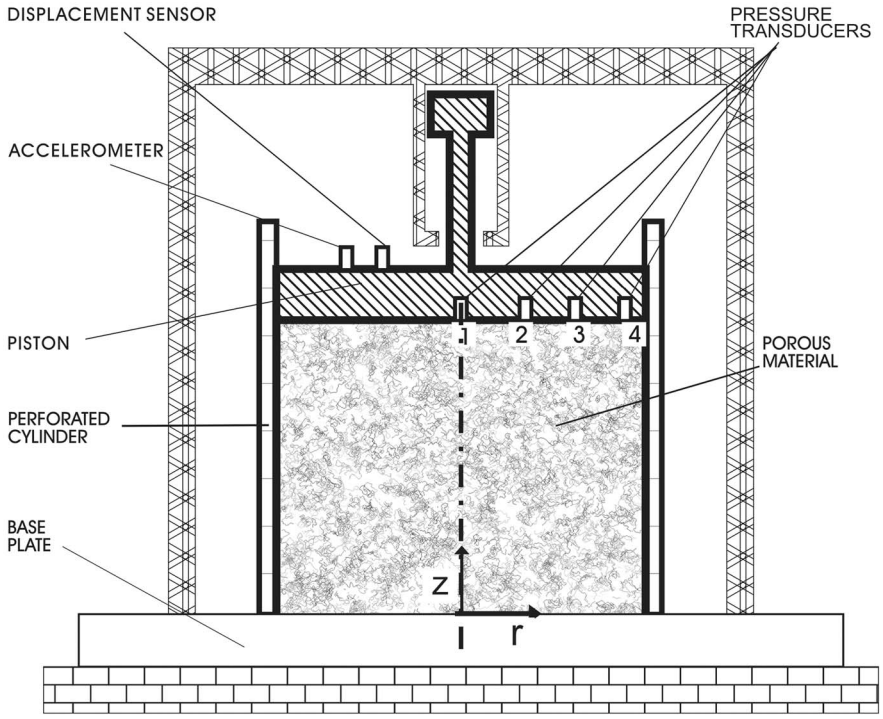

(*a*)

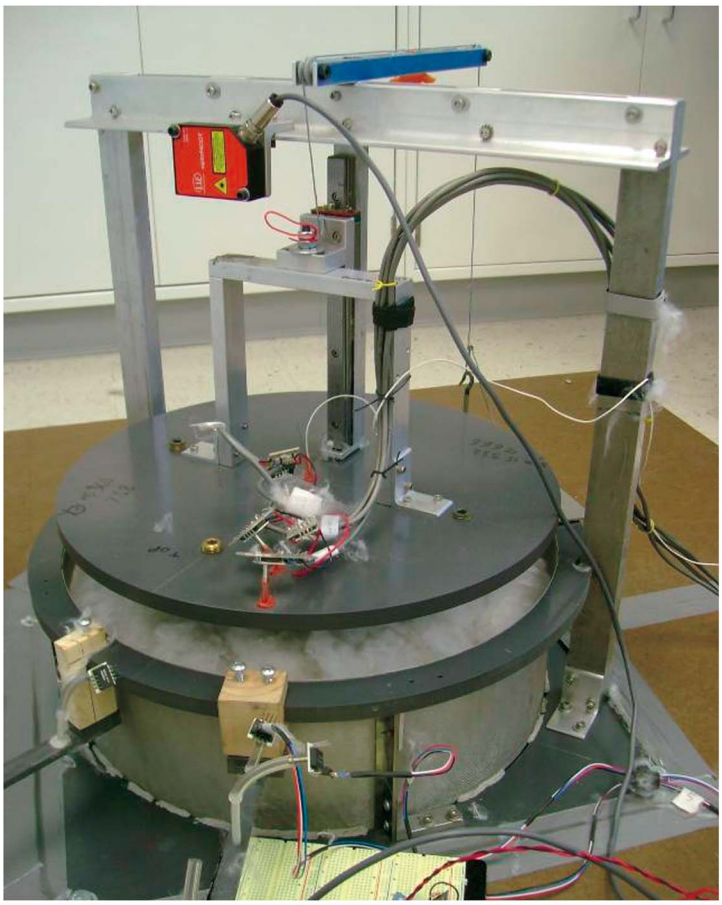

(*b*)

Fig. 1 (*a*) **Schematic of the test setup for finite domain and** (*b*) **picture of the actual test setup**

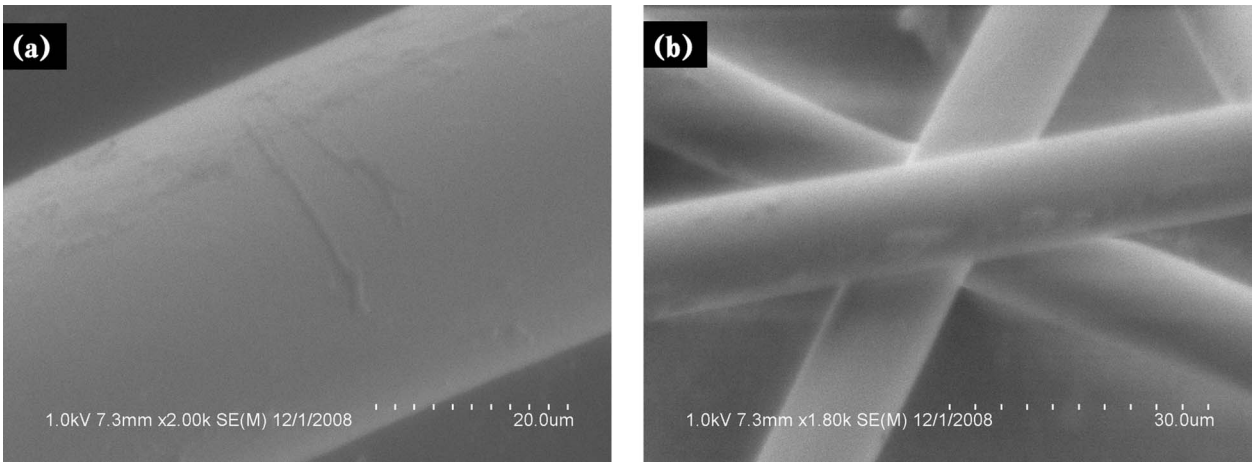

Fig. 2 SEM images for (*a*) material A at 1kV and 2000× and (*b*) material B at 1kV and 1800×

resolution of 200 μm was used to measure the displacement of the piston. The signals were captured using an USB chassis NI cDAQ9172 data acquisition system with a plug-in module NI9205, having 16 bit resolution and a maximum sampling rate of 250,000 samples/s. A LABVIEW® program was written to acquire, filter, and store the data in ASCII files for further processing with MATLAB®. Figure 1(*b*) shows the real picture of the experimental setup.

2.2 Material Characterization. Two kinds of polyester fibers, A and B, having different porosities were used for the experiments. Material A is filling material used in stuffed animals (Build-a-Bear). Material B is used in Egyptian cotton pillows. These two fibers were chosen due to their significantly different behaviors as they were being compressed. Material A tended to be more elastic, while material B was observed to be more "viscous" under rapid compaction.

Hitachi s-4800 high resolution scanning electron microscope (SEM) was used to investigate the polyester fibers. Due to the fibers being curved in loops, special care must be taken to secure the fibers onto the SEM specimen holder. First, conductive carbon tapes are firmly pressed on the SEM specimen holder, and then a small amount of the fibers are pressed onto the carbon tape by using a pair of tweezers to secure the fibers on a desirable position. A small amount of silver paint was used to further secure the fiber position, as well as to provide better electrical conductivity to reduce the charging effect. The fibers could not be glued onto the conductive carbon tapes flatly along its whole length; therefore, they would be in slightly different heights, and only portion of a fiber could be focused when a photo was taken. To avoid electron charging effect on the polyester fibers, the acceleration voltages of the SEM were kept at 5 kV or less. Figure 2(*a*) at 2000× shows some surface roughness on the surface of the fiber A. It seems that the extrusion process of the fibers was smooth, continuous, and consistent. Based on the SEM observations on these fibers, the diameters of the fibers A remain constant, which is about 40 μm. For comparison, fibers of material B were also studied by using SEM. Figure 2(*b*) is a photo taken at 1kV and 1800×, which reveals the topography of this fiber. It shows that fiber of material B has more surface irregularities than that of material A. They are not as clean as the fiber A after the extrusion process. The diameter of the fiber B is about 13 μm. Since its diameter is smaller, they were easier to be pressed onto the conductive carbon tape during the specimen mounting. No silver paint was needed to secure the positions of the fibers. It is likely that these fibers are less stiff since they are easier to deform.

In order to obtain a three-dimensional perception on the fibers, such as the space between fibers, the fiber shape, and the homogeneity of the fibers, a Zeiss stereomicroscope, model STEMI SV-11 APO, was used to characterize the fibrous materials. This stereomicroscope is equipped with a Leica DC480 digital camera to capture the images. A size of about 1.5-mm diameter specimens was investigated. For each material, three layers of fibers were taken, namely, bottom, middle, and top layers. The bottom is the farthest focused layer, while the top layer is the closest focused layer to the camera lens. The middle represents the focused in-between layer. Figures 3(*a*)–3(*c*) are taken in the order of bottom, middle, and top layers of material A. Based on the SEM pictures mentioned before, the diameter of the fiber of this material is about 40 μm; therefore, the space between the fibers for material A is estimated to be 0.7 mm (700 μm) or less. The fibers are curved and intertwined with others. It is almost impossible to identify the beginning and ending of each fiber. The length of the fibers could not be easily identified either. However, if the fibers are long enough, it is obvious that the overall length of fibers will not be a significant factor as long as there are many intertwines points where the fibers interlock with each other. It is the interlocking distance that plays an important role in the mechanical properties, assuming that the fiber stiffness and strength are kept the same. The stereographs of material B are shown in Figs. 3(*d*)–3(*f*). Figure 3(*d*) shows the bottom layer containing many very fine and dense fibers. Figure 3(*e*) shows the top layers of the fibers. Due to the dense fibers, the picture of middle layer could not be taken. Figure 3(*f*) is the top layer of the fibers in a different region at a higher magnification. From Fig. 3(*f*), again using the diameter of this fiber determined from SEM study, we can estimate that the space between the fibers is about 200 μm or less from the top view. Figures 3(*d*)–3(*f*) clearly indicate that material B has straighter fibers without too much of the twists and turns.

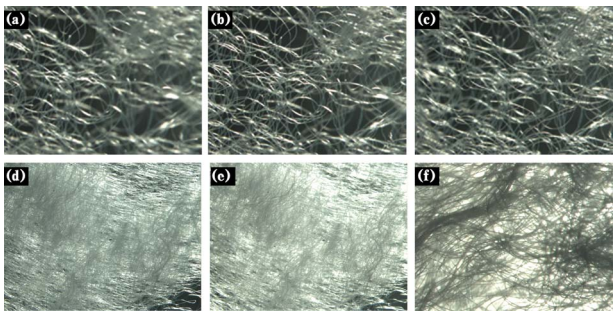

Fig. 3 Stereomicroscopy images for material A at bottom layer (*a*), middle layer (*b*), and top layer (*c*), and for material B at bottom layer (*d*), top layers (e), and top layer in a different region at a higher magnification (*f*)

Table 1 Fiber characterization test matrix

Fiber		Initial porosity	Density (kg/m^3)	Applied dynamic load (kg)
A	1	0.93	15.7	4.74, 5.14, 7.58
	2	0.90	22.2	4.74, 5.14, 7.58, 9.27
B	1	0.94	15.5	2.31, 2.71, 3.03, 4.17
	2	0.89	24.2	3.03, 4.17, 4.74
	3	0.86	28.8	4.74, 7.0, 8.71

Therefore, there will be less interlocking mechanisms among the fibers even though the space between the fibers is less. As discussed in the SEM study, material B was easier to be flattened for SEM specimen mount, probably due to its smaller diameter, less curving, and less interlocking mechanism.

For material A, two different densities were selected which consequently resulted in two different porosities. For material B, three different densities were selected. The fiber's mass was measured before filling each cylinder. These values were then divided by the volume of the cylinder based on the piston's initial height for each individual test to obtain the densities of the materials prior to compression. To measure the initial porosity of the testing material, a small graduated cylinder with a perforated piston was used. Sample material with the same density as the filling fibers was placed inside a graduated cylinder, which was then compressed completely by the perforated piston. The ratio of the volume of the air that was squeezed out to the total initial volume gives the value of the initial porosity. The density and porosity of these materials are listed in Table 1.

2.3 Experimental Methods and Results. In order to study the contribution of the solid phase to the lift generation during the dynamic compression process, we subjected the porous materials to incrementally increased static compressive loading using the same apparatus shown in Fig. 1. Since the loads were added gradually to the piston, the air in the pores had sufficient time to escape freely without generating pore pressure which is different from the dynamic experiments. This ensures the static loads are being balanced only by the solid phase of the material, and thus eliminates the inertial effect of the dropping piston and the damping effects from both the pore air pressure and the solid phase. The load on the piston and the displacement of the piston were normalized with respect to their maximum values. A representative result of this quasistatic experiment for sample B3 during compression (loading) and expansion (unloading) is shown in Fig. 4. These results are to be applied in the theoretical model that will be discussed later in this paper.

The dynamic compaction experiments were performed on two porous materials under different dynamic loading conditions as listed in Table 1. While filling the cylinder with the fibers, care was taken to ensure that the fiber was spread out evenly by hand and was put in layers inside the cylinder. The piston with applied loads (refer to the last column of Table 1 which indicates the total weight of the piston and the applied additional loads) was then suddenly released by a triggering mechanism to provide a rapid compaction on the porous material underneath. Pressure transducers captured the time-varying pore-pressure buildup. The displacement of the piston was recorded simultaneously by the displacement sensor. Figures 5(*a*) and 5(*b*) show the dynamic pressure response beneath the piston at different radial distances *r* from the center for material B3 (7.0 kg loading) and material A2 (9.25 kg loading), respectively. As shown in Fig. 5(*a*), the pressure builds up in about 0.15 s, and then relaxes in 0.1 s. The maximum pore pressure registers at the center, and the magnitude of the maximum pore pressure decreases with increasing radial distance from the center. Minimum pressure is registered at the radially outermost location. It is this pressure gradient which forces the air flow outward in the radial direction.

The difference in the general pressure response behavior for materials B3 and A2 is that one observes a negative pressure just after the pressure relaxation is complete for A2, yet this was absent for B3. This negative pressure corresponds to the rebound of the piston. It happens due to the lack of damping effect from either the trapped air or the solid phase; thus, after the air is completely purged out, the piston was pushed up and a partial vacuum is created.

A representative normalized radial pressure distribution recorded by the pressure transducers 1–4 is plotted in Fig. 6. The testing material is A2 and the loading on the piston is 9.25 kg. It is plotted at the time when peak pressure is achieved at these

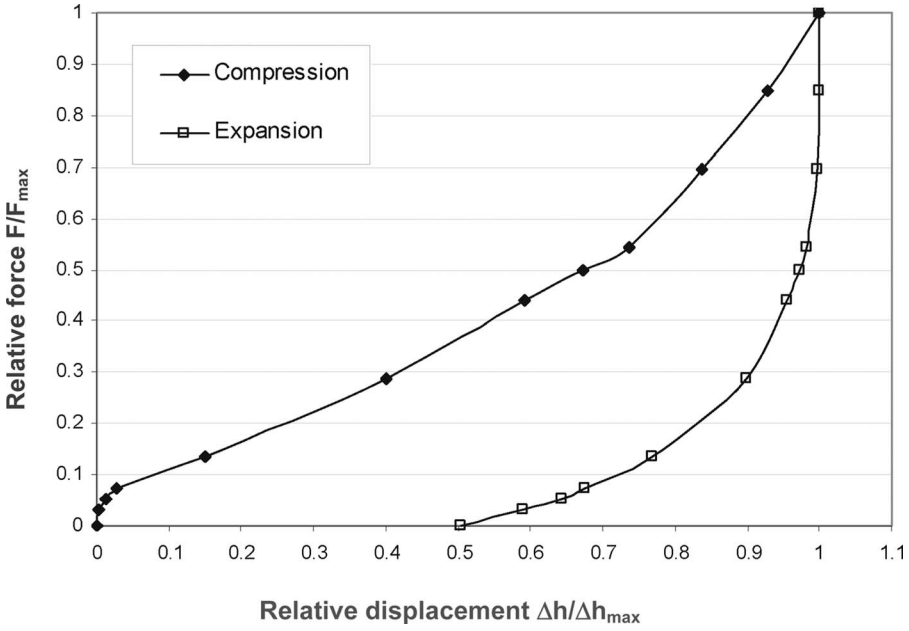

Fig. 4 Force/displacement relation obtained in the quasistatic compression experiment with fiber B3

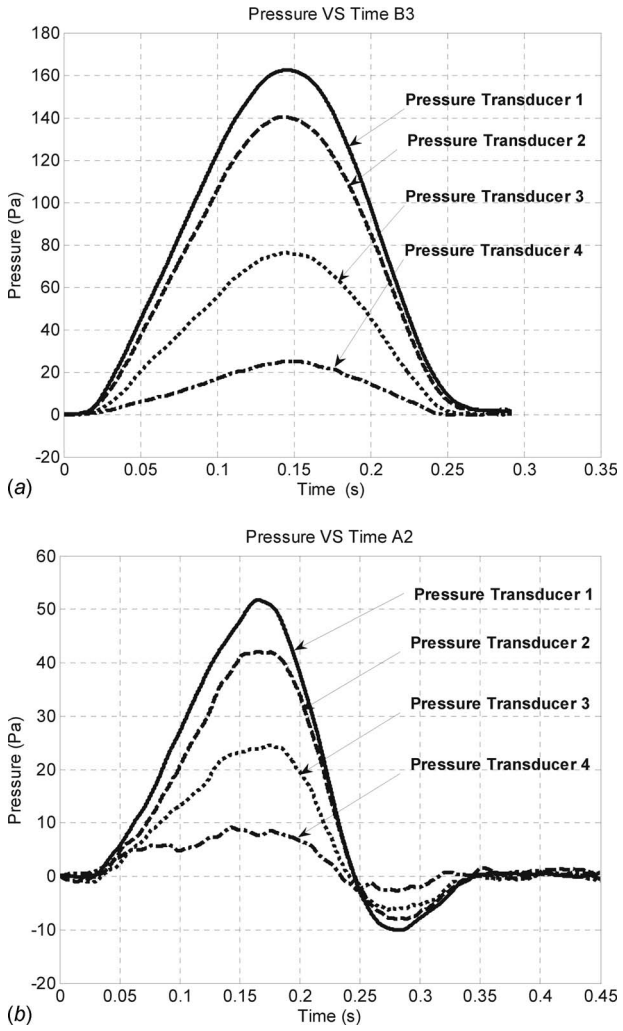

Fig. 5 Representative dynamic pressure response for (*a*) material B3 with 7.0 kg load and (*b*) material sample A2 with 9.25 kg

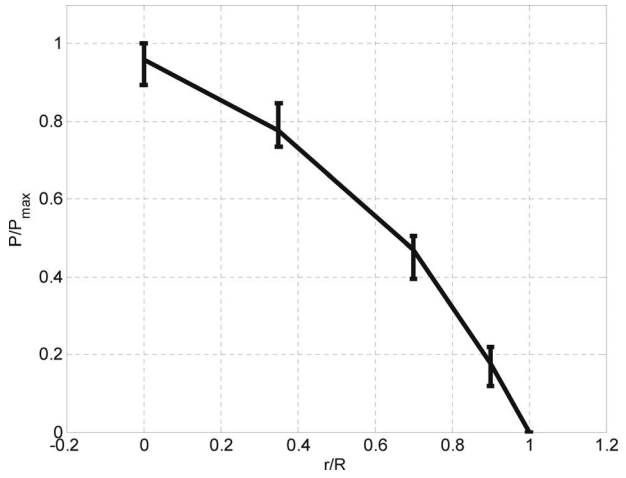

Fig. 6 Representative radial pressure measured by the pressure transducers 1–4 as shown in Fig. 1. The testing material is A2 and the loading on the piston is 9.25 kg. It is plotted at the time when peak pressure is achieved at these locations. The data have been normalized by the maximum pressure obtained by pressure transducer 1 at the center of the piston, P_{max}. The error bars in the graph indicate the range of the variation in the pressure measurements in multiple sets of experiments.

locations. As can be seen from this figure, the pressure distribution in the *r*-direction is very close to parabolic. This is not surprising since the pressure gradient in the radial direction is dominant, and a simple plug-flow model would predict a parabolic pressure distribution in this direction. In order to examine the uncertainty and repeatability of the measurements, six sets of experiments were performed under the same condition. The data have been normalized by the maximum pressure obtained by pressure transducer 1 at the center of the piston, P_{max}. The error bars in the graph indicate the range of the variation in the pressure measurements. In terms of standard deviation, the actual error is about 4%.

To examine the radial symmetry of the pressure data, two other pressure transducers were mounted at a distance of 7 cm from the center of the piston, but at 45 deg and 90 deg from the radial line where pressure transducers 1–4 are mounted. We repeated the dynamic experiments with A2 and B3. The signals obtained by these two new pressure transducers were compared with that recorded by transducer 2. The differences between them are within 6%, which justified the assumption of axisymmetry.

The rebound effect observed in Figs. 5(*a*) and 5(*b*) is better described in Figs. 7(*a*) and 7(*b*), where the time-dependent displacements of the piston for materials B3 and A2 corresponding to the dynamic compaction experiments described in Fig. 5 are presented. The displacement is normalized based on the initial thickness of the material. One can readily observe the rebound behavior for material A2.

Since we simultaneously measured the time-dependent displacement of the piston using a laser sensor and its acceleration using an accelerometer, it will be instructive to compare the acceleration obtained from the direct measurement with the time derivative of the piston displacement shown in Figs. 7(*a*) and 7(*b*). This comparison is shown in Fig. 8(*a*) for material B3 and Fig. 8(*b*) for material A2. From these two figures we can clearly see the perfect match between the readings of the accelerometer and the time derivative of the displacement data.

3 Theoretical Formulation

In Ref. [16], a consolidation theory was developed to describe the motion of the piston and the resulting pore-pressure response. The motion of the falling piston is modeled by applying Newton's law. As shown in Fig. 1, the piston is released from rest and starts falling toward a solid planar surface. The distance between the piston and the ground is assumed to be uniform in the radial direction so that the displacement, Δh, is independent of r or z and varies only with time. Balance of forces acting on the piston requires that

$$m\frac{d^2h}{dt^2} = -mg + F_{\text{air}} + F_{\text{solid-elastic}} + F_{\text{solid-damping}} \tag{1}$$

where m is the mass of the piston, h is its instantaneous height, and $F_{\text{solid-elastic}}$ and $F_{\text{solid-damping}}$ are the elastic and damping forces exerted by the solid phase. F_{air} is the integral of the pore air pressure at the piston surface,

$$F_{\text{air}}(t) = \int_0^R 2\pi r P(r,h,t)dr \tag{2}$$

As was pointed out by Joseph et al. [21], the general equation that governs the fluid flow in a saturated porous medium is

$$\rho(\mathbf{u}\cdot\nabla)\mathbf{u} + \nabla P = \mu\nabla^2\mathbf{u} - \frac{\mu}{K_p}\mathbf{u} - \frac{c\rho}{K_p^{1/2}}|\mathbf{u}|\mathbf{u} \tag{3}$$

where μ and ρ are the viscosity and density of the fluid, respectively. The origin of a nonlinear $|\mathbf{u}|\mathbf{u}$ term in Eq. (3) dates back to Dupuit [22] but is now associated with Forchheimer [23]. It arises from the pressure drag due to the wake of the fibers. In the same

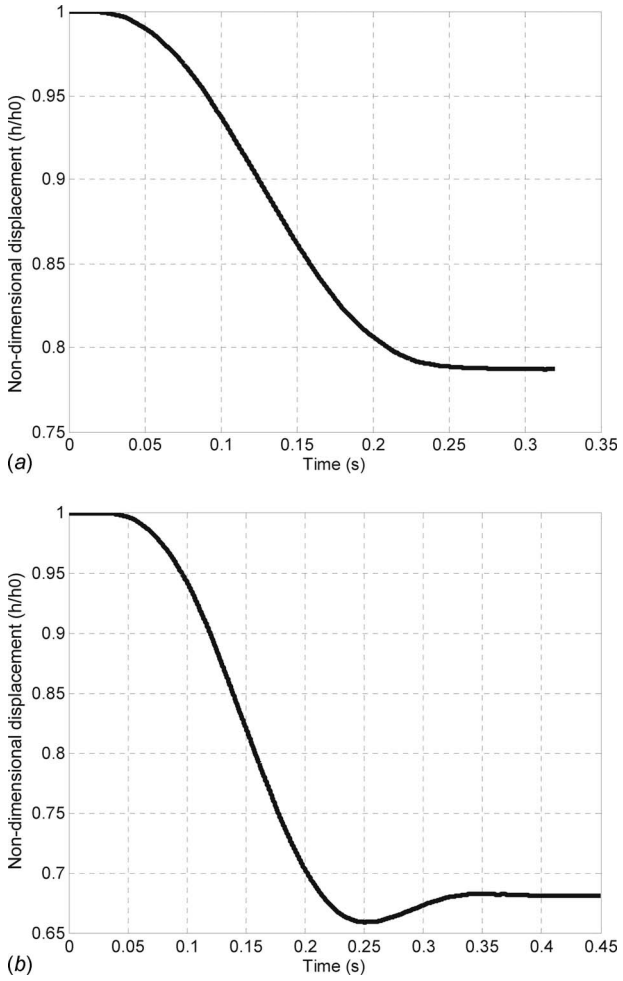

Fig. 7 Representative time-dependent displacement of the piston during the dynamic compaction experiment mentioned in Fig. 5 for (*a*) material B3 and (*b*) material A2

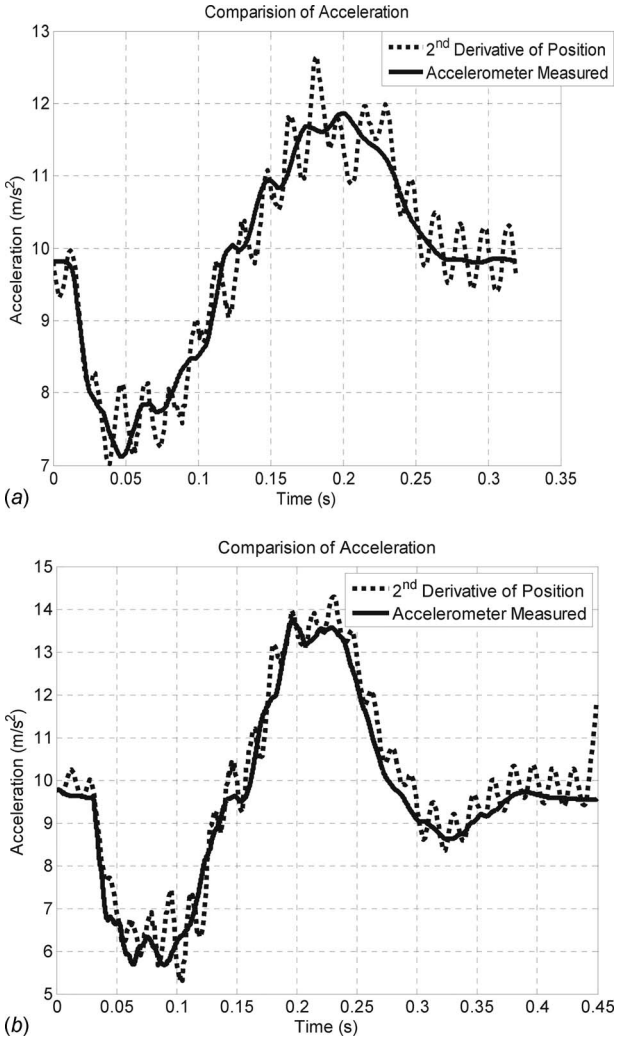

Fig. 8 Comparison between the acceleration obtained from the direct measurement using accelerometer and the time derivative of the piston displacement described in Fig. 7 for (*a*) material B3 and (*b*) material A2

way that proper averaging of the viscous term in the Navier–Stokes equations gives rise to the linear Darcy term, Joseph et al. [21] argued that proper averaging of the $(\mathbf{u}\cdot\nabla)\mathbf{u}$ term should give rise to a quadratic drag law. Available experimental evidence [24,25] appears to support this hypothesis. If one compares the magnitude of the nonlinear Forchheimer inertial term to the linear Darcy term in Eq. (3), as long as the Re based on the Brinkman length $K_p^{1/2}$, $\rho U K_p^{1/2}/\mu < 1$, the nonlinear Forchheimer inertial term is negligible while the linear Darcy term retained. In the current application, the Darcy permeability is of the order of 10^{-9} m^2 and the characteristic velocity of the air never exceeds 30 cm/s, which can be obtained from the first derivative of the displacement signals. The Re based on the $K_p^{1/2}$ is much less than unit and the Forchheimer term is neglected in Eq. (3), which leads to

$$\rho(\mathbf{u}\cdot\nabla)\mathbf{u} + \nabla P = \mu\nabla^2\mathbf{u} - \frac{\mu}{K_p}\mathbf{u} \tag{4}$$

In a more recent paper, Wu et al. [26] obtained nonlinear exact and asymptotic solutions of Eq. (4) to a stagnation-point flow in a porous medium, which show the transition in behavior that occurs between the classical solutions of Hiemenz [27] and Homann [28–30] for the two-dimensional and axisymmetric stagnation-point boundary layers, and the local expansion of the Brinkman solution for the flow past a cylinder or sphere in the stagnation regions as the Darcy permeability is decreased. In this analysis, a new fundamental dimensionless parameter emerges, $\beta = \nu/K_p A$, where ν is the kinematic viscosity and A is the characteristic velocity gradient imposed by the external flow. The structure of a new type of boundary layer is observed in the analysis that evolves as β varies from zero, the classical limit of the Hiemenz and Homann solutions, to $\beta \gg 1$, the classical Brinkman limit where inertial effects, $(\mathbf{u}\cdot\nabla)\mathbf{u}$, are negligible. These solutions show that for the case of dynamic compaction on a porous medium discussed herein, at any instant, $\beta \gg 1$, the viscous boundary layer is vanishingly thin, the inertia effect, $(\mathbf{u}\cdot\nabla)\mathbf{u}$, is negligible compared with the distributed body force, and one is left with an outer flow that is governed by linear Darcy's law,

$$\mathbf{u} = -\frac{K_p}{\mu}\nabla P \tag{5}$$

The flow in this device is time dependent, but the instantaneous flow is approximately described by a quasisteady axisymmetric flow within the cylinder, which satisfies Darcy's law, Eq. (5). In a consolidating porous medium where the porous matrix undergoes deformation during the process of transient fluid flow, $\mathbf{u}$ in Eq. (5) is the relative velocity with respect to the solid phase. In the present application, the displacement of the solid fibers is less than 22% of the 10 cm thickness of the porous layer. In contrast, the characteristic discharge distance for the air is equal to the

radius of the cylinder, which is 20 cm. As a result, the solid phase velocity is negligible compared with the air velocity, and **u** is assumed to be velocity with respect to a fixed coordinate system.

For continuity, we require that [14]

$$\nabla \cdot (\rho \mathbf{u}) + \frac{\partial(\rho\varphi)}{\partial t} = 0 \tag{6}$$

where φ is the instantaneous porosity of the porous media. During the compression process, the porosity of the porous material changes due to the motion of the upper boundary. For a porous layer with an initial uniform porosity, φ_0, and initial thickness, h_0, the deformation-dependent average porous media porosity, φ, is expressed as

$$\varphi = 1 - \frac{h_0}{h}(1 - \varphi_0) \tag{7}$$

Equation (6) describes the transient deformation of a consolidating medium. In our dynamic compression experiments, the pressure under the piston never exceeds 500 Pa above ambient pressure. Thus, the pressure change with respect to ambient pressure is only about 0.5%, the Mach number is $\ll 1$, and the air can be treated as incompressible, $\rho = \text{const}$. With this in mind, one combined Eqs. (5)–(7) and obtained a Poisson equation:

$$\frac{1}{r}\frac{\partial}{\partial r}\left(r\frac{\partial P}{\partial r}\right) + \frac{\partial^2 P}{\partial z^2} + \frac{\mu}{K_p}\frac{h_0(\phi_0 - 1)}{h^2}\frac{dh}{dt} = 0 \tag{8}$$

for solving the pressure distribution inside the porous layer at any instant. One notes that, K_p, h, and dh/dt are time-dependent parameters rather than variables in Eq. (8) due to the quasisteady condition. The solution of Eq. (8) satisfying the boundary conditions, $u_z|_{z=0} = 0$, $u_z|_{z=h} = dh/dt$, $\partial P/\partial r|_{r=0} = 0$, and $P|_{r=R} = 0$, is given by

$$P(r,z,t) = \left[\sum_{k=1}^{\infty} \frac{-\frac{\mu}{K_p}\int_0^R rJ_0(\lambda_k r)dr}{\sinh(\lambda_k h)\lambda_k \int_0^R rJ_0^2(\lambda_k r)dr} J_0(\lambda_k r)\cosh \lambda_k z + \frac{\mu(R^2 - r^2)}{4K_p}\frac{h_0(\phi_0 - 1)}{h^2} \right] \frac{dh}{dt} \tag{9}$$

where λ_k are roots of $J_0(\lambda_k R) = 0$.

K_p is a function of compression. In the current study, we employ Carman–Kozeny's semi-empirical relationship

$$K_p = \frac{d_s^2}{180}\frac{\varphi^3}{(1 - \varphi)^2} \tag{10}$$

to derive this function. Here d_s is the mean diameter of the solid particles. During the compression process, if the mean diameter, d_s remains the same and the Darcy permeability of the undeformed porous media is K_{p0}, one obtains from Eqs. (7) and (10),

$$K_p = K_{P0}\frac{\left(1 - \frac{h_0}{h}(1 - \varphi_0)\right)^3}{\left(\frac{h_0}{h}\right)^2 \varphi_0^3} \tag{11}$$

Substituting Eq. (11) into Eq. (9), one can readily obtain $P(r,z,t)$, which is then substituted into Eq. (2) to obtain $F_{\text{air}}(t)$.

In Eq. (1), the lifting force from the solid phase is composed of two parts. The elastic force is equivalent to a spring and the damping force is equivalent to a dashpot. The elastic force is determined by the quasistatic experiment mentioned before, in which the piston was loaded slowly and incrementally and thus the air in the pores can slowly escape without elevating pore pressure, in contrast to the dynamic experiments in which the air is temporarily trapped before it escapes. After each incremental weight is added, the compression Δh of the porous layer is measured. This provides an empirical expression for $F_{\text{solid-elastic}}$:

$$\frac{F_{\text{solid-elastic}}}{F_{\max}} = f\left(\frac{\Delta h}{\Delta h_{\max}}\right) \tag{12}$$

where $F_{\max} = mg$ and $\Delta h_{\max}$ is the final displacement of the piston when the full load mg is applied. Equation (12) takes different forms for loading and unloading processes, as shown in Fig. 4.

As can be seen from the stereomicroscopy images shown in Fig. 3, fibers of porous materials A and B are connected and twisted in an intricate three-dimensional structure. The bonds between fibers play an important role in determining the mechanical properties of the material. During the rapid compression, the bonds between the fibers are broken; friction between fibers creates significant damping forces which, by intuition, are proportional to the velocity of the compaction. As the piston rebounds after its maximum compression, the compressed fiber sample is aerated and expands, during which the relative motion between the fibers has to overcome the connections between fibers and a damping force from the debonding of the compressed fibers is applied. This force is intuitively expected to be proportional to velocity also, since this is the rate at which the bonds are being broken. Thus, the damping force from the solid phase is expressed as

$$F_{\text{solid-damping}} = -mg\left(\eta_i \frac{dh}{dt}\right) \tag{13}$$

where η_i is the damping coefficient and the index i indicates the damping coefficient during compression (η_d) and rebound (η_u). η_i is to be determined by comparing the theoretical predictions of the time-dependent pressure distribution and piston displacement with the corresponding experimental data. The negative sign indicates that the direction of the damping force is always opposite to the motion of the piston.

Using Eqs. (2), (12), and (13), one can integrate Eq. (1) subject to initial conditions, $h|_{t=0} = h_0$, $dh/dt|_{t=0} = 0$, numerically. The solution for $h(t)$ is then substituted into Eq. (9) to determine the time-dependent pore-pressure distribution.

4 Results and Discussion

In the previous study by Wu et al. [16], the comparison between the experiments and the theory on the pore-pressure response was employed to determine the initial Darcy permeability of the porous media. There was no direct measurement of the displacement of the piston and thus the comparison of the motion of the piston was not presented. The problem is that there might have been some solid damping force that contributed to the lift generation but was not described. In the current study, we have significantly improved the previous experimental setup, which made it possible for us to determine different forces during the dynamic compaction process. In this section, we shall compare the experimental results with the theoretical predictions based on the time-dependent displacement and pressure response, to determine the initial Darcy permeability K_{p0} and the solid damping coefficient η_i of a porous medium, and hence provide the relative contributions of different forces in lift generation.

The Darcy permeability, K_p, of a porous material denotes how easy the air can pass through the porous structure; the inverse of K_p is a measure of the resistance that the air encounters as it flows through the porous media, or equivalently, the damping force of the trapped air that acts on the piston. In the snow compaction study by Wu et al. [16], the damping force of the solid phase was absent since the frictional force between ice crystals was expected to be small. However, in the current study, if one neglects the fiber

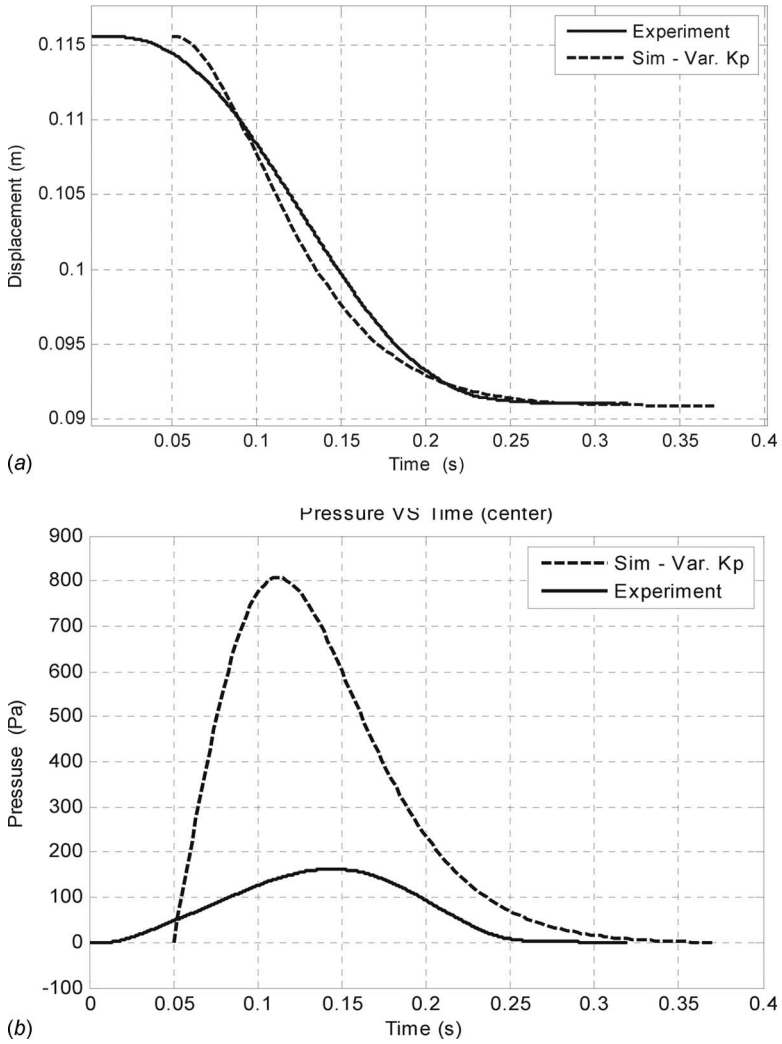

Fig. 9 Comparison between experimental results (solid line) and theoretical simulation (dash line) for the dynamic compaction experiments with material B3 at 7.0 kg loading: (*a*) displacement of the piston and (*b*) pore pressure at the center of the piston. The simulation was based on no solid damping effects during compression.

damping force during compression, as shown in Fig. 9(*a*) for the displacement of the piston in the dynamic compaction experiment with fiber B3 under 7.0 kg loading, in order to have the theoretical prediction match the experimental data, the initial Darcy permeability of the fiber needs to be 1.33×10^{-9} m^2. One substitutes this value into Eq. (9) and finds that the theoretical prediction for the peak pore pressure at the center of the piston is eight times larger than the experimental result as shown in Fig. 9(*b*). Also, the pore-pressure peak happens at 0.11 s as compared with the experimental time of about 0.15 s, approximately 0.04 s earlier. The value of Darcy permeability is obviously overestimated. This is because one neglects the fiber damping force during compression. If the solid phase damping force is absent, in order to provide the necessary damping effect to match the displacement data, a smaller Darcy permeability is needed because lower Darcy permeability indicates more resistance that the air encounters when it passes through and thus higher air damping force; also with lower permeability, air cannot escape easily and more pressure is built up.

Figure 9 leads us to believe that the fiber damping force plays a significant role in lift generation. One has to adjust both the Darcy permeability and the solid damping coefficient η_i in the simulation in order to match the theoretical predictions with the experimental data. The matching was found by trial and error. It is shown in Fig. 10 that if the permeability of the fiber is assumed to be a constant during the compression, the best fit between experiments and theory requires $K_p=6.25\times10^{-9}$ m^2, $\eta_d=4.73$ s/m, and $\eta_u=300$ s/m. If the permeability changes as a function of compression based on the Carman–Kozeny's equation (11), the initial Darcy permeability was determined to be $K_{p0}=8.79\times10^{-9}$ m^2, $\eta_d=4.73$ s/m, and $\eta_u=300$ s/m.

It is clearly demonstrated in Fig. 10 that varying permeability provides a better match. However, even with varying permeability, the theoretical model still predicts a faster pressure buildup compared with the experimental data. One attributes this behavior to the following three reasons: First, the change in permeability does not exactly follow the Carman–Kozeny's equation; second, the solid damping coefficient varies during the compression process; third, the empirical relationship obtained from the quasistatic experiment does not precisely describe the elastic lifting force from the solid phase during the rapid compaction. In an ongoing study by our group, a permeability measurement apparatus was developed which will be applied to measure the change in the Darcy permeability as a function of compression. The results will be included in the consolidation theory developed herein to pro-

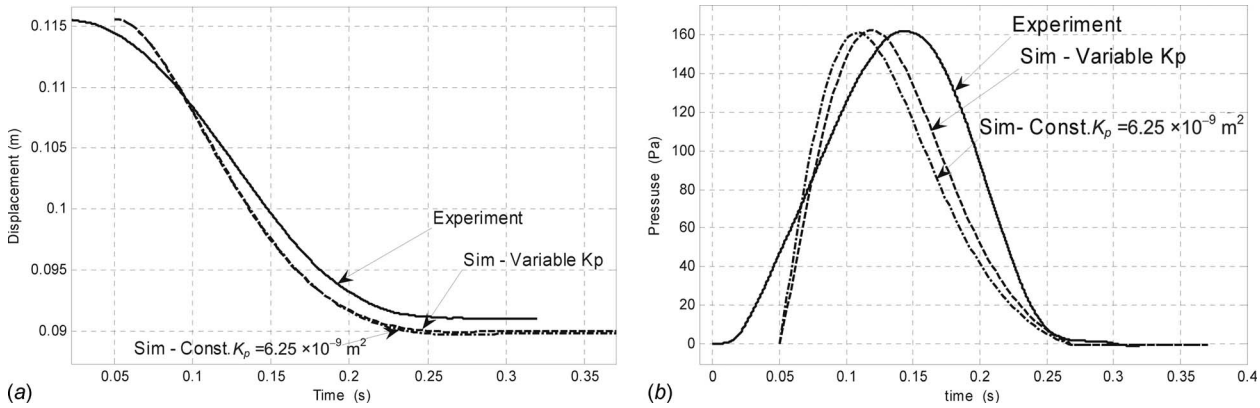

Fig. 10 Comparison between experimental results and theoretical simulation for the dynamic compaction experiments with material B3 at 7.0 kg loading: (*a*) displacement of the piston and (*b*) pore pressure at the center of the piston. Two simulations are provided, one for constant permeability at $K_p=6.25\times10^{-9}$ m^2 and the other for varying permeability following Eq. (11) with initial value of permeability $K_{p0}=8.79\times10^{-9}$ m^2. In both cases, the solid damping coefficients in compression and expansion are determined as $\eta_d=4.73$ s/m and $\eta_u=300$ s/m, respectively.

vide a better simulation. In further study, we will also improve our current experimental setup by adding a dynamic loading cell to directly measure the elastic solid phase lifting force.

In order to verify if the approach presented herein is appropriate, we performed simulations for material B3 with different loading conditions listed in Table 1. Figures 11(*a*) and 11(*b*) show comparisons between the experimental data and the theoretical predictions on the time-dependent displacement of the piston and pore-pressure generation. The applied load is 8.71 kg. Interestingly, one finds that the best fit for both the motion of the piston and the pore-pressure distribution requires $K_{p0}=8.79\times10^{-9}$ m^2, $\eta_d=3.33$ s/m, and $\eta_u=300$ s/m, the same value of permeability K_{p0} and rebound coefficient η_u as that obtained in 7.0 kg loading condition. The solid damping coefficient during the compression is relatively small. This is not surprising because the bonds between fibers are more easily broken with increased load. We repeated this cross checking for other loading conditions of material B3 and obtained consistent matches. By doing this, we have verified the validity of the theoretical and experimental methods developed in this paper.

As mentioned before, rebound behavior was observed for material A2 under 9.25 kg loading situation because of the lack of damping effects from either the trapped air or the solid phase. We performed comparisons between theory and experiments for material A2 and observed a significant rebound effect. One finds that if the permeability of the fiber changes as a function of compression based on the Carman–Kozeny's equation (11), the initial Darcy permeability was determined to be $K_{p0}=1.301\times10^{-7}$ m^2, and the solid damping coefficients for the compression and expansion are $\eta_d=3.82$ s/m and $\eta_u=7.7$ s/m, respectively. Comparing with what was found for material B3 where $K_{p0}=8.79\times10^{-9}$ m^2, $\eta_d=4.73$ s/m, and $\eta_u=300$ s/m, it is obvious that the damping effect of B3 from the pore air pressure are much higher than that of material A2, as was expected. This observation is consistent with the scanning electron microscopy and stereo microscopy study presented before. The fiber diameter of material A is three times larger than material B. Since the Darcy permeability of a porous medium is proportional to the square of the fiber dimension, as shown in Eq. (10), the permeability of A2 is expected to be higher than B3. Furthermore, one noticed that fibers of material A are stiffer. This implies the contribution of the solid phase elastic forces is a more significant for material A2.

The lumped parameter model based on the consolidation theory developed herein can reproduce the major features of the experimental data. The theoretical model provides further insight into the relative importance of the individual forces during the compression process. This is summarized in Fig. 12, which shows the

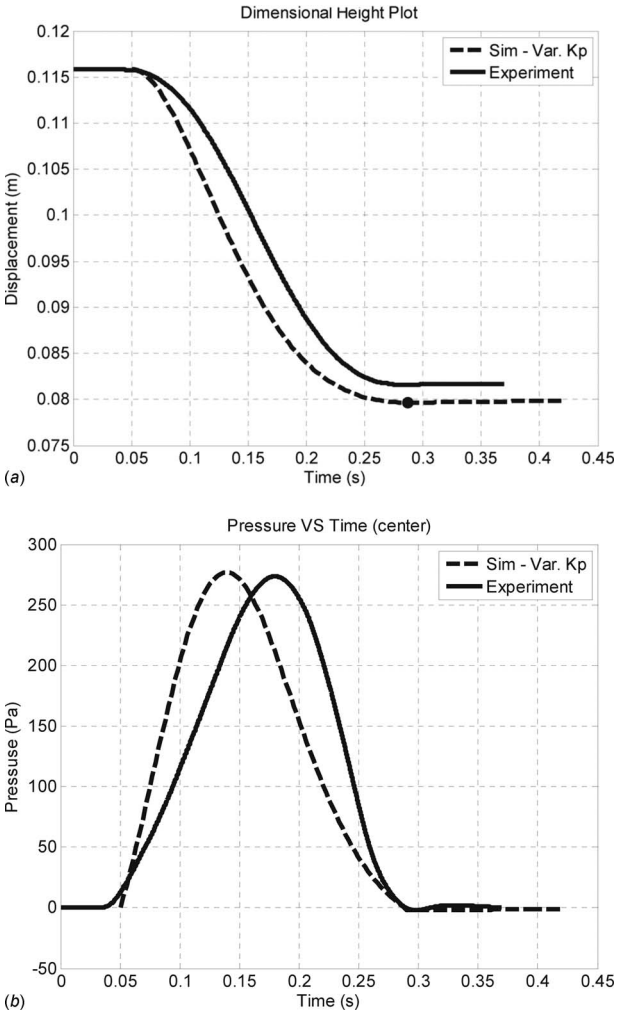

Fig. 11 Comparison between experimental results and theoretical simulation for the dynamic compaction experiments with material B3 at 8.71 kg loading: (*a*) displacement of the piston and (*b*) pore pressure at the center of the piston. The initial value of Darcy permeability $K_{p0}=8.79\times10^{-9}$ m^2, and the solid damping coefficients in compression and expansion are $\eta_d=3.33$ s/m and $\eta_u=300$ s/m, respectively.

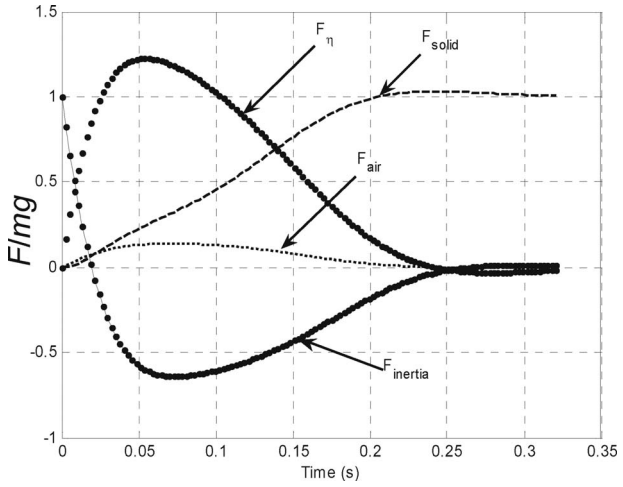

Fig. 12 Time-dependent forces during dynamic compression of fiber B3 under 7.0 kg loading

time variation in the four forces that appear in Eq. (1) normalized by the applied weight, *mg*. The summation of all the normalized forces at any time must equal unity. It is obvious that the solid damping effect of fiber B3 (in Fig. 12 is expressed as F_η) is dominant and thus the damping force from the trapped air (in Fig. 12 is expressed as F_{air}) plays a minor role in damping the inertial force of the piston (in Fig. 12 is expressed as F_{inertia}). During the compression process, the elastic solid phase force (in Fig. 12 is expressed as F_{solid}) continues to increase until it fully supports the piston weight when the air pore pressure is completely vented and the velocity of the piston reaches zero.

5 Concluding Remarks

In this paper, we have developed a systematic experimental and theoretical approach for examining the dynamic lift forces that are generated during the rapid compaction of soft porous fibrous materials with varying densities. Significant redesigning and enhanced instrumentation of the experimental apparatus yielded much improved data. Most notably, the application of a displacement sensor provided us with meaningful information on the piston movement. An important development following the work of Wu et al. [16] was the study of the solid phase damping force for different fibers. By comparing the theoretical predictions with the experimental data on the motion of the piston as well as the pore-pressure response, we were able to separate the solid phase damping force from that of the transiently trapped air. This experimental and theoretical approach has provided an important method in characterizing the relative contributions of different forces in the lift generation in a porous medium. To our knowledge, it is the first time that such forces have been considered.

Lift generation in deformable porous media is a new concept in porous media flow. The application of this concept to human skiing [16–18,26] and the design of a futuristic train track [19] were chosen for their novelty, but the basic idea could have important applications in the design of soft porous bearings with greatly increased lubrication pressures and long life. The key of such applications is to maximize the lift force generated by the pore pressure. If the transiently trapped fluid contributes more to the total lift, the solid structure's contribution will be less, and thus, the frictional force which is proportional to the normal force from the solid phase is reduced. In order to achieve this goal, finding the right material is extremely important. This material needs to be very soft so as to generate minimal elastic force under rapid compression. The interlocking between the fibers of the material need to be very week so that the solid phase damping force is reduced. The fiber diameter of the material need to be small and the spacing between the fibers need to be small too. This ensures low permeability of the porous media and higher air pressure generation. The quantified methodology presented in this paper has provided an important experimental and theoretical approach in characterizing the role of various forces during the rapid compaction of highly compressible porous media. It is of great importance in developing super lubrication bearing using soft porous materials.

One limitation in the present study is that the Darcy permeability of the porous material was not measured in parallel experiments with the same material sample to verify the theoretically predicted value of K_{p0}. The Carman–Kozeny's equation (10) that is employed in this manuscript is only an approximation for consolidating media. In an ongoing study by our group, we are developing a permeability measurement device for soft porous materials. The data to be obtained using this device will be incorporated in the theoretical simulation presented above to further evaluate the validity of our approach.

Another limitation of the current study is the preparation of the soft porous materials before the compaction. Since we manually spread the material inside the cylinder, some inconsistence is observed in different sets of experiments with the same porous material. To improve the repeatability of the experiments, a well controlled method is needed to fluffy the porous materials after each run of experiments.

In the current experimental setup, one expects the frictional force between the fibers and the side wall of the device to be relatively high because the fibers were pushed laterally toward the side wall of the cylinder during the compression. In our theoretical simulations, we introduced a solid phase damping force term to include all the damping effects other than that from the pore fluid pressure. In an ongoing research, we are upgrading our apparatus to separate the damping force between the fibers from that between the fiber and the device side wall.

The elastic lifting force from the solid structure was determined by a quasistatic experiment in the present study. One notices that this might not precisely describe the behavior of the solid phase during the dynamic compression process. In further study, we shall improve our experimental setup by experimentally measuring the solid phase lifting force during rapid compaction.

Acknowledgment

The authors acknowledge the financial support from the ONR under Grant No. N00024-07-C-4212. This research was completed in partial fulfillment of the requirements for the Master's degree of B.B. from Villanova University. We would like to acknowledge Dr. Sergey Nersesov for providing us the displacement sensor, Mr. Chris Townend, Mr. Daniel S. Walker, and Mr. Robert Crawford for their valuable technical support, and Ms. Yuejuan Ma for her help in preparation of the graphics.

Nomenclature

α = Brinkman parameter, $\alpha^2 = h^2/K_p$
d_s = mean diameter of the solid particles
K_p = Darcy permeability
K_{P0} = initial Darcy permeability of the undeformed porous layer
φ = instantaneous porosity of the porous media
φ_0 = initial uniform porosity
h = porous layer thickness
h_0 = initial porous layer thickness
dh/dt = the velocity of the piston
Δh = piston displacement
$\Delta h_{\max}$ = final displacement of the piston when the full load *mg* is applied
mg = total load applied on the porous media
F_{air} = lifting force exerted by the trapped air on the piston

$F_{\text{solid-elastic}}$ = the elastic forces exerted by the solid phase on the piston

$F_{\text{solid-damping}}$ = the damping forces exerted by the solid phase on the piston

η_i = solid phase damping coefficient with the index i indicating the damping coefficient during compression (η_d) and rebound (η_u)

μ = dynamic viscosity of the fluid

υ = fluid kinematic viscosity

ρ = fluid density

A = characteristic velocity gradient imposed by the external flow for a stagnation-point flow in a porous medium

β = fundamental dimensionless parameter for a stagnation-point flow in a porous medium, $\beta = \upsilon / K_p A$

References

[1] Grodzinsky, A. J., Lipshitz, H., and Glimcher, M. J., 1978, "Electromechanical Properties of Articular Cartilage During Compression and Stress Relaxation," Nature (London), **275**, pp. 448–450.

[2] Mow, V. C., Holmes, M. H., and Lai, W. M., 1984, "Fluid Transport and Mechanical Properties of Articular Cartilage: A Review," J. Biomech., **17**(5), pp. 377–394.

[3] Mow, V. C., and Guo, X. E., 2002, "Mechano-Electrochemical Properties of Articular Cartilage: Their Inhomogeneities and Anisotropies," Annu. Rev. Biomed. Eng., **4**, pp. 175.

[4] Damiano, E. R., 1998, "The Effect of the Endothelial-Cell Glycocalyx on the Motion of Red Blood Cells Through Capillaries," Microvasc. Res., **55**(1), pp. 77–91.

[5] Feng, J., and Weinbaum, S., 2000, "Lubrication Theory in Highly Compressible Porous Media: The Mechanics of Skiing, From Red Cells to Humans," J. Fluid Mech., **422**, pp. 281–317.

[6] Secomb, T. W., Hsu, R., and Pries, A. R., 1998, "A Model for Red Blood Cell Motion in Glycocalyx-Lined Capillaries," Am. J. Physiol., **274**, pp. H1016–H1022.

[7] Wang, W., and Parker, K. H., 1995, "The Effect of Deformable Porous Surface Layers on the Motion of a Sphere in a Narrow Cylindrical Tube," J. Fluid Mech., **283**, pp. 287–305.

[8] Tada, S., and Tarbell, J. M., 2002, "Flow Through Internal Elastic Lamina Affects Shear Stress on Smooth Muscle Cells (3D Simulations)," Am. J. Physiol. Heart Circ. Physiol., **282**, pp. H576–H584.

[9] Guo, P., Weinstein, A. M., and Weinbaum, S., 2000, "A Hydrodynamic Mechanosensory Hypothesis for Brush Border Microvilli," American Journal of Physiology-Renal Physiology, **279**(4), pp. F698–F712.

[10] Feng, J., and Weinbaum, S., 2001, "Flow Through an Orifice in a Fibrous Medium With Application to Fenestral Pores in Biological Tissue," Chem. Eng. Sci., **56**, pp. 5255–5268.

[11] Weinbaum, S., Zhang, X., Han, Y., Vink, H., and Cowin, S. C., 2003, "Mechanotransduction and Flow Across the Endothelial Glycocalyx," Proc. Natl. Acad. Sci. U.S.A., **100**(13), pp. 7988–7995.

[12] Weinbaum, S., Tarvell, J. M., and Damiano, E. R., 2007, "The Structure and Function of the Endothelial Glycocalyx Layer," Annu. Rev. Biomed. Eng., **9**, pp. 121–167.

[13] Farina, A., 1997, "Flow in Deformable Porous Media: Modeling and Simulations of Compression Moulding Processes," Math. Comput. Modell., **26**, pp. 1–15.

[14] Bear, J., 1972, *Dynamics of Fluids in Porous Media*, Elsevier, New York.

[15] Schrefler, B. A., and Scotta, R., 2001, "A Fully Coupled Dynamic Model for Two-Phase Fluid Flow in Deformable Porous Media," Comput. Methods Appl. Mech. Eng., **190**, pp. 3223–3246.

[16] Wu, Q., Andreopoulos, Y., Xanthos, S., and Weinbaum, S., 2005, "Dynamic Compression of Highly Compressible Porous Media With Application to Snow Compaction," J. Fluid Mech., **542**, pp. 281–304.

[17] Wu, Q., Igci, Y., Andreopoulos, Y., and Weinbaum, S., 2006, "Lift Mechanics of Downhill Skiing and Snowboarding," Med. Sci. Sports Exercise, **38**(6), pp. 1132–1146.

[18] Wu, Q., Andreopoulos, Y., and Weinbaum, S., 2006, "Riding on Air: A New Theory for Lift Mechanics of Downhill Skiing and Snowboarding," *The Engineering of Sport 6*, Springer, New York, pp. 281–286.

[19] Wu, Q., Andreopoulos, Y., and Weinbaum, S., 2004, "From Red Cells to Snow-Boarding: A New Concept for a Train Track," Phys. Rev. Lett., **93**(19), p. 194501.

[20] Skotheim, J. M., and Mahadevan, L., 2005, "Soft Lubrication: The Elastohydrodynamics of Nonconforming and Conforming Contacts," Phys. Fluids, **17**, p. 092101.

[21] Joseph, D. D., Nield, D. A., and Papanicolaou, G., 1982, "Nonlinear Equation Governing Flow in a Saturated Porous Medium," Water Resour. Res., **18**(4), pp. 1049–1052.

[22] Dupuit, J., 1863, *Théoriques et pratiques sur le mouvement des eaux*, Dunod, Paris.

[23] Forchheimer, P., 1901, "Wasserbewegung durch Boden," Z. Ver. Dtsch. Ing., **45**, pp. 1782–1788.

[24] Givler, R. C., and Altobelli, S. A., 1994, "A Determination of the Effective Viscosity for the Brinkman–Forchheimer Flow Model," J. Fluid Mech., **258**, pp. 355–370.

[25] Macdonald, I. F., EI-Sayed, M. S., Mow, K., and Dullien, F. A. L., 1979, "Flow Through Porous Media: The Ergun Equation Revisited," Ind. Eng. Chem. Fundam., **18**, pp. 199–208.

[26] Wu, Q., Weinbaum, S., and Andreopoulos, Y., 2005, "Stagnation Point Flow in a Porous Medium," Chem. Eng. Sci., **60**, pp. 123–134.

[27] Hiemenz, K., 1911, "Die Grenzschicht an Einem in den Gleichförmigen Flüssigkeitsstrom Eingetauchten Geraden Kreiszylinder," Dinglers Polytechnisches Journal, **326**, pp. 321–410.

[28] Homann, F., 1936, "Der Einfluss grosser Zähigkeit bei der Strömung um den Zylinder und um die Kugel," Z. Angew. Math. Mech., **16**, pp. 153–164.

[29] Homann, F., 1936, "Einfluss grosser Ziihigkeit bei Strimung um Zylinder," Forsch. Geb. Ingenieurwes., **7**, pp. 1–9.

[30] Homann, F., 1952, "The Effect of High Viscosity on the Flow Around a Cylinder and Around a Sphere," NACA TM Report No. 1344.

Upscaling of the Geological Models of Large-Scale Porous Media Using Multiresolution Wavelet Transformations

M. Reza Rasaei
Institute for Petroleum Engineering,
University of Tehran,
Tehran 11365-4563, Iran

Muhammad Sahimi[1]
Mork Family Department of Chemical
Engineering and Materials Science,
University of Southern California,
Los Angeles, CA 90089-1211
e-mail: moe@iran.usc.edu

To model fluid flow and energy transport in a large-scale porous medium, such as an oil or a geothermal reservoir, one must first develop the porous medium's geological model (GM) that contains all the relevant data at all the important length scales. Such a model, represented by a computational grid, usually contains several million grid blocks. As a result, simulation of fluid flow and energy transport with the GM, particularly over large time scales (for example, a few years), is impractical. Thus, an important problem is upscaling of the GM. That is, starting from the GM, one attempts to generate an upscaled or coarsened computational grid with only a few thousands grid blocks, which describes fluid flow and transport in the medium as accurately as the GM. We describe a powerful upscaling method, which is based on the wavelet transformation of the spatial distribution of any static property of the porous medium, such as its permeability, or a dynamic property, such as the spatial distribution of the local fluid velocities in the medium. The method is a multiscale approach that takes into account the effect of the heterogeneities at all the length scales that can be incorporated in the GM. It generates a nonuniform computational grid with a low level of upscaling in the high permeability sectors but utilizes high levels of upscaling in the rest of the GM. After generating the upscaled computational grid, a critical step is to calculate the equivalent permeability of the upscaled blocks. In this paper, six permeability upscaling techniques are examined. The techniques are either analytical or numerical methods. The results of computer simulations of displacement of oil by water, obtained with each of the six methods, are then compared with those obtained by the GM. [DOI: 10.1115/1.3167544]

Keywords: large-scale porous media, permeability, upscaling, wavelet transformation, two-phase flow

1 Introduction

Over the past 2 decades considerable progress has been made in developing techniques for measuring or estimating the properties of large-scale (LS) porous media, such as oil, gas, and geothermal reservoirs, and groundwater aquifers. At the same time, many advances have been made in the development of methods for the characterization of LS porous media. When the progress and advances are combined with modern geostatistical techniques, the resulting methodology enables one to generate a highly resolved computational grid, with up to a few million grid blocks, that represents the geological model (GM) of a LS porous medium. The GM represents the most detailed model of a LS porous medium and contains all the relevant and available information and data for a porous medium. However, computer simulations of multiphase flows and transport with the GM entail carrying out highly intensive computations, so much so that they are often not even feasible.

Thus, an important issue in the numerical simulation of multiphase flows in LS porous media is the so-called *upscaling* problem. In this problem one addresses the issue of how to upscale the properties of the grid blocks in the GM in order to develop a coarsened grid with far fewer grid blocks that, when used in the numerical simulations with an affordable amount of computation time, the results are as accurate as those obtained with the GM. As such, the problem is highly nontrivial and has been studied for a long time.

Although the GM of a LS porous medium is usually generated by the geostatistical methods, it is considered to be a deterministic model when used in a numerical simulator. That is, no uncertainties are associated with the permeabilities of the grid blocks. The effect of the uncertainties in the flow properties of a LS porous medium is then estimated through a Monte Carlo method, i.e., numerical simulation of the fluid flow and transport problem in many geostatistical *realizations* of the porous medium. Such a Monte Carlo technique differs from the stochastic approaches that are commonly used in the simulations of fluid flow and transport in ground water aquifers, in which the permeability is treated as a stochastic variable with known statistics and correlation structure. The idea is to compute directly the mean behavior of, and the uncertainty in, the results [1–4].

In the numerical simulations of multiphase flows and transport in oil reservoirs—the focus of this paper—the upscaling problem is, therefore, one of coarsening and averaging. The key issue to address is how to capture in the upscaled model the effects that are due to fine-scale heterogeneities, which may affect the global flow properties. Under such circumstances, the problem of using the correct boundary conditions for computing the upscaled properties is central to addressing some of the difficulties that one encounters in the upscaling process. One useful way of addressing the problem is by the so-called streamtube upscaling (see discussion in Ref. [5]). Moreover, the periodic, as opposed to no-flow, boundary conditions proposed by Durlofsky [6] decreases the negative effect of the boundaries on the computed properties. Up-

[1]Corresponding author.

Manuscript received October 4, 2008; final manuscript received February 3, 2009; published online July 29, 2009. Review conducted by Kambiz Vafai.

scaling, which is essentially a problem of change in scales, was also studied theoretically by various techniques, such as homogenization [7–9] and LS volume averaging [10]. Stochastic analysis applied to the infiltration problems [11] may also be extended to the case of multiphase flow in LS porous media.

Before we begin discussing the various upscaling techniques, however, it is essential to understand a fundamental point: For additive properties, such as the porosity and saturation (volume fraction) of a fluid phase, simple weighted arithmetic averages are usually accurate enough for the upscaling process. That is not, however, the case for nonadditive properties, such as the permeability, transmissibility, or hydraulic conductance. These are *tensorial* properties that depend not only on their spatial distributions but also on their *orientation* with respect to each other, as well as with respect to the direction of the flow.

Any accurate upscaling method consists of two parts: *regridding* (generating the structure of the upscaled grid) and attributing the effective properties of the upscaled grid blocks to them. The former is intended for capturing the *global* geologic features of the GM, whereas the latter focuses on preserving the *local* details of the flow properties within an upscaled block. A major concern in any upscaling is that uniform regridding generally results in excessively smoothened properties. This is particularly the case for the permeability. Such a regridding does not maintain the important details—typically at the high ends of the distributions of the nonadditive properties in the geostatistical description of the GM. This, in turn, may lead to inaccurate predictions for such important quantities as the breakthrough time of the displacing fluid, e.g., water.

We have recently introduced [12–15] a powerful and flexible regridding technique based on the wavelet transformations (WTs). The WT method is ideally suited for nonuniform coarsening, and overcomes the shortcomings associated with uniform regridding of the regions of potentially high fluid velocities, which are the highly permeable sectors. As we show below, the WT method achieves good agreement between the results obtained with the upscaled grid and the GM for (a) the global pressure-flow rate behavior of a LS porous medium, (b) the breakthrough characteristics of the displacing fluid, and (c) the *post*breakthrough flows of all the fluids in the porous medium.

For simulating single-phase flow in a porous medium, the most important parameter is the absolute Darcy permeability, for which several upscaling methods have been developed. Very good reviews of the subject were already presented elsewhere [16–18]. Classification of various upscaling methods is possible based on either the nature of the method (analytical or numerical) or their dependence on the boundary conditions (local or nonlocal) or the GM employed (deterministic or stochastic). Wen and Gómez-Hernández [17] classified the various upscaling techniques as local, nonlocal, and direct methods, while Renard and de Marsily [18] used deterministic, stochastic, and heuristic classifications.

Each upscaled block consists of several smaller cells that exist in the grid before the upscaling. Local techniques assume that the block permeability tensor is intrinsic to the cell permeabilities within the block, while in the nonlocal techniques the block permeabilities depend not only on the cells' permeabilities within the block but also on the flow boundary conditions imposed on the upscaling process. Direct techniques generate the blocks' permeabilities from the small amount of data, which are obtained by measurement without constructing a detailed GM.

On the other hand, the deterministic techniques assume that the GM is completely known (without any uncertainty), as opposed to the stochastic techniques that assume only an approximate knowledge of the model, and take a probabilistic view. The heuristic methods devise rules for calculating the *plausible* equivalent permeabilities of the upscaled blocks.

From among such a variety of approaches for computing the permeability of the blocks in the upscaled grid, we use in this paper six of the most commonly used methods. We show that WT-based regridding method that we have developed, together with a proper single-phase upscaling technique, is highly efficient and accurate for simulation of multiphase flows in LS heterogeneous porous media.

The rest of this paper is organized as follows. A brief description of the WT upscaling is given in Sec. 2. Next, the GM used in the computer simulations and its statistical properties are described. We then describe the details of the six methods of upscaling the single-phase permeabilities. Simulations of two-phase flows, in both the GM and the upscaled model, are then described and the results are presented and compared in Secs. 5 and 6. A summary of the paper is then presented.

2 Wavelet Upscaling of the Geological Model

Mallat [19] provided a good discussion of the mathematical foundations of the WTs, while Neivergelt [20] gave an excellent, easy to understand introduction. Suppose that $k(\mathbf{x})$ represents the local, spatially varying permeability at point $\mathbf{x}$ of a LS porous medium. Then, the WT of $k(\mathbf{x})$ is defined by

$$D(a,\mathbf{b}) = \int_{-\infty}^{\infty} k(\mathbf{x})\psi_{ab}(\mathbf{x})d\mathbf{x} = \frac{1}{\sqrt{a}}\int_{-\infty}^{\infty} k(\mathbf{x})\psi[(\mathbf{x}-\mathbf{b})/a]d\mathbf{x} \quad (1)$$

where $\psi(\mathbf{x})$—called the *mother wavelet*—may be selected from a *family* of such functions (see below), hence providing great flexibility in analyzing the spatial distribution of $k(\mathbf{x})$ at many length scales. $D(a,\mathbf{b})$ is also called the *wavelet detail coefficient* of $k(\mathbf{x})$. In Eq. (1), $a>0$ is a rescaling parameter, whereas $\mathbf{b}$ represents a translation of the wavelet. According to Eq. (1), the WT of $k(\mathbf{x})$ enables one to analyze its distribution at increasingly coarser ($a>1$) or finer ($a<1$) length scales, while $\mathbf{b}$ acts as a *window* that enables one to focus on a particular region. While $D(a,\mathbf{b})$ contains information on the *differences* between two approximations of $k(\mathbf{x})$ in two *successive* length scales, the most accurate approximation of $k(\mathbf{x})$ at a *fixed* scale is given by the wavelet *approximate* or *scale coefficient*, defined by

$$S(a,\mathbf{b}) = \int_{-\infty}^{+\infty} \phi_{ab}(\mathbf{x})k(\mathbf{x})d\mathbf{x} \quad (2)$$

where the wavelet *scale function* $\phi(\mathbf{x})$ is orthogonal to $\psi(\mathbf{x})$. The definition of $\phi_{ab}(\mathbf{x})$ is similar to that of $\psi_{ab}(\mathbf{x})$.

We analyze the problem in 2D porous media. Elsewhere [14] we also analyzed 3D heterogeneous porous media. Hence, consider a 2D square grid that represents the GM of a LS porous medium. We attribute to each square block of the grid the permeabilities k_x and k_y in the two principal directions. We then apply a one-level discrete WT to the permeabilities. Associated with the WT of the permeabilities of a block centered at $\mathbf{x}=(i_1,i_2)$ is a set of four wavelet coefficients that consists of one wavelet scale coefficient and three wavelet detail coefficients, which are given, in more precise forms, by

$$D_j^{(\ell)}(i_1,i_2) = \int_{\Omega} k(x,y)\psi^{(\ell)}_{j,i_1,i_2}(x,y)dxdy \quad (3)$$

$$S_j(i_1,i_2) = \int_{\Omega} k(x,y)\phi_{j,i_1,i_2}(x,y)dxdy \quad (4)$$

where j is the level of coarsening ($j=1$ represents the GM) and Ω represents the grid (the domain of the problem). Note that $S_j(i_1,i_2)$ contains information about $k(\mathbf{x})$ associated with a block centered at $\mathbf{x}$ in the *coarser* grid, whereas $D_j^{(\ell)}(i_1,i_2)$ measures the *contrast* between $k(\mathbf{x})$ in the coarser scale and those of the block's neighbors in the previous finer-scale grid, with $\ell=1$, 2, and 3 denoting the contrasts between the blocks in the x, y, and the diagonal directions, respectively.

To carry out the upscaling—or regridding—of the GM, we introduce two thresholds ϵ_s and ϵ_d. The former ϵ_s is a magnitude of the blocks' permeabilities relative to the largest permeability in the GM. It is, therefore, set as a fraction of the largest $S_j(i_1,i_2)$ in the entire 2D grid. The second threshold ϵ_d is a relative measure of the contrast between the permeabilities of the neighboring blocks. Thus, similar to ϵ_s, ϵ_d is also set as a fraction of the largest $D_j^{(\ell)}(i_1,i_2)$ in the grid. All the detail and scale coefficients in the grid are then normalized with respect to their corresponding largest values in the GM.

The upscaling or regridding is carried out by comparing the threshold ϵ_s with the scale coefficient associated with each block. If $S_j(i_1,i_2) > \epsilon_s$, it implies that the block's permeabilities (k_x and/or k_y) are relatively large and significant. We, therefore, move on to the next block. If, however, $S_j(i_1,i_2) < \epsilon_s$, we examine the block's detail coefficients $D_j^{(\ell)}(i_1,i_2)$ and set to zero those that are smaller than ϵ_d. Doing so is equivalent to merging the *neighbor* in the (ℓ) direction of the block (which, in the finer-scale grid, is just one block or one diagonal block away from (i_1,i_2)) with the block itself and forming a larger block. Therefore, depending on the broadness and the correlation structure of the spatial distribution of $k(\mathbf{x})$, as well as the numerical values of the two thresholds, a number of blocks in the original fine-scale grid are coarsened, i.e., they are merged to form larger blocks.

The WTs have recursive properties. This implies that the new upscaled grid can be coarsened further by applying again the discrete WT to the scale coefficients, obtained at the previous level, which contain information about $k(\mathbf{x})$ in the *present* upscaled grid. Doing so entails calculating a new set of four wavelet coefficients for each block of the (upscaled) grid in its current state. The new detail coefficients are again set to zero, if they are smaller than the threshold ϵ_d, and the corresponding blocks in the grid are merged. The process is repeated again until no significant number of the blocks can be merged (upscaled) to form larger blocks. Typically, for given values of ϵ_d and ϵ_s, three or four levels of coarsening suffice for generating the final upscaled grid. Clearly, the higher the two thresholds ϵ_d and ϵ_s, the larger the number of the blocks that can be upscaled (merged). The thresholds are set by the amount of computation time that one can afford. The effective permeabilities of the coarsened blocks are then computed by the methods described below.

We must now specify the wavelet functions. One way of constructing 2D wavelets, which is used in the present paper, is by the tensor products of the wavelets. Doing so gives rise to one 2D wavelet scaling function

$$\phi_{j,i_1,i_2}(x,y) = \phi_{i_1}^j(x)\phi_{i_2}^j(y) \tag{5}$$

and three 2D wavelets

$$\psi_{j,i_1,i_2}^{(1)}(x,y) = \phi_{i_1}^j(x)\psi_{i_2}^j(y)$$

$$\psi_{j,i_1,i_2}^{(2)}(x,y) = \psi_{i_1}^j(x)\phi_{i_2}^j(y)$$

$$\psi_{j,i_1,i_2}^{(3)}(x,y) = \psi_{i_1}^j(x)\psi_{i_2}^j(y) \tag{6}$$

The 1D discrete wavelets are constructed by setting $a=2^j$ and $b=2^j i$ in Eqs. (1) and (2), with i and j being integers. Rescaling and translating $\psi(x)$ and $\phi(x)$ using $\psi_i^j(x)=2^{-j/2}\psi(2^{-j}x-i)$ and $\phi_i^j(x)=2^{-j/2}\phi(2^{-j}x-i)$ enable one to also construct orthonormal wavelets that are nonzero over only small intervals of x. An important set of wavelets, developed by Daubechies [21], consists of orthonormal wavelets of order M—usually referred to as the Daubechies wavelets of order M (DBM)—which possess the properties that their first M moments are zero, with

$$\phi(x) = \sqrt{2}\sum_{i=0}^{L-1} h_i \phi(2x-i) \tag{7}$$

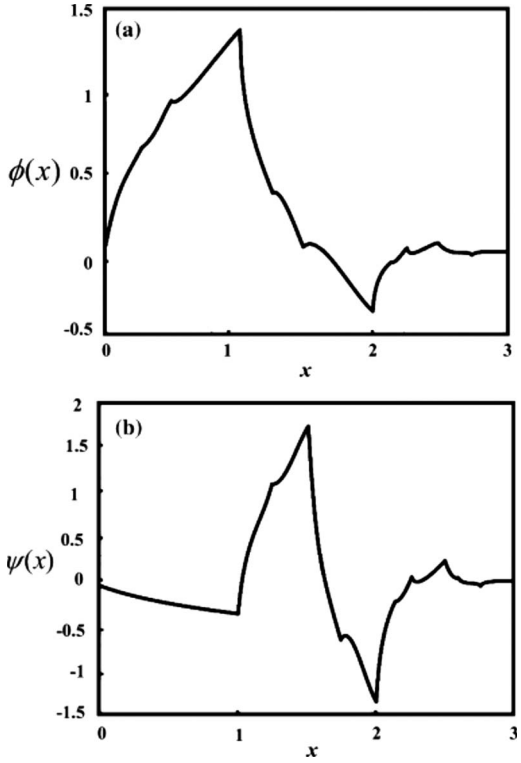

Fig. 1 The DB4 scaling (top) and wavelet (bottom) functions

$$\psi(x) = \sqrt{2}\sum_{i=0}^{L-1} g_i \phi(2x-i) \tag{8}$$

where $L=2M$. Here, h_i and g_i are the *filter coefficients* and are related by $g_i=(-1)^i h_{L-i-1}$ with $i=0,1,\ldots,L-1$. They are usually nonzero for only a few values of i. Press et al. [22] listed the values of h_k for many wavelets. Based on our previous simulations and experience [12–15], we utilized the DB4 wavelet in order to compute the results reported in this paper. Figure 1 presents the 1D DB4 wavelet and the corresponding scaling function. The filter coefficients of the DB4 wavelet are $(h_0,h_1,h_2,h_3)=\frac{1}{8}[(\sqrt{2}+\sqrt{6}),(3\sqrt{2}+\sqrt{6}),(3\sqrt{2}-\sqrt{6}),(\sqrt{2}-\sqrt{3})]$.

3 Upscaling of the Permeabilities

Once the upscaled grid is generated, one must compute the effective permeabilities of the upscaled (enlarged) grid blocks. As mentioned in the Introduction, we compare six different upscaling methods that have commonly been used in the past for calculating the permeabilities of the coarsened blocks. The first three methods that are described below utilize closed analytical relations and thus are easy to use. The numerical methods described below can also be used but at the expense of slightly more computations. In Secs. 3.1–3.6, we describe the six upscaling techniques.

3.1 Arithmetic-Harmonic Averaging. The simplest way of computing the permeability of a coarsened block is based on such averages as the arithmetic, harmonic, and geometric means of the permeabilities of the smaller cells within the block. It is well-known that the blocks' permeabilities in a 1D permeable medium with noncommunicating layers represent the arithmetic means for fluid flow parallel to the layers. The harmonic mean of the permeabilities, on the other hand, is associated with flow perpendicular to the layers [23]. For 2D fluid flow in an infinite block in which the permeability of the cells that comprise the block possess spatially distributed permeabilities with an isotropic spatial correla-

tion, the block permeability is equal to the geometric mean of the distribution. This result, which in principle should be used only for *infinite* blocks, was used extensively in the petroleum and hydrology literature [24–27] for *finite* blocks without much justification.

Durlofsky [28] investigated different permeability averages, including arithmetic, geometric, harmonic, arithmetic-harmonic (Arith-Harm), and harmonic-arithmetic, in 2D porous media and for several spatial distributions of the permeabilities (uncorrelated and correlated, isotropic and anisotropic, and sand-shale binary distributions). He concluded that there is no valid average for all the distributions that he considered. Other combined averaging methods, utilized by several groups [29–31], indicated that the geometric mean is not an accurate approximation of the block permeability, if the variance of the permeability distribution is large or if there is a finite fraction of zero or very small permeabilities (which would represent a percolation effect [23,32,33]) or if anisotropy is important.

We used the analytical relations for a combination of the arithmetic-harmonic averages, given by Henriette et al. [34] and Li et al. [35], in order to calculate the upscaled blocks' permeabilities in each direction. Note that the horizontal effective permeabilities K_x are approximately equal to the harmonic mean of the arithmetic averages of the permeabilities in the GM:

$$K_x = \frac{L_x}{L_y \sum_{i=1}^{N_x} \frac{\Delta x_i}{\sum_{j=1}^{N_y} \Delta y_j k_{x,i,j}}} \tag{9}$$

$$K_y = \frac{L_y}{L_x \sum_{j=1}^{N_y} \frac{\Delta y_i}{\sum_{i=1}^{N_x} \Delta x_i k_{y,i,j}}} \tag{10}$$

Here, L_x and L_y are the grid's dimensions, while Δx and Δy represent the corresponding dimensions of each block in the GM, with k_x and k_y being their permeabilities. N_x and N_y are the number of blocks in the GM in the two directions. If the porous medium is isotropic, then the formulas yield the same estimate of the upscaled permeability.

3.2 Analogy With Electrical Networks. There is an exact analogy between the flow between the grid that consists of blocks of permeabilities k_1, k_2,… and an electrical network (EN) of the same configuration that consists of conductors k_1, k_2,…. Thus, the electrical circuit laws that are used for computing the equivalent conductivity of an EN can also be used for determining the equivalent permeabilities of the grid or of its blocks that consist of smaller cells. Thus, if, for example, we merge four small cells configured in a square pattern, then the equivalent permeability K of the upscaled block that consists of the four small cells is given by

$$K = \frac{4k_{13}k_{24}(k_2k_4k_{13} + k_1k_3k_{24})}{k_s(k_2k_4k_{13} + k_1k_3k_{24}) + 3k_{12}k_{34}k_{13}k_{24}} \tag{11}$$

where $k_{ij}=k_i+k_j$ and $k_s=\Sigma_{i=1}^{4}k_i$. Equation (11) is then used once for each block, if the porous medium is isotropic. If the medium is anisotropic, then Eq. (11) is once used for each *direction* in order to compute the equivalent direction-dependent upscaled permeabilities.

3.3 Inverse Wavelet Transformation. Equation (1) defines a transformation $k(\mathbf{x}) \rightarrow D(a,\mathbf{b})$. The transformation may be inverted *exactly*, hence yielding a *reconstruction* formula

$$k(\mathbf{x}) = \frac{1}{C_\psi} \int_{-\infty}^{\infty} \int_{0}^{\infty} \frac{1}{a^{d+1}} D(a,\mathbf{b}) \psi_{a,b}(\mathbf{x}) da d\mathbf{b} \tag{12}$$

where C_ψ is a constant that depends on the wavelet used. Thus, the permeability distribution in the upscaled grid is reconstructed by computing the inverse discrete WT of $K(\mathbf{x})$ after coarsening the grid. Then, the blocks' permeabilities are computed based on the reconstructed distribution. Since during the coarsening process, some of the wavelet detail coefficients, corresponding to the cells that were merged to form the upscaled blocks, are set to zero (see above), the new permeability distribution in the regridded structure differs from that of the initial GM.

3.4 Pressure-Solver Method. In this method, the block that is being upscaled is isolated from the rest of the grid. A directional flow is simulated numerically by prescribing, as the boundary conditions, a pressure gradient $\Delta P/L$ between two opposite sides of a block of length L and no-flow boundary conditions in the transverse direction [36,37]. The fluid flow simulation then yields the flow rate passing through each upscaled block. If the total flow rate that crosses a block is Q, then the block's permeability in the direction of the flow is given (assuming that Darcy's law is valid) by $K=-(Q/A)(L/\Delta P)$, where A is the cross-sectional area of the upscaled block. Clearly, the same method may be used for each direction when the porous medium is anisotropic.

The method is not without any problem. The assumption that the block permeability tensors have their principal components parallel to the block sides, and the boundary conditions used to solve the flow problem, are questionable. Moreover, the mismatch between the actual boundary conditions and those used in this method may be a source of significant errors [38–40]. Holden et al. [41] extended the technique in order to compute the blocks' permeabilities using an iterative method. They calculated a block's permeability after each iteration from the calculated flow rate and pressure gradient in the flow iteration. The key idea is to stop the iterations *before* the solution to the flow equation converges under the conjecture that the components of the block's permeability tensor converge faster than the solution of the equations that govern the pressure.

3.5 Windowed Pressure Solver. This method attempts to correct the unrealistic no-flow boundary condition used in the pressure-solver (PS) technique. Inspired by the work of White and Horn [42], Gómez-Hernández [36,43] and Gómez-Hernández and Journel [44] proposed that a window around the block under consideration be used in order to impose realistic boundary conditions on the block's sides parallel to the flow. Fluid flow is simulated through the block, which is surrounded by its closest neighbors (the window) with uniform boundary conditions (i.e., a linearly varying prescribed pressure). The method yields the complete tensor of the block's permeability. Holden and Lia [45] extended the technique to 3D blocks. Efendiev [46] demonstrated theoretically the enhanced accuracy that the method achieves. The method does have some drawbacks with respect to the uniqueness of the solution that it yields [47].

3.6 An Unbiased Method. We have developed this method for computing the effective permeabilities of the coarsened block. The inspiration for the development of this method was provided by a similar method for the calculation of upscaled *relative permeabilities* used in multiphase flow simulation. As in the pressure-solver method, a local flow process is simulated on the subgrid of the upscaled block. The upscaled permeabilities will be most accurate if the simulation at the block scales reproduces, as closely as possible, the actual flow in the global GM. Wallstorm et al. [48] suggested a simple set of boundary conditions in which the magnitude of the flux is held constant at the block's inlet, whereas pressure is held constant at the outlet. The rationale for such boundary conditions is that if a constant pressure drop is imposed on two opposite sides of the block (as is commonly done), then

the pressure drop across both the high and low permeability regions inside the upscaled block will be the same. Since the flux is proportional to the permeability, one is led to biased estimates of the relative permeabilities. If, on the other hand, a constant flux is imposed on two opposite sides of a block, then the permeability field has no effect whatsoever on the flux. Therefore, by using a set of mixed boundary conditions (flux and pressure), the method interpolates between the two extreme cases. This is the method we developed for upscaling of the *single-phase* permeabilities of the coarsened blocks.

4 The Geological Model

To put the method under a stringent test, we used a synthetic GM in which not only was the distribution of the local permeabilities relatively broad (distributed over four orders of magnitude) but it also contained long-range correlations. To this end, we generate the permeabilities by the fractional Brownian motion (FBM), a stochastic process that induces long-range correlations in the permeabilities. The extent of the correlations that are generated by the FBM is as large as the grid's linear size. Briefly, the FBM is characterized by a spectral density given by

$$S(\boldsymbol{\omega}) = \frac{a(d)}{\left(\sum_{i=1}^{d} \omega_i^2\right)^{\alpha}} \tag{13}$$

where ω_i is the frequency component in the ith direction, $\alpha = H + \frac{1}{2}d$ with d being the spatial dimensionality of the system, and H is the *Hurst exponent*. As we simulate 2D porous media in this paper, $d=2$. Here, a is a coefficient that depends on both d and H. For example, for $d=1$ one has $a = c_0 H/[\Gamma(1-2H)\cos(\pi H)]$, with Γ being the gamma function and c_0 is a constant of order 1. The Hurst exponent H is such that $H > 1/2 (< 1/2)$ generates positive (negative) correlations, whereas for $H = 1/2$ the successive increments in the FBM-generated sequence are uncorrelated. Negative (positive) correlations imply that a block with a high or low permeability is less (more) likely to be a neighbor to another block with high or low permeability.

There is considerable evidence that the FBM-type correlations are ubiquitous in oil reservoirs and ground water aquifers (see, for example, Refs. [49,50]). We emphasize that the wavelet coarsening method described in this paper is independent of the spatial distribution of the permeabilities. The statistics of the permeability field generated by the FBM and used in the simulations (see below) are as follows. We used a Hurst exponent, $H=0.3$. Note that due to H being less than 0.5, a FBM permeability field is more heterogeneous than one with $H > 0.5$, which contains positive correlations. The minimum and maximum permeabilities were, respectively, 0.2 md and 14112 md. The standard deviations of log k was 1.15. An example of the permeability distribution is presented in Fig. 2. All the computations were carried out using a 2D GM represented by a grid of size 256×256 in which the blocks' sizes were 10×10 ft^2. Two wells were inserted in the GM at two opposite corners. One represented the injection well (see below), while the second one represented the production well.

5 Numerical Simulation of Water Flooding

We simulated a water-flooding process as an example of a typical two-phase flow in a heterogeneous porous medium. By combining Darcy's law and the mass conservation equation and ignoring the effect of gravity, we obtain the following equations for two-phase flow of oil and water in a porous medium:

$$B_o^{-1} \nabla \cdot (K\lambda_0 \nabla \Phi_o) - \frac{q_o}{\rho_o} = \frac{\partial}{\partial t}\left(\frac{\phi S_o}{B_o}\right) \tag{14}$$

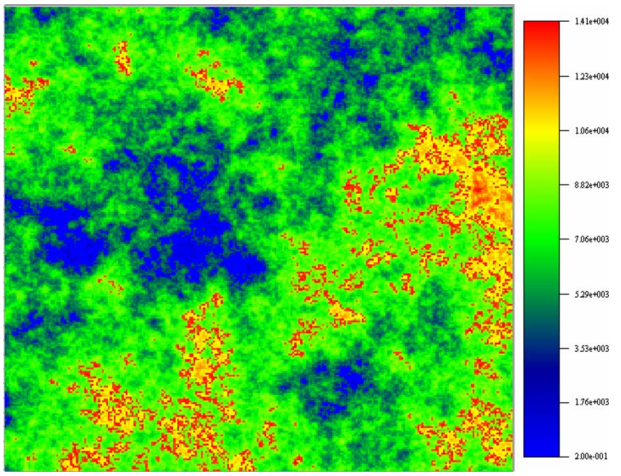

Fig. 2 A sample of the geostatistical permeability field used in the simulations

$$B_w^{-1} \nabla \cdot (K\lambda_w \nabla \Phi_w) - \frac{q_w}{\rho_w} = \frac{\partial}{\partial t}\left(\frac{\phi S_w}{B_w}\right), \tag{15}$$

where $\Phi_w = P_o - P_c$ with $P_c = P_o - P_w$ in which P_o and P_w are the pressures in the oil and water phases, λ_o and λ_w are, respectively, the mobility of the oil and water, and (B_o, q_o) and (B_w, q_w) are their corresponding formation volume factor and flow rate, respectively. The densities ρ_o and ρ_w are evaluated under the standard conditions. We then combine Eqs. (14) and (15) to obtain the governing equation for P_o, which contains no explicit time derivatives of the fluids' saturations:

$$B_o\left[\nabla \cdot \left(K\frac{\lambda_o}{B_o}\nabla P_o\right) - \frac{q_o}{\rho_o}\right] + B_w\left\{\nabla \cdot \left[K\frac{\lambda_w}{B_w}(\nabla P_o - \nabla P_c)\right] - \frac{q_w}{\rho_w}\right\} = \phi C \frac{\partial P_o}{\partial t} \tag{16}$$

where $C_i = -B_i^{-1}\partial B_i/\partial P_i$ $(i = o, w)$ represents the phase compressibility, $C_r = -\phi^{-1}\partial\phi/\partial P_o$ is the rock's compressibility, and $C = C_r + C_o S_o + C_w S_w$.

The governing equations for P_o and S_o are solved by a finite-volume (FV) method, which is most suitable for the type of irregular computational grid that we generate by the upscaling method. To utilize the FV method, we first integrate both sides of Eq. (16) over a control surface A to obtain

$$\int\int C\phi \frac{\partial P_o}{\partial t} dA = \int\int \left\{B_o\left[\nabla \cdot \left(K\frac{\lambda_o}{B_o}\nabla P_o\right) - \frac{q_o}{\rho_o}\right] + B_w\left\{\nabla \cdot \left[K\frac{\lambda_w}{B_w}(\nabla P_o - \nabla P_c)\right] - \frac{q_w}{\rho_w}\right\}\right\} dA \tag{17}$$

The left side of Eq. (17) is evaluated by assuming that the oil pressure in any block can be represented by an average value. Likewise, the flow rates q_o and q_w are assumed to represent the average rates in any block. The time derivative is approximated by a suitable finite-difference (FD) form. Therefore, the left side of Eq. (17) is written, for example, as $C\phi\Delta S(P_i^{n+1} - P_i^n)/\Delta t$, if we use a forward FD approximation, where ΔS is the surface of the block (or its side length, as it is a 2D block), P_i^n is the pressure after n time steps at grid point i representing the (center of a) block, and Δt is the time step. One then invokes the divergence theorem to convert the surface integrals on the right side of Eq. (17) to line integrals. Since the upscaled grid contains blocks of various sizes, all the terms on the right side of Eq. (17), after their conversion to

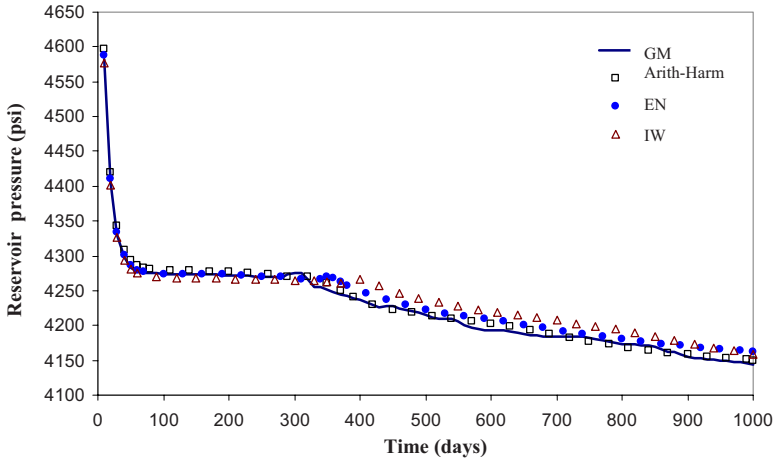

Fig. 3 Comparison of the reservoir's average pressure as computed with the upscaled model using the analytical methods of upscaling the permeabilities and in the GM. The analytical methods are the Arith-Harm averages, the analogy with ENs, and the IWT. Upscaling was done uniformly with the thresholds $\epsilon_s=\epsilon_d=1$.

line integrals via the divergence theorem, must be evaluated carefully.

Some of the details of the model porous medium in which the water-flooding process is simulated is as follows. We neglect the capillary pressure P_c so that fluid flow is dominated by viscous forces. Thus, $P_o=P_w$. If, however, P_c is not to be neglected, as we have done elsewhere [14], then, similar to the relative permeabilities and Eq. (18) that expresses their dependence on the saturations (see below), the functional dependence of P_c on the saturation must also be specified. Therefore, we need only solve Eq. (17) for P_o. At the same time, since $S_o+S_w=1$, we also need to solve only for S_o. The fluids' viscosities enter the governing equations through the mobility terms in Eqs. (14)–(17). The mobility of a fluid phase is defined as the ratio of its permeability and viscosity.

The porosity of the porous medium also enters as the coefficient of the time derivatives in the governing equations for the saturation and fluid phase pressure. While it is true that the permeability depends on the porosity, there is no known exact relation between the two. The available correlations are either empirical or semi-empirical. We do not use such correlations in the present paper. Instead, we consider a porous medium with a uniform porosity of 0.2 and, as described above, a permeability distribution generated by a FBM. However, it adds no complexity to the model if one wishes to generate a spatial distribution of the porosities by any method, including through the use of a relation between the porosity and the permeability.

The simulator first solves the governing equations for the pressure P_o of the oil phase and then computes the oil saturation S_o by solving Eq. (14). To obtain the solution, we use a combination of the implicit pressure, explicit saturation (IMPES) and the fully implicit methods. The IMPES method is conditionally stable and converges to the correct solution, if the time step Δt is selected carefully. If Δt is too large, the numerical simulator may generate saturations that are larger than one. This possibility is eliminated by imposing the condition that the saturation and pressure changes in any grid block between two consecutive time steps must remain tightly bounded, which was achieved by adjusting Δt such that the difference between the saturations between t and $t+\Delta t$ in any grid block was no more than 0.05, and the pressure changes no more than 100 psi. In addition, to guarantee the stability of the solution, an adaptive time-step method was used, which automatically increased Δt whenever the variables changed slowly and vice versa.

The advantage of the IMPES method is that when it is used appropriately, it yields accurate results at a minimum computa-

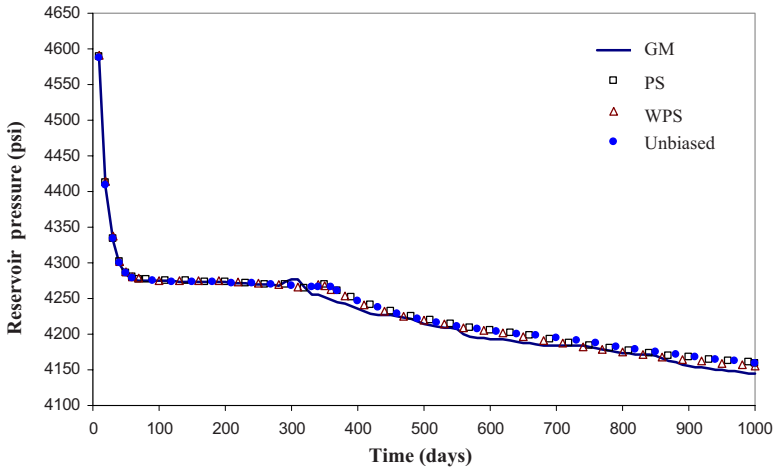

Fig. 4 Same as in Fig. 3 but using the numerical methods of upscaling the permeabilities, which are the PS, the WPS, and the unbiased methods

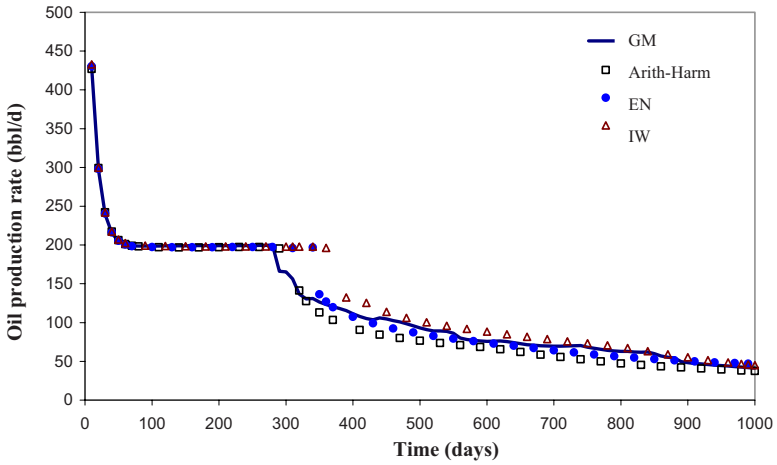

Fig. 5 Comparison of the rate of oil production as computed with the upscaled model using the analytical methods of upscaling the permeabilities and in the GM. The analytical methods are the Arith-Harm averages, the analogy with ENs, and the IWT. Upscaling was done uniformly with the thresholds $\epsilon_s=\epsilon_d=1$.

tional cost. Its limitations are that because (a) a large portion of the reservoir far from the wells may experience very slow changes in P_o and S_o, it is not efficient to use very small Δt, and (b) the IMPES method is not accurate if large variations in the dependent variables (P_o and S_o) occur rapidly. Moreover, time-truncation errors are generally larger in implicit simulators. A fully implicit method provides the required stability but at a considerably higher computational cost.

The largest variations in S_o and P_o occur in the near-well regions, which also control the maximum allowed time step Δt when the interface between the oil and water is close to them. Therefore, at the beginning of the injection, Δt must be small, but when the interface is no longer near the injection (or production) well, it can be much larger. Therefore, we consider a small zone of grid blocks around each well in which we use the fully implicit procedure for discretizing the governing equations, while the IMPES method is used in the remaining part of the grid.

For the fully implicit part, we guess the S_o distribution at time t and solve the discretized equations for P_o. The S_o distribution is then computed based on the newly calculated P_o distribution. The procedure is iterated several times (typically about eight) until converged solutions are obtained. For the IMPES part, after computing the P_o distribution for each time step, we solve Eq. (17) in which the time-derivative term is discretized explicitly. In both cases the discretized equations are solved by a combination of the Newton–Raphson and biconjugate-gradient methods. More details about the numerical techniques are given elsewhere [14,15].

We carried out simulation and upscaling of immiscible displacement of oil by water in the 2D heterogeneous model described in the this section. Water was injected at one corner of the grid at a constant injection rate of 200 STB/day, while oil and water were produced at a constant bottom-hole pressure of 4000 psi (absolute) at the opposite corner. The field's initial pressure was assumed to be 5000 psi everywhere. The relative permeability k_{rj} to fluid j at saturation S_j was assumed to be given by the conventional Corey-type function,

$$k_{rj} = \left(\frac{S_j - S_{rj}}{S_{\max,j} - S_{rj}} \right)^{n_j} \tag{18}$$

with $S_{\max,o}=S_{\max,w}=0.8$, the residual saturations $S_{or}=S_{ow}=0.2$, $n_w=1.5$, and $n_o=2.0$. The oil and water viscosities were taken, respectively, to be 3 cP and 1 cP, and gravity (as well the capillary pressure) effect was ignored. The simulations were carried out for

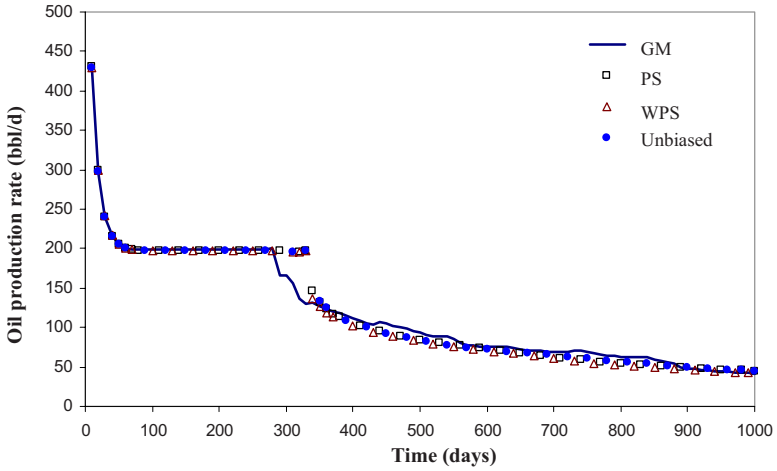

Fig. 6 Same as in Fig. 5 but using the numerical methods of upscaling the permeabilities, which are the PS, the WPS, and the unbiased methods

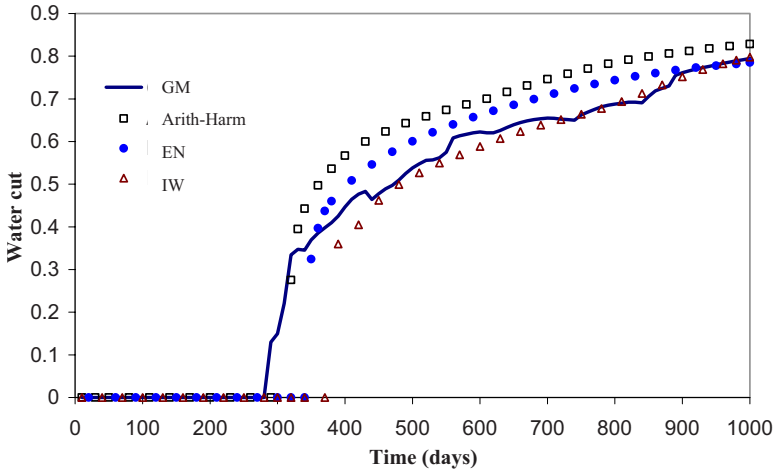

Fig. 7 Comparison of the water cuts (rate of water production) as computed with the upscaled model using the analytical methods of upscaling the permeabilities and in the GM. The analytical methods are the Arith-Harm averages, the analogy with ENs, and the IWT. Upscaling was done uniformly with the thresholds $\epsilon_s=\epsilon_d=1$.

a period of 1000 days of water flooding. Admittedly, the problem that we study is a relatively simple one but the goal is to test the accuracy of the six methods of upscaling of the permeabilities. Elsewhere [13–15] we have studied highly nonlinear flows in very heterogeneous 2D and 3D porous media.

6 Results and Discussion

In addition to using the six methods of permeability upscaling described above, two thresholds were also used for generating the upscaled grids, which were as follows:

(1) *Case 1*: $\epsilon_s=\epsilon_d=1$ (*uniform* coarsening, except around the wells, which was kept resolved)
(2) *Case 2*: $\epsilon_s=\epsilon_d=0.8$ (high level of *nonuniform* coarsening)

In each case, the average pressure of the reservoir, the rate of oil production, and the water cut at the production well (the fraction of water at the well) were calculated using the six methods of permeability upscaling. Numerical simulations of water flooding in the GM were also carried out in order to assess the accuracy of the upscaling methods used here.

Consider, first, the results for Case 1—uniform upscaling. Figure 3 compares the average reservoir pressure in the upscaled model, computed by the three analytical methods of permeability upscaling, with that in the GM, while Fig. 4 does the same for the results obtained by the three numerical methods of permeability upscaling. All the six methods provide very accurate predictions. Figure 5 compares the oil production rates in the GM with those in the upscaled model using the three analytical upscaling methods, while Fig. 6 does the same for the results obtained by the three numerical upscaling methods. Once again, all the six methods are accurate.

The differences between the accuracy of the six permeability upscaling methods become clear, when we consider the water cut. Figures 7 and 8 compare this quantity in the GM with those computed with the three analytical and the three numerical upscaling methods, respectively. All the numerical upscaling methods overestimate the water cut. Among the analytical methods of the permeability upscaling, the inverse WT (IWT) method provides accurate predictions, followed by the method based on the analogy with the ENs. The upscaling based on simple arithmetic-harmonic averages is not accurate.

Next, we consider the results for Case 2—nonuniform upscaling of the permeabilities. Once again, when it comes to accurately predicting the average reservoir pressure and the rate of oil

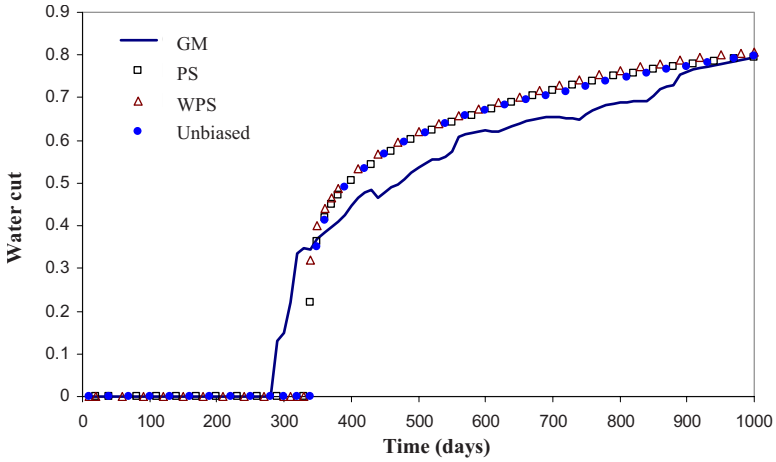

Fig. 8 Same as in Fig. 7 but using the numerical methods of upscaling the permeabilities, which are the PS, the WPS, and the unbiased methods

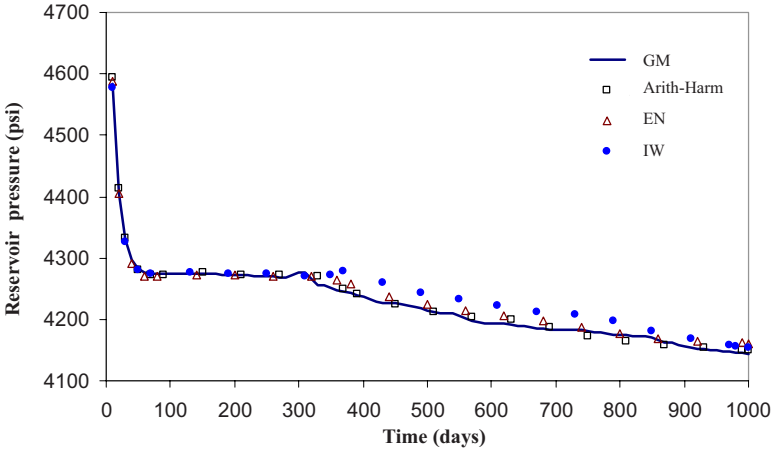

Fig. 9 Comparison of the reservoir's average pressure as computed with the upscaled model using the analytical methods of upscaling the permeabilities and in the GM. The analytical methods are the Arith-Harm averages, the analogy with ENs, and the IWT. Upscaling was done nonuniformly with the thresholds $\epsilon_s=\epsilon_d=0.8$.

production—the results for which are presented in Figs. 9–12—all the methods perform well. It is the rate of water cut that enables us to discern the most accurate permeability upscaling method. The results are presented in Figs. 13 and 14. All the numerical upscaling methods overpredict the water cut. Among the analytical methods, both the inverse WT method and the method based on the analogy with ENs are accurate for times $t>400$ days, but the latter is more accurate at earlier times and, in particular, it provides more accurate predictions for the breakthrough time—the time at which water is produced for the first time at the production well. The same is true for the uniform upscaling. However, we must note that although uniform upscaling appears to yield accurate results, this is not, in general, true for realistic simulations in which the capillary pressure and the gravity are not ignored [14,15].

Since the regions around the wells retain their resolved structures in the upscaled models, and a fully implicit model is used in these regions to solve the governing equations for the pressure and saturation (the IMPES formulation is utilized in the rest of the reservoir), we may expect very close agreement between the two sets of results in terms of the bottomhole pressures. This is clearly seen in Figs. 3, 4, 9, and 10.

Inspection of the rates of production of oil and water indicate that decreasing the wavelet thresholds from 1 to 0.8 improves the predictions for the water breakthrough time. This is expected since lower upscaling levels better preserve the high permeability regions as the thresholds are decreased. This also indicates that a uniform upscaling cannot, in general, be an accurate method. Nonuniform upscaling also prevents oversmoothening of the highly permeable sectors of the reservoir, which provide the main flow paths and influence strongly the water breakthrough time at the production well.

Another important factor in any upscaling method is the speed-up in the computations that one obtains with the upscaled methods, relative to those for the GM. The speed-up in the computations for Cases 1 and 2 are, respectively, 800 and 300, which are already very significant. But, as we showed elsewhere [12–15], the speed-up factor *increases* for more heterogeneous porous media with broader permeability distributions.

The following general conclusions may then be drawn from the computed results.

(i) Overall, the accuracy of the analytical methods may be ranked as arithmetic-harmonic averages $<$ electrical network analogy $\leq$ inverse WT.
(ii) The accuracy of the numerical methods of upscaling may be ranked as the unbiased method $>$ the windowed pressure solver (WPS) $>$ the pressure-solver method.
(iii) The difference between the various approaches decreases

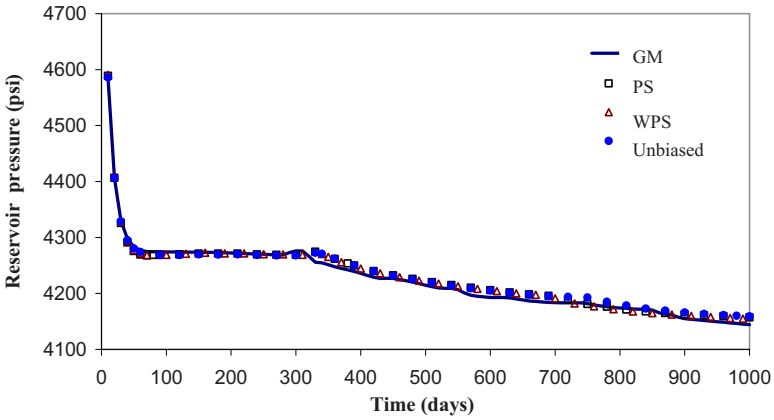

Fig. 10 Same as in Fig. 9 but using the numerical methods of upscaling the permeabilities, which are the PS, the WPS, and the unbiased methods

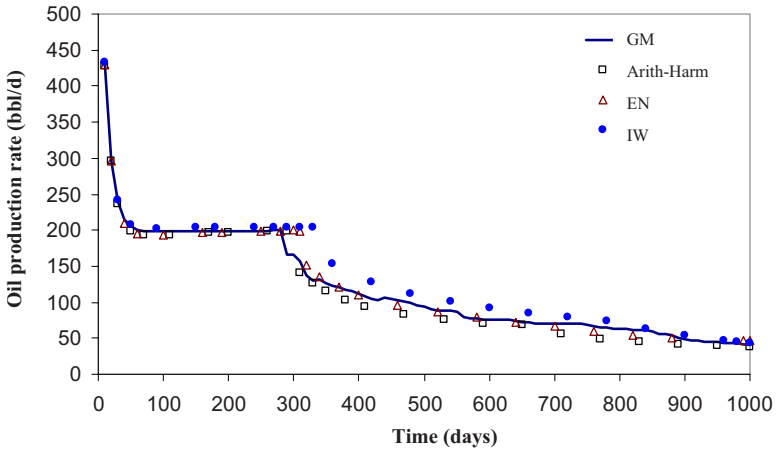

Fig. 11 Comparison of the rate of oil production as computed with the upscaled model using the analytical methods of upscaling the permeabilities and in the GM. The analytical methods are the Arith-Harm averages, the analogy with ENs, and the IWT. Upscaling was done nonuniformly with the thresholds $\epsilon_s = \epsilon_d = 0.8$.

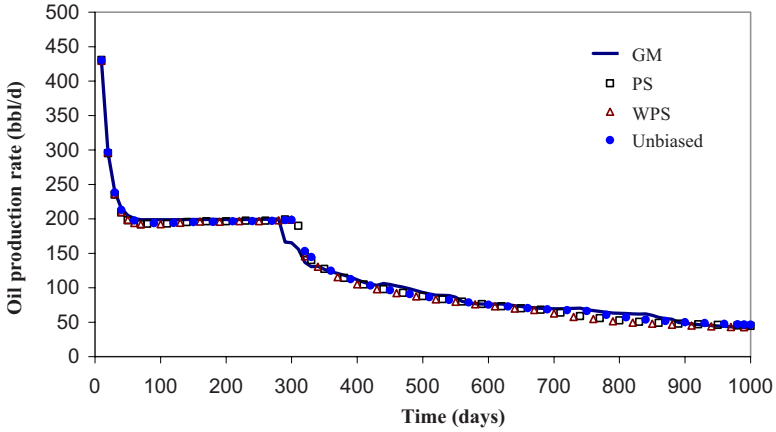

Fig. 12 Same as in Fig. 11 but using the numerical methods of upscaling the permeabilities, which are the PS, the WPS, and the unbiased methods

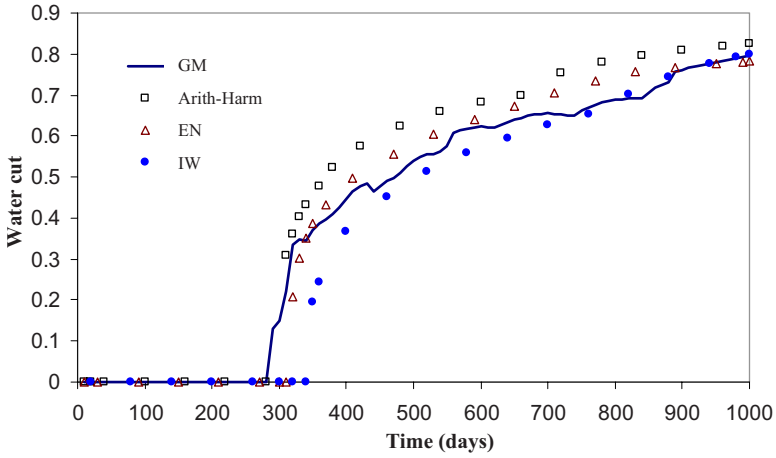

Fig. 13 Comparison of the water cuts (rate of water production) as computed with the upscaled model using the analytical methods of upscaling the permeabilities and in the GM. The analytical methods are the Arith-Harm averages, the analogy with ENs, and the IWT. Upscaling was done nonuniformly with the thresholds $\epsilon_s = \epsilon_d = 0.8$.

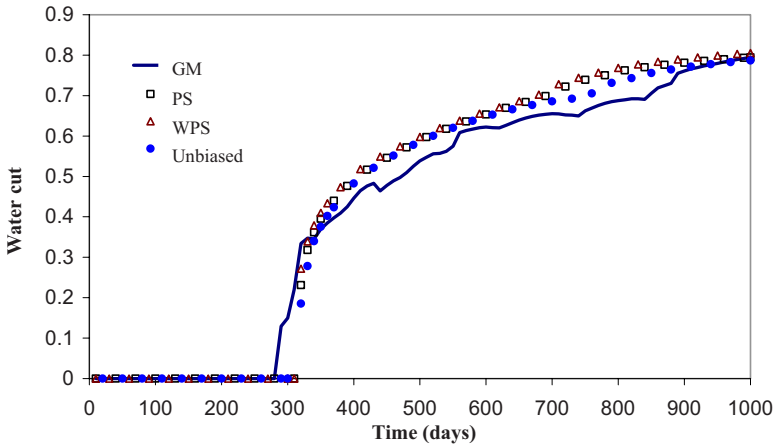

Fig. 14 Same as in Fig. 13 but using the numerical methods of upscaling the permeabilities, which are the PS, the WPS, and the unbiased methods

as the threshold values decrease, since the grid increasingly resembles the original GM.

7 Summary

We described a method for upscaling of the geological model of a large-scale porous medium based on the wavelet transformation of the medium's permeability field. The method generates a nonuniform upscaled computational grid that reduces the required computations by orders of magnitude for any fluid flow problem. We then used, in a comparative study, six distinct methods of computing the effective permeability of the upscaled blocks in the coarsened computational grid. The six methods were used, in conjunction with the wavelet upscaling of the computational grid, to study a standard water flooding in an oil reservoir in order to assess the accuracy and efficiency of the methods. Judicious choice of the wavelet thresholds, together with computing the permeability of the upscaled blocks based on either an analogy with electrical networks or the inverse wavelet transformation, yields results with an accuracy comparable with those obtained with the fine-resolution geological model of the large-scale porous medium.

The problem that we studied here and elsewhere [12–15] is one of flow in multiscale porous media. There is a growing literature on multiscale flow architectures with dendrites [51,52]. It would be interesting to study whether the technique presented here and elsewhere [12–15] may also be used for efficient simulation of multiscale flows in such systems.

Acknowledgment

The work of M.R.R. was supported by the NIOC.

Nomenclature

A = cross-sectional area
a = wavelets' rescaling parameter
b = wavelets' translation parameter
B_o = oil formation volume factor (bbl/STB)
B_w = water formation volume factor (bbl/STB)
C_i = compressibility of fluid phase i
C_ψ = wavelet renormalization constant
$D(a,\mathbf{b})$ = wavelet detail coefficient
d = spatial dimension
H = Hurst exponent
h_i = wavelet filter coefficient
g_i = wavelet filter coefficient (related to h_i)
$K(\mathbf{x})$ = single-phase permeability field
k_{rj} = relative permeability to phase j
L_x, L_y = sizes of the computational grid (in the x and y directions)
n_j = exponent in the expression that relates k_{rj} to the saturation
N_x, N_y = sizes of the geological model
P_c = capillary pressure
P_o = pressure in the oil phase
P_w = pressure in the water phase
Q = total flow rate
q_o = flow rate of oil
q_w = flow rate of water
S_o = oil saturation
S_w = water saturation
S_j = saturation of fluid phase j
S_{rj} = residual saturation of fluid phase j
$S_{\max,j}$ = maximum saturation of fluid phase j
$S(a,\mathbf{b})$ = wavelet scale coefficient
$S(\omega)$ = spectral density
t = time

Greek Letters

$\psi_{ab}(x)$ = mother wavelet
$\phi_{ab}(x)$ = wavelet scale function
Δt = magnitude of the time step (days)
Δx_i, Δy_i = sizes of the blocks in the geological model
ΔP = pressure difference
ω_i = frequency component in the ith direction
Γ = gamma function
Φ_o = oil potential
Φ_w = water potential
λ_o = mobility of oil
λ_w = mobility of water
ρ_o = oil density
ρ_w = water density
ϕ = porosity

References

[1] Dagan, G., 1987, "Theory of Solute Transport by Groundwater," Annu. Rev. Fluid Mech., **19**, pp. 183–215.
[2] Graham, W., and McLaughlin, D., 1989, "Stochastic Analysis of Nonstationary Solute Transport. 1. Unconditional Moments," Water Resour. Res., **25**, pp. 215–232.
[3] Gelhar, L. W., 1993, *Stochastic Subsurface Hydrology*, Prentice-Hall, Englewood Cliffs, NJ.
[4] Neuman, S. P., 1993, "Eulerian-Lagrangian Theory of Transport in Space-Time Nonstationary Fields: Exact Nonlocal Formulation by Conditional Moments and Weak Approximation," Water Resour. Res., **29**, pp. 633–645.
[5] Hewett, T. A., and Yamada, T., 1997, "Theory for Semi-Analytical Calculation of Oil Recovery and Effective Relative Permeability Using Streamtubes," Adv.

Water Resour., **20**, pp. 279–292.
[6] Durlofsky, L. J., 1994, "Accuracy of Mixed and Control Volume Finite Element Approximations to Darcy Velocity and Related Quantities," Water Resour. Res., **30**, pp. 965–973.
[7] Bourgeat, A., 1984, "Homogenized Behavior of Two-Phase Flows in Naturally Fractured Reservoirs With Uniform Fracture Distribution," Comput. Methods Appl. Mech. Eng., **47**, pp. 205–216.
[8] Amaziane, B., and Bourgeat, A., 1988, "Effective Behavior of Two-Phase Flow in Heterogeneous Reservoirs," *Numerical Simulation in Oil Recovery* (IMA Volumes in Mathematics and Its Applications), M. F. Wheeler, ed., Springer, New York.
[9] Sáez, A. E., Otero, C. J., and Rusinek, I., 1989, "The Effective Homogeneous Behavior of Heterogeneous Porous Media," Transp. Porous Media, **4**, pp. 213–238.
[10] Quintard, M., and Whitaker, S., 1990, "Two-Phase Flow in Heterogeneous Porous Media II: Numerical Experiments for Flow Perpendicular to a Stratified System," Transp. Porous Media, **5**, pp. 429–472.
[11] Mantoglou, A., and Gelhar, L. W., 1989, "Three-Dimensional Unsaturated Flow in Heterogeneous Systems and Implications on Groundwater Contamination," Transp. Porous Media, **4**, pp. 529–548.
[12] Mehrabi, A. R., and Sahimi, M., 1997, "Coarsening of Heterogeneous Media: Application of Wavelets," Phys. Rev. Lett., **79**, pp. 4385–4388.
[13] Ebrahimi, F., and Sahimi, M., 2004, "Multiresolution Wavelet Scale Up of Unstable Miscible Displacements in Flow Through Porous Media," Transp. Porous Media, **57**, pp. 75–102.
[14] Rasaei, M. R., and Sahimi, M., 2008, "Upscaling and Simulation of Waterflooding in Heterogeneous Reservoirs Using Wavelet Transformations: Application to the SPE-10 Model," Transp. Porous Media, **72**, pp. 311–338.
[15] Rasaei, M. R., and Sahimi, M., 2009, "Upscaling of the Permeability by Multiresolution Wavelet Transformations, and Simulation of Multiphase Flows in Heterogeneous Porous Media," Comput. Geosci., **13**, pp. 187–214.
[16] McCarthy, J. F., 1995, "Comparison of Fast Algorithms for Estimating Large-Scale Permeabilities of Heterogeneous Media," Transp. Porous Media, **19**, pp. 123–134.
[17] Wen, X.-H., and Gómez-Hernández, J. J., 1996, "Upscaling Hydraulic Conductivities in Heterogeneous Media: An Overview," J. Hydrol., **183**, pp. ix–xxxii.
[18] Renard, P., and de Marsily, G., 1997, "Calculating Equivalent Permeability, A Review," Adv. Water Resour., **20**, pp. 253–276.
[19] Mallat, S., 1999, *A Wavelet Tour of Signal Processing*, Academic, San Diego.
[20] Neivergelt, Y., 1999, *Wavelets Made Easy*, Birkhäser, Boston.
[21] Daubechies, I., 1988, "Orthonormal Basis of Compactly Supported Wavelets," Commun. Pure Appl. Math., **41**, pp. 901–996.
[22] Press, W. H., Teukolsky, S. A., Vetterling, W. T., and Flannery, B. P., 1992, *Numerical Recipes*, 2nd ed., Cambridge University, London.
[23] Sahimi, M., 1995, *Flow and Transport in Porous Media and Fractured Rock*, VCH, Weinheim.
[24] Warren, J. E., and Price, H. S., 1961, "Flow in Heterogeneous Porous Media," SPEJ, **1**, pp. 153–169.
[25] Dagan, G., 1985, "Stochastic Modeling of Groundwater Flow by Unconditional and Conditional Probabilities: The Inverse Problem," Water Resour. Res., **21**, pp. 65–72.
[26] Clifton, M. P., and Neuman, S. P., 1982, "Effect of Kriging and Inverse Modelling on Conditional Simulation of the Avra Valley Aquifer in Southern Arizona," Water Resour. Res., **18**, pp. 1215–1234.
[27] Hoeksema, R. J., and Kitanidis, P. K., 1985, "Comparison of Gaussian Conditional Mean and Kriging Estimation in the Geostatistical Solution of the Inverse Problem," Water Resour. Res., **21**, pp. 825–836.
[28] Durlofsky, L. J., 1992, "Representation of Grid Block Permeability in Coarse Scale Models of Randomly Heterogeneous Porous Media," Water Resour. Res., **28**, pp. 1791–1800.
[29] Pickup, G. E., Ringrose, P. S., Jensen, J. L., and Sorbie, K. S., 1994, "Permeability Tensors for Sedimentary Structures," Math. Geol., **26**, pp. 227–250.
[30] Lozano, J. A., Costa, L. P., Alves, L. P., and Silva, A. C., 1996, "Upscaling of Stochastic Models for Reservoir Simulation—An Integrated Approach," SPE Paper No. 36205.
[31] Gómez-Hernández, J. J., and Wen, X.-H., 1994, "Probabilitic Assessment of Travel Times in Groundwater Modeling," Stochastic Hydrol. Hydraul., **8**, pp. 19–55.
[32] Sahimi, M., 1993, "Flow Phenomena in Rocks: From Continuum Models to Fractals, Percolation, Cellular Automata, and Simulated Annealing," Rev. Mod. Phys., **65**, pp. 1393–1534.
[33] Sahimi, M., 1994, *Applications of Percolation Theory*, Taylor & Francis, London.
[34] Henriette, A., Jacquin, C. G., and Adler, P. M., 1989, "The Effective Permeability of Heterogeneous Porous Media," PCH, PhysicoChem. Hydrodyn., **11**, pp. 63–72.
[35] Li, D., Beckner, B., and Kumar, A., 2001, "A New Efficient Averaging for Scaleup of Multimillion-Cell Geologic Models," SPE Paper No. 72599.
[36] Gómez-Hernández, J., 1991, "A Stochastic Approach to the Simulation of Block Conductivity Fields Conditioned Upon Data Measured at a Smaller Scale," Ph.D. thesis, Stanford University, Stanford, CA.
[37] Sánchez-Vila, X., 1995, "On the Geostatistical Formulations of the Groundwater Flow and Solute Transport Equations," Ph.D. thesis, Universitat Politética de Catalunya, Barcelona, Spain.
[38] Abbaszadeh, M., and Koide, N., 1996, "Evaluation of Permeability Upscaling Techniques and a New Algorithm for Interblock Transmissibilities," SPE Paper No. 36179.
[39] Begg, S. H., Carter, R. R., and Dranfield, P., 1989, "Assigning Effective Values to Simulator Gridblock Parameters for Heterogeneous Reservoirs," SPE Reservoir Eng., **4**, pp. 455–463.
[40] Gautier, Y., and Noetinger, B., 1994, "Preferential Flow-Paths Detection for Heterogeneous Reservoirs Using a New Renormalization Technique," *Proceedings of the Fourth European Conference on the Mathematics of Oil Recovery*, Norway.
[41] Holden, L., Hoiberg, J., and Lia, O., 1989, "Homogenization of Absolute Permeability," Norwegian Computer Centre Report No. 1211.
[42] White, C. D., and Horn, R. N., 1987, "Computing Absolute Transmissibility in the Presence of Fine-Scale Heterogeneity," SPE Paper No. 16011.
[43] Gómez-Hernández, J. J., 1990, "Simulation of Block Permeability Conditioned Upon Data Measured at a Different Scale," *ModelCARE 90: Calibration and Reliability in Groundwater Modelling*, K. Kovar, ed., IAHS, Wallingford, Oxfordshire, IAHS Publication No. 195, pp. 407–416.
[44] Gómez-Hernández, J. J., and Journel, A. G., 1990, "Stochastic Characterization of Grid-Block Permeabilities: From Point Values to Block Tensors," *Proceedings of the Second European Conference on the Mathematics of Oil Recovery*, Paris.
[45] Holden, L., and Lia, O., 1992, "A Tensor Estimator for the Homogenization of Absolute Permeability," Transp. Porous Media, **8**, pp. 37–46.
[46] Efendiev, Y. R., 1999, "The Multiscale Finite Element Method (MsFEM) and Its Applications," Ph.D. thesis, California Institute of Technology, Pasadena, CA.
[47] Wen, X.-H., Durlofsky, L. J., Lee, S. H., and Edwards, M. G., 2000, "Full Tensor Upscaling of Geologically Complex Reservoir Descriptions," SPE Paper No. 62928.
[48] Wallstorm, T. C., Hou, S., and Durlofsky, L. J., 1999, "Application of a New Two-Phase Upscaling Technique to Realistic Reservoir Cross Sections," SPE Paper No. 51939.
[49] Molz, F. J., Rajaram, H., and Lu, S., 2004, "Stochastic Fractal-Based Models of Heterogeneity in Subsurface Hydrology: Origins, Applications, Limitations and Future Research Questions," Rev. Geophys., **42**, p. RG1002.
[50] Sahimi, M., and Tajer, S. E., 2005, "Self-Affine Distributions of the Bulk Density, Elastic Moduli, and Seismic Wave Velocities of Rock," Phys. Rev. E, **71**, p. 046301.
[51] Bejan, A., 2006, "Constructal Theory of Generation of Configuration in Nature and Engineering," J. Appl. Phys., **100**, p. 041301.
[52] Bejan, A., and Lorente, S., 2008, *Design With Constructal Theory*, Wiley, Hoboken.

A Depletion Strategy for an Active Bottom-Water Drive Reservoir Using Analytical and Numerical Models—Field Case Study

Ibrahim Sami Nashawi[1]
Department of Petroleum Engineering,
College of Engineering and Petroleum,
Kuwait University,
P.O. Box 5969,
Safat 13060, Kuwait
e-mail: is.nashawi@ku.edu.kw

Ealian H. Al-Anzi
Kuwait Oil Company,
P.O. Box 9758,
Ahmadi 61006, Kuwait
e-mail: eanzi@hotmail.com

Yousef S. Hashem
Department of Petroleum Engineering,
College of Engineering and Petroleum,
Kuwait University,
P.O. Box 5969,
Safat 13060, Kuwait
e-mail: yhashem@hotmail.com

Water coning is one of the most serious problems encountered in active bottom-water drive reservoir. It increases the cost of production operations, reduces the efficiency of the depletion mechanism, and decreases the overall oil recovery. Therefore, preventive measures to curtail water coning damaging effects should be well delineated at the early stages of reservoir depletion. Production rate, mobility ratio, well completion design, and reservoir anisotropy are few of the major parameters influencing and promoting water coning. The objective of this paper is to develop a depletion strategy for an active bottom-water drive reservoir that would improve oil recovery, reduce water production due to coning, delay water breakthrough time, and pre-identify wells that are candidates to excessive water production. The proposed depletion strategy does not only take into consideration the reservoir conditions, but also the currently available surface production facilities and future development plan. Analytical methods are first used to obtain preliminary estimates of critical production rate and water breakthrough time, then comprehensive numerical investigation of the relevant parameters affecting water coning behavior is conducted using a single well 3D radial reservoir simulation model.
[DOI: 10.1115/1.3177385]

Keywords: water coning, bottom-water drive, critical production rate, breakthrough time, water/oil ratio, reservoir anisotropy, numerical methods, analytical methods

1 Introduction

Excessive oil production from a well that partially penetrates an oil zone overlying water aquifer causes the oil/water interface to bow into a bell-shape water cone. As the production rate increases, the cone peak rises above the original water/oil contact (WOC) until it reaches the bottom perforations, and eventually water breaks through into the well. The maximum water-free oil production rate is commonly called critical oil rate.

Two forces control water coning mechanism: (1) vertical dynamic flow force and (2) gravity force. The vertical dynamic flow force is due to pressure drop in the vicinity of the wellbore caused by oil withdrawal from the reservoir. As the oil is produced, the upward force causes the water underlying the oil zone to rise to a certain height at which the dynamic force is balanced by the net gravity force. As long as these two forces are in equilibrium, the water cone is delicately stable with its apex at a distance below the bottom perforations. However, an infinitesimal increase in the oil production rate may disturb the equilibrium, and eventually water breaks through into the well.

Water coning publications can be classified into three categories: (1) critical rate calculation, (2) water breakthrough time determination, and (3) post-breakthrough performance and water/oil ratio (WOR) estimation. Critical rate is the topic that has been addressed the most. In general, critical rate calculation methods can be divided into two categories. The first category determines the critical rate analytically based on equilibrium conditions between the upward viscous forces and the net gravity forces. The second category is based on empirical correlations.

Critical rate calculation can be traced back to 1935 when Muskat and Wyckoff [1] solved Laplace equation assuming single-phase incompressible fluid under steady-state condition in isotropic reservoirs. They also assumed that the potential distribution in the oil phase is not affected by the cone shape. In a subsequent paper, Muskat [2] highlighted the effect of the anisotropy ratio k_v/k_h on the breakthrough time and oil recovery from active bottom-water drive reservoirs. Arthur [3] pursued Muskat and Wyckoff [1] reasoning to develop a graphical solution for the critical rate. Meyer and Garder [4] proposed a simple equation to calculate the critical rate when the water cone touches the bottom perforations of the well. In developing their equation, they assumed that the flow of oil and/or gas toward the wellbore is strictly radial, the flow of water from the water/oil contact to the bottom of the well is strictly vertical, and the pressure drawdown controlling the flow of oil and/or gas is restricted to gravitational pressure difference. Chaney et al. [5] used the potentiometric model technique and mathematical analysis to study the effect of completion on water and gas coning at any depth in the pay zone. This method does not consider the cone height and pressure distribution in the reservoir; moreover, it is mainly applicable to homogeneous and isotropic reservoirs. Chierici et al. [6] also used the potentiometric model method to calculate the optimum water-free oil rate. They presented their results in dimensionless curves that take into consideration reservoir anisotropy. However, their findings are only adequate for small water aquifers. The models presented by Chaney et al. [5] and Chierici et al. [6] neglected the presence of water cone, which adversely affected the accuracy of the results. Meyer and Searcy [7] and Schols [8] used Hele-Shaw models, whereas Henley et al. [9] and Khan [10] used scale models to explore the water coning phenomenon. Karp et al. [11] adopted the theory of Muskat and Wyckoff [1] to experimentally and theoretically examine the effects of horizontal barriers on water coning. Welge and Weber [12], Blair and Weinaug [13], Letkeman and Ridings [14], Chappelear and Hirasaki [15], and Fisher

[1]Corresponding author.

Manuscript received August 4, 2008; final manuscript received February 1, 2009; published online July 29, 2009. Review conducted by Kambiz Vafai.

et al. [16] used 2D numerical models to inspect water coning performance. However, due to the complexity of water coning behavior, 2D models do not provide full spectrum of the water coning process. Woods and Khurana [17] and Trimble and McDonald [18] developed 3D reservoir simulators, which provide better understanding of water coning behavior.

Sobocinski and Cornelius [19] presented a dimensionless plot, which traces the rise of water cone vertex from the moment it builds up to breakthrough into the wellbore. Bournazel and Jeanson [20] fitted the curve developed by Sobocinski and Cornelius [19] by a simple analytical expression. Kuo and DesBrisay [21] numerically investigated the effects of various reservoir parameters on water coning performance and proposed a simplified correlation for water coning behavior. This method does not provide good results when applied to reservoirs with local barriers, reservoirs with a high degree of stratification, or reservoirs with a thick oil-water transition zone. Wheatley [22] presented a trial-and-error procedure to determine the critical rate assuming constant potential at the wellbore and drainage radius. They also assumed that the water/oil contact is in static pressure equilibrium with the oil. Most importantly, Wheatley's [22] theory considered the cone shape by requiring a streamline oil/water interface. Piper and Gonzalez [23] inspected the effect of cone height on the pressure gradient within the oil zone of three-phase systems. Hoyland et al. [24] used simulated data to develop correlations for critical rate prediction in isotropic and anisotropic reservoirs.

All of the previously mentioned studies do not consider the effect of limited wellbore entry on well productivity, which adversely affects the results. Abbas and Bass [25] were the first investigators to consider the effect of partial well penetration on maximum water-free production. They showed that the optimum fractional wellbore penetration interval, completed from the top of the pay zone, should be 0.5 in oil/water coning systems. Yang and Wattenbarger [26] performed exhaustive numerical sensitivity analysis to develop empirical correlations for the prediction of critical rate, breakthrough time, and WOR after breakthrough. Guo and Lee [27] presented an analytical solution for optimum wellbore penetration to maximize the critical production rate from isotropic reservoir.

Water coning behavior in horizontal wells has been also extensively investigated using numerical reservoir simulation. Hypothetical and field data were used to generate empirical correlations that describe the water coning performance [26,28–37]. Many of the available correlations are based on steady-state approximation of the reservoir conditions. However, since steady-state cannot hold during cone development under field operating conditions, especially in the early production stage, the predicted critical rates are questionable and cannot be of practical use [38]. More recently, several numerical simulation studies [39–42] investigating water coning behavior in edge and bottom-water drive reservoirs were published in the literature. The common aim of these papers was developing an effective methodology capable of delaying water coning.

The objective of this study is to delineate a depletion strategy for an active bottom-water drive reservoir that would maximize oil recovery, minimize water production due to coning, delay water breakthrough time, and pre-identify wells that are vulnerable to excessive water production. The study is divided into three major stages. The first stage consists of using analytical methods to obtain preliminary estimates of critical production rate and water breakthrough time. The second stage involves building a single well 3D radial reservoir model to investigate the various parameters affecting water coning behavior. Finally, a reservoir depletion strategy, which takes into consideration the reservoir conditions, production requirements, and current surface facilities limitations and future expansion, is outlined.

2 Criteria for Reservoir Depletion Strategy

Four depletion criteria are adopted in this study for selecting the optimum critical fluid production rate (CFPR).

1. The CFPR should minimize the water coning phenomenon. Trying to stop the water cone implies that the well must be produced at a very low rate, which may not be economical or may not represent the production potential of the reservoir.
2. The CFPR should maximize the cumulative oil production, hence the oil recovery.
3. The CFPR should extend the plateau of water-free oil production as long as possible and confine the cumulative water production to the amount that meets the current capacity of the water handling facility. The future facility upgrade for the reservoir under investigation is planned for year 2010.
4. The optimum CFPR should lengthen the natural production life of the well up to the year 2010, when artificial lift methods are planned to be implemented.

3 Reservoir Description

The reservoir under investigation is one of the largest and most complex reservoirs in the Middle East. The overall reservoir architecture is defined by the depositional processes, which are mostly channel processes. The internal makeup of the channels was affected by marine influence, and range from fully fluvial channels, through deltaic channels, tidally-influenced channels, and more marine estuarine channel fills. Stacked and amalgamated sand-filled fluvial channels form the massive sands of the reservoir.

Fluvial processes dominate the lower part of the formation. High frequency changes in the sea level increased the marine influence in the channels of the upper part of the reservoir. This influence rendered some of the channels to be more clay rich and bioturbated with markedly lower reservoir quality, and some others to be filled with marine or tidally-influenced shales. The net/gross ratio of sands is typically high and the sand body connectivity is good. Individual channel width is slightly less than 3280 ft, which is a typical well spacing; consequently, individual sands and shales can rarely be correlated between wells.

Clean, well sorted, massive, and cross bedded sands of excellent quality dominate most of the reservoir. The reservoir porosity ranges from 15% to 27%, whereas the permeability varies from 1000 mD to 5000 mD. Bioturbation in the cleaner sands reduces the formation permeability by mixing previously discrete sand/shale laminate, and introducing ductile fines (clay) into the pore throats.

4 Well Description

Well A is located in the central crest of the field. It was drilled and completed in 1997. Open-hole logs indicated that the original WOC was at a depth of 8350 ft. A time lapse thermal decay tool (TDT) survey was performed on September 16, 1999, and located the WOC at 8313 ft. This indicates that the water level has risen 37 ft in 32 months. The well produced from 1998 to 2000 at 3000 STB/D. At the beginning of year 2000, the production rate was increased to 5000 STB/D. Just 6 months after the increase in fluid production, water cut (WC) started in the well. The historical production rate and water cut for Well A are displayed in Fig. 1. Current standoff between the WOC and the bottom perforation is 61 ft, which indicates that the water production was due to a water cone. Figure 2 illustrates the historical WOC movement in the well.

5 Analytical Methods

Analytical methods are often used in the field to obtain quick preliminary estimates of critical production rate, breakthrough time, and cone height. Then, the results are integrated with actual

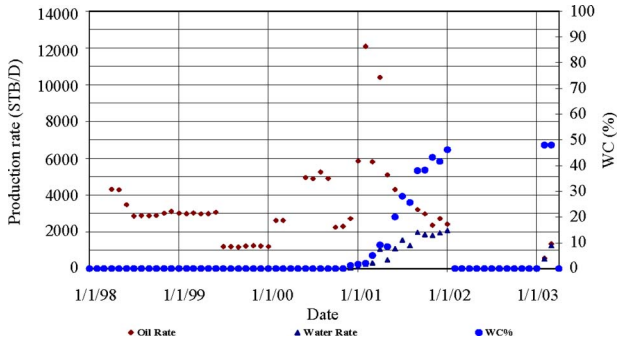

Fig. 1 Historical production rate from Well A

field data into reservoir simulation models to history match the reservoir behavior and predict future performance. While the standard coning correlations provide insight into the mechanics of water coning, reservoir simulation has the advantage of capturing local heterogeneity, anisotropy, and capillarity.

Six frequently used analytical techniques will be applied in this investigation. Four methods will be used to calculate the CFPR, and two methods will be applied to compute the water breakthrough time. All the calculations will be performed using the actual reservoir fluid and rock properties reported in Table 1. The fluid pressure-volume-temperature (PVT) properties provided in the table are measured under reservoir conditions.

5.1 Mathematical Formulation of the CFPR Methods. The methods of Meyer and Garder [4], Kuo and DesBrisay [21], Chaney et al. [5], and Chierici et al. [6] were used to calculate the CFPR. A discussion of the theoretical background of these methods was presented in the introduction. A concise description of the mathematical formulation will be given in Secs. 5.1.1–5.1.4.

5.1.1 Meyer and Garder Method. This method is one of the classical analytical techniques published in the oil literature on the mechanics of two immiscible fluid flows in porous media. Meyer and Garder [4] proposed the following equation to calculate the CFPR:

$$q_c = \frac{0.001535(\rho_w - \rho_o)k(h^2 - D^2)}{\mu_o B_o \ln(r_e/r_w)} \tag{1}$$

5.1.2 Kuo and DesBrisay Method. This method is one of the earliest techniques where a simple computer program was used for quick estimate of critical rate. Kuo and DesBrisay [21] used numerical simulation to determine the sensitivity of water coning behavior to various reservoir parameters. Using the correlations presented in Eqs. (3)–(5), the CFPR can be calculated from Eq. (2).

$$q_c = (\text{factor A})(\text{factor B})(\text{factor C}) \tag{2}$$

$$\text{factor A} = \frac{(\rho_w - \rho_o)k(h^2 - D^2)}{2049\mu_o B_o} \tag{3}$$

$$\text{factor B} = 0.432 + 3.1416/[\ln(r_e/r_w)] \tag{4}$$

$$\text{factor C} = (h/r_e)^{0.14} \tag{5}$$

5.1.3 Method of Chaney et al. Chaney et al. [5] proposed the following CFPR equation based on several potentiometric model runs

$$q_c = \frac{0.00333 q_{\text{curve}} k(\rho_w - \rho_o)}{\mu_o B_o} \tag{6}$$

where q_{curve} is defined as follows:

$$q_{\text{curve}} = 0.1313(h^2 - D^2) + 34\left(\frac{57 - h}{44}\right)^2 - 250\left(\frac{D}{h} - 0.3\right) \times \left(\frac{h - 10}{90}\right)^2 - 40 \tag{7}$$

For accurate results, the pay zone thickness should be between 10 and 100 ft, and the D/h ratio should be between 0.1 and 0.5 ($10\ \text{ft} \le h \le 100\ \text{ft}$ and $0.1 \le D/h \le 0.5$).

5.1.4 Method of Chierici et al. Chierici et al. [6] developed the following equation for CFPR calculation:

$$q_c = \frac{0.0008051 k_h h^2(\rho_w - \rho_o)(D/h)(CI/h + D/h)^{0.525}}{\mu_o B_o[(r_e/h)(k_v/k_h)^{0.5}]^{0.165}} \tag{8}$$

Equation (8) should be used in conjunction with a set of curves. The published curves are only valid for homogeneous formations, either isotropic or anisotropic.

5.2 Calculation of CFPR. The results obtained from the various analytical methods are reported in Table 2. The various methods yielded different and sometimes conflicting results; more importantly, most of the results do not represent the reservoir potential. The analytical techniques have also shown that the well will have coning problems at low production rate. However, well surveillance conducted in the field indicates that Well A is capable of producing water-free oil even at rates higher than those obtained from the analytical methods. It has been mentioned in the introduction that the analytical methods only provide good results when their fundamental assumptions are satisfied. For instance, the Meyer and Garder [4] method, which yielded the lowest CFPR value of 624 STB/D, assumes radial oil flow toward the wellbore, vertical water flow to the bottom of the well, and pressure drop in the reservoir restricted to gravitational forces. This set of ideal flow conditions can be hardly encountered in any reservoir. The method of Chierici et al. [6], which considers reservoir anisotropy, provided the highest CFPR value of 1917 STB/D. Even though, this value is close to the actual flow behavior of the reservoir under study; yet, it does not represent the actual reservoir potential. The other two methods also have limitations. The method of Chaney et al. [5] is applicable to homogeneous and isotropic reservoirs and the Kuo and DesBrisay [21] method does not provide good results when applied to reservoirs with local barriers, reservoirs with high degree of stratification, or reservoirs with thick oil-water transition zone. Consequently, it is not surprising that these methods do not provide good results due to their idealistic nature and the complexity of the reservoir of this study; nevertheless, they can be used as general guidelines for further numerical investigations.

The data set given in Table 1 is also used to calculate the CFPR for a range of oil column thicknesses and completion intervals, which can be found in various reservoir locations. The calculation showed that the techniques do not provide critical rates that reflect the reservoir capability. Figures 3–6 display the results of the different methods.

5.3 Mathematical Formulation of Water Breakthrough Time Methods. The breakthrough time of water in the producing wells should be accurately determined, because it plays a major key role in reservoir depletion strategy and overall field development plan. Prior knowledge of the water breakthrough time allows the production management to adequately design water treatment facilities capable of handling excessive water production from the field. The Sobocinski and Cornelius [19] and the Bournazel and Jeanson [20] methods are used in this study to calculate the breakthrough time. The mathematical equations of these techniques are given in Secs. 5.3.1 and 5.3.2.

5.3.1 Sobocinski and Cornelius Method. Sobocinski and Cornelius [19] proposed the following correlation to calculate the water breakthrough time:

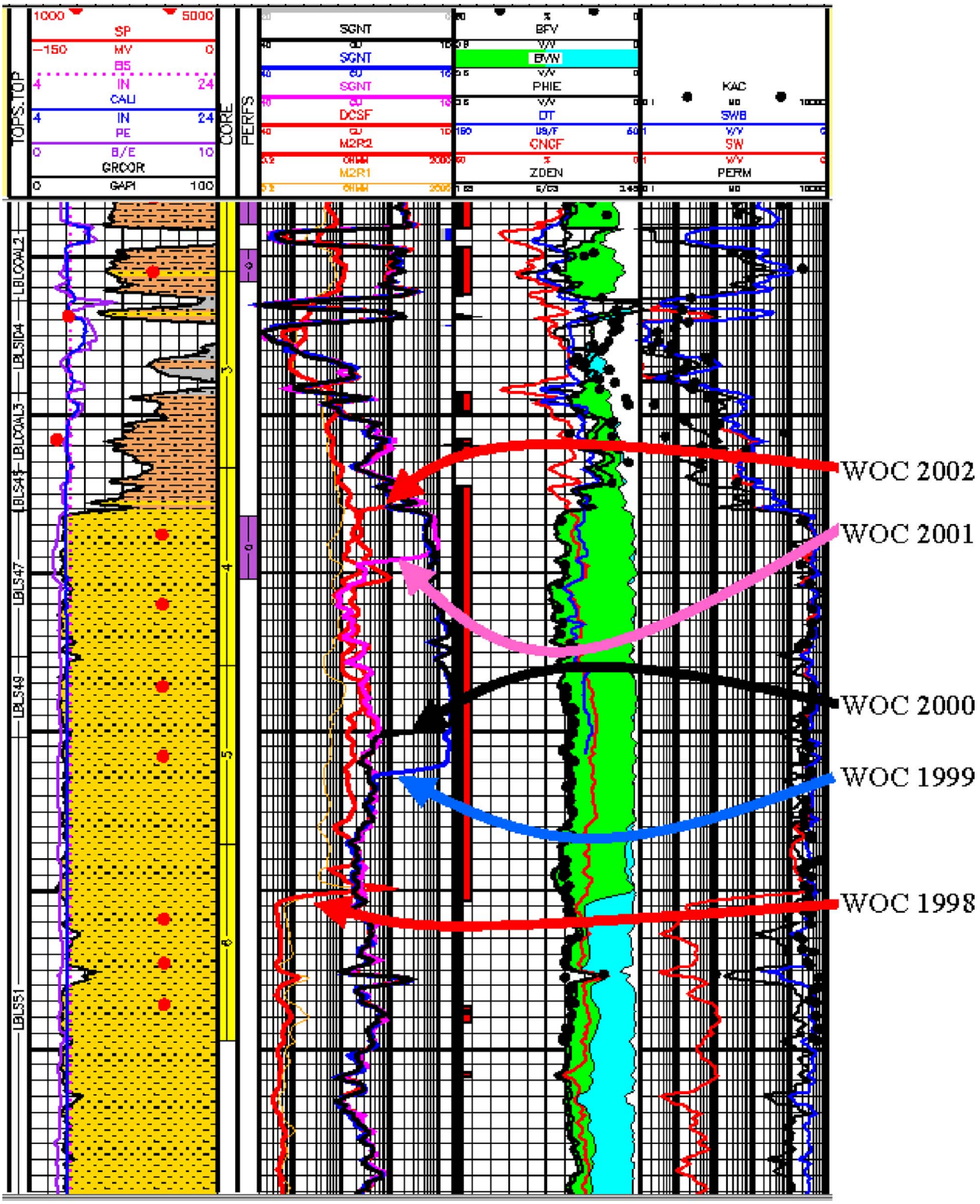

Fig. 2 Water/oil contact (WOC) tracking of Well A

$$t = \frac{\mu_o \phi h F_k t_D}{0.00137(\rho_w - \rho_o)k_h(1 + M^{\alpha})} \tag{9}$$

where the dimensionless time, t_D, and the mobility ratio, M, are, respectively, defined as follows:

$$t_D = \frac{0.00137(\rho_w - \rho_o)k_h(1 + M^{\alpha})t}{\phi h F_k \mu_o} \tag{10}$$

$$M = \frac{k_w/\mu_w}{k_o/\mu_o} \tag{11}$$

The exponent α in Eqs. (9) and (10) is equal to 0.5 for $M < 1$ and 0.6 for $M > 1$.

5.3.2 Bournazel and Jeanson Method. This technique was proposed as a quick method for predicting water breakthrough

Table 1 Pertinent reservoir and fluid properties

Reservoir/well properties	
Horizontal permeability, k_h (mD)	500
Vertical permeability, k_v (mD)	50
Formation porosity, ϕ (%)	0.177
Drainage radius, r_e (ft)	970
Wellbore radius, r_w (ft)	0.354
Pay zone thickness, h (ft)	123
Completed interval (ft)	20
Standoff from WOC (ft)	103
Mobility ratio, M (dimensionless)	1.2
Average reservoir pressure, P_r (psi)	4000
Fluid properties	
Oil formation volume factor, B_o (RB/STB)	1.43
Oil viscosity, μ_o (cp)	0.76
Oil density, ρ_o (gm/cc)	0.69
Oil production rate, q_o (STB/D)	2500
Oil saturation pressure, P_b (psi)	2480
Residual oil saturation, S_{or} (%)	19.2
Irreducible water saturation, S_{wir} (%)	10
Formation water viscosity, μ_w (cp)	0.525
Formation water density, ρ_w (gm/cc)	1.165

time. The working equation is given as follows:

$$t = \frac{\mu_o \phi h F_k (t_D)_{bt}}{0.00137(\rho_w - \rho_o)k_h(1 + M^{\alpha})} \tag{12}$$

where the dimensionless breakthrough time, $(t_D)_{bt}$, is defined as follows:

$$(t_D)_{bt} = \frac{Z}{3 - 0.7Z} \tag{13}$$

and the dimensionless cone height, Z, is given as follows:

Table 2 CFPR calculation results from the various analytical methods

Method	CFPR (STB/D)
Meyer and Garder [4]	624
Kuo and DesBrisay [21]	977
Chaney et al. [5]	1473
Chierici et al. [6]	1917

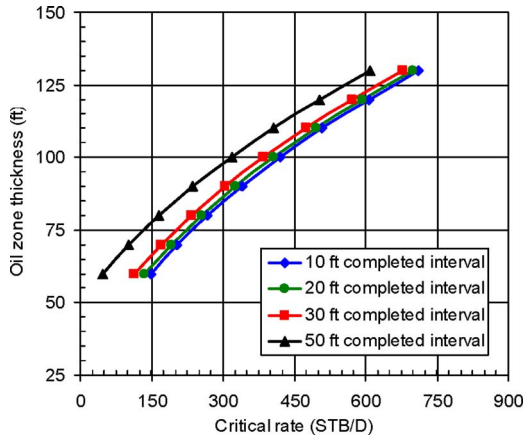

Fig. 3 Critical production rate as calculated by Meyer and Garder [4] method

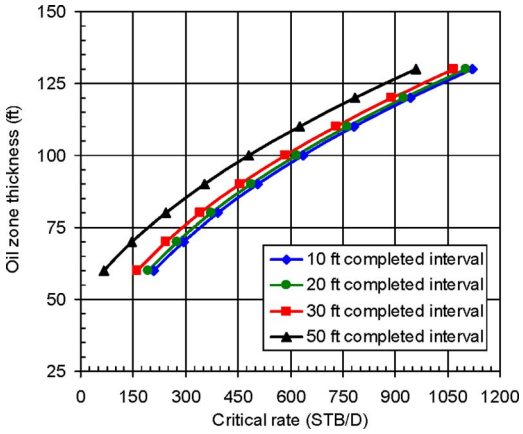

Fig. 4 Critical production rate as calculated by Kuo and DesBrisay [21] method

$$Z = \frac{0.00307(\rho_w - \rho_o)k_h h h_c}{q_o B_o \mu_o} \tag{14}$$

5.4 Calculation of Water Breakthrough Time. Water breakthrough time was calculated for a range of oil column thicknesses and perforation standoff that covers most of the well conditions in the reservoir. The calculation results are reported in Table 3. The Sobocinski and Cornelius [19] and the Bournazel and Jeanson

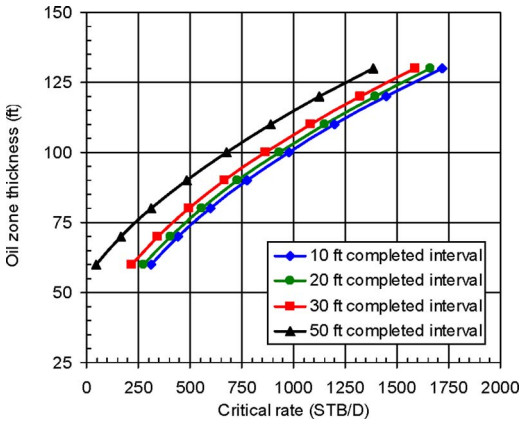

Fig. 5 Critical production rate as calculated by Chaney et al. [5] method

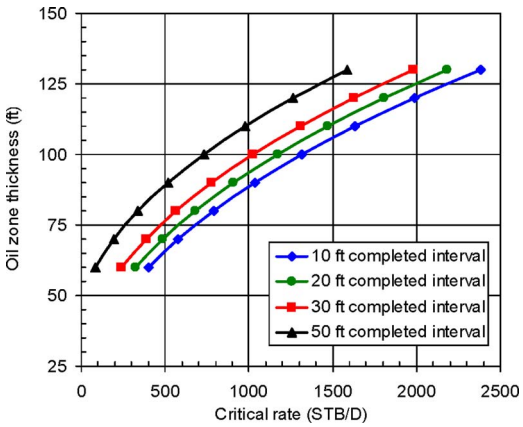

Fig. 6 Critical production rate as calculated by Chierici et al. [6] method

Table 3 Water breakthrough time for different oil column thickness and standoff from WOC

Oil column thickness, h (ft)	Standoff from WOC, h_c (ft)	Water breakthrough time, t (year)	
		Sobocinski and Cornelius [19] method	Bournazel and Jeanson [20] method
80	60	0.38	0.26
100	80	1.50	0.76
123	103	4.93	3.57
130	110	5.21	8.41

[20] methods indicate that the water will break through in Well A after 4.93 years and 3.57 years of production, respectively. The two methods indicate a delay in the water breakthrough time. In reality, the water invaded the perforations after only 2 years of production. This signifies that the two analytical methods are too naive to capture the reservoir performance; consequently, they should be used with extreme care only to provide quick estimates of water breakthrough time. Time lapse TDT surveys and actual production data are extremely important for quality checking the accuracy of the analytical techniques before adapting any of them in the field.

Due to the complex physical phenomena that take place in real 3D reservoirs, even for homogeneous and isotropic cases, and the assumptions used in the derivation and simplification of the analytical solutions, the analytical models oversimplify the water coning process and frequently yield unreliable reservoir performance results. Thus, rigorous numerical simulation model using actual field data should be developed to investigate the various reservoir parameters affecting water coning behavior, to determine the critical production rate, and to forecast reservoir performance after water breakthrough.

6 Numerical Simulation Model

6.1 Model Description. The model used in this study is a 3D radial model with the well located in the center. The inner and outer radii of the model are 0.354 ft and 970 ft, respectively, and the total thickness is 541.5 ft. The perforated zone is between 8066 ft and 8088.5 ft. The number of grid blocks has been optimized with a grid sensitivity analysis. The analysis showed that accurate results could be obtained with a total of 2025 grid blocks, 135 grid blocks in the vertical direction, and 15 grid blocks in the radial direction. The block size in the radial direction increases exponentially with distance from the wellbore. Figure 7 displays a schematic illustration of the reservoir simulation model used in this investigation.

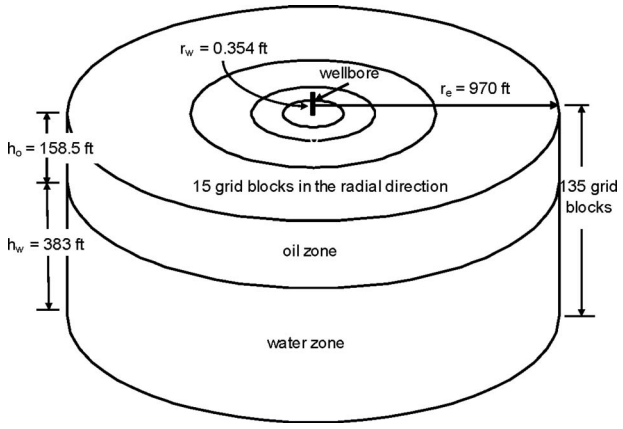

Fig. 7 Schematic illustration of the reservoir simulation model

Table 4 k_h, k_{radial}, and k_v values used for the history match

Interval thickness (ft)	k_h (mD)	k_{radial} (mD)	k_v (mD)
22.5	500	500	50
63.75	1600	1600	160
72.25	1350	1350	135
383	2351	2351	235.1

The reservoir pressure is above the saturation pressure of 2480 psi; thus, only oil and water are flowing in the reservoir. The production is subject to two constraints: (i) the total liquid production rate, oil and water, should not exceed 20,000 STB/D and (ii) the flowing bottomhole-pressure of the well should not fall below the saturation pressure. The simulated cases will run to an economic water cut limit of 95%. The following are few features of the simulation model:

1. The thicknesses of the oil and water zones are 158.5 ft and 383 ft, respectively. The total model thickness, consisting of the oil and water zones, is divided into four intervals. Each interval is assigned different horizontal and vertical permeability values as shown in Table 4. The horizontal permeability, k_h, and the radial permeability, k_{radial}, values are assumed equal. The vertical to horizontal permeability ratio, k_v/k_h, is equal to 0.1 throughout the reservoir. The oil and water relative permeability curve is displayed in Fig. 8.
2. An irreducible water saturation of 10% dominates the entire reservoir above the WOC. The residual oil saturation is equal to 19.2% and the WOC is at 8352 ft.
3. The net/gross ratio is 0.9, while the formation porosity is 17.7%. These values are considered constant for the entire formation and are characteristics of the best parts of the reservoir where coning is most likely to occur.
4. The water compressibility, viscosity, formation volume factor, and the residual oil saturation were fine-tuned for history matching purposes.

6.2 History Matching. The actual historical daily and cumulative oil, gas, and water production rates will be matched with the results of the simulation model. The simulator input data are used to determine the optimum production rate and to scrutinize various parameters affecting water coning behavior. A comparison

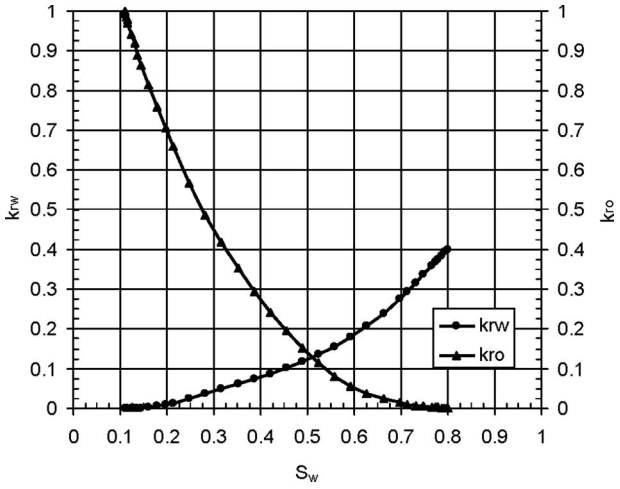

Fig. 8 Oil and water relative permeability as a function of water saturation

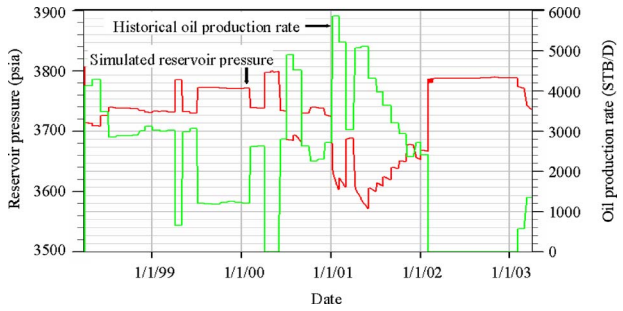

Fig. 9 Historical oil production rate versus simulated reservoir pressure

between the simulated results and the actual history data is illustrated in Figs. 9–16.

Figure 9 displays the real oil production rate and simulated bottomhole-pressure as a function of time. It is evident from the figure that as the production rate increases, the simulated pressure decreases and vice versa. This pressure behavior indicates that the model nicely simulates the actual reservoir performance.

Figures 10–12 compare the actual and simulated water cut, water production rate, and cumulative water production, respectively. All three figures show a very good match between the historical and simulated data.

Figures 13 and 14 compare the actual and simulated daily and cumulative oil, gas, water, and total fluid production. All the figures clearly illustrate that the simulated data follow the same graphical trend as the real well performance data. This proves that the developed simulator model is capable of accurately imitating the actual reservoir performance.

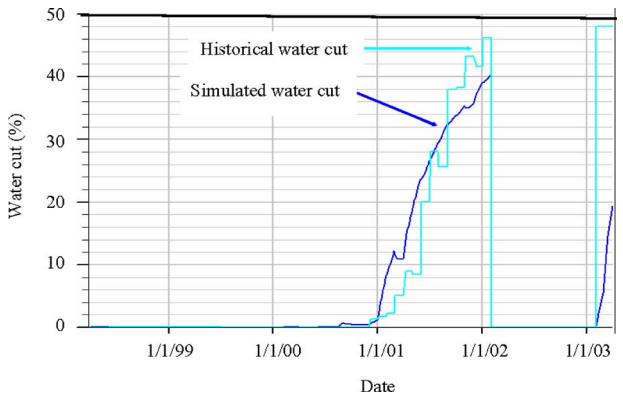

Fig. 10 Historical water cut versus simulated water cut

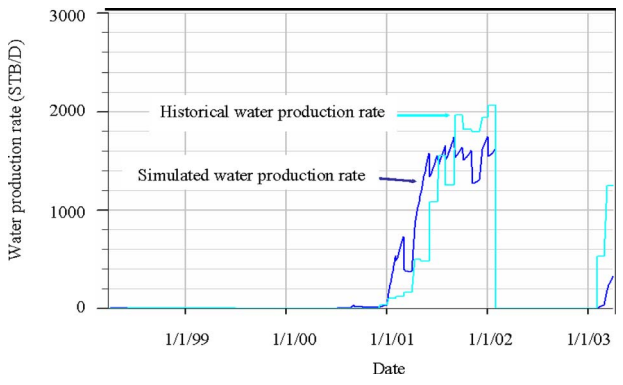

Fig. 11 Historical water production rate versus simulated water production rate

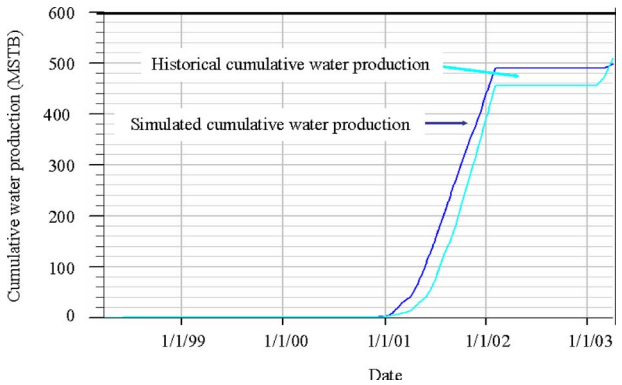

Fig. 12 Historical cumulative water production versus simulated cumulative water production

6.3 Determination of the CFPR. The simulation model is used to determine the most suitable CFPR for Well A that fulfills the four criteria requirements set in Sec. 2 of the paper. Five simulation runs with fluid production rate of 1000 STB/D, 2000 STB/D, 2500 STB/D, 5000 STB/D, and 10,000 STB/D will be conducted to determine the optimum critical rate. The simulator run will stop either when the simulation execution time reaches year 2020, or when the water cut in the well reaches the economic limit of 95%. The results of the simulated cases will be compared in terms of cumulative oil and water production, well life, and water cone height.

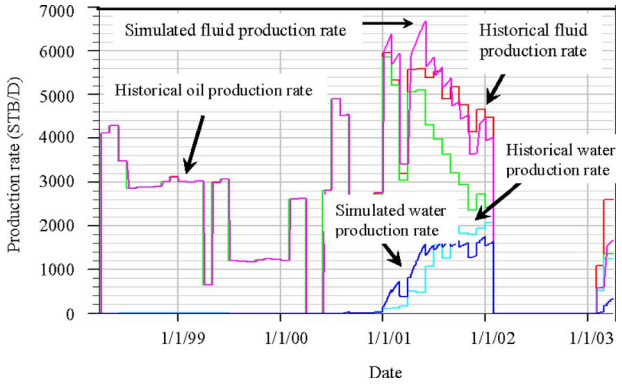

Fig. 13 Historical oil, water, and total fluid production rates versus simulated oil, water, and total fluid production rates

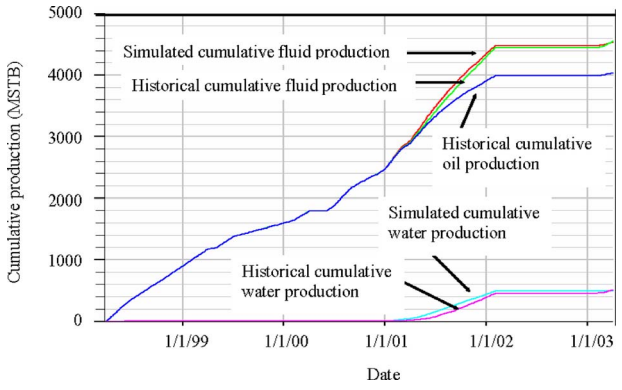

Fig. 14 Historical cumulative oil, water, and total fluid production versus simulated cumulative water and total fluid production rates

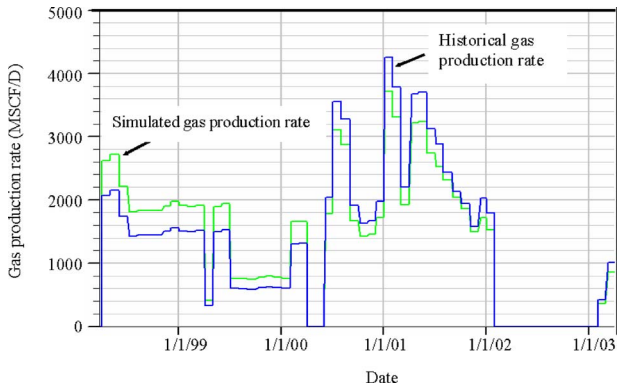

Fig. 15 Historical gas production rate versus simulated gas production rate

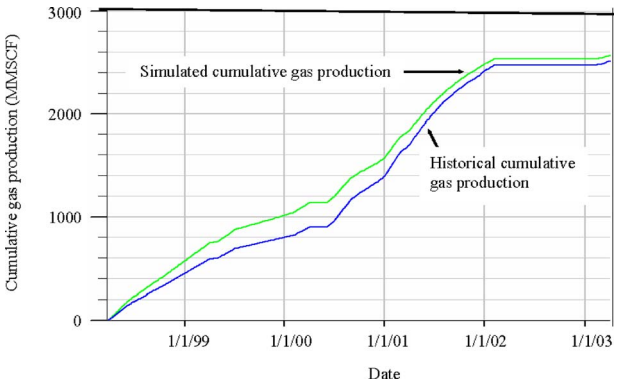

Fig. 16 Historical cumulative gas production versus simulated cumulative gas production

6.3.1 Effect of Production Rate on the Water Cone Height. The simulation results indicate that as the production rate increases from 1000 STB/D to 10,000 STB/D, the cone height underneath the perforations sharply increases and water breaks through in the well faster than the low production rate cases. This implies that the water cone formation speed and height are rate sensitive. For instance, the cone of the 1000 STB/D case will reach the perforations after 7 years of production and will be 20 ft high, whereas the cone of the 10,000 STB/D case will touch the bottom perforations after 8 months of production and will be 70 ft high. Table 5 illustrates the effects of production rate on water breakthrough time and cone height.

6.3.2 Effect of Production Rate on the Well Life. The effect of production rate on the well life is demonstrated in Table 5. The results reported in the table reveal that as the production rate increases the water-free oil production period and the well life become shorter. For a production rate of 1000 STB/D, the simulator used all the allocated execution time (up to year 2020) before stopping at 84% water cut. As the production rate increases, the well life decreases until it becomes only 5 years with a production rate of 10,000 STB/D.

6.3.3 Effect of Production Rate on Cumulative Oil and Water Production. The effect of production rate on cumulative oil and water production is also illustrated in Table 5. The results indicate that the cumulative oil production is not highly affected by the increase in production rate. However, the cumulative water production increases as the production rate increases. Production rates of 5000 STB/D and 10,000 STB/D do not have significant impact on the cumulative oil production; conversely, the amount of water which must be handled over the lifetime of the well is increased. Producing the well at either 2000 STB/D or 2500 STB/D yields similar cumulative oil production and much less cumulative water production when compared with the higher liquid production rates. Therefore, it can be concluded that a production rate of 2500 STB/D is the most appropriate optimum CFPR for Well A since it yields the most suitable results among all simulated cases; the cumulative oil production is comparable to the higher liquid production cases and the cumulative water production is lower than the higher rate cases.

7 Sensitivity Analysis

Several sensitivity analysis cases are conducted to investigate the impact of well completion conditions and reservoir properties on water coning behavior. The recommended optimal CFPR of 2500 STB/D was used in all the simulated cases.

The first sensitivity case investigated the effects of thickness/standoff of the perforations on water coning. This parameter can be controlled during the completion stage of the well; hence, any adverse effect on water cone development can be anticipated prior to fluid production and remedial actions can be taken to minimize water coning problems. Moreover, three other sensitivity cases inspected the effects of reservoir permeability, anisotropy (k_v/k_h ratio), and shale break between the perforations and the WOC. The objective of these cases is to obtain a good understanding of the effects of formation properties on water coning behavior.

7.1 Effect of Thickness and Standoff of Perforated Interval. Three simulated cases of different perforation thickness and standoff from the WOC were used to investigate the effects of perforated interval. The first two cases have perforated interval thicknesses of 30 ft and 50.75 ft, respectively. The perforated interval of the third case is divided into two zones. The first zone is 20.5 ft thick, whereas the second zone is 15 ft thick. The perforation standoff from the WOC is 93 ft, 72.25 ft, and 80.5 ft for the first, second, and third case, respectively.

The simulation results are reported in Table 6. The thickest perforation interval (50.75 ft), which has the smallest standoff distance from the WOC (72.25 ft), has the shortest well life and yields the least volume of cumulative oil production. Conversely, the two intervals completion has the longest well life and provides maximum volume of cumulative oil production among the other

Table 5 Effect of various production rates on well performance

Production rate (STB/D)	Cumulative oil production (MMSTB)	Cumulative water production (MMSTB)	Well life (year)	Date cone reaching perforation	Cone height (ft)
Actual rate	4.04	0.51	5	01/09/2000	50
1000	5.51	2.54	22	18/10/2007	20
2000	6.04	9.32	21	17/05/2002	30
2500	6.05	9.51	17	21/02/2001	50
5000	6.09	11.12	9.4	03/05/1999	60
10,000	6.09	12.66	5.1	06/08/1998	70

Table 6 Effect of perforated interval and standoff from WOC on well performance

Thickness of perforated zone (ft)	Standoff from WOC (ft)	Cumulative oil production (MMSTB)	Cumulative water production (MMSTB)	Well life (year)	Date cone reaching perforation	Cone height (ft)
22.5 (base case)	100.5	6.05	9.51	17	21/02/2001	50
30	93	6.00	9.56	17	23/11/2000	40
50.75	72.25	5.87	9.23	16.5	27/02/2000	40
20.5	80.5	6.30	12.84	21	25/08/2000	40
15						

cases; however, the cumulative water production of this case is the highest of all simulated cases.

If one of the three completion scenarios is to be selected for Well A, the two intervals completion will be a good choice. This approach increases the well life by 4 years and the oil recovery by 0.25 MMSTB over the base case. However, the cumulative water production of this completion is 3.33 MMSTB higher than the base case. To overcome this problem, the well can be completed with a space between the two perforations sets; so that when the water breaks through the bottom perforations zone, an isolation operation can be conducted to isolate the water invaded interval. From practical field experience, lowering the water cut economical limit in the bottom zone from 95% to 50%–70% will reduce the cumulative water production of the well and, at the same time, will not affect the oil recovery since the upper interval will continue producing up to 95% water cut.

7.2 Effect of Reservoir Permeability. Two simulated cases were used to investigate the effects of permeability variation on water coning behavior. In the first case, the permeability was reduced by 50% from the base case permeability, whereas the permeability of the second case was increased by 30%. A k_v/k_h value of 0.1 was used in both cases.

The results of the simulation runs are presented in Table 7. A 50% reduction in permeability caused a 0.04 MMSTB increase in oil production over the base case; however, this slight advantage was offset by 1.67 MMSTB increase in water production. The permeability reduction also extended the well life by 2 years; but, at the same time, it caused the water to break through in the well 9 months earlier, which contributed to detrimental excessive water production. Conversely, a 30% increase in permeability caused a reduction in oil production, water production, and well life when compared with the base case.

7.3 Effect of Reservoir Anisotropy (k_v/k_h Ratio). Two simulated cases were performed to inspect the effects of k_v/k_h on the well performance. In the first case, the vertical permeability k_v was reduced by 50% from the original k_v yielding a k_v/k_h ratio of 0.05. In the second case, k_v was increased by 300% resulting in a k_v/k_h ratio of 0.3.

The results of the simulation runs are reported in Table 8. It is shown in the table that the 50% reduction in k_v ($k_v/k_h=0.05$) did not have any effect on oil recovery; however, it reduced the water production by 0.81 MMSTB and the well life by 1 year. It also caused a 3-month delay in the water breakthrough time. Conversely, the 300% increase in k_v ($k_v/k_h=0.3$) did not affect the well life; however, it caused a 0.11 MMSTB reduction in oil production, a 0.19 MMSTB increase in water production, and 6 months early water breakthrough time. Therefore, an increase in the k_v/k_h ratio has adverse effects on the well performance, whereas a decrease in the k_v/k_h ratio reduces the volume of water production.

7.4 Effect of Shale Break Between Perforation and WOC. Two simulated cases were conducted to investigate the effects of shale break on water coning behavior. The radial extensions of the shale breaks were 68.96 ft and 571.9 ft for the first and second simulated cases, respectively. In both cases, the shale layer had a thickness of 10 ft and was located 73.5 ft below the perforations. The results obtained from the simulation runs are illustrated in Table 9. It is quite obvious from the presented results that the well life is not affected by the radial extension of the shale. The long-radius shale break increased the oil production by 0.28 MMSTB and reduced the water production by 0.61 MMSTB when compared with the base case. It also caused an 18-month delay in the water breakthrough time when compared with the short-radius shale. Besides, no water cone was observed in the long-radius shale case as compared with a 40 ft high water cone observed in the short-radius case.

The presence of shale between the deepest perforations and the WOC improves the oil recovery, retards the water movement in the vertical direction, delays the water breakthrough time, and reduces the water production. The shale break diverts the water to sweep parts of the reservoir that are away from the well; hence, enhancing oil recovery. Usually, the short shale break is not as affective as the long shale break in improving the well performance since water can move around it. Yet, long shale delays and/or may even prevent coning, but at the same time, it impedes the pressure support of the water aquifer.

Table 7 Effect of formation permeability on well performance

Simulated cases	Cumulative oil production (MMSTB)	Cumulative water production (MMSTB)	Well life (year)	Date cone reaching perforation
Base case	6.05	9.51	17	21/02/2001
50% reduction in k_h	6.09	11.18	19	27/05/2000
30% increase in k_h	6.03	9.16	16.6	22/05/2001

Table 8 Effect of reservoir anisotropy on well performance

k_v/k_h	Cumulative oil production (MMSTB)	Cumulative water production (MMSTB)	Well life (year)	Date cone reaching perforation
0.1 (base case)	6.05	9.51	17	21/02/2001
0.05	6.05	8.70	16	22/05/2001
0.30	5.94	9.70	17	23/11/2000

Table 9 Effect of shale break on well performance

Shale radial extension (ft)	Cumulative oil production (MMSTB)	Cumulative water production (MMSTB)	Well life (year)	Date cone reaching perforation
Base case (no shale)	6.05	9.51	17	21/02/2001
68.96	6.07	9.48	17	22/05/2001
571.90	6.33	8.90	16.9	13/11/2002

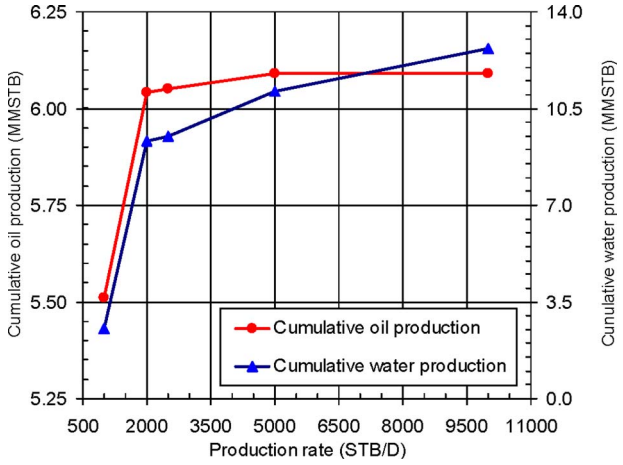

Fig. 17 Cumulative oil and water production as a function of various fluid production rates

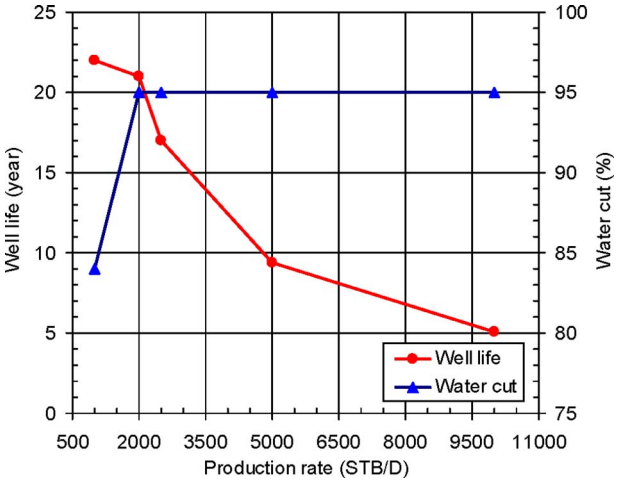

Fig. 18 Well life and water cut as a function of various fluid production rates

8 Optimum Depletion Strategy

Managing active water drive reservoirs requires collaborative efforts among production and reservoir engineers to delineate and implement an innovative production philosophy that expands the water-free oil production plateau, delays the water breakthrough time, extends the economic life of the well, and increases the oil recovery. Good depletion strategy should consider current capacity and future expansion of water handling facilities; moreover, the natural production life of the wells should be carefully assessed and extended until artificial lift equipment are ready to be installed.

Due to the complex physical phenomena existing in actual reservoirs, even for homogenous and isotropic cases, analytical models are often inadequate to describe the entire well performance behavior. Consequently, they must be used with extreme care and diligence as general guides to obtain preliminary estimates of production rate and water breakthrough time. Conversely, numerical reservoir models integrate actual rock and fluid properties as well as various parameters influencing water coning in a precise and consistent manner and efficiently capture the well performance. Furthermore, reservoir simulation models have the capability to describe pre- and post-water breakthrough performance of the wells. Several simulation runs were conducted to select the production rate scenario that best satisfies the depletion criteria set for Well A. Figures 17 and 18 display the results of the various rates and their effects on Well A.

The following observations can be withdrawn from the results reported in Table 5 and Figs. 17 and 18:

1. A production rate of 1000 STB/D yields the least amount of cumulative water production; however, this rate does not meet the production potential of Well A as specified in criterion 1. Furthermore, the cumulative oil production obtained from this rate is substantially less than those obtained from all other rates. Thus, it does not maximize the oil recovery as it is required by criterion 2. Conversely, the 1000 STB/D rate extends the well life and the dry oil production plateau more than any other rate; thus, it fulfills criteria 3 and 4.
2. Production rates of 5000 STB/D and 10,000 STB/D yield the same amount of cumulative oil production and do not cause any loss in reserve, which satisfy criterion 2. However, the 10,000 STB/D rate is higher than the production potential of Well A; hence, it does not satisfy criterion 1. Furthermore, producing the well at either 5000 STB/D or 10,000 STB/D rate does not extend the dry oil production plateau as both rates yield large amount of water production, which is beyond the handling capacity of the current water treatment facility. Thus, both rates do not meet criterion 3. Also, the two rates do not extend the natural production life of the well until the time when the artificial lift facilities will be ready for installation. Hence, both rates do not fulfill criterion 4.
3. The production rates of 2000 STB/D and 2500 STB/D almost yield the same amount of cumulative oil production, do not cause any loss in oil reserve, fall within the production potential of Well A, extend the dry liquid production plateau more than the higher rates, and expand the natural production life of the well beyond the time required for the artificial lift installation (year 2010); accordingly, they satisfy criteria 1, 2, 3, and 4.

Table 10 summarizes the observations withdrawn from the various simulated cases in terms of criterion satisfaction. It is evident that the 2000 STB/D and the 2500 STB/D rates satisfy all the criteria outlined for the reservoir depletion strategy. Therefore, they can be considered as the optimum production rate for Well A. The higher rate results in 0.17% increase in cumulative oil production and 2% increase in cumulative water production over the lower rate; however, the excess additional water production can be easily handled by the existing water treatment facility. Thus, the 2500 STB/D rate is the optimum critical rate for Well A.

Dry oil production has been the mainstay of the deliberate production strategy pursued thus far for the reservoir under investigation. The numerical simulation study has illustrated that the water-free oil production plateau from Well A can be further extended if the following activities are carefully implemented:

1. using a minimum of 40 ft standoff from the WOC
2. using two perforation intervals with a blank zone between them

Table 10 Production rate selection in light of criteria satisfaction

Production rate (STB/D)	Criterion			
	1	2	3	4
1000	X	X	✓	✓
2000	✓	✓	✓	✓
2500	✓	✓	✓	✓
5000	✓	✓	X	X
10,000	X	✓	X	X

3. recompletion of a new producing zone as soon as a current producing zone turns wet
4. producing the wells away from the water invaded areas
5. aggressive water shutoff program to reduce water cut

9 Conclusions and Recommendations

The goal of the optimum depletion strategy developed in this study is to determine the most suitable production rate that improves the oil recovery, minimizes the water production, delays the water breakthrough time as much as possible, and extends the economic life of the wells. The following pertinent conclusions summarize this study:

1. Several analytical methods for critical rate calculations were examined. None of them yielded the rate that represents the actual well potential. Moreover, two other methods were used to calculate the expected water breakthrough time into Well A. The calculated times were considerably longer than the actual water breakthrough time of the well.
2. A 3D reservoir simulation model was constructed to obtain the optimal rate that matches the historical data, delays the water breakthrough time, and achieves maximum cumulative oil production. A production rate of 2500 STB/D was found eligible of satisfying these requirements.
3. Using two perforation intervals with a gap between them increases the well life and the overall oil recovery. When the water invades the bottom interval, an isolation operation can be conducted to eliminate the water-source perforations.
4. Water coning behavior and oil recovery are highly sensitive to variations in formation permeability and reservoir anisotropy.
5. The presence of short-radius shale break between the perforations and the WOC increases the cumulative water production and accelerates the water breakthrough time when compared with the long-radius shale break, which causes an improvement in the oil recovery, a delay in the water breakthrough time, and a reduction in the cumulative water production.

Reservoir simulation investigation should constitute the main endeavor of depletion strategy formulation. Continuous integration of updated field data into the simulation model is the key element in upgrading reserve and efficiently managing and forecasting the dynamic behavior of bottom-water drive reservoirs. Exhaustive well surveillance using leading-edge technology and tools is extremely important to acquire accurate new data essential to update the simulation model. Moreover, oil demand/supply and prices are important dynamic factors that should be concurrently studied to examine their impacts on the depletion strategy, selection of the optimum rate, and overall development of field processing facilities required to handle additional water production in case of increased demand beyond the optimum rate.

Nomenclature

B_o = oil formation volume factor (RB/STB)
CFPR = critical fluid production rate (STB/D)
D = completion interval thickness, ft
F_k = ratio of horizontal to vertical permeability
h_c = standoff from WOC (ft)
h_o = net pay zone thickness (ft)
h_w = water zone thickness (ft)
k = formation permeability (mD)
k_h = horizontal permeability (mD)
k_{radial} = radial permeability (mD)
k_v = vertical permeability (mD)
M = mobility ratio (dimensionless)
MMSTB = million stock tank barrels
P_b = oil saturation pressure (psi)
P_r = average reservoir pressure (psi)
q_c = critical production rate (STB/D)
r_e = reservoir drainage radius (ft)
r_w = wellbore radius (ft)
S_{or} = residual oil saturation (fraction)
S_{wir} = irreducible water saturation (fraction)
t = water breakthrough time (year)
t_D = dimensionless time
$(t_D)_{\text{bt}}$ = dimensionless time at water breakthrough
TDT = thermal decay tool
WC = water cut (fraction)
WOC = water/oil contact
WOR = water/oil ratio
Z = dimensionless cone height

Greek Symbols

μ_o = oil viscosity (cp)
μ_w = formation water viscosity (cp)
ρ_o = oil density (gm/cc)
ρ_w = formation water density (gm/cc)
ϕ = formation porosity (fraction)

Subscripts

b = saturation pressure
bt = breakthrough
c = critical
e = drainage
h = horizontal
o = oil
or = residual oil
v = vertical
w = water
wir = irreducible water

References

[1] Muskat, M., and Wyckoff, R. D., 1935, "An Approximate Theory of Water Coning in Oil Production," Trans. AIME, **114**, pp. 144–161.
[2] Muskat, M., 1947, "The Performance of Bottom Water-Drive Reservoirs," Trans. AIME, **170**, pp. 81–111.
[3] Arthur, M. G., 1944, "Fingering and Coning of Water and Gas in Homogeneous Oil Sand," Trans. AIME, **145**, pp. 184–199.
[4] Meyer, H. I., and Garder, A. O., 1954, "Mechanics of Two Immiscible Fluids in Porous Media," J. Appl. Phys., **25**(11), pp. 1400–1406.
[5] Chaney, P. E., Noble, M. D., Henson, W. L., and Rice, T. D., 1956, "How to Perforate Your Well to Prevent Water and Gas Coning," Oil Gas J., **55**(53), pp. 108–114.
[6] Chierici, G. L., Ciucci, G. M., and Pizzi, G., 1964, "A Systematic Study of Gas and Water Coning by Potentiametric Models," J. Pet. Technol., **16**(8), pp. 923–929.
[7] Meyer, H. I., and Searcy, D. F., 1956, "Analog Study of Water Coning," J. Pet. Technol., **8**(4), pp. 61–64.
[8] Schols, R. S., 1972, "An Empirical Formula for the Critical Oil Production Rates," Erdoel-Erdgas-Z., **88**(1), pp. 6–11.
[9] Henley, D. H., Owens, W. W., and Craig, F. F., 1961, "A Scale-Model Study of Bottom-Water Drives," J. Pet. Technol., **13**(1), pp. 90–98.
[10] Khan, A. R., 1970, "A Scaled Model Study of Water Coning," J. Pet. Technol., **22**(6), pp. 771–776.
[11] Karp, J. C., Lowe, D. K., and Marusov, N., 1962, "Horizontal Barriers for Controlling Water Coning," J. Pet. Technol., **14**(7), pp. 783–790.
[12] Welge, H. J., and Weber, A. G., 1964, "Use of Two-Dimensional Methods for Calculating Well Coning Behavior," SPE J., **4**(4), pp. 345–355.
[13] Blair, P. M., and Weinaug, C. F., 1969, "Solution of Two-Phase Flow Problems Using Implicit Difference Equations," SPE J., **9**(4), pp. 417–424.
[14] Letkeman, J. P., and Ridings, R. L., 1970, "A Numerical Coning Model," SPE J., **10**(4), pp. 418–424.
[15] Chappelear, J. E., and Hirasaki, G. J., 1976, "A Model of Oil-Water Coning for Two-Dimensional, Areal Reservoir Simulation," SPE J., **16**(2), pp. 65–72.
[16] Fisher, W. G., Letkeman, J. P., and Tetreau, E. M., 1975, "The Application of Numerical Coning Models to Optimize Completion and Production Methods to Increase Oil Production in the Bellshill Lake Blairmore Pool," SPE, reprint series, **4a**, pp. 33–39.
[17] Woods, E. G., and Khurana, A. K., 1977, "Pseudofunctions for Water Coning in a Three-Dimensional Reservoir Simulation," SPE J., **17**(4), pp. 251–262.
[18] Trimble, R. H., and McDonald, A. E., 1981, "A Strongly Coupled, Fully Implicit, Three-Dimensional, Three-Phase Well Coning Model," SPE J., **21**(4), pp. 454–458.
[19] Sobocinski, D. P., and Cornelius, A. J., 1965, "A Correlation for Predicting Water Coning Time," J. Pet. Technol., **17**(5), pp. 594–600.
[20] Bournazel, C., and Jeanson, B., 1971, "Fast Water Coning Evaluation

Method," presented at the Annual Fall Meeting, New Orleans, LA, Oct. 3–6, Paper No. SPE 3628.
[21] Kuo, M. C. T., and DesBrisay, C. L., 1983, "A Simplified Method for Water Coning Predictions," presented at the Annual Technical Conference and Exhibition, San Francisco, CA, Oct. 5–8, Paper No. SPE 12067.
[22] Wheatley, M. J., 1985, "An Approximate Theory of Oil/Water Coning," presented at the Annual Technical Conference and Exhibition, Las Vegas, NV, Sept. 22–25, Paper No. SPE 14210.
[23] Piper, L. D., and Gonzalez, F. M., Jr., 1987, "Calculation of the Critical Oil Production Rate and Optimum Completion Interval," presented at the Production Operations Symposium, Oklahoma City, OK, Mar. 8–10, Paper No. SPE 16206.
[24] Hoyland, L. A., Papatzacos, P., and Skjaeveland, S. M., 1989, "Critical Rate for Water Coning: Correlation and Analytical Solution," SPE Reservoir Eng., **4**(4), pp. 495–502.
[25] Abbas, H. H., and Bass, D. M., 1988, "The Critical Production Rate in Water-Coning System," presented at the Permian Basin Oil and Gas Recovery Conference, Midland, TX, Mar. 10–11, Paper No. SPE 17311.
[26] Yang, W., and Wattenbarger, R. A., 1991, "Water Coning Calculations for Vertical and Horizontal Wells," presented at the Annual Technical Conference and Exhibition, Dallas, TX, Oct. 6–9, Paper No. SPE 22931.
[27] Guo, B., and Lee, R. L.-H., 1993, "A Simple Approach to Optimization of Completion Interval in Oil/Water Coning System," SPE Reservoir Eng., **8**(4), pp. 249–255.
[28] Miller, R. T., and Rogers, W. L., 1973, "Performance of Oil Wells in Bottom Water Drive Reservoirs," presented at the Annual Fall Meeting, Sept. 30–Oct. 3, Paper No. SPE 4633.
[29] Blades, D. N., and Stright, D. H., 1975, "Predicting High Volume Lift Performance in Wells Coning Water," J. Can. Pet. Technol., **14**(4), pp. 62–70.
[30] Kossack, C. A., Kleppe, J., and Aasen, T., 1987, "Oil Production from Troll Field: A Comparison of Horizontal and Vertical Well," presented at the Annual Technical Conference and Exhibition, Dallas, TX, Sept. 27–30, Paper No. SPE 16869.
[31] Giger, F. M., 1989, "Analytical Two-Dimensional Models of Water Cresting Before Breakthrough for Horizontal Wells," SPE Reservoir Eng., **4**(4), pp. 409–416.
[32] Lee, S. H., and Tung, W. B., 1990, "General Coning Correlations Based on Mechanistic Studies," presented at the Annual Technical Conference and Exhibition, New Orleans, LA, Sept. 23–26, Paper No. SPE 20742.
[33] Ozkan, E., and Raghavan, R., 1990, "A Breakthrough Time Correlation for Coning Toward Horizontal Wells," presented at the European Petroleum Conference, The Hague, The Netherlands, Oct. 21–24, Paper No. SPE 20964.
[34] Papatzacos, P., Herring, T. R., Martinsen, R., and Skjaeveland, S. M., 1991, "Cone Breakthrough Time for Horizontal Wells," SPE Reservoir Eng., **6**(3), pp. 311–318.
[35] Consonni, P., Thiele, M. R., Palagi, C. L., and Aziz, K., 1993, "Flexible Gridding Techniques for Coning Studies in Vertical and Horizontal Wells," presented at the Middle East Oil Technical Conference and Exhibition, Manama, Bahrain, Apr. 3–6, Paper No. SPE 25563.
[36] Menouar, H. K., and Hakim, A. A., 1995, "Water Coning and Critical Rates in Vertical and Horizontal Wells," presented at the Middle East Oil Show, Manama, Bahrain, Mar. 11–14, Paper No. SPE 29877.
[37] Recham, R., and Osisanya, S. O., 2000, "Effects of Water Coning on the Performance of Vertical and Horizontal Wells—A Reservoir Simulation Study of Hassi R'mel Field, Algeria," presented at the International Conference on Horizontal Well Technology, Alberta, Canada, Nov. 6–8, Paper No. SPE/Pet. Soc. CIM 65506.
[38] Joshi, S. D., 1991, *Horizontal Well Technology*, PennWell, Tulsa, OK.
[39] Siddiqi, S. S., and Wojtanowicz, A. K., 2002, "A Study of Water Coning Control in Oil Wells by Injected or Natural Flow Barriers Using Scaled Physical Model and Numerical Simulator," presented at the Annual Technical Conference and Exhibition, San Antonio, TX, Sept. 29–Oct. 2, Paper No. SPE 77415.
[40] Inikori, S. O., Wojtanowicz, A. K., and Siddiqi, S. S., 2002, "Water Control in Oil Wells With Downhole Oil-Free Water Drainage and Disposal," presented at the Annual Technical Conference and Exhibition, San Antonio, TX, Sept. 29–Oct. 2, Paper No. SPE 77559.
[41] Hernandez, J. C., and Wojtanowicz, A. K., 2006, "Effect of Anisotropy on Water Invasion in Edge-Water Drive Reservoirs," presented at the Canadian International Petroleum Conference, Calgary, Canada, Jun. 13–15, Paper No. CIPC 2006-199.
[42] Hernandez, J. C., and Wojtanowicz, A. K., 2007, "Optimum Well Completion Strategies in Reservoirs With Bottom and Edge Water Invasion," presented at the Canadian International Petroleum Conference, Calgary, Canada, Jun. 12–14, Paper No. CIPC 2007-105.

Effect of Thermal Modulation on the Onset of Electrothermoconvection in a Dielectric Fluid Saturated Porous Medium

N. Rudraiah
National Research Institute for Applied Mathematics,
492/G, 7th Cross, 7th Block (West),
Jayanagar,
Bangalore 560 070, Karnataka, India;
Department of Mathematics,
UGC Centre for Advanced Studies in Fluid Mechanics,
Central College Campus,
Bangalore University,
Bangalore 560 001, Karnataka, India
e-mail: rudraiahn@hotmail.com

M. S. Gayathri
Department of Mathematics,
BMS College of Engineering,
Basavanagudi, Bangalore 19, Karnataka, India
e-mail: gayathrinaren@gmail.com

An electroconvection in a horizontal dielectric fluid saturated with a densely packed porous layer is investigated under the simultaneous action of vertical electric field and vertical temperature gradient when the walls of the layer are subjected to time periodic temperature modulation. The dielectric constant is assumed to be a linear function of temperature. A regular perturbation method based on small amplitude of applied temperature field is used to compute the critical values of Rayleigh number and wave number. The shift in the critical Rayleigh number is calculated as a function of frequency of modulation, electric Rayleigh number, Prandtl number, and Darcy number, and their effects on the critical Rayleigh number are discussed. The situations which are favorable for the design of artificial organs without the side effect of hemolysis are explained.
[DOI: 10.1115/1.3180709]

Keywords: electroconvection, modulation, perturbation procedure

1 Introduction

The study of electrothermoconvection (ETC) in a porous medium is of practical importance in many fields such as material science processing, chemical engineering, geothermal activities, oil recovery techniques, purification of ground water pollution, and biomechanics of the design of artificial organs. The theoretical model developed here is of importance to overcome or at least to reduce the side effects like hemolysis (the loss of hemoglobin from red blood cell (RBC), i.e., erythrocytes) caused by artificial organs in biomechanics manufactured by metals. Such organs will produce either high or low stresses due to either rough or smooth surfaces. These stresses produce a force, which drives the RBCs in the blood to a particular region in the arteries leading to bursting of RBC releasing hemoglobin. This loss of hemoglobin due to bursting of RBC is a disease called hemolysis. The experiments of Christopherson and Dowson [1] support this. The ETC in the presence of electric field studied in this paper will help to manufacture artificial organs using dielectric materials like titanium, which prevents the side effect of hemolysis. The physical process involved in the manufacture of artificial organs by solidifying a dielectric alloy having poor electric permittivity ε, which is a function of temperature, is as follows. The solidification caused by cooling from below and heating from above produces the variation in ε with temperature, which in turn produces a dipole by shifting bound charges from the nuclei. This dipole produces polarization. The rate of change in polarization is the current called piezoelectric current. This dipole together with charge density also produces an electric force. The piezoelectric current acts as sensing and the electric force acts as actuation, which are the two properties that a material needs to be a smart material. Further, the solidification process of dielectric fluid produces a mushy layer called dendrites, which is a mixture of solid and fluid phases. The solid crystals are of the nature of nanocrystals, which are uniformly placed, and the experiments of Sri Rammurthy and Arunachalam [2] supports this. The mushy layer can be regarded as a dielectric fluid saturated porous layer. In other words, this process of solidification produces a smart material of nanostructure, which can be used to produce efficient artificial organs with maximum efficiency and minimum weight. In these practical applications naturally occurring phenomena are usually unsteady because of the periodicity of the principal driving forces, which find their origin in transient heating or cooling at the boundaries. More specifically, if heat is introduced slowly, the basic temperature gradient is uniform and convection usually manifests in the form of rolls, and a number of studies on this in the absence of electric field [3–7] or in the presence of electric field [8–11] are available. If heat is introduced rapidly, the basic temperature gradient is nonuniform, being a function of position and time, and the convection may manifest in the form of columnar rolls. The effect of a nonuniform basic temperature gradient on the onset of convection in horizontal fluid layers [12–14] and in porous layers [15–17] was investigated in the absence of electric field and showed that a nonuniform temperature gradient controls (i.e., either augments or suppresses) convection (see Refs. [18,19]).

Although Gross and co-worker [20,21] performed some preliminary experiments in a horizontal dielectric fluid layer, it seems that the mechanism of the phenomenon was not yet established theoretically. Also, the effect of general nonuniform temperature gradient, depending on both position and time, in the presence of an electric field, was not given any attention in literature to our knowledge, although it is a natural occurrence in many practical problems cited above. In this paper we are mainly concern with the onset of convection of an equilibrium state in a dielectric fluid saturated porous medium because of the nature of organs like cartilage, endothelium, and so on. This equilibrium state may be stable or unstable to infinitesimal disturbances depending on the behavior of the system. The basic flow is unstable if the disturbances grow over each modulation cycle and is stable if they decay over each cycle. It is said to be neutrally stable if it experiences neither net growth nor net decay.

A linear stability analysis of small amplitude temperature modulation is performed by Venezian [12]. He established that the

Manuscript received August 27, 2008; final manuscript received March 12, 2009; published online July 31, 2009. Review conducted by Kambiz Vafai.

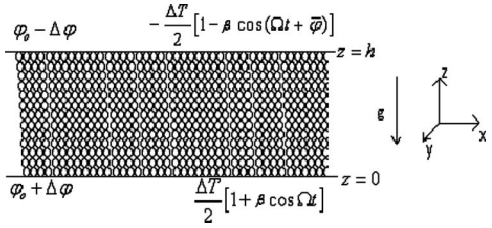

Fig. 1 Physical configuration

onset of convection can be delayed or advanced by the out-of-phase or in-phase modulation, respectively, of the boundary temperatures as compared with the unmodulated system. In particular, he found that at low frequencies the equilibrium state becomes unstable. A problem of low frequency modulation of thermal convection was investigated by Rosenblat and Herbert [13]. They obtained the asymptotic solution with arbitrary amplitude ratio and made comparison with the known experimental results. Rosenblat and Tanaka [22] studied the effect of thermal modulation on the onset of Rayleigh–Benard convection when the temperature gradient has both steady and time-periodic components. They found that, in general, there is an enhancement of the critical value of suitably defined Rayleigh number.

Finucane and Kelly [14] performed both theoretical and experimental investigations of the thermal modulation in a horizontal fluid layer. A convective analysis of the flow indicates that the linear assumption is valid at low frequencies of modulation. They also studied the nonlinear analysis using the same assumption with free boundary conditions and verified the results by conducting an experiment. They found, both experimentally and theoretically, that at low frequencies the modulation is destabilizing while stabilizing at high frequencies. A weak nonlinear stability analysis of thermal modulation was performed by Roppo et al. [23]. They also reported that at low frequencies the modulation is destabilizing and stabilizing at high frequencies. Further, Schmitt and Lucke [24], Or and co-worker [25,26], and Li [27] also investigated the effect of modulation on the thermal convection in a horizontal fluid layer. On the other hand, the studies related to the effect of thermal modulation on the onset of electroconvection in a dielectric fluid saturated porous medium have not received much attention in spite of their many applications cited above, and its study is the main objective of this paper. In particular, we try to investigate how the combined effect of nonuniform thermal field and a uniform electric field would influence electrothermoconvection arising from thermal perturbations in a dielectric fluid saturated porous layer.

2 Mathematical Formulation

We consider a horizontal layer of a dielectric fluid saturated densely packed porous medium of thickness h (see Fig. 1). The wall temperatures are externally imposed and are taken as

$$T = \frac{\Delta T}{2}[1 + \beta\cos\Omega t] \quad \text{at } z = 0 \tag{1}$$

$$T = -\frac{\Delta T}{2}[1 - \beta\cos(\Omega t + \bar{\varphi})] \quad \text{at } z = h \tag{2}$$

where β is the small amplitude of the thermal modulation, Ω is the frequency, and $\bar{\varphi}$ is the phase angle. The time dependent parts denote the modulation imposed on the adverse thermal gradient caused by the temperatures $\Delta T/2$ and $-\Delta T/2$ at the lower and upper walls, respectively. The lower wall at $z=0$ is embedded with parallel electrodes having an applied uniform voltage $\varphi_o+\Delta\varphi$ and the upper wall at $z=h$ is embedded with parallel electrodes having an applied uniform voltage $\varphi_o-\Delta\varphi$. We assume that the dielectric constant ε of the fluid is a linear function of temperature, the fluid is incompressible, and the porous medium is densely packed. For simplicity, we consider the free-free isothermal boundary conditions at the walls. In other words, the fluid is bounded by stress free nondeformable surface with temperature specified at the boundaries. With the usual assumptions and approximations made in the convection problems in a densely packed porous medium saturated with Boussinesq incompressible dielectric fluid, the governing equations are the conservation of mass

$$\nabla\cdot\boldsymbol{q} = 0 \tag{3}$$

the conservation of momentum

$$\delta^{-1}\frac{\partial\boldsymbol{q}}{\partial t} + \delta^{-2}(\boldsymbol{q}\cdot\nabla)\boldsymbol{q} = -\nabla P + \frac{\rho}{\rho_0}\boldsymbol{g} - \frac{\nu}{K}\boldsymbol{q} - \frac{E^2}{2\rho_0}\nabla\varepsilon \tag{4}$$

and the conservation of energy

$$A\frac{\partial T}{\partial t} + (\boldsymbol{q}\cdot\nabla)T = \chi\nabla^2 T \tag{5}$$

where P and A are defined in the Appendix and $\boldsymbol{q}$ is given in the Nomenclature.

Equation (4) is the modified Lapwood [28] equation where modification means the addition of the last term on the right hand side of Eq. (4).

Following Roberts [8], since the fluid is dielectric, we assume that there are no free charges. Further there are no induced and applied magnetic fields. The relevant Maxwell equations are

$$\nabla\times\boldsymbol{E} = 0 \quad \text{or} \quad \boldsymbol{E} = -\nabla\varphi \tag{6}$$

$$\nabla\cdot(\varepsilon\boldsymbol{E}) = 0 \tag{7}$$

$$\varepsilon = \varepsilon_m(1 + \eta T) \tag{8}$$

$$\rho = \rho_0(1 - \alpha T) \tag{9}$$

The above equations admit an equilibrium, which is the basic solution in which

$$\boldsymbol{q} = 0, \quad T = T_b(z,t), \quad \varphi = \varphi_b(z), \quad \boldsymbol{E} = E_b(z), \quad \text{and} \quad \varepsilon = \varepsilon_b(z,t)$$

where the quantities with suffix b represent the basic state and they satisfy the equations

$$-\nabla P_b + \frac{\rho_b}{\rho_0}\boldsymbol{g} - \frac{{E_b}^2}{2\rho_0}\nabla\varepsilon_b = 0 \tag{10}$$

$$A\frac{\partial T_b}{\partial t} = \chi\nabla^2 T_b \tag{11}$$

$$\nabla\cdot(\varepsilon_b\boldsymbol{E}_b) = 0 \tag{12}$$

$$\varepsilon_b = \varepsilon_m(1 + \eta T_b) \tag{13}$$

The solution of Eq. (11), subject to the boundary conditions (1) and (2), consists of both steady and oscillating parts and is given by

$$T_b = \frac{\Delta T}{2h}(h - 2z) + \bar{\varepsilon}\,\mathrm{Re}\{[a(\lambda)e^{\lambda z/h} + a(-\lambda)e^{-\lambda z/h}]e^{-i\Omega t}\} \tag{14}$$

where

$$a(\lambda) = \frac{\Delta T}{2}\frac{e^{-i\bar{\varphi}} - e^{-\lambda}}{e^{\lambda} - e^{-\lambda}}, \quad \lambda = (1-i)\left(\frac{A\Omega h^2}{2\chi}\right)^{1/2} \tag{15}$$

and Re stands for the real part.

Also Eq. (13) gives

$$\varepsilon_b \approx \varepsilon_m\left(1 - \frac{\Delta T}{h}\eta z\right) \tag{16}$$

Using $E_b=-\nabla\varphi_b$ in Eq. (12) and solving the resulting equation, we get the solution for φ_b in the form

$$\varphi_b = -\frac{2\Delta\varphi}{(1+\eta\Delta T/2)}\frac{z}{h} - \frac{\eta\Delta T\Delta\varphi}{(1+\eta\Delta T/2)}\frac{z^2}{h^2} + \varphi_o + \Delta\varphi \tag{17}$$

$$\therefore \quad E_b = \frac{2\Delta\varphi}{h}\left(1+\frac{\Delta T}{h}\eta z\right) \tag{18}$$

We now superimpose the infinitesimal perturbations on the basic state of the form

$$\boldsymbol{q} = \boldsymbol{q}' = (u',v',w'), \quad P = P_b + P', \quad T = T_b + T', \quad \varepsilon = \varepsilon_b + \varepsilon'$$
$$\varphi = \varphi_b + \varphi', \quad \boldsymbol{E} = \boldsymbol{E}_b + \boldsymbol{E}' \tag{19}$$

where the primes indicate the perturbed quantities.

Substituting Eq. (19) into Eqs. (3)–(9) using the basic state given by Eqs. (10)–(16) and linearizing, we obtain

$$\delta^{-1}\frac{\partial \boldsymbol{q}'}{\partial t} = -\nabla\pi + \alpha T' g\hat{k} - \frac{\nu}{K}\boldsymbol{q}' + B'\hat{k} \tag{20}$$

$$\left(A\frac{\partial}{\partial t} - \chi\nabla^2\right)T' = -\frac{\partial T_b}{\partial z}w' \tag{21}$$

$$\nabla^2\varphi' = \frac{2\Delta\varphi}{\varepsilon_m h}\frac{\partial\varepsilon'}{\partial z} + \frac{\eta\Delta T}{h}\frac{\partial\varphi'}{\partial z} \tag{22}$$

$$\varepsilon' = \varepsilon_m \eta T' \tag{23}$$

where

$$\pi = P' + \frac{\varepsilon' {E_b}^2}{2\rho_0} \tag{24}$$

$$B' = \frac{\Delta T\eta E_b\varepsilon_m}{\rho_0 h}\left(\frac{2\Delta\varphi\varepsilon'}{h\varepsilon_m} - \frac{\partial\varphi'}{\partial z}\right) \tag{25}$$

Following Roberts [8], we assume $\eta\Delta T \ll 1$. Accordingly, we discard any term involving $\eta\Delta T$ compared with a similar terms in the absence of that factor. For example, we neglect the last term in Eq. (22) in comparison with the term $\nabla^2\varphi'$ on the left since their ratio is of order $\eta\Delta T \ll 1$. Under this approximation Eq. (22), using Eq. (23), becomes

$$\nabla^2\varphi' = \frac{2\eta\Delta\varphi}{h}\frac{\partial T'}{\partial z} \tag{26}$$

and Eq. (25) becomes

$$B' = \frac{2\eta\varepsilon_m\Delta T\Delta\varphi}{\rho_0 h^2}\left(\frac{2\eta\Delta\varphi}{h}T' - \frac{\partial\varphi'}{\partial z}\right) \tag{27}$$

From Eq. (27), we get

$$\nabla^2 B' = \frac{4\eta^2\varepsilon_m\Delta T(\Delta\varphi)^2}{\rho_0 h^3}{\nabla_H}^2 T' \tag{28}$$

where

$${\nabla_H}^2 = \frac{\partial^2}{\partial x^2} + \frac{\partial^2}{\partial y^2}$$

To eliminate the pressure from Eq. (20), we take curl twice from Eq. (20) and obtain

$$\left(\frac{1}{\delta}\frac{\partial}{\partial t} + \frac{\nu}{K}\right)\nabla^2 w' = \alpha g{\nabla_H}^2 T' + {\nabla_H}^2 B' \tag{29}$$

Substituting Eqs. (21) and (28) into Eq. (29), we obtain the following equation for the vertical component of velocity:

$$\left[\left(\frac{1}{\delta}\frac{\partial}{\partial t} + \frac{\nu}{K}\right)\left(A\frac{\partial}{\partial t} - \chi\nabla^2\right)\nabla^4 + \alpha g\nabla^2\left(\frac{\partial T_b}{\partial z}{\nabla_H}^2\right)\right]w'$$
$$= -\frac{4\eta^2\varepsilon_m\Delta T(\Delta\varphi)^2}{\rho_0 h^3}\frac{\partial T_b}{\partial z}{\nabla_H}^4 w' \tag{30}$$

satisfying the boundary conditions

$$w' = \frac{\partial^2 w'}{\partial z^2} = T' = 0 \quad \text{at } z = 0,h \tag{31}$$

Equation (30) is made dimensionless using the transformations

$$(x^*,y^*,z^*) = \frac{1}{h}(x,y,z), \quad w^* = \frac{w'}{\chi/h}, \quad t^* = \frac{t}{Ah^2/\chi}, \quad \omega = \frac{\Omega}{\chi/Ah^2} \tag{32}$$

and we obtain (after dropping asterisks $*$)

$$\left[\left(\frac{1}{\delta A}\frac{1}{\mathrm{P}_r}\frac{\partial}{\partial t} + \frac{1}{\mathrm{D}_a}\right)\left(\frac{\partial}{\partial t} - \nabla^2\right)\nabla^4 + \mathrm{R}_a\ \nabla^2((-1+\bar{\varepsilon}f){\nabla_H}^2)\right]w$$
$$= -\mathrm{R}_e(-1+\bar{\varepsilon}f){\nabla_H}^4 w \tag{33}$$

$$f = \mathrm{Re}\{[A(\lambda)e^{\lambda z} + A(-\lambda)e^{-\lambda z}]e^{-i\omega t}\} \tag{34}$$

The boundary conditions (31) can also be made dimensionless using the scales given by Eq. (32) and using $\partial^4 w'/\partial z^4 = 0$. If w' and T' are zero, we obtain

$$w = \frac{\partial^2 w}{\partial z^2} = \frac{\partial^4 w}{\partial z^4} = 0 \quad \text{at } z = 0,1 \tag{35}$$

If the horizontal dependence of w in Eq. (33) is assumed to be of the form $e^{i(k_x x + k_y y)}$, where k_x and k_y are the horizontal wave numbers, then w takes the following form:

$$w = W(z,t)e^{i(k_x x + k_y y)} \tag{36}$$

It follows that

$${\nabla_H}^2 w = -k^2 W$$

where $k^2 = {k_x}^2 + {k_y}^2$ and ${\nabla_H}^2$ is as defined in Eq. (28).

Hence Eqs. (33) and (35), respectively, become

$$\left[\left(\frac{1}{\delta A}\frac{1}{\mathrm{P}_r}\frac{\partial}{\partial t} + \frac{1}{\mathrm{D}_a}\right)\left(\frac{\partial}{\partial t} - (D^2-k^2)\right)(D^2-k^2)^2\right.$$
$$\left. - \mathrm{R}_a\ k^2(D^2-k^2)(-1+\bar{\varepsilon}f)\right]W$$
$$= -\mathrm{R}_e\ k^4(-1+\bar{\varepsilon}f)W \tag{37}$$

$$W = \frac{\partial^2 W}{\partial z^2} = \frac{\partial^4 W}{\partial z^4} = 0 \quad \text{at } z = 0,1 \tag{38}$$

where the dimensionless quantities are given in the Appendix. To obtain an expression for R_a in Eq. (37), we use the following regular perturbation procedure.

3 Regular Perturbation Procedure With Small Amplitude Approximation

We seek the eigenfunctions W and eigenvalues R_a of Eq. (37) for a temperature gradient $\partial T_b/\partial z = (-1+\beta f)$ that departs from the linear temperature gradient $\partial T_b/\partial z = -1$ in modulated system by the quantities of the order β. It follows that the eigenfunctions and eigenvalues of the present problem differ from those associated with the usual Benard problem by the quantities of order β. We therefore assume the solution of Eq. (37) in the form

$$W = W_0 + \beta W_1 + \beta^2 W_2 + \cdots$$
$$\mathrm{R}_a = \mathrm{R}_{ao} + \beta\ \mathrm{R}_{a1} + \beta^2\ \mathrm{R}_{a2} + \cdots \tag{39}$$

Substituting Eq. (39) into Eq. (37) and equating the coefficients of like powers of β, we obtain the following system of equations:

$$LW_0 = 0 \tag{40}$$

$$LW_1 = k^2\ \mathrm{R}_{a0}(D^2 - k^2)(fW_0) - k^2\ \mathrm{R}_{a1}(D^2 - k^2)W_0 - \mathrm{R}_e\ k^4 fW_0 \tag{41}$$

$$LW_2 = k^2\ \mathrm{R}_{a0}(D^2 - k^2)(fW_1) - k^2\ \mathrm{R}_{a2}(D^2 - k^2)W_0 - \mathrm{R}_e\ k^4 fW_1 - k^2\ \mathrm{R}_{a1}(D^2 - k^2)W_1 + k^2\ \mathrm{R}_{a1}(D^2 - k^2)(fW_0) \tag{42}$$

where the operator L is defined in the Appendix.

W_0, W_1, and W_2 have to be determined using the boundary conditions given by Eq. (38).

The function W_0 is a solution of the problem when $\beta = 0$ and marginally stable solutions for that problem are

$$W_0^{(n)} = \sin n\pi z$$

The corresponding eigenvalues are given by

$$\mathrm{R}_{a0}{}^{(n)} = \frac{(n^2\pi^2 + k^2)^2}{\mathrm{D}_a\ k^2} - \frac{\mathrm{R}_a\ k^2}{(n^2\pi^2 + k^2)}$$

For a fixed value of wave number k, the least eigenvalue occurs at $n = 1$ and is given by

$$\mathrm{R}_{a0} = \frac{(\pi^2 + k^2)^2}{\mathrm{D}_a\ k^2} - \frac{\mathrm{R}_e\ k^2}{(\pi^2 + k^2)} \tag{43}$$

corresponding to $W_0 = \sin \pi z$.

R_{a0} assumes the minimum value R_{a0c} for $k = k_c$, where k_c satisfies the equation

$$(k_c{}^2)^4 + 2\pi^2(k_c^2)^3 - \mathrm{R}_e\ \mathrm{D}_a\ \pi^2(k_c^2)^2 - 2\pi^6 k_c^2 - \pi^8 = 0 \tag{44}$$

We observe that, in the absence of electric field, i.e., when $\mathrm{R}_e = 0$, Eqs. (43) and (44) yield the values $\mathrm{R}_{a0c} = 4\pi^2$ and $k_c = \pi$, which are the classical results of Lapwood [28] for convection in the porous layer. Equation (41) for W_1 now takes the form

$$LW_1 = k^2\ \mathrm{R}_{a0}(D^2 - k^2)(f \sin \pi z) + \mathrm{R}_{a1}\ k^2(\pi^2 + k^2)\sin \pi z - \mathrm{R}_a\ k^4 f \sin \pi z \tag{45}$$

The solubility condition requires that the time-independent part of the right hand side of Eq. (45) should be orthogonal to $\sin \pi z$. Since f varies sinusoidally in time, the only steady term is $\mathrm{R}_{a1}\ k^2(\pi^2 + k^2)\sin \pi z$ so that R_{a1} is zero. It follows that the all odd coefficients, i.e., $\mathrm{R}_{a3}, \mathrm{R}_{a5}, \ldots$, in Eq. (39) are all zero. Expanding the right hand side of Eq. (45) in a Fourier series of the form

$$e^{\lambda z} \sin m\pi z = \sum_{n=1}^{\infty} g_{nm}(\lambda) \sin n\pi z \tag{46}$$

where

$$g_{nm}(\lambda) = -\frac{4nm\pi^2\lambda[1 + (-1)^{n+m+1}e^{\lambda}]}{[\lambda^2 + (n-m)^2\pi^2][\lambda^2 + (n+m)^2\pi^2]} \tag{47}$$

it is convenient to define

$$L(\omega, n) = \left[-\frac{\omega^2}{\delta A\ \mathrm{P}_r}(n^2\pi^2 + k^2)^2 + \frac{(n^2\pi^2 + k^2)^3}{\mathrm{D}_a} - \mathrm{R}_{a0}\ k^2(n^2\pi^2 + k^2) - \mathrm{R}_e\ k^4 \right] - i\omega \left[\frac{(n^2\pi^2 + k^2)^2}{\mathrm{D}_a} + \frac{(n^2\pi^2 + k^2)^3}{\delta A\ \mathrm{P}_r} \right] \tag{48}$$

It follows that $L \sin n\pi z e^{-i\omega t} = L(\omega, n)\sin n\pi z e^{-i\omega t}$.

Now, from Eq. (45), we have

$$LW_1 = -k^2\ \mathrm{Re}\left(\sum_{n=1}^{\infty} [\mathrm{R}_{a0}(n^2\pi^2 + k^2) + \mathrm{R}_a\ k^2] B_n(\lambda) \sin n\pi z e^{-i\omega t} \right) \tag{49}$$

so that

$$W_1 = -k^2\ \mathrm{Re}\left(\sum_{n=1}^{\infty} [\mathrm{R}_{a0}(n^2\pi^2 + k^2) + \mathrm{R}_a\ k^2] \frac{B_n(\lambda)}{L(\omega, n)} \sin n\pi z e^{-i\omega t} \right) \tag{50}$$

where

$$B_n(\lambda) = A(\lambda) g_{n1}(\lambda) + A(-\lambda) g_{n1}(-\lambda) \tag{51}$$

Equation (42) for W_2 takes the form

$$LW_2 = k^2\ \mathrm{R}_{a0}(D^2 - k^2)(fW_1) + \mathrm{R}_{a2}\ k^2(\pi^2 + k^2)\sin \pi z - \mathrm{R}_e\ k^4 fW_1 \tag{52}$$

We shall not require the solution of this equation but merely use it to determine R_{a2}, the first nonzero correction to R_a. The solubility condition requires that the steady part of the right hand side of Eq. (52) should be orthogonal to $\sin \pi z$. Thus

$$\mathrm{R}_{a2} = \frac{-2\ \mathrm{R}_{a0}}{\pi^2 + k^2} \int_0^1 \overline{(D^2 - k^2) fW_1} \sin \pi z dz + \frac{2\ \mathrm{R}_e\ k^2}{\pi^2 + k^2} \int_0^1 \overline{fw_1} \sin \pi z dz \tag{53}$$

where the bar denotes a time average.

Using Eqs. (49) and (50) in Eq. (53), we obtain

$$\mathrm{R}_{a2} = \frac{-k^2}{4(\pi^2 + k^2)} \{\mathrm{R}_{a0}(\pi^2 + k^2) + \mathrm{R}_e\ k^2\} \times \sum_{n=1}^{\infty} \frac{\{\mathrm{R}_{a0}(n^2\pi^2 + k^2) + \mathrm{R}_e\ k^2\} |B_n(\lambda)|^2 [L(\omega, n) + L^*(\omega, n)]}{|L(\omega, n)|^2} \tag{54}$$

The critical value of the Rayleigh number R_a is computed up to $O(\beta^2)$ by evaluating R_{a0} and R_{a2} at $k = k_c$ for the cases where the oscillating temperature field is (a) symmetric, (b) asymmetric, and (c) when only the lower wall temperature is oscillating while the upper wall is held at constant temperature for fixed values of R_e, D_a, and P_r. These critical values are computed for different values of R_e, and the results are depicted in Figs. 2–5.

4 Discussions

The R_{a2} is computed using MATHEMATICA for the following three cases:

(a) When the oscillating temperature field is symmetric, i.e., the wall temperatures are modulated in phase so that $\bar{\varphi} = 0$.

(b) When the field is asymmetric, corresponding to an out-of-phase modulation, $\bar{\varphi} = \pi$.

(c) When only the temperature of the lower wall is modulated while the upper wall being held at a fixed constant temperature. In this case it is convenient to take the wall temperature to be $\Delta T/2[1 + \beta \cos \Omega t]$ at the lower wall and $-\Delta T/2$ at the upper wall. This can be recovered from the equations by setting $\bar{\varphi} = -i\infty$.

The variation in corrected Rayleigh number R_{a2} with frequency modulation ω is depicted in Fig. 2 when the oscillating temperature field is symmetric. From this figure, it is clear that for values of $\omega (\approx 25)$, $-\mathrm{R}_{a2}$ increases to its maximum value and then it

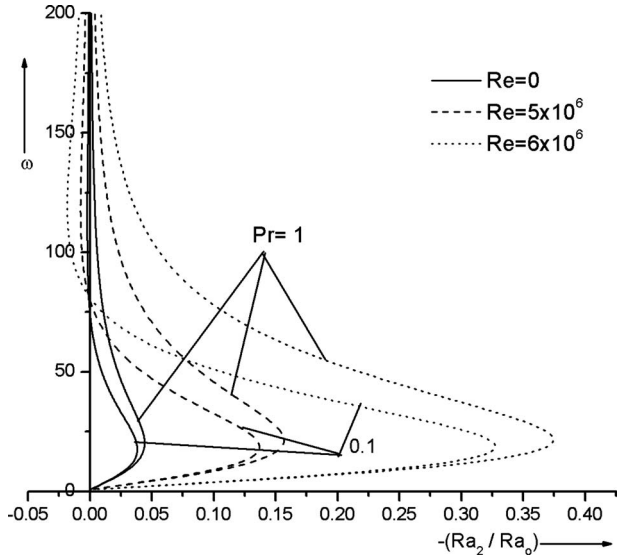

Fig. 2 Variation in R_{a2} with ω for the case of symmetric temperature modulation

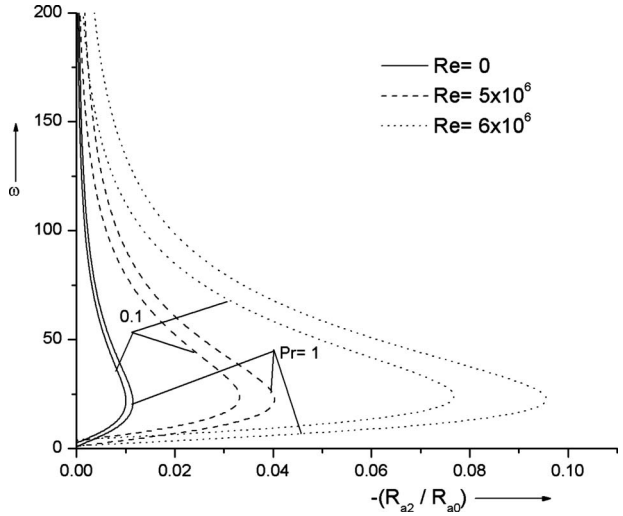

Fig. 4 Variation in R_{a2} with ω for the case of lower wall temperature modulation

decreases with further increase in ω. Also, it is observed that $-R_{a2}$ is always positive in the absence of electric field (i.e., $R_e=0$) but it is positive for other values R_e and ω only up to 75, indicating that the convection sets in at lower values of Rayleigh number than those predicted for the unmodulated system.

Figure 2 also indicates that for a given value of ω, $-R_{a2}$ increases with an increase in electric Rayleigh number R_e, indicating that the effect of electric field on the symmetric modulated porous layer is to suppress ETC implying reduction in moving RBC so that accumulation of RBC in a particular region will be prevented and hence suitable to control hemolysis. However, the effect of R_e disappears for fairly large values of ω in which case $R_{a2}\rightarrow 0$. In particular, for $\omega \geq 75$ there is a shift in the critical Rayleigh number implying that the effect of R_e is to augment the convection. We also observe from this figure that for small frequency ω, $-R_{a2}$ increases with the Prandtl number P_r, resulting in suppression of convection. Therefore, the use of large value of P_r is usually the case in synovial fluid in synovial joints. This is also useful to control hemolysis for the reason explained above.

Figure 3 displays the variation in the correction Rayleigh number $-R_{a2}$ with ω when the time-periodic boundary temperature is asymmetric. From this figure, it is clear that there is a shift in the critical Rayleigh number for small values of ω (from 0 to 50), $-R_{a2}$ is negative for $P_r<1$ and positive for $P_r>1$, indicating that the effect of modulation suppresses convection for $P_r<1$ and augments convection for $P_r>1$. For large values of ω, $-R_{a2}$ becomes positive, indicating that the asymmetric modulation augments convection for moderate and large values of frequency. Thus asymmetric modulation suppresses convection for $P_r<1$ and augments it for $P_r>1$ for small values of frequency ω while it augments convection for moderate and large values of ω. It means that small values of ω are suitable to control hemolysis. This phenomenon is also substantiated from this figure that an increase in the value of electric Rayleigh number R_e increases the magnitude of R_{a2}. At small frequencies, critical Rayleigh number increases $P_r<1$. Hence the effect of electric Rayleigh number is to suppress the convection for $P_r<1$ and hence suitable to control hemolysis.

The effect of electric Rayleigh number on the onset of convection for lower boundary temperature modulation is shown in Fig.

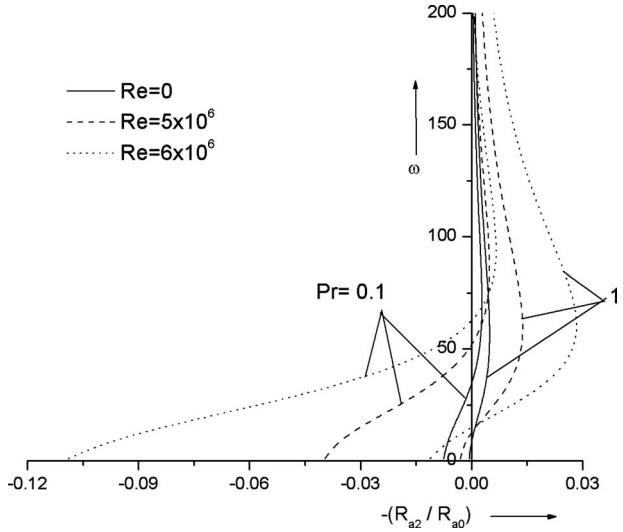

Fig. 3 Variation in R_{a2} with ω for the case of asymmetric temperature modulation

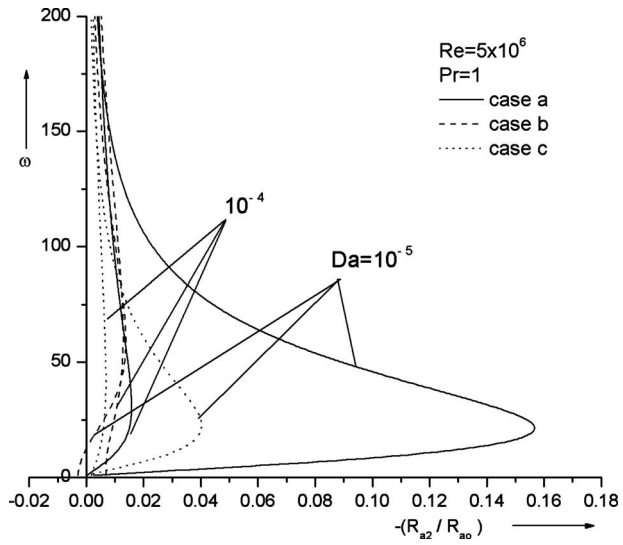

Fig. 5 Variation in R_{a2} with ω for different values of Da

4. In this case, the effect is similar to that of the symmetric temperature case. Even in this case small frequencies and $P_r < 1$ are suitable to design artificial organs using dielectric material like silicon because they prevent the side effect of hemolysis.

Figure 5 shows the variation in R_{a2} with ω for different values of Darcy number D_a. This figure indicates that for small values of ω, as D_a increases, R_{a2} increases for both cases (a) and (c) but decreases in case (b). Hence the effect of D_a is to suppress the onset of convection in cases (a) and (c) and augment the onset of convection in case (b) in the presence of modulation. From this we conclude that cases (a) and (c) are more suitable to design artificial organs using dielectric material in the presence of electric field because they control hemolysis by preventing accumulation of RBCs in a particular region and thus prevent bursting of RBCs.

5 Conclusions

Finally we summarize the following conclusions.

1. The symmetric modulation augments convection at moderate modulation frequencies while its effect disappears for high frequencies and hence is not suitable to design the artificial organs for the reasons explained in Sec. 4.
2. For low frequencies, the asymmetric modulation suppresses convection for $P_r < 1$ and hence suitable to design artificial organs because they control hemolysis by preventing accumulation of RBCs.
3. Symmetric modulation and lower wall temperature modulation cases have similar effects; however, symmetric modulation is more effective.
4. In the case of asymmetric modulation, the electric field suppresses convection for $P_r < 1$ and augments convection for $P_r > 1$. That is, the effect of small P_r and dielectric material in the presence of electric field is suitable to design artificial organs.
5. The effect of both electric Rayleigh number and Darcy number disappears for large frequencies irrespective of the type of thermal modulation and hence not suitable to design artificial organs.
6. The effect of D_a is to suppress the onset of convection in cases (a) and (c) and augment the onset of convection in case (b), as discussed in Sec. 4. Hence the mechanisms of cases (a) and (c) are ideal to design artificial organs because they prevent accumulation of RBC in a particular region, which will not allow bursting of RBC and thus prevent hemolysis.

Acknowledgment

This work was supported by ISRO under the Respond Project No. ISRO/RES/2/338/2007-08. The financial support of ISRO is gratefully acknowledged. M.S.G. is indebted to the management of BMS educational trust, in particular, to the Principal and HOD of BMS College of Engineering for their encouragement to continue the research work.

Nomenclature

α = coefficient of thermal expansion
ε = dielectric constant (electric permittivity)
φ = electric potential
R_e = electric Rayleigh number
η = expansion coefficient of electric permittivity
ν = kinematic viscosity
K = permeability of the porous medium
δ = porosity
P_r = Prandtl number
R_a = Rayleigh number
A = specific heat ratio
χ = thermal diffusivity
t = time
$\boldsymbol{q}$ = velocity

Appendix

$$P = \frac{p}{\rho_0} - E^2\frac{\partial \varepsilon}{\partial \rho}, \quad A = \frac{(\rho C_p)_m}{(\rho C_p)_f}, \quad D_a = \frac{K}{h^2}$$

$$R_a = \frac{\alpha g \Delta T h^3}{\nu\chi}, \quad R_e = \frac{4\Delta T^2 \eta^2 \varepsilon_m (\Delta\varphi)^2}{\rho_0 \nu\chi}$$

$$P_r = \frac{\nu}{\chi}, \quad A(\lambda) = \frac{\lambda}{2}\frac{e^{-i\bar{\varphi}} - e^{-\lambda}}{e^{\lambda} - e^{-\lambda}}, \quad \lambda = (1-i)(\omega/2)^{1/2}$$

$$L = \left(\frac{1}{\delta A}\frac{\partial}{P_r \partial t} + \frac{1}{D_a}\right)\left(\frac{\partial}{\partial t} - (D^2 - k^2)\right)(D^2 - k^2)^2 + R_{a0}\ k^2(D^2 - k^2) - R_e\ k^4$$

References

[1] Christopherson, D. C., and Dowson, D., 1959, "An Example of Minimum Energy Dissipation of Viscous Flow," Proc. R. Soc. London, Ser. A, **251**, pp. 550–564.
[2] Sri Rammurthy, A. M., and Arunachalam, V. S., 1982, *Eutectic Growth in Space*, S. Ramaseshan and M. K. Tiwari, eds., Indian Academy of Sciences, India, pp. 195–207.
[3] Joseph, D. D., 1976, "Stability of Fluid Motions I & II," *Springer Tracts in Natural Philosophy*, Vol. 28, Springer, New York.
[4] Cheng, P., 1978, "Heat Transfer in Geothermal Systems," *Advances in Heat Transfer*, Vol. 14, Academic Press, New York, pp. 1–105.
[5] Caltagirone, J. P., 1981, "Convection in a Porous Medium," *Convective Transport and Instability Phenomena*, G. Braun, ed., Karlsruhe, Germany, pp. 199–232.
[6] Rudraiah, N., and Balachandra Rao, S., 1982, "Nonlinear Cellular Convection and Heat Transport in a Porous Medium," Appl. Sci. Res., **39**, pp. 21–43.
[7] Rudraiah, N., and Balachandra Rao, S., 1983, "Study of Nonlinear Convection in a Sparsely Packed Porous Medium Using Spectral Analysis," Appl. Sci. Res., **40**(3), pp. 223–245.
[8] Roberts, P. H., 1969, "Electrohydrodynamic Convection," Q. J. Mech. Appl. Math., **22**, pp. 211–220.
[9] Takashima, M., and Aldridge, K. D., 1976, "The Stability of a Horizontal Layer of Dielectric Fluid Under the Simultaneous Action of a Vertical DC Electric Field and Vertical Temperature Gradient," Q. J. Mech. Appl. Math., **29**, pp. 71–87.
[10] Bradley, R., 1978, "Overstable Electroconvective Instabilities," Q. J. Mech. Appl. Math., **31**, pp. 381–390.
[11] Wong, J., and Melcher, J. R., 1969, "Thermally Induced Electroconvection," Phys. Fluids, **12**, pp. 2264–2269.
[12] Venezian, G., 1969, "Effect of Modulation on the Onset of Thermal Convection," J. Fluid Mech., **35**, pp. 243–254.
[13] Rosenblat, S., and Herbert, D. M., 1970, "Low Frequency Modulation of Thermal Instability," J. Fluid Mech., **43**, pp. 385–398.
[14] Finucane, R. G., and Kelly, R. E., 1976, "Onset of Instability in a Fluid Layer Heated Sinusoidaly From Below," Int. J. Heat Mass Transfer, **19**, pp. 71–85.
[15] Nield, D. A., 1975, "The Onset of Transient Convective Instability," J. Fluid Mech., **71**, pp. 441–454.
[16] Rudraiah, N., Kaloni, P. N., and Radhadevi, P. V., 1990, "Effect of Modulation on the Onset of Thermal Convection in a Viscoelastic Fluid-Saturated Sparsely Packed Porous Layer," Can. J. Phys., **68**(2), pp. 214–221.
[17] Rudraiah, N., Veerappa, B., and Balachandra Rao, S., 1980, "Effect of Non-Uniform Thermal Gradinet and Adiabatic Boundaries on Convection in a Porous Media," ASME J. Heat Transfer, **102**(2), pp. 254–260.
[18] Rudraiah, N., Ramachandramurthy, V., and Chandana, O. P., 1985, "Effects of Magnetic Field and Nonuniform Temperature Gradient on Marangoni Convection," Int. J. Heat Mass Transfer, **28**(8), pp. 1621–1624.
[19] Rudraiah, N., and Chandana, O. P., 1985, "Effects of Coriolis Force and Nonuniform Temperature Gradient on Rayleigh Benard Convection," Can. J. Phys., **64**, pp. 90–99.
[20] Gross, M. J., and Porter, J. E., 1966, "Electrically Induced Convection in Dielectric Liquids," Nature (London), **212**, pp. 1343–1345.
[21] Gross, M. J., 1967, *Mantles of the Earth and Terrestrial Planets*, S. K. Runcom, ed., Wiley, New York.
[22] Rosenblat, S., and Tanaka, G. A., 1971, "Modulation of Thermal Convective Instability," Phys. Fluids, **14**, pp. 1319–1322.
[23] Roppo, M. H., Davis, S. H., and Rosenblat, S., 1984, "Benard Convection With Time Periodic Heating," Phys. Fluids, **27**, pp. 796–803.
[24] Schmitt, S., and Lucke, M., 1991, "Amplitude Equation for Modulated Rayleigh Benard Convection," Phys. Rev. A, **44**(8), pp. 4986–5002.

[25] Or, A. C., and Kelly, R. E., 1999, "Time Modulated Convection With Zero Mean Temperature Gradient," Phys. Rev. E, **60**(2), pp. 1741–1747.
[26] Or, A. C., 2001, "Onset Condition of Modulated Rayleigh-Benard at Low Frequency," Phys. Rev. E, **64**, p. 050201.
[27] Li, B. Q., 2001, "Stability of Modulated-Gravity-Induced Thermal Convection in Magnetic Fields," Phys. Rev. E, **63**, p. 041508.
[28] Lapwood, E. R., 1948, "Convection of a Fluid in a Porous Medium," Proc. Cambridge Philos. Soc., **44**, pp. 508–521.

The Use of a Nano- and Microporous Surface Layer to Enhance Boiling in a Plate Heat Exchanger

Richard Furberg[1]
e-mail: richard.furberg@energy.kth.se

Björn Palm

School of Industrial Engineering and Management,
Department of Applied Thermodynamics and Refrigeration,
Royal Institute of Technology,
Stockholm 10044, Sweden

Shanghua Li

Muhammet Toprak

Mamoun Muhammed

School of Information and Communication Technology,
Division of Functional Materials,
Royal Institute of Technology,
Stockholm 10044, Sweden

Presented research is an experimental study of the performance of a standard plate heat exchanger evaporator, both with and without a novel nano- and microporous copper structure, used to enhance the boiling heat transfer mechanism in the refrigerant channel. Various distance frames in the refrigerant channel were also employed to study the influence of the refrigerant mass flux on two-phase flow heat transfer. The tests were conducted at heat fluxes ranging between 4.5 kW/m^2 and 17 kW/m^2 with 134a as refrigerant. Pool boiling tests of the enhancement structure, under similar conditions and at various surface inclination angles, were also performed for reasons of comparison. The plate heat exchanger with the enhancement structure displayed up to ten times enhanced heat transfer coefficient in the refrigerant channel, resulting in an improvement in the overall heat transfer coefficient with over 100%. This significant boiling enhancement is in agreement with previous pool boiling experiments and confirms that the enhancement structure may be used to enhance the performance of plate heat exchangers. A simple superposition model was used to evaluate the results, and it was found that, primarily, the convective boiling mechanism was affected by the distance frames in the standard heat exchanger. On the other hand, with the enhanced boiling structure, variations in hydraulic diameter in the refrigerant channel caused a significant change in the nucleate boiling mechanism, which accounted for the largest effect on the heat transfer performance. [DOI: 10.1115/1.3180702]

Keywords: enhanced boiling, flow boiling, plate heat exchanger, nanostructured, microstructured, 134a

1 Introduction

With the prospects of energy efficiency, miniaturization, product reliability, and the potentially large economic advantages, an extensive research and development effort has been undertaken in the area of enhanced boiling heat transfer over the past couple of decades. Several informative summaries have been published on the topic, such as Refs. [1–3], who all report on the boiling performance of various microscale enhancement structures. The primary industrial usage of these microsized boiling enhancement structures have been in so called shell and tube heat exchangers for large refrigeration applications [4]. At the same time, over the past 20 years, compact plate heat exchanges have replaced traditional shell-and-tube heat exchangers, since the former are more energy and space efficient and are cheaper to produce. Despite this trend, only a few attempts to enhance compact plate heat exchangers with high performing microsized, or smaller, enhancement structures have been reported on.

Hillis and Thomas [5], as part of an evaluation of heat exchangers for a large 40 MW ocean thermal energy conversion (OTEC) pilot plant in Hawaii, tested the performance a small-frame plate heat exchanger with ammonia as refrigerant. The heat exchanger plates featured a 60 deg chevron angle corrugation pattern and were coated in Linde's high-flux surface: a porous aluminum particle layer. Boiling heat transfer coefficients of about 30 kW/m^2/K were recorded at a heat flux of 26 kW/m^2, equivalent to a fivefold improvement compared to an uncoated surface.

Müller-Steinhagen [6] vacuum plasma sprayed a 250 μm thick layer of spherically shaped Inconel 625 particles on to a plate and frame heat exchanger surface. The particles had a diameter of 105–170 μm and enhanced the boiling heat transfer coefficient in R134a with up to 100%.

Matsushima and Uchida [7] tested a brazed plate heat exchanger with a novel pyramidlike structure in R22. The structural features were 1.5 mm in height, hence, not in the microsized region, but the evaporation heat transfer coefficients were estimated to be 1.5–2 times higher than those of regular herringbone-type plates. Longo et al. [8] applied 50–200 μm sized, pyramidlike surface features to a plate heat exchanger with herringbone macroscale corrugation, resulting in a 40% increase in the boiling heat transfer coefficient in R22. This enhancement was larger than the increase in heat transfer area, suggesting a real improvement in the boiling heat transfer mechanism.

Since both of these pyramidlike structures are fabricated through mechanical deformation, the possibilities to control submicron features are small. Hence, without re-entrant cavities and large area enhancements, the boiling enhancement potential of these aforementioned structures is rather limited. Recent developments within nano- and microtechnologies have made possible the creation of well defined three-dimensional connected porous network structures, Davis [9], which, so far, have mainly been used in applications such as catalysis molecular sieves, fuel cells, sorption, and separation [10]. These developments have opened up new possibilities to structure high performing boiling surfaces with well defined micro- and submicron topology, using methods more precise than mechanical deformation.

The importance of nanosized surface structures for the boiling performance of a surface was convincingly shown by Honda et al.

[1]Corresponding author.

Manuscript received September 27, 2008; final manuscript received April 15, 2009; published online July 31, 2009. Review conducted by Kambiz Vafai.

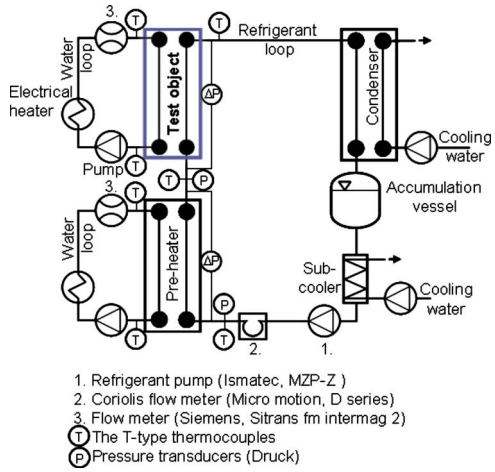

Fig. 1 Experimental set-up for thermal tests of plate heat exchanger

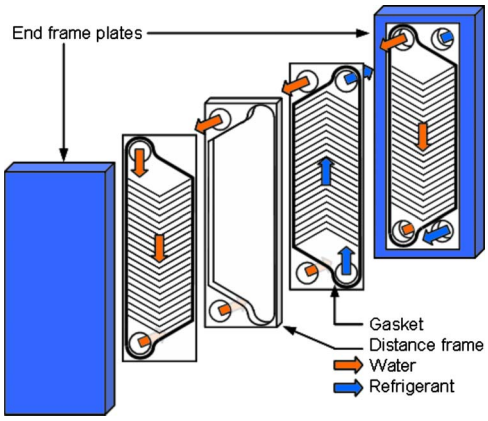

Fig. 2 Plate heat exchanger with gasket seals and distance frame

[11] and Vemuri and Kim [12]. But seemingly exclusively, these newly developed enhancement structures, with controlled nano- and microfeatures, are aimed for small scale cooling of electronics applications.

A novel nano- and microporous structure was recently shown to enhance pool boiling heat transfer in 134a with over one order of magnitude compared to a plain machined copper surface [13]. Presented research is an experimental study of the performance of a plate heat exchanger evaporator with and without this novel enhancement structure applied to the refrigerant channel. The flow boiling tests were conducted in 134a with heat fluxes ranging from 4.5 kW/m^2 to 17 kW/m^2. Various distance frames were also used to widen the refrigerant channel in order to isolate the influence of refrigerant mass flux and thereby gain a better understanding of boiling heat transfer in plate heat exchangers in general and the enhanced surface in particular.

2 Experimental Apparatus and Procedure

The schematics of the experimental test set-up are described in Fig. 1. The refrigerant flow rate in the system was induced by a refrigerant pump and measured with a Coriolis flow meter. The refrigerant inlet quality was controlled by a preheater, and the over all pressure in the system was set by the cooling load in the condenser, which was balanced by the heat input from an electrical heater connected to the water side of the test object. The data acquisition system consisted of data logger, HP 34970A, measuring and collecting all the temperature, pressure, and flow readings and transmitting the data to a PC for further processing and storage.

Test object. As illustrated in Fig. 2, the stainless steel heat exchanger plates, featuring a herringbonelike macrocorrugation pattern with a sinusoidal shape, were assembled between two end frame plates and compressed by tightening bolts. Some important characteristics of the standard stainless steel heat exchanger plates are found in Table 1. Rubber gaskets sealed the channels and directed the fluids into alternate channels. The main advantage of this set-up was that the heat exchanger could easily be reconfigured. Two different distance frames were also used in the refrigerant channel, with a thickness, δ_{frame}, of 5 mm and 10 mm, respectively, to study the influence of the refrigerant mass flux. Hence, six different heat exchanger configurations were tested, as seen in Table 2.

Enhancement structure. The boiling enhancement structure was manufactured on the surface of two herringbone patterned heat exchanger plates, on the part of the plates in contact with the refrigerant. The porous layer took on a red shade and covered the complete sinusoidal shape, as seen in Figs. 3(*a*) and 3(*b*).

The porous surface layer comprised a porous copper wall structure that defined and separated macropores, which were interconnected in the general direction normal to the surface of the substrate. The diameter of the macropores gradually increased with distance from the substrate and had an average top layer diameter of 105 μm and a top pore density of about $75/mm^2$, as seen in Fig. 3(*c*). The thickness of the surface layer measured 250 μm, as seen in Fig. 3(*d*). The porous wall consisted of dendritically shaped structures forming a large surface area and numerous cavities, in the 0.1 to 1 μm range, between its branches. The overall porosity of the surface structure was about 95%, based on the measured thickness and mass of the surface layer and the density of solid copper.

The stainless steel heat exchanger plates were first precoated with a thin copper layer before the porous structure was manufactured on the surface. The porous structure was fabricated with an electrodeposition method, wherein metallic copper nanoparticles were dendritically connected into an ordered microporous structure using hydrogen bubble evolution as a dynamic masking template followed by an annealing process, as further described in Ref. [14]. The manufacturing technique has been shown to provide ample room to control both the micro- and the nanosized features of the surface structure, hence, opening up the possibility

Table 1 Geometrical characteristics of heat exchanger plates

Macrocorrugation pattern	Sinusoidal
Plate material	316 Stainless steel
Plate thermal conductivity, λ_{plate} (W/m/K)	16.3
Fluid flow plate length, L (m)	0.357
Fluid flow plate width, W (m)	0.100
Total heat transfer area, A_{tot} (m^2)	0.032
Surface enlargement factor, ϕ (A_{tot}/A_{proj})	1.15
Corrugation angle, β (deg)	60
Corrugation pitch, P (mm)	10.0
Corrugation depth, B (mm)	2.4
Plate thickness, δ_{plate} (mm)	0.5
Surface roughness (peak height), R_p (μm)	0.55

Table 2 Tested heat exchanger configurations and the abbreviations used

	Distance frame		
	None	5 mm	10 mm
Standard plate	STD	STD+5	STD+10
Enhanced plate	$n\mu P$	$n\mu P$+5	$n\mu P$+10

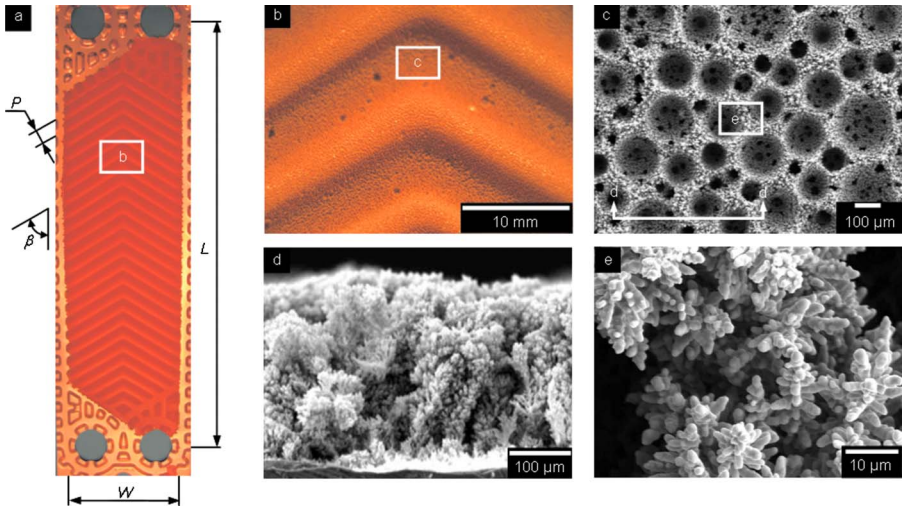

Fig. 3 (***a***) **Heat exchanger plate with enhanced surface structure fabricated on the refrigerant side.** (***b***) **Close-up view of enhanced heat exchanger plate.** (***c***) **and** (***e***) **SEM picture of the enhancement structure.** (***d***) **SEM side-view.**

to change the geometrical dimensions of the structure to suit different refrigerants. The structure may also be applied to various geometries and in fairly narrow gaps.

Test conditions. 134a was used as refrigerant for all tests at pressures varying between 3–4 bars, depending of overall performance of the heat exchanger and the heat flux. Tests were carried out under oil free conditions. The flow direction of the water and the refrigerant was countercurrent. The water side flow rate through the test object corresponded to a temperature drop from 12°C to 7°C. The incoming vapor quality was controlled to 5–15%. Results from preliminary tests showed that difference in inlet quality between 5% and 15% had a negligible effect on the heat transfer coefficient on the refrigerant side. The outgoing vapor quality was controlled with the refrigerant pump to near 100% by decreasing the refrigerant flow until the measured superheat was 0°C.

All the components of the experimental set-up, but the test object itself, were insulated with 10 mm thick foam insulation. The heat flux was varied between 4.5 kW/m^2 and 14 kW/m^2 for the standard plates (higher heat flux could not be tested at the time due to limited cooling capacity) and 4.5 kW/m^2 and 17 kW/m^2 for the enhanced heat exchanger. Each reported value was calculated as an arithmetic mean from 250 data points recorded during steady state conditions for about 15 min.

Data reduction. The overall heat transfer coefficient, U, of the heat exchanger was defined as the ratio between the exchanged heat flow rate, q, and the logarithmic mean temperature difference, $\Delta T_{\ln}$, and the nominal heat transfer area, A_{tot}

$$U = \frac{q}{A_{\text{tot}} \Delta T_{\ln}} \tag{1}$$

where q was calculated from a heat balance on the water side according to

$$q = \dot{m}_w c_{p\_w} (T_{w\_\text{in}} - T_{w\_\text{out}}) \tag{2}$$

where $\dot{m}_w$ is the water mass flow, c_{p_w} is the specific heat capacity of water, and T_{w_in} and T_{w_out} are the in- and outgoing water temperatures, respectively. The logarithmic temperature difference was calculated based on the saturated refrigerant temperature, $T_{\text{sat\_out}}$, at the outlet of the heat exchanger, according to

$$\Delta T_{\ln} = \frac{(T_{w\_\text{in}} - T_{\text{sat\_out}}) - (T_{w\_\text{out}} - T_{\text{sat\_out}})}{\ln\left(\dfrac{T_{w\_\text{in}} - T_{\text{sat\_out}}}{T_{w\_\text{out}} - T_{\text{sat\_out}}}\right)} \tag{3}$$

The overall heat transfer coefficient may be calculated using

$$U = \frac{1}{\dfrac{1}{h_w} + \dfrac{\delta_{\text{plate}}}{\lambda_{\text{plate}}} + \dfrac{1}{h_{\text{ref}}}} \tag{4}$$

where h_w and h_{ref} are the water and refrigerant side heat transfer coefficients, respectively. In order to evaluate the heat transfer performance on the refrigerant side, the heat transfer coefficient on the water side of the plates was first evaluated using a modified Wilson plot method, during which the plates in the heat exchanger were configured to form two channels. Water-to-water tests were carried out where the heat transfer coefficient was kept constant in one channel, while the water flow in the other channel was varied between Reynolds numbers of 94 and 1070.

The general heat transfer correlation for the water channel was assumed to follow the general behavior of the classical Dittus–Boelter correlation [15]

$$\text{Nu}_w = \frac{h_w d_{h\_w}}{\lambda_w} = C_1 \ \text{Re}_w^{\ n_1} \ \text{Pr}_w^{\ 1/3} \tag{5}$$

with the hydraulic diameter of the water channel, d_{h_w}, and the Reynolds number was defined as

$$d_{h\_w} = \frac{2B}{\phi} \tag{6}$$

$$\text{Re}_w = \frac{\dot{V}_w \rho_w d_{h\_w}}{W \cdot B \cdot \mu_w} \tag{7}$$

where $\dot{V}_w$ is the water volume flow. A best fitting procedure was used on the experimental data, and the constants were determined to $C_1 = 0.271$ and $n_1 = 0.668$, with an R-square value of 0.997. The heat balance between the hot and the cold side during the Wilson plot tests was within ±3%.

Uncertainty estimates. An uncertainty analysis, according to Kline and McClintock [16], of the overall heat transfer coefficient in Eq. (1), has been made. The U-value, based on the heat transfer plate surface area A_{tot}, was a function of four independent vari-

Table 3 Uncertainty contribution to the *U*-value from different variables

	STD		$n\mu P+10$	
q'' (kW/m^2)	5	14	5	17
U (kW/m^2/K)	0.8	1.4	1.3	3.4
Volume flows	0.5%	0.5%	0.5%	0.5%
Property data	0.2%	0.2%	0.2%	0.2%
Temperature differences	3.6%	2.9%	4.7%	3.8%
Combined uncertainty	2.6%	2.3%	3.4%	2.7%
Estimated heat gain	5.5%	1.8%	5.6%	1.5%

ables: water volume flow ($\dot{V}$), temperature difference between incoming and outgoing fluids (ΔT), specific heat of water (c_{p_w}), and water density (ρ_w). Table 3 presents the uncertainty of each variable and for two different test cases at low and high heat flux.

The accuracy of the temperature measurement had the major influence on the calculated *U*-value. The uncertainty interval for the temperature difference (ΔT) was estimated to 0.1°C (20:1 odds). Measurements of the enhanced heat exchanger at low heat flux and high flow rates resulted in the lowest temperature differences ΔT and therefore come with the largest overall uncertainty of less than 4%. Ambient heat gain to the heat exchanger during the tests was estimated using natural convection correlations [17] and was between 1% and 6% of the transferred heat. The results presented in this work have not been adjusted for the heat gain.

3 Experimental Results

Overall results. As seen in Fig. 4, the enhanced surface structure in the refrigerant channel improved the overall performance of the heat exchanger, the *U*-value, with 68–108% compared to the standard (STD) configuration. The *U*-value for the $n\mu P+10$ configuration was only 10–20% below the maximum limit, where the heat transfer coefficient on the refrigerant side approaches infinity. With Eqs. (4)–(7), the heat transfer coefficient on the refrigerant side, h_{ref}, was calculated for each test. As seen in Fig. 5, the refrigerant heat transfer coefficient in $n\mu P+10$ was as high as 22 kW/m^2/K at a heat flux of 17 kW/m^2, corresponding to an enhancement effect of up to 10 times compared to STD+10 and about 8 times compared to the STD configuration. This enhancement appears significantly greater than those previously reported for plate heat exchangers with surface enhancements.

In the standard heat exchanger, the thermal resistances on the water and refrigerant sides were comparable, but with the enhancement structure, the thermal resistance was about 4–7 times larger on the water side compared to the refrigerant side. Hence, it

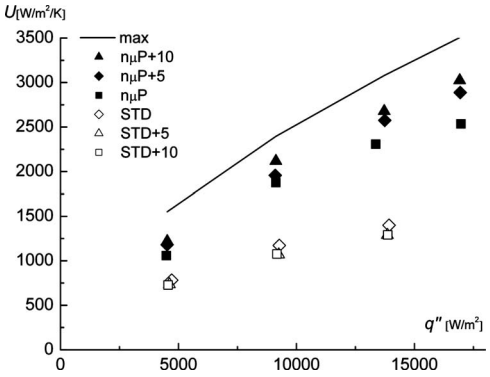

Fig. 4 Overall *U*-value as a function of heat flux for standard and enhanced heat exchangers

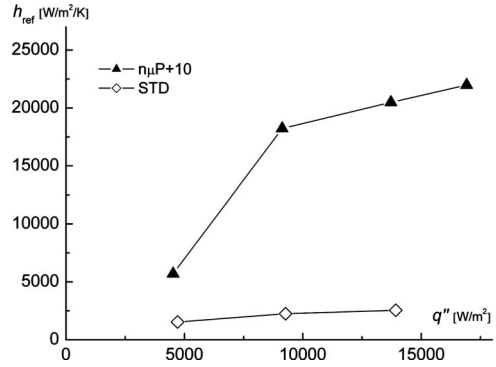

Fig. 5 Heat transfer coefficient on the refrigerant side, h_{ref}, as a function of heat flux for a standard and an enhanced heat exchanger

would be desirable to increase the Reynolds number on the water side in a real application to fully utilize this improvement in boiling heat transfer.

Standard plate heat exchanger. The isolated effect of variations in refrigerant mass flux by the use of distance frames in a plate heat exchanger has not been studied before. It would therefore be worthwhile to comment on some observations regarding the standard plate heat exchanger results. The heat transfer coefficient on the refrigerant side, h_{ref}, for the STD configuration showed 12–17% better performance than the refrigerant channels with the distance frames (STD+5 and STD+10). No significant difference was found between the configurations with the 5 and 10 mm distance frames. Even though there is no clear agreement on how to model the heat transfer in a plate heat exchanger, the general superposition approach, of a convective and a nucleate boiling term, first suggested by Rohsenow [18], made widely popular by Chen [19], and later more generalized by Zhang et al. [20], has worked fairly well for brazed plate heat exchangers, as shown by Palm and Thonon [21]. Considering that the refrigerant was completely evaporated in the heat exchanger, resulting in a low refrigerant mass flux was, ranging from 2 kg/s/m^2 to 22 kg/s/m^2, and that the Thonon criteria [22] suggests that the heat transfer is nucleate boiling dominated, the effects of the convective refrigerant flow were expected to be small. Hence, a simplified superposition model is initially tested, without the flow suppression and enhancement factors that are related to convective effects of the refrigerant flow. The refrigerant side heat transfer coefficient, h_{ref}, can therefore be calculated as the sum of a convective boiling term, h_{cb}, and nucleate boiling term, h_{nb}, according to

$$h_{\text{ref}} = h_{\text{cb}} + h_{\text{nb}} \tag{8}$$

The convective boiling term, h_{cb}, typically characterized by conduction and convection through the liquid film near the plate wall and vaporization at the liquid/vapor interface, can be calculated using the single phase heat transfer correlation in Eq. (5), with the constants, C_I and n_I, obtained for the given plate geometry. Further, the refrigerant Reynolds number, Re_{ref}, was between 99 and 336 during all tests, within the range of Eq. (5). The refrigerant Reynolds number was defined as

$$\text{Re}_{\text{ref}} = \frac{G_{\text{ref}} d_{h\_\text{ref}}}{\mu_{l\_\text{ref}}} \tag{9}$$

where G_{ref}, is the total refrigerant mass flux, calculated as

$$G_{\text{ref}} = \frac{\dot{m}_{\text{ref}}}{W(B + \delta_{\text{frame}})} \tag{10}$$

The nucleate boiling heat transfer coefficient, h_{nb}, is characterized by bubble formation, growth, and motion, taking place in a super-

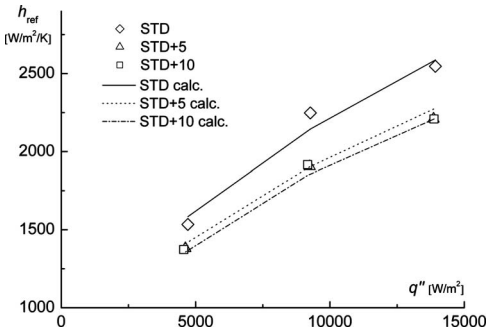

Fig. 6 Measured and calculated heat transfer coefficients on the refrigerant side, h_{ref}, as a function of heat flux standard configurations

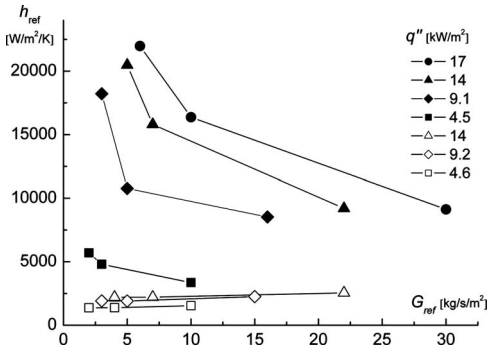

Fig. 8 Heat transfer coefficient on refrigerant side, h_{ref}, as a function of refrigerant mass flux, G_{ref} (filled symbols—$n\mu P$, white symbols—STD)

heated boundary layer and was calculated based on the Cooper [23] correlation

$$h_{nb} = C_2 \cdot p_r^{(0.12-0.2\log_{10} R_P)}(-\log_{10} p_r)^{-0.55} M^{-0.5} q''^{n_b} \quad (11)$$

A best fit iteration results in $C_2 = 5.86$ and the heat flux exponent $n_b = 0.49$, which is in fairly good agreement with other studies, such as Longo and Gasparella [24] and Claesson [25], who also found that the boiling heat transfer coefficient in a brazed plate heat exchanger was a power-law function of the heat flux with an exponent between 0.4 and 0.6. The difference in saturation pressure between data points, accounted for 5% improvement in h_{ref} between the highest (3.3 bars at lowest heat flux) and lowest saturation pressure (2.9 bars at highest heat flux). This is rather insignificant compared to the heat flux contribution to h_{ref} of 95%.

Despite its simplicity, the model captures the small effect of varying refrigerant flow rate remarkably well, as seen in Fig. 6. The convective contribution to the refrigerant side heat transfer, h_{ref}, was on average small; 17%, 8%, and 5% for the STD, STD +5, and STD+10, respectively. On average, the absolute deviation between the calculated and the measured refrigerant side heat transfer coefficient, h_{ref}, was only 2.2%, with a maximum difference of 4.6%. The conclusion is thus that the convective boiling term, h_{cb}, was affected by the introduction of the distance frames and accounted for the change in refrigerant heat transfer coefficient.

Enhanced plate heat exchanger. As seen in Fig. 7, the effect of the distance frames was the opposite with the enhanced plates compared to the standard plates, since the performance was greatly improved with the introduction of distance frames. The heat transfer coefficient on the refrigerant side, h_{ref}, was between 70% and 140% higher with the 10 mm distance frame ($n\mu P$ +10) than with the plates pressed together ($n\mu P$). The frictional pressure drop in the refrigerant channel was not noticeably affected by the porous structure.

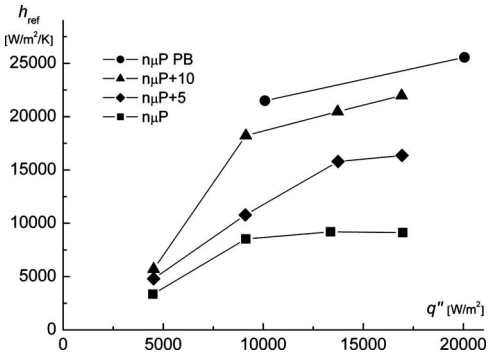

Fig. 7 Heat transfer coefficients on the refrigerant side, h_{ref}, as a function of heat flux for the enhanced configurations including results from pool boiling tests

Results from recent pool boiling experiments of the same nano- and microporous structure (R134a, saturated conditions at 5 bars) at different inclination angles, similar to those of Furberg et al. [26], show good agreement with the $n\mu P+10$ results. The two pool boiling measurement points, included in Fig. 7 and noted $n\mu P$ PB, were recorded with a 90 deg surface inclination angle. The close agreement between these pool and flow boiling results indicates that with the 10 mm distance frame, the boiling mechanism is the same as in pool boiling on the enhanced surface.

As discussed more in depth in Ref. [26], the boiling enhancement effect that is caused by the porous structure may be attributed to certain surface features: The pores form channels that penetrate the whole structure and are directed normally to the surface with increasing diameters. The high density and the shape of these channels ensure that the vapor produced, during evaporation inside the structure, can quickly be released with low resistance from the dendritic structure. Also, the high porosity of the interconnected network effectively traps vapor and facilities liquid transport within the structure and allow for communication between active nucleation sites. Finally, the dendritically shaped wall structure, with its large surface area, might facilitate formations of thin liquid films with high evaporation rate and long three-phase-lines with high heat transfer rates.

As seen in Fig. 8 the increase in mass flux seemed to have had a relatively limited impact on the standard plates, but a significant effect on the enhanced plates. The refrigerant mass flux was equivalent to a liquid refrigerant velocity of less than 20 mm/s, which was notably lower than the expected bubble rise velocity of at least 100 mm/s in an infinite pool of R134a, according to a visualization study by Maneri and Vassallo [27]. The conditions were therefore similar to pool boiling, especially for the cases where the distance frames where employed. Hence, it is probable that, for the enhanced plates, it is not the convective suppression effect of the refrigerant liquid mass flux per se that accounted for the decreased h_{ref} with increased G_{ref}, but rather the confining effect of the plate wall.

Figure 9 has therefore been added to illustrate how the heat transfer mechanism in the enhancement structure was positively affected by an increase in the hydraulic diameter of the refrigerant channel, d_{h_ref}. The effect is more pronounced at higher heat fluxes. The standard plate configurations, also included in the figure, exhibited a negative relationship to an increased hydraulic diameter, even though the absolute magnitude of the effect was much smaller than for the enhanced plates. It may also be observed from Figs. 7 and 8 how the generally positive heat flux dependence of the refrigerant heat transfer coefficient, h_{ref}, disappeared for the enhanced plates with the smallest refrigerant hy-

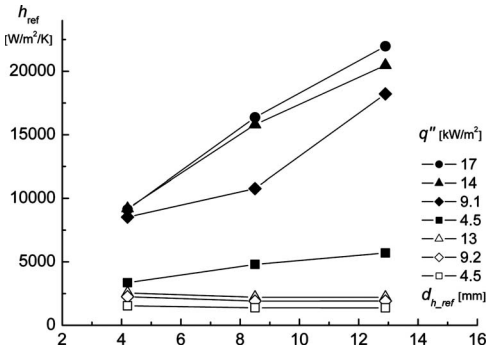

Fig. 9 Heat transfer coefficient on refrigerant side, h_{ref}, as a function of the hydraulic diameter of the refrigerant channel, d_{h_ref} (filled symbols—$n\mu P$, white symbols—STD)

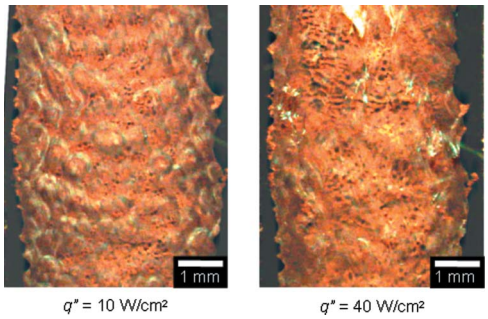

Fig. 11 Pictures from enhanced evaporator channel (d_h =2.5 mm) in a thermosyphon loop at various heat and refrigerant mass flux

draulic diameter, d_{h_ref}, at heat fluxes above 4.5 kW/m^2. This indicates that the boiling mechanism was inhibited at high heat fluxes and smaller d_{h_ref}.

This behavior of the nano- and microporous structure has been observed previously in flow boiling experiments in a thermosyphon loop. In these experiments, as reported in Ref. [28], the use of a high speed video camera showed a reduction in the number of nucleation sites at increasing heat flux for the enhancement structure, while the nucleation site density appeared to be rather constant for a smooth copper surface. Figure 10 shows how the heat transfer coefficient changed with the heat flux for the enhanced ($n\mu P$-evap.) and the smooth (s-evap.) evaporators in the thermosyphon experiments. The figure also includes pool boiling results from a surface enhanced with the nano- and microporous structure at a 90 deg surface inclination angle. The performance of the enhanced evaporator ($n\mu P$ evap.) started to decline rapidly with heat fluxes above 20 W/cm^2, while the heat transfer coefficient of the smooth surface (smooth-evap.) continued to increase with heat flux up to about 30 W/cm^2. The rapid decline of the heat transfer coefficient for the enhanced evaporator, eventually led to a critical heat flux (CHF), which is characterized by formations of a vapor film on the surface. CHF was about 20% lower for the enhanced evaporator than for the smooth one. Pool boiling experiments of the enhancement structure did not show this rapid decline of the heat transfer coefficient at corresponding heat fluxes. Apparently, the confinement imposed on the gas/bubble transport by the channel walls triggered an early onset of CHF (Fig. 11).

Hence, for the plate heat exchanger case, with an outgoing vapor quality of 100%, the large effect that the hydraulic diameter had on the heat transfer performance of the enhanced plates could be caused by the channel walls confining rising vapor bubbles. These confined bubbles may disrupt the otherwise highly active nucleation sites in the porous layer, causing temporary dry out of the dendritic structure. This could, locally within the dendritic structure, be a rather similar mechanism to CHF.

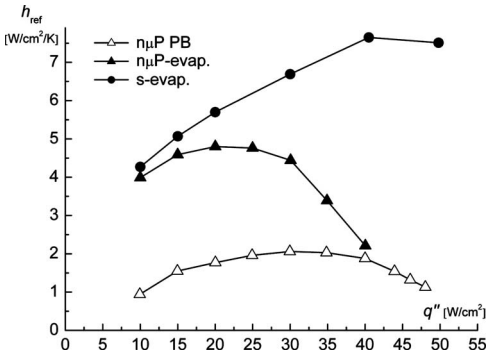

Fig. 10 Heat transfer coefficient versus heat flux, q'', for evaporator and pool boiling tests with the enhancement structure

With these observations in mind, it is clear that the model developed to predict the heat transfer in the standard plate heat exchanger can not be directly used for the enhanced configurations. Cooper's correlation did not satisfactory capture the nucleate boiling performance of the enhanced boiling surface, $h_{nb\_n\mu P}$, which rather looked like a logarithmic function, such as

$$h_{nb\_n\mu P} = C_3 \cdot \ln(q'') - C_4 \tag{12}$$

The porous enhancement structure can be expected to alter the conduction and convection through the liquid film near the plate wall to the extent that the correlation, obtained from single phase tests of standard plates, Eq. (5), is no longer useful to calculate the convective boiling term, h_{cb}. This term, h_{cb}, should also be very small relative the enhanced nucleate boiling term and was therefore excluded in the suggested correlation for the refrigerant side heat transfer coefficient of the enhanced structure, $h_{ref\_n\mu P}$.

Further, a suppression multiplier, S, was introduced to incorporate the boiling suppression effect that was observed for smaller refrigerant channel diameters, according to

$$h_{ref\_n\mu P} = S \cdot h_{nb\_n\mu P} \tag{13}$$

Since the bubble confinement effect was thought to cause the suppression of the boiling mechanism in the porous structure, the suppression multiplier was chosen as a function of the dimensionless confinement number Co, according to

$$S = \frac{C_5}{\mathrm{Co}^{0.7}} \tag{14}$$

where the confinement number was defined as

$$\mathrm{Co} = \frac{\sqrt{\sigma/(g(\rho_l - \rho_g))}}{d_{h\_ref}} \tag{15}$$

Kew and Cornwell [29] introduced the dimensionless confinement number, Co, and suggested that with Co$>$0.5, a bubble is confined in a small channel, which could affect the dominant heat transfer mechanism. Even though the average confinement number is less than 0.5 for the three different configurations, local confinement effects are probably present in the channel due to the macro corrugation pattern, particularly when no distance frame was used.

The constants C_3, C_4, and C_5 were iterated to 12,364, 96,991, and 0.15, respectively. The suppression factor was calculated to about 0.95 for the $n\mu P+10$ configuration and 0.46 for the $n\mu P$ heat exchanger. As seen in Fig. 12, the agreement between the calculated and the measure heat transfer coefficient, h_{ref}, was not as good as for the standard plates, but it captured the effects of both the boiling enhancement and the suppression effect with an average absolute deviation of 7.9% and a maximum error of 19%.

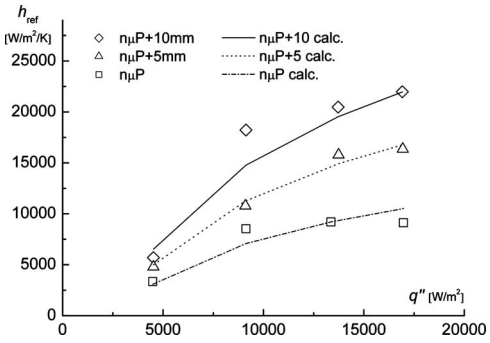

Fig. 12 Calculated and measured heat transfer coefficient, h_{ref}, as a function of heat flux, q''

4 Conclusions

The boiling heat transfer coefficient of a herringbone patterned plate heat exchanger evaporator was enhanced up to ten times in 134a by a novel nano- and microporous copper structure. As a result, the overall heat transfer coefficient was improved with over 100%. This significant boiling enhancement is in agreement with previous pool boiling experiments and confirms that the enhancement structure may be used to enhance the performance of plate heat exchangers.

A simple superposition model was used to evaluate the results and it was found that, primarily, the convective boiling mechanism was affected by the distance frames in the standard heat exchanger. On the other hand, with the enhanced boiling structure, variations in the hydraulic diameter caused a change in the nucleate boiling mechanism, which accounted for the largest effect on the heat transfer performance.

Nomenclature

A = heat transfer area, m^2
B = corrugation depth, mm
Co = confinement number, dimensionless
c_p = specific heat capacity, J/kg/K
d_h = hydraulic diameter, m
G = mass flux, $W/m^2/K$
h = heat transfer coefficient, $W/m^2/K$
h_{fg} = enthalpy of vaporization, J/kg
L = fluid flow plate length, m
M = molecular molar mass, g/mol
$\dot{m}$ = mass flow, kg/s
$n\mu P$ = nano- and microporous structure
Nu = Nusselt number, dimensionless
q = heat flow rate, W
q'' = heat flux, W/m^2
P = corrugation pitch, mm
p = pressure, Pa
R_p = Surface roughness (peak height), μm
S = suppression multiplier, dimensionless
s = smooth channel surface
STD = standard plate
Re = Reynolds number
T = temperature, K
U = overall heat transfer coefficient, $W/m^2/K$
$\dot{V}$ = volume flow, m^3/kg
W = fluid flow plate width, m

Greek Symbols

β = corrugation angle, deg
Δ = difference
δ = thickness, m
λ = thermal conductivity, W/m/K
μ = dynamic viscosity, Pa s
ρ = density, kg/m^3
σ = surface tension, N/m
ϕ = surface enlargement factor

Subscripts

cb = convective boiling
frame = distance frame
l = liquid
ln = natural logarithm
nb = nucleate boiling
plate = heat exchanger plate
proj = projected
r = reduced
ref = refrigerant
sat = saturation
tot = total
v = vapor
w = water

References

[1] Thome, J., 1990, *Enhanced Boiling Heat Transfer*, Hemisphere, New York.
[2] Bergles, A. E., 1997, "Enhancement of Pool Boiling," Int. J. Refrig., **20**(8), pp. 545–551.
[3] Webb, R. L., 1994, *Principles of Enhanced Heat Transfer*, Wiley-Interscience, New York.
[4] Webb, R. L., 2004, "Odessey of the Enhanced Boiling Surface," ASME J. Heat Transfer, **126**, pp. 1051–1059.
[5] Hillis, D., and Thomas, A., 1981, "Test and Development Program for Closed-Cycle OTEC Heat Exchangers," Oceans, **13**, pp. 883–888.
[6] Müller-Steinhagen, H., 2008, "Smart Surfaces for Improved Heat Exchangers," HTRI e-Publications, www.htri-net.com/ePubs/epubs.htm.
[7] Matsushima, H., and Uchida, M., 2002, "Evaporation Performance of a Plate Heat Exchanger Embossed With Pyramid-Like Structures," J. Enhanced Heat Transfer, **9**, pp. 171–179.
[8] Longo, G. A., Gasparella, A., and Sartori, R., 2004, "Experimental Heat Transfer Coefficients During Refrigerant Vaporisation and Condensation Inside Herringbone-Type Plate Heat Exchangers With Enhanced Surfaces," Int. J. Heat Mass Transfer, **47**, pp. 4125–4136.
[9] Davis, M. E., 2002, "Ordered Porous Materials for Emerging Applications," Nature (London), **417**, pp. 813–821.
[10] Stein, A., 2003, "Advances in Microporous and Mesoporous Solids—Highlights of Recent Progress," Adv. Mater., **15**, pp. 763–775.
[11] Honda, H., Takamatsu, H., and Wei, J. J., 2002, "Enhanced Boiling of FC-72 on Silicon Chips With Micro-Pin-Fins and Submicron-Scale Roughness," ASME J. Heat Transfer, **124**, pp. 383–390.
[12] Vemuri, S., and Kim, K., 2005, "Pool Boiling of Saturated FC-72 on Nano-Porous Surface," Int. Commun. Heat Mass Transfer, **32**, pp. 27–31.
[13] Furberg, R., 2006, "Enhanced Boiling Heat Transfer from a Novel Nanodendritic Micro-Porous Copper Structure," Licentiate thesis, Royal Institute of Technology, Stockholm, Sweden.
[14] Li, S., Furberg, R., Toprak, M., Palm, B., and Muhammed, M., 2008, "Nature-Inspired Fabrication of Nanostructured Micro-Porous Surfaces for Enhanced Boiling," Adv. Funct. Mater., **18**(15), pp. 2215–2220.
[15] Dittus, F. W., and Boelter, L. M. K., 1930, "Heat Transfer in Automobile Radiators of the Tubular Type," Univ. Calif. Publ. Eng., **2**, pp. 443–461.
[16] Kline, S. J., and McClintock, F. A., 1953, "Describing Uncertainties in Single Sample Experiments," Mech. Eng. (Am. Soc. Mech. Eng.), **75**, pp. 3–8.
[17] Incropera, F. P., and DeWitt, D. P., 2002, *Fundamentals of Heat and Mass Transfer*, Wiley, New York, pp. 545–551.
[18] Rohsenow, W. M., 1952, "A Method of Correlating Heat Transfer Data for Surface Boiling of Liquids," ASME J. Appl. Mech., **74**, pp. 969–976.
[19] Chen, J. C., 1966, "Correlation for Boiling Heat-Transfer to Saturated Fluids in Convective Flow," Ind. Eng. Chem. Process Des. Dev., **5**, pp. 322–329.
[20] Zhang, W., Hibiki, T., and Mishima, K., 2005, "Correlation for Flow Boiling Heat Transfer at Low Liquid Reynolds Number in Small Diameter Channels," ASME J. Heat Transfer, **127**, pp. 1214–1221.
[21] Palm, B., and Thonon, B., 1999, "Thermal and Hydraulic Performances of Compact Heat Exchangers for Refrigeration Systems," *Proceedings of the International Conference on Compact Heat Exchangers and Enhancement Technology for the Process Industries*, Banff, Canada, pp. 455-462.
[22] Thonon, B. R., Vidil, R., Marvillet, C., 1995, "Recent Research and Developments in Plate Heat Exchangers," J. Enhanced Heat Transfer , **2**, pp. 149–155.
[23] Cooper, M. G., 1984, "Heat Flow Rates in Saturated Nucleate Pool Boiling—A Wide Ranging Examination Using Reduced Properties," *Advances in Heat Transfer*, Academic, Orlando, FL, pp. 203–205.
[24] Longo, G. A., and Gasparella, A., 2007, "Heat Transfer and Pressure Drop During HFC Refrigerant Vaporisation Inside a Brazed Plate Heat Exchanger," Int. J. Heat Mass Transfer, **50**, pp. 5194–5203.
[25] Claesson, J., 2004, "Thermal and Hydraulic Performance of Compact Brazed Plate Heat Exchangers Operating as Evaporators in Domestic Heat Pumps,"

Ph.D. thesis, Royal Institute of Technology, Stockholm, Sweden.
[26] Furberg, R., Li, S., Palm, B., Toprak, M., and Muhammed, M., 2006, "Dendritically Ordered Nano-Particles in a Micro-Porous Structure for Enhanced Boiling," *Proceedings of the IHTC-13 Conference*, Sydney, Australia, Aug. 13–18.
[27] Maneri, C. C., and Vassallo, P. F., 2000, "Dynamics of Bubbles Rising in Finite and Infinite Media," Department of Energy Information Bridge," Report Nos. DE2004-821300; LM-00K048.
[28] Furberg, R., Khodabandeh, R., Palm, B., Li, S., Toprak, M., and Muhammed, M., 2008, "Experimental Investigation of an Evaporator Enhanced With a Micro-Porous Structure in a Two-Phase Thermosyphon Loop," *Proceedings of the 2008 ASME Summer Heat Transfer Conference, HT2008*, Jacksonville, FL, Aug. 10–14.
[29] Kew, P. A., and Cornwell, K., 1997, "Correlations for the Prediction of Boiling Heat Transfer in Small-Diameter Channels," Appl. Therm. Eng., **17**, pp. 705–715.

Therporaoustic Convection: Modeling and Analysis of Flow, Thermal, and Energy Fields

Shohel Mahmud

Roydon Andrew Fraser

Department of Mechanical and Mechatronics Engineering,
University of Waterloo,
200 University Avenue West,
Waterloo, ON, N2L 3G1, Canada

The problem of therporacoustic (thermal-porous-acoustic) convection near a porous medium, representative of a stack in a thermoacoustic engine/refrigerator, is modeled and analyzed in this paper. Assumptions (e.g., long wave, short stack, and small amplitude oscillation) are made to enable simplification of the governing unsteady-compressible-viscous forms of the continuity, momentum, and energy equations to achieve analytical solutions for the fluctuating velocity and temperature and the complex Nusselt number. Boundary walls are assumed to be very thin in thickness and the conduction heat transfer inside the boundary walls are neglected in this paper. The derived analytical results are expressed mainly in terms of the Darcy number (Da), critical temperature gradient ratio (Γ_0), Swift number (S_w), Prandtl number (Pr), and modified Rott's and Swift's parameters (f_ν and f_k). The real part of the fluctuating flow complex Nusselt number approaches to the steady result, as reported in the literature, at the zero frequency limit. While in the high frequency limit, the real part of the complex Nusselt number matches well with the limit obtained by other oscillating flow researchers with slight differences explained by additional terms included in this work. A wave equation for the pressure fluctuation is modeled by combining the continuity, momentum, and energy equations and subsequent integrations which, in the inviscid no-stack limit, approaches the Helmholtz wave equation. Based on the derived energy flux density equation performance plots are proposed, which give the Swift number at the maximum energy transfer (S_{w0}) for a given Γ_0 and Da.
[DOI: 10.1115/1.3180705]

1 Introduction

The study of convection processes in porous media is a well-developed field of investigation because of its importance to a variety of situations, for example, thermal insulation, geothermal systems, solid matrix heat exchangers, nuclear waste disposal, microelectronic heat transfer equipment, coal and grain storage, petroleum industries, and chemical catalytic beds [1–3]. Heat and mass transfer studies through saturated porous media are important developments and a rapidly growing area in contemporary heat transfer researches [4]. Although the mechanics of fluid flow through porous media has preoccupied engineers and physicists for more than a century, the study of heat transfer has reached the status of a separate field of research during the past 3 decades [1]. The reader is directed to a growing number of articles that outline the fundamentals of porous media fluid flow, heat transfer, and mass transfer [2–8].

As an example of porous media heat transfer, consider electronic package cooling. The rapid development in the design of electronic packages for modern high-speed computers has led to a demand for new and reliable methods of chip cooling. This has motivated several researchers to consider porous materials as effective media for electronic package heat removal. Due to the large surface area of porous media heat transfer rates can be enhanced significantly. Forced, mixed, and natural convections through porous channels or cavities were modeled with several electronic cooling case studies available in the references given in the previous paragraph.

Another potential application of convection processes in porous media is found in thermoacoustic prime movers/engines and heat pumps/refrigerators [9]. The stack is considered to be the most important part of the thermoacoustic devices. As of today, those wishing to build a practical thermoacoustic prime mover or refrigerator have had a limited choice of stack materials, for example, the plastic roll stack, the wire mesh stack, a metal or ceramic honeycomb stack having square and hexagonal channel sections, and the pin stack [9]. These stacks, while simple in concept, can be very labor intensive or costly thus hindering low budget fabrication.

Recently, Adeff et al. [10] tested the performance of porous *reticulated vitreous carbon* (RVC) as a stack material in a thermoacoustic engine and a refrigerator. The relatively inexpensive, lightweight, and easy to machine RVC is an open pore foam material composed solely of vitreous carbon. In addition, RVC has low thermal conductivity, high porosity, and high specific heat. However, the brittleness of RVC is its major disadvantage. A loose fitting stack can vibrate against the heat exchangers causing the filaments to break [10].

Adeff et al. [10] did not develop a theoretical model for porous media thermoacoustic systems either in general or for RVC as a particular case. Swift's [11] theories of general thermoacoustics were used to compare with the results obtained by Adeff et al. [10]. Swift [9,11] considered the overall stack as a porous medium composed of multiple individual channels, these pores or channels being of circular, rectangular, hexagonal, and cross section. Swift's theories were developed for an individual pore or channel similar to Rott's groundbreaking theories of thermoacoustics [12]. It is assumed in Swift's and Rott's theories that the individual channel is filled with nothing but a nonporous (clear) fluid (for example, air, helium, or the mixture of helium and xenon).

The primary objective of this paper is to incorporate into the fundamental thermoacoustics theory of Swift [11] and Rott [12] a modification that treats the fluid-gaps within a stack of a thermoacoustic engine/refrigerator as porous media, not simply a multichannel stack as pursued by Swift [9,11]. In order to develop the theories of thermoacoustics for porous media, Mahmud and Fraser [13–15] initially developed models for porous stacks and pre-

Manuscript received September 29, 2008; final manuscript received June 3, 2009; published online July 31, 2009. Review conducted by Kambiz Vafai.

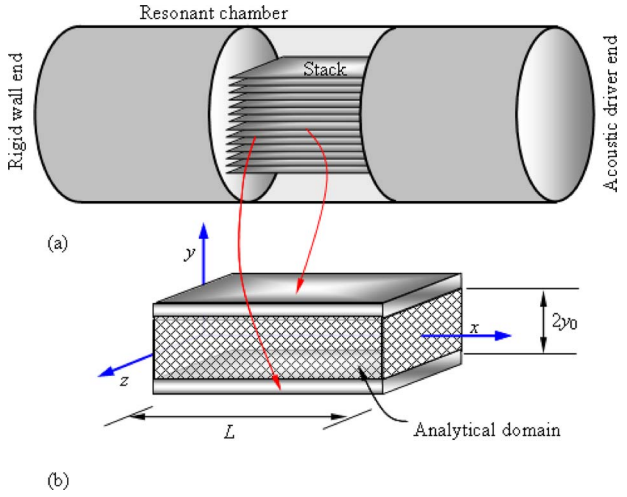

Fig. 1 (*a*) A multiplate porous thermoacoustic system and (*b*) coordinate system and dimensions of analytical domain in the porous medium

sented their results in the steady-state limit. Some non-stack-like cases are also studied [16,17] in order to capture the transient properties of thermovibrational convection. Recent studies of Leong and Jin [18,19] and Fu et al. [20] considered an oscillatory flow and heat transfer scenario in a porous channel filled with a porous medium. For a laminar incompressible flow, Kuznetsov and Nield [21] modeled the flow and heat transfer in a parallel-plate channel and in a circular tube filled with a saturated porous medium, which follows the Brinkman model. Kuznetsov and Nield [21] assumed a small amplitude fluctuating pressure with nonzero mean. However, none of the existing literature considers the hydrodynamic and thermal interactions of a small amplitude compressible wave or sound wave with a stack filled with a porous medium; this provides the primary motivation of this work to extend the theory of thermoacoustics to porous media.

There is, of course, always an academic interest to test a relatively new theory and find its potential applications. However, Organ [22] and Swift [9] pointed out many of the shortcomings of the current state of the art of thermoacoustic and Stirling systems. Considering today's shortcomings, additional approximations and extensions of the current thermoacoustic theory are required in order to achieve a better performance engine/refrigerator in the near future.

2 Problem Formulation

Current analysis is carried out for an unsteady-state, compressible, two-dimensional flow within a parallel-plate channel filled with a homogeneous and isotropic porous medium. Consider a stack of parallel plates located somewhere in a gas-filled duct or resonator (see Fig. 1(*a*)). Calculations are performed in a single (or individual) channel between a pair of plates as depicted in Fig. 1(*b*). The spacing between two consecutive plates is $2y_0$, the length of the stack is L, and the stack width is large enough such that the variables are assumed constant in a direction perpendicular to the page (see Fig. 1(*b*)). The axis perpendicular to the plate is the y-axis. The location $y=0$ is chosen to be the midpoint between the two adjacent plates. The axis parallel to the plate is the x-axis, and $x=0$ is chosen to be at the beginning of the stack to the left.

The gap between two plates is assumed to be filled with a porous material, as shown in Fig. 1(*b*). The porous medium is saturated with a single phase Newtonian fluid and is assumed to be in local thermodynamic equilibrium with the fluid. The thermophysical properties of the solid matrix and of the fluid are assumed to be constant. Although for certain porous media, such as packed beds, porosity may vary due to channeling near the walls [23], in the present study a rigid foam or wire mesh material is considered such that porosity and permeability are assumed to be constant, even close to the walls. The channel walls are assumed to be very small in thickness. Therefore, the conduction heat transfer inside the channel walls is neglected.

An acoustic driver initiates the fluid oscillation inside the resonant chamber as well as inside the porous medium. The oscillating compressible fluid interacts hydrodynamically and thermally with the porous medium and produces several thermoacoustic effects (e.g., heat flux and work flux). In order to model the physics behind such effects, accurate descriptions of the continuity, momentum, and energy equations are required. The derivations of different thermoacoustic parameters are available in Secs. 2.1–2.5. Discussions on the derivations and qualitative/quantitative variations in the derived parameters (e.g., fluctuating velocity, fluctuating temperature, and heat flux) with so called thermoacoustic variables (e.g., Swift number and critical temperature gradient ratio) are provided in Sec. 3.

2.1 Analysis of the Flow Field. The equation for mass conservation or mass continuity, according to Nield and Bejan [1], for a porous medium is

$$\frac{\mathbf{D}(\varphi\rho)}{\mathbf{D}t} + \nabla\cdot(\rho\mathbf{v}) = 0 \tag{1}$$

where φ, ρ, and $\mathbf{v}$ are the porosity of the porous medium, the density of the fluid, and the velocity vector, respectively. In contrast to the mass continuity equation (Eq. (1)), the modeling of momentum transfer in a porous medium is a complex issue. Most available models are based on several assumptions and are mainly empirical in nature [1]. The simplest one is the Darcy flow model [1,24–26], which constructs a relationship between the flow velocity in a certain direction to the pressure gradient in that direction, i.e.,

$$\mathbf{v} = \frac{K}{\mu_d}(-\nabla p + \rho\mathbf{g}) \tag{2}$$

where K, μ_d, p, and $\mathbf{g}$ are the permeability of the porous medium, dynamic viscosity of the fluid, pressure, and gravity vector, respectively. The permeability K ($\sim m^2$) is an empirical constant. A list of permeabilities is available for different porous materials in Refs. [1,5]. The Darcy flow model is valid in circumstances where the order of magnitude of the *local pore Reynolds number*, based on the local volume averaged speed ($|\mathbf{v}|^{1/2}$) and length scale $K^{1/2}$, is smaller than 1. Darcy's law neglects the effects of a solid boundary or the effect of inertial forces on fluid flow and heat transfer [27]. These neglected effects are expected to become significant near the boundary and in high-porosity media (e.g., thermoacoustic stack), invalidating the Darcy model in these locations and situations.

When a relatively high permeability and porosity porous medium (e.g., rigid foam) interacts with moderate to high frequency sound waves, it results in a local pore Reynolds number greater than 1. Such a case may be handled by Forchheimer's modification [1,25,28] of Darcy's model by adding a term $-b\rho K/\mu|\mathbf{v}|\mathbf{v}$ to the right hand side of Eq. (2), where b is the Forchheimer coefficient [1]. Furthermore, as one is dealing with a viscous fluid flow in a narrow channel, an additional modification, likely Brinkman's extension [1], is required. Brinkman's term $K\nabla^2\mathbf{v}$ may be added to the right hand side of Eq. (2) in place of Forchheimer's added term. These two modifications of the Darcy flow model, the Forchheimer model and the Brinkman model, are used by several authors (e.g., Vafai and Tien [27] and Kaviany [29]) to study forced convection boundary layer type flow and heat transfer situations. However, as discussed in Ref. [25], neither of the foregoing models account adequately for the transition from porous medium flow to pure (or clear) fluid flow in the case of high permeability (i.e., $K\to\infty$). According to Bejan [25], a model that

bridges the gap between the Darcy–Forchheimer model and the Navier–Stokes equation was proposed by Vafai and Tien [27] and is also available in Ref. [25]:

$$\rho\frac{\mathbf{D}\mathbf{v}}{\mathbf{D}t}+\frac{\rho b\varphi}{\sqrt{K}}|\mathbf{v}|\mathbf{v}=-\nabla p-\varphi\frac{\mu_d}{K}\mathbf{v}+\rho\mathbf{g}+\mu_e\nabla^2\mathbf{v} \tag{3}$$

where μ_e is the effective viscosity of fluid. Note that the ratio of μ_e to μ_d is termed as the viscosity ratio (M) [30]. In this paper M is considered to be unity, which means $\mu_e=\mu_d=\mu$. Neglecting the effect of gravity, the x-momentum equation for the current problem can be obtained from Eq. (3) as

$$\left(\rho\frac{\partial u}{\partial t}+\rho u\frac{\partial u}{\partial x}+\rho v\frac{\partial u}{\partial y}\right)+\frac{\rho b\varphi}{\sqrt{K}}u^2=-\frac{\partial p}{\partial x}-\varphi\frac{\mu}{K}u+\mu\left(\frac{\partial^2 u}{\partial x^2}+\frac{\partial^2 u}{\partial y^2}\right) \tag{4}$$

In order to linearize Eq. (4) and to model the oscillating gas in the porous channel bounded between two parallel plates, the following assumptions are made.

- The plates are perfectly rigid.
- A first order expansion in amplitude is sufficient for all variables.
- All terms that are higher than the first order are neglected, except for the energy flux, heat flux, and the work flux.
- The mean fluid velocities (u_m and v_m) are zero.
- Pressure is not a function of the y-axis.
- The acoustic wavelength (λ) is much larger than the transverse dimension $2y_0$.
- The acoustic wavelength (λ) is much larger than the penetration depths (δ_ν and δ_k).

All dependent variables are expressed in terms of a mean component and a first order fluctuating components as follows:

$$p=p_m+p_1(x)e^{i\omega t},\quad \rho=\rho_m+\rho_1(x)e^{i\omega t},\quad T=T_m+T_1(x,y)e^{i\omega t}$$
$$u=u_m+u_1(x,y)e^{i\omega t},\quad v=v_m+v_1(x,y)e^{i\omega t} \tag{5}$$

where any term with the subscript "m" represents the mean value (usually a real number) and the term with the subscript "1" represents the fluctuating value (usually a complex expression). The time dependency of a particular variable is represented by $\exp(i\omega t)$, where ω represents the circular frequency and equals $2\pi f$. The x-dependency of u_1, v_1, and T_1 comes from their dependency on the pressure. By substituting variable expansions as shown in Eq. (5) into the axial momentum equation and after considering all of the assumptions, Eq. (4) can be further simplified to [31]

$$i\omega\rho_m u_1=-\frac{\partial p_1}{\partial x}-\varphi\frac{\mu}{K}u_1+\mu\frac{\partial^2 u_1}{\partial y^2} \tag{6}$$

In order to obtain Eq. (6) the following scales are considered: $x\sim\tilde{\lambda}$, $y\sim\delta_\nu$, $u\sim u_1$, and $v\sim v_1$ where $\tilde{\lambda}$ equals $\lambda/2\pi$. Therefore, at steady-state, $u_1/\tilde{\lambda}\sim v_1/\delta_\nu$ is obtained from the continuity equation (Eq. (1)). In turn, this yields $u_1\gg v_1$ since it is already assumed that $\tilde{\lambda}\gg\delta_\nu$. After the following boundary conditions, (a) at $y=0$, $\partial u_1/\partial y=0$ and (b) at $y=y_0$, $u_1=0$, are applied, the solution to Eq. (6) becomes

$$u_1=\frac{i}{\omega\rho_m(1+\Psi)}\frac{\partial p_1}{\partial x}\left\{1-\frac{\cosh[(1+i)\sqrt{1+\Psi}y/\delta_\nu]}{\cosh[(1+i)\sqrt{1+\Psi}y_0/\delta_\nu]}\right\}$$
$$\text{with}\quad \Psi=\frac{\varphi}{2i\ \mathrm{Da}} \tag{7}$$

In Eq. (7), δ_ν and Da are the viscous penetration depth [9] and the Darcy number (K/δ_ν^2) [1], respectively. Although the origin of Da seems to be purely geometric (ratio of 2 length scales), it expresses, alternatively, the degree of internal blockage experienced by the stack after introducing the porous medium. The viscous penetration depth δ_ν ($=\sqrt{2\nu/\omega}$) indicates how far the momentum can diffuse laterally during a characteristic time interval ($=2/\omega$). The characteristic time interval is of the order of the period of oscillation ($\tau=2\pi/\omega$) divided by π. For the simplicity and convenience of presentation in this paper, the $(1+i)\sqrt{1+\Psi}/\delta_\nu$ term in Eq. (7) is expressed later in this paper as a_0. Now, introducing a dimensionless transverse distance Y ($=y/\delta_\nu$) and a nondimensional Swift number S_w ($=y_0/\delta_\nu$), Eq. (7) can be modified to

$$u_1=\frac{i}{\omega\rho_m(1+\Psi)}\frac{\partial p_1}{\partial x}\left\{1-\frac{\cosh[(1+i)\sqrt{1+\Psi}S_wY]}{\cosh[(1+i)\sqrt{1+\Psi}S_w]}\right\} \tag{8}$$

Note that the Swift number (S_w) is a measure of the narrowness (or the wideness) of the channel. By using the integration $(y_0)^{-1}\int_0^{y_0}u_1dy$, the average velocity ($u_{1,\mathrm{av}}$) can be calculated from Eq. (7) as

$$u_{1,\mathrm{av}}=\frac{i}{\omega\rho_m(1+\Psi)}\frac{\partial p_1}{\partial x}\left\{1-\frac{\tanh[(1+i)\sqrt{1+\Psi}S_w]}{(1+i)\sqrt{1+\Psi}S_w}\right\} \tag{9}$$

The parameter $(1+\Psi)$ in Eqs. (7)–(9) represents a direct influence of the presence of the porous medium on the fluctuating velocity and can be termed as a *porous-thermoacoustic-parameter* or *therporacoustic-parameter*. The fluctuating velocity (u_1) and average velocity ($u_{1,\mathrm{av}}$) expressions, shown in Eqs. (7)–(9), respectively, are complex expressions. However, only their real parts have physical meanings.

2.2 Analysis of the Thermal Field. Consider now the energy equation for the flow through a porous medium. For simplicity, it is assumed that the medium is isotropic and that radiative effects are negligible. It is also assumed that the temperatures in the fluid and at the adjacent solid matrix of the porous material are the same (i.e., local thermal equilibrium [1,25,32]). Based on the local thermal equilibrium assumption, heat conduction in the solid matrix and fluid phases takes place in parallel so that there is no net heat transfer from one phase to the other. The governing energy equation, for such a case, can be obtained by integrating the solid's energy equation over the area occupied by the solid matrix and integrating the fluid's energy equation over the area occupied by the fluid (in the pores) followed by a subsequent addition of two area averaged equations and simplifications [1,24,32]. It should be noted that when the assumption of local thermal equilibrium is abandoned, account must be taken for the local heat transfer between solid and fluid (see Ref. [25] for details).

For the current problem and assumptions, the following general form of the energy equation [32] results to

$$\rho C_p\left[\sigma\frac{\partial T}{\partial t}+(\mathbf{v}\cdot\nabla)T\right]=\nabla\cdot(k\nabla T)+\beta T\frac{\mathbf{D}p}{\mathbf{D}t}+\left(\frac{\mu}{K}+\frac{\rho b}{K^{1/2}}|\mathbf{v}|\right)\mathbf{v}\cdot\mathbf{v} \tag{10}$$

for modeling the temperature inside a porous medium where σ, k, C_p, and β are the porous medium heat capacity ratio, the overall thermal conductivity, the specific heat of the fluid, and the thermal expansion coefficient, respectively. The parameters σ and k can be defined, according to Bejan [25], as

$$\sigma=\varphi+(1-\varphi)(\rho_{\mathrm{sm}}C_{\mathrm{sm}})/(\rho C_p) \tag{11a}$$

$$k=(1-\varphi)k_{\mathrm{sm}}+\varphi k_f \tag{11b}$$

where ρ_{sm}, C_{sm}, and k_{sm} are, respectively, the density, the specific heat, and the thermal conductivity of the solid matrix material of the porous medium. Following similar scaling arguments as performed in Sec. 2.1 and applying Rott's thermoacoustic linearization, the energy equation in the porous medium can be simplified to

$$i\omega\rho_m C_p \sigma T_1 + C_p \rho_m u_1 \frac{\partial T_m}{\partial x} = k\frac{\partial^2 T_1}{\partial y^2} + i\omega\beta T_m p_1 \tag{12}$$

In Eq. (12) the subscripts m represent the mean properties in the porous medium. The general solution to Eq. (12) yields

$$T_1 = C_1 \cosh\left(\frac{1+i}{\delta_k}\sqrt{\sigma}y\right) + C_2 \sinh\left(\frac{1+i}{\delta_k}\sqrt{\sigma}y\right) + \frac{\Pr}{\sigma\ \Pr - \Psi - 1}\frac{\nabla T_m \nabla p_1}{\omega^2\rho_m(1+\Psi)}\frac{\cosh(a_0 y)}{\cosh(a_0 y_0)} - \frac{\nabla T_m \nabla p_1}{\omega^2\rho_m\sigma(1+\Psi)} + \frac{\beta T_m p_1}{\rho_m C_p \sigma} \tag{13}$$

where Pr and δ_k represent the Prandtl number and the thermal penetration depth, respectively. The thermal penetration depth indicates how far the thermal energy can diffuse laterally during a characteristic time interval ($=2/\omega$). In Eq. (13), two gradients $\partial T_m/\partial x$ and $\partial p_1/\partial x$ are expressed as ∇T_m and ∇p_1, respectively, by using the convention of the available thermoacoustic literature [9,11]. For simplicity and convenience of presentation in this paper, the $(1+i)\sqrt{\sigma}/\delta_k$ term in Eq. (13) is expressed later as b_0.

Applying the symmetry boundary condition, i.e., $\partial T_1/\partial y = 0$ at $y=0$, results in $C_2=0$ in Eq. (13). However, in order to evaluate C_1, it is necessary to apply an appropriate boundary condition at the wall. One possible approximation is to assume a zero fluctuating temperature at the wall, i.e., $T_1=0$ at $y=y_0$. Note that for such a thermal boundary condition, it is required to assume that the plate has a large enough heat capacity per unit area that its temperature will not change significantly at the acoustic frequency [9,11]. This is a very good approximation in the thin plate limit. However, the energy equation for the solid wall is required to be solved if a finite wall thickness and moderate heat capacity per unit area of the wall are considered. Finally, the fluctuating temperature inside the porous medium (T_1), after a very lengthy calculation and rearrangement, becomes

$$T_1 = \frac{\beta T_m p_1}{\rho_m C_p \sigma} - \frac{\nabla T_m \nabla p_1}{\omega^2\rho_m\sigma(1+\Psi)} \times \left\{1 - \frac{\Pr\ \sigma}{\Pr\ \sigma - \Psi - 1}\frac{\cosh[(1+i)\sqrt{1+\Psi}S_w Y]}{\cosh[(1+i)\sqrt{1+\Psi}S_w]}\right\} - \left\{\frac{1}{\Pr\ \sigma - \Psi - 1}\frac{\nabla T_m \nabla p_1}{\omega^2\rho_m\sigma} + \frac{\beta T_m p_1}{\rho_m C_p \sigma}\right\}\frac{\cosh[(1+i)\sqrt{\sigma\ \Pr}\ S_w Y]}{\cosh[(1+i)\sqrt{\sigma\ \Pr}\ S_w]} \tag{14}$$

The final expression of the fluctuating temperature (T_1), shown in Eq. (14), is a complex expression. However, only the real part of it has physical meanings. By using the integration $(y_0)^{-1}\int_0^{y_0} T_1 dy$, a space averaged temperature ($T_{1,\mathrm{av}}$) can be calculated from Eq. (14) as

$$T_{1,\mathrm{av}} = \frac{\beta T_m p_1}{\rho_m C_p \sigma}(1 - f_k) - \frac{\nabla T_m \nabla p_1}{\omega^2\rho_m\sigma}\left[\frac{(\Pr\ \sigma - \Psi - 1) - \Pr\ \sigma f_\nu + f_k(1+\Psi)}{(\Pr\ \sigma - \Psi - 1)(1+\Psi)}\right] \tag{15}$$

The definitions of f_ν and f_k are given by the following equations:

$$f_\nu = \frac{\tanh[(1+i)\sqrt{1+\Psi}S_w]}{(1+i)\sqrt{1+\Psi}S_w} \quad \text{and} \quad f_k = \frac{\tanh[(1+i)\sqrt{\sigma\ \Pr}\ S_w]}{(1+i)\sqrt{\sigma\ \Pr}\ S_w} \tag{16}$$

In the absence of a porous medium, f_ν and f_k are reduced to Rott's thermoacoustic functions proposed by Swift [9]. Therefore, expressions available in Eq. (16) are modified Rott's functions for the porous medium.

2.3 Heat Transfer From the Wall. The heat transfer rate from the wall is calculated in terms of the Nusselt number (Nu). For the current problem, the following definition of Nusselt number is used:

$$\mathrm{Nu} = \left(\frac{4y_0}{T_w - T_{\mathrm{ref}}}\right)\left.\frac{\partial T_1}{\partial y}\right|_{y=y_0} \tag{17}$$

where T_{ref} is a suitable reference temperature. For the steady-state channel flow problems, heat transfer literature uses the bulk mean temperature (T_b) or the mixing-cup temperature [32] as T_{ref} for calculating the Nusselt number. A definition of T_b is given in the following equation [32]:

$$T_b = \frac{1}{u_{1,\mathrm{av}}A}\int_A u_1 T_1 dA = \frac{1}{u_{1,\mathrm{av}}y_0}\int_0^{y_0} u_1 T_1 dy \tag{18}$$

If Eq. (14) is substituted into Eq. (18) and the integration is performed, then the expression for T_b, after a very lengthy calculation, becomes

$$T_b = \left[\frac{\beta T_m p_1}{\rho_m C_p \sigma} - \frac{\nabla T_m \nabla p_1}{\omega^2\rho_m\sigma(1+\Psi)}\right] - \frac{\nabla T_m \nabla p_1}{\omega^2\rho_m\sigma(1+\Psi)}\frac{\Pr\ \sigma}{\Pr\ \sigma - \Psi - 1}\left(1 - \frac{f_\nu^2}{1-f_\nu}\Phi_\nu\right) - \left[\frac{\beta T_m p_1}{\rho_m C_p \sigma} - \frac{\nabla T_m \nabla p_1}{\omega^2\rho_m\sigma(\Pr\ \sigma - \Psi - 1)}\right]\left(\frac{1+\Psi}{\Pr\ \sigma - \Psi - 1}\right) \times \left(\frac{f_\nu - f_k}{1-f_\nu}\right) \tag{19}$$

where Φ_ν equals $2i(1+\Psi)S_w^2$. By substituting Eq. (14) into Eq. (17), the expression of Nusselt number becomes

$$\mathrm{Nu} = \left(\frac{4}{T_w - T_{\mathrm{ref}}}\right)\left[\frac{\nabla T_m \nabla p_1}{\omega^2\rho_m\sigma}\frac{1}{\Pr\ \sigma - \Psi - 1}\left\{\frac{\Pr\ \sigma}{1+\Psi}\Phi_\nu f_\nu - \Phi_k f_k\right\} - \frac{\beta T_m p_1}{\rho_m C_p \sigma}\Phi_k f_k\right] \tag{20}$$

where Φ_k equals $2i\sigma\ \Pr\ S_w^2$. Depending on the specific thermoacoustic problems, different authors consider different definitions of T_{ref}. For example, Mahmud and Fraser [33] considered T_b as T_{ref} for a multiplate thermoacoustic problem, Lu and Cheng [34] considered a space averaged solid wall temperature as T_{ref} for a thick-wall-circular-pore thermoacoustic problem, and Liu and Garrett [35] considered a space averaged gas temperature ($T_{1,\mathrm{av}}$ in this paper) as T_{ref}. The Nusselt number expression derived in Eq. (20) is a complex quantity. Therefore, in the available thermoacoustic literature (e.g., Refs. [33,34]) it is termed the "complex Nusselt number."

2.4 Wave Equation. In the limit of the short plate approximation [11], a standing-wave-like pressure fluctuation can be used. In such an approximation, it is assumed that the plate is short enough that it does not perturb a standing-wave-like pressure fluctuation appreciably so that $p_1 = p_0 \cos(2\pi x/\lambda)$, where λ and p_0 are the wavelength and fluctuating pressure amplitude, respectively. However, for a more general case, a pressure equation (or the wave equation) needs to be modeled.

In this section an equation for the fluctuating pressure (or the wave equation) is derived. The continuity equation (Eq. (1)) can be expanded to yield

$$\frac{\partial(\varphi\rho)}{\partial t}+\rho\left[\frac{\partial u}{\partial x}+\frac{\partial v}{\partial y}\right]+\left[u\frac{\partial \rho}{\partial x}+v\frac{\partial \rho}{\partial y}\right]=0 \tag{21}$$

Following similar scaling arguments as performed in Sec. 2.1 and applying Rott's thermoacoustic linearization, the continuity equation can be simplified to

$$i\omega\varphi\rho_1+\frac{\partial}{\partial x}(\rho_m u_1)+\rho_m\frac{\partial v_1}{\partial y}=0 \tag{22}$$

Note that the $\partial\rho_m/\partial y$ term is neglected while deriving Eq. (22). Now, differentiating Eq. (6) with respect to x and using Eq. (22), the following equation is obtained:

$$-i\omega\varphi\rho_1-\rho_m\frac{\partial v_1}{\partial y}=\frac{1}{i\omega(1+\Psi)}\frac{\partial}{\partial x}\left(\mu\frac{\partial^2 u_1}{\partial y^2}\right)-\frac{1}{i\omega(1+\Psi)}\frac{\partial^2 p_1}{\partial x^2} \tag{23}$$

With the thermodynamic relation $\rho_1=-\rho_m\beta T_1+(\gamma/c^2)p_1$, ρ_1 can be eliminated from Eq. (23) to yield

$$\frac{\partial}{\partial x}\left(\mu\frac{\partial^2 u_1}{\partial y^2}\right)-\frac{\partial^2 p_1}{\partial x^2}+(1+\Psi)\left\{\omega^2\rho_m\varphi\beta T_1-\frac{\varphi\omega^2\gamma}{c^2}p_1+i\omega\rho_m\frac{\partial v_1}{\partial y}\right\}=0 \tag{24}$$

Equation (24) may be integrated between 0 to y_0 to eliminate v_1 (i.e., $v_1(0)=0$ and $v_1(y_0)=0$) and to obtain a differential equation for p_1 as a function of x. Finally, the wave equation becomes

$$\frac{\partial}{\partial x}\left\{(1-f_\nu)\frac{\partial p_1}{\partial x}\right\}+\frac{\varphi\beta\nabla T_m}{\sigma}\left\{1-\frac{\sigma\ \mathrm{Pr}\ f_\nu}{\sigma\ \mathrm{Pr}-\Psi-1}+\frac{(1+\Psi)f_k}{\sigma\ \mathrm{Pr}-\Psi-1}\right\}\frac{\partial p_1}{\partial x}-\frac{(1+\Psi)}{k_0^2}\left\{\frac{\varphi(\gamma-1)(1-f_k)}{\sigma}-\gamma\right\}p_1=0 \tag{25}$$

where k_0 is the inverse of the wave number (ω/c). For a nonporous medium, $\mathrm{Da}\to\infty$, $\Psi\to 0$, $\varphi\to 1$, and $\sigma\to 1$. For a no-stack situation, $\nabla T_m\to 0$. For inviscid flow, $f_\nu\to 0$ and $\mathrm{Pr}\to 0$. Substituting these values in Eq. (25) results in

$$\frac{\partial^2 p_1}{\partial x^2}+\left(\frac{\omega}{c}\right)^2 p_1=0 \tag{26}$$

which is well known as the Helmholtz equation [31].

2.5 Energy Flux Density. In steady-state, for a thermoacoustic engine/refrigerator without lateral heat flows to the surroundings, the time-averaged energy flux ($\langle\dot{\mathbf{E}}\rangle$) along the x-direction is independent of x [11]. The magnitude of $\dot{\mathbf{E}}$ is the amount of energy passing, in unit time, through a unit area perpendicular to the direction of the fluid velocity [36]. The energy flux density vector ($\dot{\mathbf{E}}$) is a conserved quantity for temporally periodic problems such as thermoacoustic engines and heat pumps. The general equation for $\dot{\mathbf{E}}$, according to Ref. [36], is

$$\dot{\mathbf{E}}=\rho\mathbf{v}\left(\tfrac{1}{2}|\mathbf{v}|^2+h\right)-\mathbf{v}\,.\,\boldsymbol{\sigma}-k\ \mathrm{grad}(T) \tag{27}$$

where h and $\boldsymbol{\sigma}$ are the enthalpy and the viscous stress tensor, respectively. General and simplified analytical expressions of the energy flux density vector for several multistack thermoacoustic problems are reported in the available thermoacoustic literature (e.g., Refs. [9,11]). Numerical calculation of $\dot{\mathbf{E}}$ near a thermoacoustic couple is available in Refs. [37,38]. For the present problem, the $\mathbf{v}\cdot\boldsymbol{\sigma}$ term can be neglected by considering the long-wave approximation. The flow of kinetic energy can also be neglected since it is proportional to the cube of the velocity. By considering these assumptions along with other assumptions already mentioned in this paper, Eq. (27) reduces to

$$\dot{\mathbf{E}}\approx\rho uh-k\frac{\partial T}{\partial x} \tag{28}$$

The functional relationship of the enthalpy with the entropy and pressure, i.e., $h=f(s,p)$, leads to the following [9,39]:

$$dh=\left(\frac{\partial h}{\partial s}\right)_p ds+\left(\frac{\partial h}{\partial p}\right)_s dp=Tds+\frac{dp}{\rho}=C_p dT+(1-T\beta)\frac{dp}{\rho} \tag{29}$$

Integrating Eq. (29) results in an expression for h in terms of s and p. Using a linear thermoacoustic expansion, Eq. (28) can be simplified further to

$$\dot{E}_2\approx\rho_m C_p(T_1u_1)+(1-T_m\beta)(p_1u_1)-k\frac{\partial T_m}{\partial x} \tag{30}$$

The thermodynamic relation $s_1=(C_p/T_m)T_1-(\beta/\rho_m)p_1$ is used to obtain Eq. (30). The subscript "2" in Eq. (30) signifies a second order quantity. After time and space averaging, the energy flux per unit perimeter (E_2/Π) along x becomes

$$\frac{E_2}{\Pi}=\rho_m C_p\int_0^{y_0}\overline{T_1u_1}dy+(1-\beta T_m)\int_0^{y_0}\overline{p_1u_1}dy-y_0k\nabla T_m \tag{31}$$

In Eq. (31), an overbar $(-)$ over a quantity represents time averaging. If Eqs. (7) and (14) are substituted into Eq. (31) and the integrations are performed,

$$E_2=\frac{y_0\Pi}{2}\Re\left[-\frac{ip_1\nabla\tilde{p}_1}{\omega\rho_m(1+\tilde{\Psi})}\left\{(1-\tilde{f}_\nu)+\frac{\beta T_m}{\sigma}\frac{(1+\tilde{\Psi})(\tilde{f}_\nu-f_k)}{\sigma\ \mathrm{Pr}+\tilde{\Psi}+1}\right\}+\frac{i\nabla T_m C_p}{\omega^3\rho_m\sigma}\frac{\nabla p_1\nabla\tilde{p}_1}{(1+\Psi)(1+\tilde{\Psi})}\times\left\{(1-\tilde{f}_\nu)-\frac{\sigma\ \mathrm{Pr}}{\sigma\ \mathrm{Pr}-\Psi-1}\frac{(f_\nu-\tilde{f}_\nu)-\Psi f_\nu-\tilde{\Psi}\tilde{f}_\nu}{2}-\frac{(1+\Psi)(1+\tilde{\Psi})(\tilde{f}_\nu-f_k)}{(\sigma\ \mathrm{Pr}-\Psi-1)(\sigma\ \mathrm{Pr}+\tilde{\Psi}+1)}\right\}+\left(\frac{\sigma-1}{\sigma}\right)\frac{i\beta T_m}{\omega\rho_m}\frac{p_1\nabla\tilde{p}_1}{1+\tilde{\Psi}}(1-\tilde{f}_\nu)\right]-\Pi y_0k\frac{\partial T_m}{\partial x} \tag{32}$$

where $\Re[\ ]$ signifies the real part and tilde $(\sim)$ denotes the complex conjugation.

The global work flux (W_2) alone is estimated by integrating the time-averaged product of the fluctuating velocity and pressure with respect to y [9] from the channel centerline to the wall. The resulting equation is

$$W_2=\Pi\int_0^{y_0}\overline{p_1u_1}dy=-\frac{y_0\Pi}{2}\frac{1}{\omega\rho_m}\Re\left[\frac{ip_1\nabla\tilde{p}_1}{1+\tilde{\Psi}}(1-\tilde{f}_\nu)\right] \tag{33}$$

3 Results and Discussion

The expressions for several thermoacoustic parameters (e.g., the fluctuating velocity and temperature, complex Nusselt number, fluctuating pressure, and energy flux density) are derived in Secs. 2.1–2.5. In this section, graphical results are presented along with simplifications and interpretations of the derived expressions. To avoid the confusion with the sign (+ or −), it is assumed that the porous stack is placed at the quarter wavelength $(0\le x\le\lambda/4)$ of

the sound wave. Also, it is assumed that the mean temperature gradient (∇T_m) is a positive quantity; i.e., the cold heat exchanger is placed at the beginning of the plate (near the driver side) and the hot heat exchanger is positioned at the end of the plate [11]. The thermophysical properties are assumed to be constant and are calculated at the mean temperature (T_m) except for the mean density (ρ_m), which is calculated from the mean pressure (p_m). Although nondimensional forms of the fluctuating velocity, temperature, Nusselt number, and energy flux density are adopted in this section, the properties of helium at 298 K ($=T_m$) are used if it is necessary as a pore fluid and a high-porosity porous medium is considered that is consistent with a typical thermoacoustic stack.

3.1 Discussion on the Flow Field. The expression of the fluctuating velocity (u_1), given in Eq. (7) or Eq. (8), is a superposition of two components: (a) a y-independent velocity component represented by the terms outside the curly bracket and (b) a y-dependent transverse wave represented by the hyperbolic cosine functions. As Swift number (S_w) represents the narrowness or the wideness of the channel, the fluctuating velocity u_1 approaches its boundary layer limit velocity fluctuation when S_w approaches infinity. In the limit of a very large S_w the terms with the hyperbolic cosine functions in Eq. (8) become zero, i.e.,

$$\lim_{S_w\to\infty}\left\{\frac{\cosh[(1+i)\sqrt{1+\Psi}S_wY]}{\cosh[(1+i)\sqrt{1+\Psi}S_w]}\right\}=0 \tag{34}$$

In such a case, the expression for the fluctuating velocity reduces to its y-independent velocity component only, i.e.,

$$u_{1,S_w\to\infty}=\left(\frac{1}{1+\Psi}\right)\left(\frac{i}{\omega\rho_m}\frac{\partial p_1}{\partial x}\right)=iu_p^s \tag{35}$$

It should be noted that the second bracketed term in Eq. (35), i.e., $i(\partial p_1/\partial x)/(\omega\rho_m)=iu^s$, represents a standing wave velocity expression [11] and can be obtained in the limit of a very large Darcy number (or the so called *clear fluid limit* [1]) from Eq. (35). Therefore, Eq. (35) represents the boundary layer limit fluctuating velocity inside the porous medium.

An expression for the nondimensional fluctuating velocity (U) can be obtained after dividing Eq. (8) by Eq. (9) and is given by

$$U=\left\{\frac{(1+i)\sqrt{1+\Psi}S_w}{(1+i)\sqrt{1+\Psi}S_w-\tanh[(1+i)\sqrt{1+\Psi}S_w]}\right\}\times\left\{1-\frac{\cosh[(1+i)\sqrt{1+\Psi}S_wY]}{\cosh[(1+i)\sqrt{1+\Psi}S_w]}\right\} \tag{36}$$

In the limit of a large Darcy number ($\mathrm{Da}\to\infty$), the porous-thermoacoustic-parameter ($1+\Psi$) approaches to unity. In such a case, the expression for the fluctuating velocity reduces to the clear-fluid-limit multistack thermoacoustic velocity as reported in the available literature (e.g., Refs. [9,11,33]).

For different values of S_w, U is plotted in Fig. 2 as a function of Y when $\mathrm{Da}\to\infty$. Relatively larger Swift numbers ($=10,20$) result in a thin shear layer adjacent to the wall within a few δ_ν. A large portion of the fluid away from the wall is unaffected by the viscous effect imposed by the boundary walls during a time period of oscillation. As S_w approaches a very large value ($S_w\to\infty$), the velocity profile becomes y-independent as discussed earlier in this section. In contrast to larger S_w, as S_w decreases and approaches relatively small values ($S_w\leq 1$), the velocity profile approaches a shape similar to that seen in the plane Poiseuille flow [36].

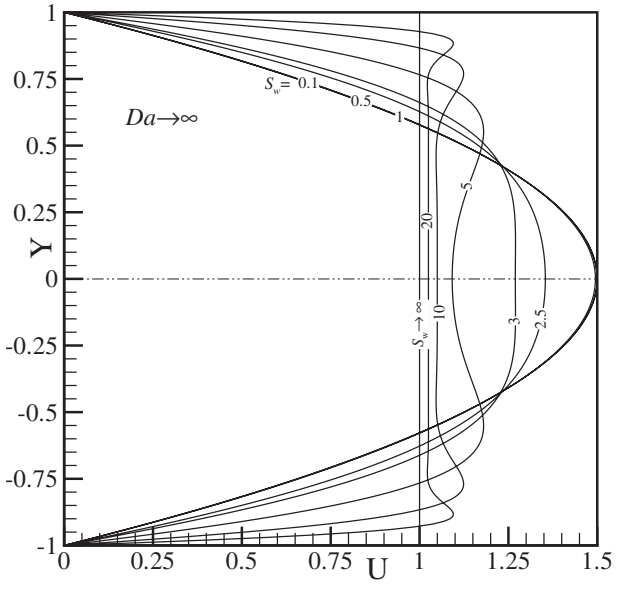

Fig. 2 Dimensionless velocity as functions of Swift numbers in the clear fluid limit

The effect of the Darcy number on the fluctuating velocity profile is discussed next. To facilitate this discussion, the dimensionless fluctuating velocity profiles are presented in Fig. 3 as a function of the Darcy number for a constant Swift number. At relatively higher Darcy numbers ($\mathrm{Da}\geq 1$), the porous medium's solid matrix induced frictional drag imposes less resistance to the flow. Therefore, the shear effect extends from the channel wall to the channel centerline for the considered Swift number in Fig. 3 and the velocity profiles are nearly parabolic for $\mathrm{Da}\geq 1$. In contrast, for relatively low Darcy numbers ($\mathrm{Da}<1$), the pore length scale becomes smaller than the viscous penetration depth, which imposes a signification amount of solid matrix induced frictional

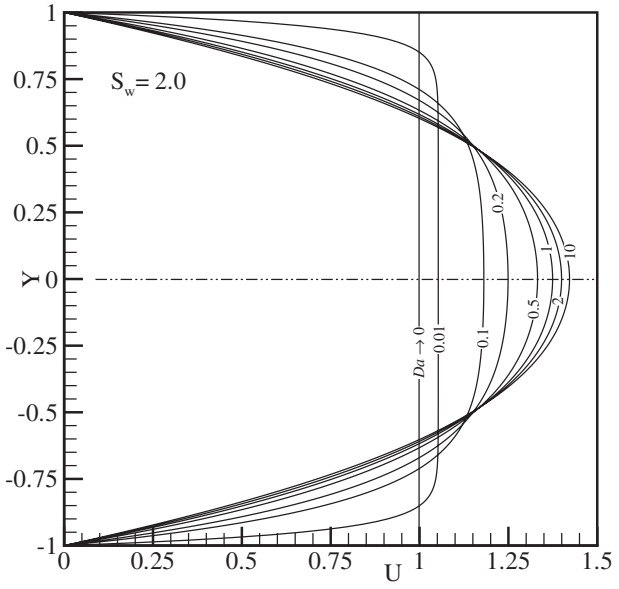

Fig. 3 Dimensionless velocity as functions of Darcy numbers at S_w=2.0

drag on the fluctuating fluid. Velocity profiles become flatter near the channel centerline with a thinner shear layer as the Darcy number decreases. In the limit of a very small Darcy number ($\mathrm{Da}\to 0$), the velocity profile approaches a slug-flow profile [32], as shown in Fig. 3.

3.2 Discussion on the Thermal Field. The expression for the fluctuating temperature T_1, given in Eq. (14), is a superposition of a y-independent temperature component represented by the terms before the first curly bracket and a y-dependent components represented by the terms with the hyperbolic cosine functions. In the limit of a very large Swift number, the terms with the hyperbolic cosine functions in Eq. (14) become zero, which results in the y-independent temperature component only, i.e.,

$$\lim_{S_w\to\infty}(T_1) = \frac{\beta T_m p_1}{\rho_m C_p \sigma} - \frac{\nabla T_m \nabla p_1}{\omega^2 \rho_m \sigma(1+\Psi)} = \frac{T_{\mathrm{ad}}}{\sigma} - \frac{T_{\mathrm{sw}}}{\sigma(1+\Psi)} = T_0 \tag{37}$$

In Eq. (37), T_{ad} ($=\beta T_m p_1/\rho_m C_p$) is the fluctuating temperature due to an adiabatic compression and expansion of the fluid in the absence of a porous medium [9] and T_{sw} ($=\nabla T_m \nabla p_1/\omega^2\rho_m$) is similar to a standing wave temperature amplitude. As the fluid oscillates along the x-direction with an equivalent displacement amplitude u_0/ω (where $u_0=\nabla p_1/\omega\rho_m$), the temperature at a given point in space oscillates by an amount $\nabla T_m u_0/\omega$ ($=T_{\mathrm{sw}}$), even if the temperature of a given piece of fluid remains constant. The appearance of σ and $(1+\Psi)$ terms in the expression of T_0 signifies the influence of the porous medium on T_{ad} and T_{sw}. Therefore, $\sigma^{-1}T_{\mathrm{ad}}$ and $\sigma^{-1}(1+\Psi)^{-1}T_{\mathrm{sw}}$ in Eq. (37), respectively, represent an equivalent adiabatic fluctuating temperature and a standing wave temperature amplitude inside the porous medium.

In Eq. (37), the fluid properties, temperature gradient, flow properties, geometry, and porous medium properties can be set in such a way that both the terms on the right hand side of Eq. (37) become equal, resulting in $T_0=0$. For such a special case, the resulting temperature gradient is proposed to be a critical temperature gradient (∇T_{cr}) and is given by

$$\nabla T_{\mathrm{cr}} = \frac{p_1}{\nabla p_1}\frac{\beta T_m \omega^2}{C_p}(1+\Psi) \tag{38}$$

The critical temperature gradient is important because it determines the transition between the heat pump and prime mover functions of thermoacoustic devices [11]. Usually, $\nabla T_m > \nabla T_{\mathrm{cr}}$ signifies a heat engine mode of operation and $\nabla T_m < \nabla T_{\mathrm{cr}}$ signifies a heat pump/refrigerator mode of operation for thermoacoustic devices. The ratio of ∇T_{cr} to ∇T_m can be termed the *porous medium temperature gradient ratio* (Γ_0) or simply the *temperature gradient ratio*. For the current problem Γ_0 can be expressed as follows:

$$\Gamma_0 = (\beta T_m)\frac{p_1}{\nabla p_1}\frac{\omega^2}{C_p \nabla T_m}(1+\Psi) = \frac{T_{\mathrm{ad}}}{T_{\mathrm{sw}}}(1+\Psi) = \Gamma_0^*(1+\Psi) \tag{39}$$

where Γ_0^* is the inverse of an ordinary temperature gradient ratio [33].

An expression for the nondimensional fluctuating temperature (Θ) can be obtained after dividing Eq. (14) by Eq. (15) and is given by

$$\Theta = \frac{(\Gamma_0 - 1) + \left[\dfrac{\mathrm{Pr}\ \sigma}{\mathrm{Pr}\ \sigma - \Psi - 1}\right]\dfrac{\cosh[(1+i)\sqrt{1+\Psi}S_w Y]}{\cosh[(1+i)\sqrt{1+\Psi}S_w]} - \left[\dfrac{1+\Psi}{\mathrm{Pr}\ \sigma - \Psi - 1} + \Gamma_0\right]\dfrac{\cosh[(1+i)\sqrt{\sigma\ \mathrm{Pr}}\ S_w Y]}{\cosh[(1+i)\sqrt{\sigma\ \mathrm{Pr}}\ S_w]}}{(1-f_k)\Gamma_0 - \left[1 + \dfrac{f_k(1+\Psi) - \mathrm{Pr}\ \sigma f_\nu}{(\mathrm{Pr}\ \sigma - \Psi - 1)}\right]} \tag{40}$$

Note that in the limit of a very large Darcy number ($\mathrm{Da}\to\infty$), the expression for Θ in Eq. (40) approaches the clear fluid limit expression reported in the thermoacoustic literature (e.g., Ref. [33]).

The influence of the Swift number in the clear fluid limit fluctuating temperature is studied next. For different values of S_w, Θ is plotted in Fig. 4 as a function of Y when $\mathrm{Da}\to\infty$. The temperature gradient ratio (Γ_0) is set equal to 2.0 because for efficient thermoacoustic device operation Γ_0 is suggested to be kept close to unity [11]. At a relatively large Swift number (i.e., a very wide channel), a considerable portion of the fluctuating fluid beyond a few thermal penetration depths does not feel the effect from the imposed wall thermal boundary condition during a time period of oscillation. This results in a thin layer of transverse temperature variation adjacent to the wall. As S_w approaches its theoretical upper limit ($S_w\to\infty$), the temperature profile becomes y-independent as expected (also discussed earlier in this section). In contrast to a large S_w, as S_w decreases and approaches relatively small values (e.g., $S_w\leq 2$), the fluctuating temperature profile approaches a parabolic shape extended from the wall to the centerline of the channel. For $\Gamma_0=2$, Fig. 5 shows the transverse variation in Θ at $S_w=0.5$, 3.5, and 10 and $\mathrm{Da}=0.001$, 0.01, 1, and ∞. For a given S_w, the shape of the temperature profile does not change significantly by the introduction of the solid matrix. The results also show that the centerline temperature decreases slightly with increases in Da. The convection process along the axial direction of the channel is suppressed due to the dampening effect produced by the solid matrix material of the porous medium on the flow field. In contrast, the transverse conduction process is enhanced due to the presence of the solid matrix material. These combined effects result in a minor variation in the dimensionless temperature profiles for a given time period of oscillation.

3.3 Discussion on the Complex Nusselt Number. In steady-state channel flow, the temperature gradient at the wall ($\partial T_1/\partial y|_{y=y_0}$) is in phase and proportional to the characteristic or bulk fluid-wall temperature difference ($T_w - T_{\mathrm{ref}}$) [32]. In such a case Nusselt number is a real number, and for a fully developed internal channel flow Nusselt number becomes a constant [32] for a particular geometry. In contrast, $T_w - T_{\mathrm{ref}}$ may not always be in phase with $\partial T_1/\partial y|_{y=y_0}$ in the case of an oscillating flow (see Figs. 4 and 5). For example, Fig. 5 clearly indicates that the near wall temperature (i.e., the thin layer with a transverse variation) leads (in-phase) the nearly constant centerline temperature for $S_w=3.5$ and 10.0. The transverse variation in temperature extends within a few thermal penetration depths (δ_k), which depends on the several fluid and flow parameters. The thinner the thermal penetration depth, the greater the temperature gradient. Therefore, the formidable-looking complex Nusselt number expression, presented in Eq. (20), always poses interpretation difficulties due to the complicated appearance of the different terms in it. Instead,

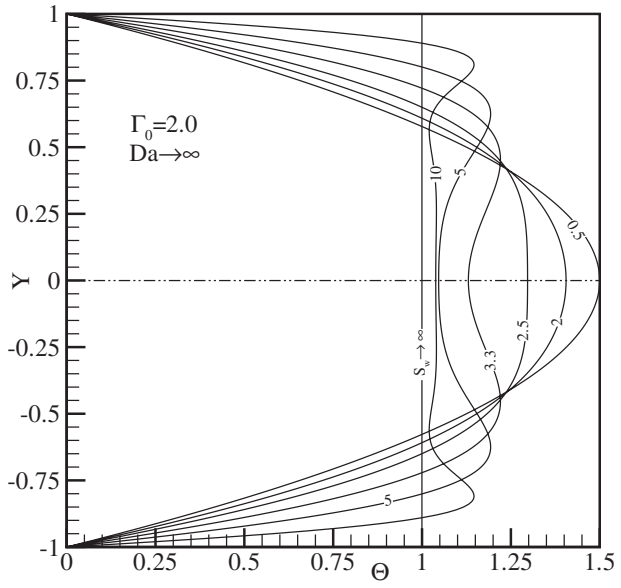

Fig. 4 Dimensionless temperature as functions of Swift numbers in the clear fluid limit

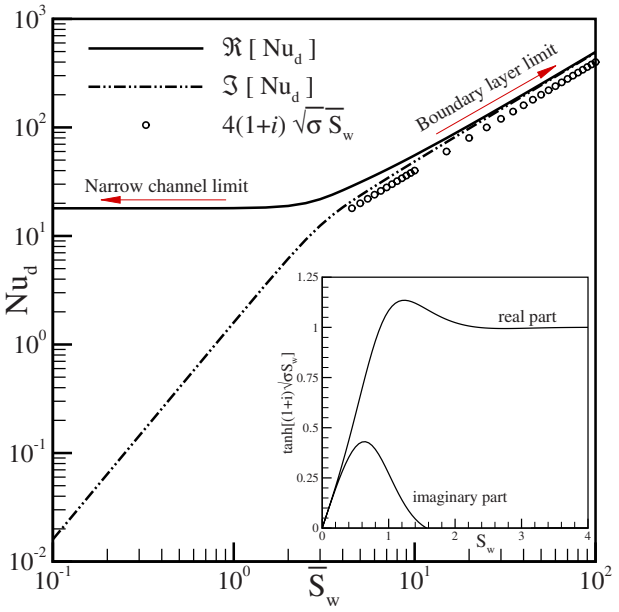

Fig. 6 Darcy limit of the complex Nusselt number at different Swift numbers

Eq. (20) will be simplified next using some reasonable assumptions in order to interpret some limiting thermoacoustic oscillation cases.

First, an inviscid limit or more precisely a Darcy limit of the complex Nusselt number is considered with a negligible longitudinal mean temperature gradient (i.e., $\nabla T_m \to 0$ and $\Gamma_0 \to \infty$). In the inviscid limit, the viscous penetration depth, the first Rott function, and the Prandtl number all approach zero (i.e., $\delta_\nu \to 0$, $f_\nu \to 0$, and $\mathrm{Pr} \to 0$). Considering these simplifications, the expression for the complex Nusselt number reduces to

$$\mathrm{Nu}_d = 8i\sigma\bar{S}_w^2\left(\frac{f_k}{1-f_k}\right) \tag{41}$$

in the Darcy limit. In Eq. (41), $\bar{S}_w$ ($=y_0/\delta_k$) is the modified Swift number. In deriving Eq. (41), $T_{1,\mathrm{av}}$ is considered to be T_{ref}. It is observed from Eq. (41) that Nu_d is independent of Da. However, it depends on the thermal boundary layer thickness because both $\bar{S}_w$ and f_k are functions of the thermal penetration depth. The real and imaginary parts of Nu_d are plotted in Fig. 6 as a function of $\bar{S}_w$. It is observed from Fig. 6 that the real part of Nu_d is larger in magnitude than the imaginary part at lower $\bar{S}_w$. That means the bulk fluid-wall temperature difference is in phase with the temperature gradient at the wall when the thermal penetration depth is larger than the channel width (i.e., $\bar{S}_w < 1$). This is also supported by the temperature profiles seen at lower Swift numbers, as shown in Figs. 4 and 5. Because of the nearly invariant wall temperature gradients at lower Swift numbers, Nu_d is nearly constant (the narrow channel limit of Nu_d). However, at higher Swift numbers, the thermal penetration depth is much smaller than the channel width, which leads Nu_d to its boundary layer limit. The hyperbolic tangent function in the expression of f_k (see Eq. (16)) approaches 1 when $\bar{S}_w$ is large in magnitude ($\bar{S}_w > 2$) (also graphically shown in Fig. 6). In such a case, f_k reduces to $(1-i)/(2\sqrt{\sigma}\bar{S}_w)$ and the expression for Nu_d (Eq. (41)) simplifies to

$$\mathrm{Nu}_d \approx \frac{8i\sigma\bar{S}_w^2}{(1+i)\sqrt{\sigma}\bar{S}_w - 1} \tag{42}$$

If Eq. (42) is expanded as a Taylor series with respect to $\bar{S}_w \to \infty$ and the leading order term is selected from that series, Eq. (42) further reduces to $4(1+i)\sqrt{\sigma}\bar{S}_w$. The boundary layer limit of Nu_d, i.e., $4(1+i)\sqrt{\sigma}\bar{S}_w$, is also plotted in Fig. 6 for larger values of $\bar{S}_w$. It is observed from Fig. 6 that $4(1+i)\sqrt{\sigma}\bar{S}_w$ underpredicts the original profiles of Nu_d a little because of several simplifying assumptions. However, both Nu_d and $4(1+i)\sqrt{\sigma}\bar{S}_w$ show similar trends at higher $\bar{S}_w$.

Next, consider a situation where viscous penetration depth (δ_ν) is no longer zero. Therefore, previous neglected parameters in the Darcy limit (e.g., Pr and f_ν) are nonzero in this case. However, the axial mean temperature gradient (∇T_m) is assumed in this case to be a fair bit larger than the critical temperature gradient (∇T_{cr}). Such an assumption makes the last term of Eq. (20) smaller than the other terms. In this approximation, the complex Nusselt number reduces to the following form:

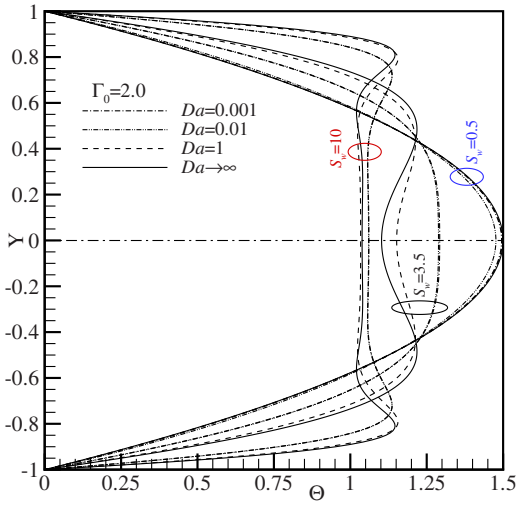

Fig. 5 Dimensionless temperature as functions of Swift numbers and Darcy numbers

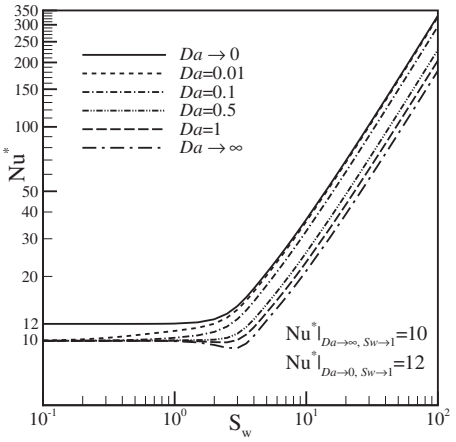

Fig. 7 Profiles of complex Nusselt numbers (Eq. (43)) at different Swift and Darcy numbers

$$\mathrm{Nu}^* = 8i(1+\Psi)\mathrm{Pr}\ \ \sigma S_w^2 \frac{f_\nu - f_k}{(\mathrm{Pr}\ \ \sigma - \Psi - 1) - \mathrm{Pr}\ \ \sigma f_\nu + f_k(1+\Psi)} \tag{43}$$

Equation (43) depends on the Darcy number and both the thermal and viscous penetration depths. The real part of Nu^* is plotted in Fig. 7 as a function of S_w at six selected Da. The profiles of Nu^* in Fig. 7 follow similar trends to that seen in Fig. 6 for Nu_d. For a given Da, variation in Nu^* with S_w is insignificant as long as S_w is small in magnitude (a narrow channel limit). For a higher S_w, Nu^* approaches the boundary layer limit for all considered Da. In the limit of a very large Darcy number ($\mathrm{Da}\to\infty$), Eq. (43) reduces, after some rearrangements, to the following form:

$$\mathrm{Nu}^*|_{\mathrm{Da}\to\infty} = 4\times 2i\ \ \mathrm{Pr}\ \ S_w^2\left[\frac{(1-f_\nu)(1-\mathrm{Pr})}{(1-f_k)-\mathrm{Pr}(1-f_\nu)} - 1\right] \tag{44}$$

A similar equation is obtained by Liu and Garrett [35] for a single pore geometry. Note that Liu and Garrett [35] used the Lautrec number ($\mathrm{Lc}_\kappa = \sqrt{\mathrm{Pr}}\,S_w$) [40] and a pore radius instead of the Swift number and a hydraulic radius, respectively, in their Nusselt number expression.

3.4 Discussion on the Energy Flux Density. By using Γ_0 from Eq. (39), a nondimensional global energy flux equation can be expressed as follows:

$$\begin{aligned}\frac{E_2}{E_0} = &-\Gamma_0 \Re\left[(1-\tilde{f}_\nu) + \frac{\beta T_m}{\sigma}\frac{(1+\tilde{\Psi})(\tilde{f}_\nu - f_k)}{\sigma\ \ \mathrm{Pr}+\tilde{\Psi}+1}\right] \\ &+ \Im\left[\frac{1}{\sigma}\left\{(1-\tilde{f}_\nu) - \frac{\sigma\ \ \mathrm{Pr}}{\sigma\ \ \mathrm{Pr}-\Psi-1}\frac{(f_\nu-\tilde{f}_\nu)-\Psi f_\nu - \tilde{\Psi}\tilde{f}_\nu}{2}\right.\right. \\ &\left.\left. - \frac{(1+\Psi)(1+\tilde{\Psi})(\tilde{f}_\nu - f_k)}{(\sigma\ \ \mathrm{Pr}-\Psi-1)(\sigma\ \ \mathrm{Pr}+\tilde{\Psi}+1)}\right\} + \left(\frac{\sigma-1}{\sigma}\right)(1-\tilde{f}_\nu)\right] \\ &- \Gamma_{\mathrm{cond}}\end{aligned} \tag{45}$$

where E_0 is a reference global energy flux given by

$$\begin{aligned}E_0 &= \frac{y_0\Pi}{2}\frac{\nabla T_m C_p}{\omega^3\rho_m}\frac{\nabla p_1 \nabla \tilde{p}_1}{(1+\Psi)(1+\tilde{\Psi})} \\ &= \frac{y_0\Pi}{2}\frac{\rho_m C_p}{(1+\Psi)(1+\tilde{\Psi})}\left(\frac{\nabla p_1}{\omega\rho_m}\right)\left(\frac{\nabla\tilde{p}_1}{\omega\rho_m}\frac{\nabla T_m}{\omega}\right) \\ &\approx \frac{y_0\Pi}{2}\frac{1}{(1+\Psi)(1+\tilde{\Psi})}\rho_m C_p(u_0 T_{\mathrm{sw}})\end{aligned} \tag{46}$$

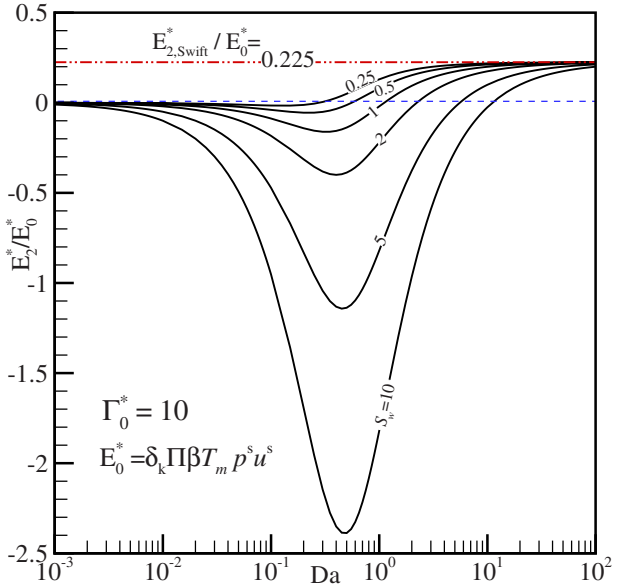

Fig. 8 Distribution of normalized E_2^* as functions of Da and $\bar{S}_w$ for $\Gamma_0^*=10$ (conduction energy flux is neglected in this figure)

In the limit of a very large Darcy number ($\mathrm{Da}\to\infty$), Eq. (45) reduces to the energy flux equations obtained by Swift [11] and Mahmud and Fraser [33] for a multiplate thermoacoustic system in its thin plate limit. In Eq. (45), Γ_{cond} is the ratio of the axial conduction term (the last term in Eq. (32)) to E_0. The formidable-looking energy flux equation (Eq. (32) or Eq. (45)) poses interpretation difficulties due to its complicated functional relationship with different parameters. Therefore, a simplified energy flux equation, using the boundary layer approximation, as discussed before, is investigated first in order to understand how energy flux changes with changes in the different thermoacoustic parameters (e.g., Da and S_w). In the inviscid boundary layer approximation, Eq. (32) (or Eq. (45)) reduces to

$$\begin{aligned}E_2^* = &-\frac{\delta_k\Pi}{2\sigma^{3/2}}\left(\frac{\beta T_m p^s u^s}{2+\mathrm{Da}^{-2}/2}\right)\left[\left(\frac{1}{\Gamma_0^*}-1\right)\right. \\ &\left. + \frac{\sigma^{3/2}\bar{S}_w}{\mathrm{Da}}\left\{\left(1+\frac{1}{\beta T_m}\right) - \frac{1}{\sqrt{\sigma}}\right\}\right] - \left[\Pi y_0 k\frac{\partial T_m}{\partial x}\right]_{\mathrm{cond}}\end{aligned} \tag{47}$$

The conduction term (the last square bracketed term in Eq. (47)) imposes a negative effect on the energy flow and efficiency of thermoacoustic devices so it is best if the x component of the thermal conductivity is as small as possible. Now, nonzero thermal conductivity in the y-direction is essential for device operation. The y component of the thermal conductivity appears in δ_k; if it were zero, there would be no thermoacoustic effects at all. Therefore, a nonisotropic conductivity is most desirable being very small in the x-direction and large in the y-direction. E_2^* is proportional to the area $\delta_k\Pi$ ($=y_0\Pi/\bar{S}_w$); therefore, if $\bar{S}_w\approx 1$ (i.e., $y_0\approx\delta_k$), then essentially the entire cross-sectional area of the fluid in the porous medium is effective in carrying energy. E_2^* depends on βT_m for liquids near their critical points and for most gases $\beta T_m\approx 1$. E_2^* is proportional to the product $p^s u^s$ and so approaches and may equal to zero if a short porous stack is placed near a pressure node or a velocity node of the standing wave oscillation. In order to understand the Da dependency of E_2^*, E_2^* is normalized by $\delta_k\Pi\beta T_m p^s u^s$ and plotted in Fig. 8 as a function of Da ($0.001\le\mathrm{Da}\le 10$) at different $\bar{S}_w$ for $\Gamma_0^*=10$. The conduction energy flux is assumed negligible in Fig. 8. For a vanishingly small Darcy number (i.e., $\mathrm{Da}\to 0$), the pore length scale becomes negligible

when compared with the thermal penetration depth. In such a case, the porous channel acts as if it is nearly a solid block. Therefore, in the $\mathrm{Da}\to 0$ limit, E_2^* (Eq. (47)) reduces to the expected conduction energy flux, and then E_2^* further reduces to zero for a negligible conduction energy flux. Therefore, it is observed in Fig. 8 that all nondimensional energy flux profiles approach to zero at very small Darcy numbers. As Da increases from its lowest possible value, $|E_2^*/E_0^*|$ increases in magnitude and approaches a maximum near $\mathrm{Da}\approx 1$ for $\bar{S}_w \geq 1$ where the penetration depth and pore scale are comparable. For a very high Darcy number (i.e., $\mathrm{Da}\to\infty$), Eq. (47) reduces to an expression obtained and discussed by Swift [11] and this reduced expression is as follows:

$$E^*_{2,\mathrm{Swift}} = -\frac{\delta_k \Pi}{4}(\beta T_m p^s u^s)\left[\frac{1}{\Gamma_0^*} - 1\right] - \left[\Pi y_0 k \frac{\partial T_m}{\partial x}\right]_{\mathrm{cond}} \quad (48)$$

For the Γ_0^* considered in Fig. 8, the Swift limit (Eq. (48)) is 0.225. As seen in Fig. 8 the nondimensional energy flux profiles approach the Swift limit at relatively high Darcy numbers.

Figure 8 is a very insightful result. Its behavior was explained in the previous paragraph; however, Fig. 8 also holds significant physical meaning for a designer of thermoacoustic devices. More insightful, Fig. 8 reveals via the large dip in E_2^*/E_0^* that there is much potential to improve thermoacoustic refrigerator efficiencies by operating in the Da range 0.1–1.0 using a channel width characterized by $S_w \geq 2$. Furthermore, for the designer, the $\mathrm{Da}\to 0$ where $E_2^*/E_0^* \to [E_2^*/E_0^*]_{\mathrm{cond}}$ is the no fluid, and it is a solid, slug-flow, conduction only, no porosity limit for the stack, while the $\mathrm{Da}\to\infty$ where $E_2^*/E_0^* \to [E_2^*/E_0^*]_{\mathrm{Swift}}$ (i.e., the Swift limit case, Eq. (48)) is understood to be the fluid or gas only, no porous material, infinite porosity limit for the stack. That is, $\mathrm{Da}\to 0$ is a solid stack with no holes, $\mathrm{Da}\to\infty$ is the typical stack composed of plates with, say, air or helium between, and if a porous medium is used much more efficient thermoacoustic engine designs are possible in the Da range 0.1–1.0.

For porous media thermoacoustic systems, σ and Da are two important parameters because their magnitudes strictly reflect a combination of the thermophysical properties and porosities of the porous medium and thermophysical properties of the working fluid. If the term Γ_{cond} can be dropped from Eq. (45), an upper limit to energy transfer and efficiency results. Nevertheless, this upper limit of energy transfer is a function of Da, S_w, and Γ_0. For a selected porous medium and working fluid, S_w is varied from a small value ($S_w = 0.1$) to a large value ($S_w = 10$) in order to identify a maximum value of E_2/E_0 from Eq. (45) for a particular combination of Da and Γ_0. The S_w corresponding to the maximum E_2/E_0 is expressed as S_{w0}. For selected ranges of Da and Γ_0, S_{w0} is calculated and presented as a function of Da and Γ_0 in Figs. 9 and 10 for $\sigma = 10$, and in Figs. 11 and 12 for $\sigma = 279$. The mesh plots (Figs. 9 and 11) are helpful for understanding the pattern of variation in S_{w0} with Da and Γ_0, while the contour plots (Figs. 10 and 12) may be used as performance plots describing stack-plate spacing at the maximum energy transfer.

Most of the results presented in this paper are applicable to any stack material including aluminum foams; however, some results are stack shape dependent and may not fit perfectly into the model presented. Specifically, Figs. 9–12 include some stack shape dependence. Investigating the degree of impact stack shape has on the results of this paper is left for future work.

4 Conclusions

The general thermoacoustic theories available in the existing literature are modified to consider a thermoacoustic stack where the fluid-gaps are filled with a porous medium. A porous medium filled stack has a larger heat transfer area in comparison to a conventional gas-only filled stack. By using a linear perturbation analysis, the governing momentum and energy equations are linearized and solved in order to obtain the fluctuating velocity and temperature, fluctuating pressure, complex Nusselt number, and energy flux inside the porous medium in terms of several dimensionless parameters, e.g., Darcy number, Swift number, temperature gradient ratio, and Rott's functions. Both fluctuating velocity and temperature have a y-dependent part and a y-independent part. For a very wide channel limit ($S_w \to \infty$), both velocity and temperature approach their y-independent parts and these y-independent expressions are identified as the boundary layer limit velocity and temperature fluctuations, respectively. Darcy number (Da), a ratio of the permeability of porous medium to the viscous penetration depth squared, is an important parameter in

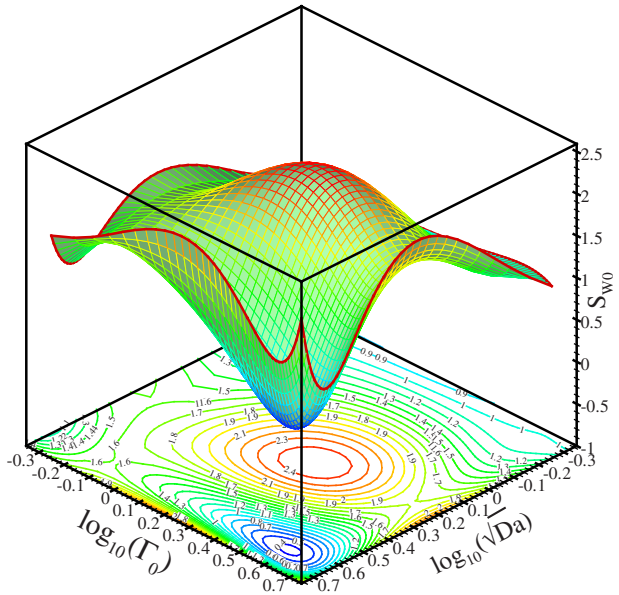

Fig. 9 Mesh-contour plot showing that the Swift number distribution corresponds to the maximum energy transfer as a function of Darcy number (Da) and temperature gradient ratio (Γ_0) for $\sigma = 10$ (note: $\log_{10}(0.5) \approx -0.3$ and $\log_{10}(5) \approx 0.7$)

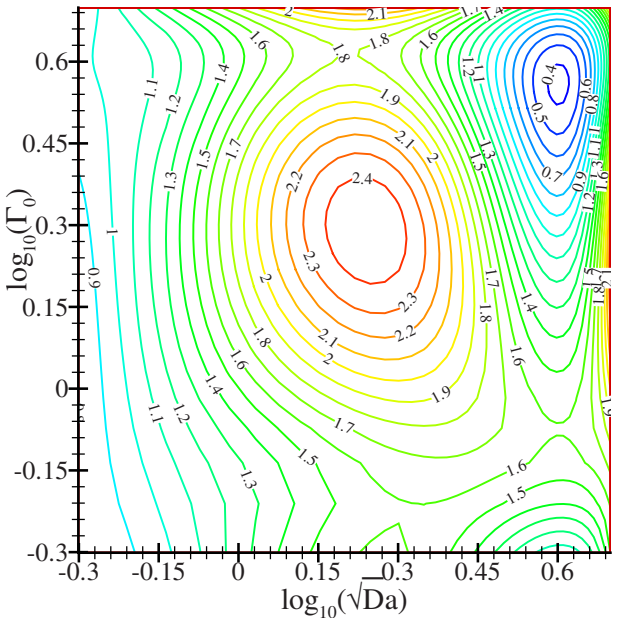

Fig. 10 Performance plot corresponds to Fig. 9 showing the magnitude of the Swift number at maximum energy transfer as a function of Darcy number and Γ_0

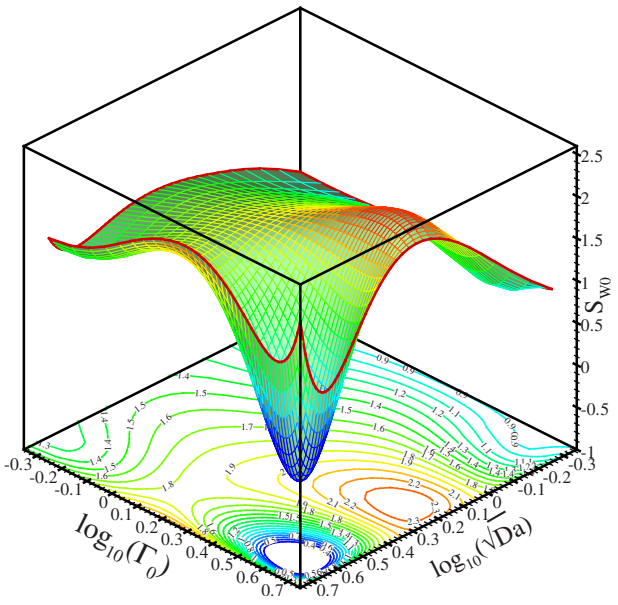

Fig. 11 Mesh-contour plot showing that the Swift number distribution corresponds to the maximum energy transfer as a function of Darcy number (Da) and temperature gradient ratio (Γ_0) for ERG AL 40 in helium (σ=279)

studying porous media thermoacoustics; it expresses the degree of internal blockage experienced by stack after introducing the porous medium.

In the limit of small Darcy number ($Da \to 0$), the velocity profile approaches a slug-flow profile. In contrast, in the limit of a large Darcy number ($Da \to 0$), the velocity profile approaches a plane Poiseuille flow profile. At very wide and very narrow channel limits, a change in the Darcy number causes an insignificant change in the temperature profile.

The complex Nusselt number for the inviscid oscillating flow in the Darcy limit (Nu_d) with negligible axial temperature gradient and the complex Nusselt number for viscous oscillating flow for relatively small temperature gradient ratio (Nu^*) are calculated. Both Nu_d and Nu^* are nearly constant when the channel is narrow. In the case of a wide channel, both Nu_d and Nu^* increase with increases in the Swift number. A wave equation is developed from simplified continuity, momentum, and energy equations. In the inviscid limit of the fluid fluctuation in a nonporous medium without any longitudinal temperature gradient, this wave equation reduces as expected to the well known Helmholtz equation.

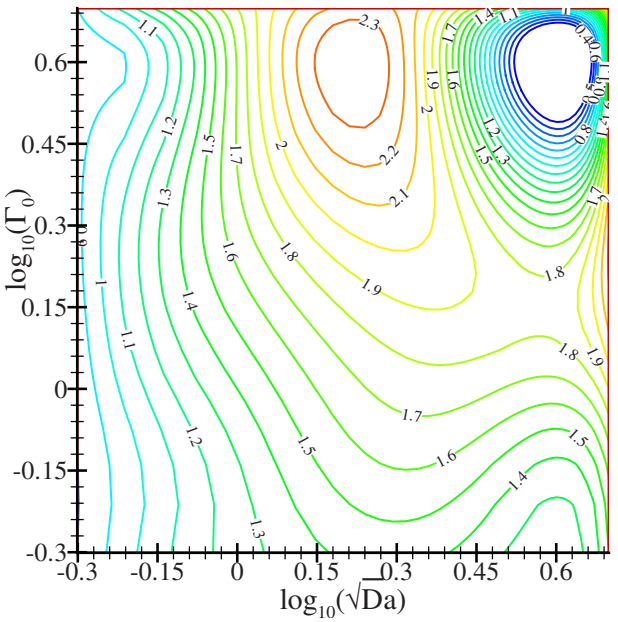

Fig. 12 Performance plot corresponds to Fig. 11 showing the magnitude of the Swift number at maximum energy transfer as a function of Darcy number and Γ_0 for ERG AL 40 [41] in helium

An energy flux density expression derived in the present study matches quantitatively with the expression derived by Swift [11] for a nonporous medium in the inviscid boundary layer limit.

Further work is required to extend the current problem to consider a full conjugate heat transfer problem and subsequent optimization based on entropy generation minimization. Numerical and experimental works are also left for future work.

Nomenclature

a_0 = complex parameter, $=(1+i)\sqrt{1+\Psi}/\delta_\nu$
b_0 = complex parameter, $=(1+i)\sqrt{\sigma}/\delta_k$
b = Forchheimer's coefficient
c = velocity of sound, m s^{-1}
C_p = specific heat of the fluid at constant pressure, J kg^{-1} K^{-1}
Da = Darcy number, $=K/\delta_\nu^2$
E_0 = reference global energy flux, W
$\dot{\mathbf{E}}$ = energy flux density vector, W m^{-2}
$\dot{E}_2$ = second order energy flux density, W m^{-2}
E_2 = global energy flux, W
f = frequency of oscillation, Hz
f_ν = first Rott's or Swift's function of thermoacoustics, $=\tanh(a_0 y_0)/(a_0 y_0)$
$\tilde{f}_\nu$ = complex conjugate of f_ν
f_k = second Rott's or Swift's function of thermoacoustics, $=\tanh(b_0 y_0)/(b_0 y_0)$
$\tilde{f}_k$ = complex conjugate of f_k
i = complex number, $=\sqrt{-1}$
h = enthalpy, J kg^{-1}
K = permeability of the porous medium, m^2
k = thermal conductivity, W m^{-1} K^{-1}
k_0 = inverse of the wave number, $=\omega/c$
L = length of the stack, m
Lc_κ = Lautrec number, $=\sqrt{\mathrm{Pr}}\ S_w$
Nu = Nusselt number
Nu_d = Darcy limit of the Nusselt number, see Eq. (41)
p = pressure, N m^{-2}
p^s = standing wave pressure [11]
Pr = Prandtl number of the fluid, $=\delta_\nu^2/\delta_k^2$
Re = Reynolds number
s = entropy, J kg^{-1} K^{-1}
S_w = Swift number, $=y_0/\delta_\nu$
$\bar{S}_w$ = modified Swift number, $=y_0/\delta_k$
t = time, s
T = temperature of the fluid, °C
T_0 = reference temperature, °C
T_{ad} = fluctuating temperature due to an adiabatic oscillation, $=T_m\beta p_1/\rho_m C_p$
T_b = bulk mean or the mixing-cup temperature of the fluid, °C
T_{sw} = standing wave temperature oscillation, $=\nabla T_m \nabla p_1/\rho_m\omega^2$
T_w = wall temperature or the solid-fluid interface temperature, °C
u = axial component of the fluctuating velocity inside the channel, m s^{-1}

U = dimensionless axial velocity, see Eq. (36)
u_0 = reference velocity, $=\nabla p_1/\omega\rho_m$
u^s = standing wave velocity, $=i(\partial p_1/\partial x)/(\omega\rho_m)$
u_p^s = standing wave velocity in porous medium, $=u^s/(1+\Psi)$
v = transverse velocity, m s^{-1}
$\mathbf{V}$, $\mathbf{v}$ = velocity vector, m s^{-1}
W_2 = total work flux, W
x = axial distance, m
y = transverse distance in fluid, m
Y = dimensionless transverse distance in the porous medium, $=y/y_0$
y_0 = half width of a channel, m

Greek Symbols

α = thermal diffusivity, m^2 s^{-1}
β = thermal expansion coefficient, K^{-1}
γ = isobaric to isochoric specific heat ratio, $=C_p/C_v$
Γ_0^* = inverse of an ordinary temperature gradient ratio, $=T_{\mathrm{ad}}/T_{\mathrm{sw}}$
Γ_0 = temperature gradient ratio in the presence of a porous medium, $=(T_{\mathrm{ad}}/T_{\mathrm{sw}})(1+\Psi)$
δ_ν = viscous penetration depth, $=\sqrt{2\nu/\omega}$
δ_k = thermal penetration depth, $=\sqrt{2\alpha_f/\omega}$
∇T_m = mean temperature gradient, $=\partial T_m/\partial x$
∇p_1 = pressure gradient, $=\partial p_1/\partial x$
∇T_{cr} = critical temperature gradient, °C m^{-1}
μ = dynamic viscosity of the fluid, N m^{-2} s
ν = kinematic viscosity, m^2 s^{-1}
$\boldsymbol{\sigma}$ = viscous stress tensor, N m^{-2}
σ = heat capacity ratio, $=\varphi+(1-\varphi)(\rho_{\mathrm{sm}}C_{\mathrm{sm}})/(\rho C_p)$
ω = circular frequency, rad s^{-1}
ρ = density of the fluid, kg m^{-3}
τ = time period, $=2\pi/\omega$
Ψ = dimensionless parameter, $=\varphi(2i\ \mathrm{Da})^{-1}$
λ = wavelength, m
$\tilde{\lambda}$ = modified wavelength, $=\lambda/2\pi$
Π = width of the plate, m
φ = porosity of the porous medium, =void volume/total volume
Φ_ν = dimensionless parameter, $=y_0^2a_0^2=2i(1+\Psi)S_w^2$
Φ_k = dimensionless parameter, $=y_0^2b_0^2=2i\sigma\ \mathrm{Pr}\ S_w^2$

Subscripts and Superscripts

0 = reference value
1 = first order variable
av = average value
f = properties of the fluid
m = mean value
sm = properties of the solid matrix material in the porous medium
w = value at wall

Symbols

$\Re[\ ]$ = real part of an expression
$\Im[\ ]$ = complex part of an expression

References

[1] Nield, D. A., and Bejan, A., 2006, *Convection in Porous Media*, 3rd ed., Springer-Verlag, Berlin.
[2] Ingham, D. B., and Pop, I., 1998, *Transport Phenomena in Porous Media*, Pergamon, Oxford.
[3] Ingham, D. B., and Pop, I., 2002, *Transport Phenomena in Porous Media II*, Pergamon, Amsterdam.
[4] Bejan, A., Dincer, I., Lorent, S., Miguel, A. F., and Reis, A. H., 2004, *Porous and Complex Flow Structures in Modern Technologies*, Springer-Verlag, New York.
[5] Scheiddeger, A. E., 1957, *The Physics of Flow Through Porous Media*, Macmillan, New York.
[6] Bejan, A., 1987, "Convective Heat Transfer in Porous Media," *Handbook of Single-Phase Convective Heat Transfer*, S. Kakaç, R. K. Shah, and W. Aung, eds., Wiley, New York.
[7] Kaviany, M., 1995, *Principles of Heat Transfer in Porous Media*, Springer-Verlag, New York.
[8] Vafai, K., 2000, *Handbook of Porous Media*, Dekker, New York.
[9] Swift, G. W., 2002, *Thermoacoustics: A Unifying Perspective for Some Engines and Refrigerators*, ASA, Melville, NY.
[10] Adeff, J. A., Hofler, T. J., Atchley, A. A., and Moss, W. C., 1998, "Measurements With Reticulated Vitreous Carbon Stacks in Thermoacoustic Prime Movers and Refrigerators," J. Acoust. Soc. Am., **104**, pp. 32–38.
[11] Swift, G. W., 1988, "Thermoacoustic Engines," J. Acoust. Soc. Am., **84**, pp. 1145–1180.
[12] Rott, N., 1980, "Thermoacoustics," Adv. Appl. Mech., **20**, pp. 135–175.
[13] Mahmud, S., and Fraser, R. A., 2004, "Flow and Heat Transfer Inside Porous Stack: Steady State Problem," Int. Commun. Heat Mass Transfer, **31**, pp. 951–962.
[14] Mahmud, S., and Fraser, R. A., 2004, "Entropy—Energy Analysis of Porous Stack: Steady State Conjugate Problem," Int. J. Exergy, **1**, pp. 385–398.
[15] Mahmud, S., and Fraser, R. A., 2005, "Conjugate Heat Transfer Inside a Porous Channel," Heat Mass Transfer, **41**, pp. 568–575.
[16] Mahmud, S., and Fraser, R. A., 2003, "Vibrational Effect on Entropy Generation in a Square Porous Cavity," Entropy, **5**, pp. 366–376.
[17] Mahmud, S., and Fraser, R. A., 2003, "Free Convection and Irreversibility Analysis Inside a Circular Porous Enclosure," Entropy, **5**, pp. 358–365.
[18] Leong, K. C., and Jin, L. W., 2004, "Heat Transfer of Oscillating and Steady Flows in a Channel Filled With Porous Media," Int. Commun. Heat Mass Transfer, **31**, pp. 63–72.
[19] Leong, K. C., and Jin, L. W., 2005, "An Experimental Study of Heat Transfer in Oscillating Flow Through a Channel Filled With an Aluminum Foam," Int. J. Heat Mass Transfer, **48**, pp. 243–253.
[20] Fu, H. L., Leong, K. C., Huang, X. Y., and Liu, C. Y., 2001, "An Experimental Study of Heat Transfer of a Porous Channel Subjected to Oscillating Flow," ASME J. Heat Transfer, **123**, pp. 162–170.
[21] Kuznetsov, A. V., and Nield, D. A., 2006, "Forced Convection With Laminar Pulsating Flow in a Saturated Porous Channel or Tube," Transp. Porous Media, **65**, pp. 505–523.
[22] Organ, A. J., 1992, *Thermodynamics and Gas Dynamics of the Stirling Cycle Machine*, Cambridge University Press, Cambridge, England.
[23] Vafai, K., and Kim, C. L., 1990, "Analysis of Surface Enhancement by a Porous Substrate," ASME J. Heat Transfer, **112**, pp. 700–706.
[24] Bejan, A., 1984, *Convection Heat Transfer*, Wiley, New York.
[25] Bejan, A., 2003, "Porous Media," *Heat Transfer Handbook*, A. Bejan and A. D. Kraus, eds., Wiley, New York.
[26] Darcy, H., 1856, *Les Fontaines Publiques de la Ville de Dijon*, Victor Dalamont, Paris.
[27] Vafai, K., and Tien, C. L., 1981, "Boundary and Inertia Effects on Flow and Heat Transfer in Porous Media," Int. J. Heat Mass Transfer, **24**, pp. 195–203.
[28] Forchheimer, P. H., 1901, "Wasserbewegung durch Boden," Z. Ver. Dtsch. Ing., **45**, pp. 1782–1788.
[29] Kaviany, M., 1985, "Laminar Flow Through a Porous Channel Bounded by Isothermal Parallel Plates," Int. J. Heat Mass Transfer, **28**, pp. 851–858.
[30] Haji-Sheikh, A., Nield, D. A., and Hooman, K., 2006, "Heat Transfer in the Thermal Entrance Region for Flow Through Rectangular Porous Passages," Int. J. Heat Mass Transfer, **49**, pp. 3004–3015.
[31] Kinsler, L. W., Frey, A. R., Coppens, A. B., and Sanders, J. V., 2000, *Fundamentals of Acoustic*, Wiley, New York.
[32] Burmeister, L. C., 1993, *Convective Heat Transfer*, Wiley, New York.
[33] Mahmud, S., and Fraser, R. A., 2005, "An Analytical Solution and Computer Simulation for a Multi-Plate Thermoacoustic System," Int. J. Exergy, **2**, pp. 207–230.
[34] Lu, G., and Cheng, P., 2000, "Friction Factor and Nusselt Number for Thermoacoustic Transport Phenomena in a Tube," J. Thermophys. Heat Transfer, **14**, pp. 566–573.
[35] Liu, J., and Garrett, S. L., 2006, "Relationship Between Nusselt Number and the Thermoviscous (Rott) Functions," J. Acoust. Soc. Am., **119**, pp. 1457–1462.
[36] Landau, L. D., and Lifshitz, E. M., 1982, *Fluid Mechanics*, Pergamon, New York.
[37] Cao, N., Olson, J. R., Swift, G. W., and Chen, S., 1996, "Energy Flux Density in a Thermoacoustic Couple," J. Acoust. Soc. Am., **99**, pp. 3456–3464.
[38] Ishikawa, H., and Mee, D. J., 2002, "Numerical Investigation of Flow and Energy Fields Near a Thermoacoustic Couple," J. Acoust. Soc. Am., **111**, pp. 831–839.
[39] Bejan, A., 2006, *Advanced Engineering Thermodynamics*, Wiley, New York.
[40] Garrett, S. L., 2004, "Resource Letter TA-1: Thermoacoustic Engines and Refrigerators," Am. J. Phys., **72**, pp. 11–17.
[41] ERG, 2005, Materials and Aerospace Corporation, 900 Stanford Avenue, Oakland, CA.

Dual-Permeability Modeling of Capillary Diversion and Drift Shadow Effects in Unsaturated Fractured Rock

Clifford K. Ho
e-mail: ckho@sandia.gov

Bill W. Arnold

Susan J. Altman

Sandia National Laboratories,
P.O. Box 5800,
Albuquerque, NM 87185-1127

The drift-shadow effect describes capillary diversion of water flow around a drift or cavity in porous or fractured rock, resulting in lower water flux directly beneath the cavity. This paper presents computational simulations of drift-shadow experiments using dual-permeability models, similar to the models used for performance assessment analyses of flow and seepage in unsaturated fractured tuff at Yucca Mountain. Comparisons were made between the simulations and experimental data from small-scale drift-shadow tests. Results showed that the dual-permeability models captured the salient trends and behavior observed in the experiments, but constitutive relations (e.g., fracture capillary-pressure curves) can significantly affect the simulated results. Lower water flux beneath the drift was observed in both the simulations and tests, and fingerlike flow patterns were seen to exist with lower simulated capillary pressures. The dual-permeability models used in this analysis were capable of simulating these processes. However, features such as irregularities along the top of the drift (e.g., from roof collapse) and heterogeneities in the fracture network may reduce the impact of capillary diversion and drift shadow. An evaluation of different meshes showed that at the grid refinement used, a comparison between orthogonal and unstructured meshes did not result in large differences.
[DOI: 10.1115/1.3180700]

Keywords: dual permeability, unsaturated flow, capillary diversion, drift shadow

1 Introduction

Performance assessment analyses of the proposed high-level radioactive waste repository at Yucca Mountain, NV, do not include the potential development of a "drift shadow," a region of reduced water flux beneath the tunnels (drifts) that will contain the waste. A region of reduced water flux directly beneath the drift may impact the flow and transport of contaminants toward the water table. However, until recently, very little data have existed regarding the possibility of drift-shadow development beneath a drift or cavity in unsaturated fractured rock.

Recent tests using X-ray absorption imaging have provided quantitative and visual evidence of the drift-shadow effect in unsaturated fractured tuff [1]. This paper presents simulations of these tests using dual-permeability models, similar to the models used for performance assessment analyses of flow and seepage in unsaturated fractured tuff at Yucca Mountain. Previous analytical solutions have been developed to predict the drift-shadow effect in porous media [2], and Houseworth et al. [3] developed a dual-permeability model of flow diversion around a simulated drift at Yucca Mountain in unsaturated fractured tuff. However, no experimental or field data were available for comparison to the theoretical results in those studies.

The purpose of this study is to present an evaluation of flow diversion and drift-shadow effects observed in experiments performed by Altman et al. [1] using a dual-permeability model. Alternative model parameters and modeling methods are investigated to determine the potential impact on simulated results.

Manuscript received September 29, 2008; final manuscript received April 1, 2009; published online July 31, 2009. Review conducted by Kambiz Vafai. Paper presented at the 2008 International High-Level Radioactive Waste Management.

2 Experimental Summary

In the experiments performed by Altman et al. [1], two machined slabs of Topopah Spring welded tuff were separated by thin wires to represent desired fracture apertures. An ~8 cm diameter circular hole cut through the slabs represented an open drift in the tuff. The slabs were held in place with an aluminum frame and encased with epoxy and Plexiglass. Water was introduced at prescribed flow rates through inflow ports at four locations along the top of the fracture aperture. The flow was allowed to reach steady-state, and the outflow was collected in five bins along the bottom of the apparatus to determine the flux distribution pattern below the drift. X-ray imaging was used to visualize solute (potassium iodide) flow paths through the fracture and tuff matrix during the experiment. Figure 1 shows a schematic of the tuff samples and test cell. Additional details of the experimental apparatus and test procedure can be found in Altman et al. [1].

Figure 2 shows some results from the 500 μm aperture experiments using X-ray imaging. The solute flow paths are distinct and appear to follow discrete "fingers" through the fracture aperture. In addition, the solute appears to be diverted around the drift opening. Heterogeneities in the tuff slabs (higher porosity pumice fragments) appear to increase the diffusion or imbibition of the solute into the tuff matrix. Locations with pumice fragments show up as "hot spots" in the X-ray images. However, it is unclear if these heterogeneities in the matrix affected the distribution of flow in the fracture aperture. The distribution of outflow beneath the drift cavity is discussed along with a comparison to the models in Secs. 3 and 4.

3 Computational Approach

The dual-permeability model has been used to model flow and transport within fractured rock at Yucca Mountain [4]. In this conceptual model, flow and transport can occur through both the

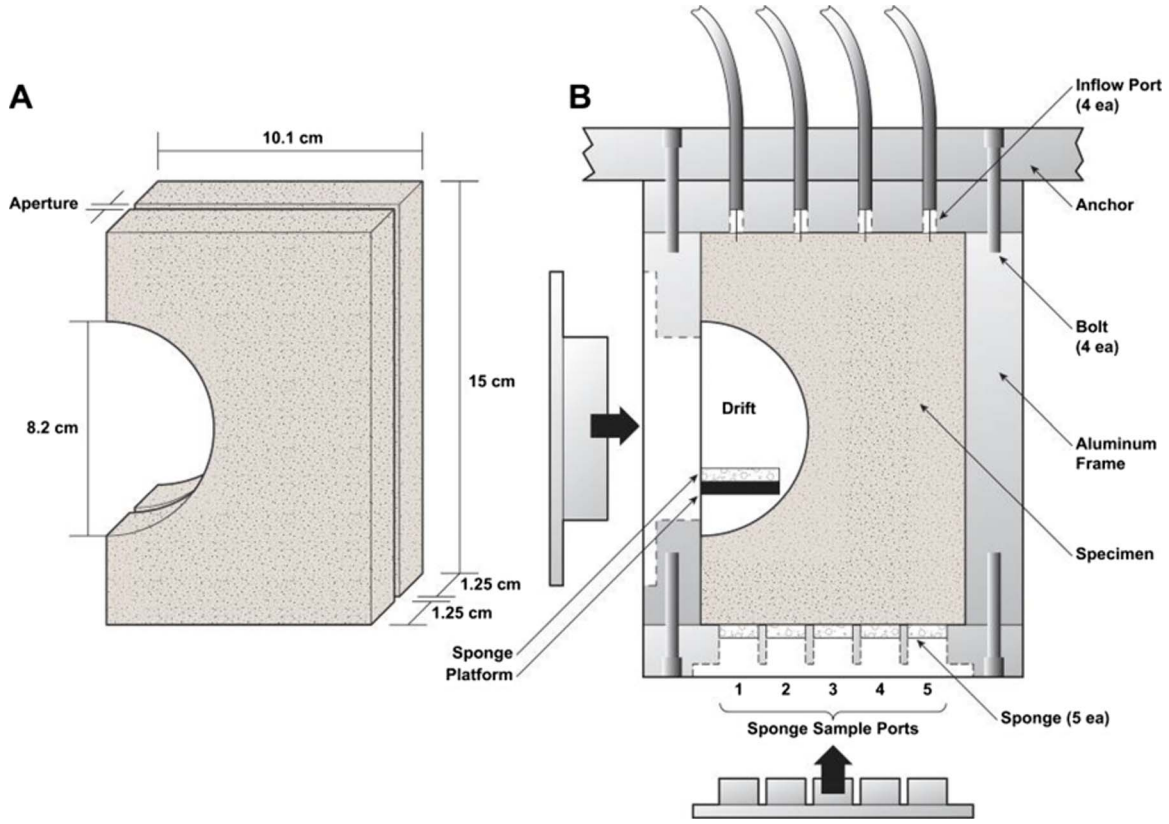

Fig. 1 Schematic of (*a*) tuff slabs and (*b*) test cell used in Ref. [1] (with permission from Elsevier)

fracture and matrix continua, as well as between the fracture and matrix continua [5]. Although a single-continuum fracture model would probably suffice for the test conditions implemented in Ref. [1] in which a single planar fracture was created between nearly saturated slabs of tuff, dual-permeability models of the experiments were developed because it was desired to replicate the models used on the Yucca Mountain project. In addition, drying of the tuff matrix (e.g., caused by heating) or pervasive fracturing through the tuff matrix may increase imbibitions and fracture/matrix interactions, and the dual-permeability model would be necessary.

Both TOUGH2 [6] and FEHM [7] were used in the numerical simulations of the drift-shadow experiments, and both codes have been used to simulate flow and transport for the Yucca Mountain project. TOUGH2 has also been used to simulate seepage into drifts and mountain-scale drift-shadow effects on flow and transport [3].

The equations governing variably saturated flow of liquid in dual-permeability media can be written as follows (shown in one dimension for brevity) [8]:

$$\frac{\partial}{\partial z}\left[\frac{\rho_l k_m k_{ml}}{\mu_l}\left(\frac{\partial P_{ml}}{\partial z}-\rho_l \boldsymbol{g}\right)\right]=\frac{\partial(\rho_l \phi_m S_{ml})}{\partial t}+\frac{\rho_l k_m k_{ml}}{\mu_l}\frac{\sigma}{d}X_{fm}k_{fl}(P_{ml}-P_{fl})-Q_{ml} \quad (1)$$

$$\frac{\partial}{\partial z}\left[\frac{\rho_l k_f k_{fl}}{\mu_l}\left(\frac{\partial P_{fl}}{\partial z}-\rho_l g\right)\right]=\frac{\partial(\rho_l \phi_f S_{fl})}{\partial t}-\frac{\rho_l k_m k_{ml}}{\mu_l}\frac{\sigma}{d}X_{fm}k_{fl}(P_{ml}-P_{fl})-Q_{fl} \quad (2)$$

where Eq. (1) describes the flow of liquid (subscript l) in the

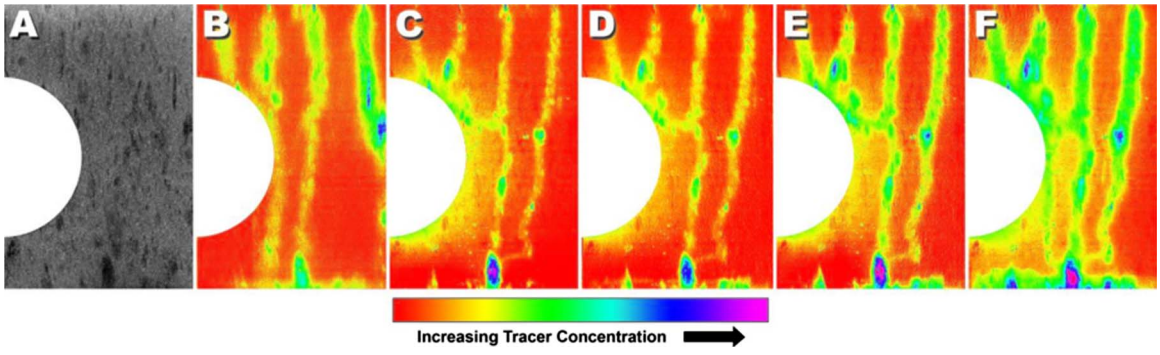

Fig. 2 X-ray absorption images of the 500 μm aperture test cell taken (*a*) before and (*b*) 5 h after the start of experiment at 0.01 ml/min, and (*c*) 1 h, (*d*) 2 h, (*e*) 3 h, and (*f*) 5 h after start of experiment with 0.23 ml/min flow rate. Image of cell without tracer (*a*) shows porous pumice fragments as darker areas. From Ref. [1] (with permission from Elsevier).

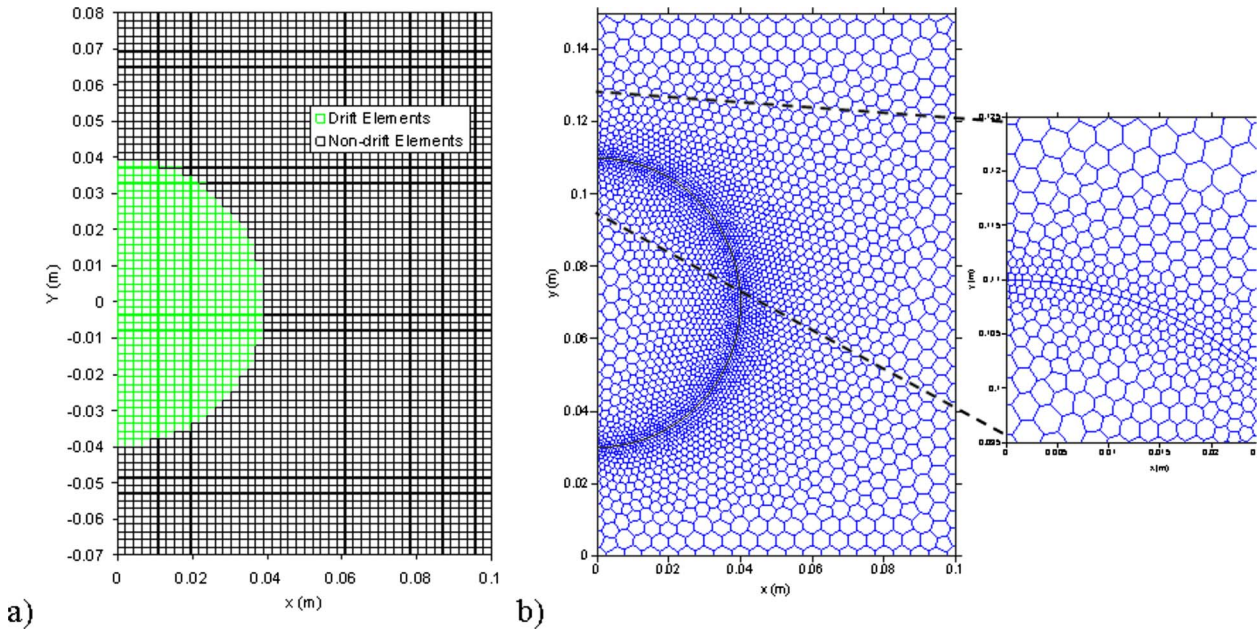

Fig. 3 Computational meshes used in the simulations. (*a*) Orthogonal mesh used in TOUGH2 simulations and (*b*) unstructured Voronoi mesh used in FEHM simulations.

matrix continuum (subscript m) and Eq. (2) describes the flow of liquid in the fracture continuum (subscript f), and k_{jl} is the relative permeability to the liquid phase, k_j is the intrinsic permeability (m^2), μ_l is the dynamic viscosity of the liquid (Pa s), P_{jl} is the liquid pressure (Pa), Q_{jl} is the external source of liquid mass, (+) injection and (−) extraction (kg/m^3 s), ϕ_m is the porosity, ρ_l is the density of the liquid (kg/m^3), σ is the specific surface of the interface between the fracture and matrix continua (m^{-1}), d is the characteristic half width of the matrix continuum between fractures (m), X_{fm} is the reduction factor for the interface area between the fracture and matrix continua, and z is the depth taken to be positive upward (m) with $j=m,f$.

In Eqs. (1) and (2), the second term on the right-hand size represents the exchange of liquid between the fracture and matrix. The reduction factor, X_{fm}, represents a reduction in the hydraulic conductance between the two continua because of small-scale features and processes such as fingering, channeling, and fracture coatings that reduce the available wetted area for fracture/matrix exchange. In the current analysis, the impact of fluid exchange between the fracture and matrix continua is not significant (most of the flow and transport is in the fracture continuum), and the reduction factor is set equal to one. Liquid pressure in the matrix and fracture continua are related to air and capillary pressure by the following relationships:

$$P_{jl} = P_{jg} - P_{jc} \tag{3}$$

where P_{jg} and P_{jc} denote air and capillary pressure in the jth continuum ($j=m,f$). In this study, the van Genuchten/Mualem capillary pressure and relative permeability relationships are given as follows [9]:

$$P_{jc} = \frac{1}{\alpha_j}[S_{je}^{-1/m_j} - 1]^{1-m_j} \tag{4}$$

$$k_{jl} = S_{je}^{1/2}(1 - (1 - S_{je}^{1/m_j})^{m_j})^2 \tag{5}$$

where m_j and α_j are fitting parameters for the jth continuum. The effective liquid saturation is

$$S_{je} = \frac{S_{jl} - S_{jlr}}{1 - S_{jlr}} \tag{6}$$

where S_{jlr} represents the residual liquid-phase saturation in the jth continuum.

3.1 Computational Domain. The domain of the drift-shadow experiment was represented in TOUGH2 with a uniform orthogonal mesh consisting of 3220 fracture elements and 3220 matrix elements, all interconnected (Fig. 3(*a*)). The resolution of the mesh was sufficient to capture capillary diversion and drift-shadow effects at the scale of the experiments. The benefits of using an orthogonal mesh include minimizing the numerical dispersion when the elements are aligned in the direction of flow and improved computational convergence. However, for nonorthogonal features, such as the circular drift, the use of orthogonal elements creates a stair-stepped interface that may artificially increase the capillary pressure required to divert water around the drift. Therefore, an alternative mesh was generated in FEHM using an unstructured Voronoi grid with 3201 primary elements (Fig. 3(*b*)). The impact of the grids on the flow distribution around the drift is investigated in Sec. 4.2.

3.2 Hydraulic Properties. Hydraulic properties of the fracture and matrix continua simulated in the dual-permeability models are summarized in Table 1. The matrix properties were based on values published by Flint [10] for samples of Topopah Spring Tuff in the lithophysal zone. The matrix van Genuchten α and n parameters were obtained using these matrix properties together with regressions from Ref. [11].

The bulk fracture porosity, ϕ_f, permeability, k_f, and van Genuchten α_f parameter were calculated as follows:

$$\phi_f = b/D \tag{7}$$

$$k_f = \frac{b^2}{12}\phi_f \tag{8}$$

Table 1 Summary of hydraulic properties used in dual-permeability models

Parameter	Value	Ref.
Matrix porosity	0.154	[10]
Matrix permeability (m^2)	8.9×10^{-18}	[10]
Matrix van Genuchten α(Pa^{-1})	1.82×10^{-6}	[11]
Matrix van Genuchten n	1.6	[11]
Fracture porosity, 100 μm aperture	0.004	Eq. (7)
Fracture bulk permeability, 100 μm aperture (m^2)	3.32×10^{-12}	Eq. (8)
Fracture van Genuchten α, 100 μm aperture (Pa^{-1})	6.94×10^{-4}	Eq. (9)
Fracture porosity, 250 μm aperture	0.0099	Eq. (7)
Fracture bulk permeability, 250 μm aperture (m^2)	5.16×10^{-11}	Eq. (8)
Fracture van Genuchten α, 250 μm aperture (Pa^{-1})	1.73×10^{-3}	Eq. (9)
Fracture porosity, 500 μm aperture	0.0196	Eq. (7)
Fracture bulk permeability, 500 μm aperture (m^2)	4.08×10^{-10}	Eq. (8)
Fracture van Genuchten α, 500 μm aperture (Pa^{-1})	3.47×10^{-3}	Eq. (9)
Fracture van Genuchten n, all apertures	3.0	[11]

$$\alpha = \frac{b\rho g}{2\sigma \cos\theta} \tag{9}$$

where b is the fracture aperture (m), D is the fracture spacing (0.025 m), ρ is the liquid density (998 kg/m^3) at 20°C, g is the gravitational constant (9.81 m/s^2), σ is the surface tension of liquid water (0.072 N/m at 20°C), and θ is the contact angle (assumed to be zero). Eq. (7) assumes one-dimensional planar fractures, Eq. (8) assumes laminar, fully developed, incompressible flow between two parallel planes, and Eq. (9) is derived from capillary pressure and force balance considerations at a liquid/air interface (Young–Laplace equation).

3.3 Boundary Conditions. Three different fracture apertures were prescribed for the tests: 100 μm, 250 μm, and 500 μm. For each of the prescribed apertures, different flow rates were introduced at four locations along the top of the fracture aperture through a needle (see Fig. 1). Table 2 summarizes the different injection rates for the different apertures. Only the low and high injection rates used in the experiments were simulated.

The lateral and top boundaries of the domain were no-flow boundary conditions. The elements located within the drift were simulated as seepage boundaries with zero capillary pressure (i.e., the liquid and gas pressure is always maintained at atmospheric pressure.). Therefore, until enough pressure head builds up above the drift, it will serve as a capillary barrier to liquid flow.

The bottom boundary was specified as gravity-drainage flow (i.e., no capillary-pressure gradient). In TOUGH2 v. 1.6, this boundary condition is applied by specifying the name of the material for the bottom boundary as "drain." The simulated outflow at the bottom of the domain was divided into five bins corresponding to the five collection bins used in the experiments. The flow in each bin was normalized to the total amount of flow that would have been collected if the flow were uniform (i.e., total inflow/5).

Table 2 Summary of injection rates for simulations

Aperture (μm)	Low injection rate per port (ml/min)	High injection rate per port (ml/min)
100	0.01	0.12
250	0.01	0.24
500	0.01	0.23

4 Results and Discussion

4.1 Impact of Capillary Pressure Curves. Figure 4 shows the simulated fracture saturation distribution resulting from the use of different capillary-pressure curves. The use of the unbounded (porous-media-based) capillary-pressure curves yields saturations that are too uniform compared with the fingerlike distributions observed in the test. The use of a linear capillary-pressure curve with an arbitrarily small maximum capillary pressure of 30 Pa yields too much seepage into the drift relative to the tests. The use of a linear capillary-pressure curve with a maximum capillary pressure of 200 Pa (which is close to the maximum capillary pressure determined by the Young–Laplace equation for an aperture bounded by parallel plates) yields a saturation distribution that is qualitatively similar to the fingerlike patterns observed in the tests (Fig. 2).

These results show that the constitutive relations for porous media that yield unbounded capillary pressures may not be appropriate for modeling capillary diversion within individual fractures. These porous-media-based capillary-pressure curves are intended to represent a broad distribution of pore sizes rather than a single fracture aperture. However, if a continuum of fractures is being modeled with a distribution of fracture apertures, the use of porous-media-based capillary-pressure curves may be appropriate.

Figure 5 shows that the measured and simulated normalized outflow at the bottom of the domain. The trend in the spatial distribution of outflow beneath the drift is generally captured using a maximum capillary pressure of 200 Pa in the model. The observed outflow in the experiments is greater in Bins 2, 3, and 4, and less in Bins 1 (under the drift) and 5 (furthest away from the drift). The match between experimental and simulated results is especially good for the 0.23 ml/min case.

In all simulations, the contribution to the outflow from the matrix was negligible, and nearly all of the outflow and diversion occurred within the fracture continuum. The simulated saturation was nearly uniform throughout the matrix continuum at a value close to one.

4.2 Impact of Mesh. The impact of the mesh on the outflow distribution was investigated using both the orthogonal mesh from the previous simulations and an unstructured mesh shown in Fig. 3. The outflow distribution resulting from the different meshes for the 250 μm aperture fracture with a maximum linear capillary pressure of 200 Pa were similar at 0.01 and 0.24 ml/min. We originally hypothesized that differences in the seepage and outflow distribution could occur because of the different representations of the curved interface along the drift. The orthogonal mesh represents the drift interface as a stair-stepped connection of elements, whereas the unstructured mesh produces a smooth curved transition between elements (see Fig. 3). The impact of this difference will likely depend on the resolution of the mesh. However, for this comparison, the mesh size was sufficiently refined such that no significant differences in the general outflow distribution between these two meshes were observed. Seepage into the drift was negligible in both the orthogonal and unstructured mesh.

4.3 Impact of Heterogeneities and Drift Collapse. In actual subsurface applications, heterogeneities in the fractures may cause additional flow diversions that were not considered in this study. Therefore, the actual distribution of flow beneath a subsurface cavity may be highly irregular. In addition, irregularities along the top surface of the cavity (e.g., drift collapse) will also impact the amount of water that diverts around the cavity or drift. An irregular interface between the cavity and the intersecting fracture may increase the amount of seepage and decrease the capillary diversion, which will reduce the impact of drift shadow.

5 Conclusions

Simulations of drift-shadow experiments have been performed to evaluate the impacts of hydrologic properties and mesh design

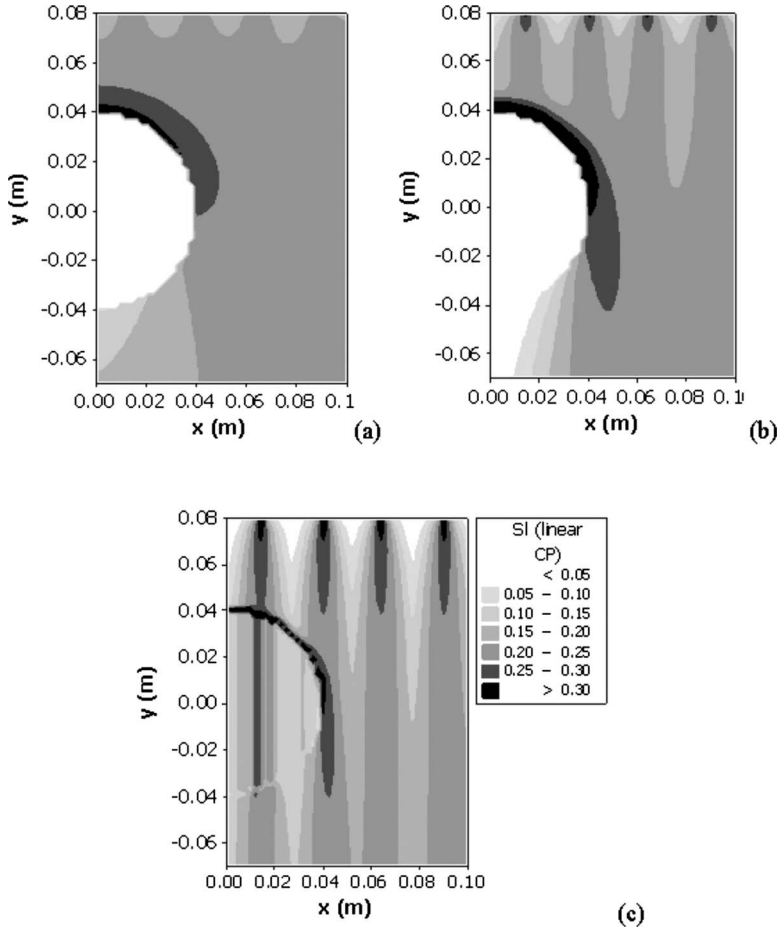

Fig. 4 Simulated fracture saturation using TOUGH2 with a 500 μm aperture and 0.23 ml/min flow rate using van Genuchten capillary-pressure curves: (*a*) unbounded maximum pressure (10^{10} Pa), (*b*) linear capillary-pressure curve with maximum capillary pressure of 200 Pa, and (*c*) linear capillary-pressure curve with maximum capillary pressure of 30 Pa

on simulated results. Comparisons with experimental data show that the phenomena of capillary diversion and drift shadow can be represented by the dual-permeability models, although the exact distribution of flux beneath the drift depends on the magnitude of the fracture capillary pressure. Van Genuchten capillary-pressure curves with an unbounded maximum capillary pressure yielded more uniform fluxes as compared with the fingerlike patterns observed in the experiments. Linear capillary-pressure curves with a smaller maximum capillary pressure of 200 Pa yielded better matches to the observed data. However, if the maximum capillary pressure was lowered to 30 Pa, the simulated seepage into the drift was much greater than that observed in the experiments. Therefore, for models of capillary diversion within individual fractures, an improvement may be to use a maximum capillary pressure defined by the Young–Laplace equation, which represents the maximum capillary pressure of a single fracture aperture bounded by two planes better than porous-media-based constitutive relations (which represent a distribution of pore sizes). Comparisons between the orthogonal and unstructured meshes yielded similar results for the outflow distribution.

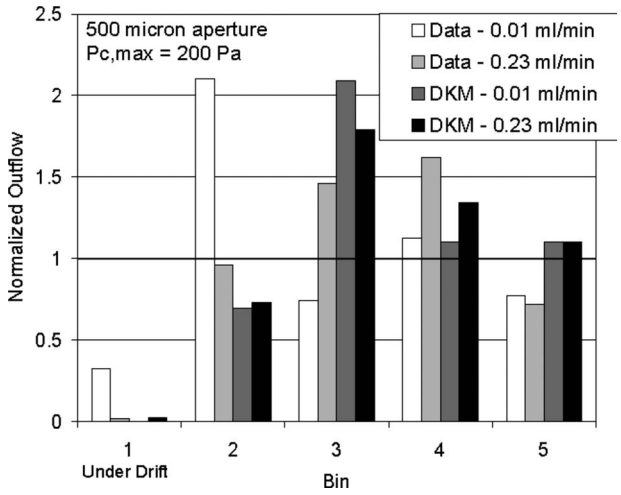

Fig. 5 Distribution of normalized outflow below the drift for a fracture aperture of 500 μm, using a linear fracture capillary-pressure curve with a maximum capillary pressure of 200 Pa (DKM=dual-permeability model)

Acknowledgment

Sandia is a multiprogram laboratory operated by Sandia Corporation, a Lockheed Martin Co. for the U.S. Department of Energy's National Nuclear Security Administration under Contract No. DE-AC04-94AL85000.

References

[1] Altman, S. J., Forsberg, A. A., Peplinski, W. J., and Ho, C. K., 2008, "Experimental Observation of the Drift Shadow Effect Using X-Ray Absorption Imaging," J. Hydrol., **348**, pp. 341–349.
[2] Philip, J. R., Knight, J. H., and Waechter, R. T., 1989, "Unsaturated Seepage

and Subterranean Holes: Conspectus, and Exclusion Problem for Circular Cylindrical Cavities," Water Resour. Res., **25**(1), pp. 16–28.
[3] Houseworth, J. E., Finsterle, S., and Bodvarsson, G. S., 2003, "Flow and Transport in the Drift Shadow in a Dual-Continuum Model," J. Contam. Hydrol., **62–63**, pp. 133–156.
[4] SNL (Sandia National Laboratories), 2007, "UZ Flow Models and Submodels," Las Vegas, NV, Report No. MDL-NBS-HS-000006.
[5] Ho, C. K., 1997, "Models of Fracture-Matrix Interactions During Multiphase Heat and Mass Flow in Unsaturated Fractured Porous Media," *Proceedings of the ASME Fluids Engineering Division*, FED-Vol. 244, pp. 401–412.
[6] Pruess, K., 1991, "TOUGH2—A General-Purpose Numerical Simulator for Multiphase Fluid and Heat Flow," Lawrence Berkeley Laboratory, Berkeley, CA, Report No. LBL-29400.
[7] Zyvoloski, G. A., Robinson, B. A., Dash, Z. V., and Trease, L. L., 1995, "Users Manual for the FEHMN Application," Los Alamos National Laboratory, Los Alamos, NM, Report No. LA-UR-94-3788.
[8] Peters, R. R., and Klavetter, E. A., 1988, "A Continuum Model for Water Movement in an Unsaturated Fractured Rock Mass," Water Resour. Res., **24**(3), pp. 416–430.
[9] van Genuchten, M. T., 1980, "A Closed-Form Equation for Predicting the Hydraulic Conductivity of Unsaturated Soils," Soil Sci. Soc. Am. J., **44**(4), pp. 892–898.
[10] Flint, L. E., 2003, "Physical and Hydraulic Properties of Volcanic Rocks From Yucca Mountain, Nevada," Water Resour. Res., **39**(5), pp. 1119–1131.
[11] Altman, S. J., Arnold, B. W., Barnard, R. W., Barr, G. E., Ho, C. K., Mckenna, S. A., and Eaton, R. R., 1996, "Flow Calculations for Yucca Mountain Groundwater Travel Time (GWTT-95)," Sandia National Laboratories, Albuquerque, NM, Report No. SAND96-0819.

Fujio Kuwahara

Yoshihiko Sano

Department of Mechanical Engineering,
Shizuoka University,
3-5-1 Johoku,
Hamamatsu 432-8561, Japan

Jianjun Liu
Department of Civil Engineering,
Wuhan Polytechnic University,
Hubei,
Wuhan 430023, China

Akira Nakayama
Department of Mechanical Engineering,
Shizuoka University,
3-5-1 Johoku,
Hamamatsu 432-8561, Japan;
Department of Civil Engineering,
Wuhan Polytechnic University,
Hubei,
Wuhan 430023, China

A Porous Media Approach for Bifurcating Flow and Mass Transfer in a Human Lung

A porous media approach was proposed to investigate the characteristics of the bifurcating airflow and mass transfer within a lung. The theory of porous media was introduced in order to deal with a large number of bifurcations and a vast scale difference resulting from bifurcations. Upon introducing a two-medium treatment for the air convection and the diffusion in its surrounding wall tissue, the oxygen mass transfer between the inhaling air and the tissue was considered along with the effects of the blood perfusion on the mass transfer within the tissue. The overall mass transfer resistance between the inlet of the trachea and the blood in the capillaries was obtained on the basis of the porous media approach. The analysis reveals that there exists the optimal number of the bifurcation levels, namely, 23, that yields the minimum overall mass transfer resistance for the mass transport from the external air to the red blood cells. The finding is consistent with Bejan's constructal law, namely, that for a flow system to persist in time, it must evolve in such a way that it provides easier access to its currents. [DOI: 10.1115/1.3180699]

Keywords: lung, porous media, bifurcation, mass transfer, gas exchange

1 Introduction

The human respiratory system is a fluid tree, which starts at the trachea and bifurcates 23 times to reach the alveolar sacs. The total area of the alveolar sacs is as large as 150 m^2, a little smaller than that of the tennis court, which enables us to exchange gases effectively within the sacs. Upon inhalation, the external air is carried through the fluid tree by convection to the alveolar sacs, as illustrated in Fig. 1. As the air passes through the fluid tree, a small portion of oxygen diffuses through the surrounding wall tissue. Subsequently, the blood perfusion within the tissue takes the diffusing oxygen into the blood. It is within the alveolar sacs that substantial oxygenation of the blood is carried out. The oxygenation takes place with a concomitant removal of carbon dioxide by diffusion between the gaseous environment and the blood in the pulmonary capillaries through the alveolar "tissue region," which consists of the alveolus membrane, interstitial fluid region, and capillary membrane. At this point, the pulmonary blood is oxygen rich, and the lungs are holding carbon dioxide. Exhalation follows, thereby ridding the body of the carbon dioxide and completing the cycle of respiration. Normal resting respirations are about 12 breaths per minute.

Substantial amount of work was carried out to investigate the characteristics of the airflow and gas exchanges within a lung [1–6] and the structure of bronchial tree in the respiratory system [7–9]. However, the reason why we have a bronchial tree with 23 levels of bifurcation has not been fully explained in the literature. By no means has this special flow structure developed by chance. Thus, in this paper, we shall focus on the flow structure in view of mass transfer, which will then guide us to find out the reason. Some [10] appealed to Bejan's [11] constructal law to explain this particular flow architecture. Others [1] were certainly successful to some extent in relating the number of the bifurcation levels to the best oxygen access to the alveolar sacs. However, one had to introduce miscellaneous assumptions such as isothermal and adiabatic flows with all species having the same chemical potential. Moreover, certain mass diffusion models introduced for an alveolar sac are often questionable since they require specific geometrical information on the sac, which is not readily accessible to us.

In this study, we shall revisit this problem, introducing a simple and yet rational model for the respiratory system. This quasisteady one-dimensional mass transfer model is similar to the one originally proposed by Nakayama et al. [12] for the mass diffusion in alveolar sacs without taking account of blood perfusion. Contrary to their model, the present model describes the entire mass transfer between the airway inlet and the red blood cell interior. In the model, a porous media approach [13,14] is introduced for the first time to account for the convective mass transfer in the airway and its surrounding wall tissue. The oxygen mass transfer between the inhaling gas and the tissue is considered along with the effects of blood perfusion on the mass transfer within the tissue. The overall mass transfer resistance between the inlet of the trachea and the blood in the capillaries is obtained on the basis of the porous media approach. It reveals that there exists the optimal number of the bifurcation levels, namely, 23, that yields the minimum overall mass transfer resistance for the mass transport from the external air to the red blood cells.

2 Pressure Drop in Bifurcating Flows

The air flow through the fluid tree is periodic. It repeats inhaling and exhaling every 5 s. This periodic fully developed flow may be approximated by a steady gas flow with its flow rate $\dot{m}$ (kg/s), going from the trachea to the sacs and coming back from the sacs to the trachea. Since the Reynolds number based on the diameter of the trachea and the inlet velocity never exceeds 1000, the flow stays laminar throughout the fluid tree. In order to estimate the flow rate for a given pressure loss Δp_{total} between the inlet of the trachea and the alveolar sacs, we may assume that fully-developed laminar flow prevails within the fluid tree. Thus, the pressure drop at the nth bifurcation level is given by

Manuscript received September 29, 2008; final manuscript received March 26, 2009; published online July 31, 2009. Review conducted by Kambiz Vafai.

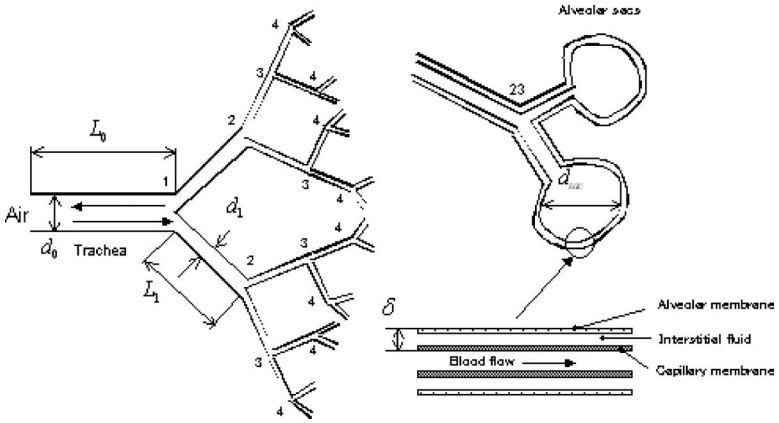

Fig. 1 Fluid tree in the respiratory system

$$\Delta p_n = \frac{128\mu L_n}{\rho\pi {d_n}^4}\left(\frac{\dot{m}}{2^n}\right) \quad \text{for } n = 0,1,2,\ldots,N \tag{1}$$

where d and L are the duct diameter and length, respectively. The subscript n refers to the duct of the nth bifurcation level, i.e., $n=0$ corresponds to the trachea such that d_0 and L_0 denote the diameter and length of the trachea, respectively. It is easy to show [11] that the minimum flow resistance at a bifurcation for a fixed total volume (i.e., ${L_{n-1}}{d_{n-1}}^2+2L_n{d_n}^2=\text{const}$) is achieved when the ratio between consecutive duct diameters follows Murray's [15] law:

$$d_n/d_{n-1} = 2^{-1/3} \tag{2}$$

Furthermore, we expect the same pressure drop sequence for inhalation and exhalation. Therefore, the pressure drop at each level of bifurcation should be equal, which gives us the ratio between consecutive duct lengths:

$$L_n/L_{n-1} = 2^{-1/3} \tag{3}$$

The pressure losses at bifurcation points are only minor and can be neglected. Hence, we obtain the mass flow rate and total pressure drop relationship

$$\Delta p_{\text{total}} = \sum_{n=0}^{n=N} \frac{128\mu(L_0 2^{-n/3})}{\rho\pi(d_0 2^{-n/3})^4}\left(\frac{\dot{m}}{2^n}\right) = (N+1)\frac{128\mu L_0}{\rho\pi {d_0}^4}\dot{m} \tag{4}$$

The maximum space which could be allocated to the lung may be estimated by the total length corresponding to the infinite number of bifurcations:

$$\sum_{n=0}^{\infty} L_n = \frac{1}{1-2^{-1/3}}L_0 = 4.85L_0 \tag{5}$$

Thus, the space remaining for the sacs to occupy may be estimated in terms of the diameter of the alveolar sacs d_{sac} as

$$d_{\text{sac}} = 4.85L_0 - \sum_{n=0}^{N} L_n = 4.85L_0 - \frac{1-2^{-(N+1)/3}}{1-2^{-1/3}}L_0 = \frac{4.85}{2^{(N+1)/3}}L_0 \tag{6}$$

3 Two-Medium Treatment for Mass Transfer in Airway Walls

The inhaling air carries oxygen from the trachea inlet to the sacs and returns with carbon dioxide from there to the trachea inlet. Nakayama et al. [12] proposed a one-dimensional mass transfer model, as illustrated in Fig. 2. In their model, convection is the main driving force for the oxygen and dioxide flow through the pulmonary airflow tree, while it is the mass diffusion that takes place between the sac surface and the blood in the pulmonary capillaries through the alveolar tissue region. However, the mass diffusion does take place also along the airflow tree in which the oxygen diffuses through the surrounding tissue walls. Within the tissue, the blood perfusion is responsible for taking the oxygen into the blood. Therefore, in this study, we shall introduce a two-medium treatment to account for such effects on the mass transfer between the inhaling air and the blood in the capillaries. Nakayama and Kuwahara [16] introduced a porous media approach and applied volume averaging to obtain a set of bioheat equations between blood vessels and tissues. We may use a two-medium treatment similar to their volume averaging to find a set of macroscopic mass transfer equations. Upon referring to Nakayama and Kuwahara [16] and Fig. 3, we may integrate the mass transfer equations for the air and the surrounding tissue to obtain two macroscopic oxygen transfer equations in the cylindrical coordinate system, one for each of the air and the surrounding tissue phases.

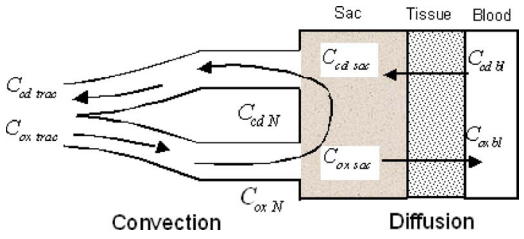

Fig. 2 One-dimensional mass transfer model

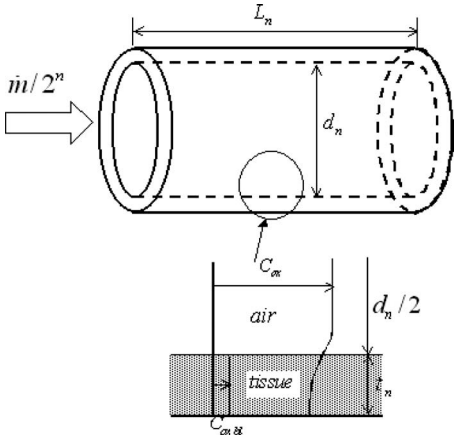

Fig. 3 Airway and its surrounding tissue

For the air flow,

$$\frac{\dot{m}}{\rho_f}\frac{d\langle C_{\mathrm{ox}}\rangle^f}{dn} = 2^n \pi d_n L_n D_{\mathrm{ox}\ f}\ \left.\frac{\partial C_{\mathrm{ox}}}{\partial r}\right|_{r=d_n/2} \quad :0 \le r \le \frac{d_n}{2} \tag{7}$$

For the mass diffusion in the surrounding tissue,

$$\frac{d}{dr}\left(rD_{\mathrm{ox}\ s}\frac{d\langle C_{\mathrm{ox}}\rangle^s}{dr}\right) - r\omega_{\mathrm{bl}}(\langle C_{\mathrm{ox}}\rangle^s - C_{\mathrm{ox\ bl}}) = 0$$

$$:\frac{d_n}{2} \le r \le \frac{d_n + 2t_n}{2} \tag{8}$$

where the intrinsic averages of the oxygen concentration C_{ox} over an elementary control volume $V_{f,s}$ are defined by

$$\langle C_{\mathrm{ox}}\rangle^f = \frac{1}{V_f}\int_{V_f} C_{\mathrm{ox}} dV \tag{9}$$

and

$$\langle C_{\mathrm{ox}}\rangle^s = \frac{1}{V_s}\int_{V_s} C_{\mathrm{ox}} dV \tag{10}$$

The sub- and superscripts f and s stand for the air (fluid) and the tissue (solid), respectively. The subscript ox denotes oxygen, while trac, sac, and bl refer to as trachea, sac, and blood, respectively. D_{ox} is the effective diffusivity and ρ_f is the density of the air. Moreover, ω_{bl} (1/s) is the perfusion rate within the tissue. The boundary and compatibility conditions are given by

$$D_{\mathrm{ox}\ f}\ \left.\frac{\partial C_{\mathrm{ox}}}{\partial r}\right|_{r=d_n/2} = D_{\mathrm{ox}\ s}\ \left.\frac{d\langle C_{\mathrm{ox}}\rangle^s}{dr}\right|_{r=d_n/2} \tag{11}$$

and

$$D_{\mathrm{ox}\ s}\ \left.\frac{d\langle C_{\mathrm{ox}}\rangle^s}{dr}\right|_{r=(d_n+2t_n)/2} = 0 \tag{12}$$

Upon integrating Eq. (8) for $d_n/2 \le r \le (d_n+2t_n)/2$ and using the foregoing conditions, we have

$$D_{\mathrm{ox}\ f}\ \left.\frac{\partial C_{\mathrm{ox}}}{\partial r}\right|_{r=d_n/2} = D_{\mathrm{ox}\ s}\ \left.\frac{d\langle C_{\mathrm{ox}}\rangle^s}{dr}\right|_{r=d_n/2} = -t_n\omega_{\mathrm{bl}}(\langle C_{\mathrm{ox}}\rangle^s - C_{\mathrm{ox\ bl}}) \tag{13}$$

Substitution of the foregoing relation into Eq. (7) yields

$$\frac{\dot{m}}{\rho_f}\frac{d\langle C_{\mathrm{ox}}\rangle^f}{dn} = -2^n \pi d_n L_n t_n \omega_{\mathrm{bl}}(\langle C_{\mathrm{ox}}\rangle^s - C_{\mathrm{ox\ bl}}) \tag{14}$$

where the axial diffusion is neglected as usually done in the tube flow. We further note $t_n \propto d_n$ assuming the geometrical similarity and $\langle C_{\mathrm{ox}}\rangle^f \simeq \langle C_{\mathrm{ox}}\rangle^s$ such that

$$\frac{d(\langle C_{\mathrm{ox}}\rangle^f - C_{\mathrm{ox\ bl}})}{(\langle C_{\mathrm{ox}}\rangle^f - C_{\mathrm{ox\ bl}})} = -\frac{\pi d_0 L_0 t_0}{\dot{m}}\rho_f\omega_{\mathrm{bl}} dn \tag{15}$$

Hence, we obtain the oxygen concentration at the last bifurcation $n=N$,

$$\langle C_{\mathrm{ox}}\rangle^f{}_N - C_{\mathrm{ox\ bl}} = (C_{\mathrm{ox\ trac}} - C_{\mathrm{ox\ bl}})\exp\left(-\frac{\pi d_0 L_0 t_0}{\dot{m}}\rho_f\omega_{\mathrm{bl}}(N+1)\right) \tag{16}$$

4 Quasisteady Mass Transfer Model

As the inhaling air carries oxygen from the trachea inlet to the last level of bifurcation at $n=N$, a part of the oxygen diffuses through the tissue along the airway wall so that the oxygen concentration in the air decreases from $\langle C_{\mathrm{ox}}\rangle^f = C_{\mathrm{ox\ trac}}$ to $\langle C_{\mathrm{ox}}\rangle^f = \langle C_{\mathrm{ox}}\rangle^f{}_N$, just before entering the sacs. Within the sacs, the oxygen diffusion takes place between the sac surface and the blood in the pulmonary capillaries through the alveolar tissue region, as illustrated in Fig. 2. Therefore, we have the following mass balance relationship for the oxygen supply rate to the blood $\dot{m}_{\mathrm{ox}}$:

$$\dot{m}_{\mathrm{ox}} = \frac{\dot{m}}{\rho_f}(C_{\mathrm{ox\ trac}} - \langle C_{\mathrm{ox}}\rangle^f{}_N) + \frac{\dot{m}}{\rho_f}(\langle C_{\mathrm{ox}}\rangle^f{}_N - \langle C_{\mathrm{ox}}\rangle^f{}_{\mathrm{sac}}) \tag{17}$$

where

$$\frac{\dot{m}}{\rho_f}(C_{\mathrm{ox\ trac}} - \langle C_{\mathrm{ox}}\rangle^f{}_N) = \frac{\dot{m}}{\rho_f}(C_{\mathrm{ox\ trac}} - C_{\mathrm{ox\ bl}})\left(1 - \exp\left(-\frac{\pi d_0 L_0 t_0}{\dot{m}}\rho_f\omega_{\mathrm{bl}}(N+1)\right)\right) \tag{18}$$

According to Eq. (16) and

$$\frac{\dot{m}}{\rho_f}(\langle C_{\mathrm{ox}}\rangle^f{}_N - \langle C_{\mathrm{ox}}\rangle^f{}_{\mathrm{sac}}) = \frac{2^N \pi d_{\mathrm{sac}}{}^2 D_{\mathrm{ox}\ s}}{\delta}(\langle C_{\mathrm{ox}}\rangle^f{}_{\mathrm{sac}} - C_{\mathrm{ox\ bl}}) = \frac{\langle C_{\mathrm{ox}}\rangle^f{}_N - C_{\mathrm{ox\ bl}}}{\frac{\rho_f}{\dot{m}} + \frac{\delta}{2^N \pi d_{\mathrm{sac}}{}^2 D_{\mathrm{ox}\ s}}}$$

$$= \frac{C_{\mathrm{ox\ trac}} - C_{\mathrm{ox\ bl}}}{\frac{\rho_f}{\dot{m}} + \frac{\delta}{2^N \pi d_{\mathrm{sac}}{}^2 D_{\mathrm{ox}\ s}}}\exp\left(-\frac{\pi d_0 L_0 t_0}{\dot{m}}\rho_f\omega_{\mathrm{bl}}(N+1)\right) \tag{19}$$

the total sac area is $2^N \pi d_{\mathrm{sac}}{}^2$ such that the mass transfer resistance between the sac surface and the blood is given by $\delta/2^N \pi d_{\mathrm{sac}}{}^2 D_{\mathrm{ox}\ s}$. Then, substituting Eqs. (18) and (19) into Eq. (17), we finally have

$$\dot{m}_{\mathrm{ox}} = \frac{1 + \frac{\delta\dot{m}}{2^N \pi d_{\mathrm{sac}}{}^2 D_{\mathrm{ox}\ s}\rho_f}\left(1 - \exp\left(-\frac{\pi d_0 L_0 t_0}{\dot{m}}\rho_f\omega_{\mathrm{bl}}(N+1)\right)\right)}{\frac{\rho_f}{\dot{m}} + \frac{\delta}{2^N \pi d_{\mathrm{sac}}{}^2 D_{\mathrm{ox}\ s}}} \times (C_{\mathrm{ox\ trac}} - C_{\mathrm{ox\ bl}}) \tag{20}$$

The blood perfusion rate ω_{bl} within the tissue of the airway wall is sufficiently small so that we may have the following approximate expression:

$$\dot{m}_{\mathrm{ox}} = \frac{1 + \frac{\delta d_0 L_0 t_0 \omega_{\mathrm{bl}}}{2^N d_{\mathrm{sac}}{}^2 D_{\mathrm{ox}\ s}}(N+1)}{\frac{\rho_f}{\dot{m}} + \frac{\delta}{2^N \pi d_{\mathrm{sac}}{}^2 D_{\mathrm{ox}\ s}}}(C_{\mathrm{ox\ trac}} - C_{\mathrm{ox\ bl}}) \tag{21}$$

Furthermore, assuming the thickness of the alveolar tissue to be $\delta = 0.2 d_{\mathrm{sac}}$ as in Ref. [12] and substituting Eqs. (4) and (6) into Eq. (21), we obtain the oxygen supply rate to the blood as follows:

$$\dot{m}_{\mathrm{ox}} = \frac{1 + \frac{0.2(N+1)}{2^N(4.85/2^{(N+1)/3})}\left(\frac{d_0 t_0 \omega_{\mathrm{bl}}}{D_{\mathrm{ox}\ s}}\right)}{(N+1)\frac{128\mu L_0}{\pi d_0{}^4 \Delta p_{\mathrm{total}}} + \frac{0.2}{2^N \pi (4.85 L_0/2^{(N+1)/3}) D_{\mathrm{ox}\ s}}} \times (C_{\mathrm{ox\ trac}} - C_{\mathrm{ox\ bl}}) \quad :\text{oxygen} \tag{22}$$

A similar procedure can be taken to get the carbon dioxide removal rate from the blood as follows:

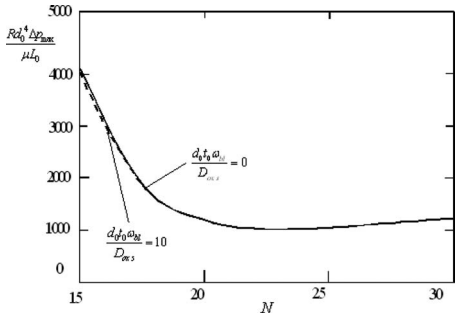

Fig. 4 Overall mass transfer resistance as a function of the number of bifurcations

$$\dot{m}_{\text{cd}} = \frac{1 + \dfrac{0.2(N+1)}{2^N(4.85/2^{(N+1)/3})}\left(\dfrac{d_0 t_0 \omega_{\text{bl}}}{D_{\text{cd}\,s}}\right)}{(N+1)\dfrac{128\mu L_0}{\pi d_0{}^4 \Delta p_{\text{total}}} + \dfrac{0.2}{2^N \pi (4.85 L_0/2^{(N+1)/3}) D_{\text{cd}\,s}}} \times (C_{\text{cd bl}} - C_{\text{cd trac}}) \quad \text{:carbon dioxide} \tag{23}$$

Both Eqs. (22) and (23) give the same total mass transfer resistance R for the species concentration difference between the inlet of trachea and the blood in the capillaries:

$$R = \frac{(N+1)\dfrac{128\mu L_0}{\pi d_0{}^4 p_{\text{total}}} + \dfrac{0.2}{2^N \pi (4.85 L_0/2^{(N+1)/3}) D_{\text{ox}\,s}}}{1 + \dfrac{0.2(N+1)}{2^N(4.85/2^{(N+1)/3})}\left(\dfrac{d_0 t_0 \omega_{\text{bl}}}{D_{\text{ox}\,s}}\right)} \tag{24}$$

where $D_{\text{ox}\,s} = D_{\text{cd}\,s}$ is assumed. Thus, the oxygen supply rate to the blood may be given by $\dot{m}_{\text{ox}} = (C_{\text{ox trac}} - C_{\text{ox bl}})/R$, whereas the carbon dioxide removal rate from the blood is given by $\dot{m}_{\text{cd}} = (C_{\text{cd bl}} - C_{\text{cd trac}})/R$. The convective part of the resistance (i.e., the first term in the numerator) increases with the number of bifurcations N since the flow rate $\dot{m}$ decreases. On the other hand, its diffusive part (i.e., the second term in the numerator) decreases as N increases since the active diffusion area of the sacs grows exponentially. The dimensionless number $(d_0 t_0 \omega_{\text{bl}}/D_{\text{ox}\,s})$ in the denominator accounts for the blood perfusion responsible for the diffusion through the tissue wall of the airway, which works to decrease the total mass transfer resistance.

It is clearly seen from the foregoing equation that there will be the number of N, which yields the minimum resistance, leading to the most effective oxygenation of the blood and the concomitant removal of the carbon dioxide. Typical values for the trachea are $L_0 = 0.11$ m and $d_0 = 0.017$ m. Furthermore, we have $\mu = 1.7 \times 10^{-5}$ Pa s for the air, $\Delta p_{\text{total}} = 1.3$ Pa, and $D_{\text{ox}} = 2.45 \times 10^{-9}$ m^2/s [4,17]. Upon substituting these values into Eq. (24), the variations in the dimensionless mass transfer resistance $(Rd_0{}^4 \Delta p_{\text{total}}/\mu L_0)$ with respect to the number of bifurcations N are shown in Fig. 4 for the cases of the dimensionless blood perfusion rate $(d_0 t_0 \omega_{\text{bl}}/D_{\text{ox}\,s}) = 0$ and 10. It is seen that the effect of the blood perfusion on the mass transfer resistance is so minor that the following expression for the case of zero perfusion rate may be used to estimate the value of N, which gives the minimum mass transfer resistance:

$$N = 2.16 \ln\left(1.88 \times 10^{-4} \frac{d_0{}^4 \Delta p_{\text{total}}}{\mu L_0{}^2 D_{\text{ox}}}\right) \tag{25}$$

The physiological values listed above are substituted into the foregoing equation (25), which readily gives $N = 22.9$. Since N is an integer, the total number of bifurcations must be $N = 23$, which agrees with the physiology literature. Possible uncertainties in values of the numerical parameters may best be illustrated by applying the law of propagation of errors to Eq. (25), which yields the relative error in N:

$$\frac{\delta N}{N} \approx \frac{2.16}{N}\left(\frac{\delta\zeta}{\zeta} + 4\frac{\delta d_0}{d_0} + \frac{\delta \Delta p_{\text{total}}}{\Delta p_{\text{total}}} - \frac{\delta\mu}{\mu} - 2\frac{\delta L_0}{L_0} - \frac{\delta D_{\text{ox}}}{D_{\text{ox}}}\right) \tag{26}$$

Since $2.16/N \approx 0.1$, none of the numerical parameters is influential enough to change the value of N drastically from 23 estimated above. In fact, any reasonable set of the values may be chosen to estimate N, which is after all fairly insensitive to the chosen values because of the logarithmic nature of Eq. (25). The finding in this study is consistent with Bejan's constructal law, namely, that for a flow system to persist in time, it must evolve in such a way that it provides easier access to its currents.

5 Conclusions

In this study, a porous media approach was proposed to investigate the characteristics of the bifurcating airflow and mass transfer within a lung. The blood perfusion responsible for the mass transfer through the tissue of the airway wall was considered for the first time, introducing a two-medium treatment for the air convection and the diffusion in its surrounding tissue wall. However, its effects on the total mass transfer resistance are found to be only marginal, and thus, the formula obtained for the case of zero blood perfusion rate may well be used to find the optimum number of bifurcations. The proposed mass transfer model based on a porous media approach reveals that the bronchial tree is constructed such that it promotes the easiest access to the external air. Naturally, there exists the optimal number of the bifurcation levels, namely, 23, that yields the minimum overall mass transfer resistance for the mass transport from the external air to the red blood cells.

Nomenclature

D = diffusion coefficient
C = concentration
d = tube diameter
L = tube length
$\dot{m}$ = mass flow rate
n = number of levels of bifurcation
N = number of bifurcations
p = pressure
r = cylindrical coordinate
R = overall mass transfer resistance
t = thickness of tissue
V = representative elementary volume
ρ = density
μ = viscosity
ω = perfusion rate

Subscripts and Superscripts

bl = blood
cd = carbon dioxide
f = fluid (air)
n = number of levels of bifurcation
ox = oxygen
s = solid (tissue)
sac = alveolar sacs

Special Symbols

$\langle\rangle^{f,s}$ = intrinsic average

References

[1] Reis, A. H., Miguel, A. F., and Aydin, M., 2004, "Constructal Theory of Flow Architecture of the Lungs," Med. Phys., **31**(5), pp. 1135–1140.
[2] Andrade, J. S., Jr., Alencar, A. M., Almeida, M. P., Mendes Filho, J., Buldyrev, S. V., Zapperi, S., Stanley, H. E., and Suki, B., 1998, "Asymmetric Flow in Symmetric Branched Structures," Phys. Rev. Lett., **81**, pp. 926–929.
[3] Mauroy, B., Filoche, M., Andrade, J. S., and Sapoval, B., 2003, "Interplay

Between Geometry and Flow Distribution in an Airway Tree," Phys. Rev. Lett., **90**, p. 148101.
[4] Koulich, V., Lage, J. L., Hsia, C. C. W., and Johnson, R. L., Jr., 1999, "A Porous Medium Model of Alveolar Gas Diffusion," J. Porous Media, **2**, pp. 263–275.
[5] Koulich, V., Lage, J. L., Hsia, C. C. W., and Johnson, R. L., Jr., 2002, "Three-Dimensional Unsteady Simulation of Alveolar Respiration," J. Biomed. Eng., **124**, pp. 609–616.
[6] Koulich, V., and Lage, J. L., 2001, "Fundamentals of Alveolar Diffusion: A New Modeling Approach," Automedica, An International Journal of Bio-Medical Engineering & Physics, Information and Technology, **20**(3-4), pp. 225–268.
[7] Karau, K. L., Krenz, G. S., and Dawson, C. A., 2001, "Branching Exponent Heterogeneity and Wall Shear Stress Distribution in Vascular Trees," Am. J. Physiol. Heart Circ. Physiol., **280**, pp. H1256–H1264.
[8] Phillips, C. G., Kaye, S. R., and Schroter, R. C., 1994, "A Diameter-Based Reconstruction of the Branching Pattern of the Human Bronchial Tree; Description and Application," Respir. Physiol., **98**, pp. 193–217.
[9] Phillips, C. G., and Kaye, S. R., 1995, "Diameter-Based Analysis of the Branching Geometry of Four Mammalian Bronchial Tree," Respir. Physiol., **102**, pp. 303–316.
[10] Bejan, A., 2005, "Review: The Constructal Law of Organization in Nature: Tree-Shaped Flows and Body Size," J. Exp. Biol., **208**, pp. 1677–1686.
[11] Bejan, A., 2000, *Shape and Structure, From Engineering To Nature*, Cambridge University Press, Cambridge.
[12] Nakayama, A., Kuwahara, F., and Sano, Y., 2009, "Why Do We Have a Bronchial Tree With 23 Levels of Bifurcation?" Heat Mass Transfer, **45**, pp. 351–354.
[13] Cheng, P., 1978, "Heat Transfer in Geothermal Systems," *Advances in Heat Transfer*, Vol. 14, Academic, New York, pp. 1–105.
[14] Vafai, K., and Tien, C. L., 1981, "Boundary and Inertia Effects on Flow and Heat Transfer in Porous Media," Int. J. Heat Mass Transfer, **24**, pp. 195–203.
[15] Murray, C. D., 1926, "The Physiological Principle of Minimal Work in the Vascular System and the Cost of Blood-Volume," Proc. Natl. Acad. Sci. U.S.A., **12**, pp. 207–214.
[16] Nakayama, A., and Kuwahara, F., 2008, "A General Bioheat Transfer Model Based on the Theory of Porous Media," Int. J. Heat Mass Transfer, **51**, pp. 3190–3199.
[17] Comroe, J. H., Forster, R. E., Dubuis, A. B., Briscoe, W. A., and Carlsen, E., 1962, *The Lung Clinical Physiology and Pulmonary Functions Tests*, Year Book Medical, Chicago, IL, pp. 117–121.

A Robust Asymptotically Based Modeling Approach for Two-Phase Flow in Porous Media

M. M. Awad[1]
e-mail: awad@engr.mun.ca

S. D. Butt
e-mail: sbutt@engr.mun.ca

Faculty of Engineering and Applied Science,
Memorial University of Newfoundland,
St. John's, NF, A1B 3X5, Canada

A simple semitheoretical method for calculating the two-phase frictional pressure gradient in porous media using asymptotic analysis is presented. The two-phase frictional pressure gradient is expressed in terms of the asymptotic single-phase frictional pressure gradients for liquid and gas flowing alone. In the present model, the two-phase frictional pressure gradient for $x \cong 0$ is nearly identical to the single-phase liquid frictional pressure gradient. Also, the two-phase frictional pressure gradient for $x \cong 1$ is nearly identical to the single-phase gas frictional pressure gradient. The proposed model can be transformed into either a two-phase frictional multiplier for liquid flowing alone (ϕ_l^2) or a two-phase frictional multiplier for gas flowing alone (ϕ_g^2) as a function of the Lockhart–Martinelli parameter X. The advantage of the new model is that it has only one fitting parameter (p), while the other existing correlations, such as the correlation of Larkins et al., Sato et al., and Goto and Gaspillo, have three constants. Therefore, calibration of the new model to the experimental data is greatly simplified. The new model is able to model the existing multiparameter correlations by fitting the single parameter p. Specifically, $p=1/3.25$ for the correlation of Midoux et al., $p=1/3.25$ for the correlation of Rao et al., $p=1/3.5$ for the Tosun correlation, $p=1/3.25$ for the correlation of Larkins et al., $p=1/3.75$ for the correlation of Sato et al., and $p=1/3.5$ for the Goto and Gaspillo correlation. [DOI: 10.1115/1.3180808]

Keywords: asymptotic, two-phase, pressure drop, porous media

1 Introduction

Two-phase flow in porous media can be found in many engineering fields such as agricultural, biomedical, chemical, mechanical, petroleum, and nuclear engineering. Classical research of petroleum engineering dealing with porous media includes oil reservoir engineering. It is necessary to predict design parameters like friction factors, pressure drops, bubble sizes, gas holdups, heat and mass transfer coefficients to determine the desired operating conditions, and the size of the equipment required for the specific purposes. For example, the pressure drop in the two-phase flow through porous media constitutes an important parameter because pumping costs could be a significant portion of the total operating cost. As a result, expressions are needed to predict the pressure drop in the two-phase flow through porous media accurately.

In the present study, new two-phase flow modeling in porous media is proposed based on an asymptotic modeling method. The two-phase frictional pressure gradient is expressed in terms of the asymptotic single-phase frictional pressure gradients for liquid and gas flowing alone. Asymptotes appear in many engineering problems, such as steady and unsteady internal and external conduction, free and forced internal and external convection, fluid flow, and mass transfer. Often, there exists a smooth transition between two asymptotic solutions [1–4]. This smooth transition indicates that there is no sudden change in slope and no discontinuity within the transition region.

The asymptotic analysis method was first introduced by Churchill and Usagi [1] in 1972. After this time, this method of combining asymptotic solutions proved quite successful in developing models in many applications like predicting forced convection for a wide range of Prandtl numbers from flat plates [5,6], in circular ducts [5,6], and from a rotating disk [7], natural convection [8], and a two-phase flow in circular pipes, minichannels, and microchannels [9].

2 Literature Review

Brownell and Katz [10] enlarged the general correlation developed in Part I [11] for a single-phase flow through porous media to cover simultaneous flow of two fluid phases. The basic concept in their work was that all the variables that affected the flow should be included in the friction factor and Reynolds number. This concept permitted the Reynolds number-friction factor plot for the flow of single phases to be used for the simultaneous flow of two homogeneous fluid phases through porous media. They treated each fluid as a single phase with modifications for the effect of one fluid on the other. They considered the wetting fluid as flowing through the same porous media as would a single phase, but a velocity correction should be applied to account for the proportion of the wetting fluid that was replaced by the other fluid. They considered the nonwetting fluid as flowing through a porous bed that had a sphericity change and a porosity reduction due to the layer of the other fluid. Also, they developed an additional correlation to predict the quantity of fluid held in a porous bed by capillary forces. They corrected the saturation for capillary forces that held a portion of the wetting fluid in interstices of the porous media. In their work, they calculated both countercurrent and parallel flows of the two phases by the use of the general flow equation.

Schwarz [12] presented another approach to the problem of the flow of two phases through porous media. This approach was by means of model studies. By using dimensional or inspectional analysis, the variables that governed a two-phase flow could be combined to dimensionless groups with the aid of which process

[1]Corresponding author.

Manuscript received March 10, 2008; final manuscript received September 8, 2008; published online August 4, 2009. Review conducted by Kambiz Vafai. This paper was presented at ASME 27th International Conference on Offshore Mechanics and Arctic Engineering (OMAE2008), Session: Offshore Technology, Petroleum Technology II, OMAE2008-57792, Estoril, Portugal, June 15–20, 2008.

could be defined. Then, laboratory tests could be designed with the purpose of determining the functional relationship between the groups. The results were also, in principle, generally applicable to many natural oil-bearing rocks; the dimensions of which were some orders of magnitude larger than the laboratory models. The results of such model studies were important to the technique of recovering petroleum because crude oil occurred in underground porous formations from which it was displaced by water and/or gas.

Larkins [13] studied a two-phase cocurrent flow in packed beds. He showed that the two-phase pressure drop could be related to the single-phase gas pressure drop as a function of gas holdup as follows:

$$\frac{\Delta P_{f,t}}{L} = \frac{\Delta P_{f,g}}{L} H_g^{-m} \tag{1}$$

$$H_g = 1 - H_l \tag{2}$$

Ford [14] studied the fluid kinetics of cocurrent flow through a fixed bed of particles in the turbulent regime. The container had a diameter (d)=1.75 in. (44.75 mm) and a length (L)=14 in. (355.6 mm). The container was packed with 1 mm glass spheres to a porosity of 36%. The liquid phase and gas phase could be supplied to the porous mass at rates of 10 gal/min (630.9 cm^3/s) and 4 gal/min (252.36 cm^3/s), respectively. The liquids used were water, industrial methylated spirits, sugar solutions, and a saturated solution of pine oil. The gas used was air. The viscosities of liquids varied from 1.24×10^{-3} kg/m s to 7.58×10^{-3} kg/m s. The surface tensions of liquids varied from 31×10^{-3} N/m for fine oil to 75×10^{-3} N/m for water. The ranges of Reynolds numbers for liquids and gas were 5.24–140 and 15–1000, respectively. The range of the pressure drop measured was 10–110 psi(gauge). The researcher measured experimentally the degree of liquid saturation of the porous mass using a radiation absorption technique with a $Thulim^{170}$ source. The range of liquid saturation was 25–85%. The experimental solution of the dimensional equation showed that the driving force should be expressed in the form of a product of only three dimensionless numbers. These three dimensionless numbers were the liquid Reynolds number (Re_l), the gas Reynolds number (Re_g), and the ratio of liquid viscosity and gas viscosity (μ_l/μ_g). The indices of dimensionless numbers have either of the two values depending on the respective range of saturation as follows.

Below the transition saturation

$$\frac{\Delta P_{f,t}}{L} = 0.0407 \times 1412.17\rho_l \ \mathrm{Re}_l^{0.29} \ \mathrm{Re}_g^{0.57}\left(\frac{\mu_l}{\mu_g}\right)^{0.28} \tag{3}$$

Above the transition saturation

$$\frac{\Delta P_{f,t}}{L} = 0.0485 \times 1412.17\rho_l \ \mathrm{Re}_l^{0.67} \ \mathrm{Re}_g^{0.3}\left(\frac{\mu_l}{\mu_g}\right)^{0.8} \tag{4}$$

Ford [14] found that the value of the degree of saturation, at which the transition from one to the other of the above equation occurs, was constant at 43% for all the liquids used.

In Ford's correlation, the units of $\Delta P_{f,t}$, L, and ρ_l are psi, ft, and lb_m/ft^3, respectively. To convert the units of ΔP_t, L, and ρ_l to SI units in the Nomenclature, the conversion factor of 1412.17 is used.

Larkins et al. [15] studied pressure drop and liquid saturation accompanying two-phase concurrent flow different packings (d_p =0.125–0.375 in. (3.175–9.525 mm) and ε=0.357–0.52) and with gas-liquid systems having a wide range of fluid properties (U_g=0–26.4 ft/s (0–8.047 m/s), U_l=0–0.87 ft/s (0–0.265 m/s), $\mu_g=12\times10^{-6}-19\times10^{-6}$ kg/m s, and $\mu_l=329\times10^{-6}-41\times10^{-3}$ kg/m s). Two basic flow patterns with nonfoaming systems were observed. Correlations of pressure drop and liquid-saturation data were obtained in terms of the single-phase friction losses for the liquid phase and the gas phase when each phase flows alone in the bed at the same temperature and pressure as the two-phase case. The researchers used the Ergun equation [16] to calculate the single-phase friction losses for the liquid phase and the gas phase, respectively. Their pressure drop correlation was

$$\log\left(\frac{\Delta P_{f,t}/L}{\Delta P_{f,l}/L + \Delta P_{f,g}/L}\right) = \log\left(\frac{\phi_g^2}{1+X^2}\right) = \frac{0.416}{(\log X)^2 + 0.666} \tag{5}$$

$$X = \left(\frac{\Delta P_{f,l}/L}{\Delta P_{f,g}/L}\right)^2 \tag{6}$$

$$\frac{\Delta P_{f,l}}{L} = \frac{150(1-\varepsilon)^2}{\varepsilon^3 d_p^2}\mu_l U_l + \frac{1.75(1-\varepsilon)}{\varepsilon^3 d_p}\rho_l U_l^2 \tag{7}$$

$$\frac{\Delta P_{f,g}}{L} = \frac{150(1-\varepsilon)^2}{\varepsilon^3 d_p^2}\mu_g U_g + \frac{1.75(1-\varepsilon)}{\varepsilon^3 d_p}\rho_g U_g^2 \tag{8}$$

It is clear that Eq. (5) is symmetrical about X=1 in the logarithmic scale. Thus, this equation implies that the influence of the liquid flow superimposed on gas single-phase flow and the influence of gas flow superimposed on liquid single-phase flow are the same with respect to the two-phase pressure drop.

In addition, Larkins et al. [15] discussed the deviations from the correlation with foaming systems and illustrated with sample data.

Turpin and Huntington [17] investigated the two-phase, gas-liquid concurrent flow in packed beds with the use of an air-water system and 2 in., 4 in., and 6 in. (50.8 mm, 101.6 mm, and 152.4 mm) diameter columns packed with tabular alumina particles of 0.025 ft and 0.027 ft (7.62 mm and 8.2296 mm) in diameter. The range of gas mass flux (G_g) was 0.02–6.5 kg/m^2 s, while the range of liquid mass flux (G_l) was 6.26–54.4 kg/m^2 s. The researchers measured the total pressure drop, column operating pressure, and liquid saturation as functions of the gas flow rate, fluid temperatures, and flow direction at several constant liquid flow rates for each column. The correlation of the frictional pressure loss was achieved in terms of a defined two-phase friction factor (f_t) and a second correlating parameter (Z) that was a function of the liquid and gas Reynolds numbers. This correlation for upward flow data was

$$\ln f_t = 8.0 - 1.12(\ln Z) + 0.0769(\ln Z)^2 + 0.0152(\ln Z)^3, \quad 0.3 \le Z \le 500 \tag{9}$$

$$Z = \frac{\mathrm{Re}_g^{1.167}}{\mathrm{Re}_l^{0.767}} \tag{10}$$

This correlation for downward flow data was

$$\ln f_t = 7.96 - 1.34(\ln Z) + 0.0021(\ln Z)^2 + 0.0078(\ln Z)^3, \quad 0.2 \le Z \le 500 \tag{11}$$

where the Turpin and Huntington parameter (Z) is defined by Eq. (10).

Turpin and Huntington [17] found that a viscosity correction factor was required to extend the friction factor correlation to include liquid viscosities that are widely divergent from that of water in terms of the ratio of mass flow rates of the respective phases.

Sato et al. [18] studied pressure loss and liquid holdup in a packed bed reactor with cocurrent gas-liquid down flow. The researchers obtained new experimental data for air-water flow in 65.8 mm and 122 mm inside diameter (i.d.) columns packed with glass spheres of six different sizes between d_p=2.59 mm and 24.3 mm. A similar expression to that of Larkins et al. [15] was obtained with different constants. Their pressure drop correlation was

$$\log\left(\frac{\Delta P_{f,t}/L}{\Delta P_{f,l}/L + \Delta P_{f,g}/L}\right) = \log\left(\frac{\phi_g^2}{1+X^2}\right) = \frac{0.70}{(\log(X/1.2))^2 + 1.0} \tag{12}$$

$$X = \left(\frac{\Delta P_{f,l}/L}{\Delta P_{f,g}/L}\right)^2 \tag{13}$$

$$\frac{\Delta P_{f,l}}{L} = \frac{150(1-\varepsilon)^2}{\varepsilon^3 d_p^2}\mu_l U_l + \frac{1.75(1-\varepsilon)}{\varepsilon^3 d_p}\rho_l U_l^2 \tag{14}$$

$$\frac{\Delta P_{f,g}}{L} = \frac{150(1-\varepsilon)^2}{\varepsilon^3 d_p^2}\mu_g U_g + \frac{1.75(1-\varepsilon)}{\varepsilon^3 d_p}\rho_g U_g^2 \tag{15}$$

It is clear that Eq. (12) is symmetrical about $X=1.2$ in the logarithmic scale.

Saada [19] studied the fluid mechanics of the cocurrent flow of gas and liquid mixtures through packed beds of glass spheres. In his study, he found two regimes of flow inside the pores. These regimes were interpreted on the basis of two flow configurations; one where the pores were predominant in single-phase flow below the transition saturation, and the other where they were predominant in two-phase flow above the transition saturation. These regimes were identified on beds with other packings and checked the interpretation by means of liquid holdup measurements using a gamma-radiation absorption technique. Based on dimensional analysis, correlations were given for the pressure drop for each of the two regimes as follows.

Below the transition saturation

$$\frac{\Delta P_{f,t}}{L} = 0.024\rho_l g \ \mathrm{Re}_l^{0.60} \ \mathrm{Re}_g^{0.39}\left(\frac{d_p}{d}\right)^{-1.1} \tag{16}$$

Above the transition saturation

$$\frac{\Delta P_{f,t}}{L} = 0.027\rho_l g \ \mathrm{Re}_l^{0.35} \ \mathrm{Re}_g^{0.51}\left(\frac{d_p}{d}\right)^{-1.15} \tag{17}$$

Saada [19] reported an equation that could be used to predict which of the two regimes was prevailing based on the assumption that at the transition point, the driving force was the same in both regimes of flow. This equation was

$$\mathrm{Re}_g^* = 0.44 \ \mathrm{Re}_l^2\left(\frac{d_p}{d}\right)^{0.38} \tag{18}$$

Midoux et al. [20] studied flow patterns, pressure loss, and liquid holdup for gas-liquid concurrent downflow in glass beds and in cylindrical and spherical CoMo Al_2O_3 catalyst packings with foaming and nonfoaming liquids. The researchers gathered the different flow patterns encountered in this study in a flow pattern diagram. Correlations of the pressure loss and the liquid holdup were proposed in terms of the single-phase friction loss or frictional energy for the liquid and the gas when each flowed along the bed. The types of correlation were dependent on the tendency of the fluid to foam or not. The researchers correlated their data from seven nonfoaming systems, two column diameters (5 cm and 10 cm), and three particle sizes in exactly the same manner of the Lockhart–Martinelli type. Their best-fit curve for pressure drop was given by

$$\phi_l = 1 + \frac{1}{X} + \frac{1.14}{X^{0.54}}, \quad 0.1 < X < 80 \tag{19}$$

Midoux et al. [20] also presented a comparison of the flow diagram and the pressure drop and holdup correlation of this work with those of other published studies.

Specchia and Baldi [21] correlated the pressure drop and the liquid holdup for the two-phase concurrent downward flow in packed beds for different types of packings by taking into account two hydrodynamic regimes: a poor and a high gas-liquid interaction regime. In their experiments, the gas used was air while the liquids used were water, 9% glycerol, 29% glycerol, and 8 ppm and 16 ppm surfactants. The range of gas mass flux (G_g) was 0.12–1.31 $\mathrm{kg/m^2\,s}$ while the range of liquid mass flux (G_l) was 1–29.7 $\mathrm{kg/m^2\,s}$. The packing shapes used were spheres and cylinders. They considered foaming and nonfoaming systems in their study. In the poor interaction regime, the researchers calculated the pressure drop as due to the gas flowing in a bed restricted by the presence of the liquid. They proposed and used a correlation valid for a free liquid trickling, modified to consider the effect of the pressure drop, to correlate liquid holdup in the presence of a concurrent gas flow. In the high interaction regime, empirical correlations were proposed for both foaming and nonfoaming systems. Their model was derived from the one proposed by Turpin and Huntington [17]. They expressed the pressure drop in terms of a two-phase friction factor (f_t) that was assumed to be a function of the dimensionless number (Z). The pressure drop was dependent on the physical properties of the fluids also through the parameter (ψ) previously introduced by Charpentier and Favier [22]. Their correlation was

$$\ln f_t = 7.82 - 1.30\ln\left(\frac{Z}{\psi^{1.1}}\right) + 0.0573\left[\ln\left(\frac{Z}{\psi^{1.1}}\right)\right]^2 \tag{20}$$

$$Z = \frac{\mathrm{Re}_g^{1.167}}{\mathrm{Re}_l^{0.767}} \tag{21}$$

$$\psi = \frac{\sigma_w}{\sigma_l}\left[\frac{\mu_l}{\mu_w}\left(\frac{\rho_w}{\rho_l}\right)^2\right]^{1/3} \tag{22}$$

Specchia and Baldi [21] claimed that all the employed correlations fitted experimental results from several authors better than those proposed in the literature.

Clements and Schmidt [23] studied a two-phase pressure drop in cocurrent downflow in packed beds. The gas used was air while the liquid used was silicone oil. The range of gas mass flux (G_g) was 0.05–0.55 $\mathrm{kg/m^2\,s}$ while the range of liquid mass flux (G_l) was 0.6–25 $\mathrm{kg/m^2\,s}$. The packing shapes used were spheres and extrudate. The researchers related the two-phase pressure drop to the single-phase gas pressure drop in an empirical correlation as follows:

$$\left(\frac{\Delta P_{f,t}/L}{\Delta P_{f,g}/L}\right) = 190 \times 7936.45\mu_l d_p\left(\frac{\varepsilon}{1-\varepsilon}\right)^3\left(\frac{\mathrm{We}_g \ \mathrm{Re}_g}{\mathrm{Re}_l}\right)^{-0.033} \tag{23}$$

In Clements and Schmidt's correlation, the units of μ_l and d_p are $\mathrm{lb}_m/\mathrm{ft\,h}$ and ft, respectively. To convert the units of μ_l and d_p to SI units like in the Nomenclature, the conversion factor of 7936.45 is used.

Rao et al. [24] studied pressure drop and liquid saturation in cocurrent downflow through packed beds. A macroscopic model was formulated based on momentum balance for the condition of no radial pressure gradients. The researchers included the effect of bubble formation on the pressure drop and holdup in their model. They compared the results of their study with the experimental data of the earlier investigators. The model provided a functional form for correlating pressure drop and liquid saturation, but some parameters had to be determined by fitting the experimental data.

Rao et al. [25] determined experimentally the two-phase pressure drop and the dynamic and the total liquid saturation for the air-water system under cocurrent downflow through packed beds using packing differing widely in geometry like spheres, cylinders, Raschig rings, and Berl saddles. A new correlation of the Lockhart–Martinelli type was proposed for the pressure drop. Their pressure drop correlation was

$$\phi_l = 1 + \frac{0.99}{X} + \frac{1.14}{X^{0.5}} \tag{24}$$

Also, Rao et al. [25] correlated satisfactorily the experimental data of their study as well as that available in literature in terms of the Reynolds numbers defined for the respective phases and the bed porosity, taking into account the flow behavior of the phases through the packed bed.

Tosun [26] reviewed the past work in the literature of gas-liquid cocurrent downflow packed bed reactors. He examined the most significant correlations against measurements from his work on six nonfoaming gas-liquid systems with a glass column of 5.1 cm inside diameter packed with spherical glass beads of 1.9 mm diameter to a height of 85 cm. The experiments set used covered gases and liquids of different nature (air-water, He-50% glycerin in water, He-(32%glycerin+30%ethanol+38%water), He-80% methanol in water, air-80% methanol in water, and air-28% glycerin in water). The range of gas mass flux (G_g) was 0.0005–1.0 $\mathrm{kg/m^2\,s}$, while the range of liquid mass flux (G_l) was 3–30 $\mathrm{kg/m^2\,s}$. He proposed a new correlation of the Lockhart–Martinelli type. His correlation was

$$\phi_l = 1 + \frac{1}{X} + \frac{1.424}{X^{0.576}} \tag{25}$$

Tosun's correlation agreed well with two similar correlations in the literature. Pinna et al. [27] mentioned that the best literature pressure drop model was the one presented by Tosun [26]. Yet, amidst the tested literature correlations, the Tosun [26] model was the only one that led to accurate predictions of pressure drop for all the packings examined in the work of Pinna et al. [27].

Sai and Varma [28] measured experimentally pressure drop in cocurrent gas-liquid downflow through packed beds for nonfoaming, foaming Newtonian, and non-Newtonian liquids. The researchers conducted experiments in two different columns covering a wide range of variables. The following parameters were included in their study: the column diameter, packing size and shape, liquid and gas flow rates, and their physical properties. In their experiments, the gas used was air while the liquids used were water, glycerine, kerosene, *n*-hexane, and carboxymethyl cellulose (CMC). The ranges of gas mass flux (G_g) were 0.18–1.54 $\mathrm{kg/m^2\,s}$ and 0.17–2.32 $\mathrm{kg/m^2\,s}$ for column I and column II, respectively, while the ranges of liquid mass flux (G_l) were 4.3–50 $\mathrm{kg/m^2\,s}$ and 3–58.8 $\mathrm{kg/m^2\,s}$ for column I and column II, respectively. The packing shapes used were Raschig rings, spheres, and cylinder particles. For the data of their study as well as the data available in the literature, unified correlations were presented in terms of flow variables, packing characteristics, and the Lockhart–Martinelli parameter (X). Also, they modeled the data using a dynamic interaction model.

Goto and Gaspillo [29] measured pressure drops and liquid holdups for gas/air-liquid (aqueous solution) upflow and downflow modes in small packing diameters of 0.46 mm, 0.92 mm, and 1.83 mm, respectively. The gas flow rates were changed while the liquid flow rate was kept constant in their experiments. The viscosities of liquid were varied by adding propylene glycol in water. The researchers found multiple hydrodynamic states for both the upflow and the downflow. Some correlations were derived from experimental results. The modified Ergun equation [30] was used to calculate the single-phase friction losses for the liquid phase and the gas phase, respectively. Their pressure drop correlation was

$$\log\left(\frac{\Delta P_{f,t}/L}{\Delta P_{f,l}/L + \Delta P_{f,g}/L}\right) = \log\left(\frac{\phi_g^2}{1+X^2}\right) = \frac{0.55}{(\log(X/1.2))^2 + 0.666} \tag{26}$$

$$X = \left(\frac{\Delta P_{f,l}/L}{\Delta P_{f,g}/L}\right)^2 \tag{27}$$

$$\frac{\Delta P_{f,l}}{L} = \frac{180(1-\varepsilon)^2}{\varepsilon^3 d_p^2}\mu_l U_l + \frac{1.8(1-\varepsilon)}{\varepsilon^3 d_p}\rho_l U_l^2 \tag{28}$$

$$\frac{\Delta P_{f,g}}{L} = \frac{180(1-\varepsilon)^2}{\varepsilon^3 d_p^2}\mu_g U_g + \frac{1.8(1-\varepsilon)}{\varepsilon^3 d_p}\rho_g U_g^2 \tag{29}$$

It is clear that Eq. (26) is symmetrical about $X=1.2$ in the logarithmic scale.

Khan et al. [31] studied flow regime identification and pressure drop in cocurrent upflow of air and water through a bed of ceramic spheres. The identified flow regimes in their study were bubble flow, pulse flow, and spray flow. The researchers presented the criteria for transition from one regime to another. They measured experimentally pressure drop for the two-phase flow. The two-phase friction factor (f_t) was correlated for the different flow regimes. For bubble flow, their correlation was

$$f_t = 3 \times 10^7\ \mathrm{Re}_g^{0.18}\ \mathrm{Re}_l^{-1.7}\left(\frac{d_p}{d}\right)^{1.5} \tag{30}$$

For pulse flow, their correlation was

$$f_t = 2.36 \times 10^7\ \mathrm{Re}_g^{0.26}\ \mathrm{Re}_l^{-1.7}\left(\frac{d_p}{d}\right)^{1.5} \tag{31}$$

For spray flow, their correlation was

$$f_t = 3.91 \times 10^5\ \mathrm{Re}_g^{1.12}\ \mathrm{Re}_l^{-1.82}\left(\frac{d_p}{d}\right)^{1.5} \tag{32}$$

Fourar and Lenormand [32] presented a new model for describing the two-phase flow at high velocities in porous media and fractures. The researchers based their model on the generalization of the single-phase Forchheimer's equation [33] by introducing a function F as a multiplier factor of the superficial velocity during the two-phase flow. They assumed that this function was dependent on the saturation and fluid properties but not on the flow regime (or Reynolds number). The function F could be derived from experiments performed at a given flow rate or from a theoretical model of the relative permeability Kr in the viscous flow regime. For use in petroleum engineering, their model was presented in terms of Kr as follows:

$$Kr_l = \frac{1}{F_l(1 + F_l\ \mathrm{Re}_l)} \tag{33}$$

$$Kr_g = \frac{1}{F_g(1 + F_g\ \mathrm{Re}_g)} \tag{34}$$

For $F\ \mathrm{Re} \ll 1$, Eqs. (33) and (34) reduce to

$$F_l = \frac{1}{Kr_l} \tag{35}$$

$$F_g = \frac{1}{Kr_g} \tag{36}$$

As a result, the relative permeability for flows with both viscous and inertial effects could be easily derived from the Kr measured in the viscous regime (but with negligible capillary forces).

For use in chemical engineering, Fourar and Lenormand [32] presented their model in terms of the Lockhart and Martinelli parameter (X) as follows:

$$\phi_l^2 = \frac{F_l(1 + F_l\ \mathrm{Re}_l)}{(1 + \mathrm{Re}_l)} \tag{37}$$

$$\phi_g^2 = \frac{F_g(1 + F_g\ \mathrm{Re}_g)}{(1 + \mathrm{Re}_g)} \tag{38}$$

$$X^2 = \frac{\rho_g}{\rho_l}\frac{\mu_l^2}{\mu_g^2}\frac{\mathrm{Re}_l(1+\mathrm{Re}_l)}{\mathrm{Re}_g(1+\mathrm{Re}_g)} \tag{39}$$

For the viscous flow regimes ($\mathrm{Re} \ll 1$), Eqs. (37)–(39) reduce to

$$\phi_l = \sqrt{F_l} \tag{40}$$

$$\phi_g = \sqrt{F_g} \tag{41}$$

$$X = \sqrt{\frac{\mu_l U_l}{\mu_g U_g}}, \quad F\ \mathrm{Re} \ll 1 \tag{42}$$

For the purely inertial flow regime ($F\ \mathrm{Re} \gg 1$), Eqs. (37)–(39) reduce to

$$\phi_l = F_l \tag{43}$$

$$\phi_g = F_g \tag{44}$$

$$X = \sqrt{\frac{\rho_l}{\rho_g}}\frac{U_l}{U_g}, \quad F\ \mathrm{Re} \gg 1 \tag{45}$$

Fourar and Lenormand [32] validated their model using experimental results obtained at high flow rates of air and water in an artificial rough fracture.

Jamialahmadi et al. [34] studied pressure drop, bubble size, gas holdup, and convective heat transfer experimentally and theoretically at constant wall heat flux for the single and two-phase flows through unconsolidated porous media. The researchers measured the single-phase pressure drop and heat transfer coefficients over a wide range of particle sizes, heat fluxes, and liquid flow rates. They used the conservation equations and the Kozeny–Carman equation [35] to describe the single-phase flow pressure drop and convective heat transfer through the porous media. The measured pressure drop was used to evaluate the validity of the predictive expressions available in the literature. Mathematical models were developed for the prediction of temperature profiles and single-phase heat transfer coefficients that predicted the experimental data with good accuracy. They presented a large number of new experimental data two-phase pressure drop, bubble size, gas holdup, and heat transfer coefficients for cocurrent upward gas/liquid flow through beds of different particle sizes under constant wall heat flux. The experimental data suggested the existence of two distinct regimes, i.e., homogeneous and heterogeneous flows. The researchers compared the experimental data on two-phase pressure drops and gas holdups with the prediction of published correlations. A correlation for the prediction of the two-phase pressure drop through porous media was presented using analogies to the single-phase flow. Their correlation was

$$\frac{\Delta P_{f,t}}{L} = \frac{f_t}{2}\frac{6(1-\varepsilon)}{d_p \varepsilon^3} \tag{46}$$

Jamialahmadi et al. [34] found that the two-phase friction factor (f_t) was a function of the gas phase Reynolds number (Re_g) and the liquid phase Reynolds number (Re_l) and could be determined from experimental data. For this purpose, the researchers compiled a data bank containing a large number of data points over a wide range of operating conditions. They used these data to develop the following correlation:

$$\frac{f_t}{2} = 94\left(\frac{\mathrm{Re}_l^{1.11}}{\mathrm{Re}_g^{1.8}}\right) + 4.4 \tag{47}$$

Using Eqs. (46) and (47), the absolute mean average error between measured and predicted values was about 5.6%. This value demonstrated the applicability of the suggested model.

Jagadeesh Babu et al. [36] studied the prediction of two-phase pressure drops and liquid holdups in cocurrent gas-liquid downflow of air-Newtonian systems through packed beds. The researchers analyzed the dependency of pressure drop and liquid holdup on phase velocities, geometry of the column, and packing materials, as well as on the physical properties of gas and liquid. In their work, the gas used was air while the liquids used were water, 25% glycerol, 56% glycerol, and ethylene glycol. In their work, the packing materials were spherical and Berl saddles. The particle diameter range was 10.25–16.05 mm. The porosity range was 0.373–0.618. They used their experimental data (825 data points obtained using four liquid systems and 3 different particles) along with those of the available literature (776 data points from 5 different sources) for the analysis. They evaluated the applicability and the limitations of the literature correlations using the available data. Based on the analysis, new correlations were developed for the estimation of pressure drops and liquid holdups, valid for low and high interaction regimes using the available data, with a wide range of variables. They determined the criteria for discriminating between the low and high interaction regions using the relation $(G_l G_g^{0.4})/(\varepsilon^2 d_p^{0.6})$ where values <350 indicate the low interaction region and values >350 indicate the high interaction region, as suggested by Venkataratnam and Varma [37]. In order to develop these correlations, they considered comprehensively the effect of different parameters on the pressure drop and liquid holdup such as the gas Reynolds number (Re_g), the liquid Reynolds number (Re_l), the Morton number for the liquid phase (Mo_l), the bed porosity (ε), and the equivalent diameter (d_e). They considered the following variable range for their study: $2.73 < \mathrm{Re}_l < 1899.4$, $2.88 < \mathrm{Re}_g < 2267.56$, $0.0026 < d_e/d < 0.126$, $0.508 < [\varepsilon/(1-\varepsilon)] < 3.545$, and $1.377 \times 10^{-11} < \mathrm{Mo}_l < 1.366 \times 10^{-6}$. The pressure drop correlations were as follows.

For the low interaction regime,

$$\frac{\Delta P_{f,t}}{L} = 0.48\rho_t g\ \mathrm{Re}_l^{0.01}\ \mathrm{Re}_g^{0.29}\left(\frac{\varepsilon}{1-\varepsilon}\right)^{-0.74}\left(\frac{d_e}{d}\right)^{-0.61}\mathrm{Mo}_l^{0.09} \tag{48}$$

For the high interaction regime,

$$\frac{\Delta P_{f,t}}{L} = 0.39\rho_t g\ \mathrm{Re}_l^{0.1}\ \mathrm{Re}_g^{0.35}\left(\frac{\varepsilon}{1-\varepsilon}\right)^{-0.67}\left(\frac{d_e}{d}\right)^{-0.59}\mathrm{Mo}_l^{0.14} \tag{49}$$

Jagadeesh Babu et al. [36] claimed that their proposed correlations matched their experimental data as well as the literature data, covering a wide range of experimental conditions satisfactorily. Statistical analysis of their correlations for low (Eq. (48)) and high (Eq. (49)) interaction regions showed arithmetic average relative deviations (AARDs) of 19% and 17% with biases of 1.023 and 1.052, respectively. The applicability of their correlations for highly viscous and non-Newtonian solutions still had to be verified with more experiments.

Jagadeesh Babu et al. [38] studied the pressure drop and liquid holdup in cocurrent gas-liquid downflow of air-CMC solutions through packed beds. The researchers analyzed the dependency of pressure drops and liquid holdups on system variables. In their work, the gas used was air, while the liquids used were water and CMC solutions (0.2%, 0.5%, 0.8%, and 1% by weight). The CMC solution was a power law model liquid (pseudoplastic fluid) and had a thixotropic nature. As a result, they evaluated the flow consistency index (k) and the flow behavior index (n) using the power law model. In their experiments, they obtained 863 data points (low interaction regime (128) and high interaction regime (735)) on pressure drop and 735 data points on liquid holdup. They used the modified Reynolds number and Morton's number involving flow consistency index (k) and flow behavior index (n) along with other variables for the development of unified correlations to represent the available data. The pressure drop correlations were as follows.

For the low interaction regime,

$$\frac{\Delta P_{f,t}}{L} = 2.4.10^{-3}\rho_t g \ \mathrm{Re}_{lm}^{0.6} \ \mathrm{Re}_g^{0.35}\left(\frac{\varepsilon}{1-\varepsilon}\right)^{-0.83}\left(\frac{d_e}{d}\right)^{-2.38}\mathrm{Mo}_m^{0.55} \tag{50}$$

For the high interaction regime,

$$\frac{\Delta P_{f,t}}{L} = 4.4.10^{-4}\rho_t g \ \mathrm{Re}_{lm}^{0.6} \ \mathrm{Re}_g^{0.49}\left(\frac{\varepsilon}{1-\varepsilon}\right)^{-0.72}\left(\frac{d_e}{d}\right)^{-2.22}\mathrm{Mo}_m^{0.26} \tag{51}$$

Table 1 gives a summary of earlier studies on the two-phase frictional pressure gradient correlations.

3 Proposed Methodology

In the asymptotic model, the dependent parameter y has two asymptotes. The first asymptote is y_0, which corresponds to a very small value of the independent parameter z. The second asymptote is y_∞, which corresponds to a very large value of the independent parameter z. The two asymptotes y_0 and y_∞ can be expressed as follows [1–4]:

$$y_0 = c_0 z^i, \quad z \to 0 \tag{52}$$

$$y_\infty = c_\infty z^j, \quad z \to \infty \tag{53}$$

The two asymptotes y_0 and y_∞ are based on the analytical solution. They consist of a constant, which has a positive real value. The two constants are called c_0 as $z \to 0$ and c_∞ as $z \to \infty$. The values of the two exponents i and j are often 0,1,1/2,1/4,1/3 [1–4].

From analytical, experimental, or numerical methods, it is known that y frequently transitions in a smooth manner between the two asymptotes y_0 and y_∞.

For the case of the two-phase frictional pressure gradient in porous media, the two asymptotes y_0 and y_∞ increase with increasing values of z, and the solution y is concave upward. This trend is also found in the case of external free and forced convection from single isothermal convex bodies.

3.1 Superposition of Asymptotes. Since $y_0 > y_\infty$ as $z \to 0$, the solution y is concave upward, and the two asymptotes y_0 and y_∞ can be combined in the following method [1–4]:

$$y = [y_0^p + y_\infty^p]^{1/p} \tag{54}$$

The parameter p is a fitting or "blending" parameter whose value can be determined in a simple method. The effect of the parameter p in Eq. (54) is only important in the transition region. The results for small and large values of the independent parameter z remain unchanged with changing the parameter p.

To determine a value of p, there are a number of methods as discussed by Churchill and Usagi [1]. For example, we can select an intermediate value of $z = z_{\mathrm{int}}$ corresponding or near the intersection of the two asymptotes for which $y(z_{\mathrm{int}})$ is known from analytical, experimental, or numerical methods. Using Eqs. (52)–(54), we can write for the intermediate value of $z = z_{\mathrm{int}}$,

$$y(z_{\mathrm{int}}) = [(c_0 z_{\mathrm{int}}^i)^p + (c_\infty z_{\mathrm{int}}^j)^p]^{1/p} \tag{55}$$

Although the fitting or blending parameter p is unknown, it can be calculated by numerical methods for solving a nonlinear equation or by means of computer algebra systems like MAPLE™ software [39].

In another method, p is chosen as the value, which minimizes the root mean square (rms) error e_{rms} between the model predictions and the available data. The fractional error (e) in applying the model to each available data point is defined as follows:

$$e = \left|\frac{\text{predicted} - \text{available}}{\text{available}}\right| \tag{56}$$

For groups of data, the rms error e_{rms} is defined as follows:

$$e_{\mathrm{rms}} = \left[\frac{1}{N}\sum_{K=1}^{N} e_K^2\right]^{1/2} \tag{57}$$

If p is a weak function of different parameters, a single value may be chosen, which best represents all of the available data for the two-phase frictional pressure gradient.

The approximate solution y is often presented in a form, which is based on one of the two asymptotes y_0 and y_∞. For example, if the approximate solution y is presented in terms of the asymptote y_0, then the model can be expressed as follows [1–4]:

$$\frac{y}{y_0} = \left[1 + \left(\frac{y_\infty}{y_0}\right)^p\right]^{1/p} \tag{58}$$

On the other hand, if the approximate solution y is presented in terms of the asymptote y_∞, then the model can be expressed as follows [1–4]:

$$\frac{y}{y_\infty} = \left[1 + \left(\frac{y_0}{y_\infty}\right)^p\right]^{1/p} \tag{59}$$

3.2 Asymptotic Methods in Two-Phase Flow. Using the asymptotic analysis method, the two-phase frictional pressure gradient $(dp/dz)_f$ can be expressed in terms of the single-phase frictional pressure gradient for liquid flowing alone $(dp/dz)_{f,l}$ and single-phase frictional pressure gradient for gas flowing alone $(dp/dz)_{f,g}$ as follows:

$$\left(\frac{dp}{dz}\right)_f = \left[\left(\frac{dp}{dz}\right)_{f,l}^p + \left(\frac{dp}{dz}\right)_{f,g}^p\right]^{1/p} \tag{60}$$

Equation (60) reduces to $(dp/dz)_{f,l}$ and $(dp/dz)_{f,g}$ as $x=0$ and 1, respectively.

If the two-phase frictional pressure gradient $(dp/dz)_f$ is presented in terms of the single-phase frictional pressure gradient for liquid flowing alone $(dp/dz)_{f,l}$, then the model can be expressed using the Lockhart–Martinelli parameter (X) as follows:

$$\left(\frac{dp}{dz}\right)_f = \left(\frac{dp}{dz}\right)_{f,l}\left[1 + \left(\frac{1}{X^2}\right)^p\right]^{1/p} \tag{61}$$

Equation (61) can be expressed in terms of a two-phase frictional multiplier for liquid flowing alone (ϕ_l^2) as follows:

$$\phi_l^2 = \left[1 + \left(\frac{1}{X^2}\right)^p\right]^{1/p} \tag{62}$$

On the other hand, if the two-phase frictional pressure gradient $(dp/dz)_f$ is presented in terms of the single-phase frictional pressure gradient for gas flowing alone $(dp/dz)_{f,g}$, then the model can be expressed using the Lockhart–Martinelli parameter (X) as follows:

$$\left(\frac{dp}{dz}\right)_f = \left(\frac{dp}{dz}\right)_{f,g}[1 + (X^2)^p]^{1/p} \tag{63}$$

Equation (63) can be expressed in terms of a two-phase frictional multiplier for gas flowing alone (ϕ_g^2) as follows:

$$\phi_g^2 = [1 + (X^2)^p]^{1/p} \tag{64}$$

One of the principal types of correlations given in the literature to correlate the two-phase pressure drop uses the dimensionless parameters ϕ_l and ϕ_g versus the Lockhart–Martinelli parameter (X) originally used by Lockhart and Martinelli [40] for the two-phase flow in horizontal pipes. The correlations relating ϕ_l and ϕ_g versus the Lockhart–Martinelli parameter (X) were successfully adopted by Larkins et al. [15], Sato et al. [18], Midoux et al. [20], Rao et al. [25], Tosun [26], Sai and Varma [28], and Goto and Gaspillo [29]. As shown in Eqs. (62) and (64), the advantage of the new model is that it has only one fitting parameter (p), while the other existing correlations, such as those of Larkins et al. [15],

Table 1 Summary of earlier studies on two-phase frictional pressure gradient correlations

Author	Dimensions	Fluids	Range of variables	Techniques, basis, observations
Ford [14]	$d=44.75$ mm $L=355.6$ mm $d_p=1$ mm	Air-water Air-industrial methylated spirits Air-sugar solutions Air-saturated solution of pine oil	Glass spheres ($\varepsilon=36\%$) $\sigma_l=31\times10^{-3}-75\times10^{-3}$ N/m $\mathrm{Re}_l=5.24-140$ $\mathrm{Re}_g=15-1\,000$ Liquid saturation=25–85%	Frictional pressure gradients correlation as a function of ρ_l, Re_l, Re_g, and (μ_l/μ_g) for below the transition saturation (43%) and above the transition saturation
Larkins et al. [15]	$d_p=3.175-9.525$ mm	Air-water	Rasching ring and spheres ($\varepsilon=0.357-0.52$) $U_g=0-8.047$ m/s $U_l=0-0.265$ m/s $\mu_g=12\times10^{-6}-19\times10^{-6}$ kg/m s $\mu_l=329\times10^{-6}-41\times10^{-3}$ kg/m s $0.05<X<30$	Two-phase frictional multiplier correlation as a function of the Lockhart–Martinelli parameter (X) Symmetrical about $X=1$ in the logarithmic scale
Turpin and Huntington [17]	$d=50.8$ mm, 101.6 mm, and 152.4 mm $d_p=7.62$ mm and 8.2296 mm	Air-water	Tabular alumina particles $0.02<G_g<6.5$ kg/m^2 s $6.26<G_l<54.4$ kg/m^2 s $0.3\leq Z\leq500$ for upward flow $0.2\leq Z\leq500$ for downward flow	Two-phase friction factor correlation as a function of the Turpin and Huntington parameter (Z) for upward flow and downward flow
Sato et al. [18]	$d=65.8$ mm and 122 mm $d_p=2.59$ mm and 24.3 mm	Air-water	Glass spheres $0.1<X<20$	Two-phase frictional multiplier correlation as a function of the Lockhart–Martinelli parameter (X) Symmetrical about $X=1.2$ in the logarithmic scale
Saada [19]	$d=45.2$ mm $L=400$ mm $d_p=0.514$ mm, 0.974 mm and 2.064 mm	Air-water	Glass spheres ($\varepsilon=34.6\%$) $\mathrm{Re}_l=2-200$ $\mathrm{Re}_g=8-900$	Frictional pressure gradients correlation as a function of ρ_l, g, Re_l, Re_g, and (μ_l/μ_g) for below the transition saturation and above the transition saturation
Midoux et al. [20]	$d=50$ mm and 100 mm $d_p=3$ mm, 1.8×6 mm^2, and 1.4×5 mm^2	Air-water Air-cyclohexane N_2-cyclohexane CO_2-gasoline N_2-gasoline He-gasoline N_2-petroleum ether CO_2-petroleum ether Air-kerosene I N_2-kerosene II CO_2-desulfurized gas oil Air-desulfurized gas oil He-desulfurized gas oil CO_2-nondesulfurized gas oil Air-nondesulfurized gas oil He-nondesulfurized gas oil	Glass beads ($\varepsilon=0.385$) $\rho_l=650-1000$ kg/m^3 $\mu_l=0.31\times10^{-3}-5\times10^{-3}$ kg/m s $\sigma_l=19\times10^{-3}-75\times10^{-3}$ N/m $0.5<G_l<40$ kg/m^2 s $0.1<X<80$	Two-phase frictional multiplier correlation as a function of the Lockhart–Martinelli parameter (X)
Specchia and Baldi [21]	$d=80$ mm Air-9% glycerol $d_p=6$ mm, 5.4 mm, and 2.7 mm	Air-water $0.12<G_g<1.31$ kg/m^2 s Air-29% glycerol Air-8 and 16 ppm surfactant	Spheres and cylinders $1<G_l<29.7$ kg/m^2 s	Two-phase friction factor correlation as a function of the Turpin and Huntington parameter (Z) and the Charpentier and Favier parameter (ψ)
Clements and Schmidt [23]	$d=55$ mm $L=1\,500$ mm	Air-silicone oil	Spheres and extrudate $0.05<G_g<0.55$ kg/m^2 s $0.6<G_l<25$ kg/m^2 s	Related two-phase frictional pressure gradients to single-phase gas frictional pressure gradients in an empirical correlation as a function of μ_l, d_p, $(\varepsilon/1-\varepsilon)$, and $(\mathrm{Re}_g\ \mathrm{We}_g/\mathrm{Re}_l)$
Rao et al. [25]	$d=92.4$ mm $L=1\,835$ mm $d_p=6.72$ mm, 4 mm, 13.07×13.97 mm^2, 8.18×7.91 mm^2, 3.14 mm, and 4.08 mm	Air-water Air-20% glycerol Air-n-hexane	Spheres, cylinders, Raschig rings, and Berl saddles $0.16<G_g<3.2$ kg/m^2 s $4.13<G_l<99.1$ kg/m^2 s	Two-phase frictional multiplier correlation as a function of the Lockhart–Martinelli parameter (X) Correlated satisfactorily the experimental data in terms of the Charpentier and Favier parameter (ψ) for gas continuous flow, pulse flow, and dispersed bubble flow

Table 1 (*Continued.*)

Author	Dimensions	Fluids	Range of variables	Techniques, basis, observations
Tosun [26]	$d=51$ mm $d_p=1.9$ mm $L=850$ mm	Air-water He-50% glycerin in water He-(32%glycerin+30%ethanol +38%water) He-80% methanol in water Air-80% methanol in water Air-28% glycerin in water	Spherical glass beads $3<G_l<30$ kg/m^2 s	Two-phase frictional multiplier correlation as a function of the Lockhart–Martinelli parameter (X) The only correlation that led to accurate predictions of pressure drop for all the packings examined in the work of Pinna et al. [27]
Sai and Varma [28]	$d=92.4$ mm for column I $d=25$ mm for column II $d_p=3.14$ mm, 11.72 mm, 6.72 mm, and 8.18×7.91 mm^2 for column I $d_p=1.59$ mm, 4.32 mm, 2.39 mm, and 5.08×5.71 mm^2 for column II	Air-water Air-glycerine Air-kerosene Air-n-hexane Air-carboxymethyl cellulose (CMC)	Raschig ring, spheres, and cylinders particle $0.18<G_g<1.54$ kg/m^2 s for column I $0.17<G_g<2.32$ kg/m^2 s for column II $4.3<G_l<50$ kg/m^2 s for column I $3<G_l<58.8$ kg/m^2 s for column II	Modeled the data using a dynamic interaction model for gas continuous flow, pulse flow, and dispersed bubble flow
Goto and Gaspillo [29]	$d_p=0.46$ mm, 0.92 mm, and 1.83 mm	Air-water Air-11.5% propylene glycol in water Air-20% propylene glycol in water	$\rho_l=998-1016$ kg/m^3 $\mu_l=1\times10^{-3}-2\times10^{-3}$ kg/m s $\sigma_l=55\times10^{-3}-72.6\times10^{-3}$ N/m	Two-phase frictional multiplier correlation as a function of the Lockhart–Martinelli parameter (X) Symmetrical about $X=1.2$ in the logarithmic scale
Khan et al. [31]	$d=91$ mm $L=1\,000$ mm $d_p=6$ mm	Air-water	Ceramic spheres	Two-phase friction factor correlation as a function of Re_g, Re_l, and (d_p/d) for bubble flow, pulse flow, and spray flow
Fourar and Lenormand [32]				Introducing a function F and relating it to the relative permeability Kr for use in petroleum engineering Two-phase frictional multiplier correlation as a function of the Lockhart–Martinelli parameter (X) for use in chemical engineering
Jamialahmadi et al. [34]	$d=32$ mm $L=580$ mm $d_p=3$ mm, 1.5 mm, 1 mm, 0.4–0.6 mm, 0.18–0.25 mm, and 0.25–0.425 mm	Air-water	Glass beads and mineral sand $U_l=0.004-0.7$ cm/s $U_g=0-30$ cm/s	Frictional pressure gradients correlation with introducing two-phase friction as a function of Re_l and Re_g
Jagadeesh Babu et al. [36]	$d=115$ mm $d_p=12.74$ mm, 16.05 mm, and 10.25 mm $1.377\times10^{-11}<\mathrm{Mo}_l<1.366\times10^{-6}$	Air-water Air-25% glycerol Air-56% glycerol Air-ethylene glycol	Spherical and Berl saddles ($\varepsilon=0.373$, 0.386 and 0.618) $2.73<\mathrm{Re}_l<1899.4$ $2.88<\mathrm{Re}_g<2267.56$ $0.0026<d_e/d<0.126$ $0.508<[\varepsilon/(1-\varepsilon)]<3.545$	Frictional pressure gradients correlation as a function of ρ_l, g, Re_l, Re_g, $(\varepsilon/1-\varepsilon)$, (d_e/d), and Mo_l for the low interaction regime and the high interaction regime
Jagadeesh Babu et al. [38]	$d=92$ mm $d_p=11.72$ mm, 8.09 mm and 3.14 mm	Air-0.2%CMC solution Air-0.5%CMC solution Air-0.8%CMC solution Air-1%CMC solution	Spherical, cylindrical, and Raschig ring ($\varepsilon=0.373$, 0.337 and 0.707) $\rho_l=996-1009$ kg/m^3 $k=0.027-1.083$ kg/m^{-1} s^{n-2} $n=0.641-0.82$ $\sigma_l=70\times10^{-3}$ N/m	Frictional pressure gradients correlation as a function of ρ_l, g, Re_{lm}, Re_g, $(\varepsilon/1-\varepsilon)$, (d_e/d), and Mo_m for the low interaction regime and the high interaction regime

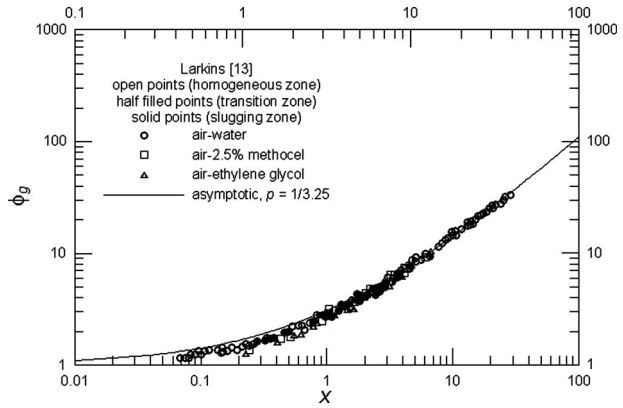

Fig. 1 Comparison of the present asymptotic model with Larkins's [13] data on 0.375 in. (9.525 mm) Raschig rings

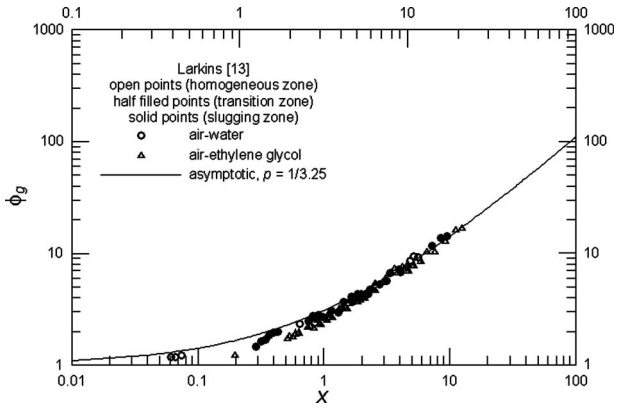

Fig. 2 Comparison of the present asymptotic model with Larkins's [13] data on 0.375 in. (9.525 mm) spheres

Sato et al. [18], and Goto and Gaspillo [29], have three constants. As a result, the calibration of the new model to the experimental data is greatly simplified.

4 Results and Discussion

Examples of the two-phase frictional pressure gradient in porous media for published data of different working fluids at different packing shapes with different diameters are presented to show the features of the asymptotes, asymptotic analysis, and the development of simple compact models. Also, asymptotic forms for ϕ_l versus Lockhart–Martinelli parameter (X) correlations, such as those of Midoux et al. [20], Rao et al. [25], and Tosun [26], are presented using one fitting parameter only. Moreover, asymptotic forms for ϕ_g versus Lockhart–Martinelli parameter (X) correlations, such as the correlation of Larkins et al. [15], the correlation of Sato et al. [18], and the Goto and Gaspillo correlation [29], are presented using one fitting parameter only instead of three constants.

4.1 Comparison of the Present Asymptotic Model With Data. Figure 1 shows a comparison of the present asymptotic model with Larkins's [13] data for the two-phase cocurrent pressure drop on 0.375 in. (9.525 mm) Raschig rings in terms of ϕ_g versus the Lockhart–Martinelli parameter (X). The used working fluids are air-water, air-2.5% methocel, and air-ethylene glycol. The open points represent the homogeneous zone, the half filled points represent the transition zone, while the solid points represent the slugging zone. Equation (64) represents the present asymptotic model. It can be seen that the present model with fitting parameter $p=1/3.25$ represents Larkins's [13] data in a successful manner. The rms error e_{rms} is equal to 12.42%. From Fig. 1, it seems that most of the error comes from the data for $X<1$. For the data points in the region of $X<1$, the rms error e_{rms} is equal to 13.62%.

Figure 2 shows a comparison of the present asymptotic model with Larkins's [13] data for the two-phase cocurrent pressure drop on 0.375 in. (9.525 mm) spheres in terms of ϕ_g versus the Lockhart–Martinelli parameter (X). The used working fluids are air-water and air-ethylene glycol. The open points represent the homogeneous zone, the half filled points represent the transition zone, while the solid points represent the slugging zone. Equation (64) represents the present asymptotic model. It can be seen that the present model with fitting parameter $p=1/3.25$ represents Larkins's [13] data in a successful manner. The rms error e_{rms} is equal to 13.62%. From Fig. 2, it seems that most of the error comes from the data for $X<1$. For the data points in the region of $X<1$, the rms error e_{rms} is equal to 19.00%.

Figure 3 shows a comparison of the present asymptotic model with Larkins's [13] data for the two-phase cocurrent pressure drop for hydrocarbon systems on 3 mm glass beads in terms of ϕ_g versus the Lockhart–Martinelli parameter (X). The data of hydrocarbon systems include natural gas lube, CO_2-lube oil, and plant data taken from the laboratories and facilities of the Humble oil, TX, and refining company. Equation (64) represents the present asymptotic model. It can be seen that the present model with fitting parameter $p=1/3.25$ represents Larkins's [13] data in a successful manner. The rms error e_{rms} is equal to 15.99%.

On the basis of the experimental data shown in Figs. 1–3, it is clear that the experimental points set in the form $\phi_g \to 1$ as $X \to 0$ and $\phi_g \to \infty$ as $X \to \infty$ in line with the expected asymptotic behavior of the Lockhart and Martinelli [40] correlation.

4.2 Asymptotic Forms for ϕ_l and ϕ_g Versus Lockhart–Martinelli Parameter (X) Correlations in Porous Media. Figures 4–6 show ϕ_l versus the Lockhart–Martinelli parameter (X) in porous media using the different correlations available in the literature such as the correlation of Midoux et al. [20] (Eq. (19)) in Fig. 4, the correlation of Rao et al. [25] (Eq. (24)) in Fig. 5, and the Tosun correlation [26] (Eq. (25)) in Fig. 6 with the present asymptotic model. Equation (62) represents the present model with fitting parameter $p=1/3.25$, 1/3.25 and 1/3.5, respectively.

From Figs. 4–6, it can be seen that the present model represents the different correlations available in the literature in a successful manner.

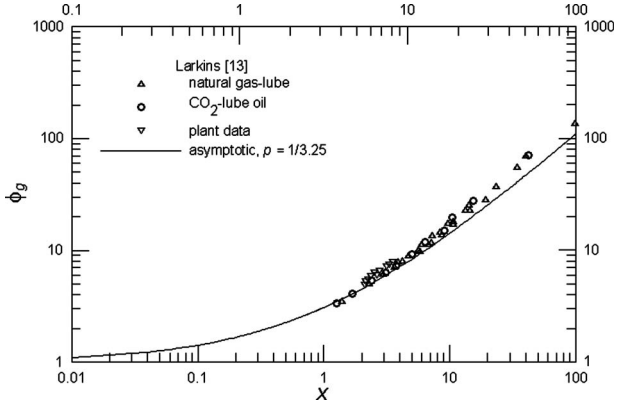

Fig. 3 Comparison of the present asymptotic model with Larkins's [13] data for hydrocarbon systems on 3 mm glass beads

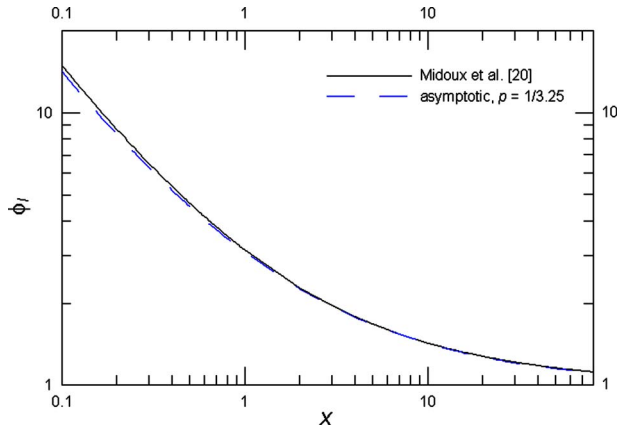

Fig. 4 Comparison of the present asymptotic model with the correlation of Midoux et al. [20]

Figures 7–9 show ϕ_g versus the Lockhart–Martinelli parameter (X) in porous media using the different correlations available in the literature such as the correlation of Larkins et al. [15] (Eq. (5)) in Fig. 7, the correlation of Sato et al. [18] (Eq. (12)) in Fig. 8, and the Goto and Gaspillo [29] correlation (Eq. (26)) in Fig. 9 with the present asymptotic model. Equation (64) represents the present model with fitting parameter $p=1/3.25$, 1/3.75, and 1/3.5, respectively.

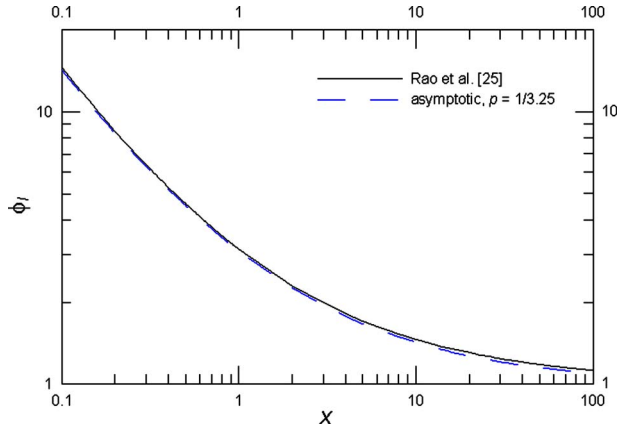

Fig. 5 Comparison of the present asymptotic model with the correlation of Rao et al. [25]

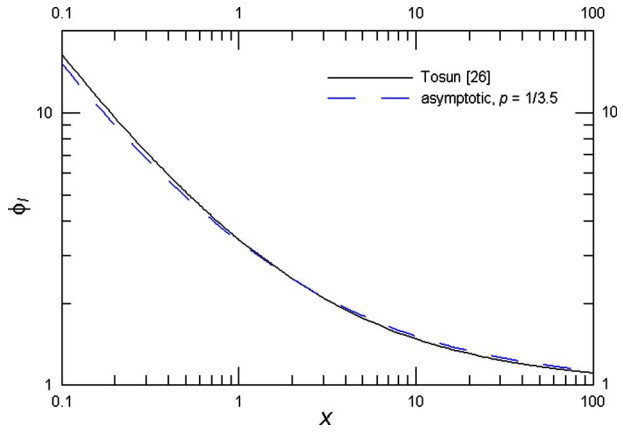

Fig. 6 Comparison of the present asymptotic model with Tosun's [26] correlation

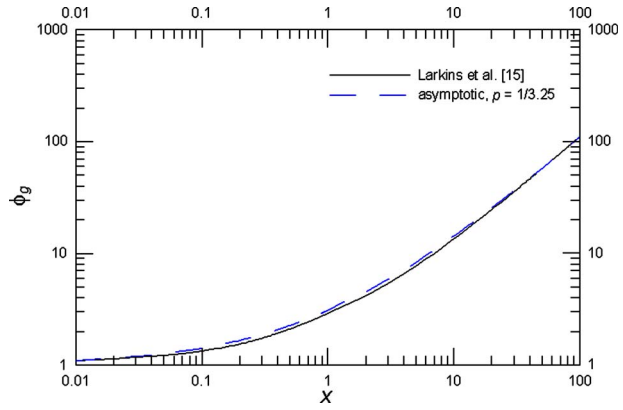

Fig. 7 Comparison of the present asymptotic model with the correlation of Larkins et al. [15]

From Figs. 7–9, it can be seen that the present model represents the different correlations available in the literature in a successful manner.

Table 2 shows fitting parameter (p) values of asymptotic forms for ϕ_l and ϕ_g versus Lockhart–Martinelli parameter (X) correlations in porous media.

5 Summary and Conclusions

A new two-phase flow modeling in porous media is proposed based on an asymptotic modeling method. The main advantage of the asymptotic modeling method in a two-phase flow takes into

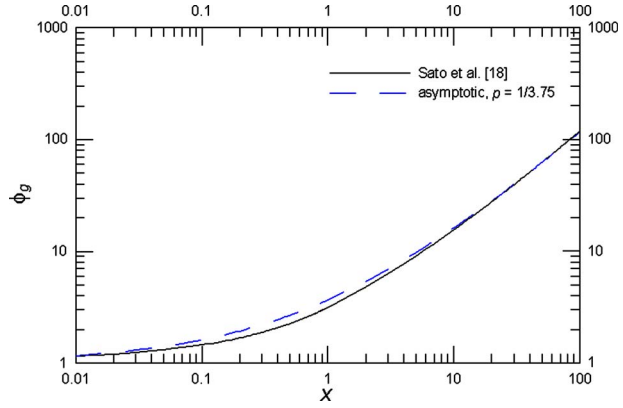

Fig. 8 Comparison of the present asymptotic model with the correlation of Sato et al. [18]

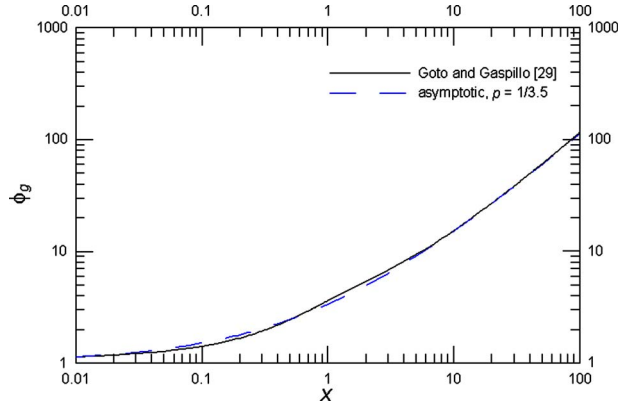

Fig. 9 Comparison of the present asymptotic model with Goto and Gaspillo's [29] correlation

Table 2 Fitting parameter (p) values of asymptotic forms for ϕ_l and ϕ_g versus X

Correlation	p
Midoux et al. [20]	1/3.25
Rao et al. [25]	1/3.25
Tosun [26]	1/3.5
Larkins et al. [15]	1/3.25
Sato et al. [18]	1/3.75
Goto and Gaspillo [29]	1/3.5

account the important frictional interactions that occur at the interface between liquid and gas because the liquid and gas phases are assumed to flow dependently of each other. The only unknown parameter in the asymptotic modeling method in a two-phase flow is the fitting parameter (p). The value of the fitting parameter (p) corresponds to the minimum rms error e_{rms} for any data set. Specifically, $p=1/3.25$ for the correlation of Midoux et al. [20], $p=1/3.25$ for the correlation of Rao et al. [25], $p=1/3.5$ for the Tosun correlation [26], $p=1/3.25$ for the correlation of Larkins et al. [15], $p=1/3.75$ for the correlation of Sato et al. [18], and $p=1/3.5$ for the Goto and Gaspillo [29] correlation. The advantage of the new model is that it has only one fitting parameter, while the other existing correlations such as the correlation of Larkins et al. [15], the correlation of Sato et al. [18], and the Goto and Gaspillo [29] correlation have three constants. Therefore, the calibration of the new model to experimental data is greatly simplified.

Acknowledgment

The authors acknowledge the financial support of Natural Sciences and Engineering Research Council of Canada-Collaborative Research and Development (NSERC-CRD) and Petroleum Research Atlantic Canada (PRAC). Also, the authors would like to thank Stephanie Dohey, the Writing Center, Memorial University of Newfoundland, for reviewing the paper. In addition, the authors acknowledge the insightful comments and suggestions of the anonymous reviewers that have improved the quality of this paper.

Nomenclature

c = constant in asymptotic solution
d = column diameter, m
d_e = equivalent diameter $=(3\Phi_s d_p \varepsilon)/(3(1-\varepsilon))$, m
d_p = particle diameter, m
e = error
F = function in the Fourar and Lenormand model
G = mass flux, kg/m s^2
H = holdup
i = exponent in asymptotic solution for $z \to 0$
j = exponent in asymptotic solution for $z \to \infty$
K = index for summation
k = flow consistency index, kg/m^{-1} s^{n-2}
Kr = relative permeability
L = height of testing section for pressure drop, m
m = exponent
Mo = Morton number $=g^{3n-2}k^4/\rho^{2-n}\sigma^{n+2}$
Mo_m = modified Morton number $=g^{3n-2}k^4/\rho^{2-n}\sigma^{n+2}$
N = number of data points
n = flow behavior index
p = fitting parameter
dp/dz = pressure gradient, Pa/m
Re = Reynolds number $=(d_p U \rho)/\mu$
Re_g^* = gas Reynolds number at which transition occurs
Re_{lm} = modified liquid Reynolds number $=(d_p^n U_l^{2-n} \rho_l)/k$
U = velocity, m/s
X = Lockhart–Martinelli parameter
x = mass quality
y = dependent parameter
Z = Turpin and Huntington parameter $=\text{Re}_g^{1.167}/\text{Re}_l^{0.767}$
z = independent parameter

Greek Symbols

ε = porosity
ρ = density, kg/m^3
Φ_s = sphericity
ϕ_g^2 = two-phase frictional multiplier for gas alone flow
ϕ_l^2 = two-phase frictional multiplier for liquid alone flow
μ = dynamic viscosity, kg/m s
σ = surface tension, N/m
ψ = Charpentier and Favier parameter

Subscripts

0 = corresponding to a very small value
∞ = corresponding to a very large value
f = frictional
g = gas
int = intermediate value
l = liquid
rms = root mean square
t = two-phase
w = water

References

[1] Churchill, S. W., and Usagi, R., 1972, "A General Expression for the Correlation of Rates of Transfer and Other Phenomena," Am. Inst. Chem. Eng. Symp. Ser., **18**(6), pp. 1121–1128.
[2] Churchill, S. W., 1988, *Viscous Flows: The Practical Use of Theory*, Butterworths, Boston, MA.
[3] Kraus, A. D., and Bar-Cohen, A., 1983, *Thermal Analysis and Control of Electronic Equipment*, Hemisphere, New York.
[4] Yovanovich, M. M., 2003, "Asymptotes and Asymptotic Analysis for Development of Compact Models for Microelectronic Cooling," *Proceedings of the 19th Annual Semiconductor Thermal Measurement and Management Symposium and Exposition (SEMI-THERM)*, San Jose, CA.
[5] Churchill, S. W., and Ozoe, H., 1973, "Correlations for Laminar Forced Convection With Uniform Heating in Flow Over a Plate and in Developing and Fully Developed Flow in a Tube," ASME J. Heat Transfer, **95**(1), pp. 78–84.
[6] Churchill, S. W., and Ozoe, H., 1973, "Correlations for Laminar Forced Convection in Flow Over an Isothermal Flat Plate and in Developing and Fully Developed Flow in an Isothermal Tube," ASME J. Heat Transfer, **95**(3), pp. 416–419.
[7] Awad, M. M., 2008, "Heat Transfer From a Rotating Disk to Fluids for a Wide Range of Prandtl Numbers Using the Asymptotic Model," ASME J. Heat Transfer, **130**(1), pp. 145–148.
[8] Raithby, G. D., and Hollands, K. G. T., 1998, *Handbook of Heat Transfer*, W. M. Rohsenow, J. P. Hartnett, and Y. I. Cho, eds., McGraw-Hill, New York, Chap. 4.
[9] Awad, M. M., 2007, "Two-Phase Flow Modeling in Circular Pipes," Ph.D. thesis, Memorial University of Newfoundland, Newfoundland, Canada.
[10] Brownell, L. E., and Katz, D. L., 1947, "Flow of Fluids Through Porous Media. Part II. Simultaneous Flow of Two Homogeneous Phases," Chem. Eng. Prog., **43**(11), pp. 601–612.
[11] Brownell, L. E., and Katz, D. L., 1947, "Flow of Fluids Through Porous Media. I. Single Homogeneous Flow," Chem. Eng. Prog., **43**(10), pp. 537–548.
[12] Schwarz, N., 1956, "Two-Phase Flow Through Porous Media," Ingenieur, **68**(4–5), pp. 1–7.
[13] Larkins, R. P., 1959, "Two-Phase Co-Current Flow in Packed Beds," Ph.D. thesis, University of Michigan, Ann Arbor, MI.
[14] Ford, L. H., 1960, "Multiphase Flow Through Porous Media With Special Reference to Turbulent Region," Ph.D. thesis, University of London, London, UK.
[15] Larkins, R. P., White, R. R., and Jeffrey, D. W., 1961, "Two-Phase Concurrent Flow in Packed Beds," AIChE J., **7**(2), pp. 231–239.
[16] Ergun, S., 1952, "Fluid Flow Through Packed Columns," Chem. Eng. Prog., **48**, pp. 89–105.
[17] Turpin, J. L., and Huntington, R. L., 1967, "Prediction of Pressure Drop for Two-Phase Two-Component Co-Current Flow in Packed Beds," AIChE J., **13**(6), pp. 1196–1202.

[18] Sato, Y., Hirose, T., Takahashi, F., and Toda, M., 1973, "Pressure Loss and Liquid Holdup in Packed Bed Reactor With Cocurrent Gas-Liquid Down Flow," J. Chem. Eng. Jpn., **6**(2), pp. 147–152.
[19] Saada, M. Y., 1975, "Fluid Mechanics of Co-Current Two-Phase Flow in Packed Beds: Pressure Drop and Liquid Holdup Studies," Period. Polytech., Chem. Eng., **19**(4), pp. 317–337.
[20] Midoux, N., Favier, M., and Charpentier, J. C., 1976, "Flow Pattern, Pressure Loss and Liquid Holdup Data in Gas-Liquid Downflow Packed Beds With Foaming and Nonfoaming Hydrocarbons," J. Chem. Eng. Jpn., **9**(5), pp. 350–356.
[21] Specchia, V., and Baldi, G., 1977, "Pressure Drop and Liquid Holdup for Two Phase Concurrent Flow in Packed Beds," Chem. Eng. Sci., **32**(5), pp. 515–523.
[22] Charpentier, J. C., and Favier, M., 1975, "Some Liquid Holdup Experimental Data in Trickle-Bed Reactors for Foaming and Non-Foaming Hydrocarbons," AIChE J., **21**(6), pp. 1213–1218.
[23] Clements, L. D., and Schmidt, P. C., 1980, "Two-Phase Pressure Drop in Cocurrent Downflow in Packed Beds: Air-Silicone Oil Systems," AIChE J., **26**(2), pp. 314–317.
[24] Rao, V. G., Ananth, M. S., and Varma, Y. B. G., 1983, "Hydrodynamics of Two-Phase Cocurrent Downflow Through Packed Beds. Part I: Macroscopic Model," AIChE J., **29**(3), pp. 467–473.
[25] Rao, V. G., Ananth, M. S., and Varma, Y. B. G., 1983, "Hydrodynamics of Two-Phase Cocurrent Downflow Through Packed Beds. Part II: Experiment and Correlations," AIChE J., **29**(3), pp. 473–483.
[26] Tosun, G., 1984, "Study of Cocurrent Downflow of Nonfoaming Gas-Liquid Systems in a Packed Bed. 2. Pressure Drop: Search for a Correlation," Ind. Eng. Chem. Process Des. Dev., **23**(1), pp. 35–39.
[27] Pinna, D., Tronconi, E., and Tagliabue, L., 2001, "High Interaction Regime Lockhart-Martinelli Model for Pressure Drop in Trickle-Bed Reactors," AIChE J., **47**(1), pp. 19–30.
[28] Sai, P. S. T., and Varma, Y. B. G., 1987, "Pressure Drop in Gas-Liquid Downflow Through Packed Beds," AIChE J., **33**(12), pp. 2027–2036.
[29] Goto, S., and Gaspillo, P. A., 1992, "Multiple Hydrodynamics States in Gas-Liquid Upflow and Downflow Through Beds of Small Packing," Ind. Eng. Chem. Res., **31**(2), pp. 629–632.
[30] Macdonald, I. F., El-Sayed, M. S., Mow, K., and Dullien, F. A. L., 1979, "Flow Through Porous Media—The Ergun Equation Revisited," Ind. Eng. Chem. Fundam., **18**(3), pp. 199–208.
[31] Khan, A., Khan, A. A., and Varma, Y. B. G., 1997, "Flow Regime Identification and Pressure Drop in Cocurrent Gas-Liquid Upflow Through Packed Beds," Bioprocess Biosyst. Eng., **16**(6), pp. 355–360.
[32] Fourar, M., and Lenormand, R., 2001, "A New Model for Two-Phase Flows at High Velocities Through Porous Media and Fractures," J. Pet. Sci. Eng., **30**(2), pp. 121–127.
[33] Forchheimer, P., 1901, "Wasserbewegung durch Böden," Z. Ver. Dtsch. Ing., **45**, pp. 1736–1741 and 1781–1788.
[34] Jamialahmadi, M., Müller-Steinhagen, H., and Izadpanah, M. R., 2005, "Pressure Drop, Gas Hold-Up and Heat Transfer During Single and Two-Phase Flow Through Porous Media," Int. J. Heat Fluid Flow, **26**(1), pp. 156–172.
[35] Kozeny-Carman, J., 1927, "Über kapillare Leitung des Wassers im Boden," Ber. Wien. Akd., **136**, pp. 271–306.
[36] Jagadeesh Babu, P. E., Arunagiri, A., and Murugesan, T., 2006, "Pressure Drop and Liquid Holdup in Co-Current Gas-Liquid Downflow of Air-Newtonian Systems Through Packed Beds," J. Chem. Technol. Biotechnol., **81**(1), pp. 70–81.
[37] Venkataratnam, G. S., and Varma, Y. B. G., 1991, "Effective Interfacial Area in Gas-Liquid Cocurrent Downflow Through Packed Beds," Bioprocess Eng., **7**(1), pp. 29–34.
[38] Jagadeesh Babu, P. E., Arunagiri, A., Reghupathic, I., and Murugesan, T., 2007, "Pressure Drop and Liquid Holdup in Co-Current Gas-Liquid Downflow of Air-CMC Solutions Through Packed Beds," Chem. Biochem. Eng. Q., **21**(2), pp. 121–129.
[39] MAPLE™, Release 9, 2003, Waterloo Maple Software, Waterloo, ON.
[40] Lockhart, R. W., and Martinelli, R. C., 1949, "Proposed Correlation of Data for Isothermal Two-Phase, Two-Component Flow in Pipes," Chem. Eng. Prog., **45**(1), pp. 39–48.

The Modeling of Form Drag in a Porous Medium Saturated by a Power-Law Fluid

D. A. Nield
Department of Engineering Science,
University of Auckland,
Private Bag 92019,
Auckland 1142, New Zealand
e-mail: d.nield@auckland.ac.nz

The alternative ways of modeling form drag in a porous medium saturated by a power-law fluid in current usage are discussed. It is argued that the best alternative is to use the same expression as that used in the case of a Newtonian fluid, but with a modified Forchheimer coefficient. [DOI: 10.1115/1.3180809]

Keywords: porous medium, form drag, power-law fluid, Forchheimer coefficient

1 Introduction and Discussion

In the experience of the author as a reviewer, there is currently a considerable amount of uncertainty about how the Forchheimer form drag term should be modeled in the case where a porous medium is saturated by a power-law fluid. Whereas many authors [1–6] used a term in u^2, where u denotes the velocity, some authors [7,8] used a term in u^{2n}, where n is the index that appears in the Darcy drag term as u^n. This note is an attempt to reduce the amount of that uncertainty.

A popular form of the momentum equation, as expressed by Chen and Hadim [9], who cited Shenoy and co-worker [3,4], is

$$\frac{\rho}{\varepsilon}(\mathbf{v}\cdot\nabla)\left(\frac{\mathbf{v}}{\varepsilon}\right) = -\nabla p - \frac{\mu^*}{K^*}|\mathbf{v}|^{n-1}\mathbf{v} - \frac{\rho C_F}{\sqrt{K}}|\mathbf{v}|\mathbf{v} + \frac{\mu^*}{\varepsilon}\nabla\left[\frac{1}{\varepsilon^{n-1}}\left(\frac{\Delta:\Delta}{2}\right)^{(n-1)/2}\Delta\right] \tag{1}$$

where ρ is the fluid density, ε is the porosity, $\mathbf{v}$ is the Darcy velocity, p is the pressure, μ^* is the consistency index, K^* is the modified permeability, K is the permeability, C_F is a Forchheimer drag coefficient, and Δ is the rate of deformation tensor. Here, we are concerned about the third term on the right hand side of Eq. (1). The authors who use such an expression typically then adopt the Ergun formula

$$C_F = \frac{1.75}{\sqrt{150}\varepsilon^{3/2}} \tag{2}$$

This formula was originally derived for a packed bed of spheres. In their numerical simulation, Inoue and Nakayama [6] obtained a similar result but with the coefficient 1.75 replaced with a value of about 0.5. These authors commented that Ergun's functional form should hold, whether or not the fluid is Newtonian. Shenoy [5], who was cited in Ref. [10], made a similar remark. He wrote that the Forchheimer term should be left unchanged because it is independent of the viscosity.

In principle one should be able to decide between the alternatives by performing some averaging over a representative elementary volume, but in practice, there is difficulty. The surface integrals that arise in this procedure need to be found, or estimated somehow, in order to achieve closure. In their investigation, Hayes et al. [11] achieved the closure by assuming that the Forchheimer expression took the same form for a power-law fluid as for a Newtonian fluid. Thus, they did not provide any independent information on which one can decide between alternative formulations.

The argument used by Shenoy and his colleagues is very plausible. If the nonlinear drag is indeed the form drag, as Joseph et al. [12,13] argued, and if the expression for the form drag is indeed independent of the viscosity, then it immediately follows on dimensional grounds that the expression must be quadratic in the velocity. However, the situation is not as clear cut as it seems at first sight.

It was pointed out by Nield [14] that, because the viscosity acts throughout the fluid and not just at the solid boundaries, viscous dissipation is a process that occurs throughout the space occupied by fluid. As a result, the total drag is influenced by what happens throughout the fluid. Although the Forchheimer form drag term does not explicitly involve the viscosity as a factor in the expression, it does arise from the action of the viscosity, mediated by the inertial effects affecting the distribution of pressure that also contributes to the stress at the solid boundaries. On this argument one should thus expect that the non-Newtonian aspects of the fluid (dilatancy or pseudoplasticity) would affect the form drag. The question now becomes: What is the best way of modeling the non-Newtonian effects?

The author suggests that the following stepwise approach is useful. One can retain the form of the expression for the form drag but allow the Forchheimer coefficient C_F to become a function of the power-law index n. A further option is to go another step and suppose that C_F is a weak function of the velocity u. If one takes that option, then a reasonable additional hypothesis is that C_F is of the form

$$C_F = C_{F0}(1 + \delta u^{2(n-1)}) \tag{3}$$

where δ is a constant small in comparison with unity, so that then

$$C_F u^2 = C_{F0}u^2 + \delta C_{F0}u^{2n} \tag{4}$$

Thus the net effect is that the expression for the form drag is now the sum of two terms: the first as used in Refs. [1–6] and the second as used in Refs. [7,8]. The results from Ref. [6] (indicating a reduction in the value of the coefficient in C_F from 1.75 to about 0.5) suggest that the sign of δ will be negative.

It is clear that further progress on this problem is dependent on more experimental work being carried out. Until that is done, the author recommends that the simple quadratic expression for the form drag be used as the default option in theoretical work on convection in porous media, with the understanding that the coefficient is not necessarily given by the Ergun formula.

Nomenclature

C_F = Forchheimer coefficient
K = permeability
K^* = modified permeability
p = pressure
u = magnitude of the Darcy velocity
$\mathbf{v}$ = Darcy velocity

Greek Symbols

Δ = rate of deformation tensor
δ = constant defined in Eq. (3)
ε = porosity
μ = fluid viscosity
μ^* = consistency index
ρ = fluid density

References

[1] Nakayama, A., and Shenoy, A. V., 1992, "A Unified Similarity Transformation for Darcy and Non-Darcy Forced-, Free- and Mixed-Convection Heat Transfer

Manuscript received March 31, 2008; final manuscript received November 18, 2008; published online July 29, 2009. Review conducted by Kambiz Vafai.

in Non-Newtonian Inelastic Fluid-Saturated Porous Media," Chem. Eng. J., **50**, pp. 33–45.
[2] Nakayama, A., and Shenoy, A. V., 1993, "Combined Forced and Free-Convection Heat-Transfer in Power-Law Fluid-Saturated Porous Media," Appl. Sci. Res., **50**, pp. 83–85.
[3] Nakayama, A., and Shenoy, A. V., 1993, "Non-Darcy Forced Convective Heat Transfer in a Channel Embedded in a Non-Newtonian Inelastic Fluid-Saturated Porous Medium," Can. J. Chem. Eng., **71**, pp. 168–173.
[4] Shenoy, A. V., 1993, "Darcy–Forchheimer Natural, Forced and Mixed Convection Heat Transfer in Non-Newtonian Power-Law Fluid-Saturated Porous Media," Transp. Porous Media, **11**, pp. 219–241.
[5] Shenoy, A. V., 1994, "Non-Newtonian Fluid Heat Transfer in Porous Media," Adv. Heat Transfer, **24**, pp. 101–190.
[6] Inoue, M., and Nakayama, A., 1998, "Numerical Modeling of Non-Newtonian Fluid Flow in a Porous Medium Using a Three-Dimensional Periodic Array," ASME J. Fluids Eng., **120**, pp. 131–135.
[7] Kumari, M., and Jayanthi, S., 2004, "Non-Darcy Non-Newtonian Free Convection Flow Over a Horizontal Cylinder in a Saturated Porous Medium," Int. Commun. Heat Mass Transfer, **31**, pp. 1219–1226.
[8] Kumari, M., and Nath, G., 2004, "Non-Darcy Mixed Convection in Power-Law Fluids Along a Non-Isothermal Horizontal Surface in a Porous Medium," Int. J. Eng. Sci., **42**, pp. 353–369.
[9] Chen, G., and Hadim, H. A., 1998, "Numerical Study of Non-Darcy Forced Convection in a Packed Bed Saturated With a Power-Law Fluid," J. Porous Media, **1**, pp. 147–157.
[10] Nield, D. A., and Bejan, A., 2006, *Convection in Porous Media*, 3rd ed., Springer, New York.
[11] Hayes, R. E., Afacan, A., Boulanger, B., and Shenoy, A. V., 1996, "Modelling the Flow of Power Law Fluids in a Packed Bed Using a Volume-Averaged Equation of Motion," Transp. Porous Media, **23**, pp. 175–196.
[12] Joseph, D. D., Nield, D. A., and Papanicolaou, G., 1982, "Nonlinear Equation Governing Flow in a Saturated Porous Medium," Water Resour. Res., **18**, pp. 1049–1052.
[13] Joseph, D., Nield, D., and Papanicolaou, G., 1982, "Correction to ′Nonlinear Equation Governing Flow in a Saturated Porous Medium' by Joseph et al.," Water Resour. Res., **19**, p. 591.
[14] Nield, D. A., 2000, "Resolution of a Paradox Involving Viscous Dissipation and Nonlinear Drag in a Porous Medium," Transp. Porous Media, **41**, pp. 349–357.